AIR FLOW OVER BARCHAN DUNES:

MEASUREMENTS ~~Sand dune dynamics~~:

field ~~experimentation~~, mathematical modelling and wind tunnel testing

A thesis submitted for the degree of Doctor of Philosophy

in

The University of London

by

Giles F.S. Wiggs

August 1992

ABSTRACT

There are few empirical measurements of velocity, shear velocity, sand transport, morphological change on the windward slopes of dunes. This thesis compares field measurements on a barchan dune in Oman with calculations using a mathematical model (FLOWSTAR) and measurements in a wind tunnel.

All three techniques demonstrate similar patterns of velocity, confirming the acceleration of flow up the windward slope, deceleration between the crest and brink and significant flow deceleration upwind of and at the toe of the dune. The FLOWSTAR model is unable accurately to predict airflow at the brink and its predictions near the surface are highly susceptible to small-scale terrain irregularities. The measurements of shear velocity in the field and those predicted by the FLOWSTAR model reflect observations of previous studies including the widely reported upwind reduction in shear velocity. Such a reduction in shear velocity upwind of the dune should result in a reduction in sand transport and sand deposition. This is not observed in the field.

Wind tunnel modelling using a near-surface pulse-wire probe suggests that the field and FLOWSTAR methods of shear velocity derivation are inadequate. The wind tunnel results exhibit no reduction in shear velocity upwind of or at the toe of the dune. This maintenance of upwind shear stress may be caused by concave (unstable) streamline curvature, which is not taken into account by the field and FLOWSTAR techniques. From this hypothesis, a new model of dune dynamics is developed relying on the establishment of an equilibrium between windward slope morphology, streamline curvature and streamwise acceleration.

With grateful thanks to my parents

TABLE OF CONTENTS

ACKNOWLEDGEMENTS

This research was funded by a Natural Environment Research Council (U.K.) Research Studentship held at the Department of Geography, University College London.

Permission to work in Oman was granted by the Diwan of Royal Court Affairs and field equipment was loaned by Petroleum Development Oman. I thank George Gamlen and Samir Hanna at Sultan Qaboos University for providing invaluable help and I am greatly indebted to Mark Ashby, Adrian Chappell, Richard Ledger, Neil Scoble and Mark Hedley for their unstinting field assistance and companionship.

The FLOWSTAR model was generously provided by Cambridge Environmental Research Consultants Ltd. and valuable help was given by Julian Hunt and Wensong Weng.

The wind tunnel was provided by the Department of Mechanical Engineering at the University of Surrey and I thank Khalfan, Frank McCluskey, Stan Bennett and the technical staff for their helpful advice and labour. I particularly appreciate the patient support of Ian Castro.

During all stages of my work kind support was given by many staff members at University College London but I particularly appreciate the technical know-how of Don Monteith and Jim Chambers.

Finally, I am deeply grateful for the continued advice and guidance of my supervisors, Andrew Warren and Ian Livingstone and I would like to thank my fellow postgraduates in the Geography Department for their support and friendship.

GLOSSARY

α	turbulent intensity (u'/u).
α	angle of repose of sand (38°).
D	standard particle diameter (0.25 mm).
d	particle diameter (mm).
d	zero-plane displacement.
δs	fractional speed-up ratio / velocity perturbation.
δs_{max}	maximum fractional speed-up ratio.
$\delta h/\delta t$	rate-of-change of height.
$\delta\theta/\delta x$	horizontal rate-of-change of slope angle.
$\Delta s/\delta x$	horizontal rate-of-change of fractional speed-up ratio.
$\Delta u_*/\delta x$	horizontal rate-of-change of surface shear velocity perturbation (cross-wire probe derived).
$\Delta u_{*_1}/\delta x$	horizontal rate-of-change of surface shear velocity perturbation (pulse-wire probe derived).
g	gravitational acceleration (9.81 ms^{-2}).
γ	bulk density of sand (2.65).
H	dune height.
h	local height.
κ	von Karman's constant (0.4).
k	surface roughness without saltation.
K	surface roughness element height (wind tunnel).
L	hill (dune) half-length.
L	cup-anemometer distance constant (m).
l	inner-layer depth (after Jackson & Hunt, 1975).
l_1	inner-layer depth (after Jensen *et al.*, 1984).
l_s	inner-surface-layer depth.
ϕ	streamline angle from horizontal (°).

q	sand transport rate on a flat surface ($gm^{-1}s^{-1}$).
q_s	sand transport rate on a sloping surface ($gm^{-1}s^{-1}$).
RI	Richardson number.
ρ	fluid density (air = 0.00122 gcm^{-3}).
θ	local slope angle (°).
θ	air temperature (°K).
T_0	surface reference temperature (°K).
τ	surface shear stress.
Ur	mean reference velocity (ms^{-1}).
u	mean wind velocity [horizontal downwind component] (ms^{-1}).
v	mean wind velocity [horizontal span-wise component] (ms^{-1}).
w	mean wind velocity [vertical component] (ms^{-1}).
u'	local fluctuating component of wind velocity (ms^{-1}).
u_*	shear velocity (ms^{-1}).
-uwb	shear stress (b denotes bar or mean value).
usb	horizontal component of Reynold's stress (s denotes square, b denotes bar or mean value).
wsb	vertical component of Reynold's stress (s denotes square, b denotes bar or mean value).
u_t	threshold velocity for grain entrainment (ms^{-1}).
u_{*_t}	threshold shear velocity for grain entrainment (ms^{-1}).
ν	kinematic viscosity (0.015).
z	height.
z_0	aerodynamic roughness with saltation.

LIST OF FIGURES

LIST OF TABLES

LIST OF EQUATIONS

CHAPTER 1 INTRODUCTION

Bagnold's pioneering work "The Physics of Blown Sand and Desert Dunes" stimulated an enormous interest in the dynamic interaction between wind and sand and the physical processes behind dune formation and maintenance. Although empirically based, many of Bagnold's hypotheses were highly speculative. Research has proceeded at a variety of scales ranging from the large atmospheric scale (on entire sand seas) (Allen, 1968; Hanna, 1969; Wilson, 1972, 1973), to small-scale studies of grain entrainment and motion (Zingg, 1953; Chepil, 1959; White, 1979; Hardisty & Whitehouse, 1988; Anderson *et al.*, 1991). The two approaches have seldom connected, but in the last decade, a small number of workers have demonstrated the value of careful monitoring of dune movement and windflow at the scale of the individual dune (Knott, 1979; Tsoar, 1978, 1983; Livingstone, 1985, 1986; Warren & Kay, 1986, 1987; Mulligan, 1988). This thesis is concerned with this intermediate scale of study.

By studying dune dynamics at this scale one can examine the effect of the intrusion of a dune into the atmospheric boundary layer. Dunes should alter the airflow in such a way so as to maintain and regulate their form through a feedback mechanism, eventually resulting in an equilibrium form for a given wind regime. The feedback mechanism (termed 'wind-dune-coupling' by Knott (1979)) has been the focus of attention for several investigators (Tsoar, 1978, 1983; Howard *et al.*, 1977), although there is still much debate as to the character of the flow field surrounding dunes (Lancaster, 1985, 1987; Watson, 1987).

Concurrent with the work of geomorphologists, there has been parallel research by engineers, physicists and mathematicians concerned with the character of turbulent wind flow over low hills. This research has included the mathematical deduction and empirical testing (principally in wind tunnels) of formulae relating to the apparent acceleration of wind and convergence of streamlines toward the crests of low hills. The most celebrated of these formulae is that of Jackson & Hunt (1975) which calculates the fractional speed-up ratio (flow acceleration) from easily available aerodynamic and morphological information. Such derived formulae have since been developed and incorporated into numerical models concerned with the prediction of dune movement (Howard *et al.*, 1977; Walmsley & Howard, 1985; Wippermann & Gross, 1986). However, the appraisal of such models has proven difficult because of the lack of empirical data. Only Livingstone (1985) has been able to show their direct applicability to measurements of flow over dunes in the Namib desert. The rate of advance of the power of computer predictions has surpassed the empirical database required to test them (Castro, 1984).

Investigations and discussions by geomorphologists concerning the acceleration of wind over the crests of dunes has proven useful. Both Lancaster (1985) and Tsoar (1985) have made use of the meteorologists' models. Tsoar (1985) noted that the amplification factor (flow acceleration) on the windward slopes of dunes was accelerated at a progressive rate toward the crest where it reached a maximum, reducing in value toward the lee. He stated that flow acceleration determined the rate of sand loss and this determined the rate of advance of the dune. There is, however, little evidence of this effect which assumes a direct relationship between wind velocity and change in dune form. Such assumptions have been criticised by Watson (1987) who contended that it would be more useful to relate the actual sand flow at a point to the *shear stress* at that point.

Some studies have demonstrated that as wind approaches a dune its velocity is reduced at the toe and just upwind, before increasing up the windward slope (Howard *et al.*, 1977; Tsoar, 1985). Such circumstances would tend to promote deposition of sand upwind of the toe as the sand transporting capacity of the wind was reduced. This would be reflected in upwind dune advance, a situation not observed in the field. This is a further argument for obtaining assessments of shear stress rather than wind velocity, for such assessments may better describe the morphological dynamics of dunes than wind velocity measurements alone.

The major research deficiencies were highlighted by Watson (1987) and Lancaster (1987). Watson pointed out that;

> *"The relationship between changes in shear stress and the amplification of wind velocity up the windward face of a dune must be established in order to ascertain how flow patterns influence rates of erosion and deposition. Since variations in shear stress are related to variations in flow velocity and pressure gradient, future work should attempt to elucidate the interaction of these parameters."*

Lancaster (1987) supported Watson in this respect and claimed that the;

> *"..major research need in aeolian bedform research is the measurement of patterns of erosion and deposition and surface shear stress on dunes of all types."*

Both authors comment on the need for more reliable empirical data in order to model the form-flow interactions and development of equilibrium morphology.

Such an attempt was made by Mulligan (1988). He investigated the way in which acceleration of flow over a dune altered the turbulence structure near the surface. He found that velocity profiles on slopes where the acceleration of wind was significant were not log-linear. This was

an important finding because it cast doubt on the accepted assumption of log-linear velocity profiles in calculations of shear stress. Indeed, an appropriate question is; "How can shear stress be determined on the windward slope of a sand dune ?"

In the light of these discussions and uncertainties, this thesis has three principal aims:

1. To collect reliable empirical data concerning the nature and structure of airflow over a sand dune in relation to its morphological characteristics. This particularly concerns the determination of the shear stress distribution across the windward slope.

along

2. To compare measurements and predictions acquired from three techniques of study; field work, mathematical modelling and wind tunnel modelling.

3. To use the collected data and technique comparisons to elucidate questions regarding the nature of dune dynamics and methods of research.

This thesis is limited to the study of a single barchan dune located in eastern Oman. A transverse dune-type was chosen for investigation for two reasons:

1. Barchan dunes represent the simplest dune-type for they are a response to a uni-directional wind regime.

2. They exhibit a common form towards which other types of dune approach in periods of wind directional constancy.

The thesis is divided into two parts. Part One consists of three chapters which describe the methods and results for each of the three techniques. Chapter 2 details the field work component; Chapter 3, the mathematical modelling and Chapter 4, the wind tunnel modelling. Each of these chapters incorporates a separate technique-specific review of the literature, and an account of the methods employed and results gained.

Part Two of the thesis is concerned with a comparison between the techniques and the significance of the results to dune dynamics and development. Chapter 5 compares the wind velocity and shear stress evaluations acquired from each of the techniques and Chapter 6 describes the methods of calculation of shear stress in the field and compares these assessments to those gained from the wind tunnel and mathematical model. The shear stress calculations are

used in Chapter 7 to determine the distribution of sand transport rates and, hence, the amount of erosion and deposition predicted by each of the techniques. The latter half of Chapter 7 contrasts the predicted rates of dune surface change with those measured in the field and from these discussions a new model of dune dynamics is developed which is founded on a balance between the stresses imposed by the processes of streamwise flow acceleration and streamline curvature.

The conclusions, presented in Chapter 8, summarise the degree to which the aims of the thesis were satisfied and describe potential strategies for future research.

CHAPTER 2 FIELD TECHNIQUES

2.1 Introduction

Three types of data are required for a study of the dynamics of sand dunes. These are:

1. Vertical and horizontal wind velocity profiles from which the areal distribution and direction of shear stress can be calculated.

2. Bulk sand transport (rates and direction)

3. Pattern of relative erosion and deposition on the dune's surface.

Dune dynamics research has endeavoured to link these three components in an attempt to understand the feedback mechanisms which relate them.

The volume and accuracy of empirical data of this type are, however, severely lacking. Many of the widely quoted dune studies were undertaken with a remarkably small collection of equipment (one or two anemometers), rarely achieving accurate instrumentation of the complex flow patterns around a dune form (Rasmussen *et al.*, 1985). Tsoar (1985) used just one "wind recorder" measuring one hour averages of wind speed and direction at a height of 11 m, although he had used more in an earlier investigation (Tsoar, 1978). Knott (1979) used five anemometers at one metre height and Howard *et al.* (1977) measured wind velocity at only 13 points in their similar study. None of these studies yielded sufficient data realistically to model wind flow patterns over dunes. They could only be used to support the results of wind tunnel studies. However, if sand transport and erosion and deposition are also to be evaluated, then reliance cannot be made on wind tunnels alone. Due to the problems of scaling and practicality a wind tunnel study of saltation over a model dune has never been achieved.

It is therefore necessary to measure wind speed and sand transport distributions simultaneously in the field. It is only relatively recently, as the complex nature of the physics of airflow over dunes has become clearer, that the limitations of simplistic field methods have been understood. The need for more detailed studies is now clear and maintained in the literature (Lancaster, 1985; Watson, 1987). Livingstone (1988, 1990) recognised that;

> *"..dune morphology cannot be viewed simplistically as a response to regional wind patterns".*

The complexities inherent in studies involving the measurement of wind and saltation over a three-dimensional body have emerged from research in two allied disciplines. One is the small scale investigation of the processes of saltation and its relationship to shear stress. This has highlighted the limitations of many of Bagnold's assumptions (Rasmussen *et al.*, 1985; Anderson & Hallett, 1986; Willetts & Rice, 1986a, 1986b; Sarre, 1987; Anderson & Haff, 1988; McEwan & Willetts, 1991; Butterfield, 1991). The other area is the examination and modelling of boundary layer flow and turbulent structures over low hills (Jackson & Hunt, 1975; Jackson, 1977; Mason & Sykes, 1979; Bradley, 1980; Walmsley *et al.*, 1982; Taylor *et al.*, 1987) [see Chapters 3 and 4]. This work has demonstrated the speed-up and non-logarithmic nature of velocity profiles over hills and defined such important structures as the inner-layer, which is that depth of flow above the dune's surface where changes in shear stress have a significant effect on the surface (see Chapter 2.2).

Using the ideas and conclusions from these investigations, much more valuable research is now being conducted in sand dune dynamics, particularly in relation to the relative speed-up of flow at the crest. Examples are the velocity profiles over a transverse dune carried out by Mulligan (1988); the relationship between dune form and amplification factor on a linear dune by Livingstone (1986, 1988); the studies in the Namib on linear and star dunes by Lancaster (1985, 1988, 1989a, 1989b); the studies by Hesp (1988) and Hesp *et al.* (1989) on coastal foredune development and the investigation of a reversing transverse dune in South Africa by Burkinshaw & Rust (1992, in press). Even so, many of these studies have avoided the complications of measuring sand transport and ignored the inner-layer by placing anemometers at a standard one metre height. Furthermore, many followed the arguments of Bagnold and believed that sand transport and shear stress could be calculated from single velocity measurements, ignoring the non-logarithmic nature of the airflow (see Chapter 2.4).

There is still a need for a detailed field investigation to link the three components of velocity distribution, sand transport, and surface change. The aim of the field experiments described here was to measure horizontal and vertical velocity profiles (from which shear velocity could be calculated) on a barchan dune and to link the results with the distribution of sand transport. The shear velocity (u_*), calculated form the wind velocity profiles, is related to the surface shear stress (τ) by:

$$u_*^2 = \tau/\nu$$

where:

ν = kinematic viscosity

An understanding of the relationship between the pattern and profile of the wind (including shear stress) and the distribution of erosion and deposition is then accomplished by measuring the change in dune form simultaneously. This Chapter describes the techniques used, and presents field data which will be compared to those of the mathematical modelling and wind tunnel modelling in Chapters 5 and 6.

2.2 Site Description and Requirements

The Area

Field experiments were carried out on a barchan dune in the eastern part of the Sultanate of Oman during July and August of 1989 and 1990, although only data collected in the latter period are presented here. The study area Figure 2.1) is dominated in the summer months (April-October) by the south-westerly monsoon or Kharif (Warren, 1988a; 1988b). The coastal plain, running north-east toward Ras-al-Hadd, has a discontinuous cover of dunes with a small sand supply. The low supply of sand is caused by a combination of a narrow continental shelf (reducing sediment input to the beach), an absence of aeolianite, and high wind turbulence (Warren, 1988a; 1988b). Coupled with the strong, uni-directional nature of the Kharif winds, such an environment is ideal for the growth of barchan dunes (Wasson & Hyde, 1983).

Requirements

In choosing the study dune several criteria were implemented. The dune had to be active (*i.e.* eroding and moving) and free from vegetation. Furthermore, it needed to be free from disturbance by people and animals and have an unobstructed upwind environment. In addition, the size of the dune was important as it is this which primarily governs the depth of the inner-layer (l) as defined by Jackson & Hunt (1975):

$$\frac{l}{L}\ln\left(\frac{l}{z_0}\right)=2\kappa^2 \qquad (2.1)$$

where:

l = inner-layer depth
L = characteristic length scale.
z_0= aerodynamic roughness
κ = von Karman's constant (0.4)

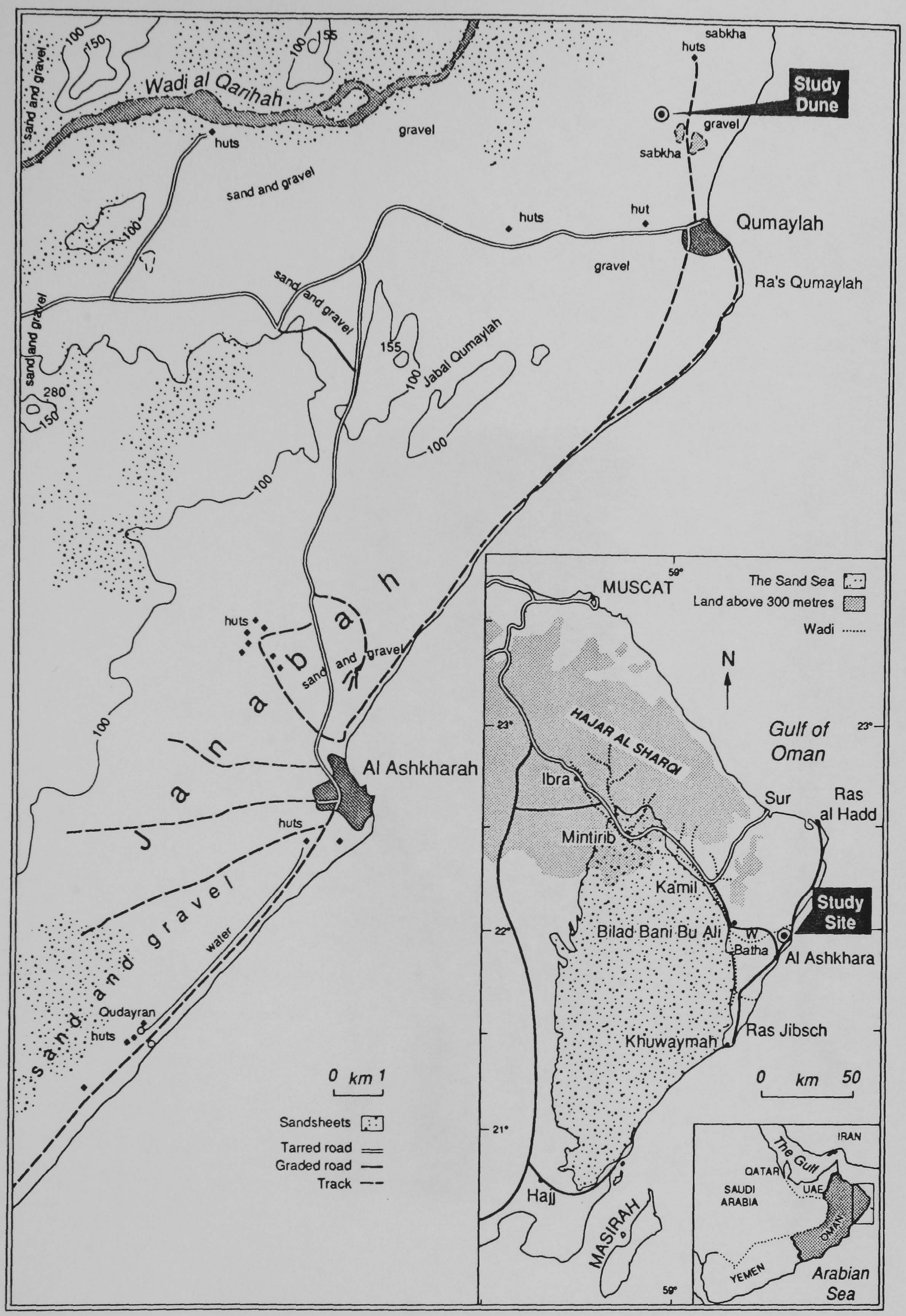

Figure 2.1 Map of Oman showing study site.

Figure 2.2 The study dune viewed from the north. Wind direction is from the right.

In this case, L is taken as "the distance from the hilltop to the upstream point where the elevation is half its maximum" (Jackson & Hunt, 1975) (Figure 2.3). It is within the inner-layer that the turbulent transfer processes are dynamically significant. In other words, it is within this depth that the changes in shear stress and turbulent structure caused by the intrusion of the dune into the airflow are greatest, and where feedback mechanisms between the airflow and the dune surface can be assumed to be important (Taylor *et al.*, 1987). In order to measure wind velocity characteristics that are important to the morphology of the dune, it is therefore necessary to measure velocity profiles within the inner-layer. The operation of Equation 2.1 has been examined by Rasmussen *et al.* (1985). They noted that the equation overestimated the value of l by about one third. They preferred the alternative relationship presented by Jensen *et al.* (1984):

$$l = 0.3 \left(\frac{L}{z_0}\right)^{2/3} z_0 \qquad (2.2)$$

where:

l_1 = inner-layer depth
L = characteristic half-length
z_0 = aerodynamic roughness

However, the definition of the inner-layer given by Rasmussen *et al.* (1985) is the height from the surface to the level of maximum flow speed-up. This is not the same as the definition provided by Jackson & Hunt (1975), although a re-analysis of the Jackson & Hunt solution by Hunt *et al.* (1988a) produced similar results to the Jensen *et al.* expression. The validity of all the expressions for the depth of the inner-layer on sand dunes is uncertain as none have been empirically tested. Nevertheless, a calculated inner-layer depth of at least one metre is desirable where cup anemometers are to be used. Hence, a large dune is favoured for these types of measurement, regardless of the equation applied.

Conversely, a large dune is unlikely to be in equilibrium with its environment because it reacts slowly to contemporary conditions. This concept has been labelled as a dune's "memory" by Warren & Kay (1987). All dunes lie between the qualitative extremes of high and low memory (Livingstone, 1987), with small dunes re-orientating themselves to new winds more quickly than large dunes. If a study is to be based on a dune which is in equilibrium with its prevailing wind, then a small dune should be selected which has little inertia or reaction time (Allen, 1974). This is particularly important on the coastal plains of eastern Oman because the winter monsoon (January-March) is north-easterly and reverses the dunes' movement. The large dunes in this area are therefore in a constant flux, seldom in a permanently stable state. This study is concerned

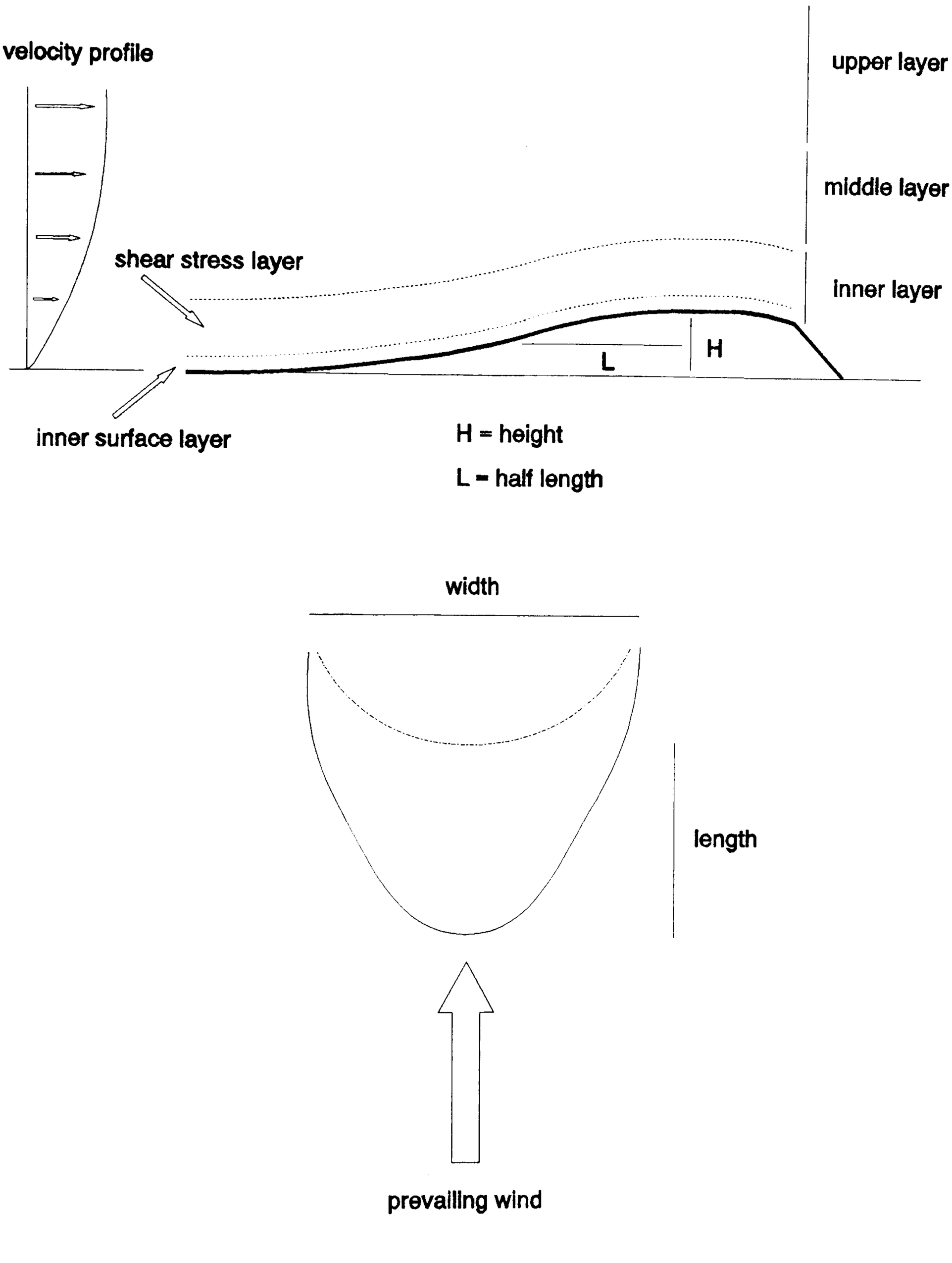

Figure 2.3 General length scales and measuring conventions.

with identifying the mutual associations between airflow and dune morphology. The investigation of a dune in at least a near-equilibrium state is therefore desirable for three reasons:

1. Measurements can be taken of the 'end-state' toward which dunes develop. Knowledge of the dynamics generated at the time of equilibrium make conjectures concerning the dynamics of dunes not in equilibrium more simple.

2. Knowledge of antecedent conditions is unnecessary.

3. The study is applicable generally to dune dynamics and is not restricted to a single dune.

Hence, when the size of the study dune was chosen, a trade-off was necessary between the size of the inner-layer and the relative equilibrium of the dune.

Relevant to this discussion are the problems involved in the practical recognition of a dune in equilibrium, for no criteria have yet been devised for their definition. For the purposes of choosing a study dune it was decided that equilibrium could be recognised by the following criteria; the crest and brink are not separated along the centre-line; there is continuous sand movement up the windward slope (Tsoar, 1985); and typical windward slope surface angles are 12°-13° at maximum (Watson, 1987). For added assurance of dune equilibrium its size was kept to the minimum necessary for an inner-layer depth sufficient to insert an array of four anemometers.

Dune Description and Local Conditions

The dune chosen for study was an asymmetrical barchan north-east of the town of Ashkhara and near Qumailah (see Figure 2.1). According to the classification of McKee (1979) it was a simple barchan, with no superimposed forms (Figure 2.2). The shape of the dune was open and short with a distance from crest to toe of 86 m and a height of 9.6 m, resulting in an inner-layer depth (l) of 1.90 m as calculated by Equation 2.1 and 0.55 m as calculated by Equation 2.2. The distance between the outside edges of the horns was 130 m (defined as width in Figure 2.3). The centre-line was not crest-brink separated (*i.e.* the highest point of the dune was also at the slip-face), although both flanks were. The trend of movement was on a magnetic bearing of 11°.

what are these

The dune was positioned in a field of discontinuous barchan dunes, to the east of a network of barchanoid ridges and to the west of a flat coastal plain. Approximately 100 m upwind of the

dune was a second smaller barchan (about 1-2 m in height) which was severely crest-brink separated. The sand being blown from the horns of this upwind dune created some differential sand supply onto the study dune. With more sand coming from the southern horn of the upwind dune, via a flat playa, the centre-line of the study dune was shifted slightly to the south, although it was the northern horn of the study dune which was elongated. Both horns of the study dune trailed downwind into vegetated mounds of sand (nebkha) and had no clearly defined endpoint.

The surface grain size of the dune at the crest, as calculated by optical laser techniques (Chappell, 1991), was normally distributed with grain parameters as shown below:

Average grain size	- 0.24 mm
Standard deviation	- 0.61 mm
Skewness	- 1.00 mm
Kurtosis	- 0.51 mm

The dune was positioned on a flat gravel surface, consisting of coarse (2-3 mm) platy fragments. The loose infill matrix was of sand sized particles (Figure 2.4).

The local meteorological conditions were investigated with a meteorological station consisting of a cup-anemometer and wind direction vane at a height of 1.5 m positioned 50 m upwind of the dune centre-line. Figure 2.5 shows typical five-minute average wind speed and direction measurements for a 20 hour period on July 10th/11th, 1990. Figures 2.5a+b indicate that the dominant wind direction was from the south-west between 190° and 225°, with the highest wind speeds occurring when the wind blew from between 205° and 215°. The time of maximum wind speed is between 10.00 and 16.00 hrs with little sand movement outside of these times. It was within this period that most of the velocity measurements over the dune were made. The wind direction variation during this interval was only about 15°, becoming more southerly as the day progressed. This small variation in wind direction did not alter the depth of the inner-layer or the amount of velocity acceleration at the crest because the effective half-length of the dune (L) did not change.

The predictable nature of the diurnal wind regime (shown in Figure 2.5) made the planning of field work much simpler than would otherwise have been the case. The anemometer arrays were set-up in the morning along the required profile line, but only started recording when the wind had veered around to a bearing parallel to the anemometer arrays.

Figure 2.4 The upwind inter-dune surface matrix. Tape measure for scale.

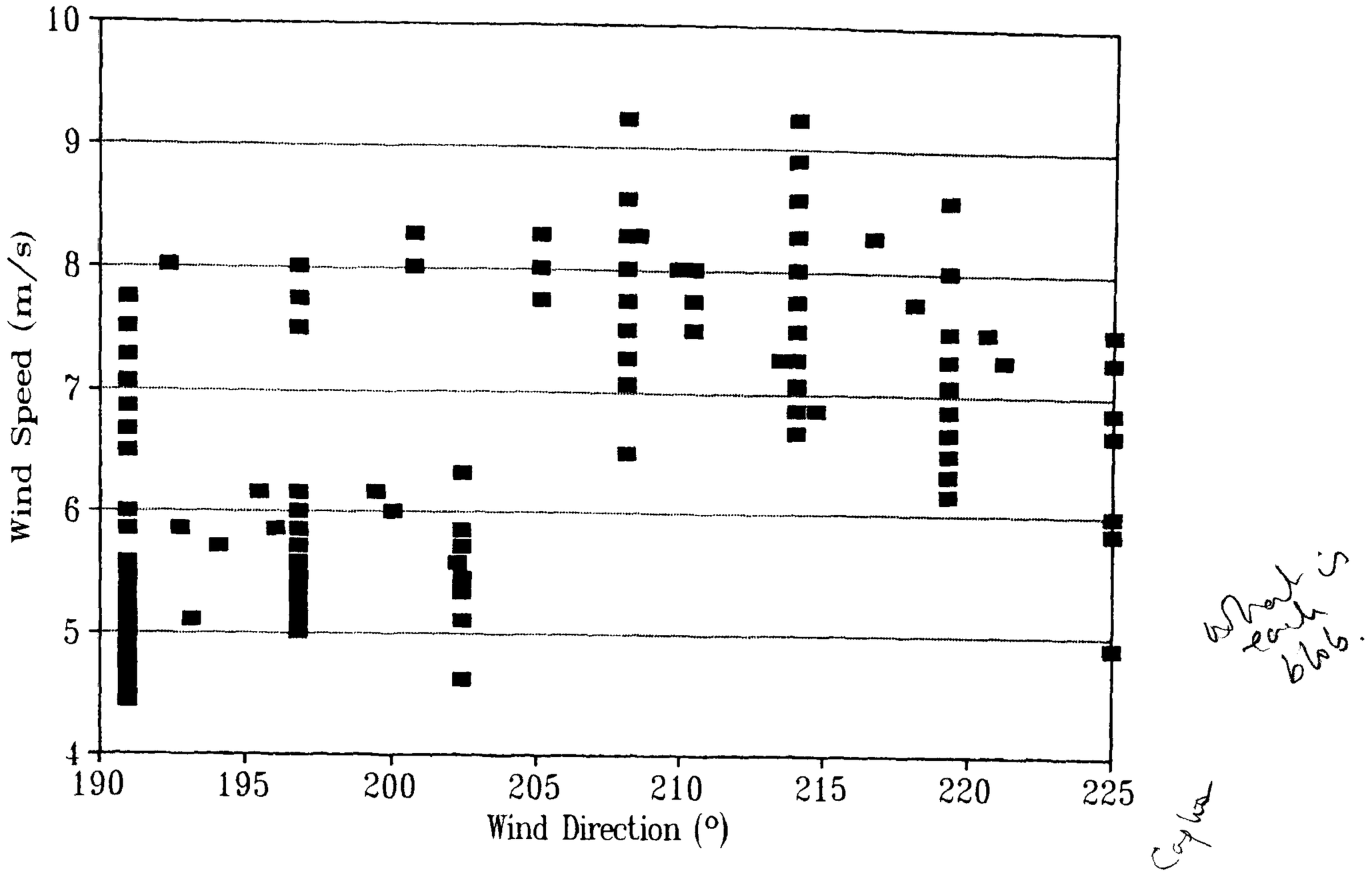

Figure 2.5a Wind speed and direction as measured at the reference site on 10.7.90 -11.7.90.

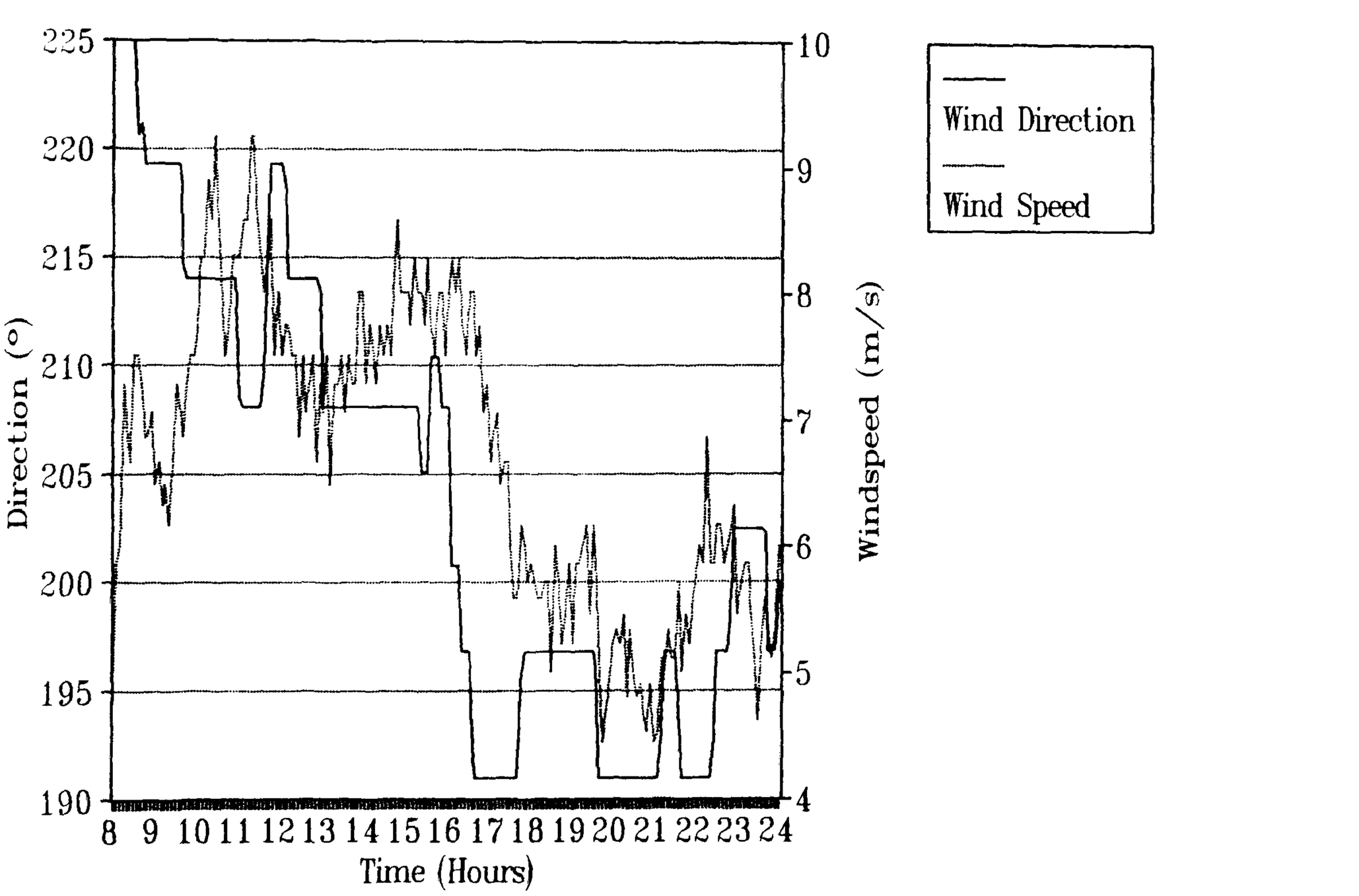

Figure 2.5b The daily pattern of wind direction at the reference site..

2.3 Methods

2.3.1 Anemometry

Type, Design and Calibration

Previous studies (*e.g.* Bagnold, 1941; Tsoar, 1983, 1985; Lancaster, 1985; Livingstone, 1985, 1986, 1989; Warren & Kay, 1987; Mulligan, 1988) have all utilised the cup-anemometer as a method of determining mean wind speed in the field. However, close to the surface, such anemometers become unreliable because of increased turbulence around the body of the instrument and the effect of saltation impact on the cups. Where measurements close to the surface with short-term fluctuations have to be made, use has been made of hot-wire probes and films (Rasmussen *et al.*, 1985; Butterfield, 1991). However, these probes are expensive, fragile and are particularly prone to breakage within the saltation layer. For the investigation presented here, 26 rotating cup-anemometers were employed with the added design feature of small (diameter ~2 cm) cups and thin bodies. This design reduces turbulence around the instrument and allows more accurate velocity measurements close to the surface, but outside the intense saltation layer (Rasmussen *et al.*, 1985).

The design of the anemometers is shown in Figure 2.6. A reed switch closes an electrical circuit with every complete rotation of the cups. The number of contact closures in a specified time interval is a measurement of the wind speed. Grant 1600 Series data loggers were used to record the number of contact closures in any time interval, and this data was downloaded onto a Toshiba 1200 portable computer for analysis.

Calibration of the anemometers was undertaken in a wind tunnel at the Department of Mechanical Engineering, University of Surrey. The anemometers were placed in the centre of the wind tunnel and subjected to free stream velocities (as measured by an upwind pitot-tube) of between 0.1 ms^{-1} and 15 ms^{-1}. The number of contact closures per minute was logged and regression analysis used to predict the windspeed from the number of rotations. A typical graph of the calibration, showing the linear response of the number of contact closures to increasing wind speed is shown in Figure 2.7.

Re-calibration of the anemometers was performed at the end of the field season to discover how much the calibration had changed. Typical results are shown in Table 2.1, which demonstrates that the maximum deviation in calibration was only ±6%. The change in calibration is also shown to be systematic, with no variation in error with windspeed.

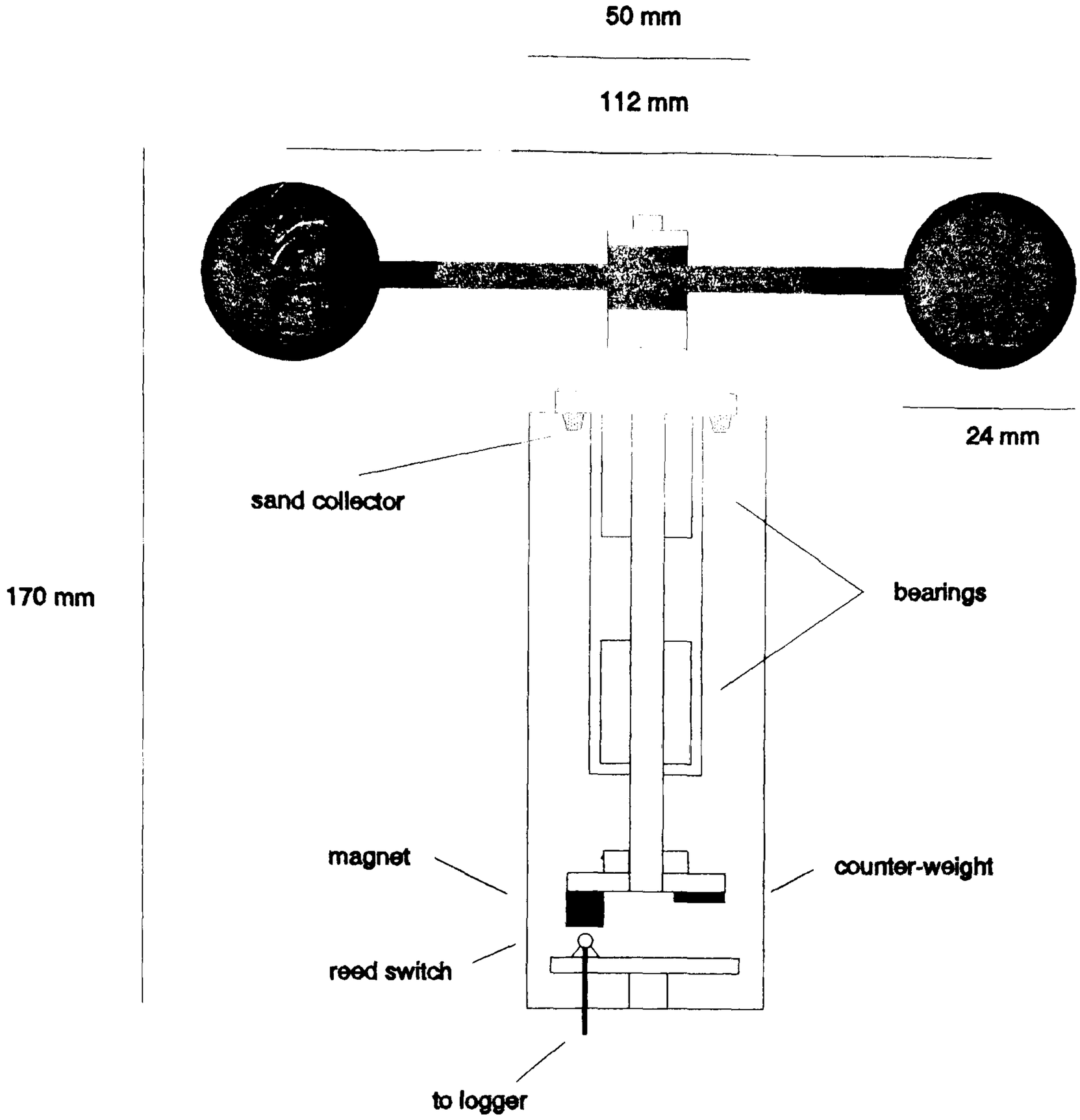

Figure 2.6 Design of the rotating cup-anemometer.

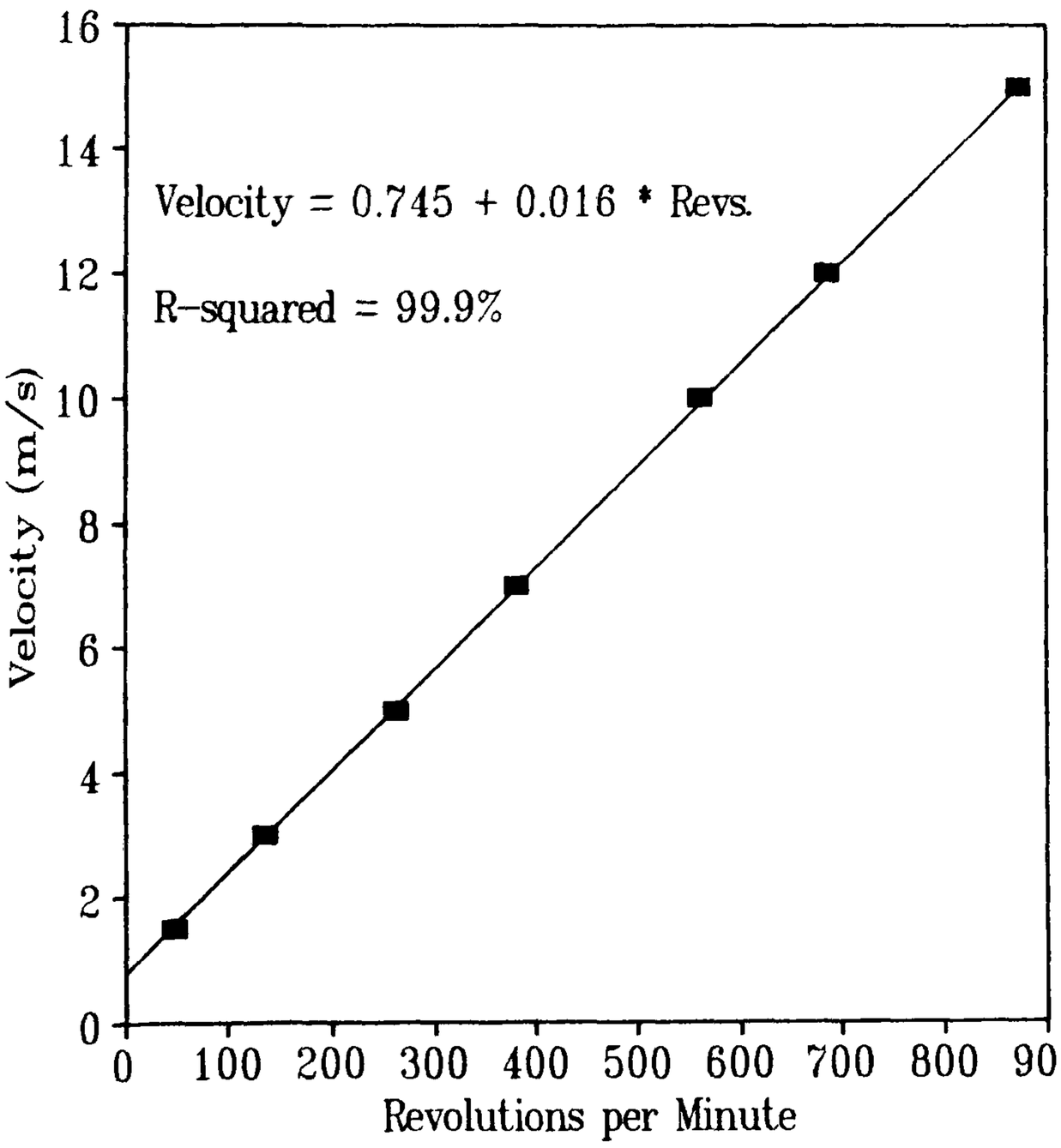

Data Table	
Velocity	Revs.
1.5	48
3	135
5	263
7	381
10	561
12	685
15	873

Figure 2.7 Cup-anemometer calibration curve.

Such calibration changes are typical over this period of time with use in desert conditions (Knott, 1979), but they reduce the accuracy of all the velocity measurements to a best estimate of ±6%. This degree of accuracy is common with cup anemometers (Knott & Warren, 1981).

Calibration checks on the anemometers were also attempted in the field. Every five days the anemometers were aligned at equal heights above the surface and their output checked against an anemometer which had not been exposed to the desert conditions. Similar cross-calibrations in field conditions have been used by Lancaster (1985), Mulligan (1988) and Burkinshaw & Rust (1992). Owing to the spatial fluctuations in wind velocity and turbulence in the field, this process could only be used to determine severe bias. Where necessary, maintenance of the apparatus was undertaken.

All cup-anemometers display a delayed response in changes to windspeed due to inertia. As recognised by Kaganov & Yaglom (1976), a hysteresis effect exists, with the response of the anemometers to an increase in windspeed being faster than that to a decrease. Knott & Warren (1981) noted that instruments with a high inertia might overestimate windspeed by up to 15%. The dynamic response characteristics of the anemometers (*i.e.* the length of time for the instrument to respond to step changes in free stream velocity) were determined experimentally in the wind tunnel using the methods described by MacCready & Jex (1964) and MacCready (1965) and followed by Knott (1979). Some typical dynamic response characteristics are given in Table 2.2 below.

The distance constant (L) was calculated in a steady airstream by stopping the rotation of the anemometer and noting the time for it to reach 50% of the free-stream value after release. Knowing the wind velocity and response time allows calculation of the response distance (1 second at 1 ms^{-1} gives an L of 1 m). The advantage of the response distance over the response time is that it is constant at all windspeeds (MacCready, 1965). The measurements of L shown in Table 2.2 are only approximate as logging intervals of less than one second could not be achieved with the data logger. However, there is no doubt that the values were small (probably < 1 m), indicative of a fast response (MacCready, 1965). The hysteresis effect was not measured in this experiment because of the difficulties involved in quickly stopping the airflow through the tunnel. However, with the values of L being so small, and the lightweight construction of the anemometers, it was felt that the effect of inertia on measurements of mean windspeed would be fairly small.

Table 2.1 Pre- and post-season anemometer calibrations (A-E are selected anemometers)

	Calibration Speed (ms^{-1})	Pre-season Calibration	Post-season Calibration	Change (%)
A	5	5	4.7	6
	10	10	9.35	6.5
	15	15	14.15	5.5
B	5	5	5.3	6
	10	10	10.4	4
	15	15	15.8	5.5
C	5	5	5	0
	10	10	10.1	1
	15	15	15.15	1
D	5	5	4.75	5
	10	10	9.55	5
	15	15	14.2	5.5
E	5	5	5.15	3
	10	10	10.2	2
	15	15	15.3	2

Table 2.2 Dynamic response characteristics of selected anemometers (A-E)

Anemometer	Starting Speed (ms^{-1})	Distance Constant (L) (m)
A	0.6	1
B	0.2	1
C	0.5	1
D	1.0	1
E	0.7	1

The angular response of the anemometers was tested in the wind tunnel for two reasons. First, to discover whether the anemometers were preferentially susceptible to wind gusts from a particular vertical angle (considering the existence of the body of the anemometer below the cups), and secondly, to find whether positioning the anemometer at an angle to the horizontal affected the calibration. Figure 2.8 indicates that even at an angle of ±40° the anemometer still records 90-95% of the free stream velocity, within the accuracy of the calibration. Hence, it can be concluded that the anemometers do not have a significant differential angular response. In practical terms, this means that the anemometers did not have to be positioned parallel to the oncoming streamline angle (which changes along the windward slope of a dune) in order accurately to measure mean velocity.

Field Procedures

STUDY PROFILES

Most studies of dune dynamics have focused on a single section line across the dune in the case of linear dunes (*e.g.* Livingstone, 1986), or along the centre-line of transverse dunes (Mulligan, 1988). Those studies which have attempted to investigate the three-dimensional nature of the barchan dune (Howard *et al.*, 1977; Knott, 1979) have made only cursory wind speed measurements on the flanks. In the present study, velocity was measured along the dune centre-line, both flanks, the right edge, in the lee, and upwind of all section lines (Figure 2.9). In this way it was hoped that an understanding of the relationships between the airflow across different parts of the dune would be gained. Such relationships are particularly interesting in this case because of the difference in crest-brink separation between the flanks and centre-line.

VERTICAL SPACING AND POSITIONING

The vertical spacing of the anemometers is governed by the height of the inner-layer (Chapter 2.2). With the equipment available for this experiment, determinations of shear velocity had to be made from velocity measurements above the surface. The best method of shear velocity determination is the subject of some controversy (see Chapter 6). A typical method involves the calculation of a regression line through a log-linear velocity profile. In order to measure a meaningful velocity profile it is necessary to place a number of anemometers within the inner-layer through which a regression line can be calculated. The depth of the inner-layer for the study dune was calculated from Equations 2.1 and 2.2 to be between 0.55 m and 1.90 m. The true nature of the inner-layer is still unresolved, but its maximum extent can be assumed to lie within the region of 0.55 m and 1.90 m depth. Taking the cautious view, it was decided to have the majority of the anemometers in the study profiles below 1.0 m.

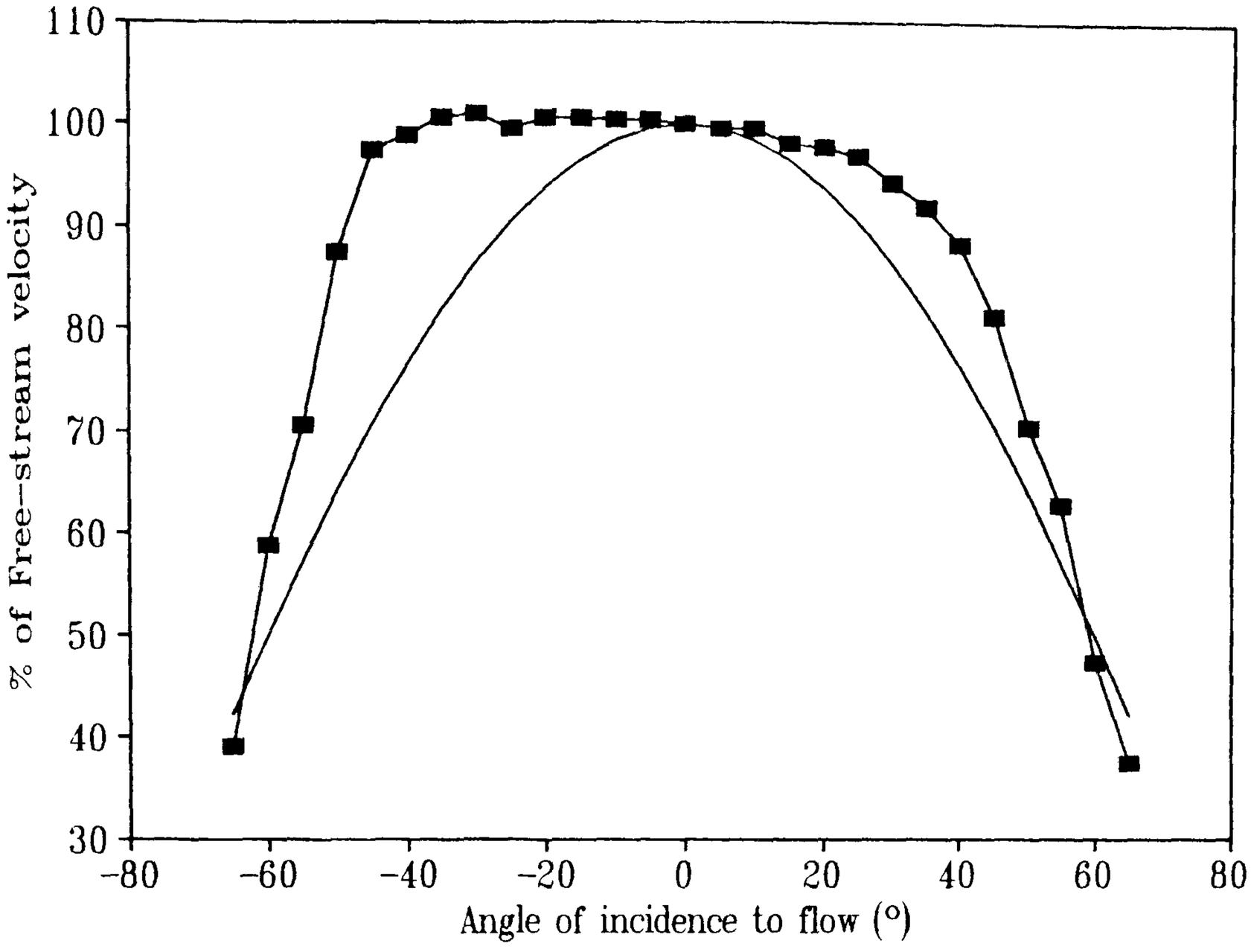

Figure 2.8 Cosine-response of the cup-anemometer. Solid line represents cosine-curve.

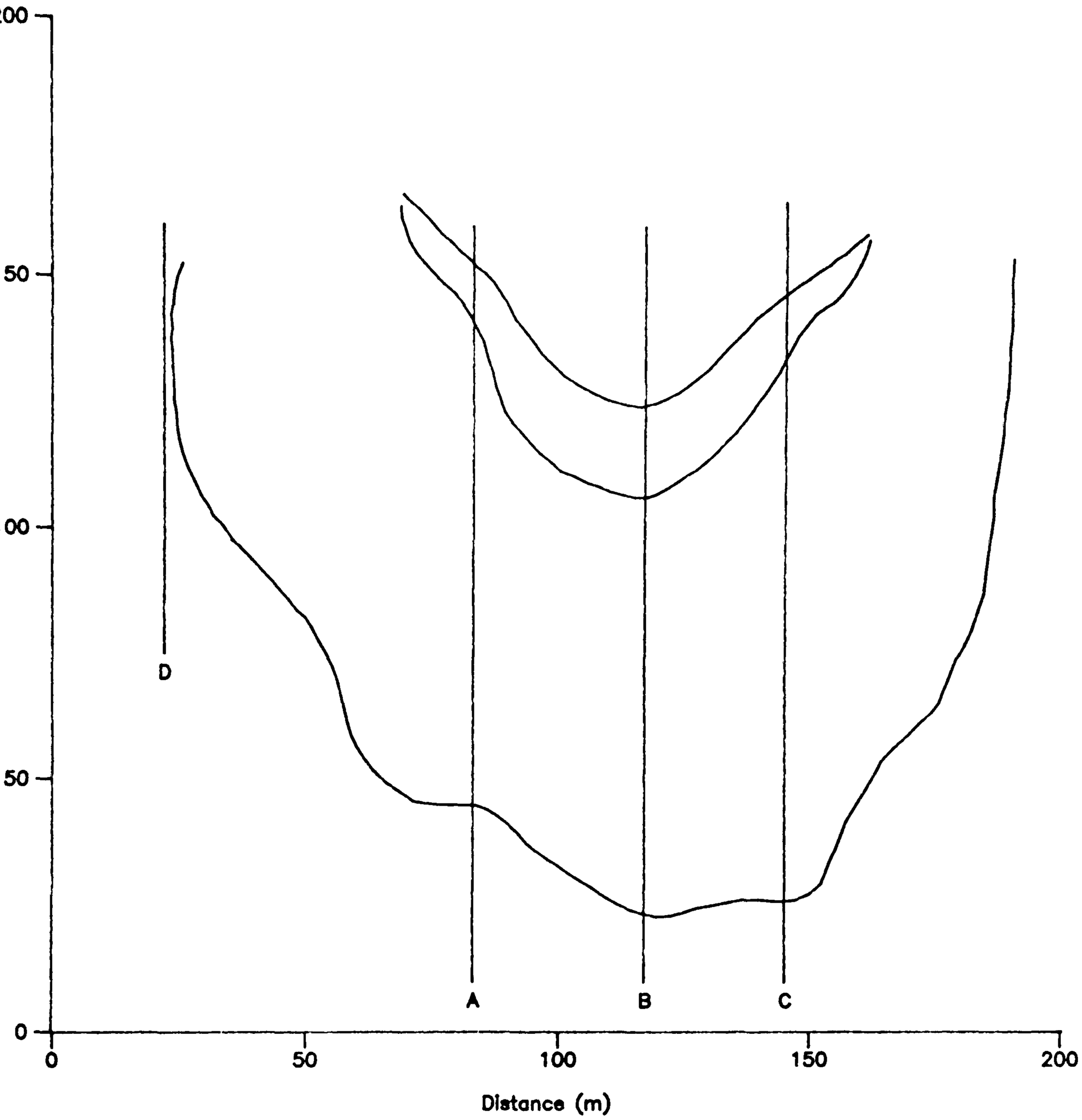

Figure 2.9 Section lines measured on the dune. A = right flank; B = centre-line; C = left flank; D = right edge.

A lower height limit on the array is imposed by the level of the saltation layer. Measurements with a cup-anemometer placed within the saltation layer have no real value because the effect of sand bombardment has an uncertain effect on its efficiency. Some consequence is expected because of the presence of grain-borne shear stress (recognised by Bagnold, 1941 and Owen, 1964) which tends to decrease flow velocities within the inner-layer (McEwen & Willetts, 1991), and the practicalities involved in using a cup-anemometer in this zone have not been debated. Furthermore, the calibration of an anemometer in a saltation layer would be seriously effected by the intrusion of sand grains into the bearings (a problem experienced by Lancaster (1985) with anemometers 5 cm from the surface). In consequence, the placing of the anemometers within the saltation layer was avoided. Sand trapping results suggested that 99% of the saltation occurred within 0.2 m of the surface.

The number and height of anemometers in the vertical profiles varied according to circumstances. Where vertical velocity profiles were to be studied in some detail (*e.g.* where the depth of the inner-layer was to be investigated) then seven anemometers were incorporated into the profile at heights of 0.25 m, 0.35 m, 0.6 m, 0.75 m, 1.0 m, 1.25 m and 1.5 m. The limited number of anemometers dictated that when detailed profiles of this sort were being measured then only three arrays could be used. Where a more expansive horizontal section was required (*e.g.* during sand trapping) then the number of anemometers in the profiles was set at four, spaced within the upper and lower bounds described above, at heights of 0.25 m, 0.35 m, 0.60 m and 1.00 m.

On the dune, the anemometer arrays were fixed in position by clamps attached to a reinforcing rod hammered into the sand (Figure 2.10). The height of the rotors of each anemometer above the sand surface was measured with a tape measure to an accuracy of about 0.5 cm.

HORIZONTAL SPACING

The horizontal distance between anemometer arrays along the test section lines varied according to individual circumstances. In general, the distance was between 8 m and 12 m, similar to the separation chosen by Livingstone (1986), Lancaster (1989b) and Mulligan (1988). In this way, a substantial portion of the test line could be covered in one recording session. At certain points on the dune surface (*e.g.* at the toe) the separation distance was reduced to 2 m or 3 m in order to gain more detailed measurements in this region of particular interest (see Chapter 1).

Figure 2.10 Typical vertical anemometer array at the crest of the dune. Anemometers at heights of 0.25 m, 0.35 m, 0.6 m and 1.0 m. Note positioning of nearby sand traps.

RECORDING INTERVAL

The recording interval over which windspeeds are averaged depends on the type of data required. Where sand trapping is involved, the wind speed needs to be known over periods of about one to ten minutes. This is because sand traps are only exposed for periods of this order of magnitude; any longer and their accuracy decreases due to sand saturation and wind direction changes (Rasmussen *et al.*, 1985) (see Chapter 2.3.2). Conversely, in order to measure all of the turbulent eddy sizes at a point, it is necessary to average wind speeds over a period of 30 to 60 minutes. Furthermore, where horizontal velocity profiles along a particular dune section are required, then the maximum averaging period is equal to the length of time that the wind direction stays constant along that section line. Over longer periods of time, the continuous erosion of the dune surface would also alter the relative heights of the anemometers. With regard to these arguments, it was decided to average the windspeed over a period of one minute, hence allowing correlation with sand trap data. However, on any one section line, the period of exposure of the anemometers was about two hours (depending upon wind direction changes), hence allowing measurement of the maximum number of eddy sizes. Averaging periods of this order of magnitude were also used by Lancaster (1985), Tsoar (1985) and Livingstone (1986).

NORMALISATION PROCEDURE

With a maximum of 26 anemometers it was not possible to measure vertical windspeed profiles along a whole section line (upwind to the brink) at once. It was therefore necessary to cover one line with a series of two or three measurement episodes. In order to compare the results of these episodes, the data were normalised by measurements at the reference station positioned 50 m upwind of the toe on the centre-line. This is common practice where associated measurements have to be taken at different times (*e.g.* Livingstone, 1986; Mulligan, 1988; Lancaster, 1989b). Such a technique has been substantiated by Bradley (1980) who noted that the variability in windspeed has little effect on the shape of a normalised profile. The two procedures used in this study are normalisation:

$$U_n = U_z/U_{z\infty}$$

where:

U_n = normalised velocity
U_z = velocity at height z on test profile
$U_{z\infty}$= velocity at height z at reference station.

and calculation of the perturbations:

$$\delta s = (U_z - U_{z\infty})/U_{z\infty} \qquad (2.3)$$

where:

δs = velocity perturbation.

The perturbation calculation is the same as that for the "fractional speed-up" ratio of Jackson & Hunt (1975), as used by Tsoar (1985). The result occurs as a fraction which is analogous to the percentage speed-up (*e.g.* $\delta s = 0.15$ represents an increase in speed as compared to the reference of 15%).

Conclusion

With careful calibration and maintenance of the anemometers in the field it was assumed that the overall accuracy of the velocity measurements was about ±5-6%. Using the techniques described concerning decisions on vertical separation, recording interval and position of the test sections on the dune, data were collected which were relevant to the stated aims of measuring the vertical and horizontal wind velocity distributions over the dune.

2.3.2 Sand Transport Rate

Several investigators have measured sand transport rate on near-horizontal beach surfaces (*e.g.* Hesp, 1983, 1988; Sarre, 1988; Sherman, 1990; Chapman, 1990). However, there is no record in the literature of similar studies of sand transport rate over sand dunes. More common is research into the design of sand traps. The justification for the design and calibration of the trap used in this investigation is noted in the section below.

Design and Calibration

In order to measure the sand transport rate, a collecting device has to be inserted into the airflow for a known period of time. However, because traps inevitably cause airflow disturbance they cannot intercept the total amount of sand in transport. For acceptable results, traps must be designed and calibrated carefully and the results must be cautiously analysed to minimise errors and account for inaccuracies.

Nearly all trap designs have been derived from two basic prototypes. The horizontal-type consists of rectangular boxes with small partitions on the bottom to stabilise the sand. The length

of the box in the wind direction is chosen so that it traps all the saltating sand. The major advantage of this design is that it does not disturb the upstream airflow. However, selecting the length of the box is problematic (Horikawa & Shen, 1960) and the trapped sand is prone to re-entrainment after deposition.

Vertical traps are more commonly used. Most designs are based on Bagnold's collector (*e.g.* Chepil & Woodruff, 1963; Gillette & Goodwin, 1974) which collects particles through a vertical slot 1 cm wide and 76 cm high. A modified version consists of vertical separators so that the vertical flux can also be established (Kawamura, 1951; Crofts, 1971). However, there are two major problems involving vertical traps; back-pressure and scouring around the base.

There has been much discussion concerning the problem of back-pressure. It has been argued that airborne particles have sufficient momentum to allow passage into the trap despite some wind deflection (Jones & Willetts, 1979). The majority of researchers, however, agree that some form of flow bleeding from the trap is necessary to reduce flow stagnation and scouring (Horikawa & Shen, 1960; Gillette & Goodwin, 1974; Fryrear *et al.*, 1991).

There have been many attempts to design a trap which allows the free passage of airflow but also removes the airborne sediment (Horikawa & Shen, 1960; Leatherman, 1978; Jones & Willetts, 1979). To accomplish this it is necessary for the collector to present a thin section to the wind (0.5-2.0 cm) to minimise wind deflection and to possess an open structure with smooth walls to reduce back-pressure.

The efficiencies (*i.e.* the proportion of moving sand collected) of the various types of trap vary considerably. That of the Bagnold trap has been reported to be as low as 20% (Knott & Warren, 1981) and as high as 60% for the modified version of Gillette & Goodwin (1974). A more recent design by Leatherman (1978) reportedly achieves a 70% efficiency (Marston, 1986). However, the determination of efficiencies is fraught with problems, and Jones and Willetts (1979) have shown that small differences in the operation of traps in the field may give rise to large contrasts in efficiency. More advanced sand traps which include load cells and provide continuous recording of the rate of transport are now in use (*e.g.* Lee, 1987; Butterfield, 1991), but these are expensive and only give measurements of total transport, not differentiating with height. Despite their advanced measuring systems, these traps still suffer from some scouring and back-pressure problems.

The trap design used in this experiment is shown in Figure 2.11 and is similar to the Aarhus design (Rasmussen *et al.*, 1985). It is made from thin polycarbonate and is small and thin, keeping flow disturbance to a minimum. Back-pressure is reduced by bleeding air from the rear through a fine gauze. Vertical variations in flux are measurable because the trap is separated into eight vertical sections each 2.5 cm high, giving a total height of 20 cm. This height is approximately equivalent to the upper limit of the saltation layer. The advantages of this trap design are its cheapness, high manoeuvrability, and differentiation of vertical sand flux.

The efficiency of the trap was tested in a wind tunnel. Hot-wire anemometer traverses were conducted in the free stream just upwind of the trap entrance at a variety of windspeeds and compared to the velocity measured at the same position when no trap was present. To simulate the trap becoming blocked by sand, the same traverse was undertaken with the gauze made impermeable with tape. Figure 2.12 shows how the percentage of flow capture with a free-stream velocity of 10 ms^{-1} is reduced markedly within the limit of the trap walls, falling to 40% at the centre. When the trap is blocked, with no bleeding of air, this declines to 23%. However, across the whole trap aperture the percentage air capture of the bled and blocked traps are 50% and 37% respectively. It is clear that the traps should be exposed to sediment transport for as short time as possible in order to reduce the effect of sand blocking the gauze. In practice the traps were exposed for 2-10 minutes, depending on the wind velocity, resulting in a reduction in permeability through the gauze of about 50%.

It should be noted that these efficiencies are only for air capture, not sand capture. Following the arguments presented above (Jones & Willetts, 1979), it is possible that the momentum of the grains approaching the trap would be large enough for them to pass through the low velocity zone at the entrance. Support for this hypothesis is shown in Figure 2.13, which indicates that the wind velocity only 50 mm in front of the trap is still 90% of its upwind value. Also, recent tests undertaken on the original Aarhus design sand trap showed that the overall trap efficiency even with sand in saltation was 49% (Rasmussen, pers. comm.). This suggests that the low velocity zone through which moving grains have to pass is fairly small.

Table 2.3 implies that the efficiency of the trap is independent of velocity, concurring with the conclusions of Horikawa & Shen (1960) and Gillette & Goodwin (1974). This infers that the efficiency of the trap is also independent of height. This may be true away from the surface, but flow visualisation carried out around the trap employing the "ink-dot" method (described in Chapter 4.3.1) suggests the existence of a reverse flow vortex and stagnation point upwind of the trap entrance (Figure 2.14). Figure 2.14 also shows the speed-up of the flow around the trap

base (represented by the extension of the ink lines due to increased velocity). It is these effects which cause scouring and under-recording of sand in reptation (as defined by Ungar & Haff, 1987) which has been a criticism of this type of trap (Rasmussen & Mikkelsen, 1988; Anderson *et al.*, 1991).

Table 2.3 Sand trap efficiency at selected wind tunnel speeds

VELOCITY (m/s)	EFFICIENCY (%)
3	49.3
5	49.3
7	49.5
10	50.3

To overcome this problem, sand transport close to the surface has commonly been predicted by extrapolating to the surface a log-linear transport rate profile from data collected higher in the sand trap, above the scouring zone (as proposed by Williams, 1964). However, Rasmussen & Mikkelsen (1988) demonstrated that the true transport rate is considerably larger than that found by using this method and Gillette & Goodwin (1974) suggested that an empirical equation which treats sand as a diffusion agent rather than a projectile gives a better estimation. In contrast, Werner (1990) believed that an inverse power law best described the mass flux dependence on height so that mass flux profiles were roughly linear on a dual logarithmic scale, except at the top and bottom of the saltating layer.

Figure 2.15 shows a typical vertical flux profile measured in this study. It appears that the log-linear extrapolation method (Williams, 1964) is appropriate in this case. Plotting the data shown in Figure 2.15 on dual log scales does not improve the linearity of the line. Furthermore, using the log-linear method, the lowest 25 mm of the profile increases its proportion of the total flux from 30.5% to 34.8%. The latter figure is a more reasonable value when compared to the common assertion that about 25% of the saltation profile is transported as "surface creep", although Rasmussen (pers. comm.) considers that 50% of sand in saltation occurs in the lowest 2 cm.

A practical method of reducing scouring at the trap entrance was also used in the field. This involved wetting the surface sand 5-10 mm in front of the trap entrance, immediately prior to a trapping run. This had the effect of almost entirely halting the scouring. However, the

technique does not stop the turbulent flow characteristics at the trap entrance (recognised in Figure 2.14) from deflecting incoming grains.

The efficiency of the trap in field conditions could not be determined. In addition to scouring and back-pressure other factors which may affect efficiency include the exposure angle between the trap entrance and the oncoming wind and the fact that sand is transported in sinuous "sand-streams", which frequently by-pass a sand trap during a measurement run.

The effect of exposure angle was tested by positioning several traps at increasing angles to the oncoming wind and measuring the transport rate simultaneously. The results are shown in Figure 2.16 which suggests that exposure angle may be an important parameter. A local deviation in wind direction of only 10° during a trapping run results in a 37% error. All sand trapping in this study was carried out over short intervals (between two and ten minutes) and the wind direction over the study area was fairly consistent (see Chapter 2.2). It is therefore considered that changes in wind direction have had only a slight effect on sediment capture efficiencies, being dwarfed by the other difficulties already mentioned.

The "sand streams" present a different problem which was not tackled in this study. The streams weave across the dune in no easily identifiable pattern, sometimes encroaching into trapping areas and sometimes not. The errors in sand trapping resulting from these sand streams are probably systematic, affecting all traps to the same degree. Hence, the errors should average out in a stochastic process. The phenomenon is worthy of further study.

The efficiency of the trap is variable with time, and can only be discovered with wind tunnel tests where saltation could be introduced into the flow. In the absence of the necessary facilities, and in consideration of the arguments presented above, the efficiency of the trap for the purposes of this study was considered to be 50%.

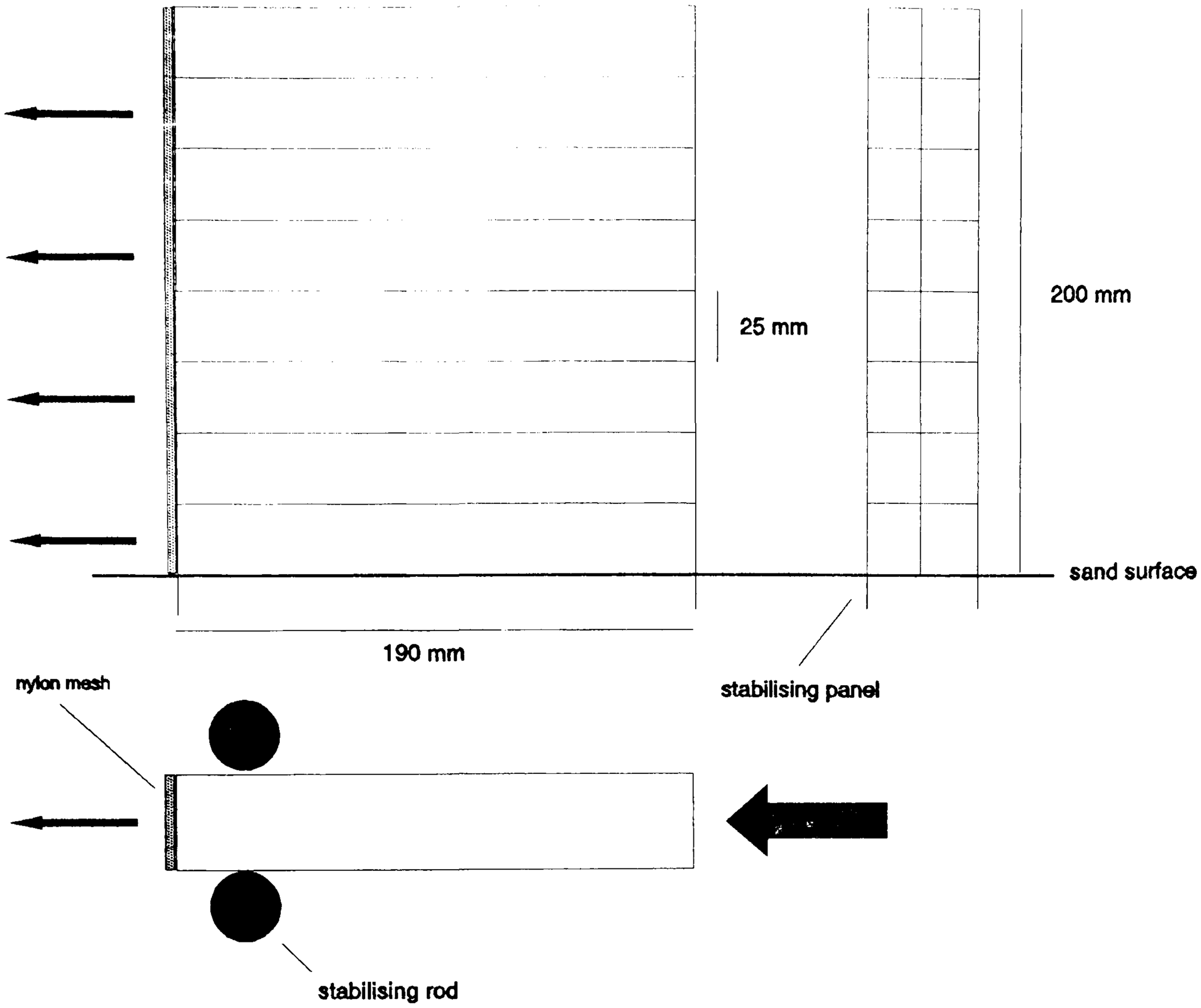

Figure 2.11 Design of the sand trap.

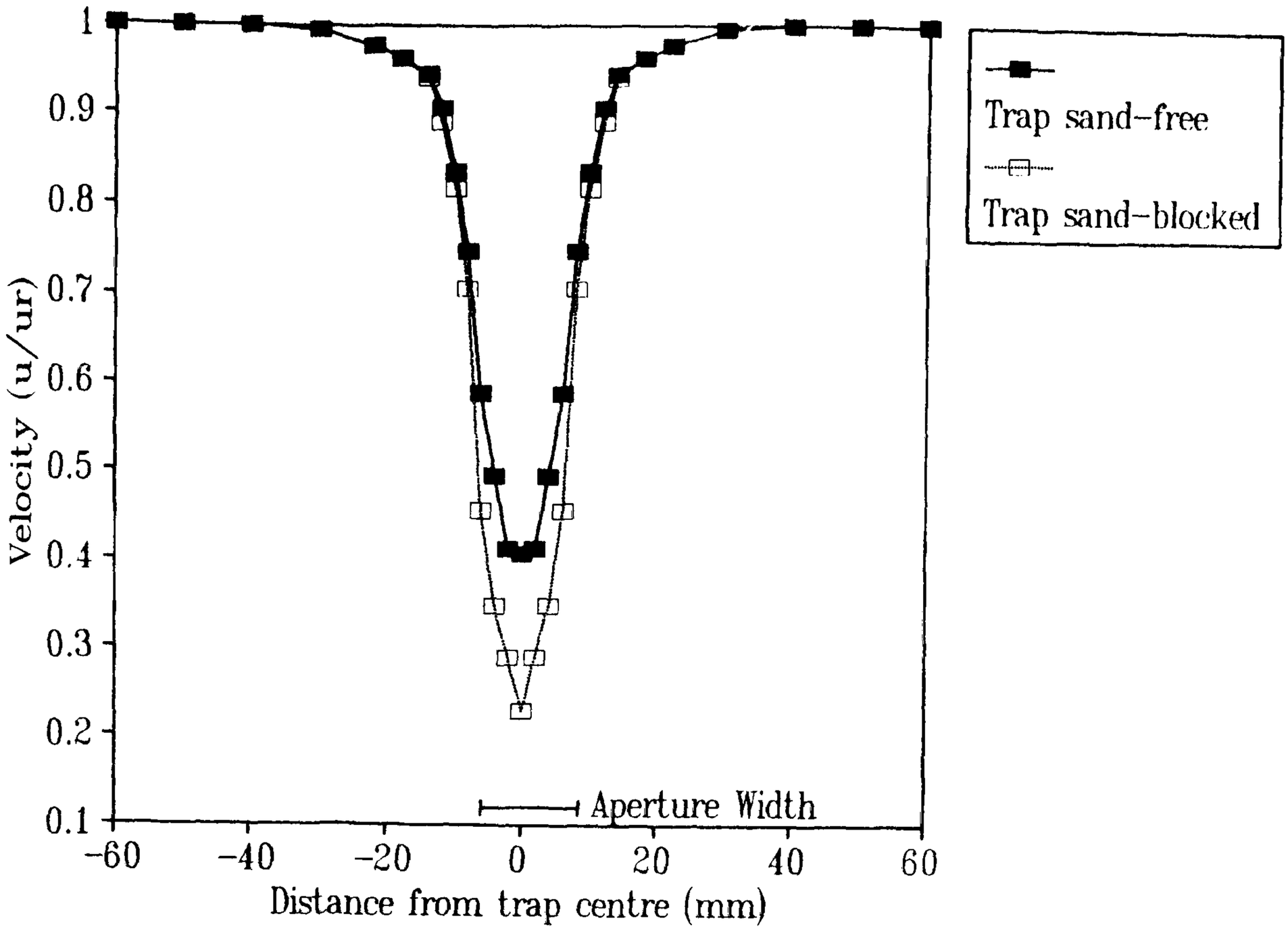

Figure 2.12 Efficiency of air-capture of the sand trap, measured in the wind tunnel.

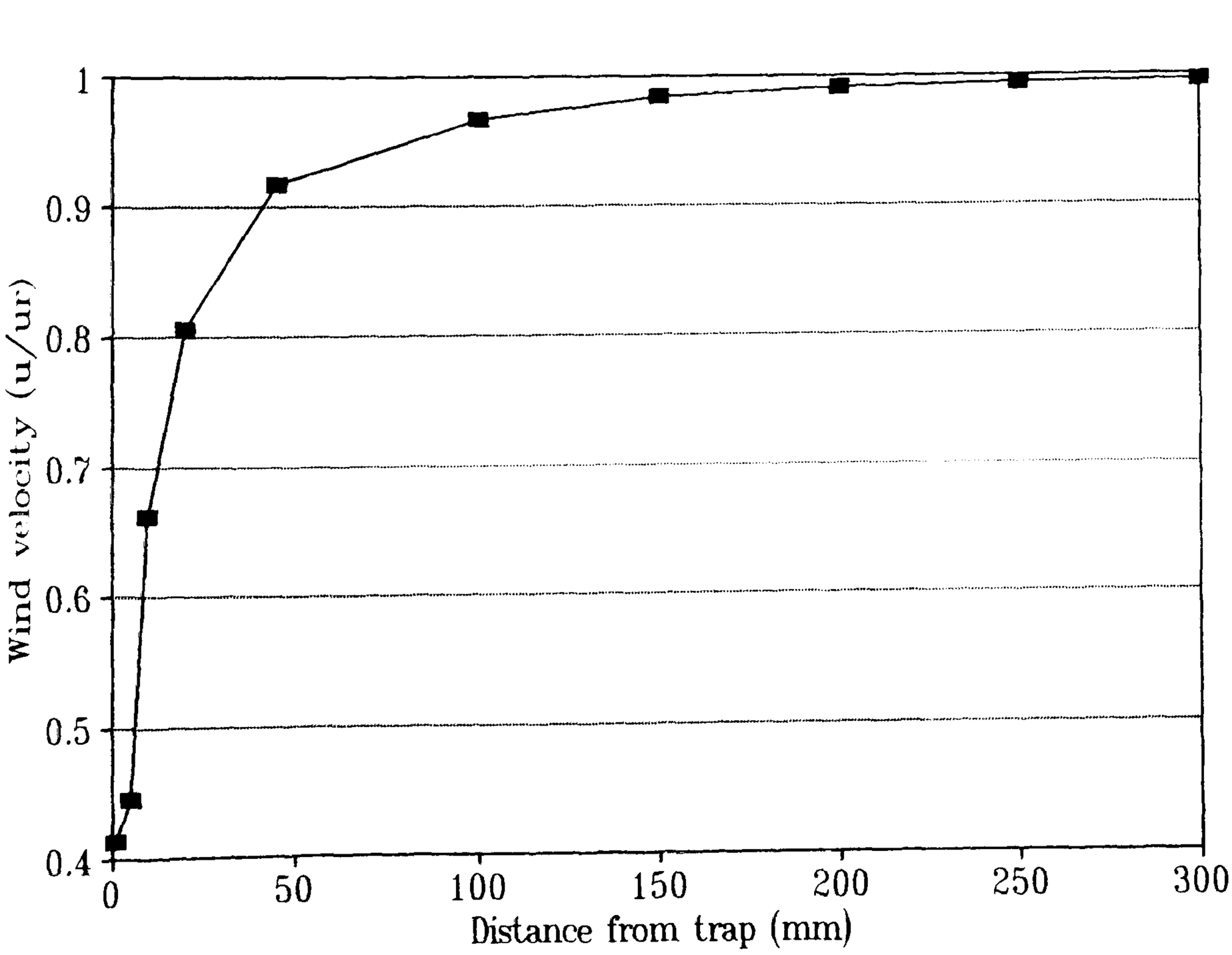

Figure 2.13 Low velocity zone upwind of the sand trap, measured in the wind tunnel.

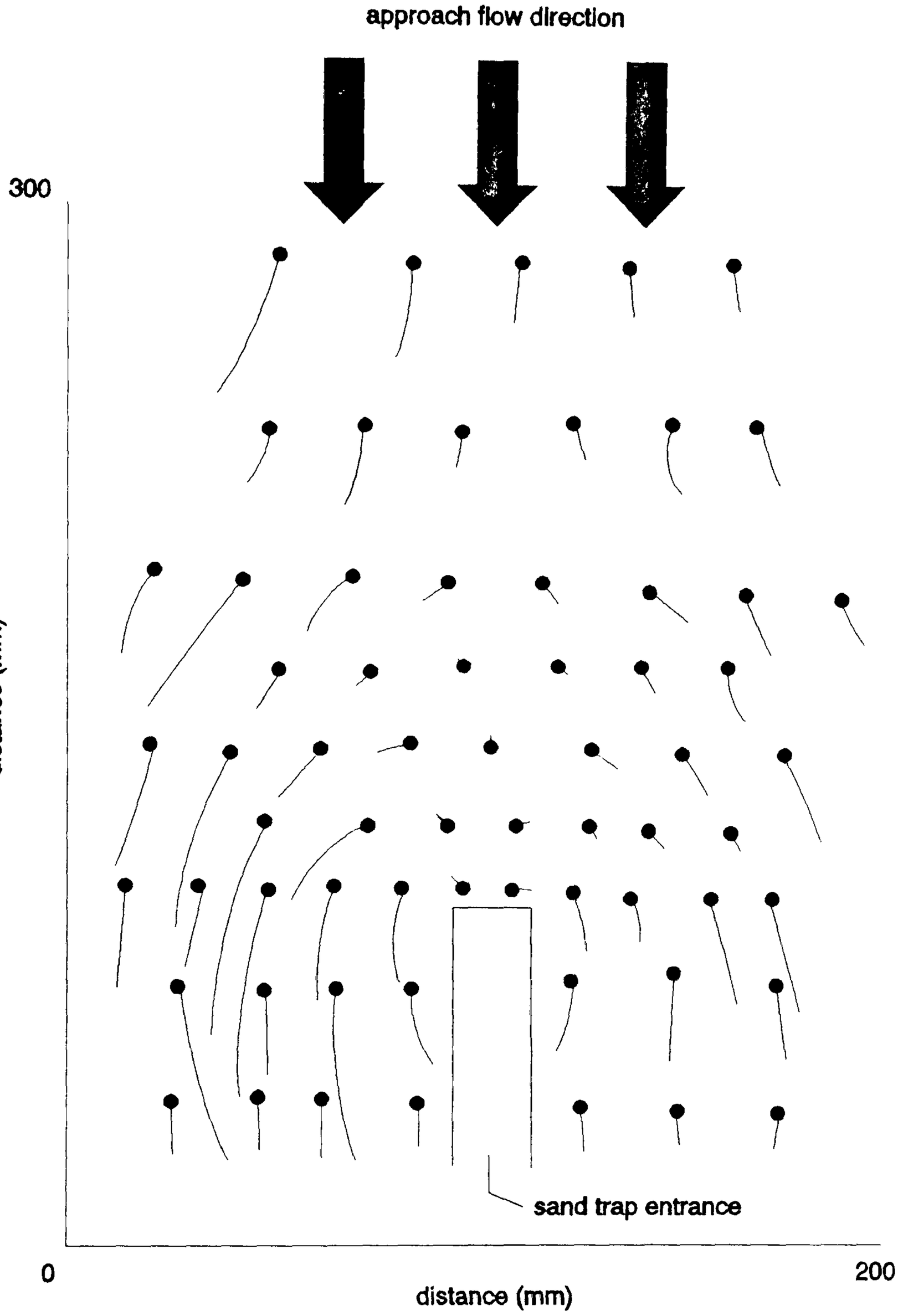

Figure 2.14 Surface streamlines at the sand trap entrance. Tails indicate flow direction. Note flow stagnation and possible reverse flow vortex immediately upwind of the trap entrance.

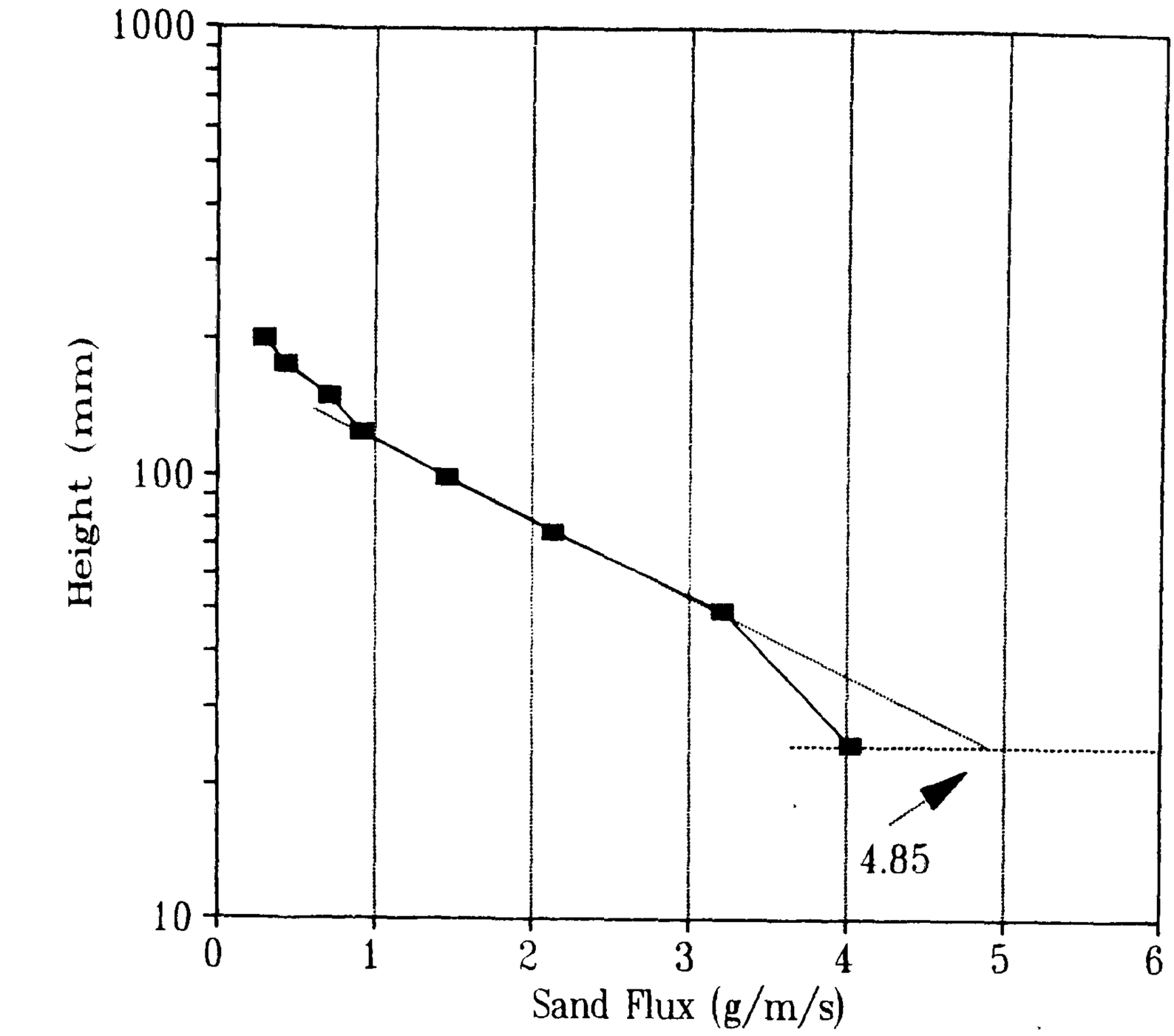

Figure 2.15 The log-linear method of correcting for the amount of sand trapped in the lowest compartment.

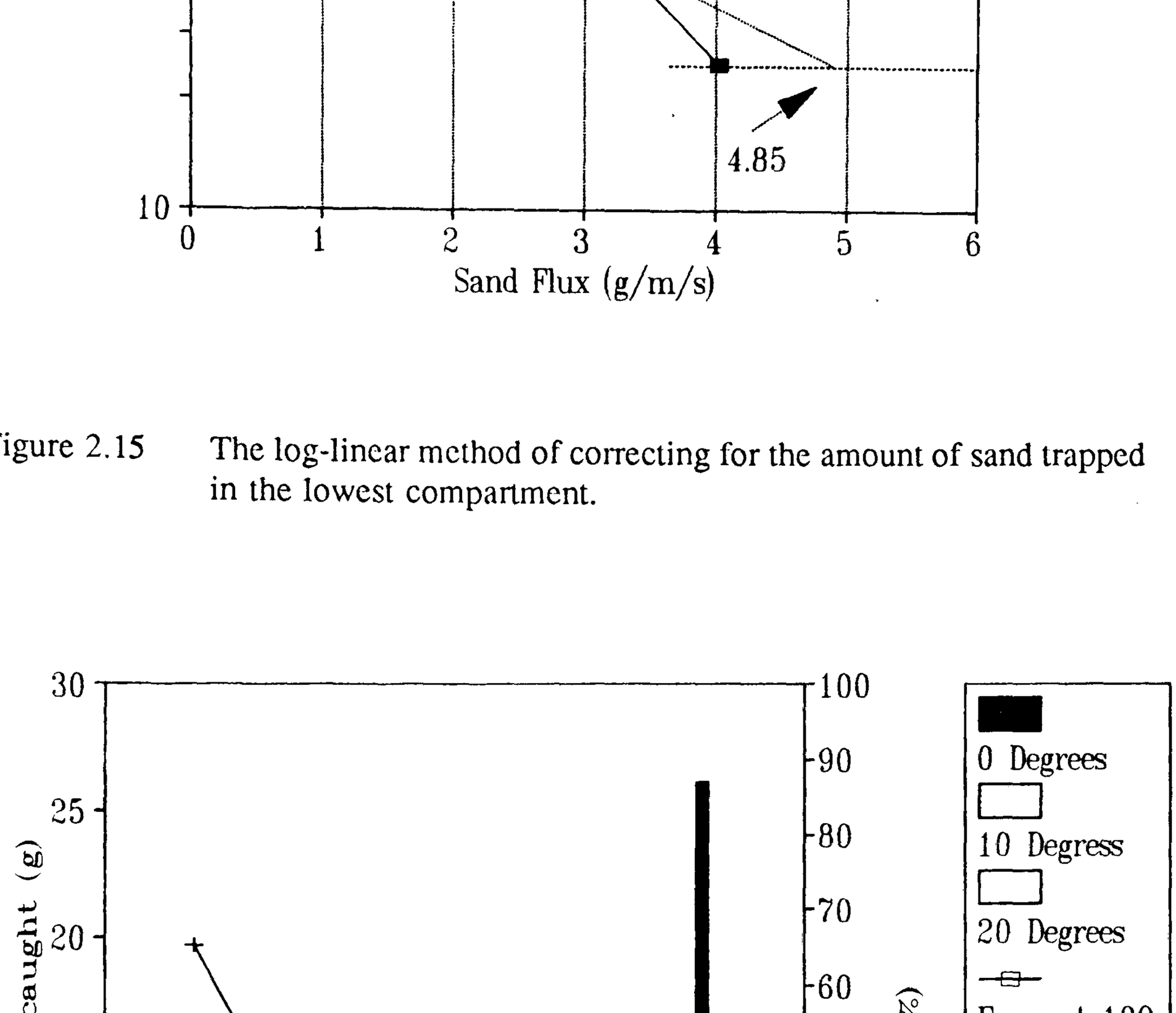

Figure 2.16 Effect of exposure angle on sand trap efficiency.

Field Procedures

In the field, the sand traps were initially secured between two stakes positioned next to the anemometer arrays with the gauze facing upwind, hence prohibiting sand capture. Once water had been sprinkled in front of the traps to reduce scouring, and the anemometers had begun a one-minute recording sequence, all the sand traps were reversed at once so that their open apertures faced into the wind (Figure 2.17). At the end of the recording interval the traps were retrieved and the height of sand in each compartment was measured. The equivalent weight of sand trapped and the resulting flux were calculated using Equation 2.4 below:

$$q_{act} = (h * 0.284 + 0.416)/t/w \qquad (2.4)$$

Where:

q_{act}= measured sand transport rate ($gm^{-1}s^{-1}$)
h = height of sand in trap compartment (mm)
t = time of trapping interval (seconds)
w = width of sand trap compartment (0.007 m)

Equation 2.4 was derived from regression analysis of the height of sand in the trap compartments and the corresponding weight (Figure 2.18). The measured sand transport rate (q_{meas}) was then corrected to the actual sand transport rate (q_{act}), first by extrapolating for the lowest 25mm (see Figure 2.15) and secondly by assuming that the efficiency of the trap was 50% (*i.e.* doubling the estimate).

It has been assumed that there is no lag between shear stress change and sand transport rate change (*i.e.* sand traps and anemometer arrays were positioned at the same point on the dune and not separated by a distance equivalent to a time-lag). There has been debate as to the importance of the fact that the amount of sand arriving at a trap is a function of shear stress at some distance upwind (Howard *et al.*, 1977; Rasmussen *et al.*, 1985). Recent computer simulations carried out by Anderson & Haff (1988, 1991) and McEwen & Willetts (1991) indicate that an equilibrium between shear stress and sand transport rate is reached almost instantaneously (1-2 seconds). This translates into a distance lag in the field of between 5 m and 10 m. However, Howard *et al.* (1977) found that accounting for a lag between shear stress change and sand transport rate change did not improve the predictive power of their computer model and considering that the equivalent distance lag in the field is dependent upon the windspeed, which was constantly varying, no attempt was made to account for this inertia.

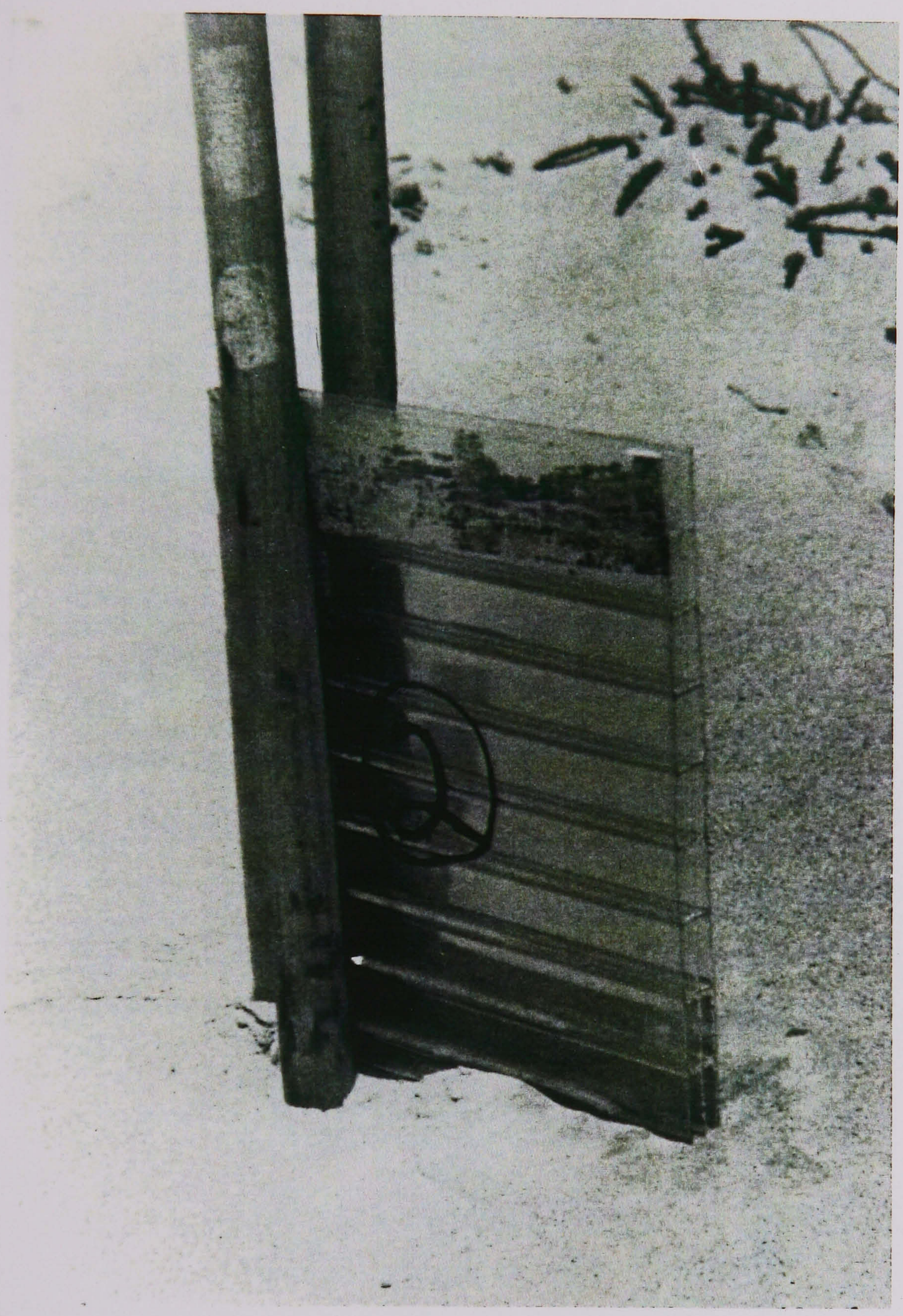

Figure 2.17 Configuration of sand trap in the field. Wind direction is from the right.

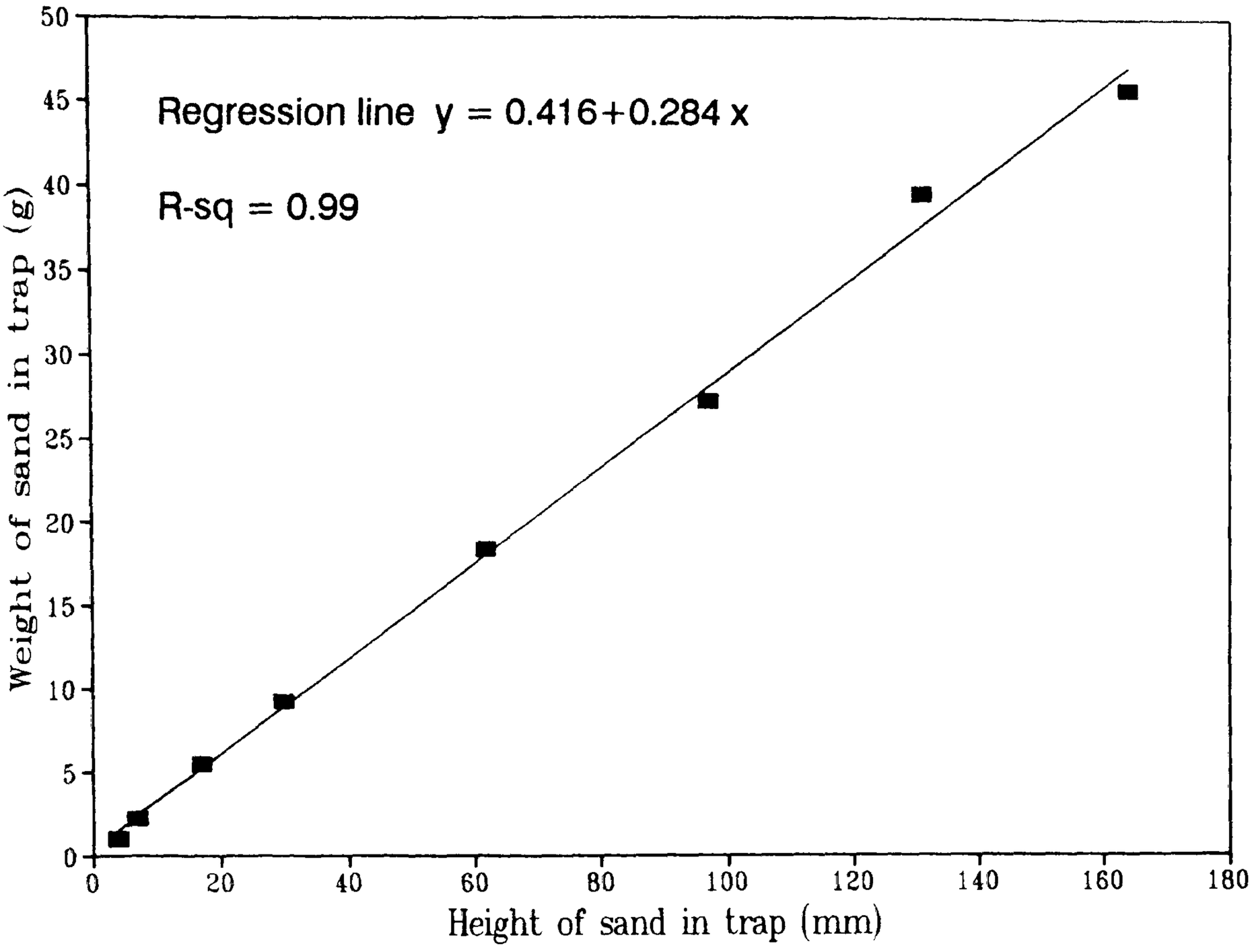

Figure 2.18 Relationship between height and weight of sand in each trap compartment.

Conclusion

The design of the trap used in this study is not 100% efficient. However, it is cheap, easy to use and its limitations have been understood. It is believed that by appreciating the problems and taking steps to alleviate them, the sand flux results presented here are of sufficient resolution to be useful. In the analysis of actual and predicted sand transport rates presented in Chapter 7 it is noted that the determination of the relative change in the sand transport rate between points on the dune is far more important than determining the actual values of sand transport. Where this is the case, the trap design presented here is of great value, as the errors described are nearly all systematic.

2.3.3 Wind Direction

Wind direction at a height of one metre was logged by a wind vane every 5 minutes at the reference station, 50 m upwind of the dune. These measurements were used to assess the prevailing wind direction during the measurement of wind velocity across different parts of the dune. In order to achieve an understanding of the degree of deflection of the near-surface wind around the three-dimensional dune form, two methods of wind direction measurement were used.

Flow Visualisation

Turbulence around the erosion pins on the windward slope (see Chapter 2.3.4) created small wake trains of sand during intense saltation. It was assumed that these wake trains were representative of the wind direction, and that a measurement of their angle with a magnetic compass represented wind direction at the surface. A similar technique was used by Howard *et al.* (1977) and Warren & Kay (1987).

Ripple Angle

Mapping of surface ripple patterns on the windward slope was undertaken, assuming a direct relationship between saltation direction and wind direction. A similar technique has been used by Nielson & Kocurek (1987), Havholm & Kocurek (1988) and Lancaster (1989a, 1989b). There is some evidence that ripple orientations deviate from wind direction on sloping surfaces (Howard *et al.*, 1977), but Lancaster (1989b) found no confirmation of this in his study on star dunes.

2.3.4 Dune Morphology

Dune Survey

A tacheometric survey of the dune was carried out at the beginning of the study period using theodolite and electronic distance measurement (EDM) techniques, similar to those described by Kay (1988). Approximately 900 data points were surveyed (at a density of about one survey point in every 3 m^2) from three fixed points. The survey covered not only the windward slope, brink/crest lines, and the base of the slip-face, but also the upwind gravel surface. The survey data was transferred onto a VAX-VMS mainframe computer and converted into cartesian co-ordinates. MAPICS software was then employed to interpolate isometric block diagrams and contour maps from the point data. The field survey points were more closely spaced along the brink-line of the dune in order for the sharp change in slope to be accurately modelled by the MAPICS interpolation algorithm. A contour map of the dune, interpolated from the survey data, is shown in Figure 2.19.

Pattern of Erosion and Deposition

Erosion and deposition on the dune were monitored by measuring changes in the elevation of the dune surface on steel rods (erosion pins). Ninety-three steel rods (15 mm diameter) were hammered into the windward slope of the dune along transects from toe to brink at approximately 10 m intervals. The tops of the rods were then surveyed with a theodolite and EDM and the length of rod visible above the dune surface was measured to the nearest 0.5 cm with a steel tape. The measuring of the rods was repeated approximately every two days for a period of 28 days. The rods caused some scouring at their base, but where this had occurred the measurements recorded were related to the elevation of the immediately surrounding surface. Similar techniques for assessing the pattern of erosion and deposition on sand surfaces have been employed by Ward (1984), Besler (1975, 1980), Howard *et al.* (1977), Lancaster (1985, 1989b), Livingstone (1985, 1989) and Warren and Kay (1987).

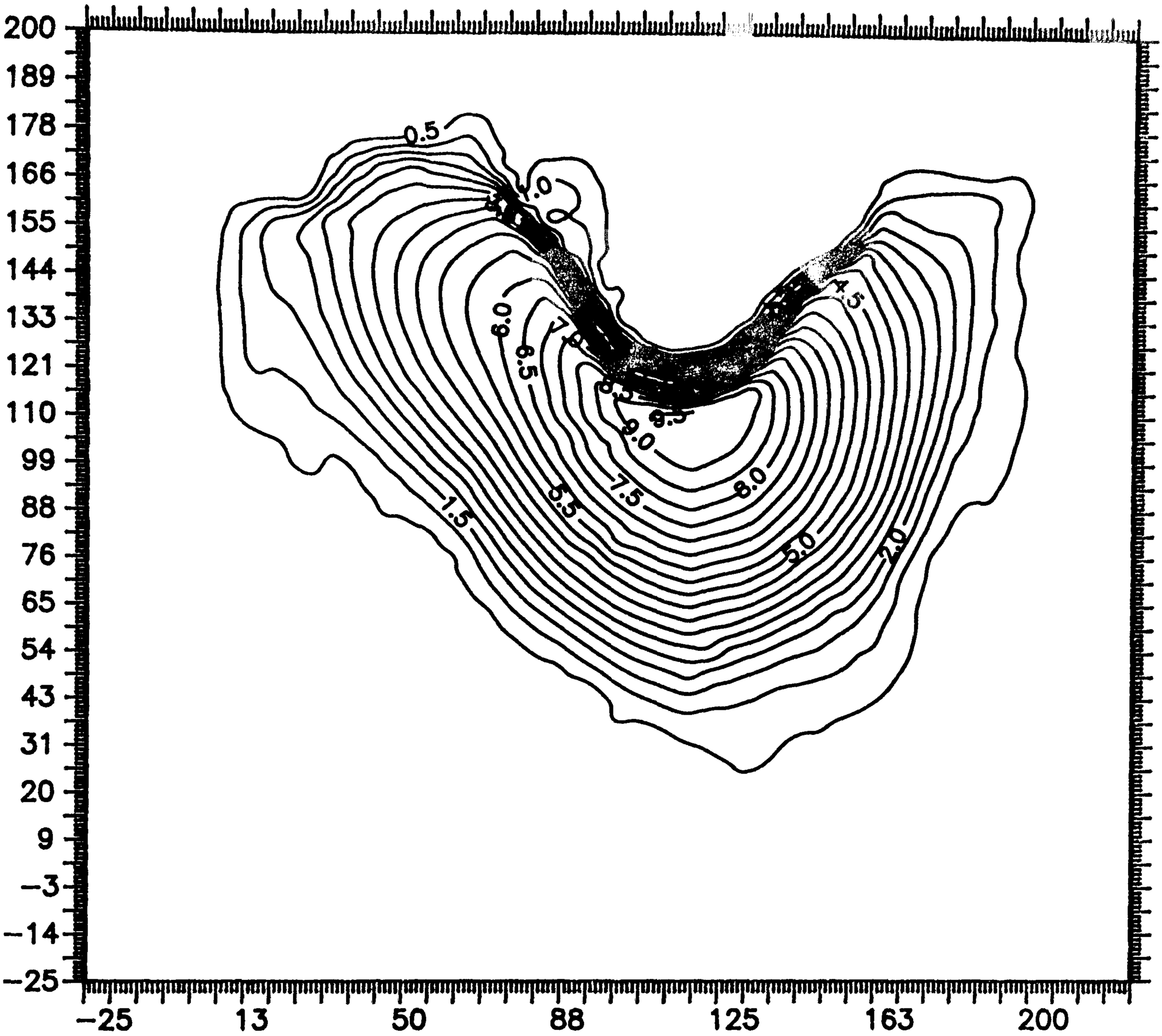

Figure 2.19 Contour map of the study dune. Contour interval is 0.5 m, wind direction from bottom to top.

2.4 Experimental Observations

2.4.1 Wind Direction

Figures 2.20 and 2.21 show the wind direction on the windward slope of the dune derived from the angular measurement of erosion pin wake trains and ripple patterns (see Chapter 2.3.3). The wake-train measurements (Figure 2.20) show less irregularity than the ripple pattern measurements (Figure 2.21). This is because the sinuous nature of the ripple patterns made their directional character more difficult to interpret than the wake train directions. Nevertheless, the general character of the flow pattern can be observed.

The centre-line flow direction does not generally deviate from the free-stream direction. However, on the flanks there is evidence that the airflow diverges away from the centre-line. This deviation appears to reach a maximum on the lower half of the slopes within 40 m of the centre-line. The degree of deviation in these regions is between 5° and 15° from the free stream direction (*ie.* the centre-line). These results are consistent with the direction measurements over barchan dunes of Allen (1968) in a flume and Howard *et al.* (1977) in the field. Both of these investigations found airflow divergence of similar degree on the flanks of their dunes. However, both Allen and Howard *et al.* also found a convergence of streamlines at the brink. The flow direction measurements shown in Figures 2.20 and 2.21 do not reveal a convergence in this region.

The flow direction measurements presented here are compared to similar flow direction assessments from the mathematical model and wind tunnel in Chapters 3 and 4. Before such comparisons are made the errors particular to the field measurements should be noted. Both sets of measurements (*i.e.* wake train and ripple pattern) were carried out at the same time on 30.7.92. The measurements took a total of two hours (13.00 hrs - 15.00 hrs), in which time the direction of the free stream flow had moved 2.5° from the centre-line of the dune in a southerly direction. The field direction measurements may therefore not strictly be analogous to each other. However, considering the errors involved in the accurate assessment of the direction of the wake trains and ripple patterns and also the time lag between wind direction change and ripple direction change, the effect of this wind shift on the results is likely to be negligible.

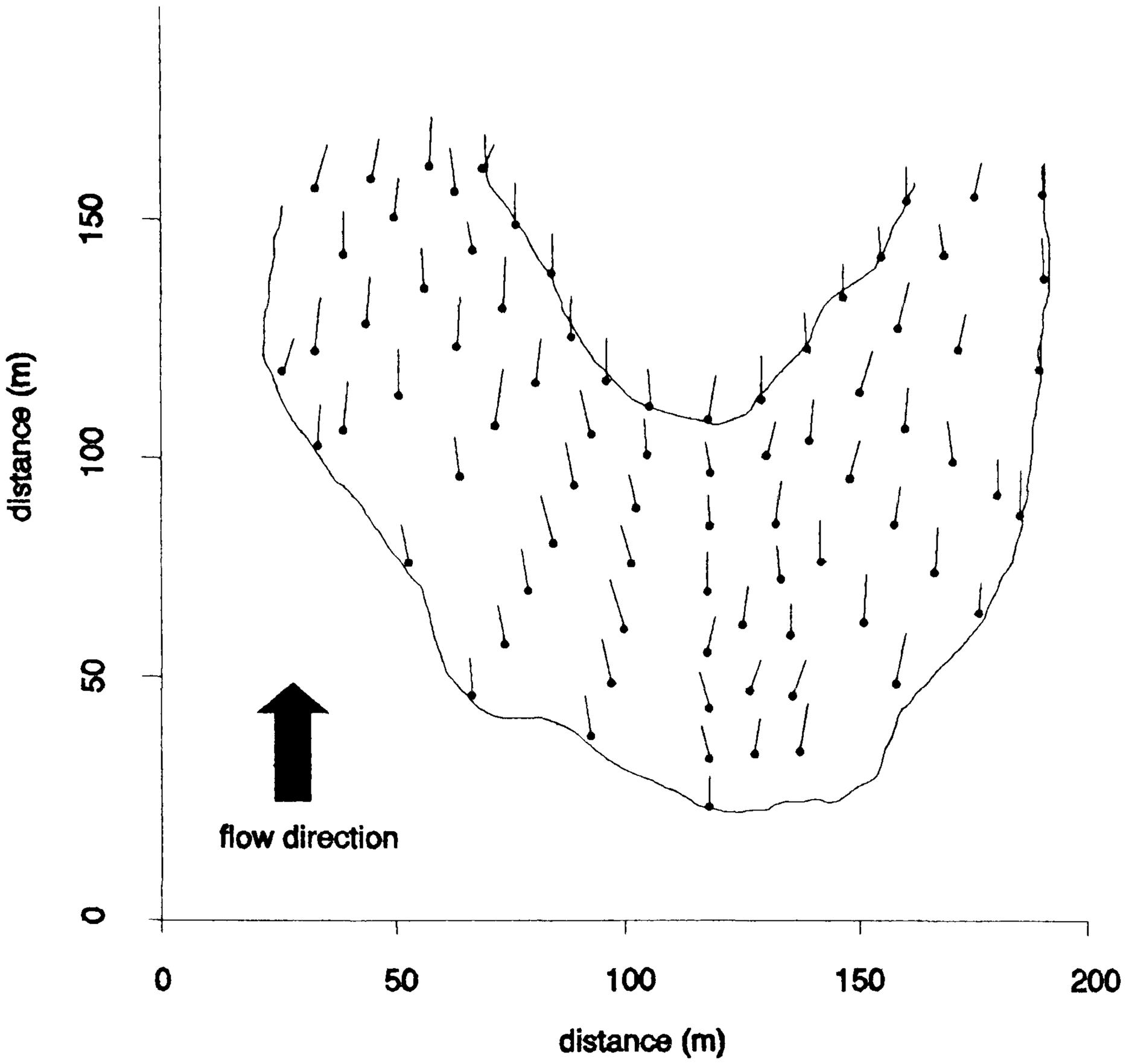

Figure 2.20 Field measurements of wind direction derived from wake-trains behind erosion pins. Tails indicate flow direction.

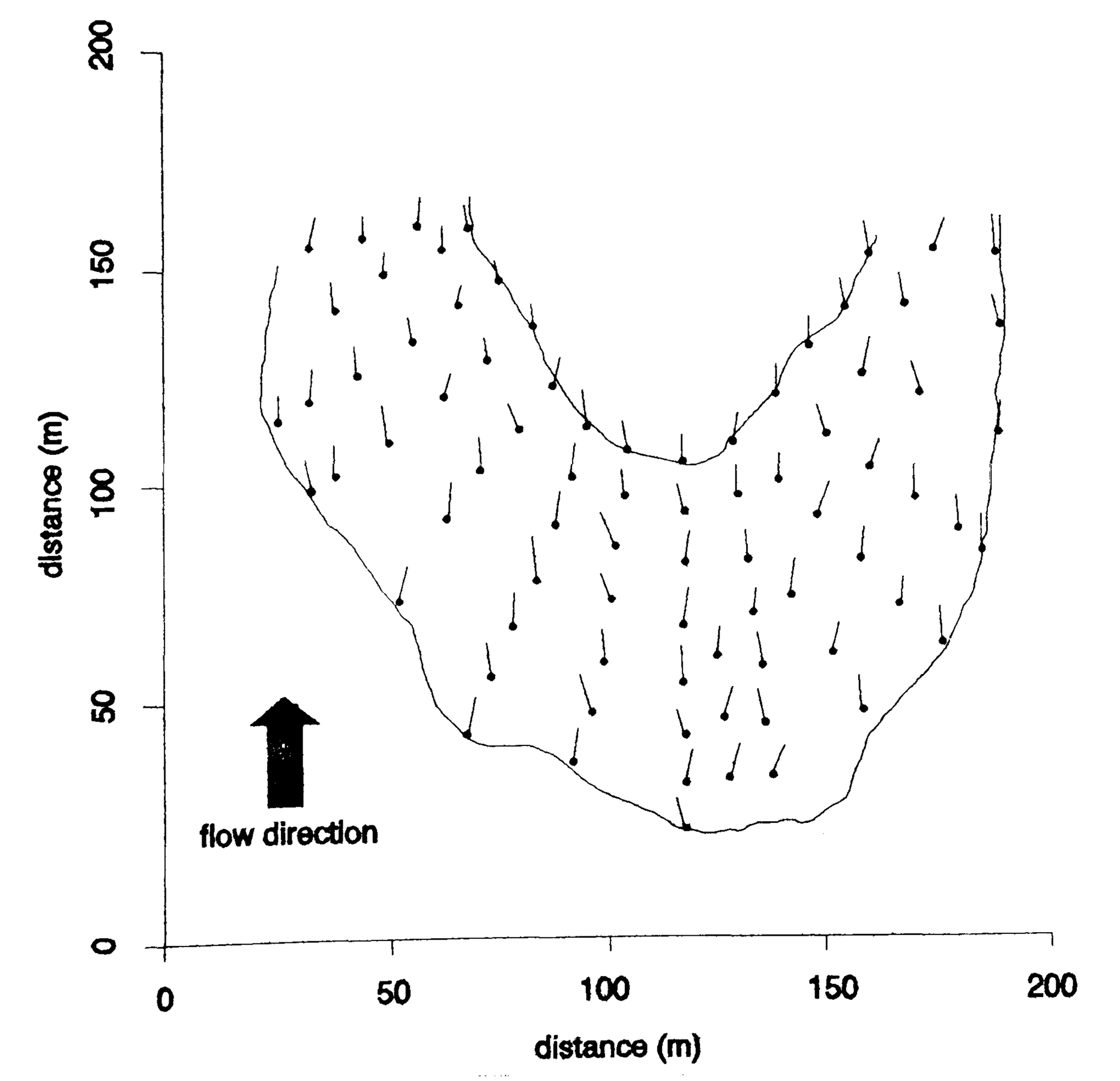

Figure 2.21 Field measurements of wind direction derived from relative ripple orientations. Tails indicate flow direction.

2.4.2 Patterns of Surface Change

The total surface change and dune movement over a 28 day period apparent from the erosion pin measurements are shown in Figure 2.22. The movement of the toe is uncertain because the precise definition of the toe at the beginning of the study period was difficult. This was due to the presence of small nebkha at both edges. The approximate toe movement within the period was 8 m. This is relatively consistent with the movement apparent at the brink-line where the downwind advance was a fairly constant 5-6 m across the width of the dune. The plan-shape of the dune over the measurement period therefore remained fundamentally unchanged.

The patterns of erosion and deposition on the dune surface are similar to those found by Howard *et al.* (1977). Figure 2.22 indicates that the windward slope was dominated by erosion and the downwind flanks were dominated by deposition. The maximum erosion (-0.93 m) occurred near the centre-line mid-way up the windward slope. This erosion was reduced downwind and deposition occurred to either side of the centre-line, reaching a maximum (+1.32 m) on the brinks of the flanks at their furthest downwind extent. The brink-line is characterised by a small amount of erosion (-0.15 m) at the centre-line and immediately either side of it, developing to increasing amounts of deposition toward both flanks.

Figure 2.23 compares the erosion and deposition measurements with the slope angle (as interpolated from the dune survey) in the direction of the prevailing wind. There is a clear relationship between the mode of surface change (erosion or deposition) and the sign of the slope angle. At all points on the windward slope where the surface angle was positive (*i.e.* upslope in the direction of the wind) erosion occurred. In contrast, wherever a negative angle was apparent deposition was dominant. It is also evident that the region of maximum erosion coincides with the maximum positive surface slope angle whilst the regions of maximum deposition are coincident with the areas of maximum negative slope angle. The point of inflection between erosion and deposition on the windward slope is approximately defined by the crest-line, where the surface slope angle is zero.

Figure 2.24 confirms the strong linear relationship between surface slope angle and erosion and deposition. A regression of the two parameters reveals a significant relationship with an r^2 value of 0.87.

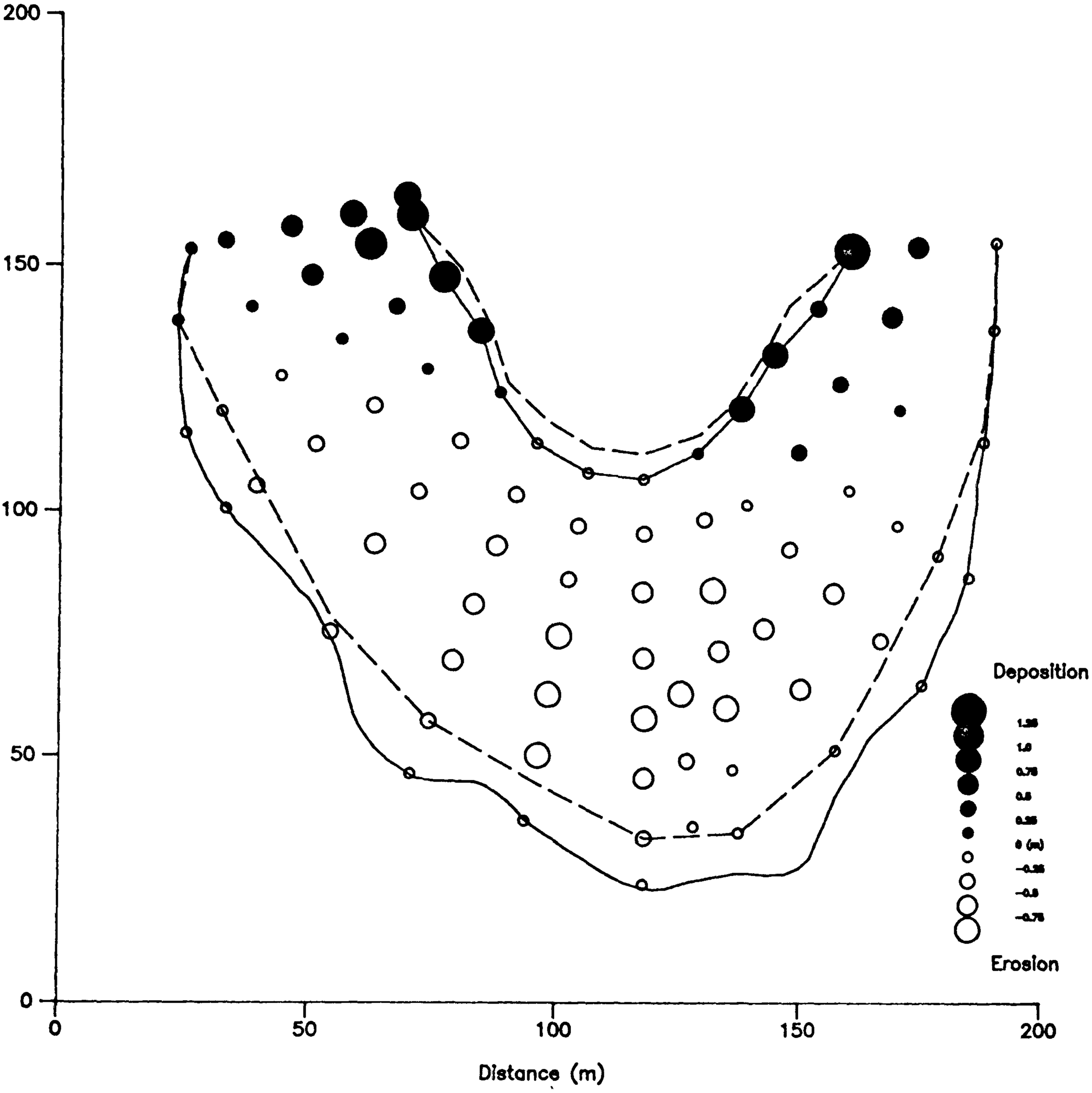

Figure 2.22 Erosion and deposition measured on the study dune and relative movement of brink and toe over a 28 day period.

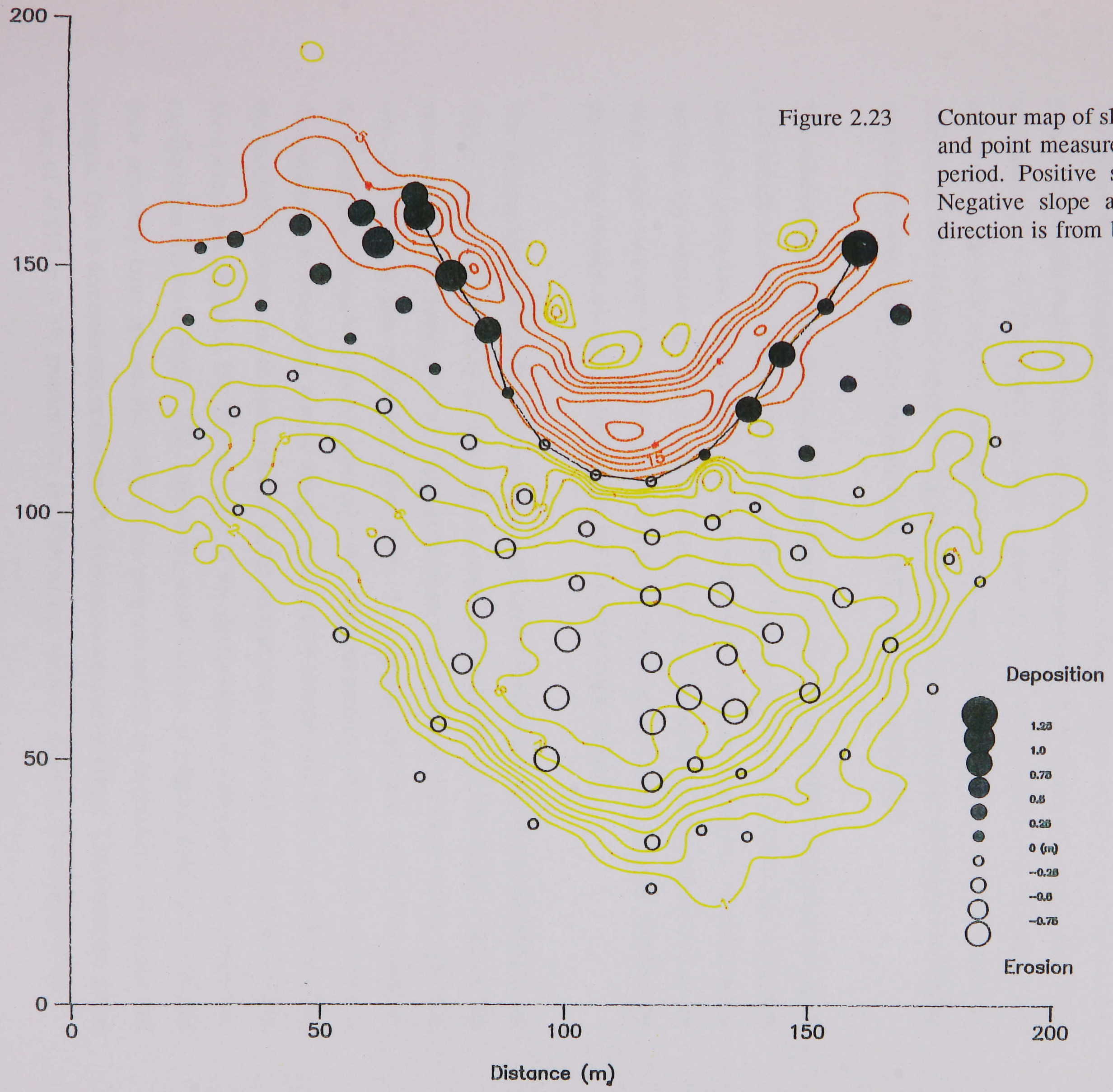

Figure 2.23 Contour map of slope angle in the direction of the prevailing wind and point measurements of erosion and deposition over a 28-day period. Positive slope angle contour interval (yellow) is 1 m. Negative slope angle contour interval (orange) is 5 m. Flow direction is from bottom to top.

Relationships such as those shown in Figure 2.24 led Bagnold (1941) to develop a predictive equation to calculate amounts of erosion and deposition from the tan of the slope angle:

$$\delta Q/\delta x = \gamma_s \, c \tan \theta \qquad (2.5)$$

where:

$\delta Q/\delta x$ = rate of erosion or deposition per unit area.
γ_s = specific weight of sand.
c = horizontal distance of dune advance.
θ = local slope angle.

Derivations of this relationship have been used to good effect to predict erosion and deposition on barchan and linear dunes respectively by Howard *et al.* (1977) and Lancaster (1987). Figure 2.25 shows the relationship between the actual erosion and deposition measured from the erosion pins in the present study and that predicted using Equation 2.5, assuming an average downwind translation of 5 m. The model provides a good fit (r^2 = 0.87) between the predicted and measured amounts of erosion and deposition, and the regression line is comparable to that of unity (1:1). This is despite Equation 2.5 generally underestimating amounts of deposition. Similar results have been reported by Howard *et al.* (1977) and Lancaster (1987).

The relationship between erosion and deposition and slope angle is further supported by Figure 2.26 which shows the dune morphology, surface slope angle and total erosion and deposition along the centre-line. The measured erosion is indicated by the open square plot. The relationship between the measured erosion and the surface slope angle is one of increasing erosion as the slope angle increases to a maximum mid-way up the windward slope. This is followed by decreasing erosion toward the crest as the surface slope angle reduces.

The comparison between the measured and interpolated erosion and deposition (dotted line on Figure 2.26) was necessary in order to construct similar graphs for the flanks. Because the erosion pins were distributed in a radial rather than a grid pattern, the flank section lines had very few erosion pins positioned upon them. To compare the dune survey and velocity measurements along these section lines with the measured amounts of erosion and deposition it was necessary to interpolate surface change from nearby erosion pins. This was achieved using the MAPICS software in the same manner as the contour map of the dune was constructed from the survey data (Figure 2.19). The accuracy of the interpolation is indicated by the centre-line interpolation shown in Figure 2.26. Due to the small number of original data points (93) and their relatively large spread, the interpolation program tended to overestimate the peaks and troughs. This is demonstrated at the point of maximum erosion on Figure 2.26 where the actual value of -0.815 m is 3% smaller than the interpolated value of -0.84 m. The shapes of the

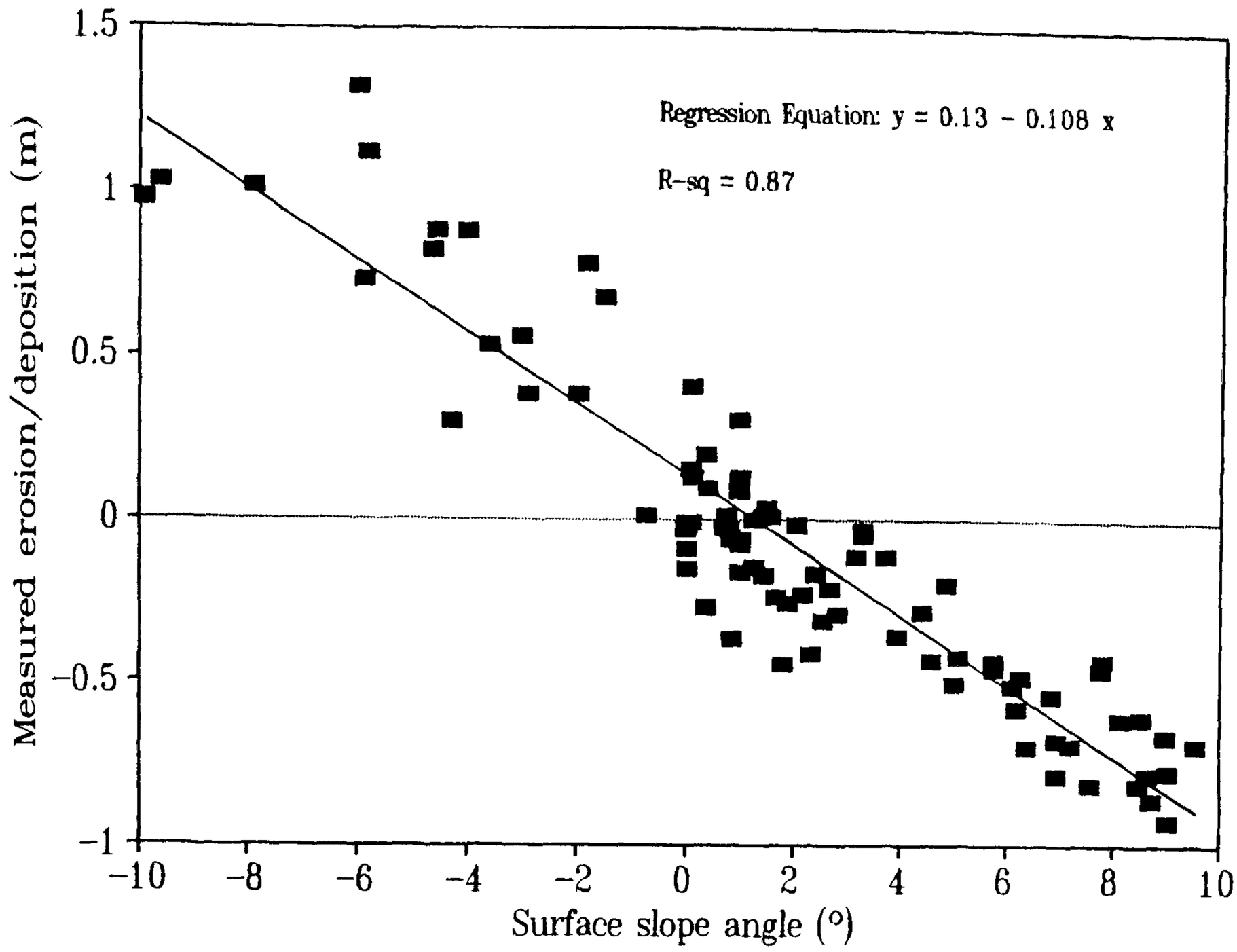

Figure 2.24 Surface slope angle and measured surface change over a 28 day period.

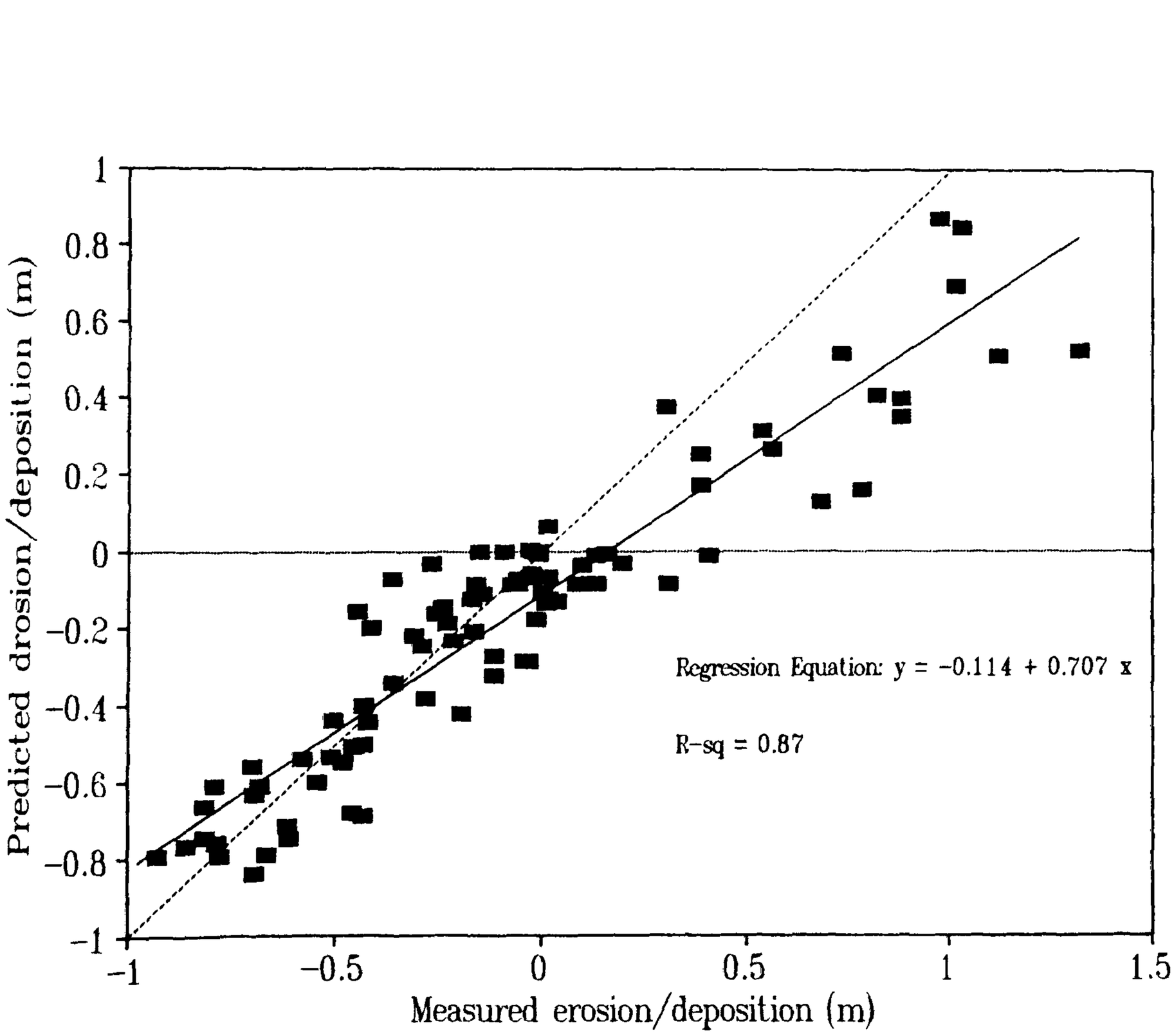

Figure 2.25 Measured surface change plotted against surface change predicted from the Bagnold (1941) model; Equation 2.5. Regression line (solid), equal surface change (dotted).

Figure 2.26 Surface height, slope angle and measured (act.) surface change over a 28 day period on the centre-line. See text for explanation of interpolated erosion and deposition.

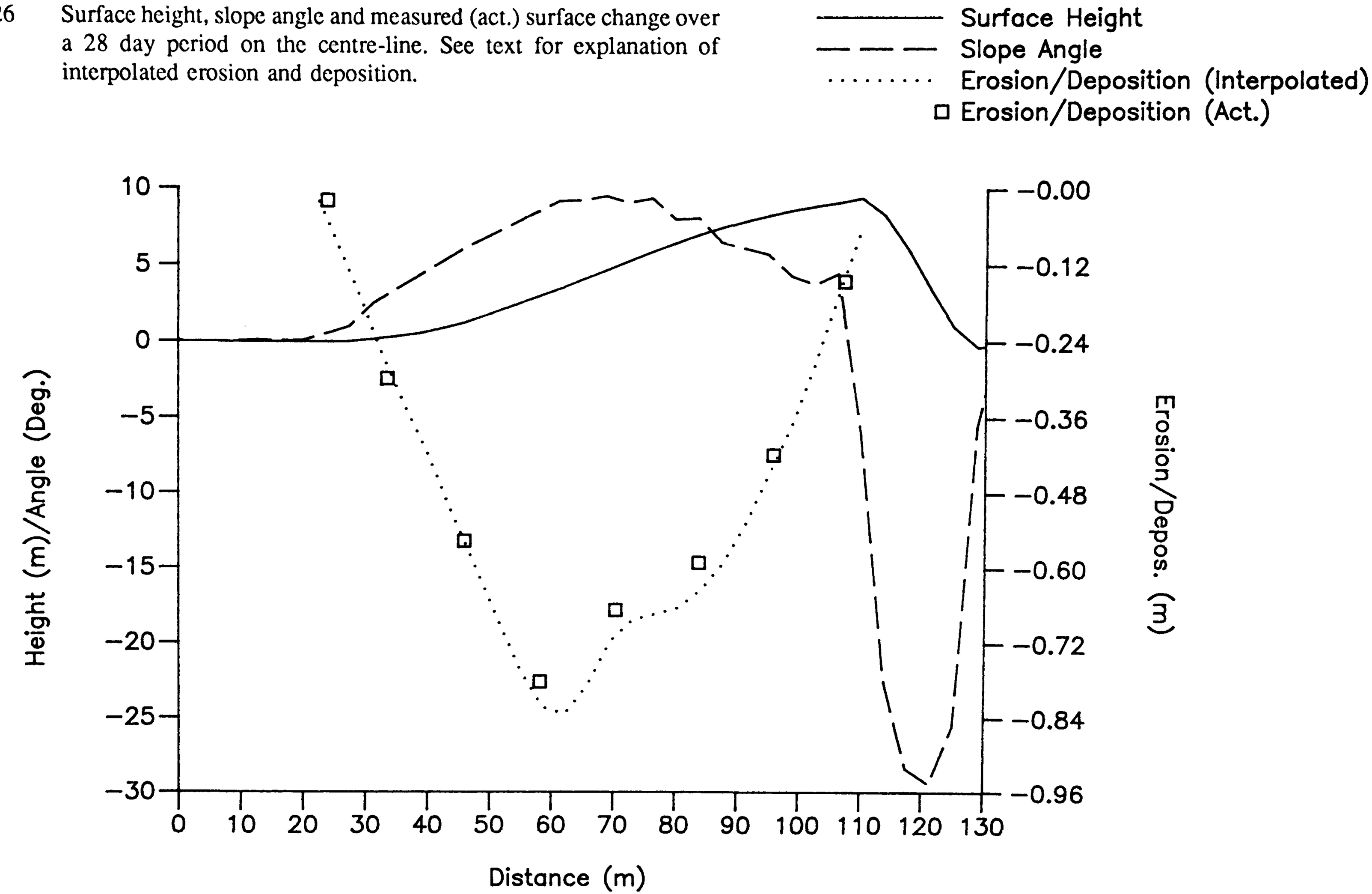

erosion patterns demonstrated by the actual and interpolated values are very similar and it is concluded that the interpolated erosion and deposition values for the two flank section lines shown in Figures 2.27 and 2.28 are probably within a 10% overestimation. For future studies it is suggested that erosion pins are distributed in a grid pattern so that cross-reference between erosion and wind velocity measured along a straight section line (parallel to the prevailing wind direction) can be more easily achieved.

The resulting interpolations of erosion and deposition on the flanks compared to dune form and surface slope angle are shown in Figures 2.27 and 2.28. The right flank (Figure 2.27) exhibits a similar relationship to the centre-line with maximum erosion (-0.73 m) at the largest positive surface slope angle. This is succeeded by a declining degree of erosion and increasing deposition to a maximum of +0.84 m at the brink, where the maximum negative surface slope angle (upwind of the slip-face) is found. Once more, the change from erosion to deposition is defined by the point of highest elevation and zero surface slope angle.

The left flank (Figure 2.28) is comparable to the right flank in that it exhibits maximum erosion (-0.64 m) at the largest positive surface slope angle and maximum deposition (+0.88 m) just upwind of the brink. The slight reduction in deposition between the point of maximum deposition and the brink itself is probably an artefact from the interpolation. However, the major difference between the surface change on the left flank and that found on the right flank and centre-line is that the point of change between erosion and deposition occurs about 10 m upwind of the crest. This means that deposition occurred on a slope facet with a positive surface angle (<+2°), countering the model proposed by Equation 2.5.

The effect that this has on the slope profile is shown in Figure 2.29. Both the centre-line and right flank slope profiles (a and b in Figure 2.29) generally maintained their shape throughout the study period as they moved downwind, following the model of Equation 2.5. However, the left flank (c) increased in height by about 0.6 m downwind from the original crest. The amount of height increase shown in Figure 2.29 is likely to be an overestimation caused by the interpolation program. However, such overestimation is unlikely to wholly account for the increase in crest height. This highlights the problems associated with a model which uses a purely geometric relationship, as discussed by Watson (1987). Equation 2.5 is only applicable to wholly equilibrium conditions as it allows for neither erosion nor deposition at the crest, where the surface slope angle is zero. It merely maintains the convex nature of the windward slope. This inaccuracy is apparent despite the significant relationship between the measured and

Figure 2.27 Surface height, slope angle and interpolated surface change over a 28 day period on the right flank.

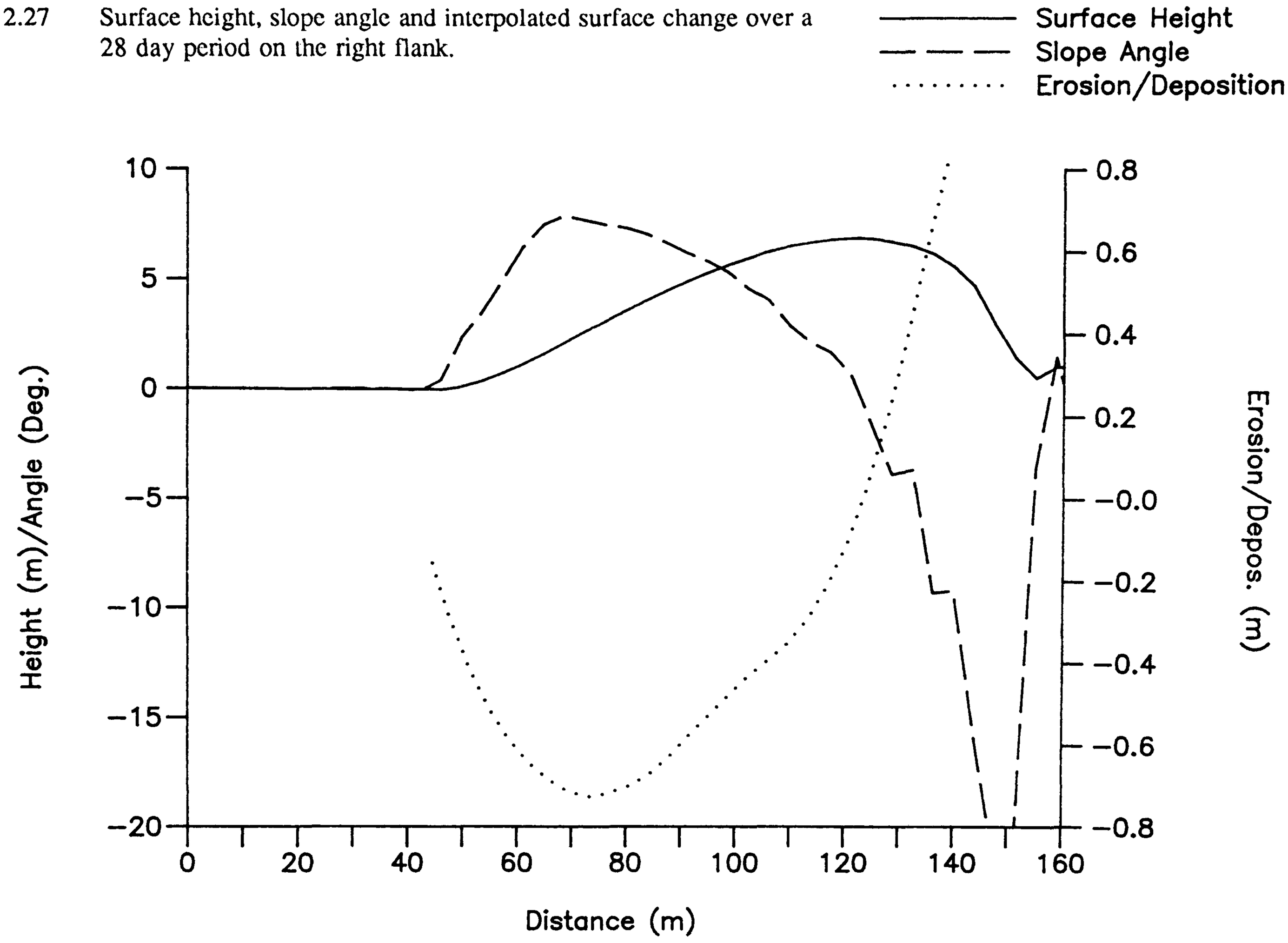

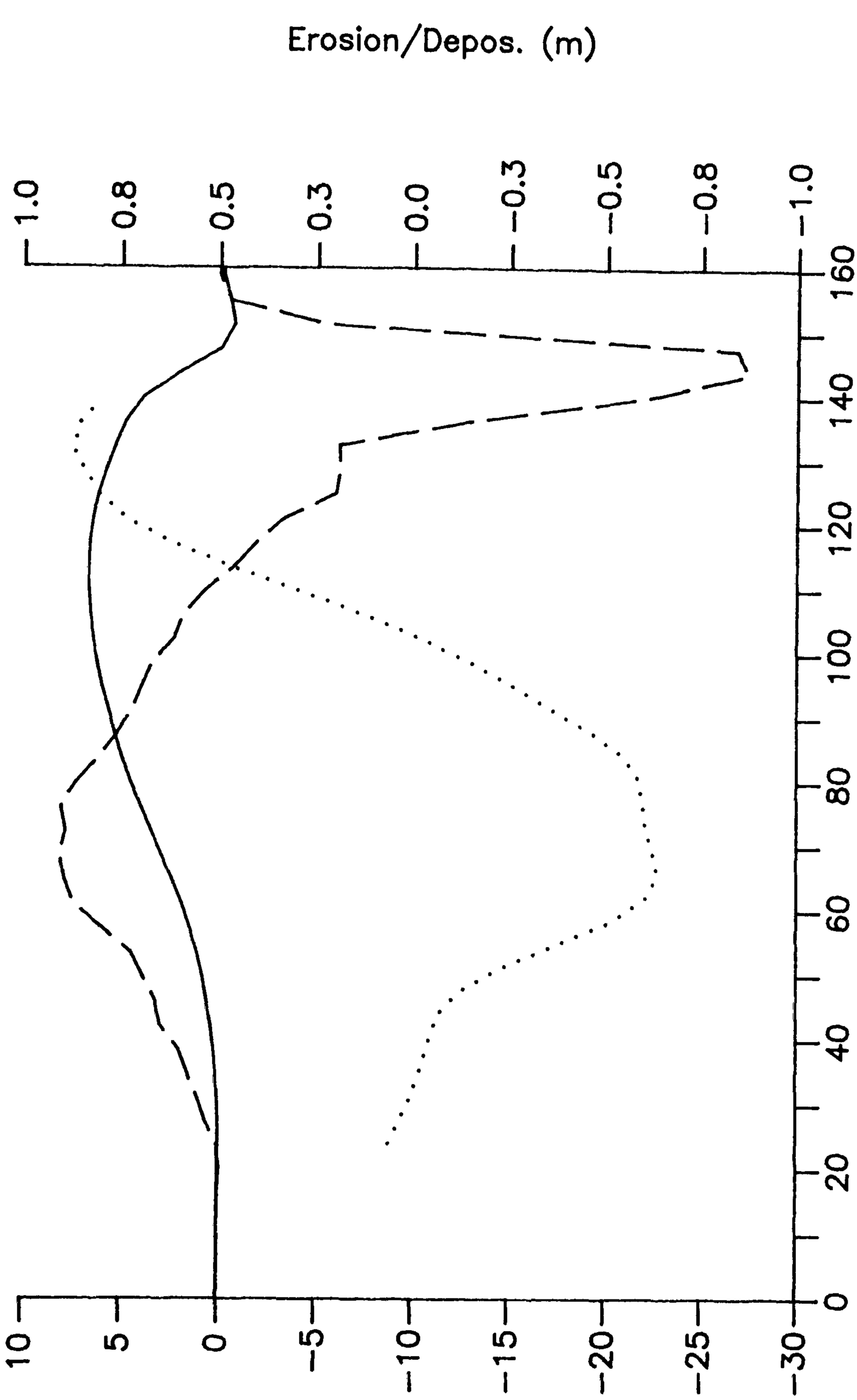

Figure 2.28 Surface height, slope angle and interpolated surface change over a 28 day period on the left flank.

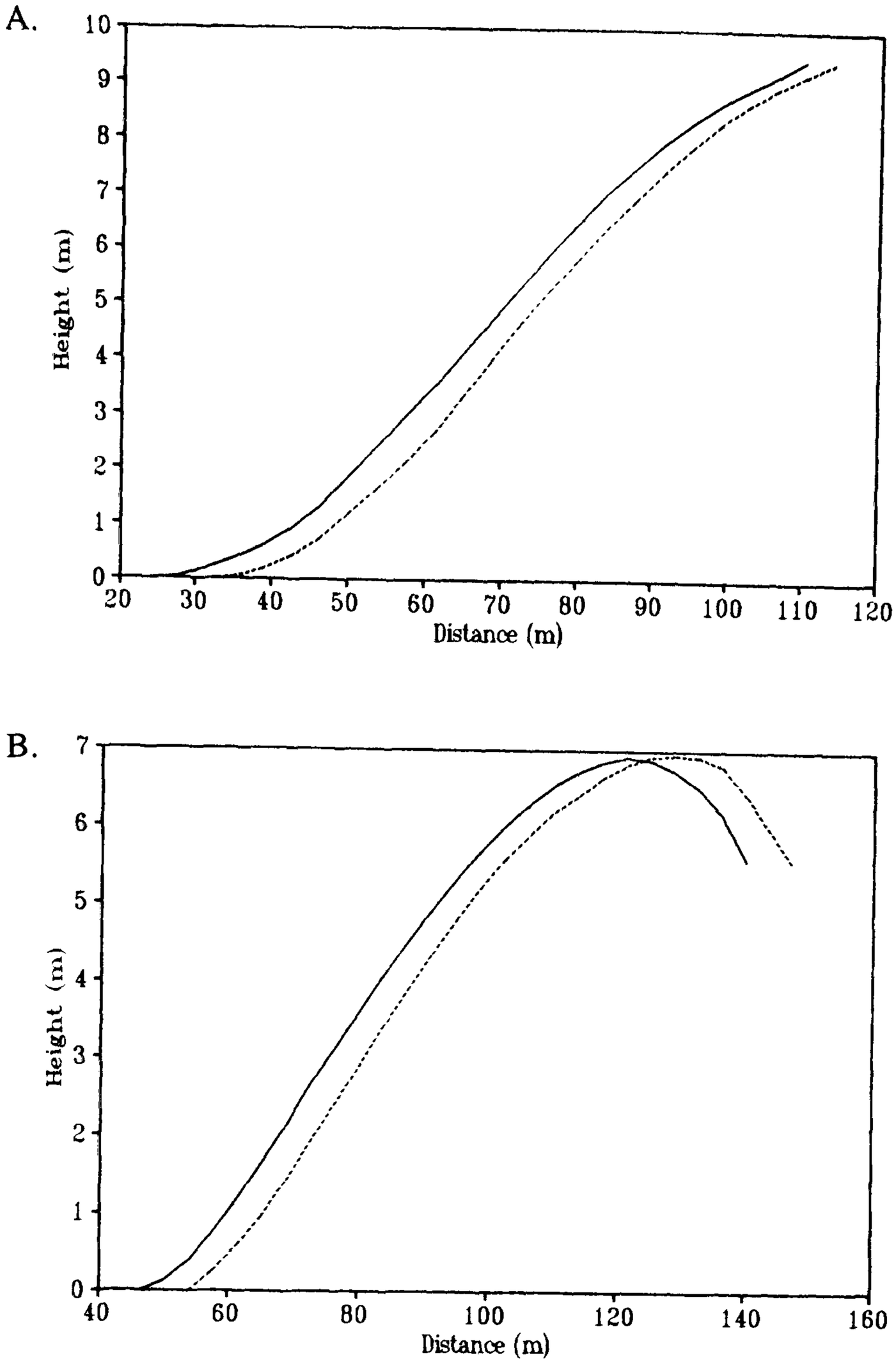

Figure 2.29 Development of the section line windward slope profiles over a 28 day period. A = centre-line; B = right flank; C = left flank.

predicted surface change (using Equation 2.5) shown in Figure 2.25. It appears that simple statistical analysis is not sufficient to prove a dynamic relationship.

The study dune therefore appears to be in a state of semi-equilibrium. The right flank and centre-line demonstrate an equilibrium form whereas the left flank is in dis-equilibrium, resulting in the accumulation of sand upwind of the crest. This conclusion has some intriguing implications. First, different parts of a dune may be in (quasi-)equilibrium with prevailing conditions at different times. Secondly, crest-brink separation may illustrate one type of equilibrium form. Lancaster (1987) argued that crest-brink separated dunes may still be growing. He suggested that deposition downwind of the crest would cause the dune to grow vertically until the crest and brink coincide. This is an attractive argument, and one which appears to describe the dynamics of the left flank of the study dune (Figure 2.29c). However, it does not describe the right flank (Figure 2.29b) where the downwind translation of the dune occurred with no change in crest height. Lancaster's (1987) hypothesis suggested that crest-brink separated dunes are in dis-equilibrium, but this appears to be a simplification.

The inadequacy of Equation 2.5 in describing the dynamics of dunes, caused by the fact that it takes only geometric relationships into account, was recognised by Watson (1987). He noted that formulae which included the effects of airflow (*i.e.* shear stress) variation on the windward slopes of dunes were necessary to accurately describe dune dynamics.

2.4.3 Velocity Measurements

Effects of Atmospheric Turbulence and Instability

In flows with low Reynold's numbers the effect of thermal stability or instability on wind velocity profiles can become significant. If strong thermal heating or stratification occurs then the turbulence may be driven by buoyant forces, rather than mechanical forces and the velocity profile can become non-logarithmic. In order to determine aerodynamic roughness (z_0) and shear velocity (u_*) from such profiles, correction factors have to be employed. Rasmussen *et al.* (1985) and Rasmussen (1989) stated that omitting the stability correction could lead to errors in u_* of the order of 15-25%.

Correction factors have been proposed by Businger *et al.* (1971), Dyer (1974) and Högström (1988) and involve calculation of either the Monin-Obukhov length (L) or Richardson number (RI). The Monin-Obukhov length is a measure of the change in type of turbulence (mechanically

or thermally driven) with height. Hence, it is a measure of the height at which velocity profiles can be measured before the effects of buoyancy need to be taken into account. The Richardson number, however, is more commonly used and more simply calculated. It describes the ratio of free to forced convection:

$$RI = g(\delta\theta/\delta z)/T_0(\delta u/\delta z)^2 \qquad \textbf{(2.6)}$$

Where:

g = gravitational acceleration
$\delta\theta/\delta z$ = average potential temperature gradient
T_0 = surface reference temperature
$\delta u/\delta z$ = average velocity gradient.

The Richardson number is positive for a stable layer and negative for an unstable one. Where RI exceeds +1, spontaneous turbulent motions are impossible and eddies penetrating such a region are quickly absorbed. Sufficient damping of turbulent motion to produce laminar conditions can occur where $RI \geq 0.2$ (McIntosh & Thom, 1981). In contrast, where $RI \leq -0.1$ the extra turbulence resulting from free convection is enough significantly to disturb the logarithmic velocity profile (McIntosh & Thom, 1981). The range of RI within which logarithmic velocity profiles can be expected is:

$$-0.01<RI<0.01$$

Outside these limits the effects of buoyancy should be accounted for, although McIntosh & Thom (1981) state that limits of ±0.04 are fairly reasonable.

In order to confirm the neutrality of the boundary layer in the present study, temperature gradients were measured with self-aspirating temperature probes (Figure 2.30) concurrently with wind velocity at heights of 0.35 m and 1.0 m at the reference station site. The Richardson number was then calculated using the finite difference equation:

$$RI = g/T.\ \delta T.\delta z/(\delta u)^2$$

where:

T = average ambient temperature at z/2 (°K)

This calculation method (from McIntosh & Thom, 1981) has the advantage over Equation 2.6 because it does not require terms for potential temperature or surface reference temperature, both of which are difficult to measure. Figure 2.31 shows the calculated RI over a period of 12 hours (observations averaged over one minute) on 24.8.90. At all times the boundary layer is slightly unstable as a result of excess heating, seldom within the strict limits ±0.01. However, the wind velocity measurements presented in this study were undertaken between 10.00 and 18.00 hrs. In this period the average RI is -0.028, well within the "reasonable" limits of McIntosh & Thom (1981). The error in measured velocity due to such instability is a function of height, and at elevations below 0.5 m the correction required is unimportant (Rasmussen *et al.*, 1985). Indeed, from the data presented in Rasmussen (1989), the error in velocity resulting from an RI of -0.03 (with $u_* = 0.4$ ms^{-1}) at 1 m height is only 1.2%. This error is insignificant when compared to the accuracy of the anemometers of ±6% (see Chapter 2.3.1). For these reasons, the boundary layer was considered to be essentially neutral and no correction was made for the effects of excess heating or instability.

Observations of Mean Velocity

As discussed in Chapter 2.1, there is little good empirical data concerning vertical and horizontal velocity profiles over sand dunes. Most studies merely document the change in velocity at a fixed height between the crest and toe (Lancaster, 1985) or the progression of wind velocity up the centre-line at a single height (Howard *et al.*, 1977; Tsoar, 1983, 1985; Livingstone, 1986). Very few studies have highlighted the development of vertical velocity profiles up the windward slope (Mulligan, 1988; Hesp *et al.*, 1989; Burkinshaw & Rust, 1992), and these have only presented three or four profiles with little discussion as to their significance or relationship to other studies. More detailed work has been accomplished in wind tunnels and these will be discussed in Chapter 4. However, comparable measurements to those presented here have been undertaken over coastal and inland hills such as Brent Knoll (Mason & Sykes, 1979), Askervein (Jensen & Zeman, 1985; Mickle *et al.* 1988) Nyland Hill (Mason, 1986) and Blashaval (Mason & King, 1985). These studies are published in the engineering literature and have not previously been compared to sand dune studies. However, due to their more detailed nature when compared to equivalent sand dune studies they are important reference points for the data presented in this study. Such comparisons are also applicable because the critical values of H/L (where H is height and L is half-length; see Figure 2.3) and L/z_0 in this study (0.24 and 0.8 x10^4 respectively) are comparable to those of the studies cited above (0.1 to 0.7 and 0.8 x10^4 to 5 x10^4 respectively).

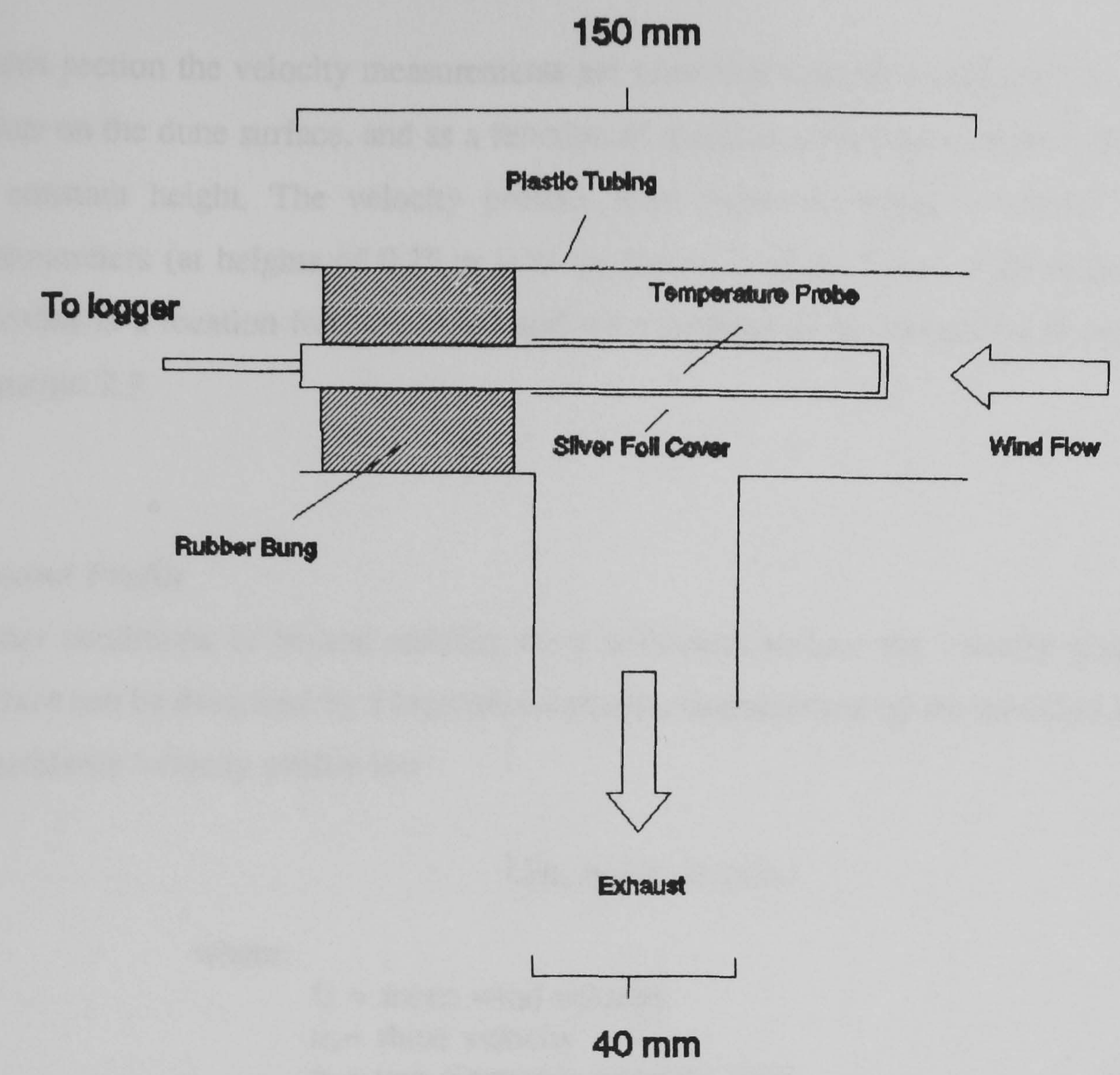

Figure 2.30 Design of the temperature probe.

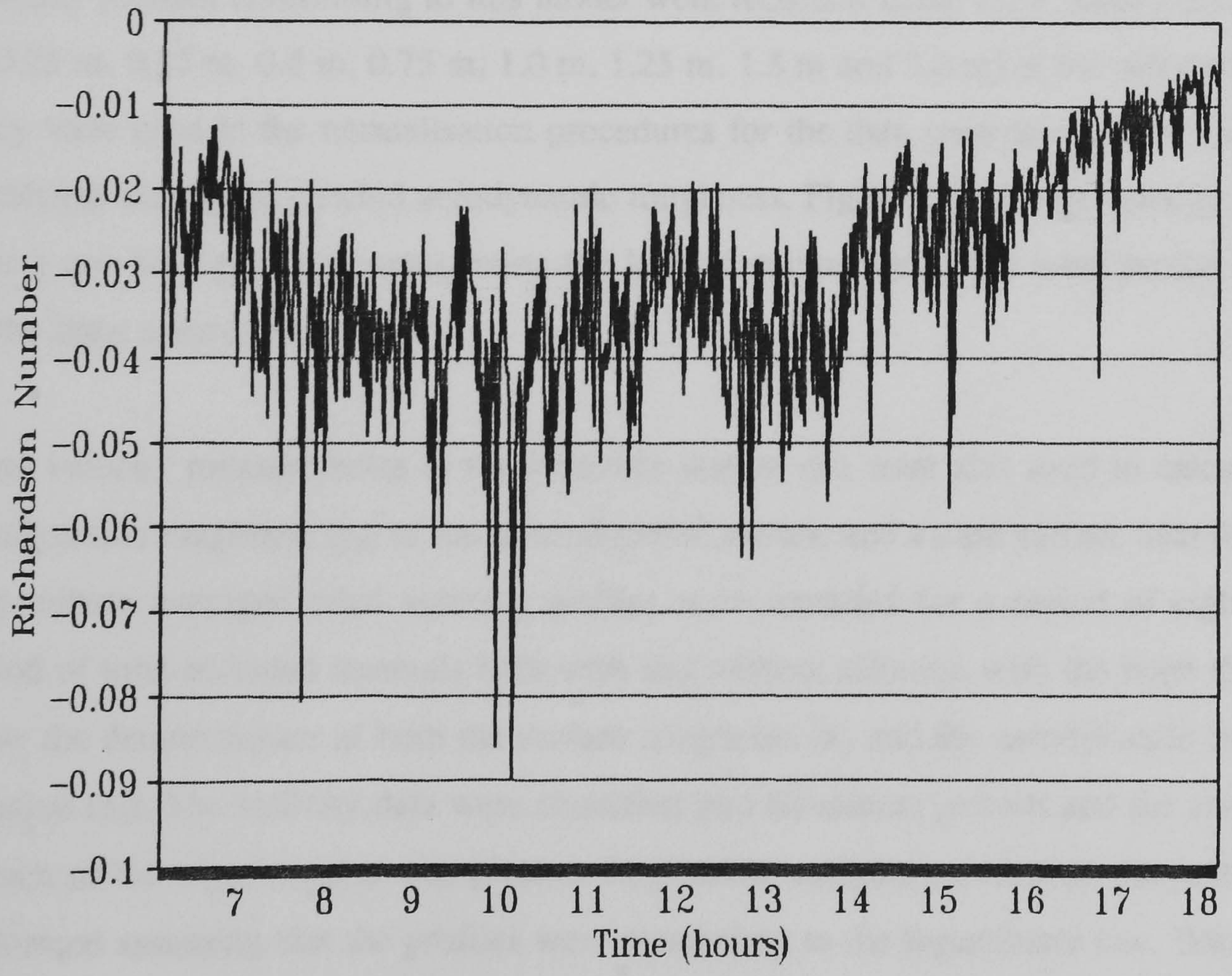

Figure 2.31 One-minute averaged measurements of the Richardson number (Ri) on 24.8.90.

In this section the velocity measurements are presented both as vertical profiles above selected points on the dune surface, and as a function of distance across the windward slope along a line of constant height. The velocity profiles were measured using a vertical array of seven anemometers (at heights of 0.25 m 0.35 m, 0.6 m, 0.75 m, 1.0 m, 1.25 m and 1.5 m) which recorded at a location for 30 minutes and were normalised by an upwind reference array using Equation 2.3.

Upwind Profile

Under conditions of neutral stability on a horizontal surface the velocity gradient above the surface can be described by a logarithmic profile, characterised by the modified Karman-Prandtl logarithmic velocity profile law:

$$U/u_* = 1/\kappa . \ln (z/z_0) \qquad (2.7)$$

where:

U = mean wind velocity
u_*= shear velocity
κ = von Karman's constant (0.4)
z = measurement height
z_0= aerodynamic roughness length.

Velocity profiles conforming to this model were recorded using eight anemometers (at heights of 0.25 m, 0.35 m, 0.6 m, 0.75 m, 1.0 m, 1.25 m, 1.5 m and 3.0 m) at the reference station site. They were used in the normalisation procedures for the data presented in this section and also in calculations of the upwind aerodynamic roughness. Figure 2.32 shows velocity data recorded over a one-hour period demonstrating the logarithmic nature of the wind profile 50 m upwind of the dune centre-line.

Wind velocity measurements at the reference station site were also used in calculations of the aerodynamic roughness (z_0) of the upwind gravel surface and a sand surface near the study dune. One minute averaged wind velocity profiles were recorded for a period of eight hours. This period of time included intervals both with and without saltation with the hope that this would allow the determination of both the surface roughness (k) and the aerodynamic roughness with saltation (z_0). The velocity data were classified into 60-minute periods and the average velocity at each of the eight heights was plotted. Regression analysis on each of the profiles was then performed assuming that the profiles were concordant to the logarithmic law. With this process the shear velocity (u_*) can be calculated from the slope of the regression line and the roughness

length (z_0) can be determined from the x-axis intercept (see Chapter 7 for further discussion of this method).

The resulting velocity profiles shown in Figure 2.33 demonstrate a log-linear increase in velocity with height. However, no focus is clearly defined in either of the graphs and the extrapolations to zero velocity in order to determine k and z_0 range from heights of 0.001 m to 0.02 m. There is no distinct contrast between periods of stable sand and periods of saltation, nor is there a discernible difference between the gravel and sand sites. From this data it is not possible to define either k or z_0 with any confidence. Other workers (Sarre, 1987, 1988; Mulligan, 1988) have had similar problems with the determination of z_0 in the field. A possible explanation for this could be inaccuracy in the anemometer readings. However, experimenters using wind tunnels and more accurate methods of velocity measurement (pitot tubes) have also experienced difficulty in defining a single focal height (Zing, 1953; Chiu, 1972; Gerety, 1985). Gerety (1985) noted that in most cases the picking of a single focal point is arbitrary.

To model the atmospheric boundary layer in the wind tunnel (see Chapter 4) and to simulate upwind conditions in the numerical model (Chapter 3) it was necessary to have an impression of the average upwind conditions in the field. From the data presented in Figure 2.33 it was possible to calculate a mean upwind roughness value (z_0) of 0.005 m and to estimate a reasonably characteristic u_* during sand driving conditions of about 0.4 ms^{-1}. The calculated roughness length agrees with typical values used in other studies (Rasmussen *et al.*, 1985)

It should be noted that there are considerable errors in determining these two parameters using the process of fitting a logarithmic profile to the velocity data. A method for evaluating the statistical errors associated with logarithmic velocity profiles was presented by Wilkinson (1983/1984). Using his arguments and taking a typical velocity profile measured in this study (Figure 2.34) a u_* of 0.43 ms^{-1} and a z_0 of 0.0045 m were calculated. However, statistical analysis showed that despite a correlation coefficient of 0.98 between the natural log of height above the surface and wind velocity, the errors associated with the estimates of u_* and z_0 were immense. The dashed lines on Figure 2.34 represent the 95% confidence limits of the calculated regression line (solid line). These lines, and their extrapolation to zero velocity, represent errors in u_* of ±23% and errors in z_0 of ±127%. Considering these errors (compounded by the efficiency of the anemometers, described in Chapter 2.3.1), the method of averaging to find a value of z_0 (as used above) and the estimate of a characteristic u_* appear reasonable.

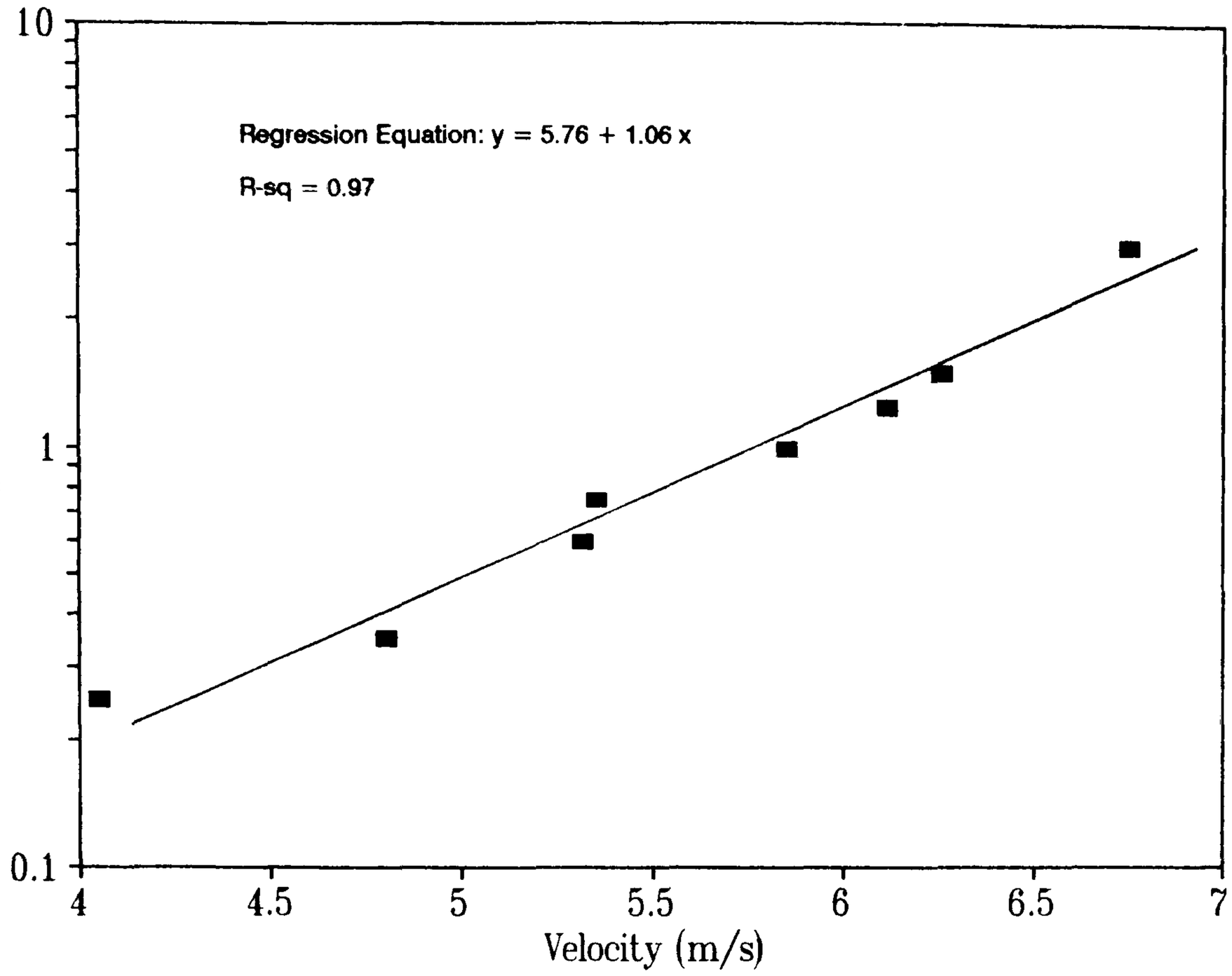

Figure 2.32 The upwind velocity profile measured at the reference site and averaged over one hour.

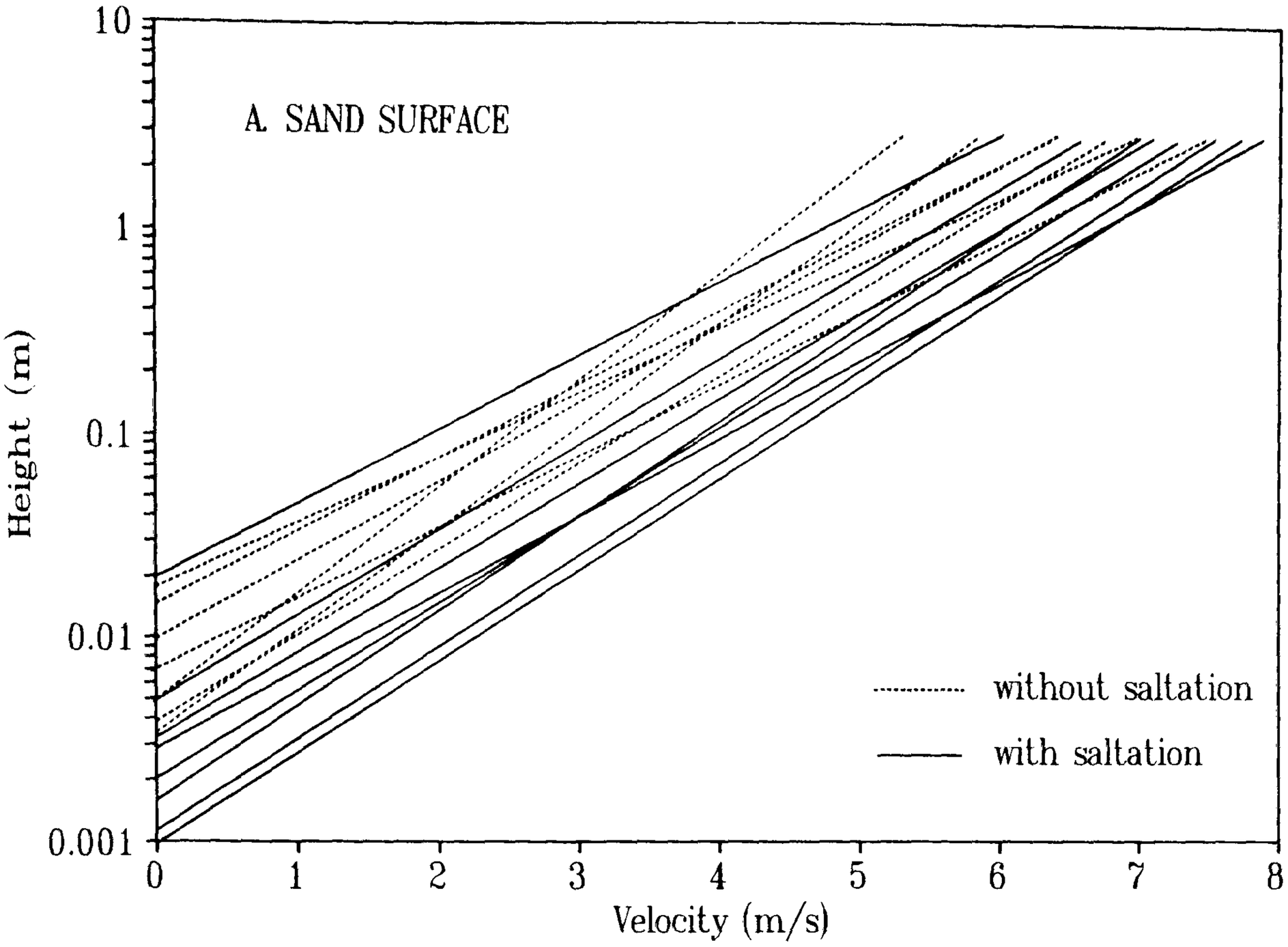

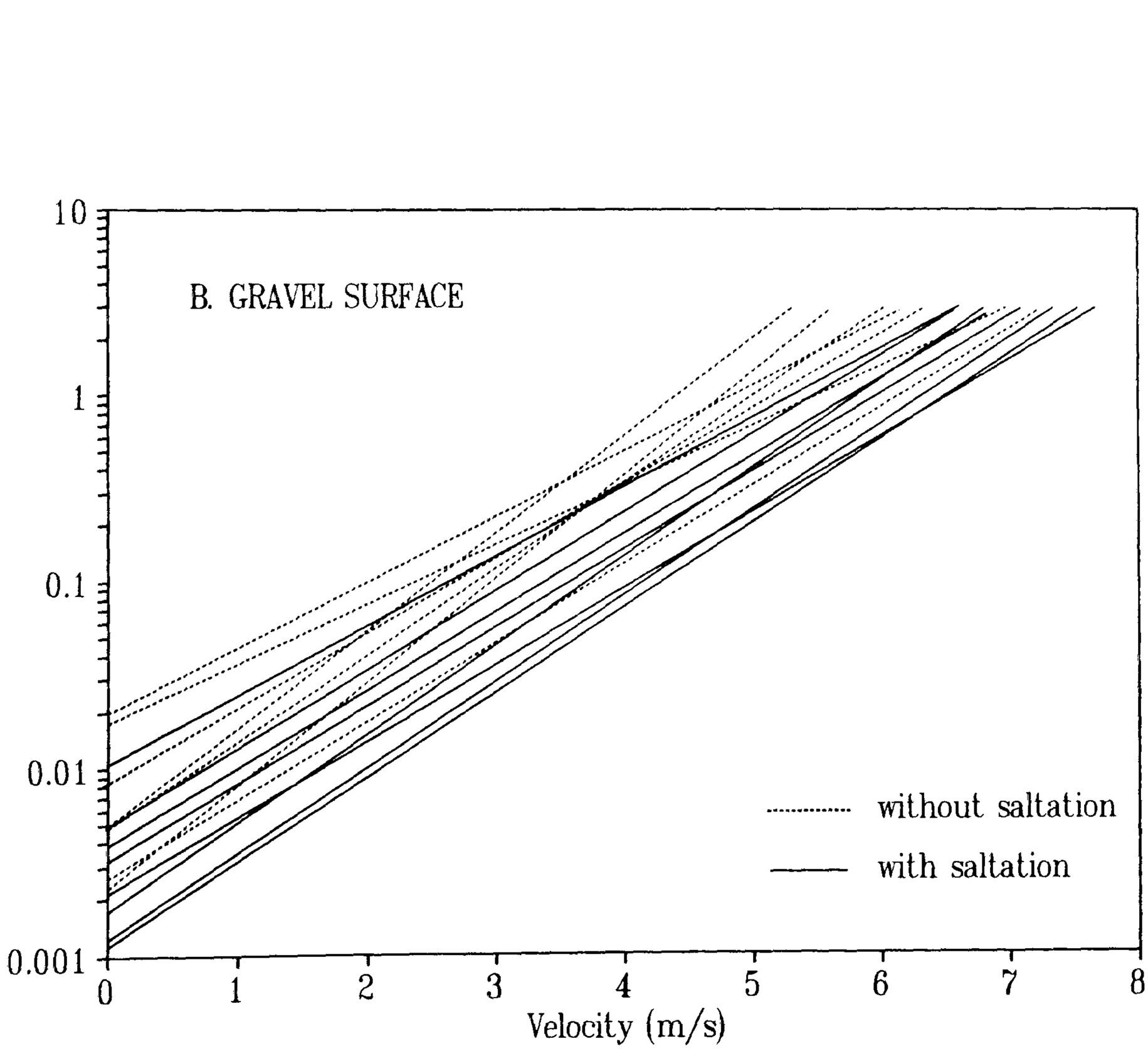

Figure 2.33 Sixty-minute averaged velocity profiles measured at the upwind gravel reference site (B) and on a neighbouring sand surface (A).

The Centre-line

The centre-line section is shown in Figure 2.9. The fractional speed-up ratio (δs) calculated from Equation 2.3 for four constant heights along the dune centre-line is shown in Figure 2.35. It indicates a reduction in near-surface wind velocity (at z = 0.25 m) at the toe of 11%. This compares with a reduction at a height of 1 m of only 5 or 6 %. This drop in wind velocity at the toe is succeeded by a uniform increase in wind speed at all heights to a maximum near the crest. This maximum in windspeed is greatest at z = 1 m where it attains a δs of 39%. This is in contrast to the speed-up at 0.25 m height where the δs is only 27%-28%. The speed-up becomes positive at x = ~45 m. This is upwind of the point where H/h = 0.3 (where H = maximum dune height and h = local surface height) which is the generally accepted location of speed-up inflection. On the study dune the point of inflection where δs=0 would be expected is at about x = 60 m.

The trend of the horizontal profile (Figure 2.35) in which there is a reduction in wind velocity at the toe and a rise to a peak at the crest is similar to that found by Livingstone (1986) and Howard *et al.* (1977). This trend has also been demonstrated on Askervein Hill (Walmsley & Salmon, 1984; Jensen & Zeman, 1985; Taylor *et al.*, 1987). It conforms to the expected pressure gradient over the dune with the approach flow being retarded, resulting in an adverse (increasing) pressure gradient and a reduction in velocity. This is succeeded by a decline in pressure as the streamlines converge over the windward face of the dune, resulting in velocity speed-up. The decline in the rate of acceleration in the crestal region is consistent with a crestal convexity in the dune profile and has also been found by Nϕrstrud (1982), Walmsley *et al.* (1982) and Tsoar (1985).

The maximum speed-up of ~39% is slightly less than the maximum calculated by the Jackson & Hunt (1975) formula of 44%.

$$\delta s_{max} = 2H/L \qquad \textbf{(2.8)}$$

Where:

δs_{max} = maximum fractional speed-up
H = maximum hill height
L = hill half-length

The height of the δs_{max} is more easily seen in Figure 2.36 which shows selected vertical profiles of speed-up along the dune centre-line. In each of the profiles where δs > 0 (profiles D, E and F) the maximum speed-up is at the highest measurement level of 1.5 m, although it is relatively

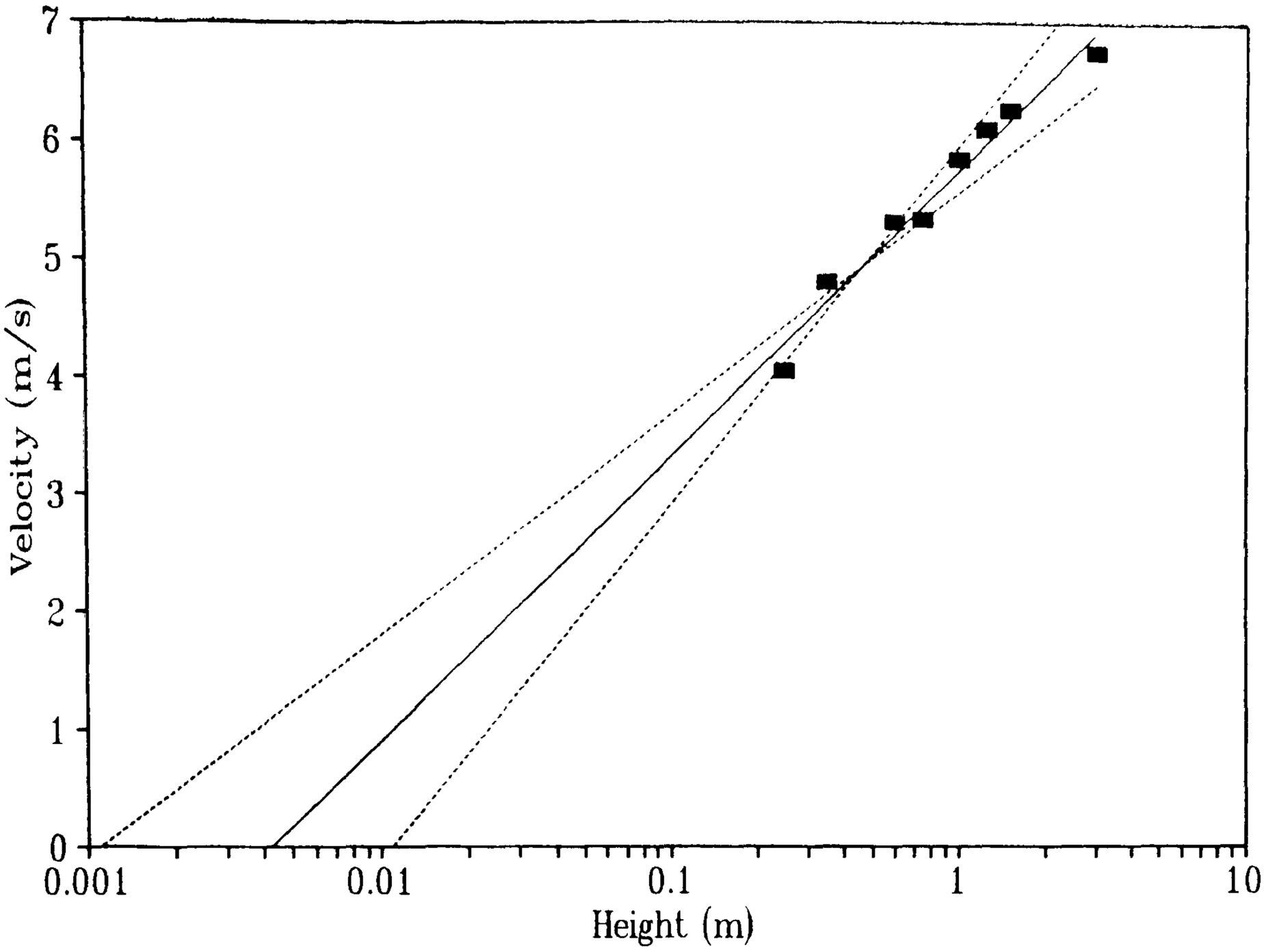

Figure 2.34 The 95% confidence limits (dashed line) of the regression line (solid) calculated through the upwind velocity profile. $u_* = 0.43$ ms^{-1} (±23%); $z_0 = 0.0045$ m (±127%).

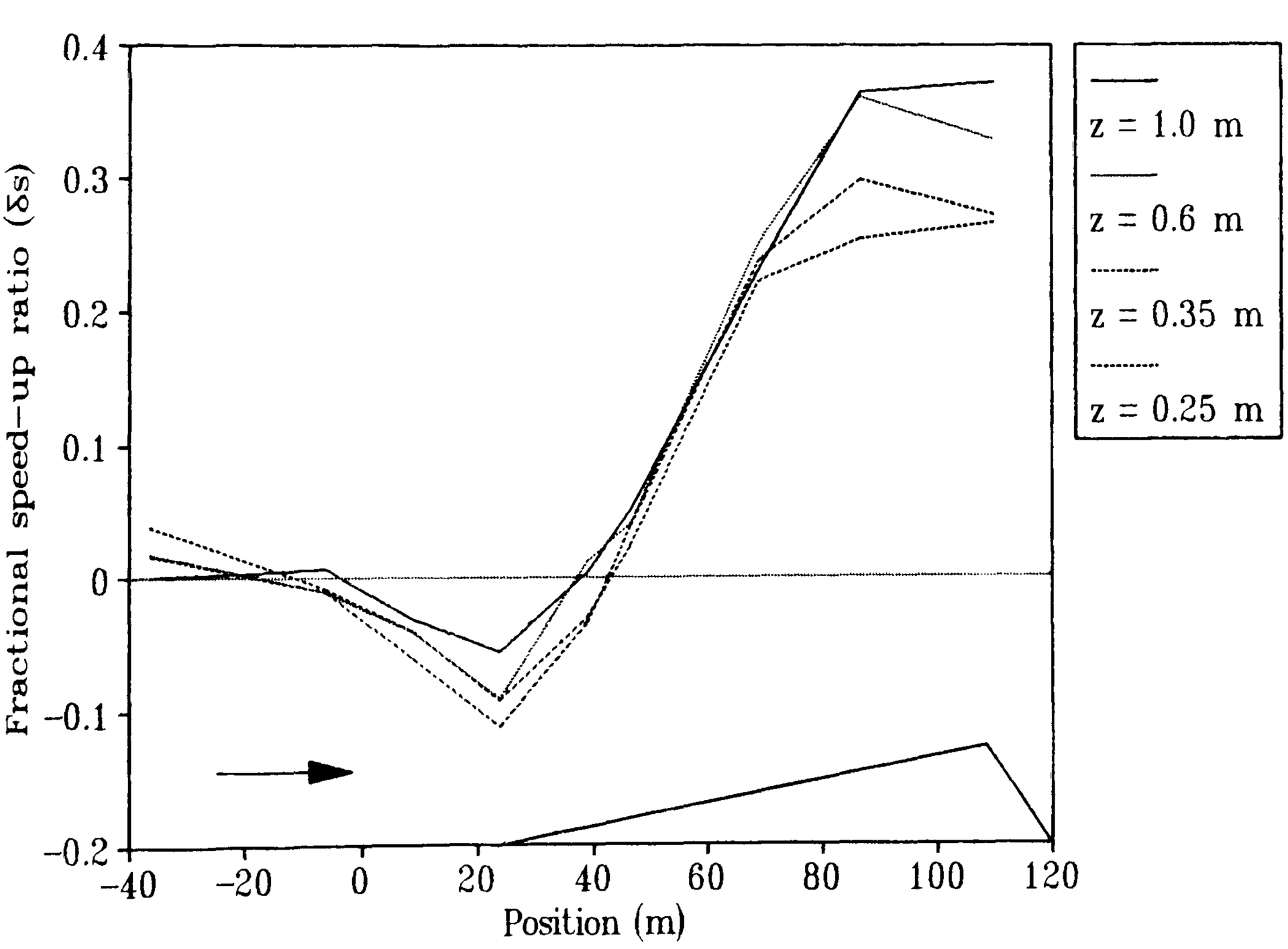

Figure 2.35 Fractional speed-up ratio (δs) on the dune centre-line at four heights.

constant upwards of 1 m. This is higher than that predicted by the inner-layer depth calculation of 0.55 m using the Jensen *et al.* (1984) expression (Equation 2.2), although it is in quite close agreement with the depth calculated from the original Jackson & Hunt (1975) theory of 1.90 m (Equation 2.1). However, vertical velocity profiles measured over Askervein Hill (Taylor *et al.*, 1987; Teunissen *et al.*, 1987; Mickle *et al*, 1988) and Nyland Hill (Mason, 1986) suggested that the maximum speed-up was at about l/3 (where l = the Jackson & Hunt inner-layer height) and that the Jensen *et al.* (1984) expression described this height better than the JH solution. A reworking of the Jackson & Hunt theory by Hunt *et al.* (1988a) also suggested that the δs_{max} should occur at a height of about l/3, dismissing the earlier JH hypothesis that it occurred at the boundary between the inner- and middle-layers. In this study the Hunt *et al.* (1988a) solution for the depth of the inner-layer is 0.68 m. The height of the δs_{max} in this study may therefore reasonably be expected anywhere between 0.22 m (*i.e.* 0.68/3) and 1.90 m (the depth of the inner-layer using the original JH solution). Gong & Ibbetson (1989) stated that it was reasonable to expect that the maximum speed-up might occur at some height intermediate between the three estimates. Furthermore, the Jackson & Hunt (1975), Jensen *et al.* (1984) and Hunt *et al.* (1988a) formulae are order-of-magnitude estimates and in the past have been tested on hills with much larger inner-layers (10 m to 20 m in depth). The results presented here are therefore considered to be in reasonable agreement with the theory.

The height of minimum speed-up in the upwind profiles (A, B and C in Figure 2.36) is consistently at the lowest measurement height of 0.25 m, showing that the reduction in velocity around the toe is more important close to the surface.

The non-uniform nature of the vertical profiles of speed-up shown in Figure 2.36 has an important effect on the character of the wind profile. Figure 2.37 shows the wind velocity profiles with the ordinate on a logarithmic scale. The upwind profile (A) exhibits a log-linear profile. However, at B (15 m upwind of the toe of the dune) the profile is retarded at the base, resulting in a non-logarithmic profile. The acceleration of flow up the windward slope, with maximum acceleration at a height of about 1 m, results in increasingly non-logarithmic profiles up to the crest (profile F). Figures 2.38 and 2.39 show in more detail the profiles at the toe (Profile C on Figure 2.37) and crest (Profile F on Figure 2.37), confirming their non-logarithmic nature.

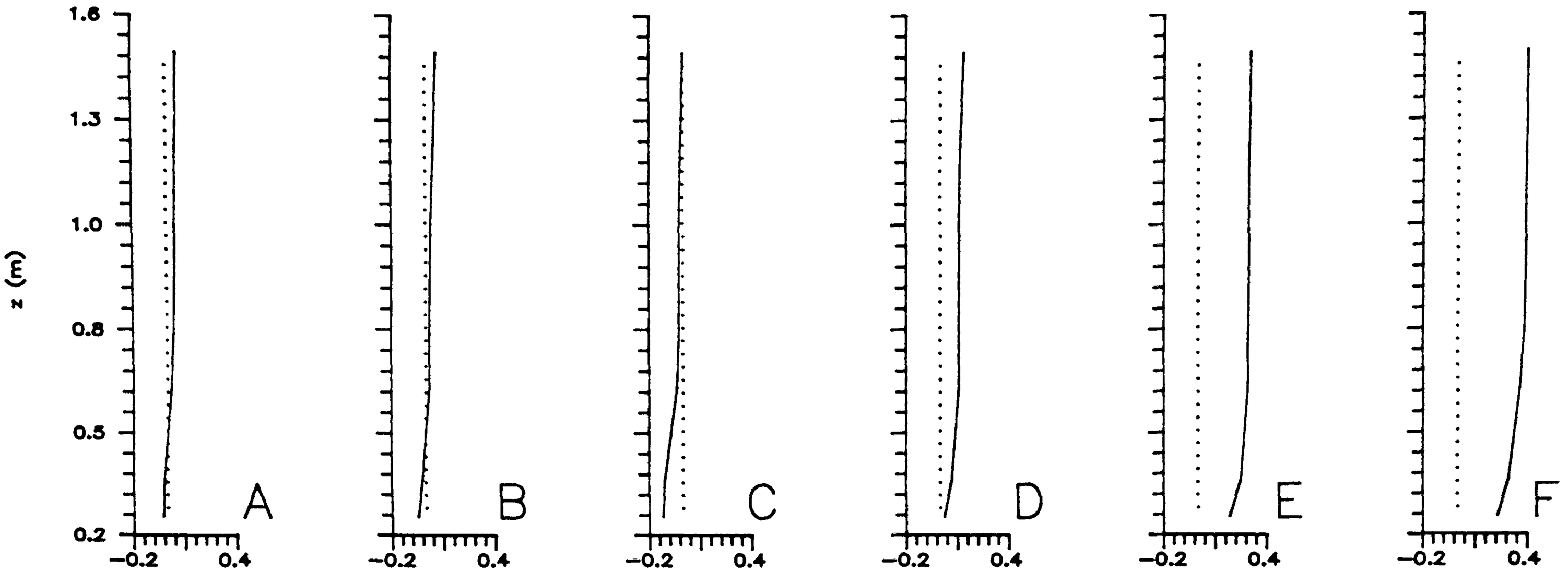

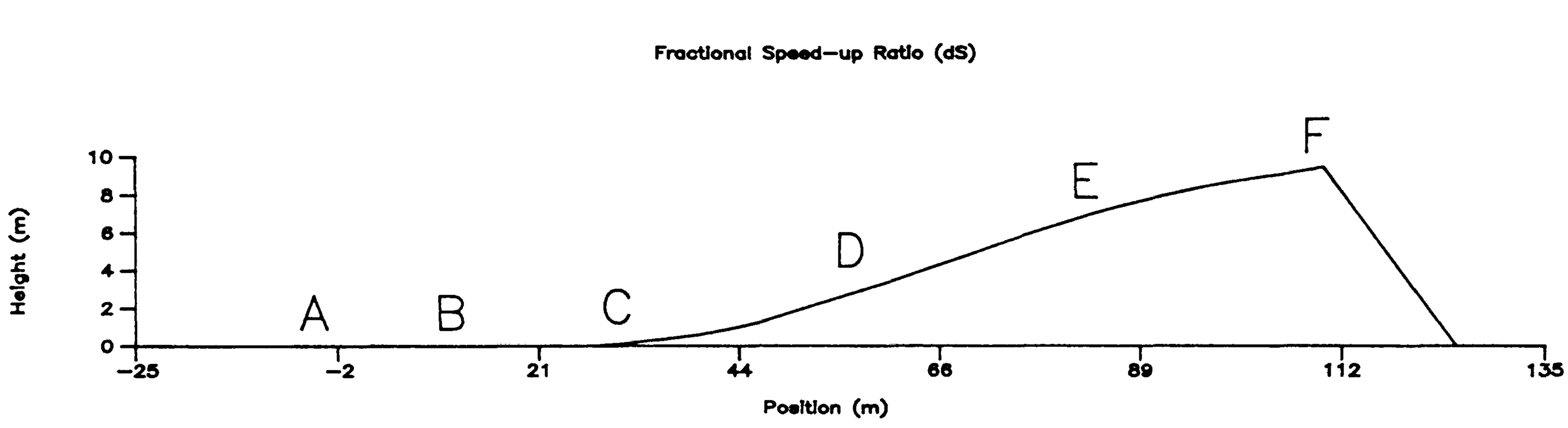

Figure 2.36 Vertical profiles of fractional speed-up ratio on the dune centre-line.

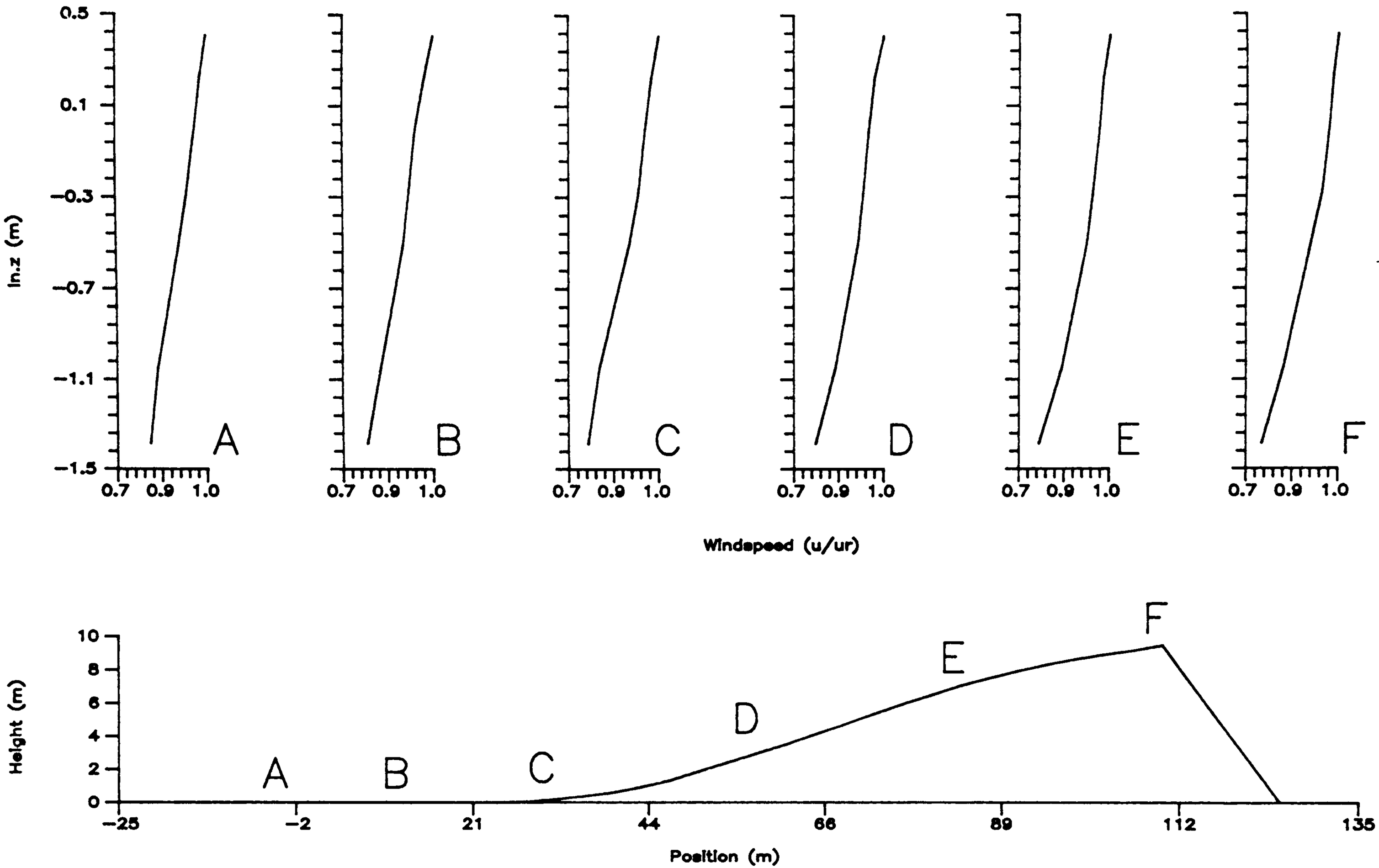

Figure 2.37 Vertical profiles of normalised windspeed on the dune centre-line (normalised by local windspeed at 1.5 m).

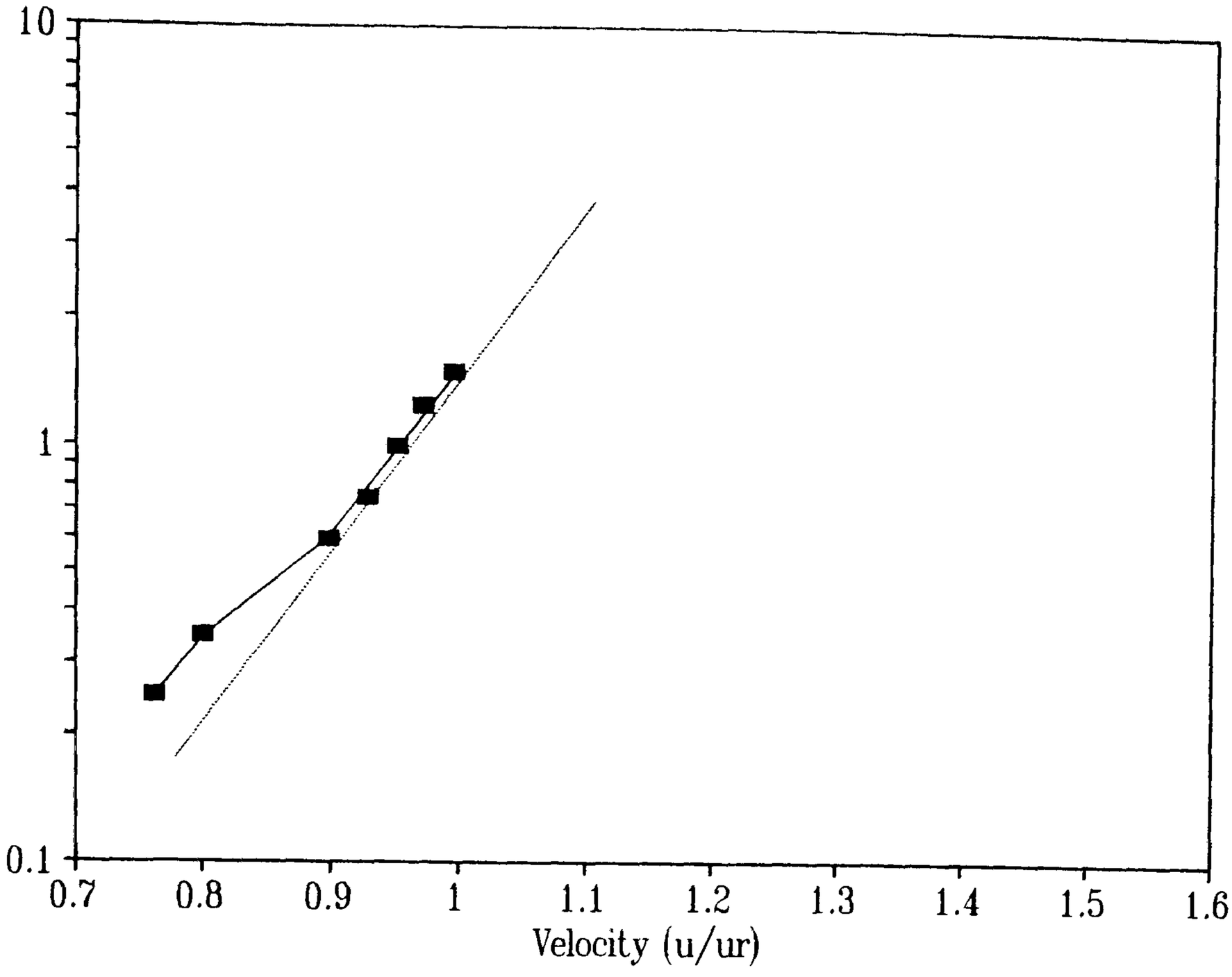

Figure 2.38 Velocity profile at the toe of the centre-line.

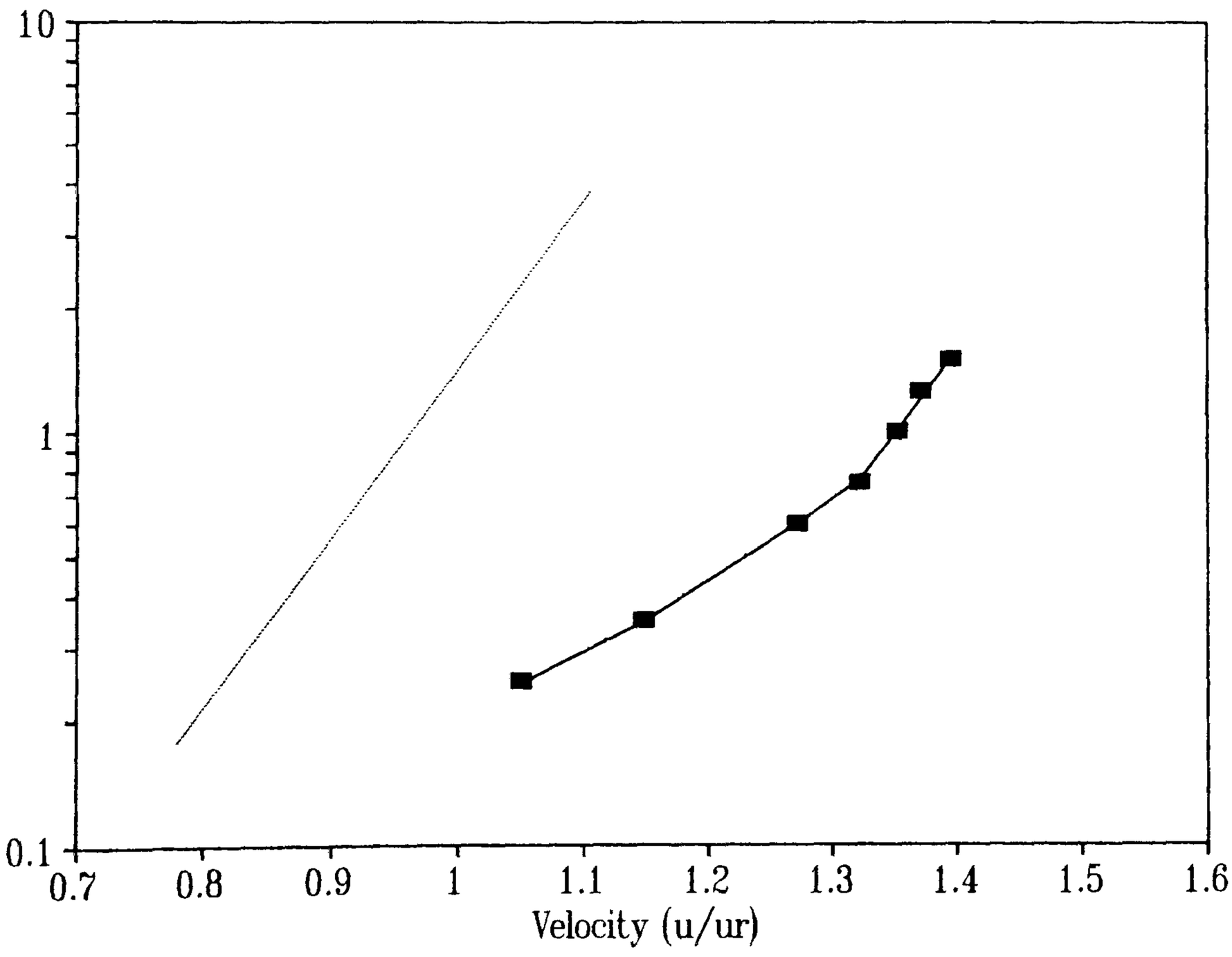

Figure 2.39 Velocity profile at the crest of the centre-line.

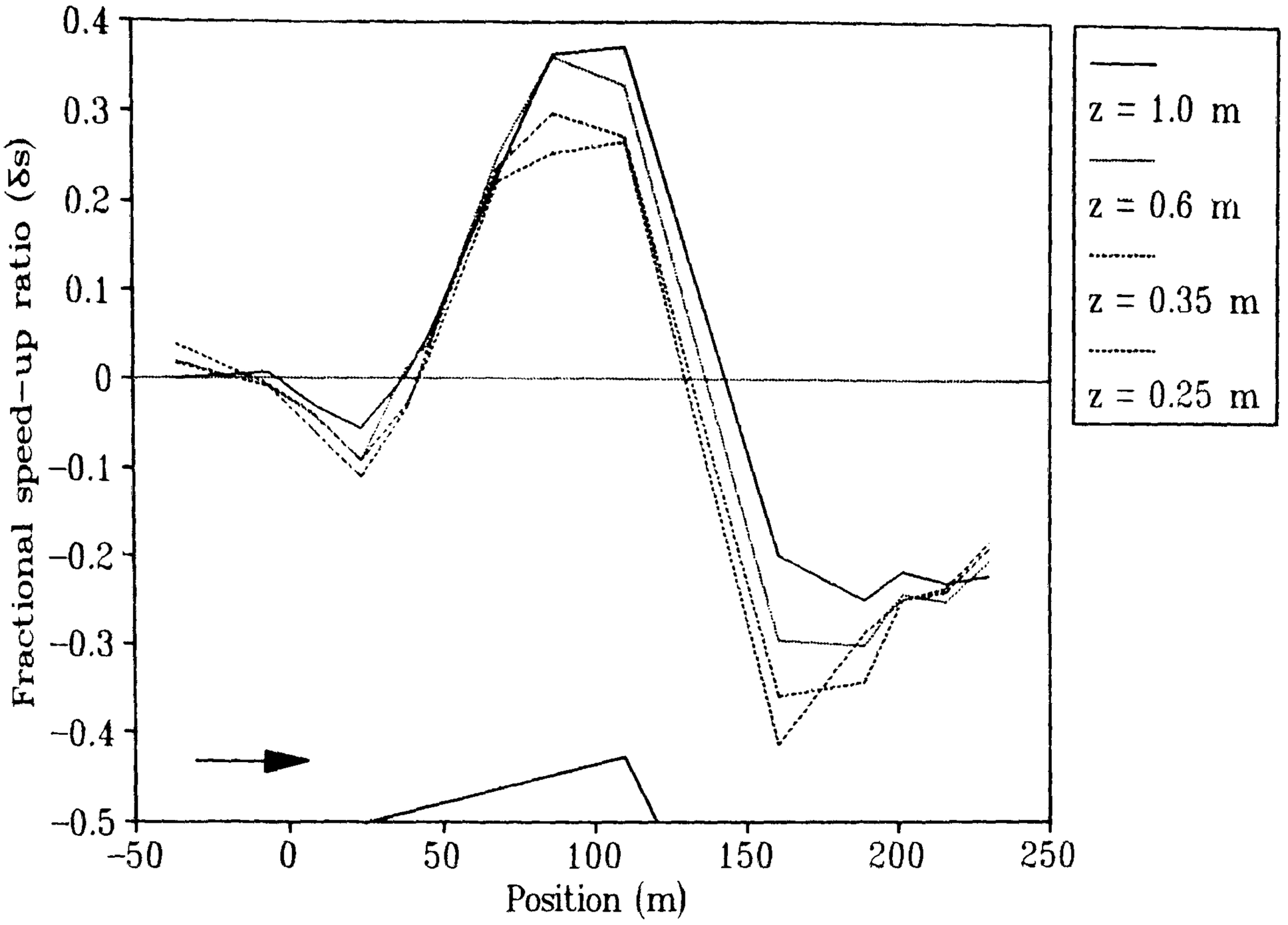

Figure 2.40 Fractional speed-up ratio on the centre-line of the windward slope and in the lee.

Similar non-logarithmic profiles have been found by Mulligan (1988), Butterfield (1991) and Burkinshaw & Rust (1992) over transverse sand dunes and the crest of Kettles and Nyland hills respectively by Mickle *et al.* (1988) and Mason (1986). However, this is the first evidence for the existence of non-logarithmic profiles in the basal regions of dunes due to the near-surface negative δs.

Further velocity measurements were carried out to the lee of the dune along the centre-line axis. These measurements were carried out downwind of the zone of re-attachment (as determined by nebkha orientations). The fractional speed-up ratios from these measurements are shown in Figure 2.40. The first downwind measurement is at 32 m from the base of the slip-face and shows a reduction in velocity compared to upwind values at a height of 0.25 m of over 40%. The degree of deceleration is strongly height dependent with the reduction in velocity at a height of 1 m of only ~25%. Measurements at all heights below 1 m then increase to a value 20% below their upwind level at a distance of over 100 m from the base of the slip-face. At this rate the velocity profile would recover its upwind character at a distance of about 170 m from the base of the slip-face, 17 times the height of the dune.

The Flanks

The velocity measurements on the left and right flanks (taken along the section lines shown in Figure 2.9) demonstrate similar patterns to those on the centre-line. Figures 2.41 and 2.42 show the calculated fractional speed-up ratios over the two flanks. In each case the velocity is retarded at the toe and increases to a maximum at the crest. The velocity is retarded between the crest and the brink on these crest-brink separated profiles.

On the left flank (Figure 2.41) the maximum retardation at the toe is at a height of 1 m and represents a velocity reduction of about 4%. This contrasts with the centre-line where the reduction in velocity at the toe was greatest near to the surface (at 0.25 m) and exhibited a reduction of about 11% (Figure 2.35). The smaller reduction on the left flank may be expected as the mass of the dune affecting the wind is less. However, the reversal in the degree of vertical retardation cannot be so easily explained. The development of δs up the windward slope of the left flank is fairly constant with height, and the maximum speed-up is at the crest (x = 110 m) where it reaches 43% at a height of 1 m. This contrasts with the δs at 0.25 m which is only 27%. This maximum speed-up is larger than the 33% calculated by Equation 2.8. The speed-up at all heights reduces to a value of about 15% at the brink as the streamlines diverge and the pressure gradient increases.

Figure 2.43 shows the development of δs with height at selected vertical profiles across the left flank. Profiles A, B and C show that the near-surface velocity is more accelerated when compared to higher levels as the flow progresses up the windward slope, contrasting with the speed-up found along the centre-line (Figure 2.36). However, profiles D and E exhibit similar profiles to the crest region of the centre-line with maximum speed-up at a height (1 m) generally equating with the height of the inner-layer. Profile F exhibits an almost constant δs with height.

The effect that these accelerations have on the nature of the wind profile is shown in Figure 2.44. Profile A, at the toe, exhibits a near logarithmic profile which might be expected considering the small amount of velocity reduction at this point. However, profiles B and C both show a deviation from the logarithmic profile as the near-surface velocity is accelerated up the windward slope. This effect is noticeable higher in the profiles in D and E, where the maximum δs at 1 m height significantly modifies the profile shape. The sharp reduction in velocity at the brink results in a distinctly non-logarithmic profile at F.

The development of δs across the right flank (Figure 2.42) is similar to that across the left flank. The reduction in velocity at the toe is the same, at 4%, but it occurs at a lower level (0.35 m) than the left flank (1 m in Figure 2.41). This is more in line with the relationship found at the centre-line (Figure 2.35). The speed-up on the windward flank shown in Figure 2.42 is less uniform than along the left flank and centre-line and the maximum δs of 35% occurs nearer the surface at a height of 0.35 m. In conflict with measurements on both the left flank and centre-line, the minimum δs at the crest (x = 117 m) occurs at a height of 1 m, the height at which the other measurements exhibited a maximum. Despite this, the maximum δs of 35% corresponds almost exactly with the δs_{max} of 34% calculated by Equation 2.8. At the brink, the δs at all measured heights is reduced to between 3% and 5%, with the more extreme reduction from crest to brink being at the lower measurement heights. This is expected considering that the maximum divergence of streamlines in this region is near the surface. Similar results have been presented by Mulligan (1988).

Figure 2.45 shows the vertical profiles of δs along the right flank of the dune. The shapes of the profiles are comparable to the left flank (Figure 2.43) and centre-line (Figure 2.36) profiles. However, Figure 2.45 demonstrates that the height of the maximum δs is highly variable along the windward slope. Profiles B, C and E exhibit maxima in δs close to the surface at 0.25 m. In contrast, D and F have maximum speed-up at higher levels. It is noticeable, that at the brink on both the left and right flanks (Profile F in Figures 2.43 and 2.45) the variation in δs with height is nearly uniform.

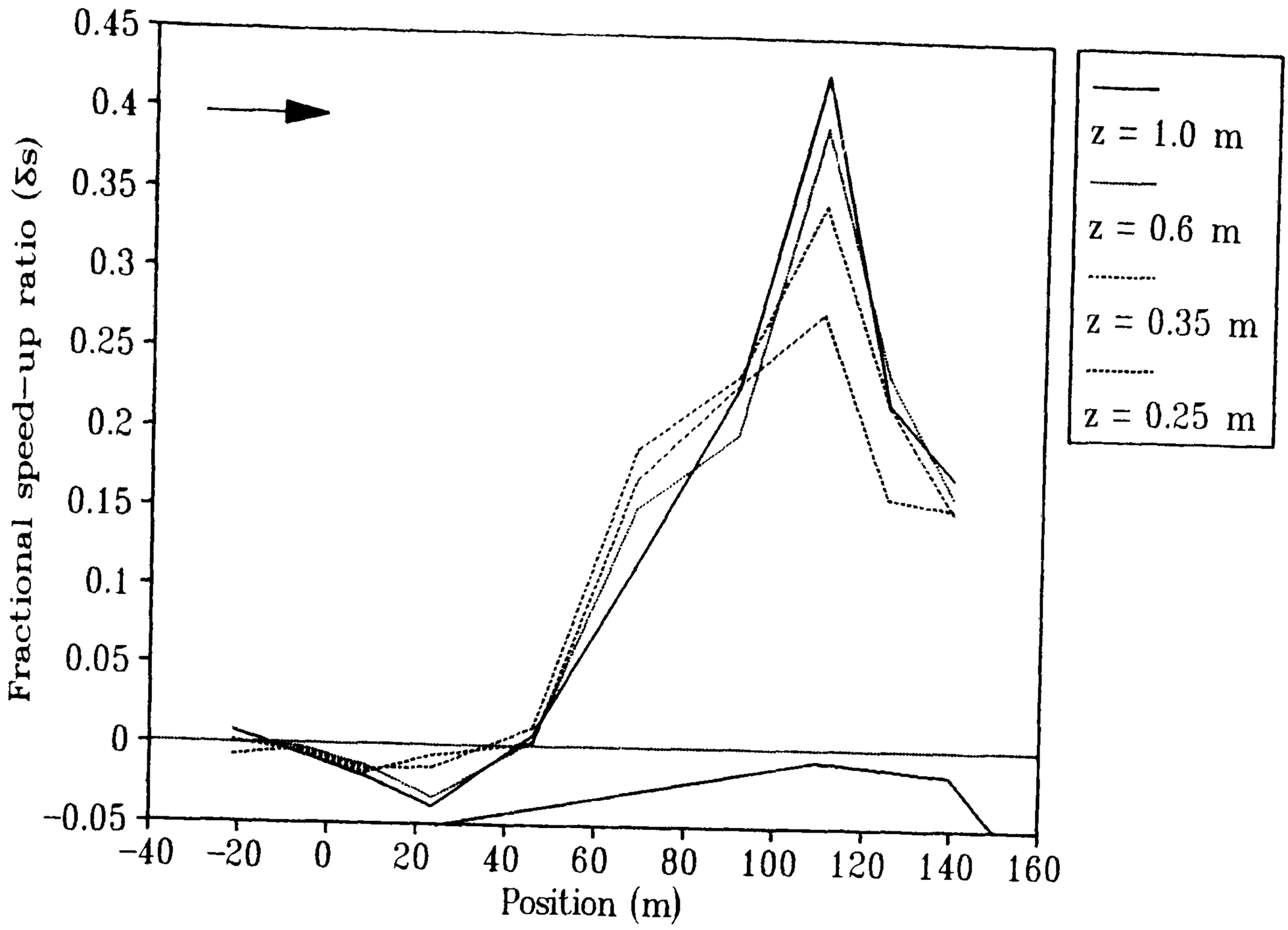

Figure 2.41 Fractional speed-up ratio (δs) on the left flank at four heights.

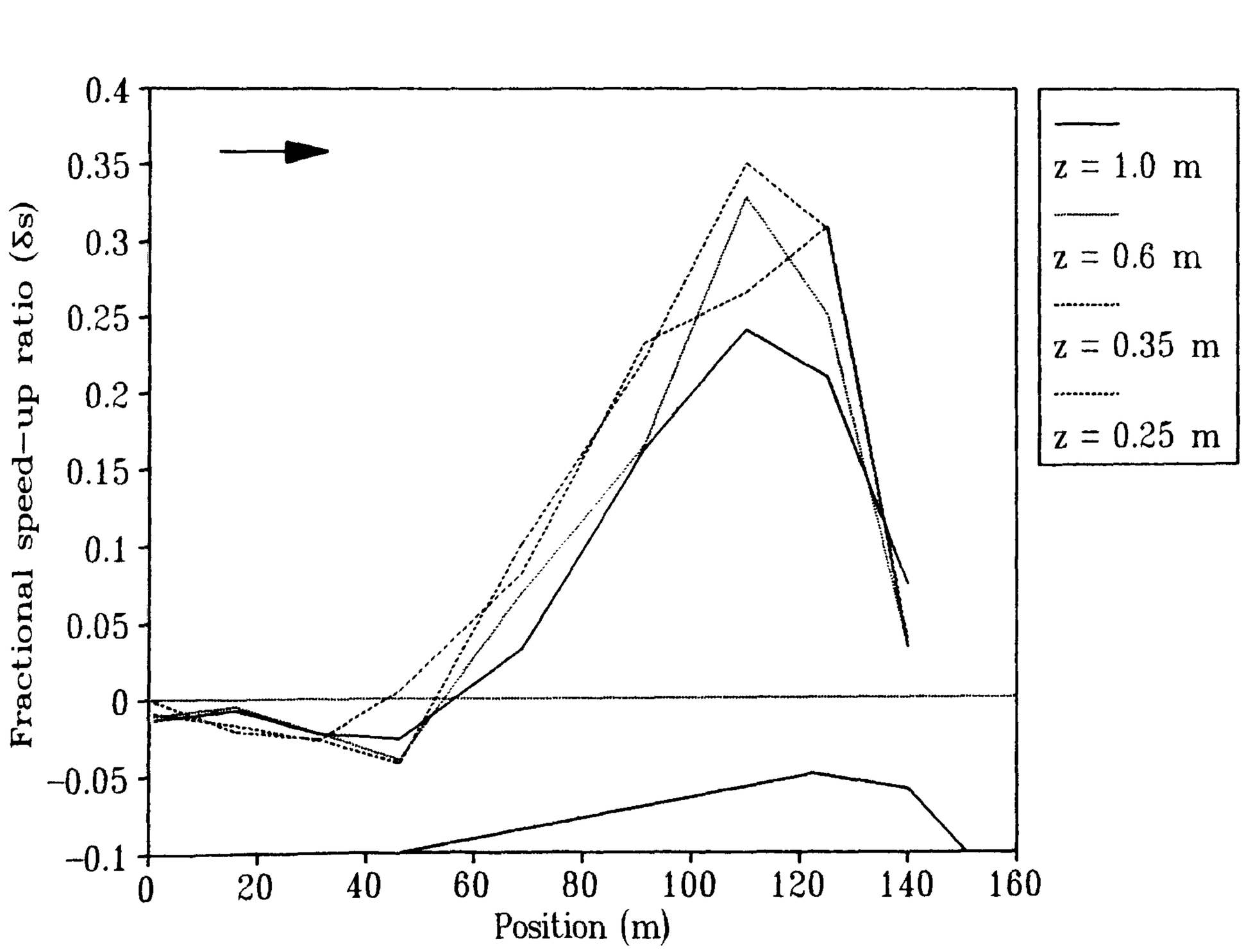

Figure 2.42 Fractional speed-up ratio (δs) on the right flank at four heights.

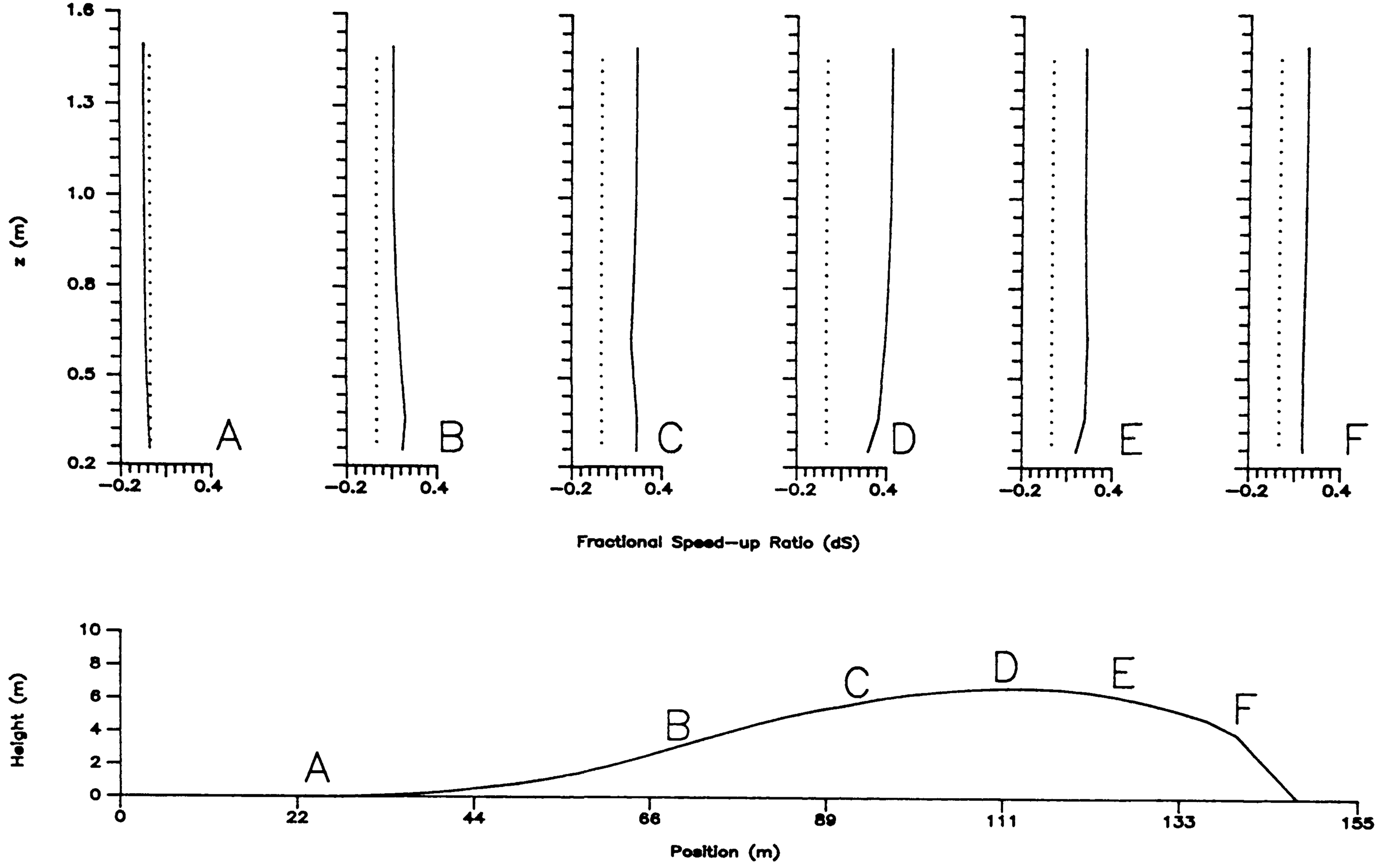

Figure 2.43 Vertical profiles of fractional speed-up ratio on the left flank.

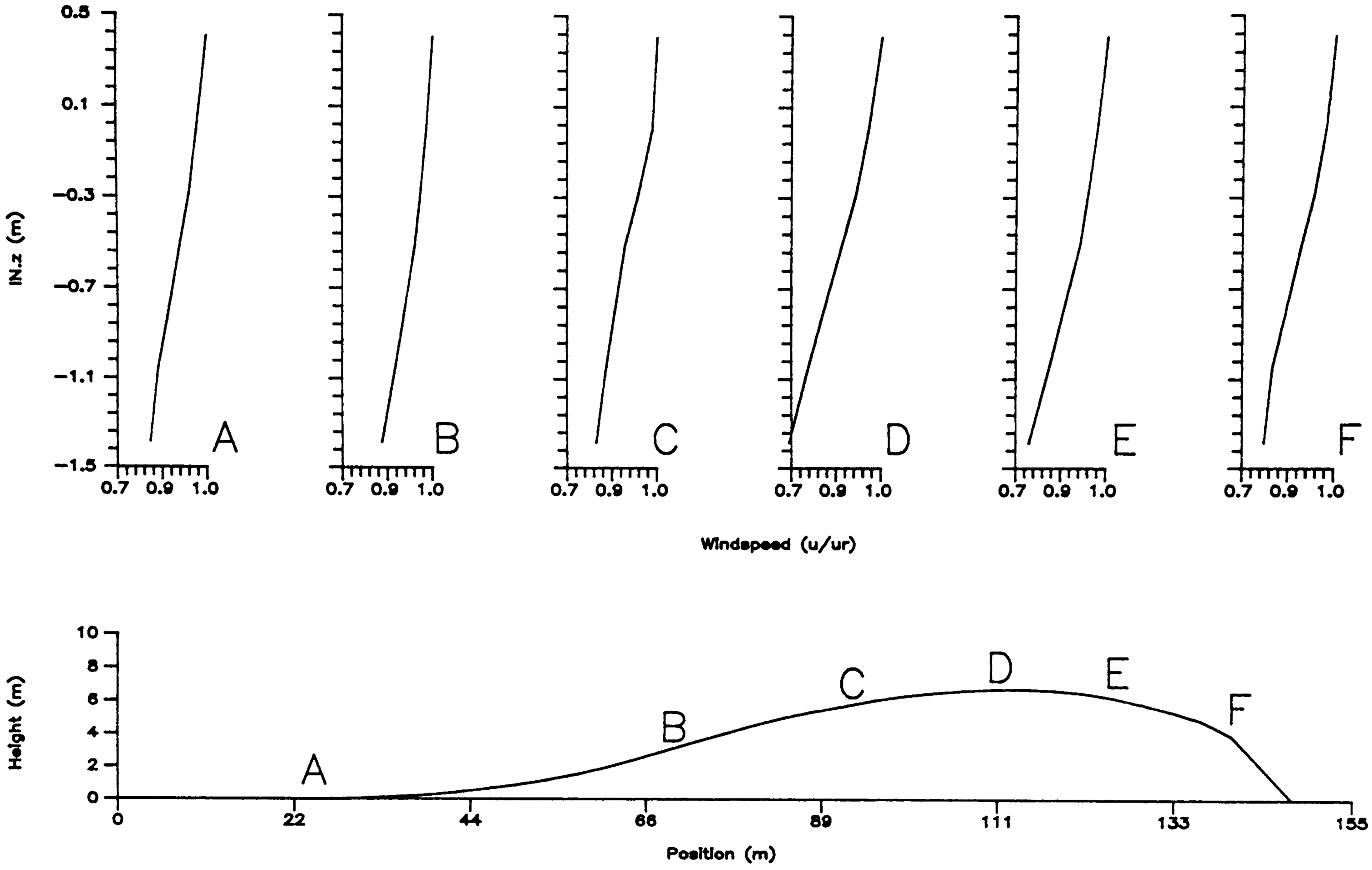

Figure 2.44 Vertical profiles of normalised windspeed on the left flank (normalised by local windspeed at 1.5 m).

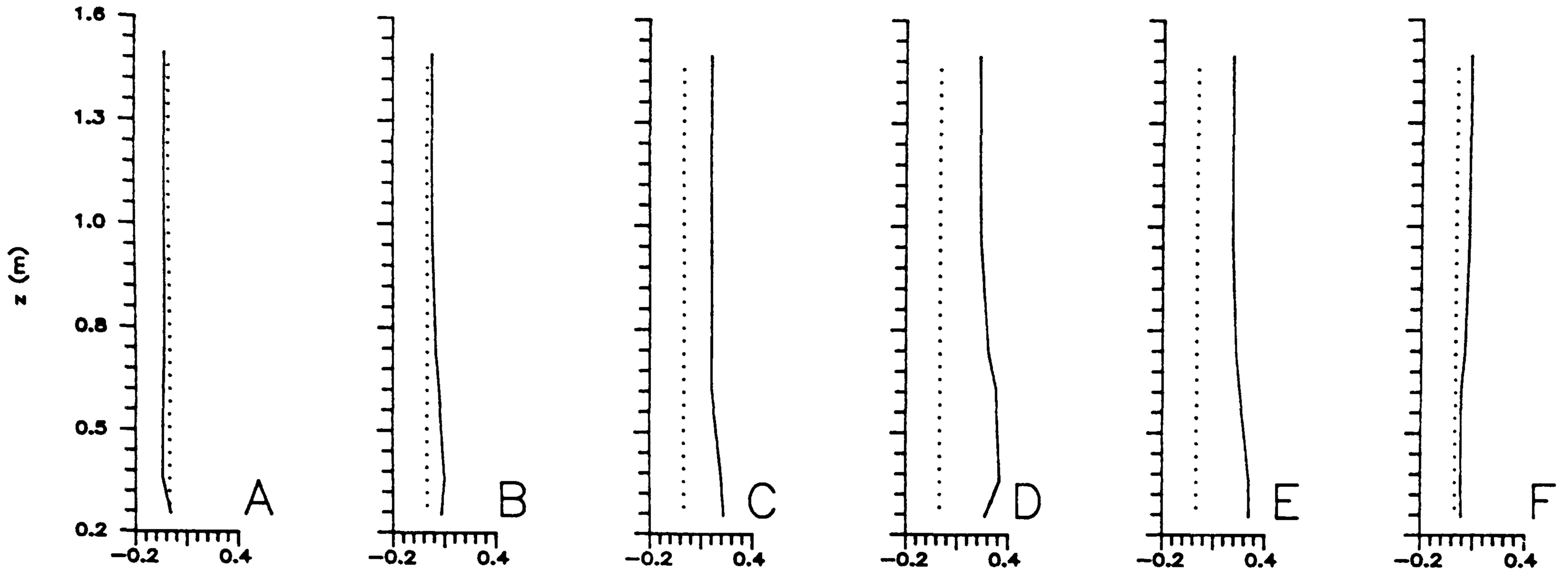

Figure 2.45 Vertical profiles of fractional speed-up ratio on the right flank.

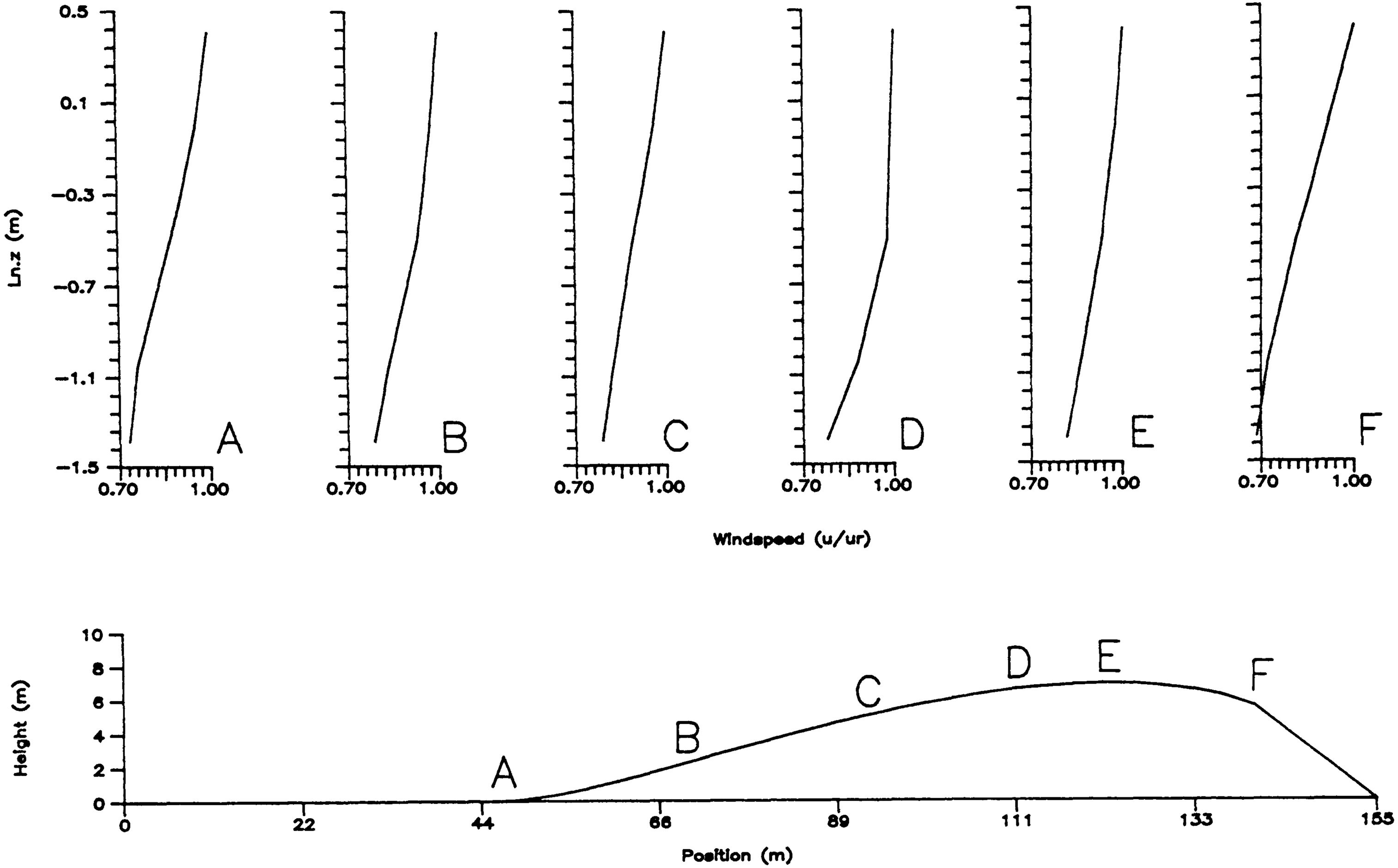

Figure 2.46 Vertical profiles of normalised windspeed on the right flank (normalised by local windspeed at 1.5 m).

The velocity profiles over the right flank (Figure 2.46) show the same non-logarithmic nature as the profiles along the left flank (Figure 2.44) and the centre-line (Figure 2.37). Unlike the left flank, a non-logarithmic structure is also evident at the toe of the dune (Profile A).

The Edge

Velocity measurements were also undertaken along the right edge of the dune (see Figure 2.9) using vertical arrays of four anemometers. Figure 2.47 shows a small (5%) reduction in windspeed at all measured heights on approaching the dune edge. This develops into an increase in δs of about 5% at the right edge itself. It is also noticeable that the near-surface δs at the dune edge is larger than that at higher levels (5% at 0.25 m compared to 1.5% at 1 m height).

These relationships might be due to a lateral deflection of airflow around the dune. This would cause a blockage to incoming air upwind of the edge, hence increasing the pressure gradient and leading to a decline in velocity. Due to the convergence of streamlines around the body of the dune, a region of windspeed increase would be expected at the edge itself, leading to decreasing pressure and flow acceleration. This effect would be dominant close to the surface where streamline convergence would be greatest. This argument is supported by the data in Figure 2.47. An alternative explanation is offered by the existence of a series of nebkha at this location which created a 1 m high ridge of sand extending laterally away from the dune. The velocity measurements may therefore have been strongly affected by the slope of the sand surface.

The data presented in Figures 2.20 and 2.21 showed no deflection of airflow at the surface around the edge of the dune, hence diminishing the likelihood of the former argument. It is therefore considered that the measurements presented in Figure 2.47 are a result of the non-uniform nature of the terrain.

2.4.4 Morphological Relationships

Figures 2.48 to 2.50 show the relationships between the surface slope angle and the rate-of-change of fractional speed-up ratio along each of the section lines. In every case there appears to be an association between the two variables with the maximum rate-of-change of speed-up generally coinciding with the maximum surface slope angle. The relationship is more noticeable close to the surface at 0.25 m height. On both the left and right flanks (Figures 2.49 and 2.50) the change in slope angles from positive to negative (*i.e.* at the crest and towards the brink) are characterised by a distinct drop in the rate-of-change of speed-up.

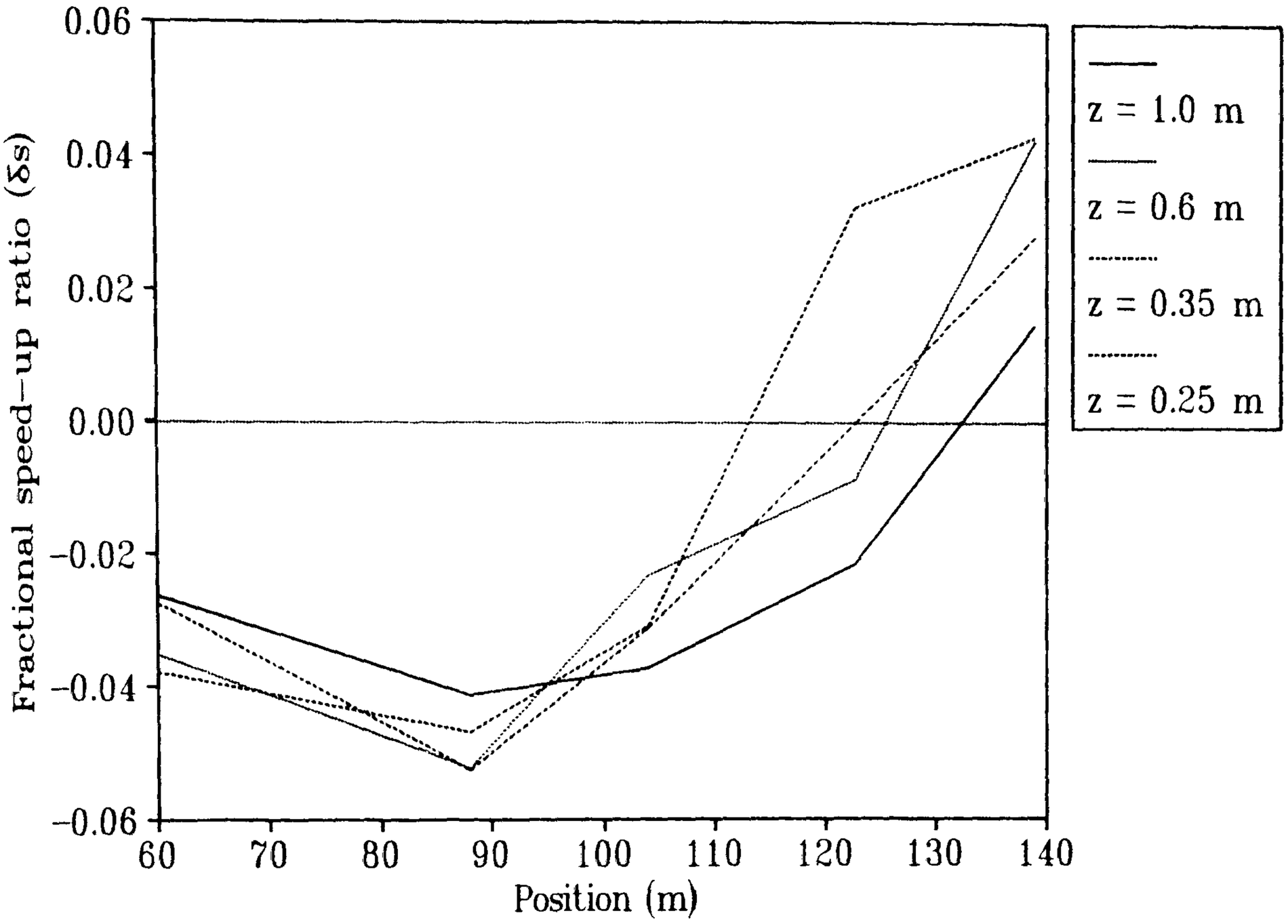

Figure 2.47 Fractional speed-up ratio (δs) at the right edge at four heights.

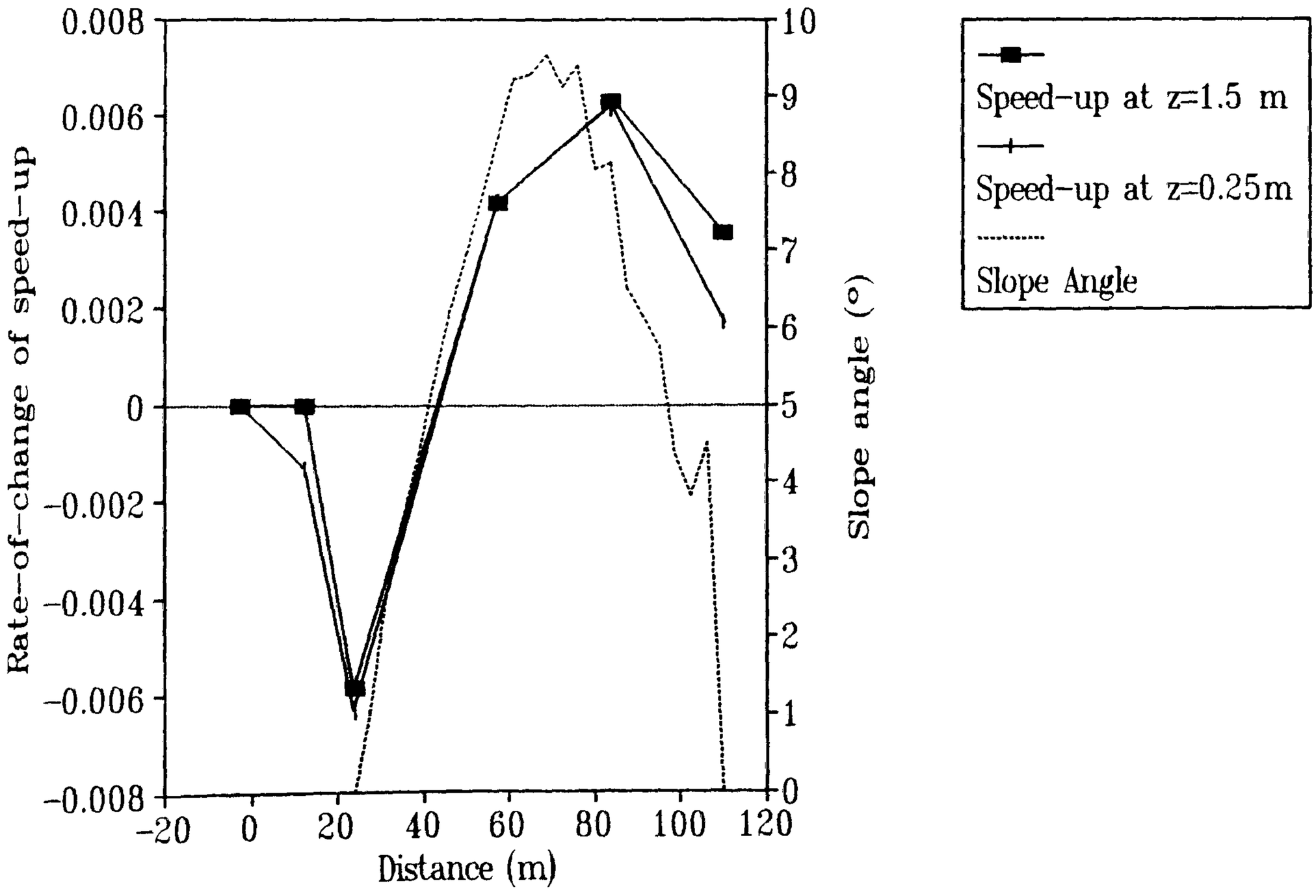

Figure 2.48 Relationship between slope angle and rate-of-change of fractional speed-up ratio on the centre-line.

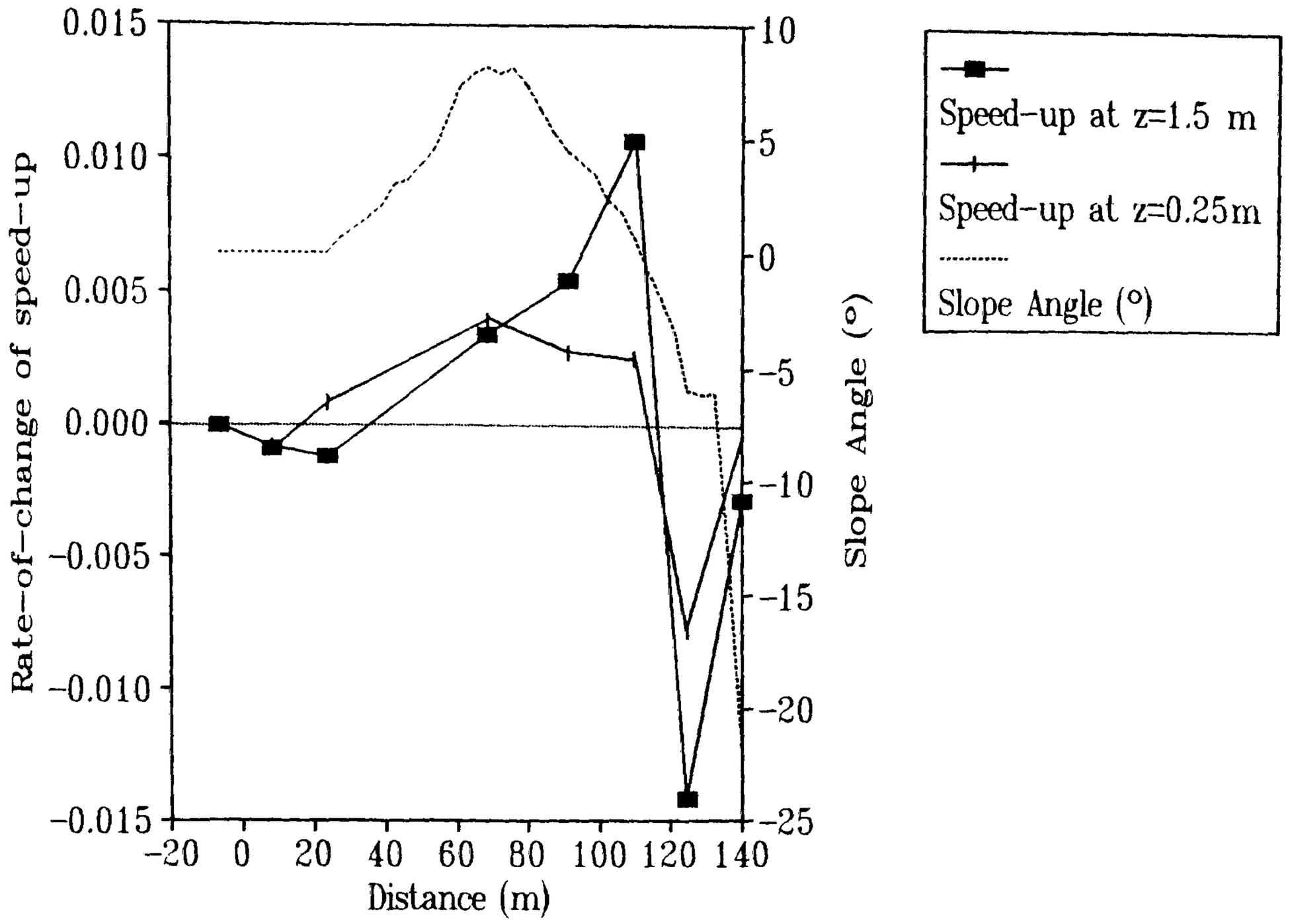

Figure 2.49 Relationship between slope angle and rate-of-change of fractional speed-up ratio on the left flank.

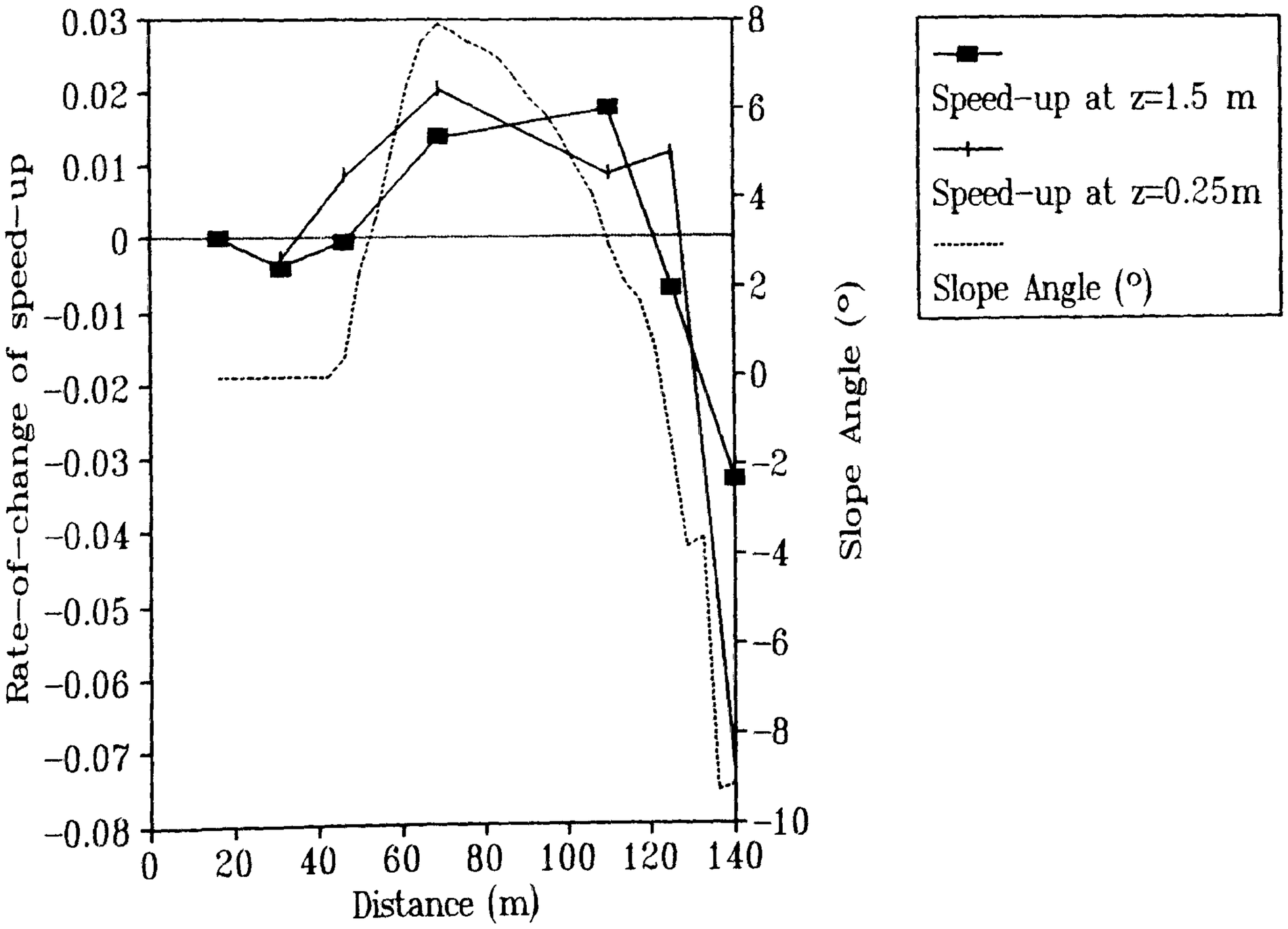

Figure 2.50 Relationship between slope angle and rate-of-change of fractional speed-up ratio on the right flank.

The reverse of this general relationship is demonstrated near the toe regions on each of the section lines. In these basal zones there is a negative rate-of-change of speed-up with an increasing surface slope angle. It seems likely that in these regions the wind velocities are responding more to the increasing (adverse) pressure gradient caused by the intrusion of the dune as a whole rather than to the changes in the local surface slope angles.

2.5 Discussion and Conclusion

Measurements of windspeed over the centre-line and flanks exhibit similar relationships to each other and to previously published work over both sand dunes and hills. The acceleration of windspeed up the windward slopes of transverse dunes, as recorded by Lancaster (1985), Mulligan (1988), Burkinshaw & Rust (1992) and predicted by Bagnold (1941) and Wilson (1972) is confirmed. The reduction in windspeed at the toe (identified in each of the measured section lines) is also proved. The minimum in windspeed at the toes of dunes has been reported by Howard *et al.* (1977) and Lancaster (1985) in the field and by Tsoar (1985) in a wind tunnel. It has also been demonstrated in measurements of flow over low hills by Jensen & Zeman (1985), Walmsley & Salmon (1984), Mason & King (1985), Mason (1986) and Taylor *et al.* (1987). However, in geomorphological studies it has always been ignored. The significance of this reduction in terms of sand transport and geomorphological dynamics is discussed in Chapter 7, but as an illustration of its neglect in the literature it is worth noting that Lancaster (1985), who remarked that:

"the windspeed drops to a minimum at the upwind base of the dune"

then calculated the comparative speed-up at the crest as a ratio to the velocity at the base. He used the Mason & Sykes (1979) formula:

$$S = U_{crest}/U_{base} \qquad \textbf{(2.9)}$$

where:

S = velocity speed-up
U_{crest} = windspeed at crest
U_{base} = windspeed at base

This is not an effective calculation when it is considered that the degree of windspeed retardation at the toe is a function of the height and length of the dune section line. The attempts by Lancaster (1985) to compare his results to the theoretical calculations of Jackson & Hunt (1975) and others then fail because these calculations use the upwind velocity as the denominator in

speed-up formulae. Equation 2.9 is also ineffective because it does not give any measure of the degree of velocity reduction at the toe.

Proof that the degree of deceleration of flow at the toe is dependent upon the size of the dune section line is given by Figures 2.35, 2.41 and 2.42. The centre-line (Figure 2.35) exhibits a larger decrease than either of the flanks. This deceleration is also likely to be a function of the degree of flow divergence near the toe of the dune, recognised in the flow direction measurements in Chapter 2.4.1. The acceleration of flow up the windward slope is nearly uniform at all measurement heights and the peak in acceleration is at the crest of the section line in all cases. The size of this peak was inconsistently predicted by the Jackson & Hunt (1975) approximation (Equation 2.8). The over-estimation of δs at the crest by Equation 2.8 may be due to the fact that the formula was developed for use on 2-D forms. It is likely that due to some airflow deflection around the 3-D study dune the acceleration at the crest was reduced. Similar results were found by Howard *et al.* (1977), Lancaster (1985) and Walmsley & Howard (1985). This argument does not, however, explain the underestimation of δs_{max} on the left flank.

On the flanks, where crest-brink separation was evident, a deceleration occurred downwind of the crest. This deceleration resulted in a reduction in wind velocity by about 30% at the brink. A reduction in windspeed at the brinks on crest-brink separated dunes has also been noted by Tsoar (1985) and Mulligan (1988). However, in neither case was the deceleration as pronounced as that shown in this study. Without more information on the shape of their test profiles no further comparison can be made.

The vertical velocity profiles suggest that measurements should have been carried out at greater elevations so that a clearer examination of the extent of the inner-layer could be carried out. The data presented here are limited to close to the maximum calculated elevation of the inner-layer and there is no evidence to suggest whether Equation 2.1 or the Jensen *et al.* (1984) formula (Equation 2.2) is the more applicable. The constantly varying height of the maximum speed-up may have been due to inaccuracies in the anemometers, identified in section 2.3.1. However, inspection of the profile data did not distinguish any unusual observations or systematic errors. The three profiles presented by Mulligan (1988) also show a δs_{max} which varies considerably with height as the wind traverses the windward slope.

Previous tests of Equations 2.1 and 2.2 in predicting the height of the maximum speed-up and inner-layer (Mason, 1986, Teunissen *et al.* 1987 and Mickle *et al.* 1988) have relied upon profile measurements only at the crests of hills. With the more detailed study presented here it is

reasonable to conclude that the height of δs_{max} changes up the windward slope, perhaps varying in relation to local surface irregularities. A clear relationship between the change in speed-up and the surface slope angle was determined on each of the section lines, particularly evident close to the surface. However, it should be noted that this study is concerned with velocity variations much closer to the surface and with a much thinner inner-layer than has been previously undertaken in research on low hills. The order of magnitude estimates of the inner-layer depth provided by Jackson & Hunt (1975), Jensen *et al.* (1984) and Hunt *et al.* (1988a) can therefore be seen to agree quite well with the data presented in this study.

Vertical profile data confirmed that the wind velocity profiles at all locations on the dune (including the toe) are non-logarithmic due to differential flow acceleration and deceleration. The progressively non-logarithmic nature of the velocity profiles on the windward flanks of desert dunes has been reported by Lancaster (1987), Mulligan (1988), Hesp *et al.* (1989) and Burkinshaw & Rust (1992). The study of Hesp *et al.* (1989) is alone in measuring non-logarithmic profiles on the windward slope and yet a logarithmic profile at the crest of a small coastal dune. The small size of their study dune (1 m height, resulting in an unmeasurable inner-layer) and the existence 15 m upwind of a dune of equal size are likely to have combined to make their results unrepresentative. Their explanation of the logarithmic profile at the crest as being an adjustment to local surface conditions seems unlikely. The increasingly non-logarithmic nature of velocity profiles up the windward slope has implications for the calculation of u_*, as discussed in Chapter 7.

CHAPTER 3 MATHEMATICAL MODELLING

3.1 Introduction

In the last 15 years there has been growing interest in the theory of boundary layer flow over low hills. This has largely been a result of the shortcomings of the techniques of investigation. Wind tunnel studies are frequently forced to make measurements too far from the surface for any practical interest because of the modest depth of a scaled inner-layer (see Chapter 4) and, whilst field studies furnish data close to the surface, terrain irregularities make local measurements difficult to interpret (Mason, 1986). Analytical approaches by meteorologists have now significantly increased the understanding of this type of flow and improvements in modelling turbulent boundary layers have made possible the calculation of the wind field over complex terrain. However, experimental evidence lags behind computational power and;

> *"...the ability to produce numerical results should not be equated with the ability to predict flow adequately"*
>
> (Castro, 1984)

Turbulent characteristics must be incorporated into calculations if accurate modelling of laminar flow over low hills is to be achieved (Mason & Sykes, 1979). A linear 2-D theory for low slopes which included the effects of turbulence was developed by Jackson & Hunt (1975), hereafter referred to as JH. Despite criticism by Sykes (1980) who claimed that the theory was inaccurate close to the surface, the JH solution, which is based on fluid dynamic principles, has been widely used. Indeed, Mason & Sykes (1979) developed the JH theory into three dimensions, a model referred to as MS3DJH. These models have been shown to predict mean velocities over hills fairly well (Mason & King, 1985; Mason, 1986), although comparisons with wind tunnel measurements (Pearse *et al.*, 1981; Taylor *et al.*, 1987; Mason & King, 1985) have tended to be far enough from the surface for only inviscid dynamics to dominate the flow behaviour, avoiding the important shear layer (inner-layer) close to the surface. Furthermore, field observations of turbulent stresses (Bradley, 1980; Britter *et al.*, 1981; Mason & King, 1985) have not shown good agreement with the JH theory although these comparisons have also been too far from the surface for the Reynold's stresses to affect the mean flow.

The advancements made in the mathematical modelling of the turbulent boundary layer have encouraged attempts to model airflow over isolated desert dunes with the aim of predicting their movement and growth (Howard *et al.*, 1977; Cekirge *et al.*, 1982, 1983, 1984; Howard & Walmsley, 1985; Walmsley & Howard, 1985; Wippermann & Gross, 1986; Zeman & Jensen,

1988). However, few studies have successfully modelled the patterns of erosion and deposition on sand dunes.

Howard & Walmsley (1985) used an adaptation of the MS3DJH model (by Walmsley *et al.*, 1982) and whilst predicting mean velocities consistent with field observations, their study was beset with problems of numerical instability caused by the sensitivity of the model to small-scale topographic perturbations, particularly for near-surface simulations. Wippermann & Gross (1986) were partly successfully in their attempts to simulate the development of a barchan dune from a conical pile of sand using flux-gradient relationships and mixing-length theory. However, their *FITNAH* model involved only a first-order (and less accurate) turbulent closure and involved some strict limiting assumptions.

The model used in this study is the revised FLOWSTAR model of C.E.R.C. (Cambridge Environmental Research Consultants Ltd.) which is based on the Hunt *et al.* (1988a) improvements on the original JH theory. The details of these improvements are described in the next section. The model is used to simulate the velocity, shear stress and surface shear stress distributions over a static representation of the prototype dune. The results from the simulation modelling presented in this Chapter are compared to the experimental observations from the field and wind tunnel studies in Chapters 4 and 5.

3.2 Model Description

A detailed explanation of the analytical computations employed by the FLOWSTAR model is given by Weng *et al.* (1991) and only a brief description, based on that work, is presented here in order to clarify basic assumptions and analyses.

The model assumes that:

1. The mean slope of the study form is small (<1/4).
2. The changes in the logarithm of the roughness height are small (<1).
3. The upwind velocity profile increases from the ground upwards and does not have an elevated shear layer.
4. Rapid cooling or heating of the surface is absent.

Hunt *et al.* (1988a, 1988b) have followed the work of Walmsley *et al.* (1982) and derived formulae for the Fourier transforms of the perturbation of the velocity and shear stress

distribution over complex terrain. The method of calculation is to use a Fast Fourier Transform (FFT) algorithm for computing the Fourier transform of the terrain height and roughness length. The algorithm for the analytical solution is then used to compute the Fourier transform of the velocity and shear stress fields. The transforms are then inverted to calculate the actual flow variables at the required point. Using analytical solutions in this way, rather than iterations (as used in most numerical [finite-difference] models), the program runs much more quickly and can be run on a modified IBM personal computer.

The model assumes that the flow can be divided into two main regions according to different predominant physical processes; the inner and outer regions (see Figure 2.3). The inner region (a distance l from the surface) represents the length scale within which changes in shear stress significantly affect the mean flow and the turbulence is in approximate equilibrium with the surface. The outer region is that zone where changes in shear stress have negligible effect on the mean flow and the flow can be treated as inviscid. A major improvement on the original JH theory is the division of the inner-layer into two sub-layers, the inner-surface-layer and the shear stress layer. The shear stress layer is characterised by the decrease in shear stress from a maximum at the surface but with only first order affects on the velocity perturbation. The inner-surface-layer (l_s, of order of magnitude z_0) is the depth in which the velocity perturbation is reduced to zero. This solution has little effect on the maximum values of velocity and stress but greatly improves their distribution and vertical profiles (Hunt *et al.*, 1988a). A further improvement involves the inclusion of a middle-layer (the lower part of the outer region) which increases the efficiency of the coupling between the inner- and outer- regions. A major effect of the improvements is that the distribution of turbulent stresses is now more comparable with the field observations of Bradley (1980), Britter *et al.* (1981) and Mason & King (1985).

The improved solutions (described by Hunt *et al.*, 1988a) for the perturbations of velocity and shear stress are:

$$u = \frac{H/L}{U(l)} \alpha \left[1 + \delta \left(1 - \ln\zeta - 4K\right)\right] \qquad 3.1$$

$$w=\frac{H/L}{U(l)}\alpha\{-\delta ik2\kappa^2+\delta^2 2\kappa^2[2+ik\zeta(\ln\zeta-2)+4\zeta\frac{\delta K}{\delta\zeta}]\} \qquad 3.2$$

$$\tau=-\frac{2H/L}{U^2(l)}\alpha\{1+4\zeta\frac{\delta K}{\delta\zeta}\} \qquad 3.3$$

and the surface shear stress perturbation is:

$$\tau=\frac{2H/L}{U^2(l)}\alpha\{1+\delta(2\ln k+4\gamma+1+i\pi)\} \qquad 3.4$$

where:

H = height
L = characteristic half length
U(l)= mean velocity at inner-layer height (l)
κ = von Karman's constant (0.4)
δ = $1/(\ln(l/z_0))$
l = $l \ln (l/z_0) = 2\kappa^2 L$
K = modified Bessel function
ζ = Z/l, where Z is the displaced co-ordinate in the z direction
ξ = normalised pressure perturbation
Δ = Euler's constant (0.57721)
k = Fourier transform variable

A comparison of the results of these solutions by Hunt *et al.* (1988a) with experimental observations over Askervein Hill (Taylor and Teunissen, 1987) revealed that the theory overestimated the velocity and shear stress perturbations near the surface, particularly near the hill-crest. Similar problems have been observed with the original JH theory (Britter *et al.*, 1981; Walmsley & Howard, 1985; Gong & Ibbetson, 1989). For more accurate estimations the solutions incorporated into the revised FLOWSTAR model are of a higher-order (second order turbulence closure model) and solved for three-dimensions, as described in detail by Carruthers *et al.* (1988) and Weng *et al.* (1991).

However, as with all current models of turbulent airflow, there is no solution available for modelling separated flow. This is of little consequence where flow over low hills is simulated because the region of separation is often very small. However, in the case of transverse sand dunes and other environmental conditions, this is not the case.

3.3 Input Parameters

Terrain Modelling

The FLOWSTAR model requires the input of terrain data in the form of cartesian co-ordinates. The terrain is then modelled using the Fourier transform method, described above, and interpolated onto a user-specified grid with sides of 8, 16, 32 or 64 cells. All subsequently calculated velocity and shear stress vectors are related to these grid nodes.

The FLOWSTAR terrain modelling of the field survey data on a 32 x 32 grid was found to be inaccurate, particularly at the breaks of slope at the toe and brink. For the present study, an improved model was achieved by first using MAPICS software to interpolate co-ordinates on a 60 x 60 grid and then using the FLOWSTAR interpolation routine. However, inaccuracies were still evident at the toe where an upwind depression was interpolated. To overcome this problem a contour map of the MAPICS interpolated data was digitised resulting in over 7000 co-ordinates. Subsequent interpolation of this data by FLOWSTAR resulted in a terrain model comparable with the field survey on the windward slope (Figure 3.1).

The finest grid spacing is the most desirable mesh to specify because it provides the maximum number of predictions. However, in this study a 32 x 32 grid was chosen because it was not only the finest mesh which provided an accurate terrain model, but it also furnished simulations with closely corresponding co-ordinates to the field measurement sites. At this resolution the FLOWSTAR model can calculate the velocity field at one height above the surface in about 40 minutes.

Wind Profile Parameters

Parameters concerning the upstream wind profile are easily inserted into the model. The data presented in this chapter resulted from an upwind profile which was comparable to that of both the field study (Chapter 2) and wind tunnel study (Chapter 4) and is summarised in Table 3.1 below;

Table 3.1 Description of the FLOWSTAR upwind profile.

Shear Velocity, u_* (ms^{-1})	0.375
Aerodynamic Roughness, z_0 (m)	0.004
Temperature Profile	Neutral
Wind Direction (°)	0

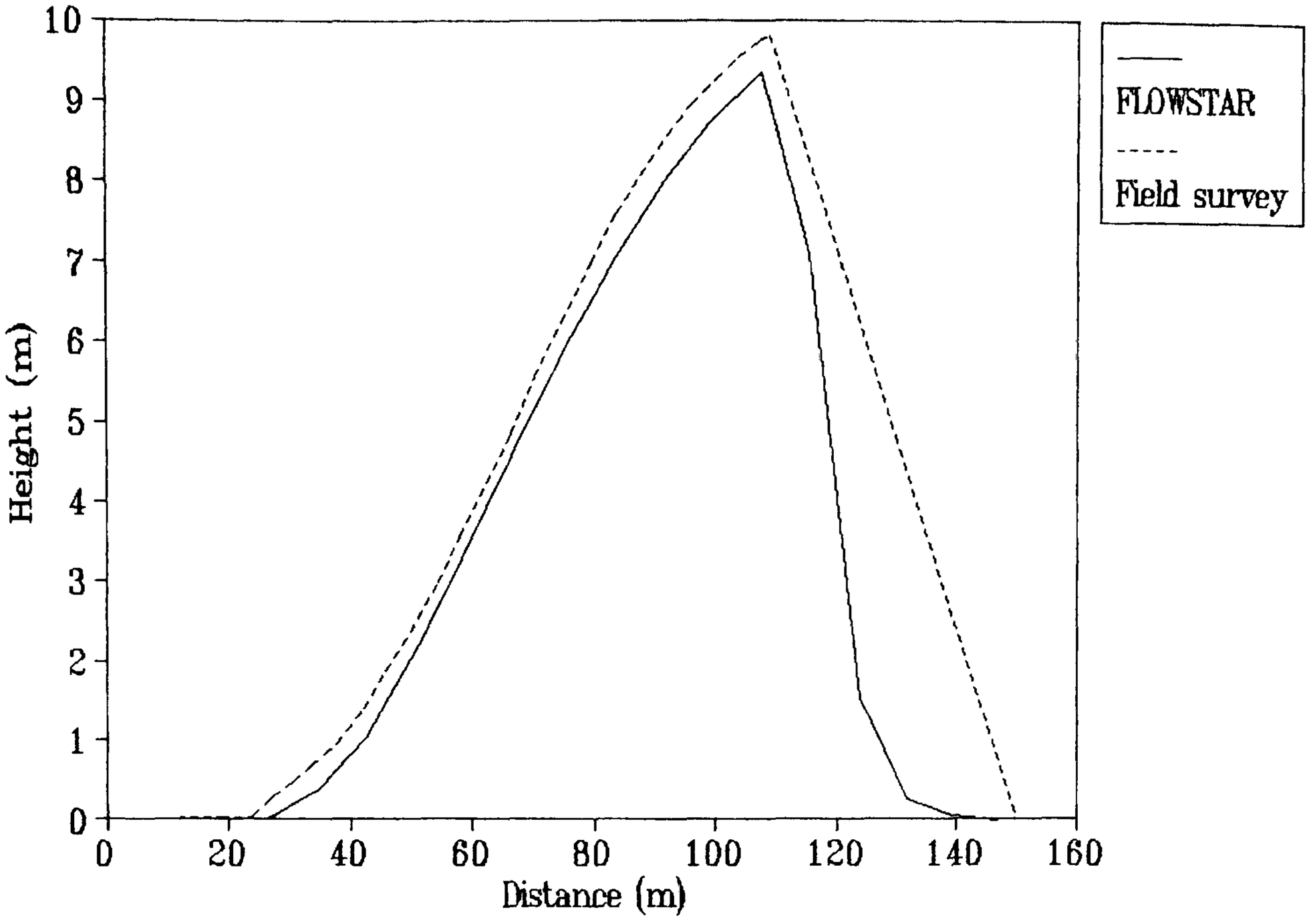

Figure 3.1 Comparison between the FLOWSTAR interpolation and the field survey of the dune centre-line.

The temperature profile can be specified as either neutral or with 4 differing degrees of stratification. Considering the Richardson number calculations in Chapter 2, a neutral temperature profile was considered most appropriate. The wind direction of 0° describes flow parallel to the dune centre-line in this case. The aerodynamic roughness of the surface was considered constant for the purposes of this simulation run. This was principally because the variations in surface roughness between the dune surface and the upwind surface, and indeed over the dune surface itself, were unknown (see Figure 2.33). A similar assumption was made concerning the wind tunnel modelling in Chapter 4 and further discussion relating to this assumption is presented in Chapter 7.

3.4 Experimental Results

Simulations were carried out at heights comparable with the field measurement heights and wind tunnel experimentation. The minimum level of calculation was 0.25 m and the maximum 30 m. The FLOWSTAR output files were transferred onto a VAX mainframe for analysis and presentation.

The mean velocity perturbations (fractional speed-up ratio, δs) were calculated from the simulated velocity vectors using Equation 3.5;

$$\delta s = \frac{\sqrt{u^2 + (w^2 \cos\theta)} - U_\infty}{U_\infty} \qquad 3.5$$

where:

δs = fractional speed-up ratio
u = u-vector of velocity
w = w-vector of velocity
θ = surface slope angle
U_∞ = upwind mean velocity in the u plane

This equation was used because the resulting mean velocity was then in approximately the same form as that measured by the anemometers in the field, assuming a cosinusoidal response of the cup-anemometers to the vertical velocity vector (w) (shown in Chapter 2.3.1). No account was made for the horizontal (v) velocity vector for two reasons. First, it was found that the v-vector was very small and would have a negligible effect on the data (<0.4%) (see below). Secondly,

the co-ordinate system used for all three techniques (field, FLOWSTAR and wind tunnel modelling) is cartesian (not streamline) and so does not allow for horizontal flow vectors divergent from the free stream direction. Disregarding the v-component of velocity (and also shear stress) in the FLOWSTAR simulations therefore made the predictions analogous to the field and wind tunnel measurements.

Flow Direction Simulations

Figure 3.2 shows a contour map of the deflection of airflow around the dune. The degree of deflection from the free-stream direction was calculated from the u- and v- vectors of velocity simulated at a height of 0.25 m:

$$x° = \tan (v/u)$$

where:

$x°$ = degree of deflection

The simulations shown in Figure 3.2 are comparable to the field measurements (Chapter 2.4) with the greatest degree of deflection (8-10°) at the base of the flanks. On the centre-line and mid-slope on the flanks no airflow deflection is apparent. However, in contrast to the field measurements, the flow is shown to converge in the crest and brink regions. The magnitude of this convergence is equivalent to the divergence at the base of the flanks. Both Allen (1968) and Howard *et al.* (1977) found flow convergence at the brink of their dunes, but not to the same degree as apparent from Figure 3.2. It is likely that the FLOWSTAR simulations of airflow deflection at the brink of the dune are influenced by the simulations in the reverse flow region, downwind of the brink. The FLOWSTAR program is unable satisfactorily to predict airflow in this region (See Chapter 3.2) and the erratic direction simulations here are likely to have prejudiced both the upwind brink simulations and also the contouring interpolation. The relatively large (10°) convergence of airflow at the brink of the dune is therefore considered to be an over-estimation FLOWSTAR.

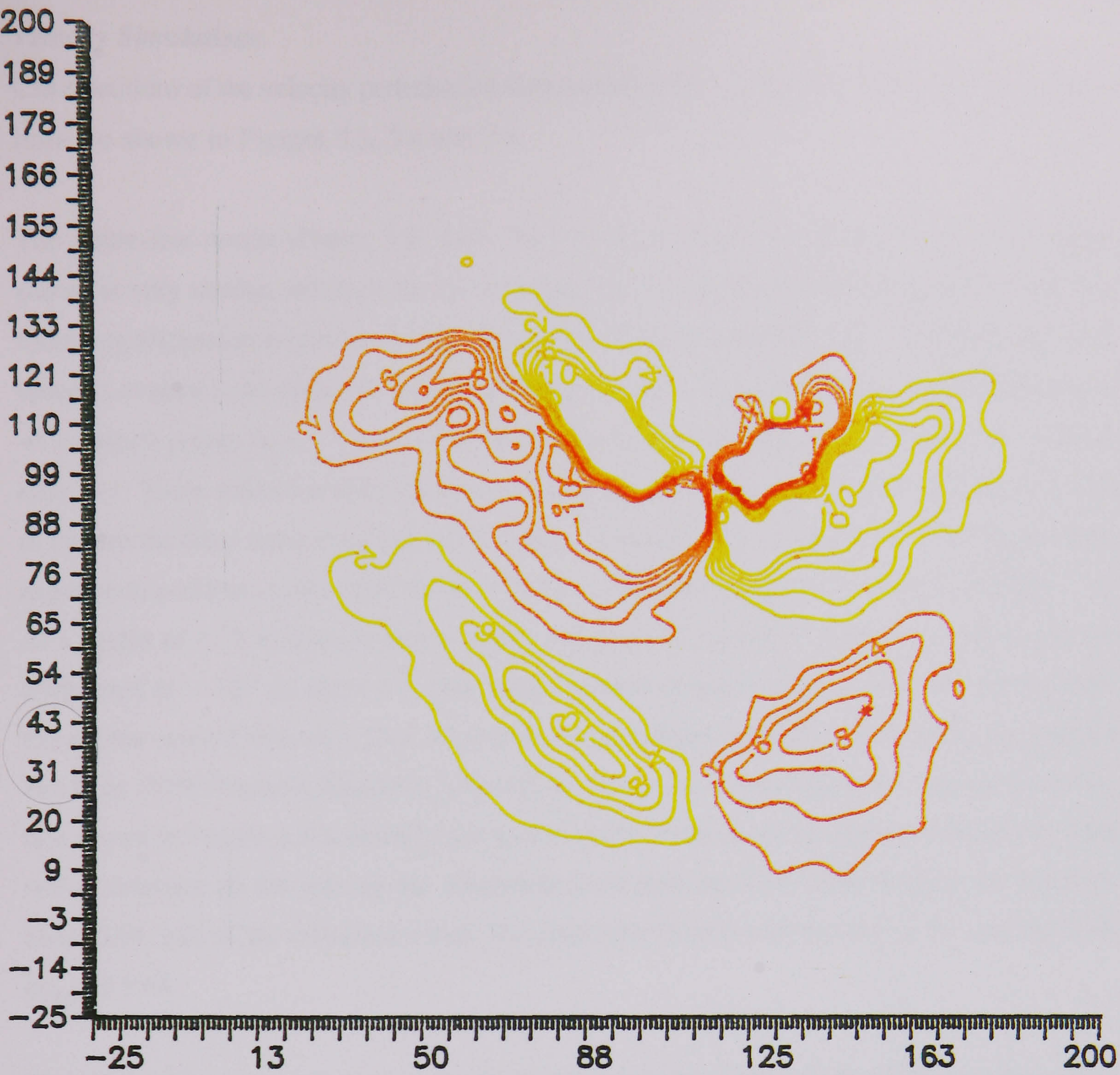

Figure 3.2 Calculated airflow deflection at a height of 0.25 m. Contour interval is 2°. Flow direction is from bottom to top.

Velocity Simulations

Cross-sections of the velocity perturbation simulations at four height levels over the three section lines are shown in Figures 3.3, 3.4 and 3.5.

The centre-line results (Figure 3.3) show that the development of speed-up at the four heights shown is very similar, although the lower height values tend to show larger perturbations. The following discussion is concerned with the lowest simulated height (0.25 m). A decreasing wind-speed is evident from about 35 m upwind of the toe. The minimum fractional speed-up ratio is -0.19 which occurs at x = 51 m (25 m downwind of the toe). The speed-up at the toe itself is only -0.1. There follows a sharp increase in speed-up toward a positive value of 0.04 at x = 60 m (where the local dune elevation (h) is about 1/3 of the total elevation, H). The change from negative to positive values of δs at h/H = 0.3 is a common feature at all heights on Figure 3.3. At a height of 0.25 m there is then a steady rise in δs to a value of 0.57 at x = 100 m. At the brink/crest (x = 107 m) there is a very sharp increase in speed-up to a value of 1.36 (a 136% rise on the upwind velocity). This value of δs is much higher than that predicted by the Jackson and Hunt (1975) formula (Equation 2.8) of 0.44. The peak in speed-up at the crest of the centre-line shown in Figure 3.3 is entirely due to one point. If the speed-up had maintained the same rate of increase all the way up the windward slope then the final value at the crest would be about 0.65, half of the simulated value. This expected value is much closer to the calculated JH δs_{max} of 0.44.

The value of δs_{max} was assumed in the JH theory to occur at l (the height of the top of the inner-layer), although the precise definition of l (given by Jackson & Hunt, 1975) is the height below which the shear stress perturbations become important to the flow. The FLOWSTAR calculation evaluated l at 0.68 m (using the modified JH theory of Hunt *et al.*, 1988a). The simulated speed-up at the crest at a height of 0.6 m was 1.1, still much larger than the JH expected value. However, if it is assumed that the rate of speed-up increase along the windward slope remains constant then the simulated δs_{max} would be about 0.58, a much closer figure to the one predicted by the JH equation. It appears that the FLOWSTAR simulation tends to over-predict velocity in the brink region by a factor of two. Downwind of the brink the simulated values of δs drop to minimum values of between -0.5 and -1.5. However, these results have no meaning because they lie in a region of separated airflow which cannot be modelled by the FLOWSTAR program.

The progression of δs on the left flank shows similar relationships to those along the centre-line, as shown in Figure 3.4. The development of speed-up at each of the heights shown is very similar, although the lowest height (0.25 m) again shows the largest perturbations. At this height

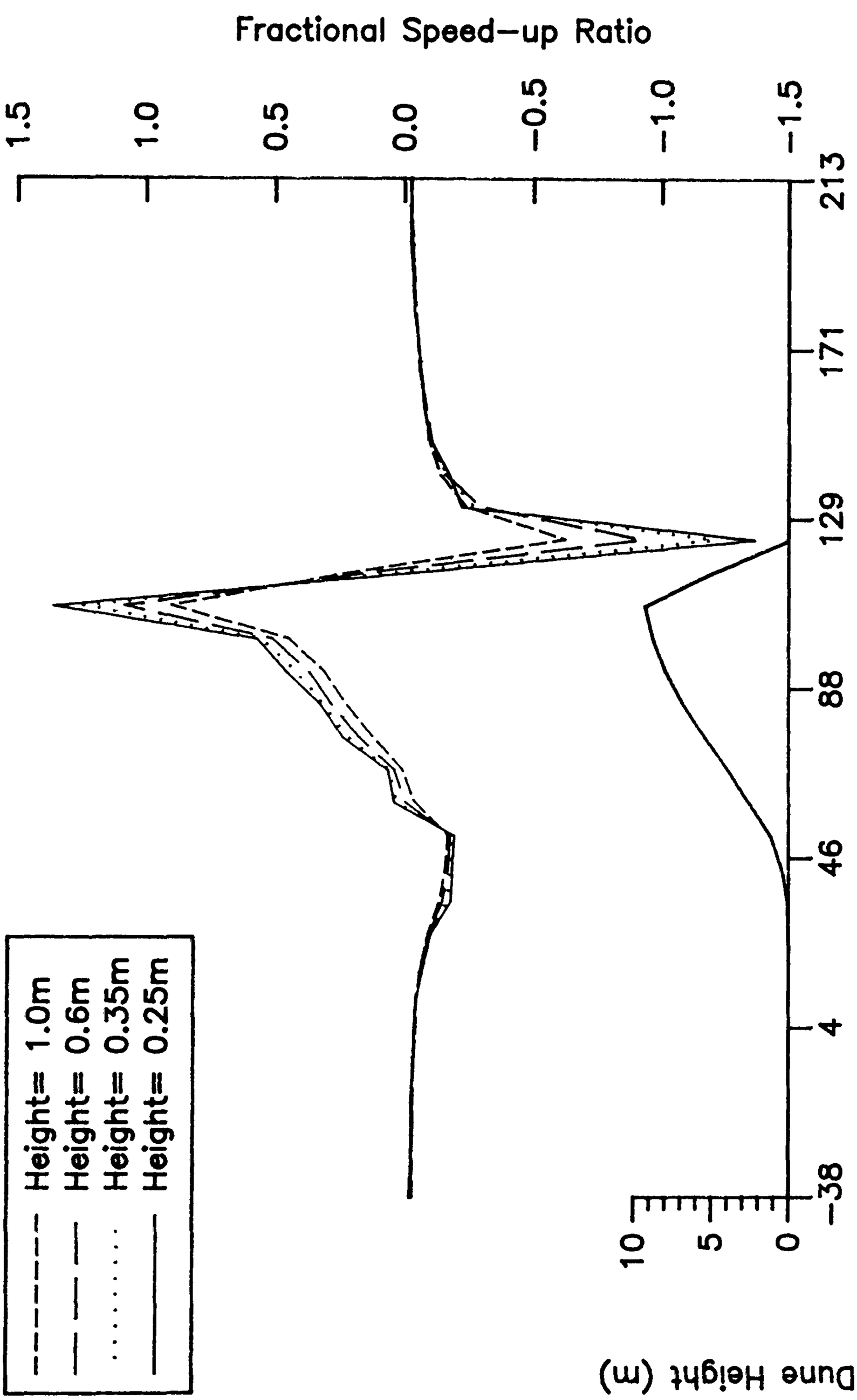

Figure 3.3 Calculated fractional speed-up ratio on the centre-line.

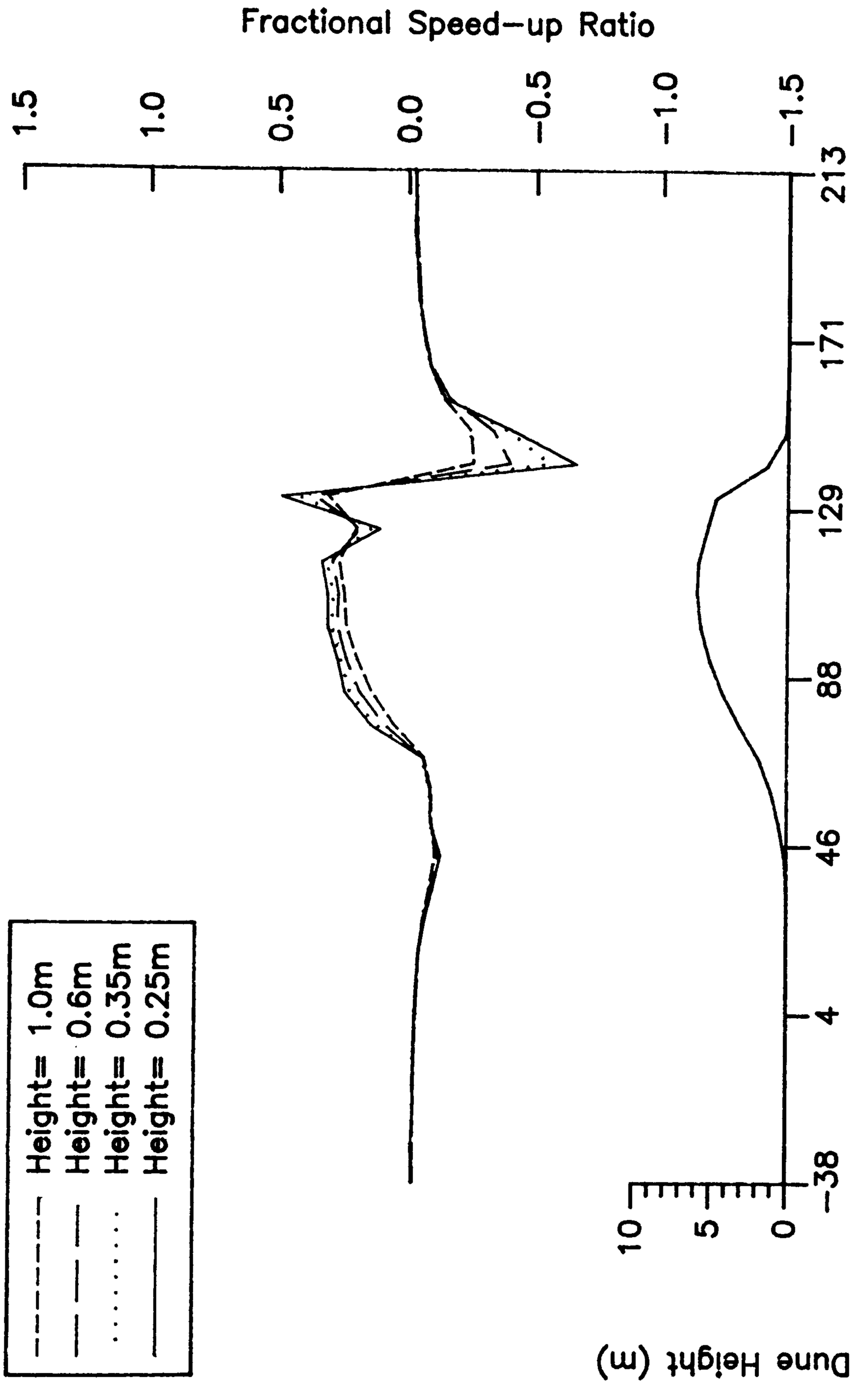

Figure 3.4 Calculated fractional speed-up ratio on the left flank.

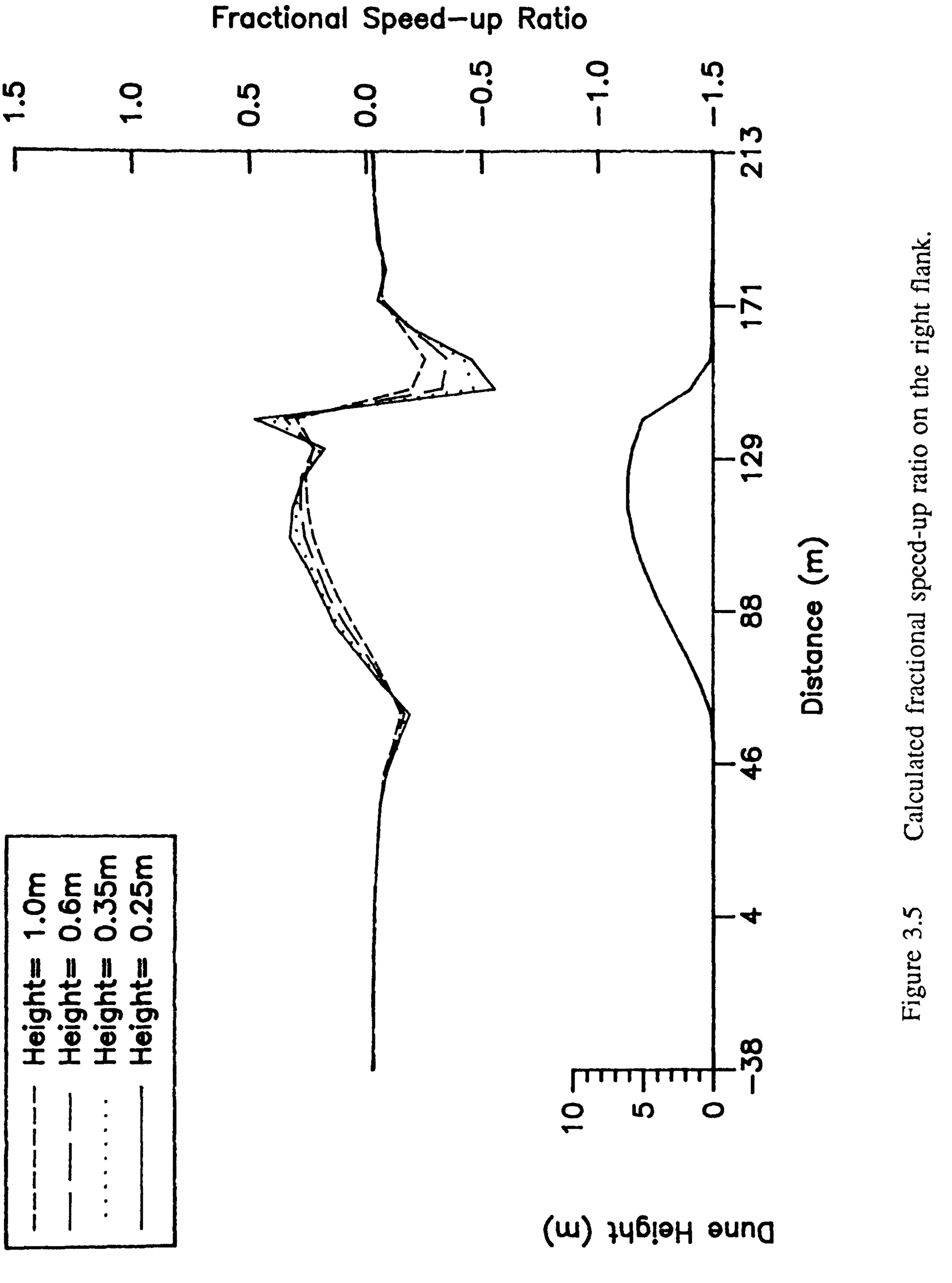

Figure 3.5 Calculated fractional speed-up ratio on the right flank.

a significant reduction in δs (-0.03) is evident at about x = 3 m, which is 24 m upwind of the toe. The minimum δs of -0.12 is found 15 m downwind from the toe. The toe itself exhibits a speed-up of -0.07. Similar to the centre-line progression, there follows a sharp increase in δs to positive values between x = 67 m and 75 m. The terrain height at this point of inflexion is approximately h/H = 0.3. Downwind of this point the speed-up increases at a steadily decreasing rate (*i.e.* with a convex profile, similar to that portrayed by the terrain itself) to a maximum at the crest of 0.34. This is comparable with the 2H/L calculation for δs_{max} of 0.33 (Equation 2.8). At first, between the crest and brink, the speed-up reduces to a value of 0.11. This trend is expected as an adverse pressure gradient develops downwind of the crest. However, at the brink itself, the δs rises sharply to 0.49. A more expected trend would be for the speed-up to reduce further to a minimum at the brink, in-line with the adverse pressure gradient development.

The general relationships described for the left flank speed-up progression also characterise those of the right flank (Figure 3.5). The upwind reduction in δs begins at about x = 19 m which is 27 m upwind of the toe. The toe itself has a speed-up of -0.1 and the minimum δs of -0.18 occurs 13 m downwind of the toe at x = 59 m. The rise in δs downwind from this point is not as sharp as that evident on either the centre-line or left flank, although a switch from negative to positive values occurs at x = 75 m which corresponds to h/H = 0.3. Toward the crest the relationships between the simulations at the four heights differ. The speed-up at 0.25 m and 0.35 m peak just upwind of the crest, while the maximum values at 0.6 m and 1.0 m are at the crest. It should be noted that the difference between the peak in δs at 0.25 m height and its value at the crest itself is only 0.04. The simulated δs_{max} is 0.33, consistent with the 2H/L calculation of 0.34 (Equation 2.8). Between the crest and brink the value of δs is reduced to 0.18, in a similar manner as the left flank. However, at the brink itself there is a very sharp rise in speed-up to a value of 0.48. Again, this is an unexpected and unrealistic result.

A more detailed illustration of the change in speed-up with height on each of the section lines is shown in the vertical profiles in Figures 3.6, 3.7 and 3.8. Ignoring the brink profiles in each case (profile H on the centre-line and J on the flanks) it can be seen from each of the three Figures that the change in δs is almost negligible above 15 m from the surface. It is also noticeable that the maximum perturbation in each case (whether positive or negative) occurs at the lowest simulated height (0.25 m). In none of the profiles is there a clear depiction of the inner-layer height (calculated at 0.68 m) where the maximum perturbations might be expected to occur according to the arguments of Jackson & Hunt (1975). The model seems to indicate that the maximum perturbation is at the surface, where one might more reasonably expect a perturbation of zero, assuming a no-slip condition at the surface (Jensen & Zeman, 1985).

The upwind profiles (A and B) in Figures 3.7 and 3.8 demonstrate little or no change in δs. It is only at the toe and downwind toward the windward break of slope (profiles C and D) that negative speed-ups at the lower heights become apparent. Profiles E, F and G all show an increasing perturbation at lower heights as the crest is approached. The brink profiles (J) on the flanks (Figures 3.7 and 3.8) maintain this progression although a sharp reduction in δs would be expected in the lower two to three metres, as is demonstrated by the intermediate H profiles.

The effect that the vertical δs profiles have on the logarithmic nature of the velocity profiles is shown in Figures 3.9 to 3.11. In each of these Figures the dotted line represents the upwind velocity profile. On all three section lines the velocity profiles become noticeably non-log linear as the flow decelerates at the toe and just downwind (profiles C and D). At the point of transposition between negative and positive speed-up (Profile E on Figure 3.9) the profile once again equates with the upwind profile. However, as the flow progresses toward the crest the profile becomes progressively non-log linear due to the high velocity accelerations. Between the crest and brink on the flanks (profile H on Figures 3.10 and 3.11) the profile becomes strongly non-log linear as the velocity at lower heights is retarded. The profiles for the brinks on each of the section lines (profile H for the centre-line and J for the flanks) clearly demonstrate the sharp increase in velocity close to the surface.

In profiles E to J in Figures 3.9 to 3.11 there is a noticeable kink in the velocity profile at log $z \approx -0.35$. This corresponds to a height of 0.7 m, and equates with the FLOWSTAR calculated inner-layer height of 0.68 m. The upper edge of the inner-layer, as determined by FLOWSTAR, is therefore characterised by an alteration in the rate-of-change of speed-up with height. This visible definition is in contrast to that offered by Jensen *et al.* (1984) and Gong & Ibbetson (1989) who state that it is comparable with the height of maximum flow acceleration. However, the improved model calculations of Hunt *et al.* (1988a) recognise that a more reasonable height for δs_{max} is about 1/3 (coincident with the maximum gradient in shear stress), as suggested by Jensen *et al.* (1984) and observed in several studies (Sykes, 1980; Mason, 1986). In this case the height of δs_{max} would be expected to occur at about 0.22 m. Figures 3.6 to 3.8 indicate that the fractional speed-up ratio increases toward the surface, at least as far as the lowest measurement point at 0.25 m. In the absence of any velocity perturbation simulations below this height a reduction in δs between 1/3 and the surface cannot be proven.

Figure 3.12 shows a contour map of the fractional speed-up ratio as simulated at a height of 0.25 m. It clearly shows the extent of the low velocity zone upwind of and at the toe of the dune and the progressive increase in δs up the windward slope. An interesting point to note is that the

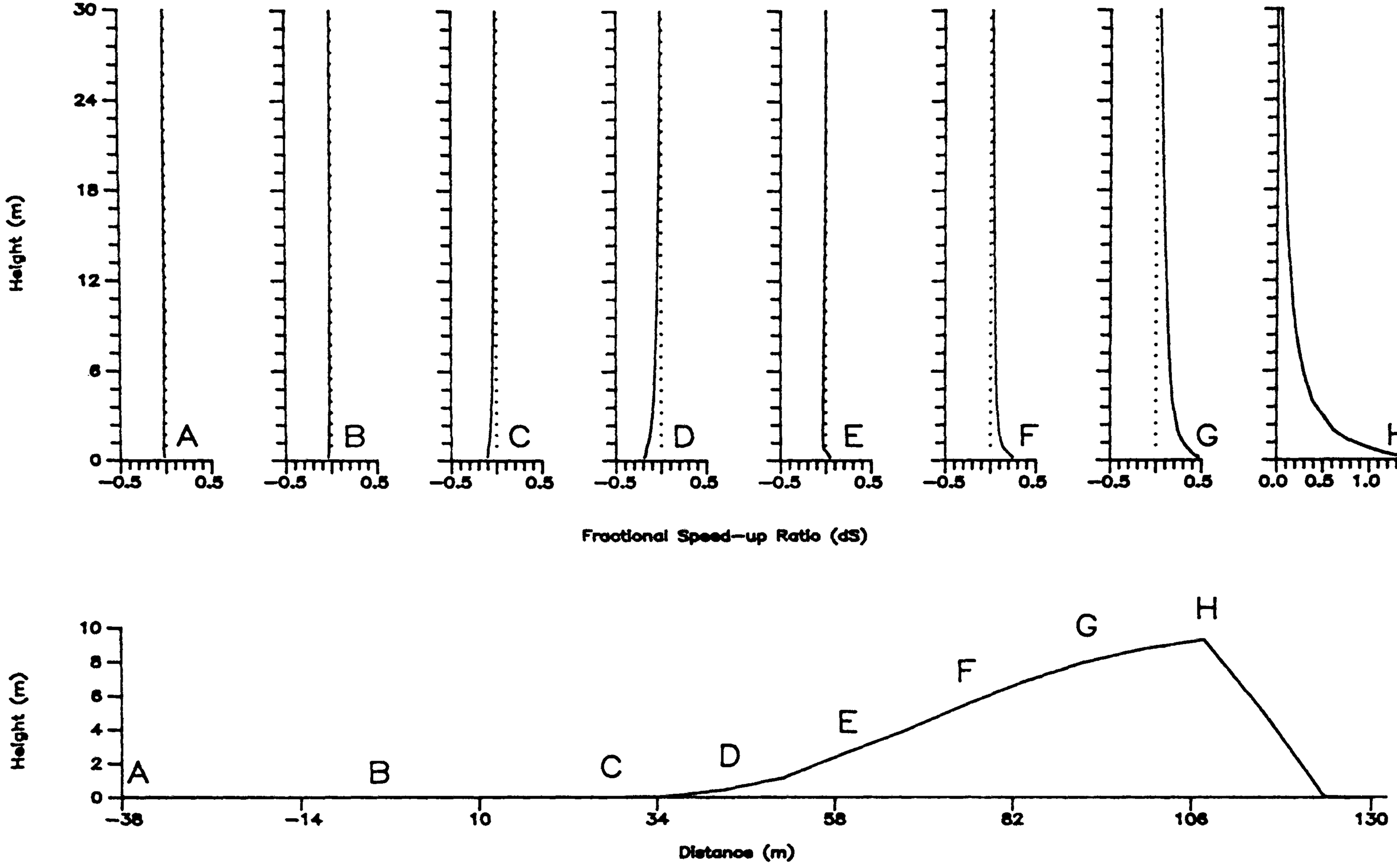

Figure 3.6 Calculated vertical profiles of fractional speed-up ratio on the centre-line.

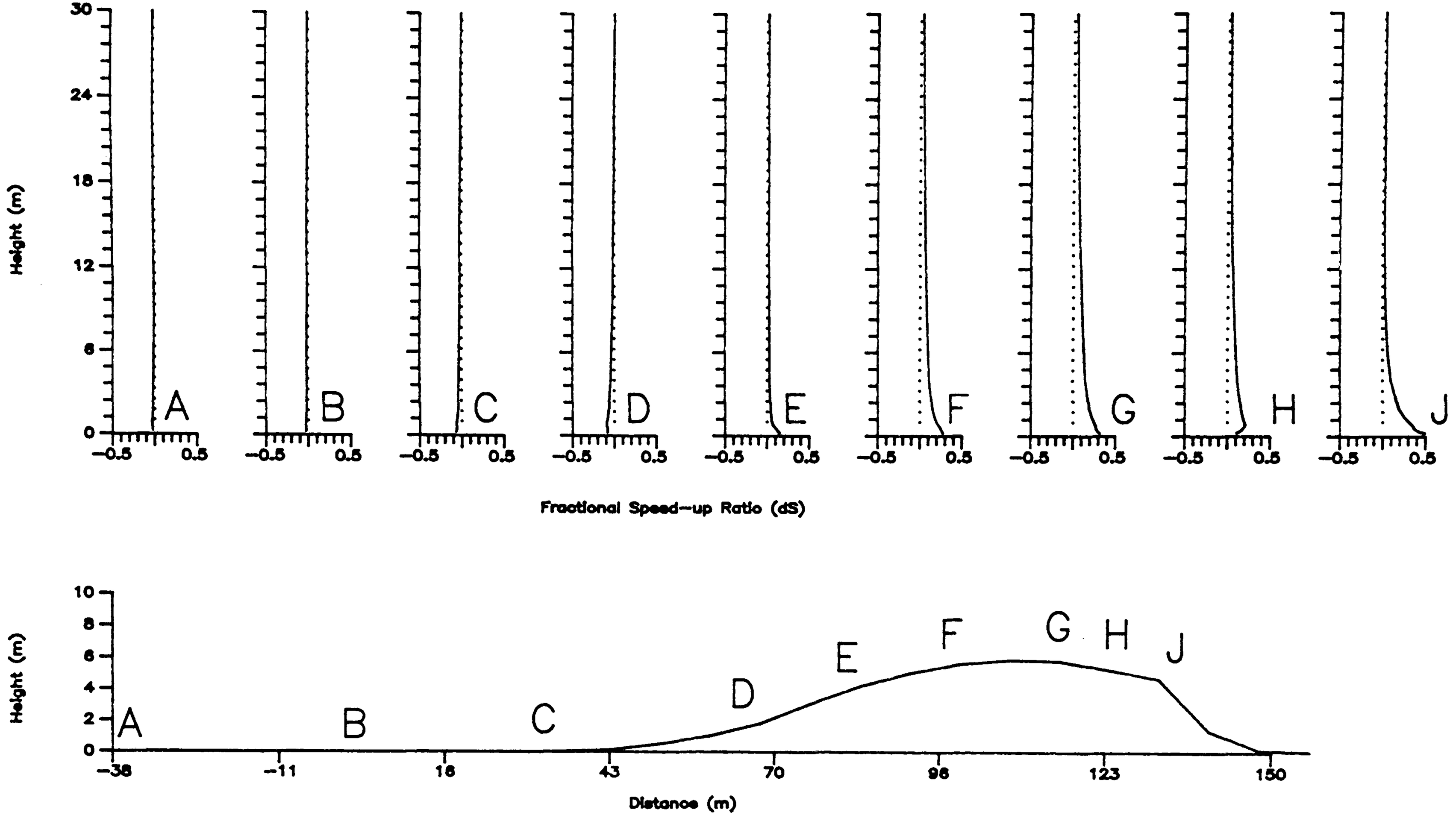

Figure 3.7 Calculated vertical profiles of fractional speed-up ratio on the left flank.

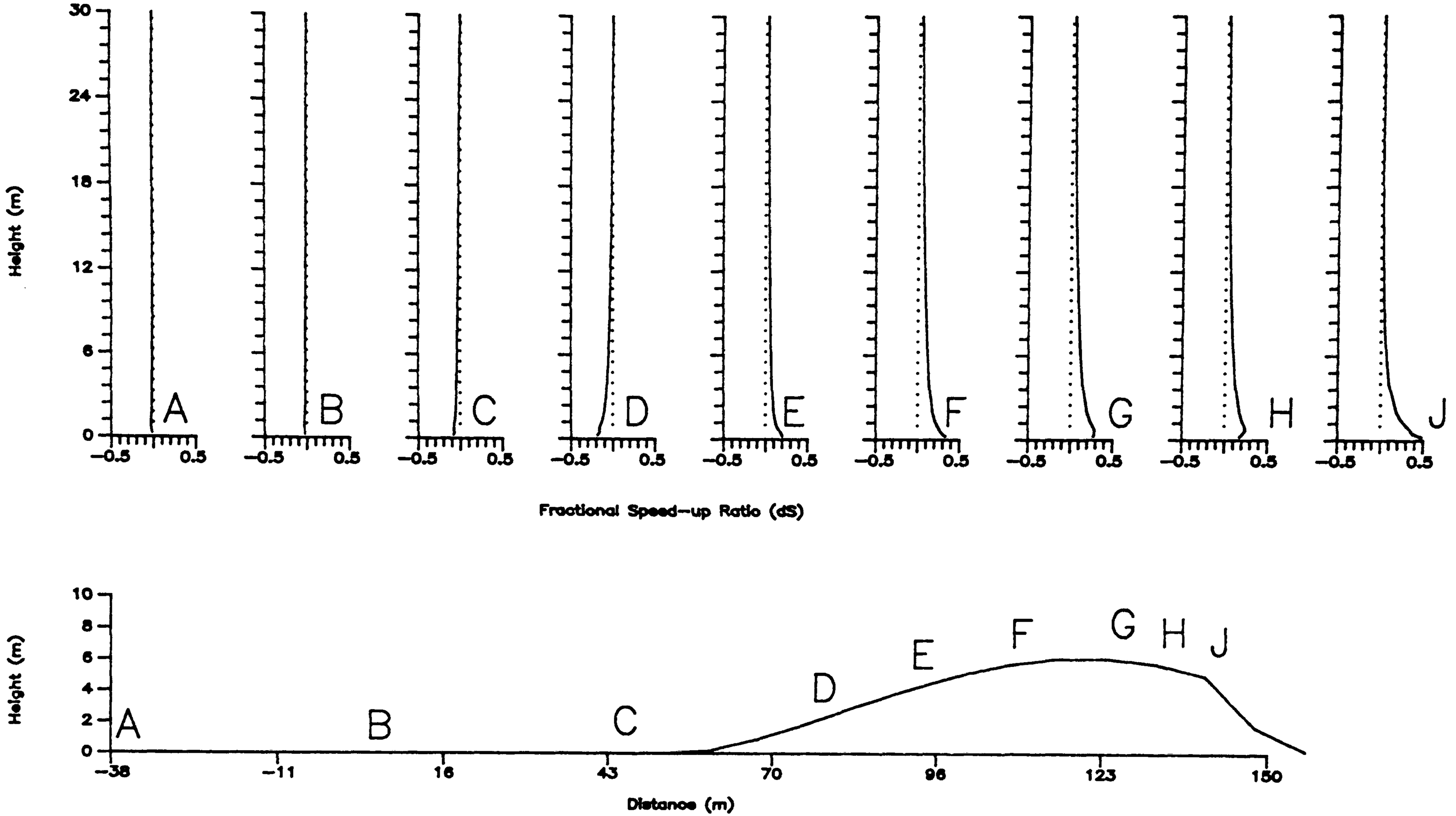

Figure 3.8 Calculated vertical profiles of fractional speed-up ratio on the right flank.

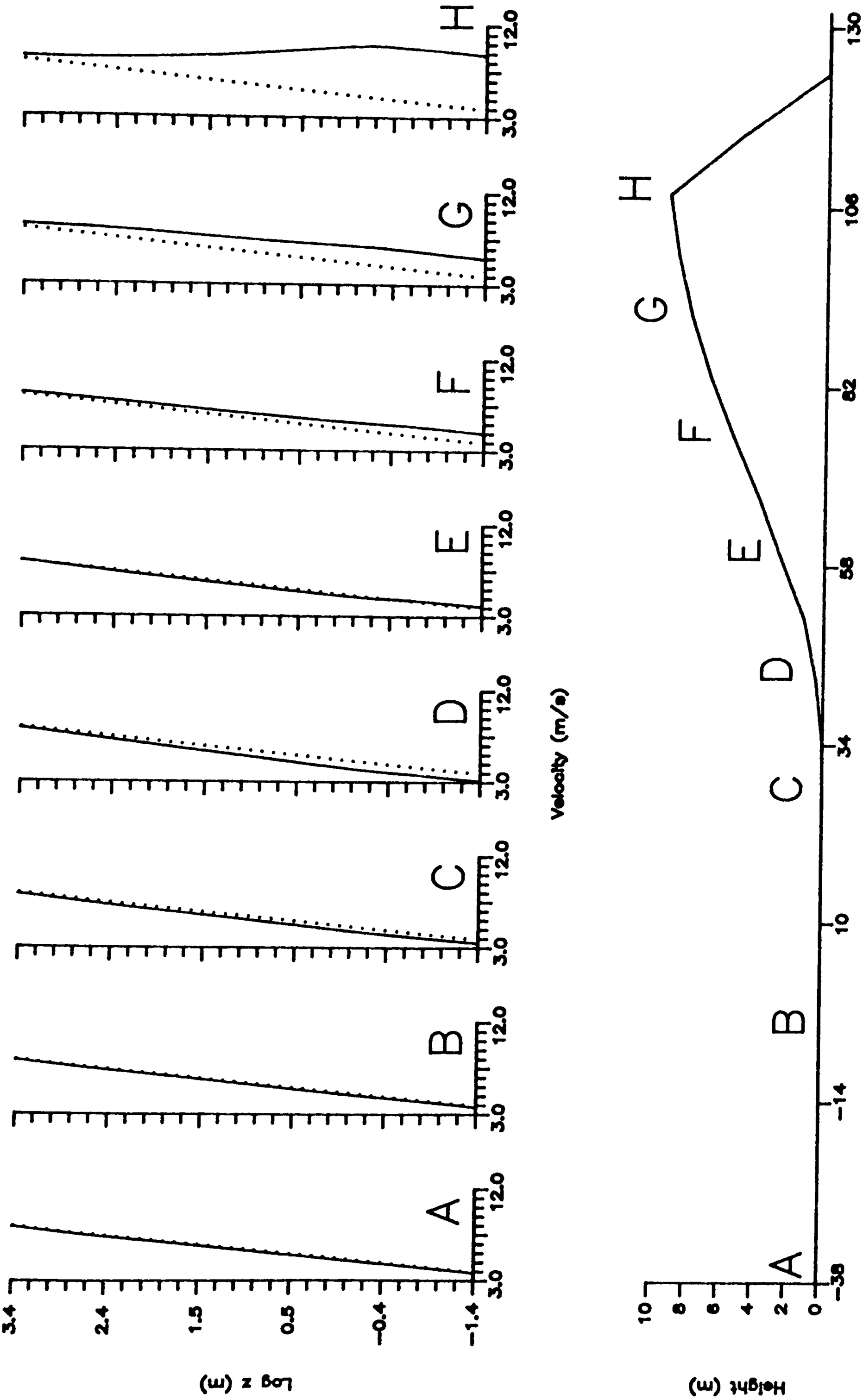

Figure 3.9 Calculated vertical velocity profiles on the centre-line.

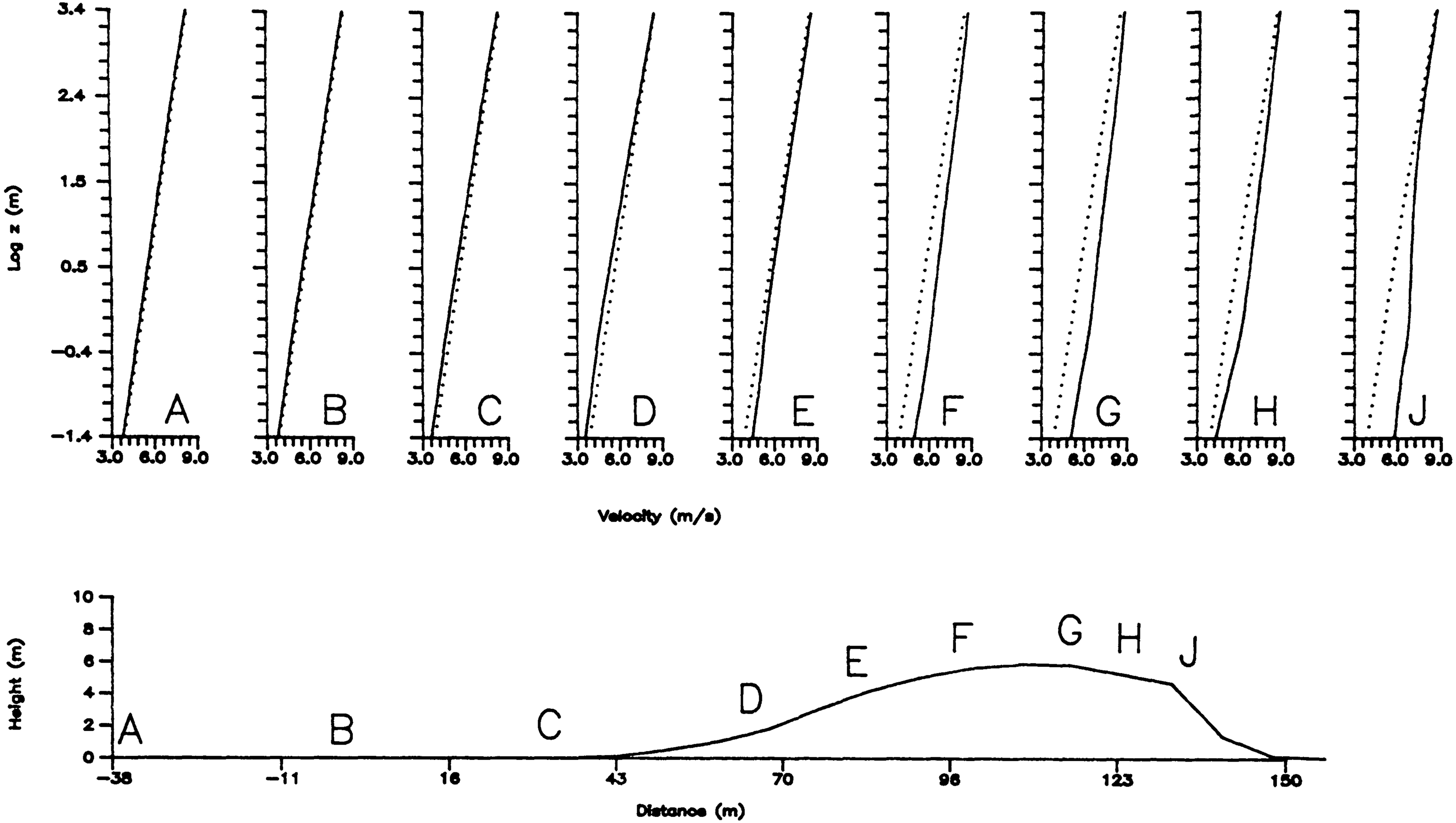

Figure 3.10 Calculated vertical velocity profiles on the left flank.

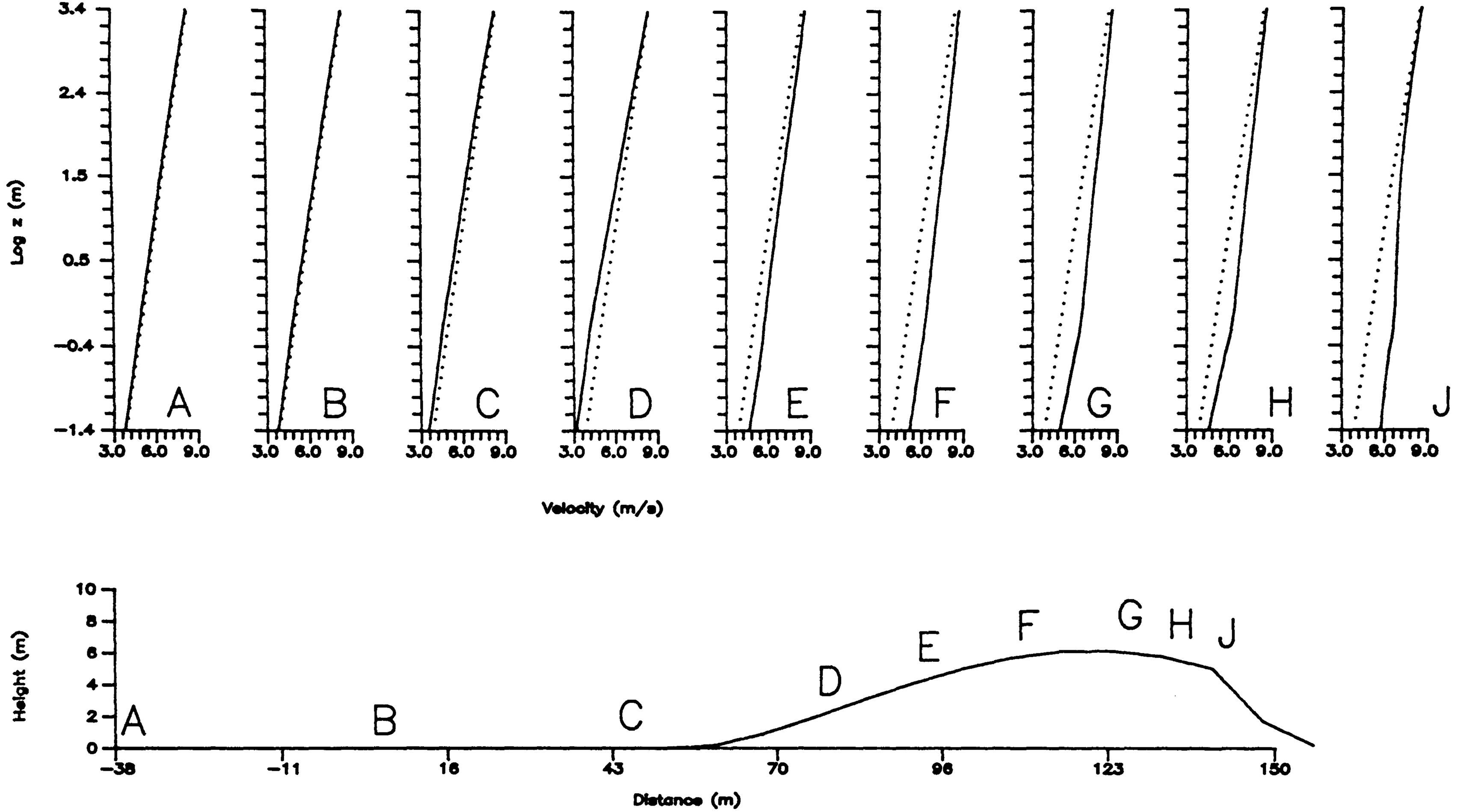

Figure 3.11 Calculated vertical velocity profiles on the right flank.

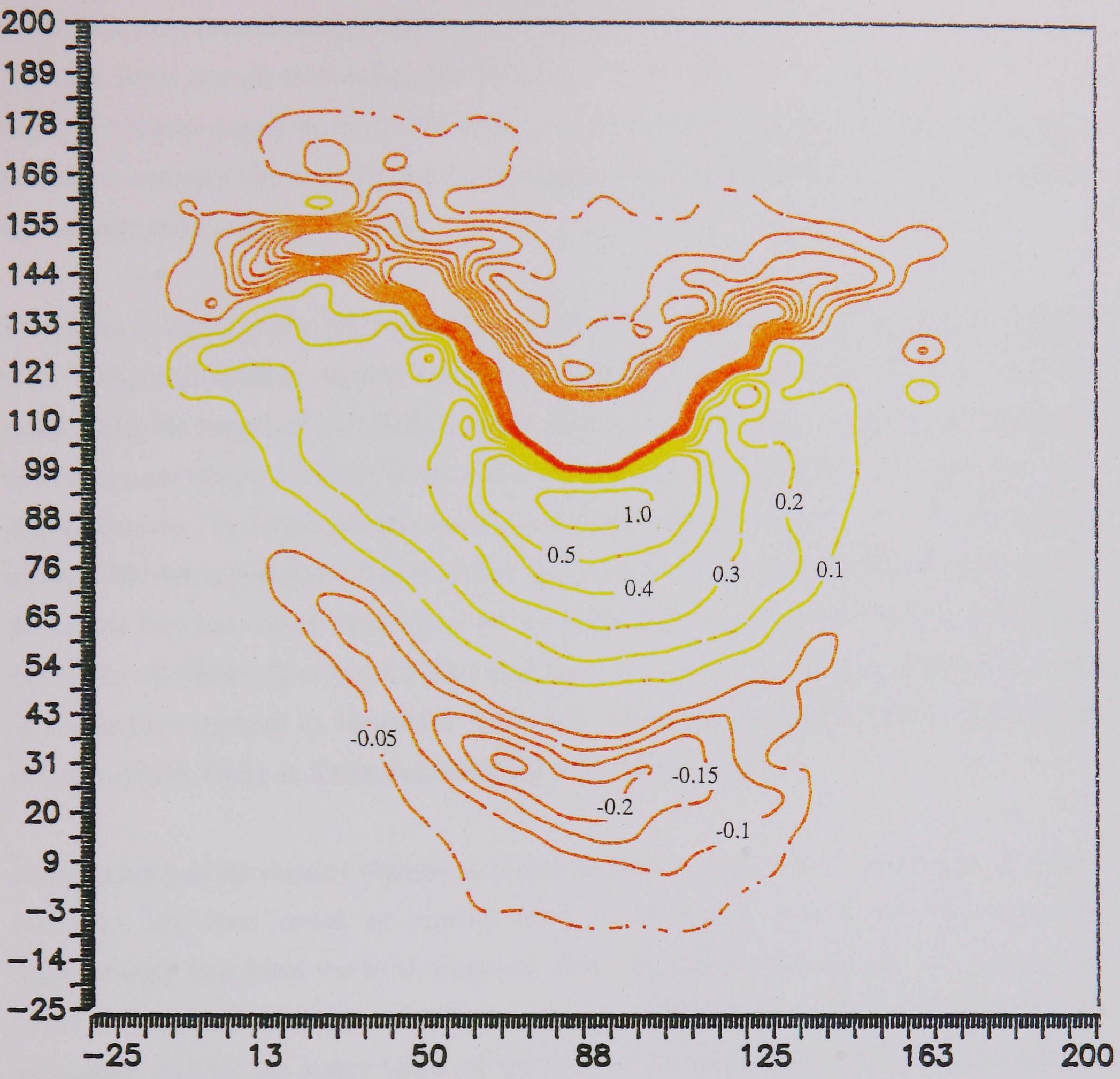

Figure 3.12 Contour map of fractional speed-up ratio calculated at 0.25 m. Orange is deceleration (negative speed-up); yellow is acceleration (positive speed-up). Flow direction is from bottom to top.

region of minimum δs upwind of the dune is offset from the centre-line. One would expect the minimum speed-up to occur on a section line coincident with the highest part of the dune. This lateral offsetting toward the right flank is probably due to the asymmetrical nature of the dune. The right flank extends horizontally almost a third further than the left flank. This is likely to result in a higher degree of lateral deflection of flow toward the right flank and a consequent decrease in velocity. The flow divergence simulations (Figure 3.2) showed more flow divergence on the right flank than the left flank.

The extent of the high velocity zones along the brink of the dune are also illustrated by Figure 3.12. These high velocity regions (identified in Figures 3.3 to 3.5) seem to occur in distinct peaks along the length of the brinkline rather than as one continuous ridge. It appears that the two flank lines chosen for study (Figures 3.4 and 3.5) dissect two of the more prominent peaks of high velocity. The reason for this overestimation of flow velocity is likely to be the inability of FLOWSTAR to model the region of flow separation which starts immediately downwind of the brink. This has a significant effect on the simulation of velocity in the cell immediately upwind (at the brink). Over-predictions in this region on a similar scale by mathematical models have also been reported by Howard & Walmsley (1985), Mason & King (1985), Walmsley & Howard (1985), Gong & Ibbetson (1989) and Weng *et al.* (1991).

A comparison of the velocity changes over each of the three section lines reveals their inherent similarity. All three reveal an upwind reduction in velocity which becomes significant approximately four times the local maximum dune height upwind of the toe. As expected, the flanks demonstrate a smaller reduction in velocity near the toe than the centre-line. This is anticipated because the larger height of the dune at the centre-line induces a larger adverse pressure gradient, hence retarding the flow. However, the right flank section line displays a considerable flow reduction in this zone, probably because of the increased lateral deflection of the flow at the leading edge of the flank, as described above. On each of the section lines the shape of the fractional speed-up ratio cross-sections display a similarity to the shape of the dune terrain. Hence, the flanks demonstrate a convex cross-section of speed-up whilst the centre-line is more triangular in appearance. As expected the centre-line exhibits a larger δs_{max} at the crest than either of the flanks, although this may partly be due to the overestimation of velocity at the brink.

Shear Stress Simulations

The simulations of shear stress perturbations (-uwb) along each of the section lines are shown in Figures 3.13 to 3.15. An examination of the results is made difficult first by the very irregular predictions and, secondly, because of the questionable results at the brink-line. However, an examination of the centre-line (Figure 3.13) reveals a possible division between the progression of shear stress at different heights. The shear stress perturbations at all the heights presented along the centre-line remain varying around zero until x ≈ 80 m, which is 55 m downwind of the toe. Between this point and the crest the shear stress at the higher levels (1.0 m and 0.6 m) appears to decrease to a perturbation of around -0.05, whilst that at lower levels (0.25 m and 0.35 m) has a generally increasing trend to between 0.03 and 0.05 at the crest itself. Downwind of the crest the stress perturbations at all four heights rise and then drop sharply.

The simulations of shear stress perturbations on the left and right flanks (Figures 3.14 an 3.15 respectively) are moderately less irregular and show analogous results to the centre-line. Both flanks demonstrate positive perturbations (0.02 to 0.04) on the upper half of the windward slopes at heights of 0.25 m and 0.35 m. At these heights there is then a drop to a near-zero perturbation at the crest, followed by a rise to peak values (0.05 to 0.07) near the brink. This is in contrast to the values at 0.6 m and 1.0 m which both show a small (-0.01 to -0.02) but steady decline to the crest and then a rise to near positive values toward the brink. On both flanks the perturbations at all heights at the brinks themselves plunge to negative values (-0.03 to -0.05).

These simulations broadly correspond to cross-sectional measurements of shear stress over a low hill in a wind tunnel undertaken by Finnigan *et al.* (1990). They found an increase in shear from the toe to half-way up the windward slope, a minimum at the crest and then a rise within the leeside wake. Ignoring the drop in shear at the brink, this describes the FLOWSTAR simulations on both flanks at 0.25 m and 0.35 m. The irregular nature of the centre-line simulations makes a comparison meaningless, although at 0.6 m and 1.0 m a crestal minimum can be identified.

The large variation in shear stress with height is indicated by Figures 3.16 to 3.18 which show the vertical profiles of stress at selected points on the section lines. Considering the irregular nature of the shear stress simulations presented in Figures 3.13 to 3.15 the actual values of stress exhibited by these profiles is less important than their overall shape. The centre-line (Figure 3.16) shows a stress divergence from upwind values at both the toe and crest at a height consistent with that of the middle-layer (4.17 m, as determined by FLOWSTAR). The crestal profile displays negative perturbations until a height of about 0.7 m is reached (the inner-layer) when the rate-of-change becomes positive. However, the values of shear stress only exceed

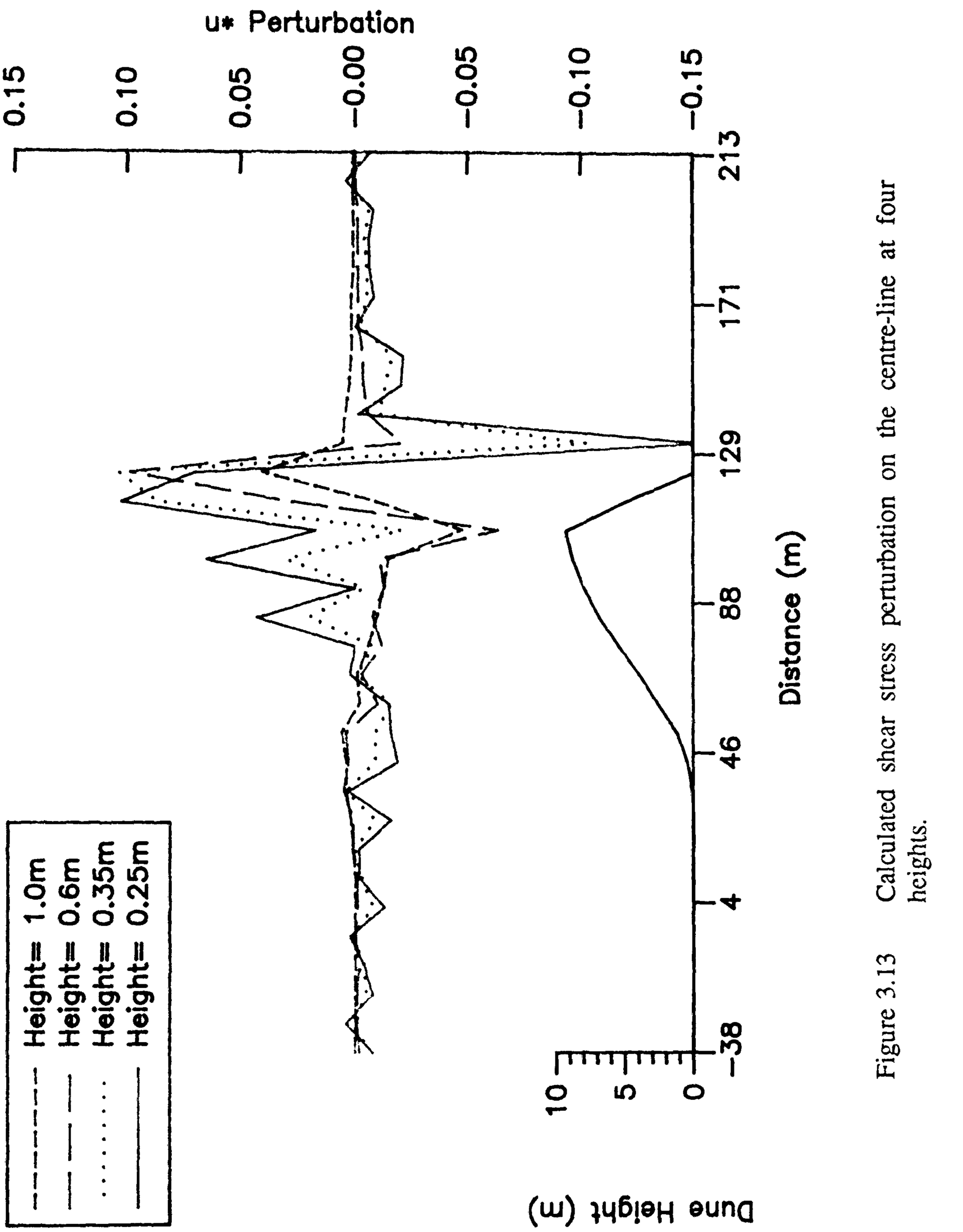

Figure 3.13 Calculated shear stress perturbation on the centre-line at four heights.

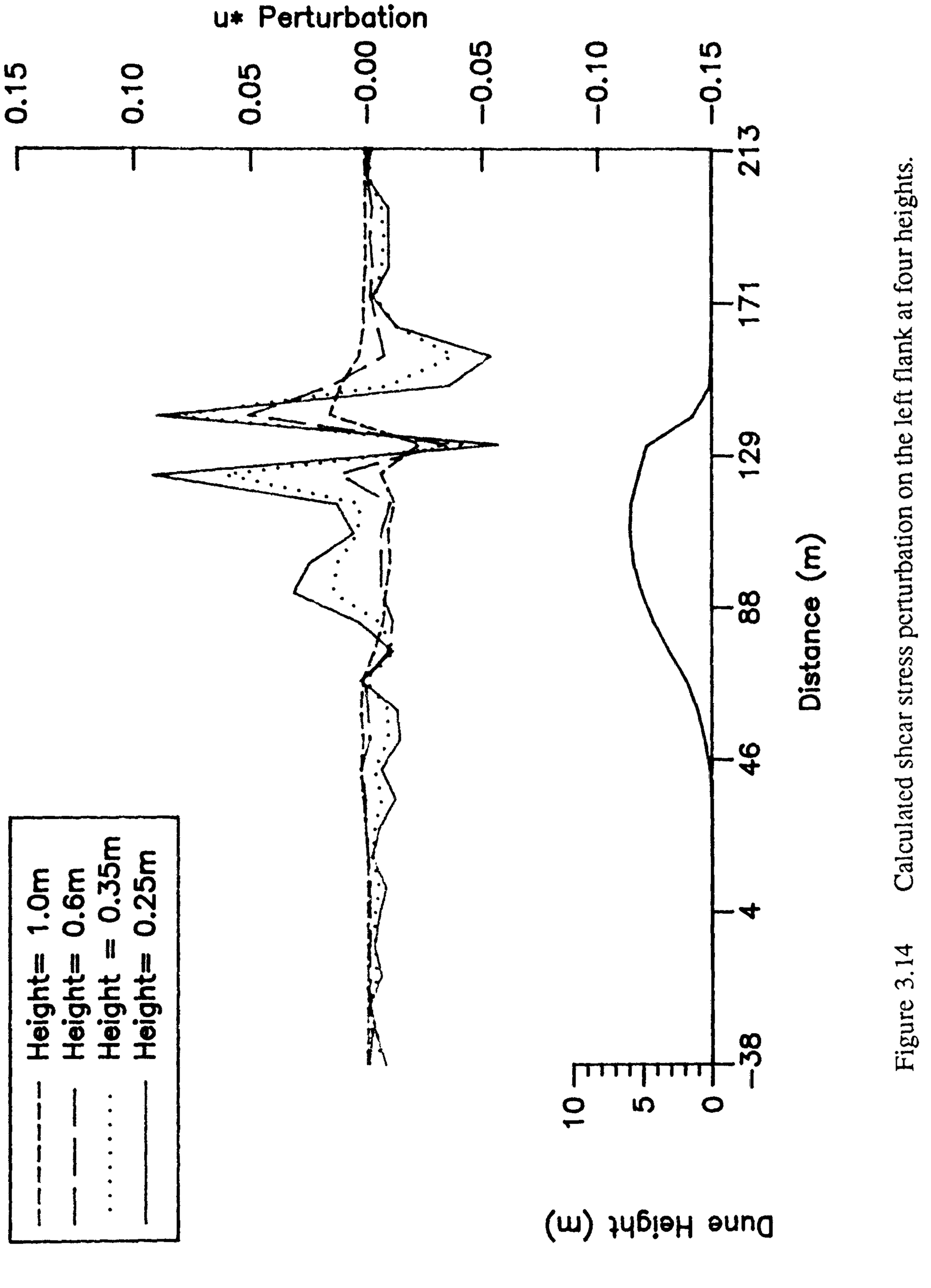

Figure 3.14 Calculated shear stress perturbation on the left flank at four heights.

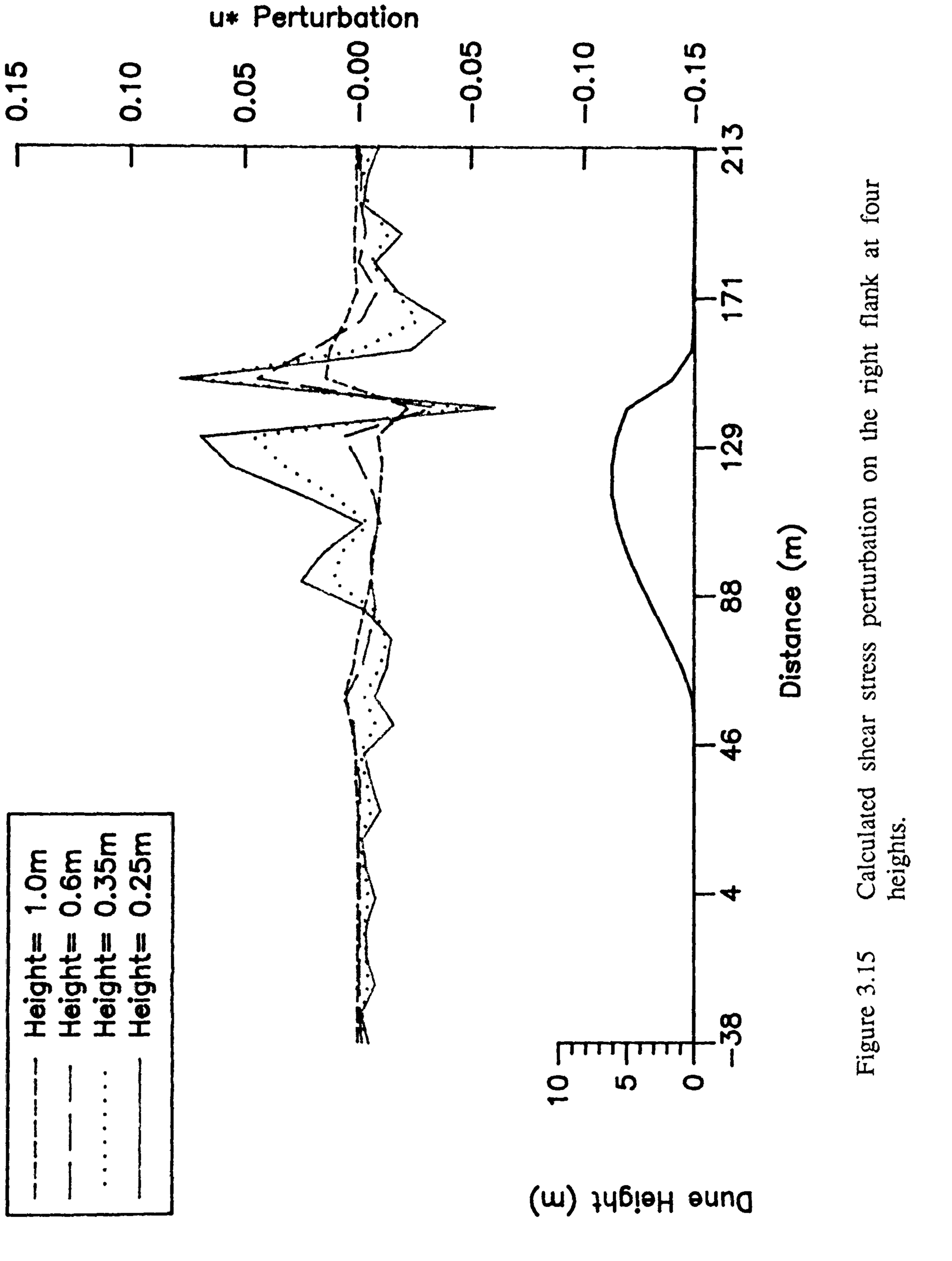

Figure 3.15 Calculated shear stress perturbation on the right flank at four heights.

upwind levels very close to the surface (~0.3 m). In contrast, the toe profile in Figure 3.16 shows a small positive perturbation up to the top of the inner-layer and then a gradual decrease to negative values at the surface. Comparable profiles for the crests and brinks of the flanks are demonstrated in Figures 3.17 and 3.18. The degree of perturbation on each section line is very different (*e.g.* the right flank shows the largest near-surface perturbation at its crest) but the shapes of the profiles and their points of departure from upwind values are very similar. Both the left and right flanks (Figures 3.17 and 3.18) demonstrate a decreasing stress perturbation at their brinks below the middle-layer. Although this reduction is briefly checked at the top of the inner-layer.

The shapes of the crest profiles presented in Figures 3.16 to 3.18 are very similar to those modelled and measured at the crests of low hills. Analogous results have been presented from measurements over Nyland Hill by Mason (1986), Askervein by Zeman & Jensen (1987) and from modelling of flow over Blashaval by Mason & King (1985). Gong & Ibbetson (1989) presented wind tunnel measurements of shear stress perturbations not only at the crest of a model hill but also at the upwind toe and mid-slope, downwind from the crest. These wind tunnel measurements are consistent in shape with the simulations presented here for the toe, crest and downwind. One of the principal reasons for the reworking of the original JH solution of turbulent modelling by Hunt *et al.* (1988a) was to improve the shear stress perturbation profile so that at the crest there was a minimum negative shear stress perturbation at a height l, of a similar size to the positive value close to the surface. All of the crestal profiles shown in Figures 3.16 to 3.18 demonstrate this basic shape although only the left flank (Figure 3.17) exhibits a positive perturbation near the surface of an equal size to the negative one at the top of the inner-layer.

Notwithstanding this variation it appears that the simulations of horizontal and vertical shear stress profiles over the model dune, despite being "noisy" and irregular in places, are consistent with state-of-the-art knowledge of flow over low hills.

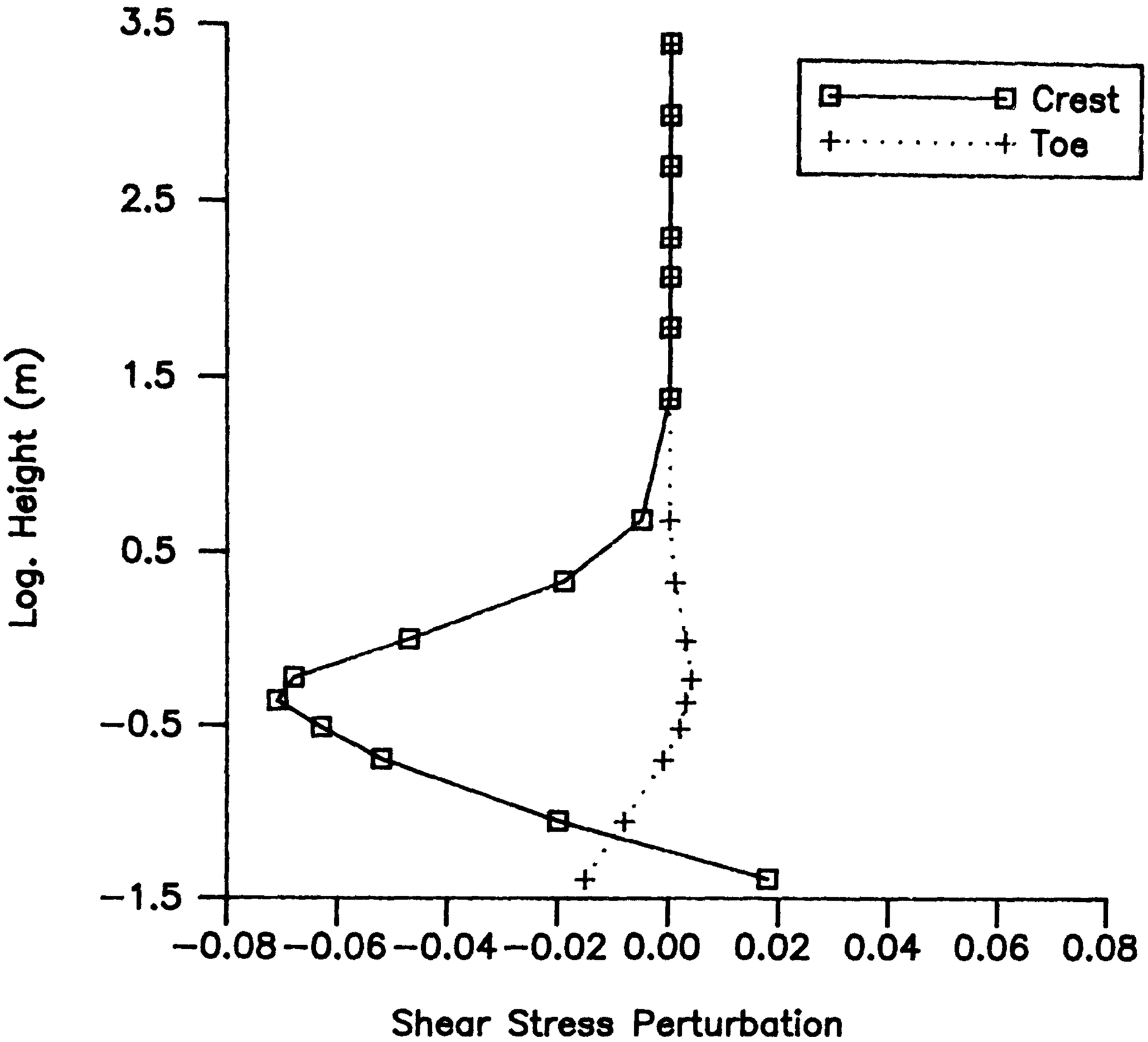

Figure 3.16 Vertical profile of shear stress perturbation calculated at the crest and toe on the centre-line.

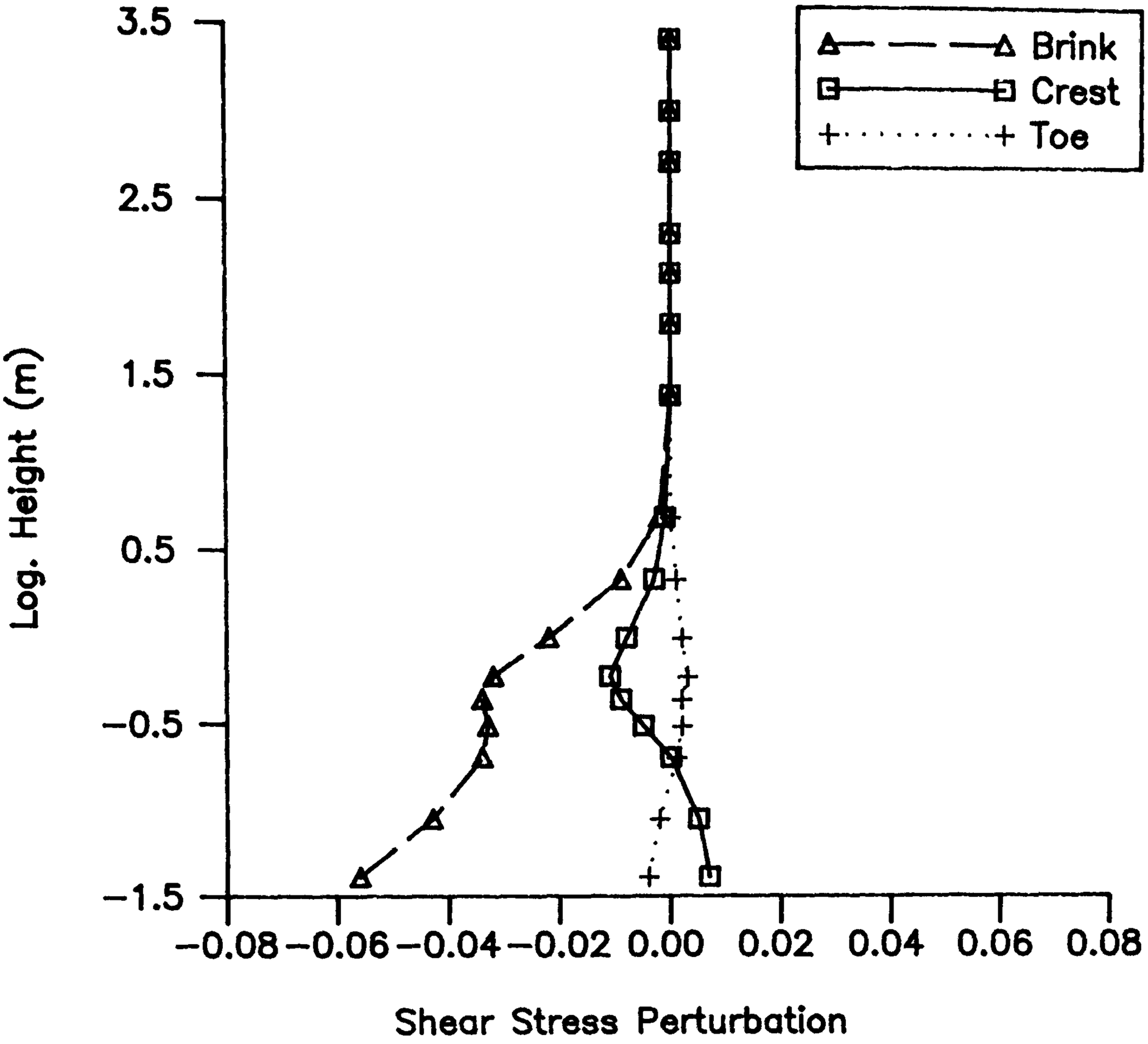

Figure 3.17 Vertical profile of shear stress perturbation calculated at the brink, crest and toe on the left flank.

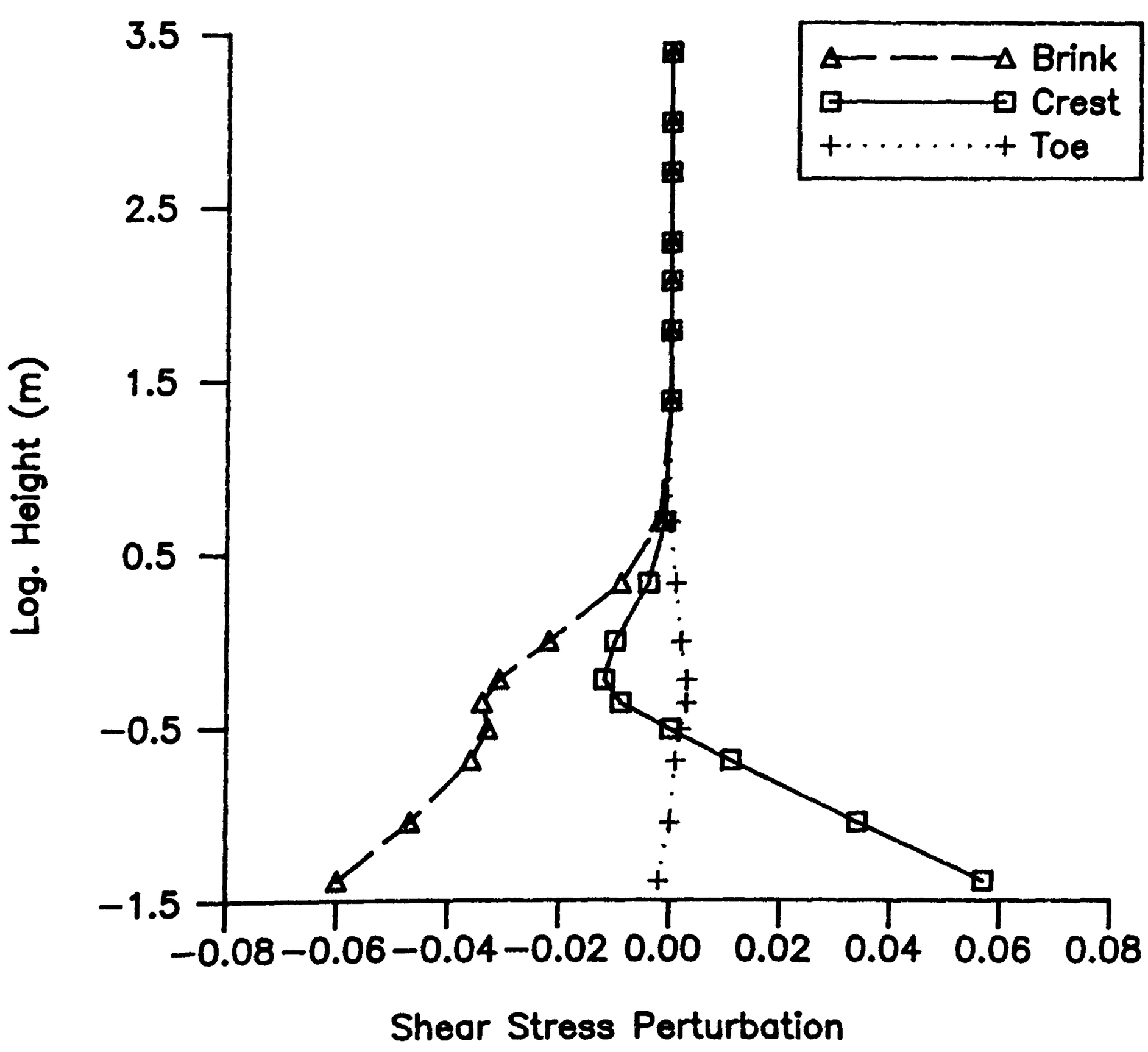

Figure 3.18 Vertical profile of shear stress perturbation calculated at the brink, crest and toe on the right flank.

Surface Shear Stress Simulations

Cross-sections of simulated surface shear stress perturbations (τ = -uwb at the surface) for each of the section lines are shown in Figures 3.19 to 3.21. The centre-line (Figure 3.19) exhibits a gradual upwind reduction in surface shear stress from x≈ 5 m to a minimum of -0.063 at x = 51 m, 24 m downwind of the toe. This is followed by a sharp rise to positive perturbations and a general increase toward the crest. At x = 100 m (just upwind of the brink) the stress perturbation is +0.15. At the brink, however, this has risen sharply to a maximum of +0.5 before dropping rapidly beyond the point of flow separation.

The left and right flanks (Figures 3.20 and 3.21) demonstrate similar developments in surface shear stress perturbation. Both exhibit negative perturbations which become significant as the flow reaches the toe. The left flank (Figure 3.20) reaches a minimum perturbation of -0.036 at x = 43 m. This is 16 m downwind of the toe and only half the minimum demonstrated by the centre-line. In contrast, the right flank reaches a minimum 16 m downwind of the toe (at x = 59 m) of -0.058, comparable in size to the drop in stress at the centre-line. Downwind of these minima both flanks present a rapid increase in perturbation to positive values, with irregular increases toward the crests. The left flank has a maximum surface stress perturbation of +0.11 at the crest. The right flank exhibits a similar maximum of +0.10 almost 20 m upwind of the crest, although the value at the crest itself is almost the same at +0.09. Between the crests and brinks of the flanks the perturbation is in decline with the left flank dropping to +0.03 and the right flank becoming reduced to +0.054. However, at the brinks, as at the centre-line, there is a sudden rise in perturbation to +0.16 and +0.12 on the left and right flanks respectively. These maxima are followed by sharp reductions beyond the brink.

A clearer display of the development of surface shear stress across the windward slope of the dune is presented by the contour map in Figure 3.22. As with the map of velocity speed-up (Figure 3.12) the negative perturbations in surface shear stress upwind of the toe show a minimum which is offset from the centre-line toward the right flank. This is likely to be a consequence of the larger lateral extent of the right flank compared to the left flank. A further similarity between Figures 3.22 and 3.12 are the erratic maxima in stress perturbation along the length of the brink line. The presence of these nodes of increase explains the abrupt escalation in stress perturbations at the brinks (shown in Figures 3.20 and 3.21). Again, it appears that the simulation of surface shear stress is unrepresentative at the brink, because of the close proximity of the reverse flow region.

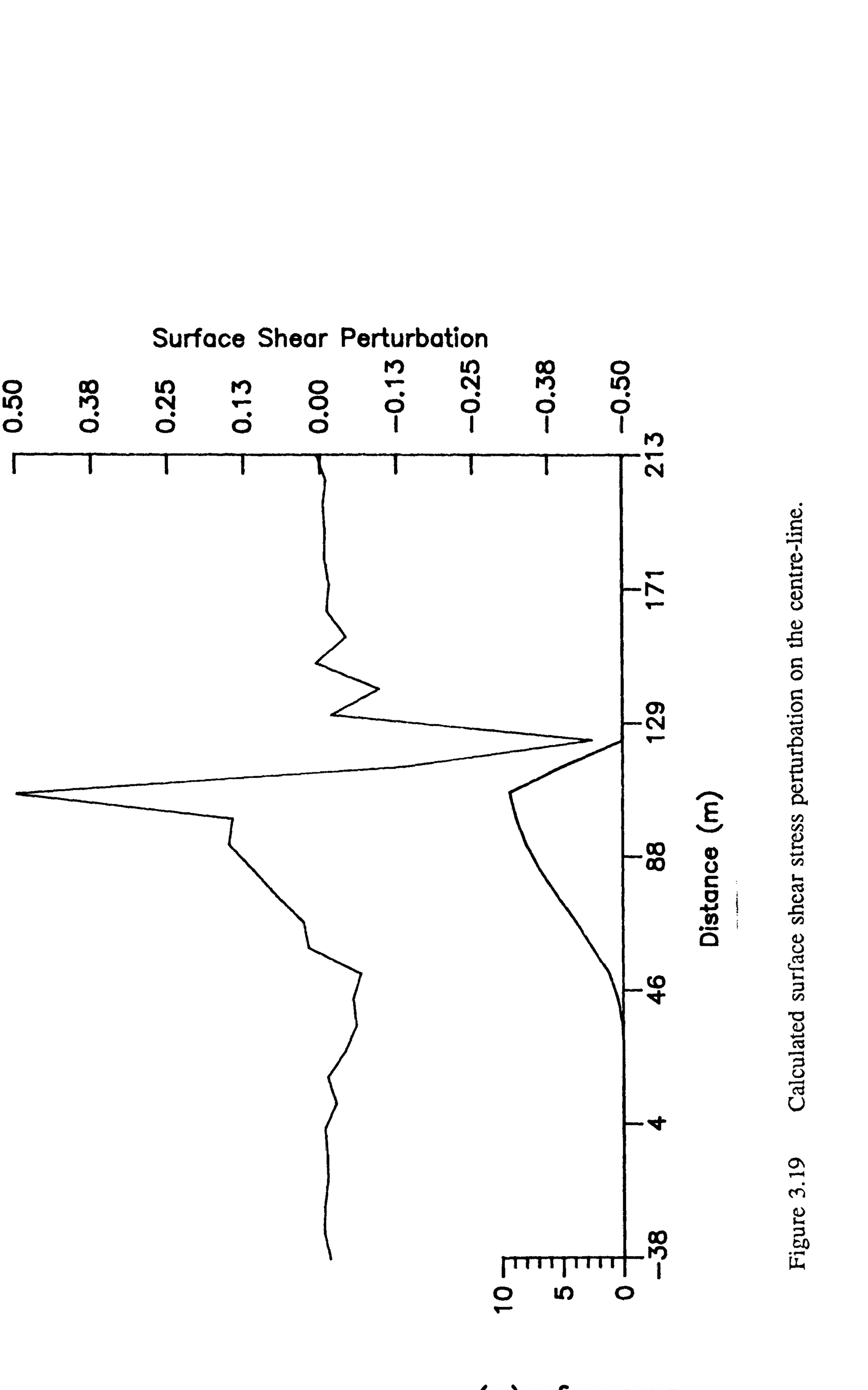

Figure 3.19 Calculated surface shear stress perturbation on the centre-line.

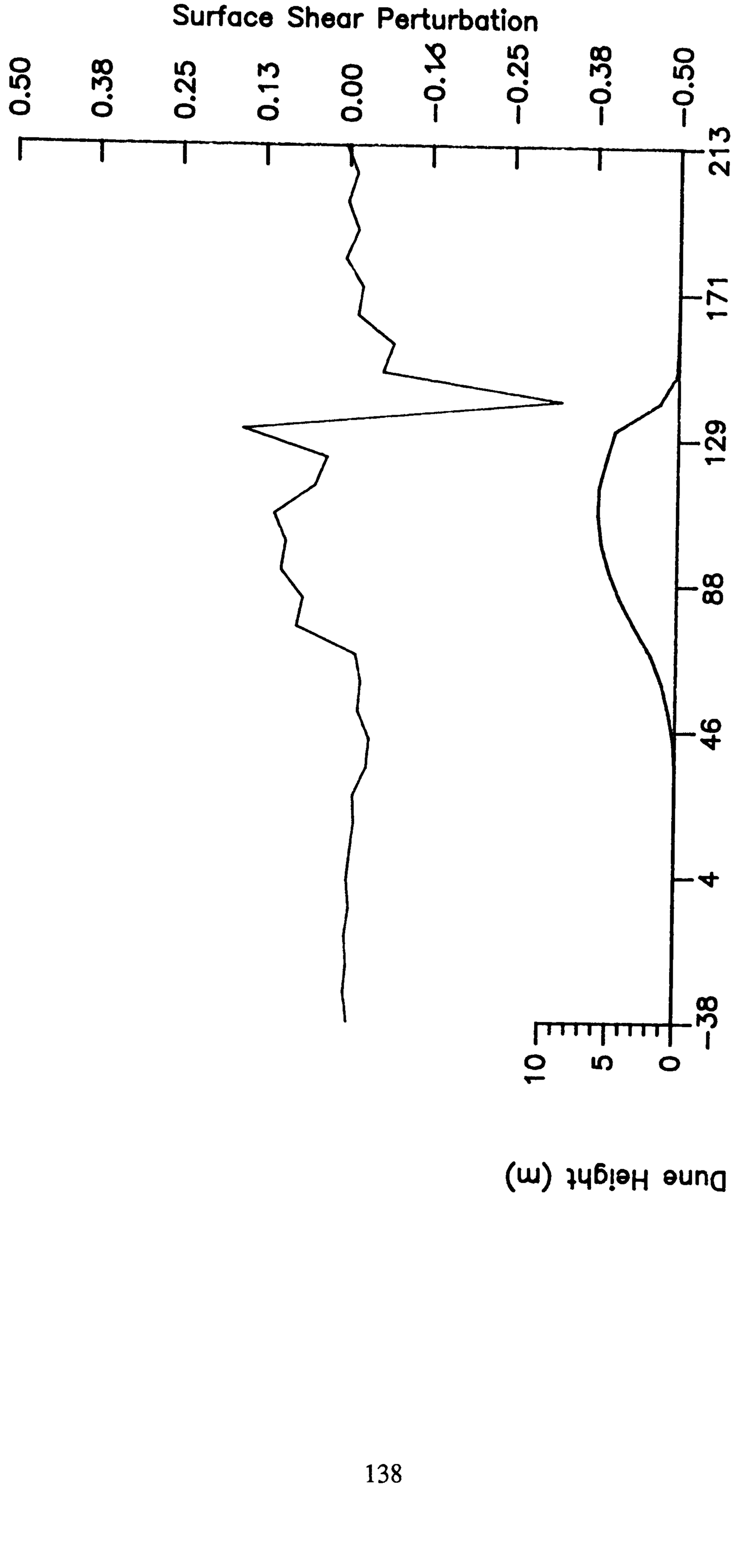

Figure 3.20 Calculated surface shear stress perturbation on the left flank.

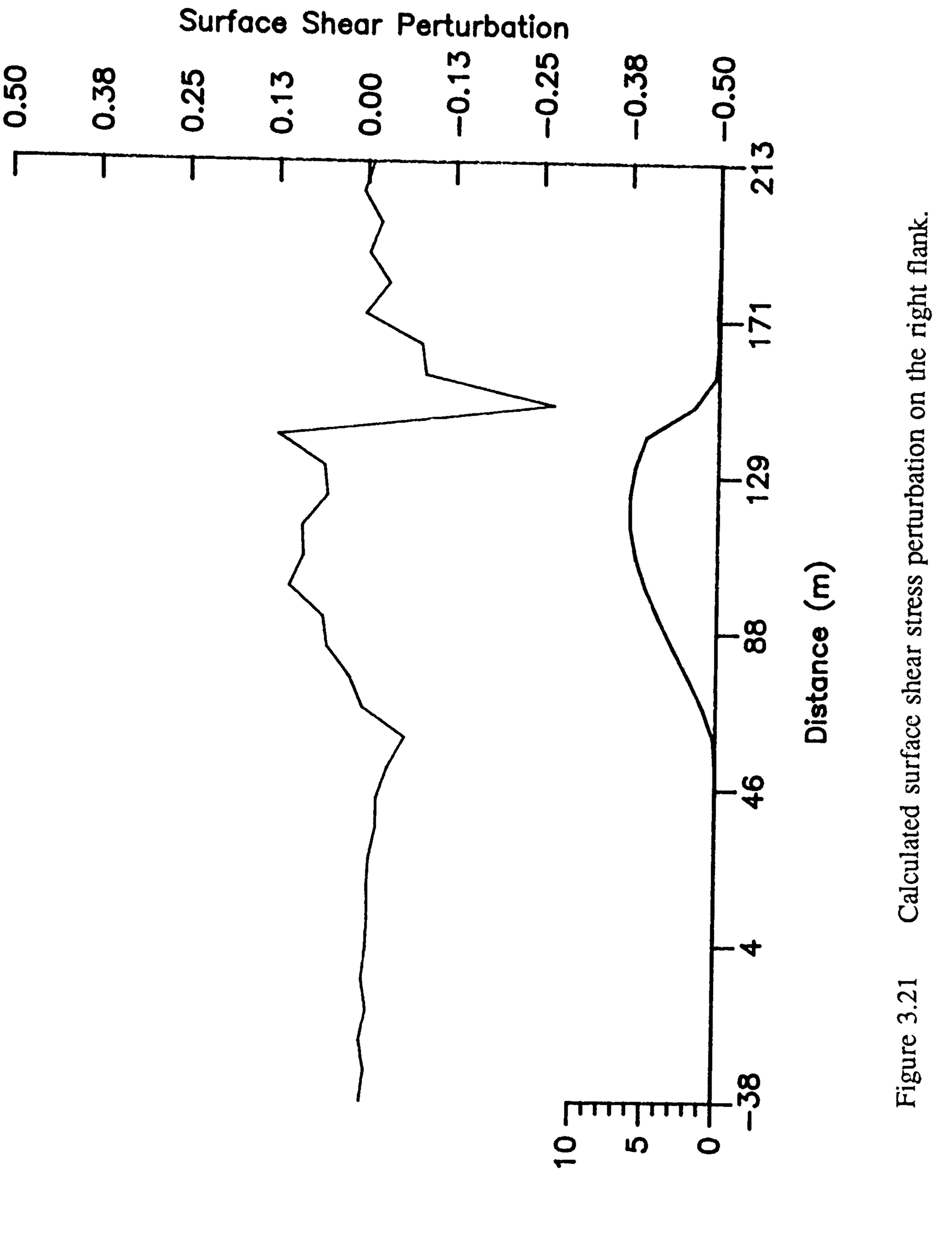

Figure 3.21 Calculated surface shear stress perturbation on the right flank.

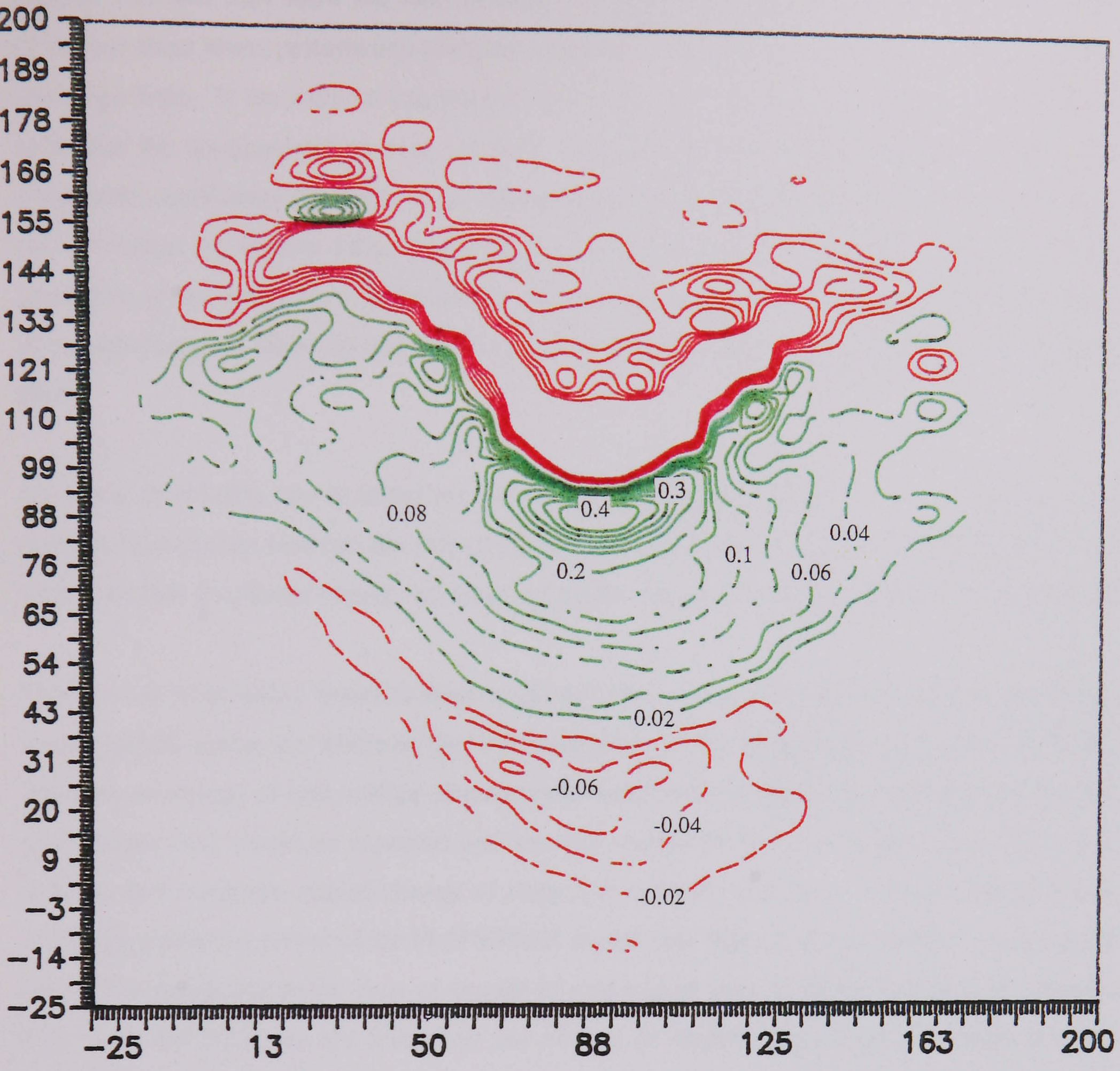

Figure 3.22 Contour map of calculated surface shear stress perturbation. Red is negative perturbation; green is positive perturbation. Flow direction is from bottom to top.

Morphological Relationships

Figures 3.23 and 3.24 show the rate-of-change of fractional speed-up ratio and rate-of-change of surface shear stress perturbation along the centre-line and their relationship to the dune height and slope angle. If the value at the brink (x = 107 m) is ignored in each case then it becomes clear that the development of both variables is highly dependent upon the slope angle. The correlation coefficients for slope angle with rate-of-change of speed-up (at 0.25 m height) and rate-of-change of surface shear stress along the centre-line are 0.67 and 0.50 respectively (exclusive of the predictions at the brink). An increase in angle is associated with an increase in rate-of-change of speed-up and surface shear stress whilst a decreasing angle has the opposite effect.

The same association can be identified on the flanks, as shown in Figures 3.25 to 3.28. In each case the relationship between the rate-of-change of surface shear stress and slope angle is less clear than that for rate-of-change of speed-up because the perturbations are that much smaller.

This general relationship between slope angle and rate-of-change of δ_s and surface shear stress seems reliable across the whole of the windward slope of the dune except at the toe and brink. The rates-of-change of both surface shear stresses and fractional speed-up ratios at the brinks are much larger than would be expected and are only related to the slope angle in that the peaks occur at the maximum rate-of-change of slope (*i.e.* onto the slip face). This is a result of the unreliable predictive power of the FLOWSTAR model near regions of reverse flow, as discussed above. The reductions in the rates-of-change of speed-up at the toes of the section lines (Figures 3.23, 3.25 and 3.27) are not related to any change in surface slope angle or terrain. Similar reductions in the rates-of-change of surface shear stress (Figures 3.24, 3.26 and 3.28) are more difficult to identify because of the irregular simulation pattern. The upwind negative rate-of-change of speed-up is more likely to be a response to the adverse pressure gradient in this region rather than any direct response to changes in the dune terrain. However, between the toe and the brink there appears to be a distinct and instantaneous association between rate-of-change of both speed-up and surface shear stress to the surface slope angle.

The sensitivity of simulations of shear stress and velocity perturbation to small changes in topography has also been noted by Walmsley *et al.* (1982), Howard & Walmsley (1985) and Hunt *et al.* (1988a). It is a feature of the JH solution and necessitates very careful smoothing of the terrain to be undertaken if erratic results are to be avoided. Howard & Walmsley (1985) cited this sensitivity as a possible cause of the over-prediction of velocity at the brink of their transverse dune and Walmsley *et al.* (1982) used seven successive smoothing functions to

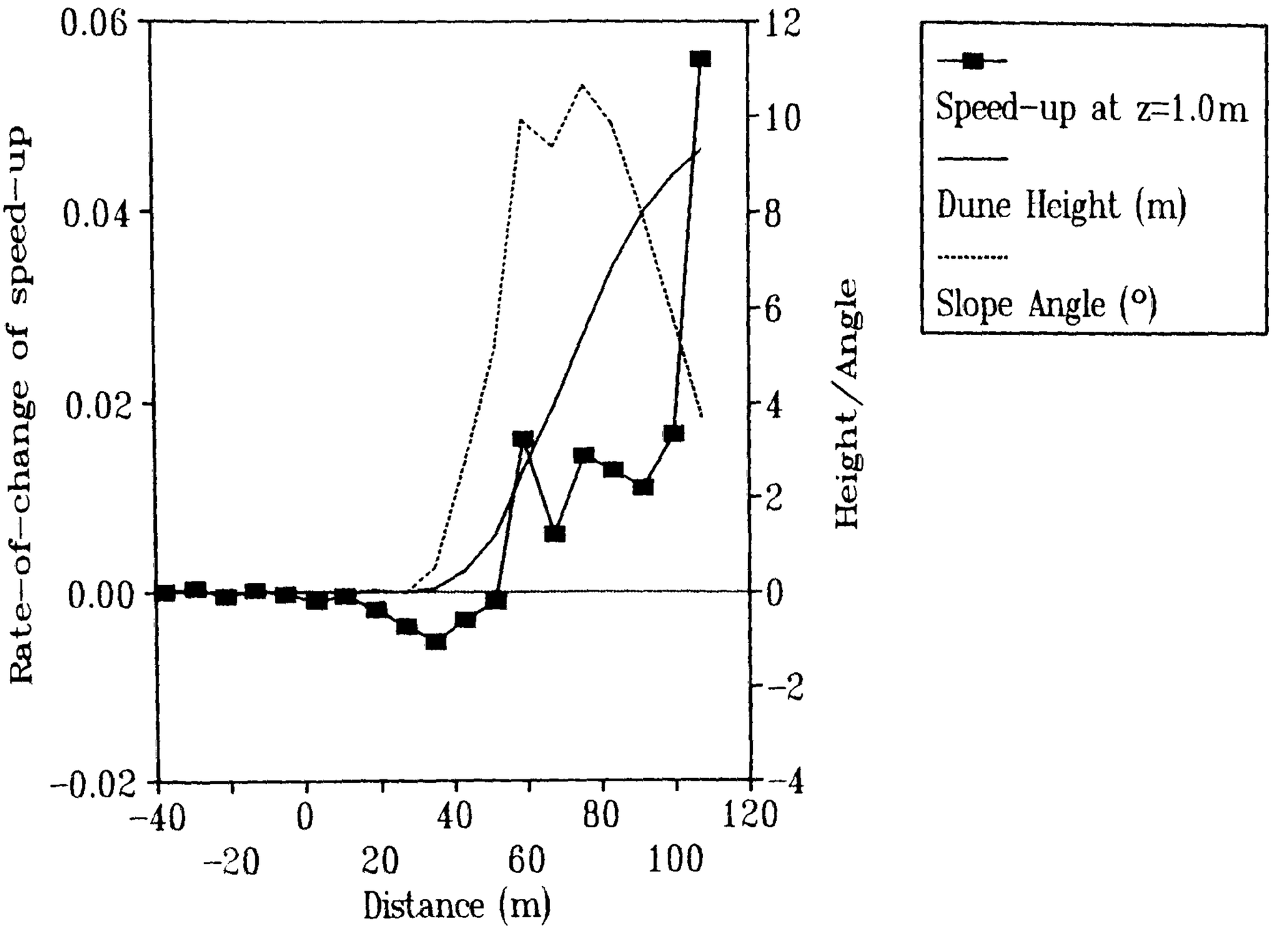

Figure 3.23 Relationship between surface height, slope angle and rate-of-change of calculated fractional speed-up ratio on the centre-line.

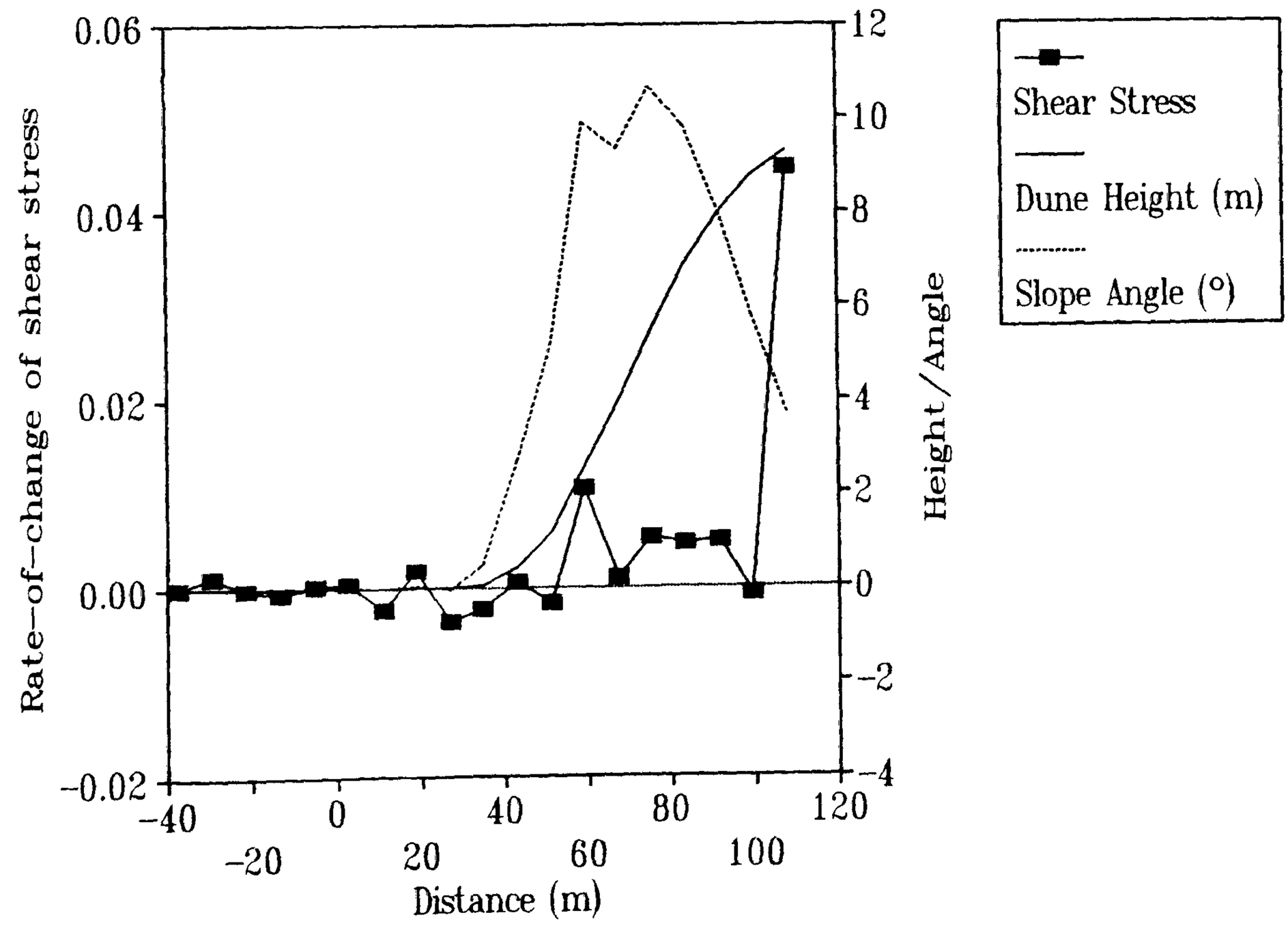

Figure 3.24 Relationship between surface height, slope angle and rate-of-change of calculated surface shear stress perturbation on the centre-line.

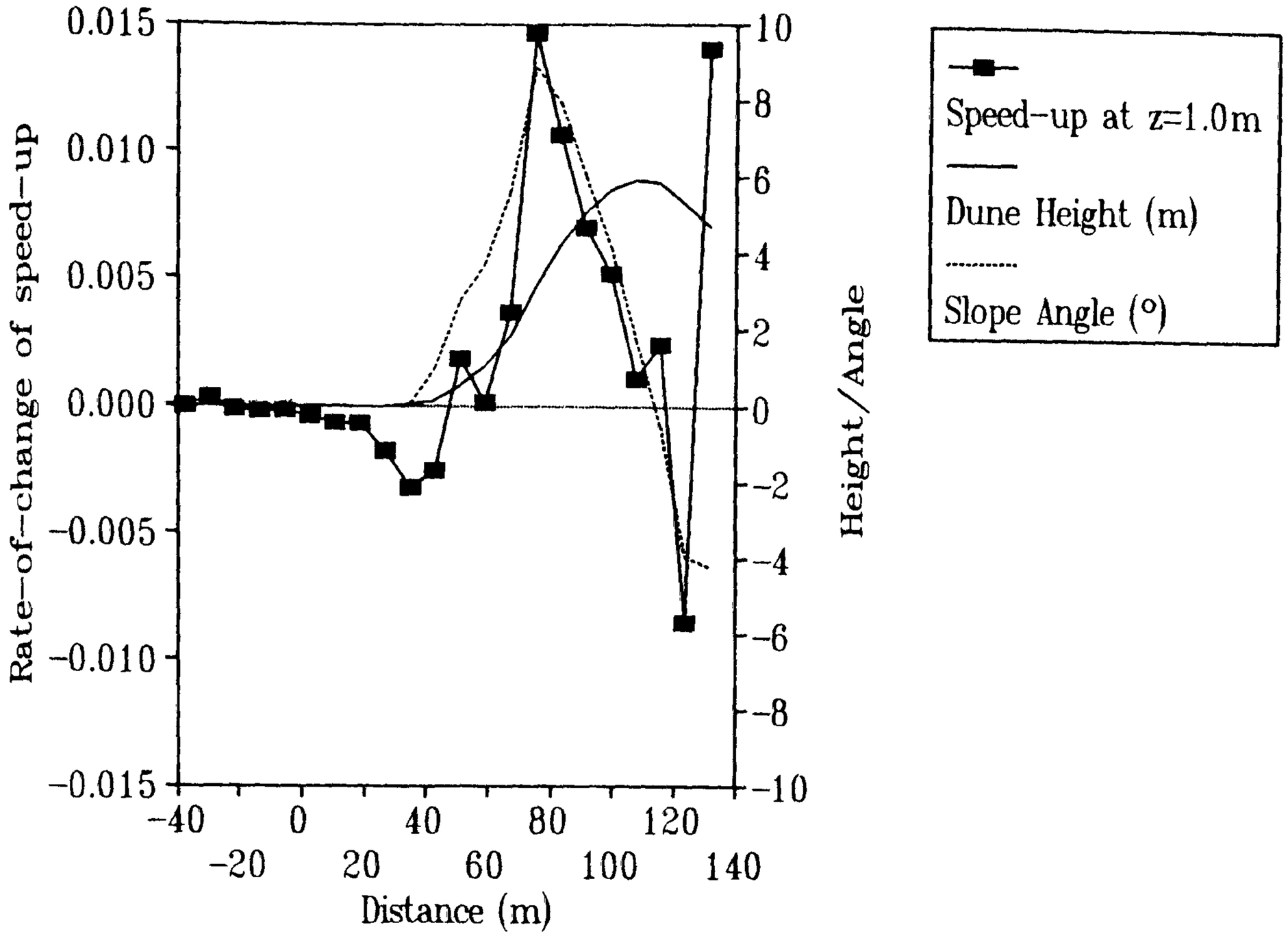

Figure 3.25 Relationship between surface height, slope angle and rate-of-change of calculated fractional speed-up ratio on the left flank.

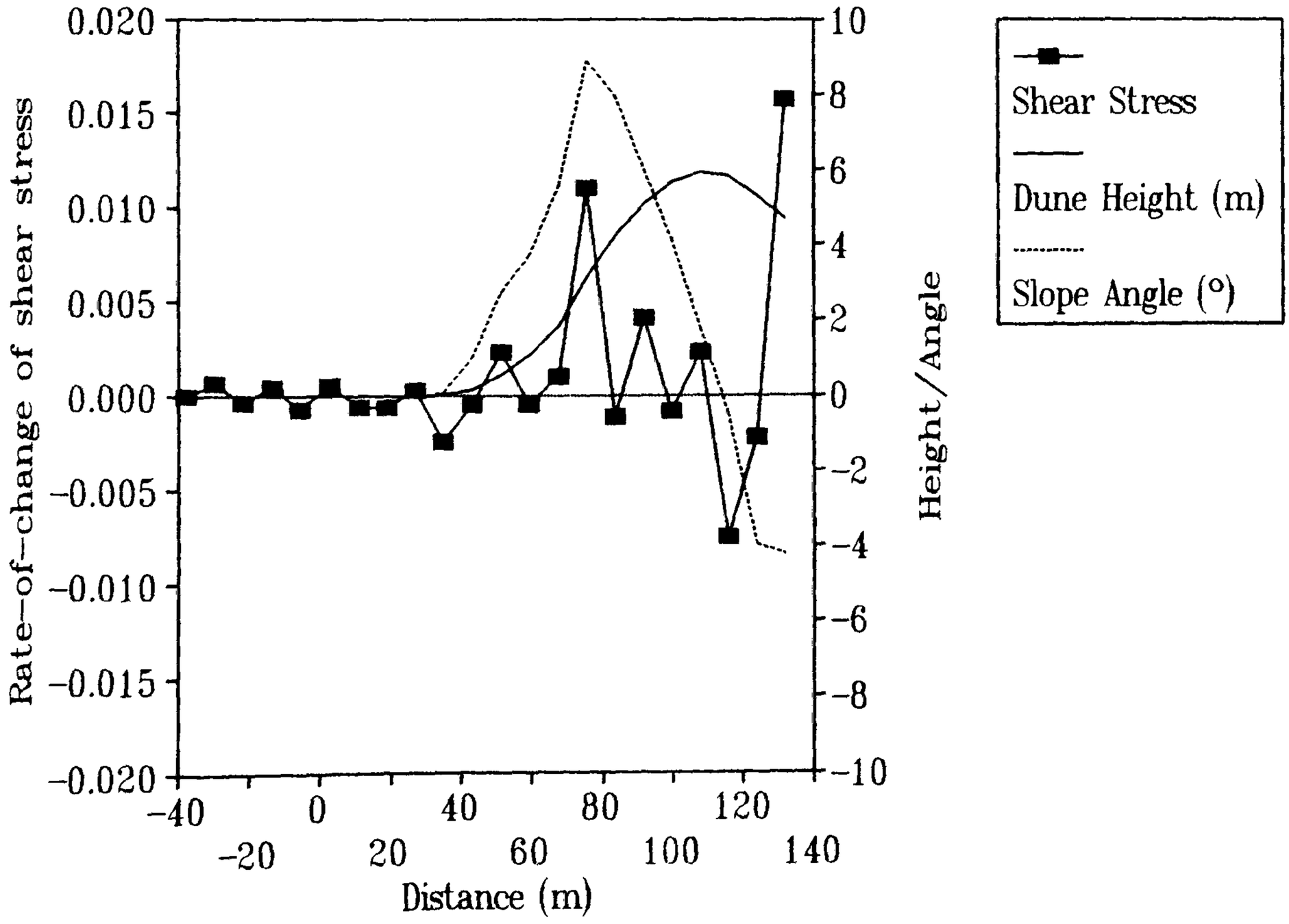

Figure 3.26 Relationship between surface height, slope angle and rate-of-change of calculated surface shear stress perturbation on the left flank.

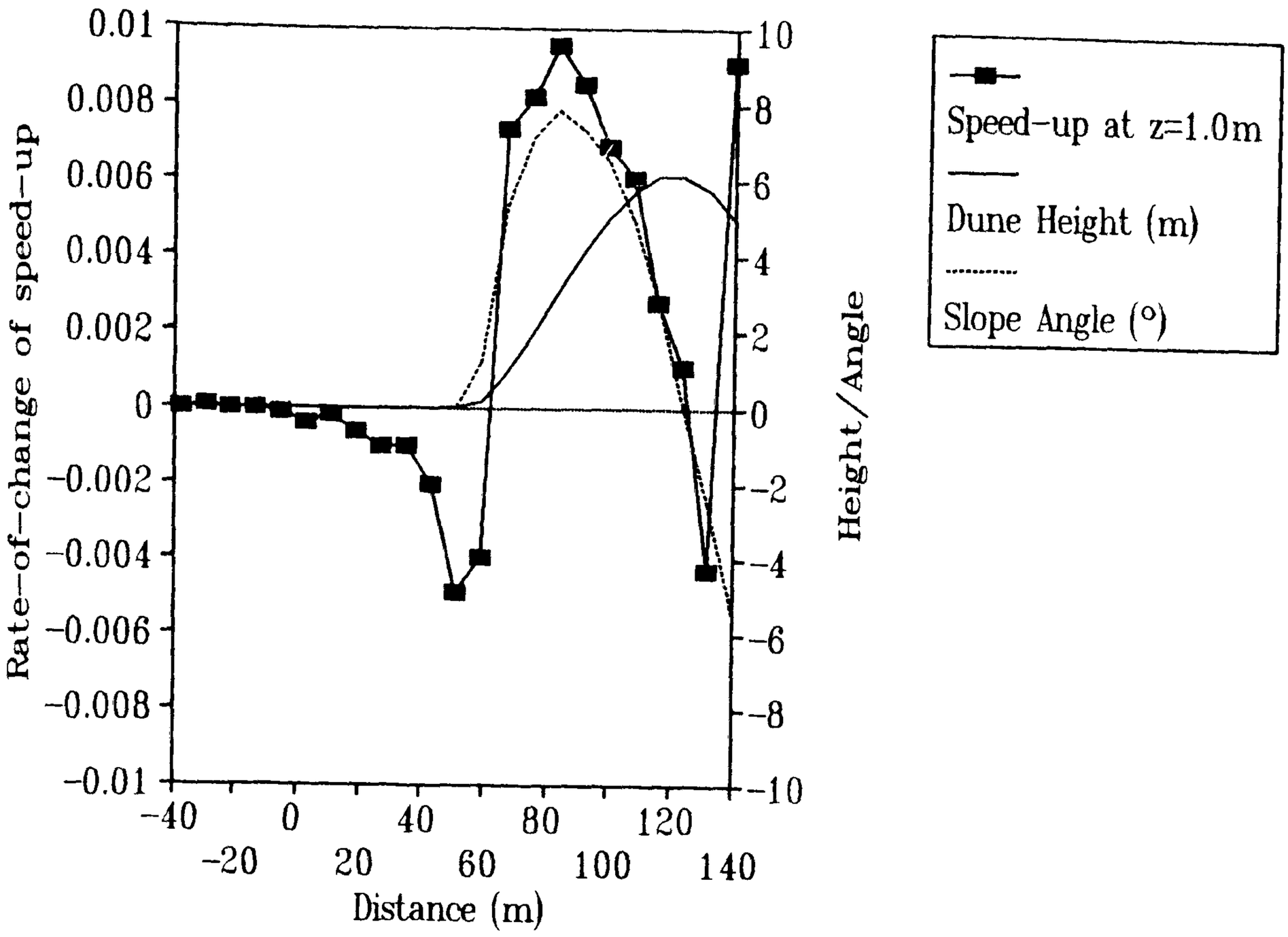

Figure 3.27 Relationship between surface height, slope angle and rate-of-change of calculated fractional speed-up ratio on the right flank.

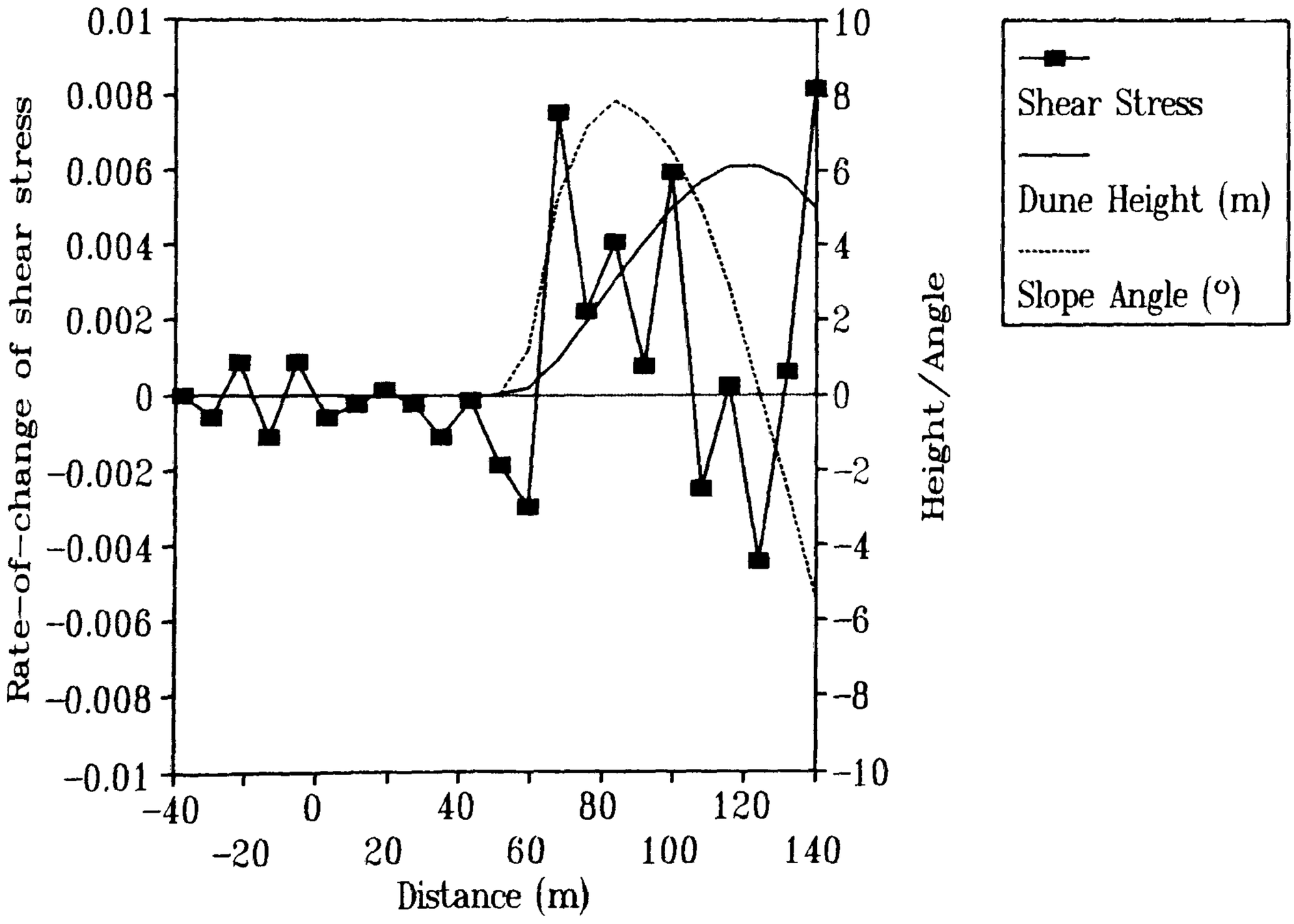

Figure 3.28 Relationship between surface height, slope angle and rate-of-change of calculated surface shear stress perturbation on the right flank.

eradicate the small scale "noise" in their velocity simulations. As discussed earlier, the over-prediction of both velocity and shear stress perturbations at the brink of the study dune in this investigation is more likely to be caused by the inability of the FLOWSTAR program to model the region of flow separation downwind of the brink. However, the need for an accurate terrain interpolation routine and reliable survey data is evident.

3.5 Conclusion

The revised FLOWSTAR model based on the Hunt *et al.* (1988a) solution for turbulent flow over low hills is an improvement on the original JH theory. The calculated velocity field over the prototype dune resembles that of other models (over similar dune forms) and corresponds with measurements of velocity perturbations over low hills. However, FLOWSTAR does appear to grossly overestimate velocity at the brink. This is a response of the model to the region of downwind flow separation. The inability of the model to predict velocity vectors in the reverse flow region also causes an over-estimation of flow convergence at the brink. The divergence of flow predicted at the base of the flanks, however, is comparable to that of the field measurements.

The development of the velocity field over the dune involves a region of negative perturbation near the toe followed by acceleration toward the crest. In the case of the flanks, there is a drop in velocity between the crest and brink, excepting the overestimation at the brink itself. The non-uniform nature of flow acceleration resulted in vertical profiles of velocity becoming non-log linear along the windward slope, even at the toe. Confirming the findings of previous studies using variations of the JH theory, it was established that the changes in velocity and shear stress perturbations were very sensitive to small-scale fluctuations of the dune terrain.

Previous tests of numerical models of turbulent flow over sand dunes have relied on such examinations of velocity field calculations to determine the reliability of the model (Howard & Walmsley, 1985). They have then proceeded to calculate sand transport and the resultant erosion/deposition. However, such a technique avoids an examination of the turbulent stress simulations which are, after all, responsible for sand transport. The results presented in this chapter have shown that, despite much "noise" within the simulation, the calculated Reynold's stresses correspond to measurements and observations made over low hills. The simulations predict a rapidly changing shear stress above the surface of the dune which could cause

considerable difficulties in estimating surface shear stress in a field situation from near-surface velocity measurements. These complications are discussed in more detail in Chapter 7.

An examination of the vertical profiles of velocity and shear stress revealed that the inner-layer is characterised by a positive gradient in shear stress and not the maximum velocity perturbation. However, it does incorporate the maximum velocity perturbation at a height equivalent to 1/3.

It now remains for the predictions of velocity and shear stress presented here to be compared to the field and wind tunnel measurements (Chapters 5 and 6).

CHAPTER 4 HARDWARE MODELLING

4.1 Introduction

Earlier Chapters have shown that advances have been made in the study of air-flow over hills utilising empirical data from field studies and theoretical concepts in mathematical modelling. However, despite the abundance of wind-tunnel simulations, hardware modelling has had little input to the development of this theory. This is initially surprising in view of the advantages of wind tunnels where the type, scale, uniformity, endurance and direction of flow can be controlled. The reasons for this lack of confidence in wind tunnels centre on the analytical model of Jackson & Hunt (1975). Britter *et al.* (1981) noted that in order to achieve fully turbulent conditions in a wind tunnel (where $u_* z_0/\nu > 3$, if ν= kinematic viscosity) it is often necessary to increase the size of the roughness elements relative to the scale model. In such circumstances the depth of the inner-layer (l), as defined by Jackson & Hunt (1975), is of the order of the size of the roughness elements. Hence, the scaling factor l/k (where l = inner-layer thickness and k = roughness element height) may be reduced to 1.0. In these conditions it is impossible to measure flow parameters within the inner-layer. Furthermore, the majority of field studies have been concerned with relatively steep sided hills which tend to induce flow separation and turbulent wakes. The wind tunnel techniques to measure airflow in such regions have yet to be perfected. The combination of these problems has resulted in the poor representation of wind-tunnel data-sets in the forum of boundary-layer flow over hills.

A few geomorphologists have employed hardware models to study airflow patterns over dunes. Indeed, much of the recent discussion of the geomorphological dynamics of dunes has stemmed from wind-tunnel research over isolated dune models (Howard *et al.*, 1977; Lai & Wu, 1978; Knott, 1979; Tsoar, 1985; Tsoar *et al.*, 1985; Greeley, 1986) Of these investigations, only those of Howard *et al.* and Tsoar *et al.* have attempted to relate their data to those of mathematical theory. The increasing prominence of hardware modelling in geomorphological discussion makes the omission of wind-tunnel studies in the classical theory of airflow modelling all the more important. It is necessary to compare a geomorphological-type wind tunnel study with theory so that the contemporary analysis of geomorphologists can be contrasted and substantiated.

Most of the geomorphological studies cited above, and similar investigations, have been at a very simplified level and, apart from Knott (1979), the published accounts lack details of experimental methods. Tsoar (1985) described velocity traverses over two typical dune profiles and compared wind tunnel experimentation with field results, but did not specify the height of measurements

above the surface. Without these details, it is not possible to make comparable measurements or conclusions.

The difficulties of measuring within the inner-layer and an understanding of the roughness element height ratio are crucial to this kind of study. Two approaches can be taken to overcome these problems. First, models can be constructed which ignore the roughness restriction and are not fully-rough (Teunissen *et al.*, 1987), hence allowing the inner-layer to be investigated. However, the degree to which the relationships between turbulence structure, separation, and near-surface velocity of smooth models compare to the real world is not fully understood. The second approach is to develop a fully-rough boundary layer and use the results as a representation of the airflow over a highly rough surface (*e.g.* urban or wooded roughness). Such an approach was used by Britter *et al.* (1981), Gong & Ibbetson (1989) and Finnigan *et al.* (1990), but is not applicable to dunes, where the aerodynamic roughness is very small.

The present study uses a combination of near-fully-rough boundary conditions which satisfy the "law-of-the-wall" parameters (z_0, u_* and d [zero-plane displacement]) and careful measurement close to the surface, to measure velocity and turbulence elements within the inner-layer, upwind of the brink of a barchan dune model. These measurements, in combination with surface shear stress measurements using a modified pulse-wire probe, are compared to the mathematical theory and field measurements in Chapters 5 and 6.

4.2 Wind Tunnel Description and Requirements

4.2.1 Experimental Apparatus

The Wind Tunnel

The wind tunnel used for the present work was located at the Department of Mechanical Engineering, University of Surrey. It was of the blower-type consisting of an 800 r.p.m motor driving air via baffles, diffuser and contraction into a 4m-long, straight, rectangular tunnel with a height of 0.6 m and width of 0.9 m (Figure 4.1). The tunnel walls were constructed from wood and plexiglass in removable sections which allowed ease of access. The control of airflow into the tunnel was achieved by varying the speed of the motor. The characteristic flow velocity in these experiments was 10 ms^{-1}.

Velocity and Shear Stress Sensors

i. Single Hot-wire Anemometer.

The inherent difficulties in making accurate measurements within a turbulent boundary layer are that a sensor must be placed within the flow, thus disrupting it, and that the flow is rapidly fluctuating and difficult to determine. Hence it is necessary to use equipment which makes instantaneous velocity and fluctuation measurements whilst also negligibly impeding the flow. The statistically quantifiable time-averaged velocity can then be determined.

The instrument most widely used in these situations is the hot-wire anemometer. It determines velocity fluctuations from the resistance of a thin wire placed in the flow, the electro-conductivity of which is controlled by its temperature. The thin wire is usually made of platinum and has a diameter of about 5 microns. Each end of the wire is gold-plated to inhibit conduction between itself and the two supports. The active portion of the wire is therefore quite small and of the order of 1 mm. Figure 4.2a shows the details of a single-wire probe.

In the present set of experiments, the *DISA* constant temperature anemometer system was employed. In this apparatus the temperature of the active wire is kept constant by an amplifier in a feedback loop (Wheatstone bridge). As long as the probe has been accurately calibrated, the velocity of flow can be deduced from the voltage required to keep the probe at a constant temperature. The relation between output voltage (V) and velocity (U) is described by King's Law;

$$V^2 = a+bU^n \tag{4.1}$$

where the constants a and b are deduced from the calibration and the exponent n is assumed to be 0.45 for speeds less than 20 ms^{-1} (Castro, 1986).

Owing to its wide use, the hot-wire anemometer has come under very close scrutiny and the literature on its use and limitations is extensive. Two concise descriptions are to be found in Bradshaw (1971) and Castro (1986). The agreed advantages of the hot-wire over other measurement techniques (*e.g.* the pitot-tube) are that;

1. Its small size offers minimum disturbance to the flow and allows measurements "at-a-point", not the mean over a wide spatial range.

2. It has a fast response time, thus being capable of measuring rapid flow fluctuations.

Figure 4.1 The wind tunnel at the Department of Mechanical Engineering, University of Surrey.

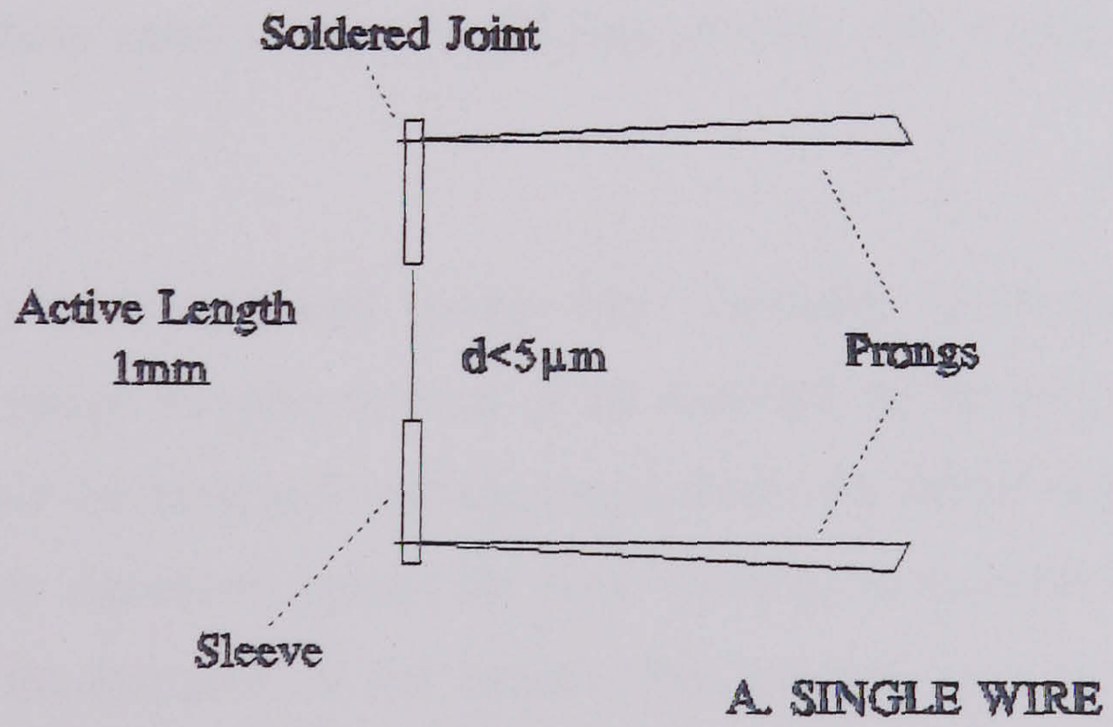

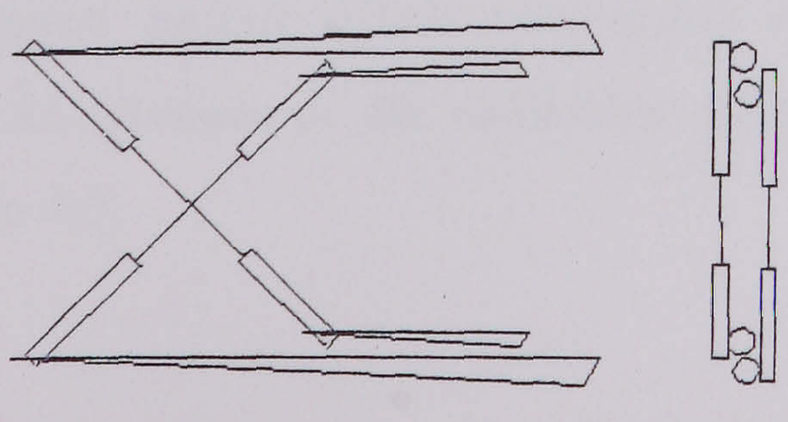

Figure 4.2 Hot-wire anemometers. A = single-wire; B = cross-wire (after Bradshaw, 1971).

PAGE

MISSING

IN

ORIGINAL

3. It measures both the amplitude and frequency of fluctuations.

However, it is important to appreciate the limitations of the hot-wire and the errors which may occur so that steps can be taken to minimise them. The major limitations (Castro, 1986) are;

1. It cannot identify reverse flows.

2. It is inaccurate in highly turbulent flows (*e.g.* >40% turbulent intensity).

3. It is liable to calibration drift because of a change in the ambient air temperature or build-up of dirt on the active wire.

Owing to the first limitation above, it was not possible in the present experiments to take any measurements downwind of the dune brink, although some shear stress measurements were made in this region using a pulse-wire probe (See iii. below). Limitation (2), concerned with highly turbulent flows, is not applicable in this case because nowhere over the model surface was the turbulence found to be in excess of 32% (see section 4.5). Limitation (3) was counteracted by frequent calibration. Before and after each traverse a reference velocity was measured. If the two values were appreciably dissimilar (±½%) then the results were dismissed. In some instances, despite changing wires, the calibration was found to be consistently irregular. Sometimes by as much as 3%. In these cases a linear coefficient-of-error was determined and applied to each measured value.

The calibration of the single-wire probe, after adjusting for frequency response, involved measuring 6000 voltage samples (a total of 60 seconds) in the empty tunnel at five different wind velocities over the expected velocity range above the model dune (2-12 ms^{-1}). The output voltage was linearly regressed against the flow velocity, as measured by a pitot-tube 170 mm from the roof at the entrance of the tunnel. This processing was carried out on-line using *PROSSER* software on a *BBC* Master microcomputer. The output from the regression consisted of the constants a and b, required by Equation 4.1. A "look-up" table of voltage output and flow velocity was then computed against which subsequent voltage measurements could be automatically compared. An example of the calibration output is shown in Table 4.1 and a calibration curve in Figure 4.3.

Table 4.1 Single hot-wire calibration data.

Voltage (Volts)	Velocity (ms^{-1})	Constant A	Constant B
4.753	10	-	-
4.563	7.483	8.157	5.121
4.335	5.107	8.029	5.168
3.975	2.53	7.879	5.227
3.757	1.497	**7.844**	**5.241**

When taking velocity measurements over the dune model, 6000 voltages were sampled at a frequency of about 100 Hz.

ii. Cross Hot-wire Anemometer (x-wire).

The single hot-wire probe measures only the u-component fluctuations of velocity. In order to calculate the Reynold's stresses at a point it is necessary to measure both the u- and w-components of the flow (the horizontal downwind and vertical components respectively). This can be accomplished by using a pair of wires arranged in an "X" formation at approximately ±45° to the flow direction. One wire measures u+w, and the other u-w. The configuration of the cross-wire probe is shown in Figure 4.2b.

The wire-calibration technique for this type of probe is similar to that for the single-wire probe. However, an additional yaw-response calibration is required. This consists of rotating the probe in the w-plane through known angles at a constant and known flow velocity, and recording the voltage apparent for each wire. The cross-wires were yaw-calibrated in the empty tunnel at $\approx$10 ms^{-1} at ±5°, ±10° and ±15°. Bradshaw (1971) noted that calibrating the wires beyond ±15° was not pertinent as this was beyond the directional response of the wires. Sample results of a cross-wire yaw calibration are shown in Table 4.2 and a graphical representation of the response of each wire to the change in angle is shown in Figure 4.4.

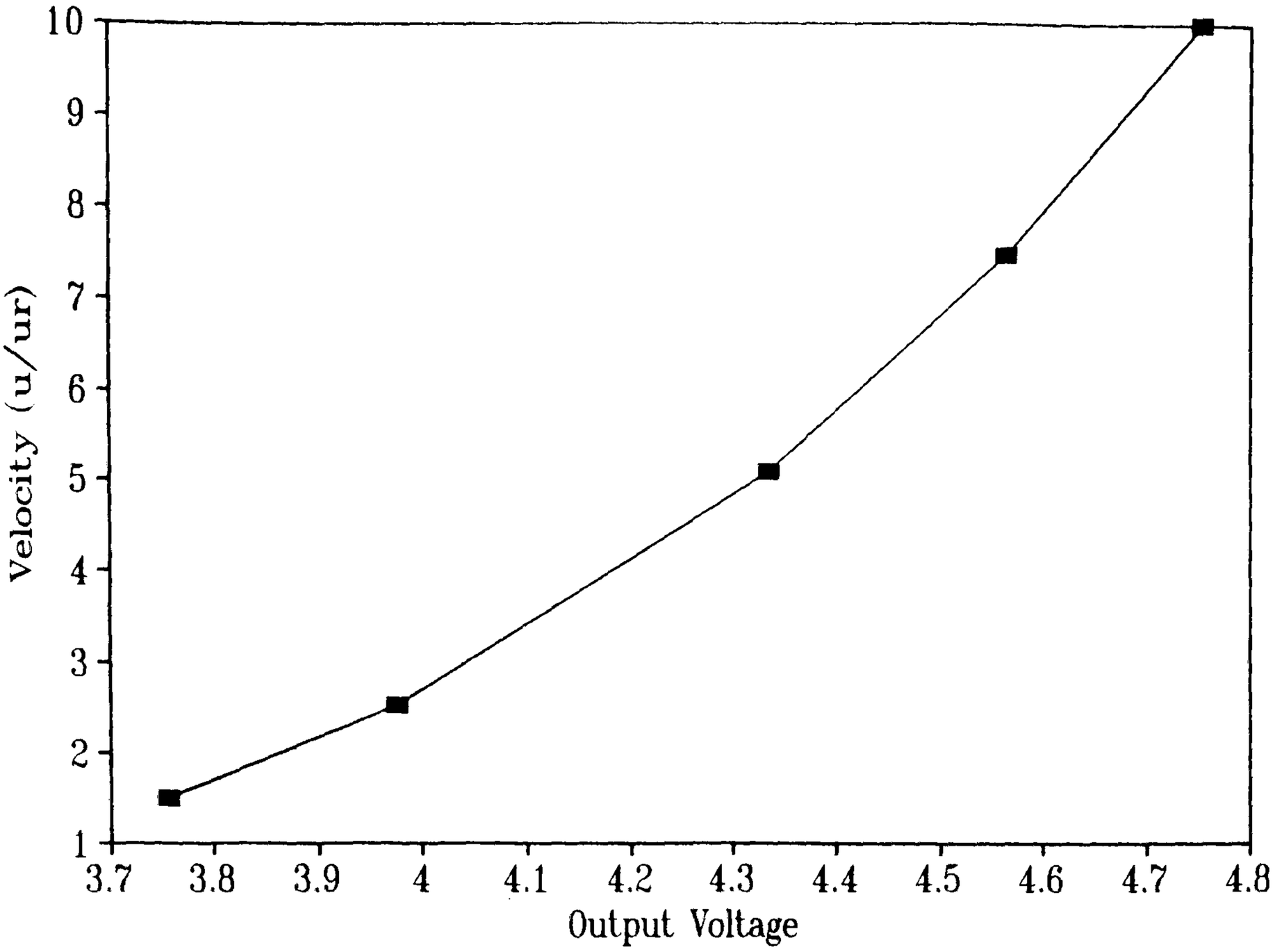

Figure 4.3 Single-wire calibration curve.

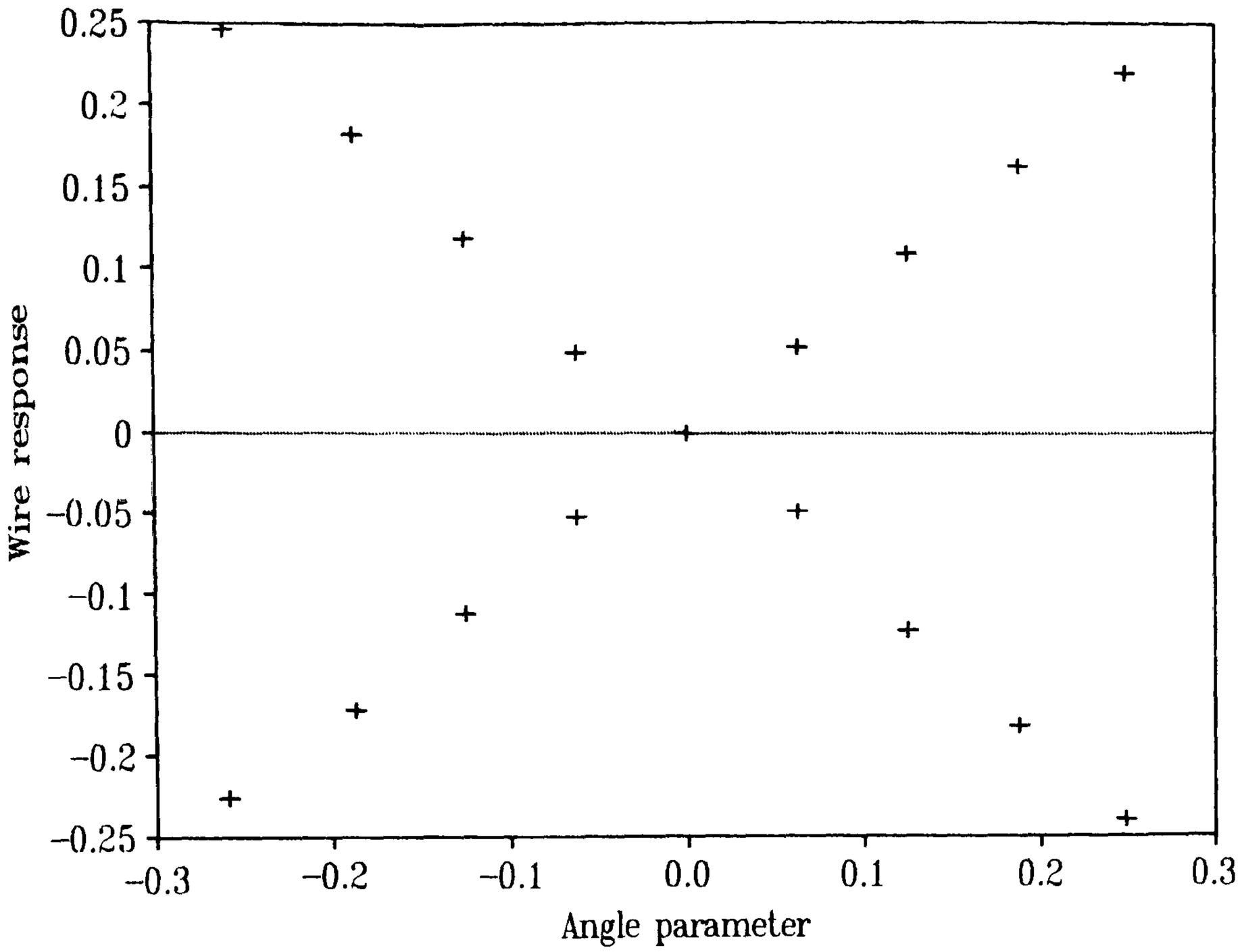

Figure 4.4 Cross-wire yaw-response calibration.

Table 4.2 Cross hot-wire yaw-response calibration data.

X	Y1	Y2	P1	P2
0	0	0	0	0
0.1253	-0.1224	0.1098	44.32	41.22
0.1874	-0.1817	0.1636	44.18	41.15
0.2487	-0.2406	0.2201	44.11	41.35
-0.2587	0.2458	-0.2265	44.31	41.7
-0.1874	0.1832	-0.1718	44.32	41.84
-0.1253	0.1189	-0.1122	44.26	41.84
-0.06279	0.04923	-0.05267	**44.16**	**41.81**

X = Angle Parameter
Y1= Response of Wire 1
Y2= Response of Wire 2
P1= Angle of Inclination of Wire 1 (°)
P2= Angle of Inclination of Wire 2 (°)

The effect of the inclination angle of each of the wires (P1 and P2) is included in the look-up table computed by the software. The yaw-calibration was carried out only once for each cross-wire as the yaw-response of the wires deviates only with the inclination angle and not ambient temperature *etc*.. The wire-calibration was carried out as for the single-wire.

The limitations of the cross-wire probe are similar to that of the single-wire, but the results are significantly more sensitive to turbulence fluctuations higher than about 15%. In this instance correction factors derived by Tutu & Chevray (1975) were utilised (see Section 4.5 for a detailed discussion).

Where measurements of Reynold's stress were being carried out over the dune model 12000 voltages were sampled at a frequency of about 100 Hz.

iii. Pulsed-wire Anemometer.

This type of probe is designed specifically to make measurements in highly turbulent or separated flow regions where traditional hot-wire probes cannot be used because of their lack of sensitivity to angular changes in the velocity vector normal to the wire axis (Castro, 1991). The principle behind pulse-wire anemometry (PWA) is the measurement of the "time-of-flight" of a heat tracer generated as a pulse in one thin wire and detected by a second sensor wire. The velocity can then be deduced from the reciprocal of the flight time.

The method has recently been adapted for measurements in the near-wall region where it is the only available technique that can measure the fluctuating component of wall shear-stress (Castro, 1991). It is particularly problematic to measure within this region, first because it is so thin and, secondly, because the influence of the wall on the probe can be significant. However, detailed measurements by Castro & Dianat (1990) have shown that the PWA technique is ideally suited to measurement within this region.

The arrangement of the near-wall probe used in this experiment is shown in Figure 4.5. The heat tracer is generated in the central wire by passing a short pulse of electric current through it. The sensor wires then act as resistance thermometers and detect the arrival of the tracer. With a sensor wire each side of the pulse wire, it is possible to measure instantaneous velocities in both directions, and hence measure elements downwind of a dune brink within the re-circulation zone. Further details concerning the use of the probe in the tunnel are given in Chapter 4.3.4.

Several authors (Bradbury & Castro, 1971; Castro *et al.*, 1987; Handford & Bradshaw, 1989; Castro & Dianat, 1990; Castro, 1991) have reviewed the uses of PWA and the relevant calibration techniques. Castro (1991) stated that the most accurate calibration was;

$$U = A/T + B/T^3 \qquad (4.2)$$

where:

U = velocity
T = time-of-flight of heat tracer

If the probe is mounted in the near-wall region, close to the surface, then it can be calibrated for surface shear stress, with u_*^2 being substituted for U in Equation 4.2. However, Castro *et al.* (1987) found that the most accurate calibration fit for surface shear stress was reached using;

$$u_*^2 = A/T + B/T^2 + C/T^3 \qquad (4.3)$$

The calibration of the probe close to the surface is different for turbulent and laminar conditions, with shear stress measurements differing by up to 20% (Castro *et al*, 1987; Castro, 1991). This implies that calibration in a laminar boundary layer results in significant shear stress errors where measurements are taken in a turbulent boundary layer. This contrast has yet to be fully explained. Standard practice is to calibrate the shear probe in a smooth wall turbulent boundary layer if subsequent measurements are to be carried out in a turbulent environment.

The pulse-wire probe was initially calibrated against a Preston tube in the empty tunnel, apart from a castellated trip fence at the front of the working section to generate some turbulence (See

Chapter 4.2.2). The pulse-wire probe was inserted through the roof of the tunnel flush with the interior surface, with the wires perpendicular to the flow direction, and calibrated for u_* (shear velocity). Subsequent calibrations required only the input from the pitot-tube positioned at the tunnel entrance. The probe was interfaced with an *Apple Macintosh* computer and on-line processing of the measurement and calibration routines was achieved through *Labview* software.

For both calibration and flow measurements 10,000 individual samples were taken at ≈20 Hz, giving an averaging time of ≈5 minutes, easily long enough to account for the lowest turbulent frequencies. Each calibration extended over a tunnel velocity range as measured by the pitot tube of between 2 and 20 ms^{-1}, giving a u_* range of about 0.15 to 0.7 ms^{-1}. The calibration routine automatically calculates the required constants for Equation 4.3 and transfers them into the measurement routine. A sample of the calibration output for the positive wire is shown in Figure 4.6.

The Traverse System

The traverse system situated on the roof of the tunnel, above the dune model (Figure 4.7) allowed the position of the hot-wire probes to be exactly defined. The traverse gear was operated through a *Macintosh* computer and errors of <0.3 mm could be achieved. However, the accuracy of the initial origin depended upon manual measurement from the floor of the tunnel with a steel rule. The system could operate in any two planes simultaneously.

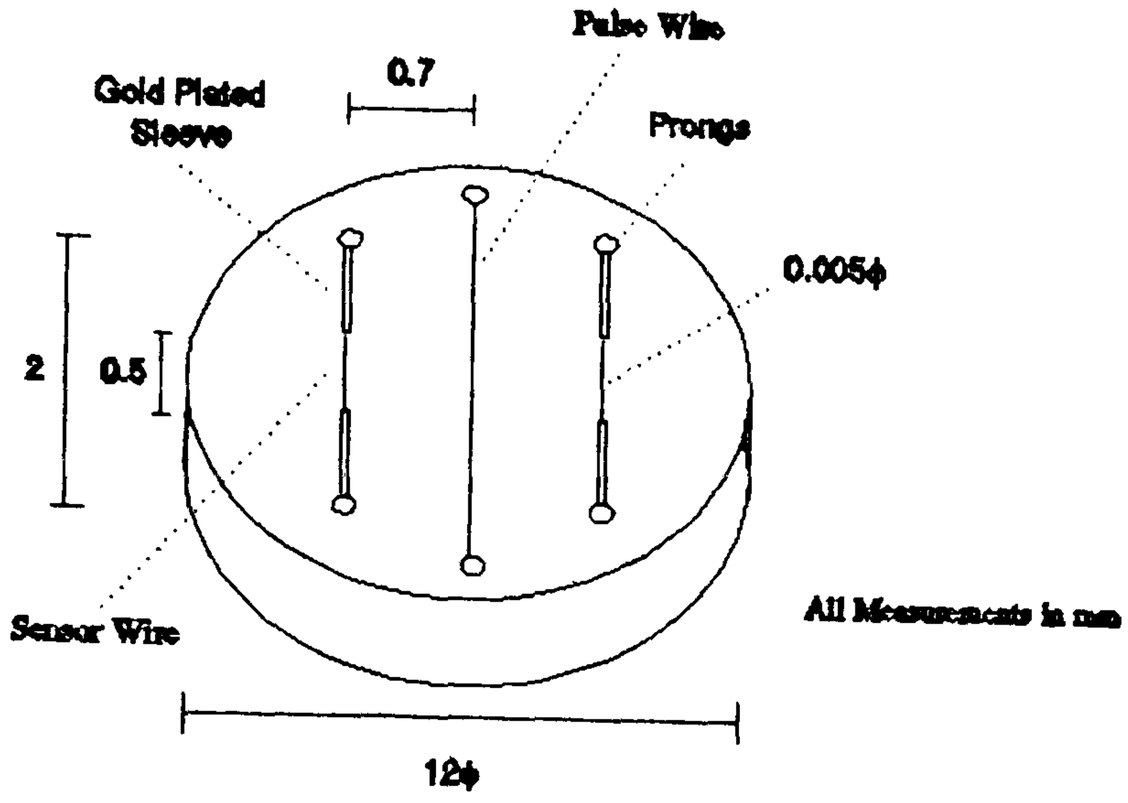

Figure 4.5 The head of the near-surface pulse-wire probe

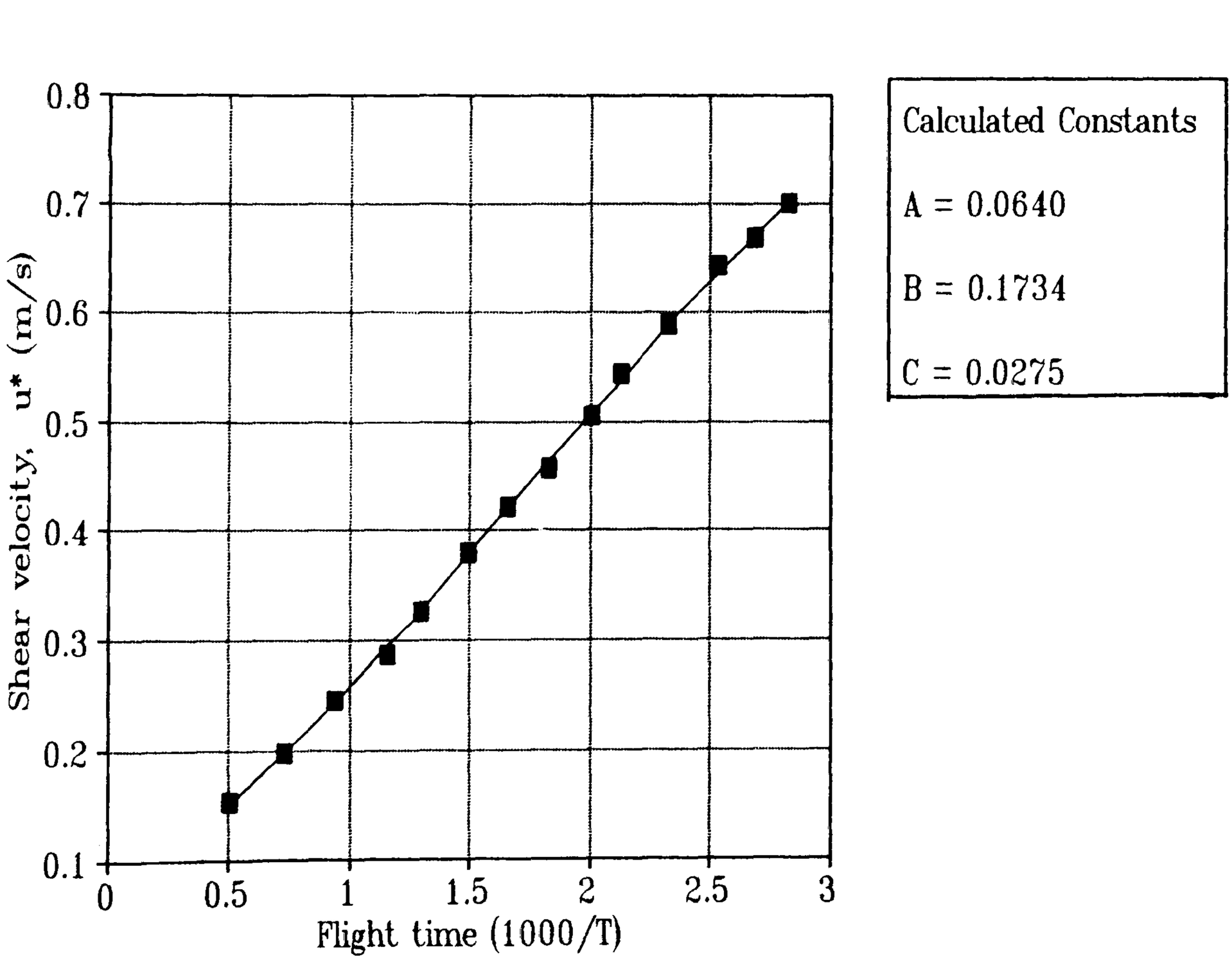

Figure 4.6 Positive (downwind) wire calibration curve for the pulse-wire probe.

4.2.2 Similarity Requirements

When scaling factors are used to place a model of a dune into a wind tunnel there are certain similarity requirements which must be satisfied in order to attain the satisfactory duplication of the full-scale environment. The scaling parameters concerning the ratios of inner-layer height to roughness element height were briefly discussed in Chapter 4.1. This section describes the rationale for using particular scaling parameters and compares the relevant wind-tunnel and field ratios.

There are two types of similarity requirement. The tunnel airflow must be dynamically similar to the actual dune environment, and the dune model must be geometrically similar to the full-scale version. To facilitate these requirements a number of non-dimensional parameters have been derived which need to be replicated as closely as possible, although Pankhurst (1952) and Knott (1979) note that it is rarely practical or possible to reproduce all of them simultaneously. No attempt was made at introducing sand into the flow because of the excessive practical complications and restrictive scaling requirements (viscosity, density *etc.*).

Simulation of the Atmospheric Boundary Layer

In order accurately to simulate the field conditions the "law-of-the-wall" parameters (u_*, z_0 and d) must be reconstructed so that they satisfy the Karman-Prandtl logarithmic law (Equation 2.7).

There are several methods of simulating the atmospheric boundary layer (ABL) as reviewed by Davenport & Isyumov (1967) and Cermak & Arya (1970). They both concluded that a naturally grown boundary layer over simulated roughness was more characteristic of the ABL than that resulting from the use of artificial methods of growth (*e.g.* grids, rods and vortex generators). The artificial methods tend to allow the decay of turbulence characteristics downstream. Cook (1977), however, noted that a boundary layer of only 380 mm depth was generated over simulated rural roughness with a tunnel length of 25 m, so that;

> *"The naturally grown boundary layer gives excellent agreement with the atmospheric data, but is restricted to the research institutions that can justify the expense of a very long wind tunnel"*
>
> Cook (1977)

The purely artificial methods of growth proposed by Elder (1959), Cockerell & Lee (1966) and Cowdrey (1967) tend only to recreate the velocity profile and not the turbulence characteristics. A compromise is required between the two methods of generation and such a technique has been suggested by Counihan (1969, 1970) with several researchers subsequently using methods of

similar design (Cook, 1977; Castro, 1979; Britter *et al.*, 1981; Gong & Ibbetson, 1989; Finnigan *et al.*, 1990). In these designs an upwind barrier produces an initial momentum deficit and depth to the boundary layer whilst a surface roughness acts as a momentum sink, thus establishing a profile of Reynold's stresses which controls the mean velocity and profile characteristics. A mixing device (a mesh of vertical and horizontal rods) upwind of the barrier creates turbulence and mixes the momentum deficit produced by the barrier into the boundary layer;

> *"The flow is tricked by the barrier into believing the fetch of roughness to be longer, and by the mixing device that the barrier is not there at all"*
>
> Cook (1977)

A fine balance exists between the fetch of roughness, size of barrier, coarseness of mesh and scale of the model. The correct dimensions for these parameters can only be judged on a trial-and-error basis.

In order to simulate the ABL the tunnel was set up as shown in Figure 4.7, but without the dune model in place. The roughness on the tunnel floor was made from sheets of Lego base board. Such a material had been used by Castro (1979) who found that it had suitable qualities for simulating the appropriate aerodynamic roughness (z_0) at a scale of ≈ 1:200. The horizontal rods of the mixing mesh could be moved vertically and added or removed as necessary. The toothed fence design was adopted to improve the mixing efficiency of the fence (Cook, 1977).

After calibration of a single hot-wire probe, the tunnel speed was set so that the reference velocities measured 170 mm from the tunnel roof were ≈ 10 ms^{-1}. Velocity profiles were then measured above the proposed position of the dune model (3500 mm downwind of the fence). Each profile consisted of 32 points with the spacing between the points varying logarithmically with height. Hence, at the surface they were measured at 0.5 mm intervals with the lowest at 3 mm from the surface, and toward the roof of the tunnel this separation was extended to 80 mm, with the highest value measured at an elevation of 400 mm.

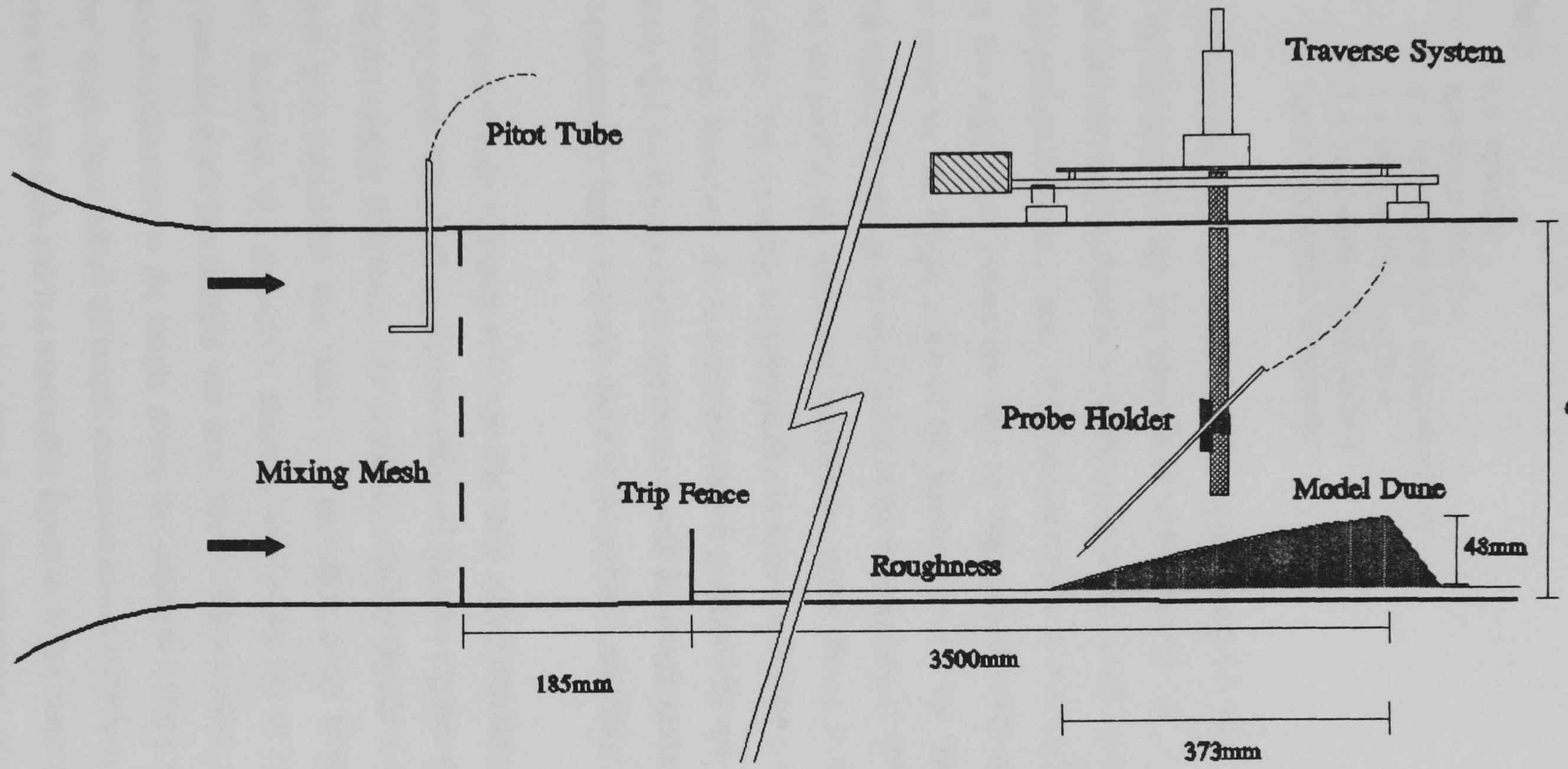

Figure 4.7 Configuration of the wind tunnel showing relative positions of mixing mesh, trip fence, roughness elements and dune model.

The velocity profiles from the traverses (carried out with differing horizontal rod positions and fence sizes) were plotted in the log-law form and compared with the modified Karman-Prandtl (compare with Equation 2.7) distribution of;

$$u/u_* = 1/\kappa.\ln(z\text{-}d/z_0) \qquad (4.4)$$

where:

u = velocity
u_*= shear velocity
κ = von Karman's constant (0.41)
z = height above surface
d = zero-plane displacement
z_0= aerodynamic roughness

A sample of the velocity profile results is shown in Figure 4.8. The straight line represents that described by Equation 4.4 and has been fitted to the data by eye. It is noticeable that between 10 mm and 100 mm height, there is a parabolic deviation away from the log-law. This is called the velocity-defect-law layer (Cook, 1977) and occurs as a result of the fence (shown in Figure 4.7) being too high. This causes the flow to "lose touch" with the physical surface and be controlled more by the length scale of the barrier than by the aerodynamic roughness. This profile was measured with an upwind fence of the dimensions of Fence 1 in Figure 4.9. In order to improve the profile, the fence was reduced in height (Fence 2, Figure 4.9) so that it would have less effect. The resulting velocity profile is shown in Figure 4.10. The defect-law-layer has been eradicated. However, the momentum deficit produced by the fence is too small, with the consequence that the flow is not in equilibrium with the rough surface. This situation is indicated by the unrealistically high velocities close to the surface, resulting in an unreasonably small z_0.

A further fence (Fence 3, Figure 4.9) was also used which had the same overall height as Fence 1 but deeper teeth. This had the desired effect of maintaining the momentum deficit whilst also increasing the mixing efficiency. The resulting velocity profile is shown in Figure 4.11. From this Figure it is noticeable that there is a deviation away from the log-law line at lower elevations. However, if a zero-plane displacement height (d) of 1.9 mm is subtracted from all the data then the result is a straight line described by Equation 4.4, as shown in Figure 4.12. The zero-plane-displacement is the height above the physical surface where the velocity is zero. It is a "false" origin from which all height measurements should be made. The chosen value of 1.9 mm seems to fit the data and is a reasonable figure as it lies beneath the height of the roughness elements (2 mm). The relationship between the roughness element height, the zero-plane displacement and the measurement convention is shown in Figure 4.13.

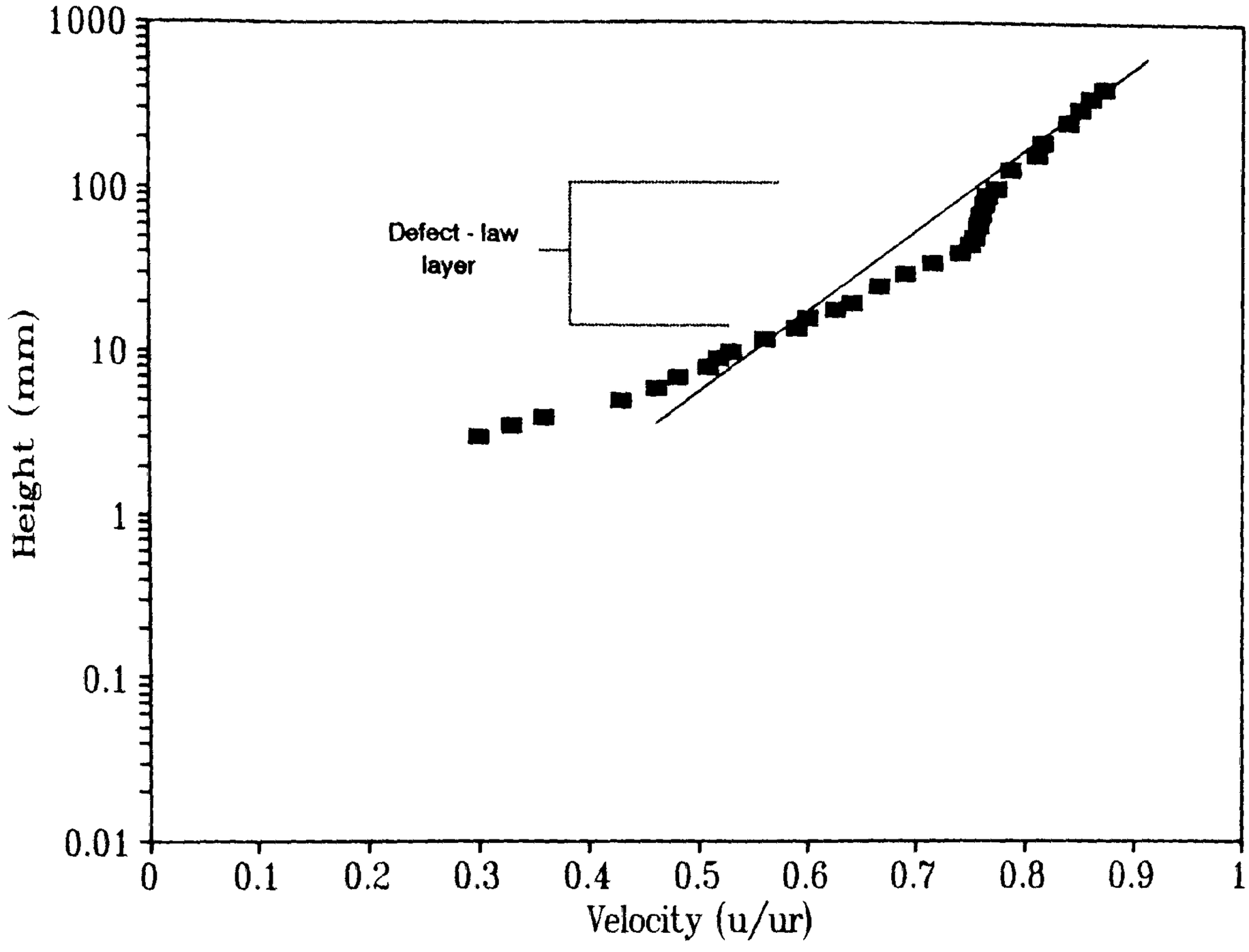

Figure 4.8 Vertical velocity profile using fence 1 (in Figure 4.9). Note defect-law layer.

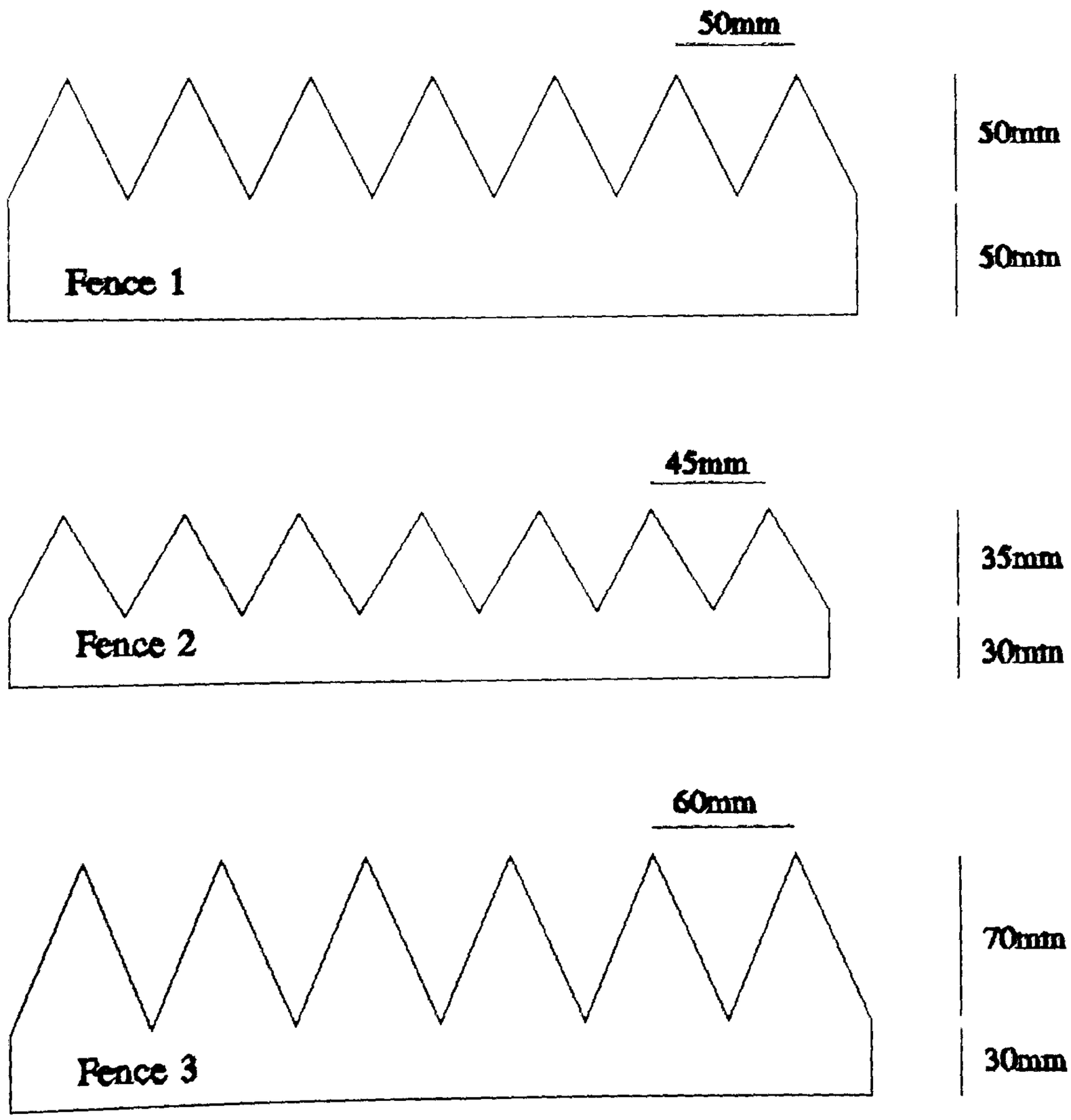

Figure 4.9 Experimental trip fences used in the simulation of the atmospheric boundary layer.

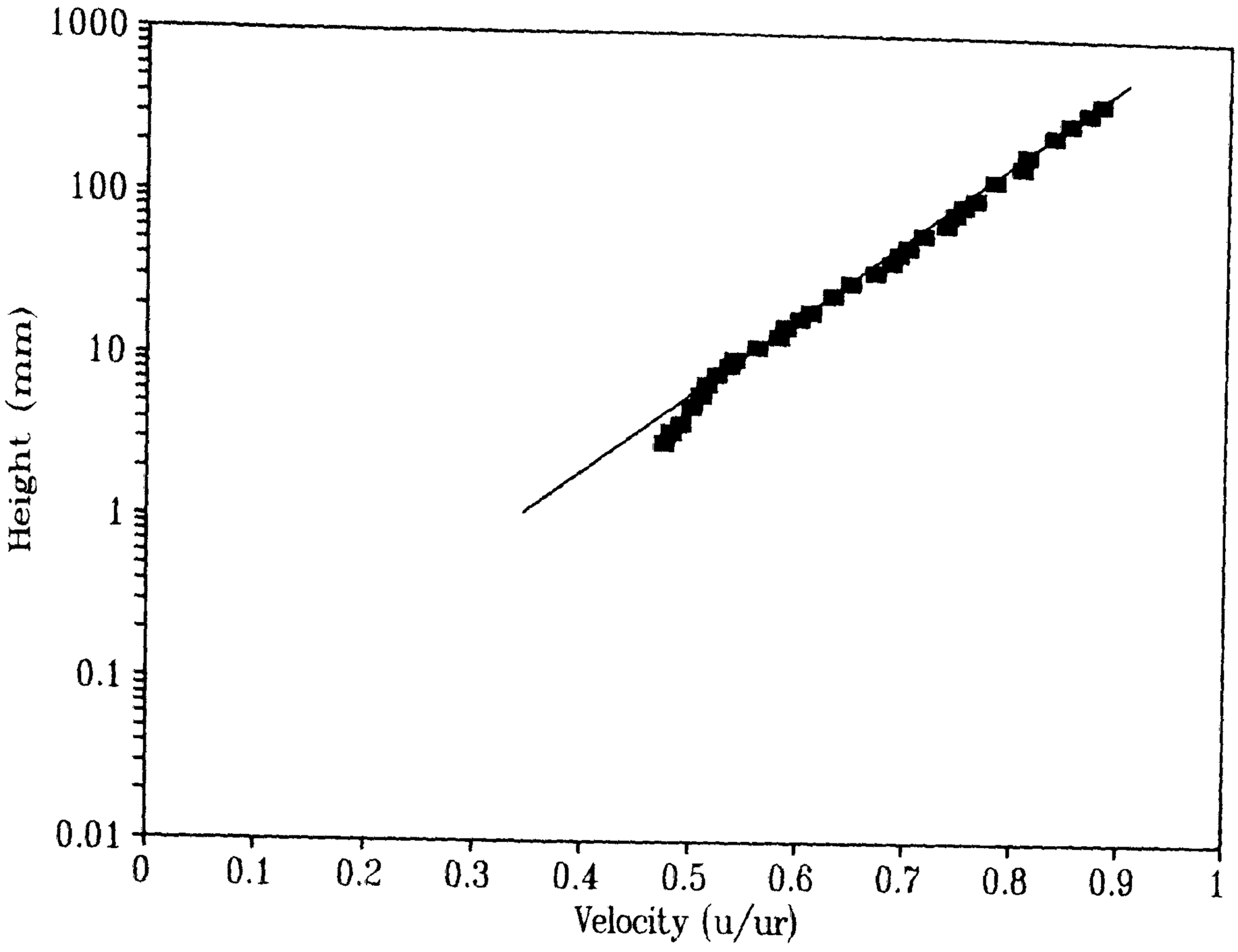

Figure 4.10 Vertical velocity profile using fence 2. Note near-surface velocity deficit.

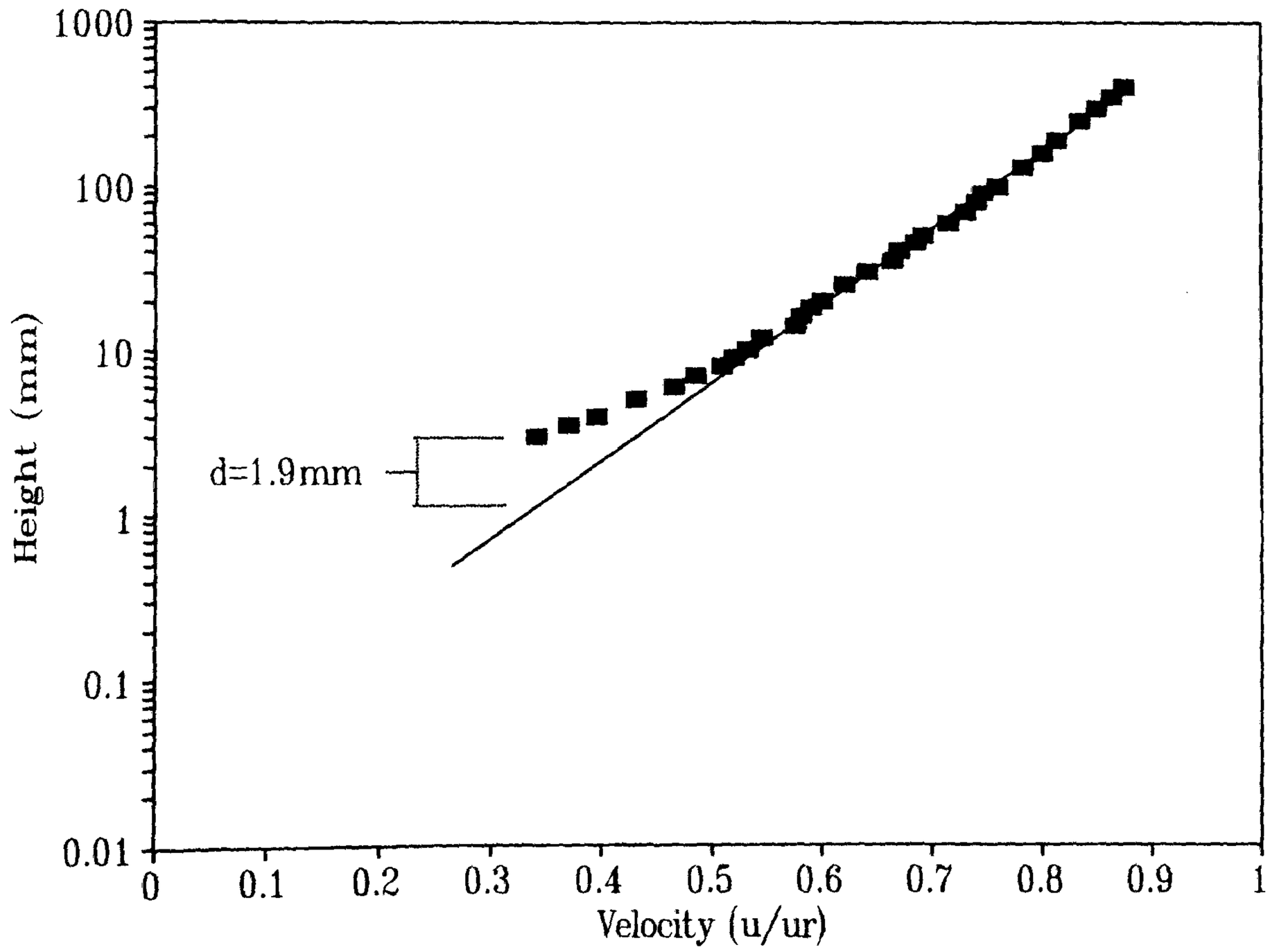

Figure 4.11 Vertical velocity profile using fence 3 showing zero-plane displacement (d).

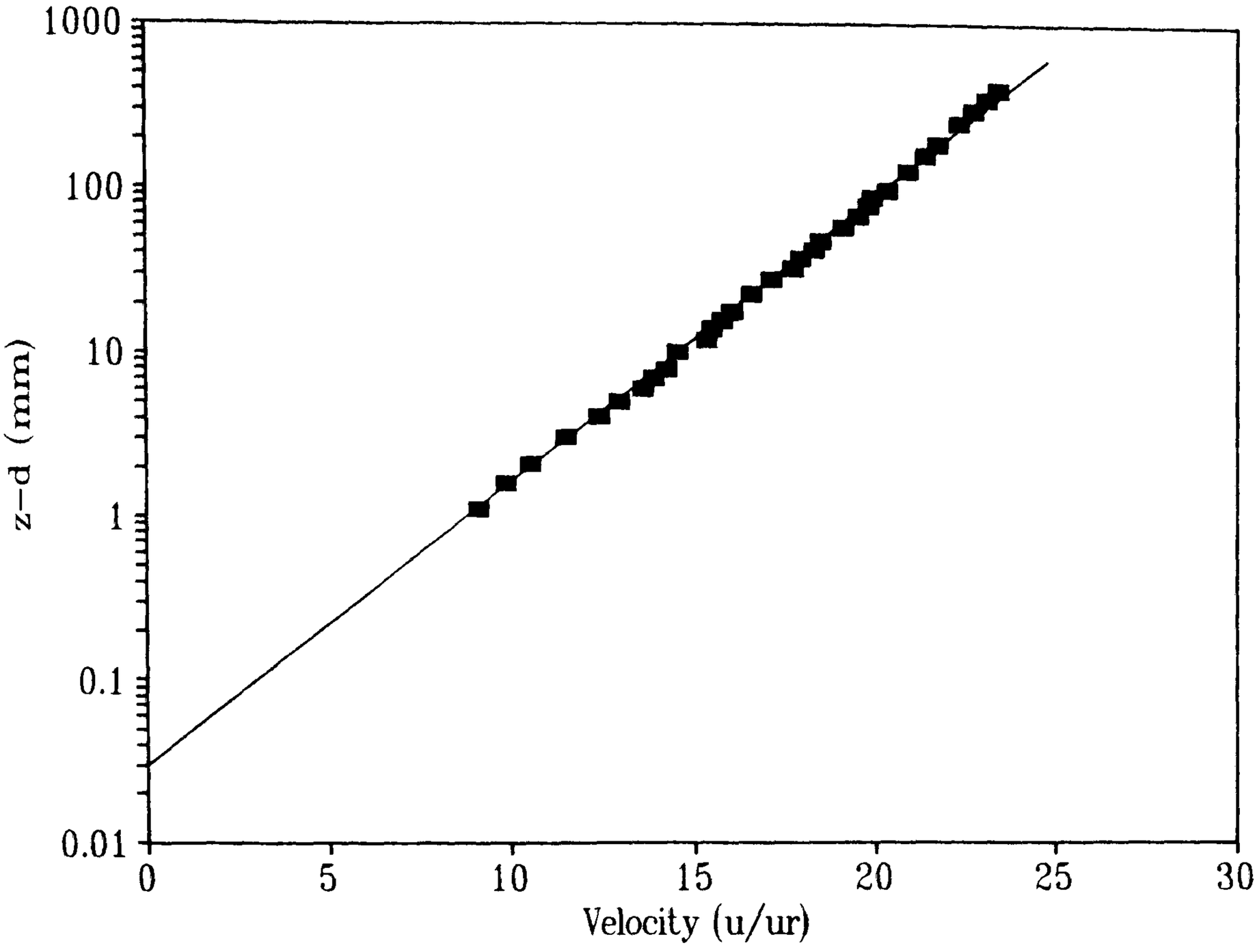

Figure 4.12 Vertical velocity profile using fence 3 with zero-plane displacement subtracted from height data.

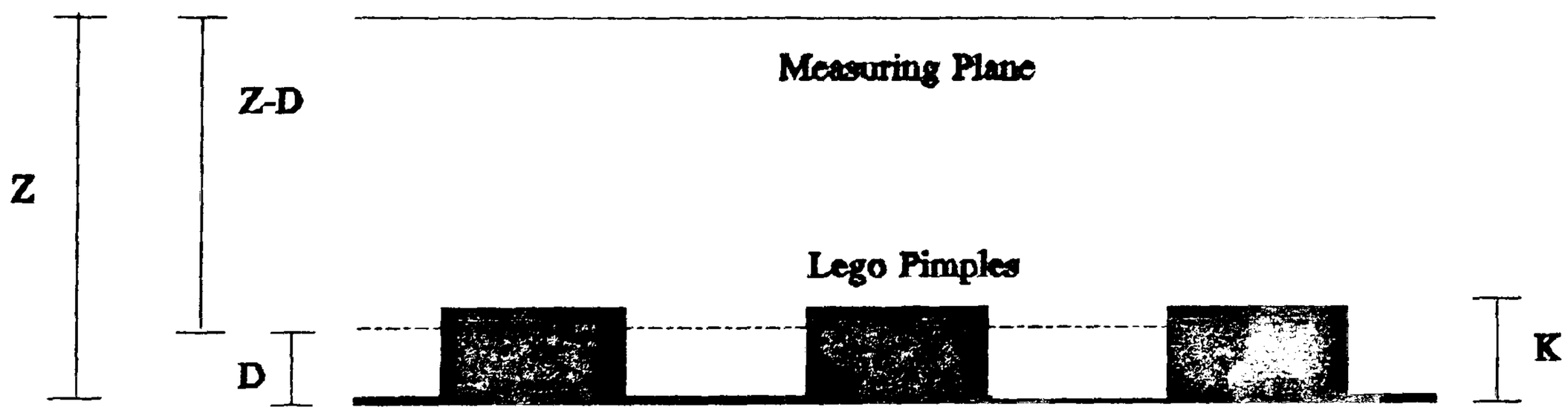

Figure 4.13 Measuring convention. K = roughness element height; D = zero-plane displacement; Z = height from surface.

From Figure 4.12 a z_0 of ≈ 0.03 mm can be estimated. At a scaling of 1:200 this represents a full-scale roughness of 6 mm, comparable with the mean value deduced from the field data of 5.0 mm. It appears that the chosen configuration of fence, roughness and mixing mesh gives a reasonable duplication of the ABL measured in the field. However, it is unsatisfactory to determine d, z_0 and u_* by using qualitative methods alone. Owen & Gillette (1985) stated that the deduction of u_* from log-profiles cannot be more accurate than ±10-15%. More consistent results can be achieved by determining u_* from measured Reynold's stresses, thus reducing the unknowns from three (d, z_0 and u_*) to two (d and z_0). If u_* is known then the fitting by eye of the log-law to the measured profile becomes much simpler and more accurate.

Reynold's stress profiles were measured using a cross-wire probe (Figure 4.2b) orientated so that it calculated the mean uw component of flow. Owing to the design of the probe it was not possible to measure closer than z ≈ 3.5 mm. However, the mean shear stress (-uwb) was fairly constant below heights of 75 mm (see Figure 4.14), so a surface value of -uwb (*i.e.* surface shear stress) could be extrapolated, as shown in Figure 4.15. As indicated in this figure, the required normalised surface shear velocity (u_*/u_τ) and gradient of the log-line ($u_\tau/\kappa u_\tau$) can be derived in the following manner;

$$\text{if} \qquad u/u_\tau = u_*/\kappa u_\tau.\ln.(z\text{-}d/z_0) \qquad (4.5)$$

and $\quad uwb/u_\tau^2$ at z-d= 0 is 0.00140

then $\quad u_*/u_\tau = \sqrt{(0.00140)} = \mathbf{0.03742}$

and $\quad u_*/\kappa u_\tau = 0.03742/0.4 = \mathbf{0.09126}$

Figure 4.16 shows the superimposition of the log-line gradient (0.09126) onto the velocity profile measured in Figure 4.12. This shows that the d, z_0 and u_* estimates agree well with the measured u_* (0.037), which is also comparable to the field shear velocities of between 0.3 and 0.4 ms^{-1}. A check of the satisfaction of Equation 4.4 is given in Figure 4.17 where u/u_* is plotted against $1/\kappa.\ln.(z\text{-}d/z_0)$ (using κ= 0.4; z_0= 0.03 mm; d= 1.9 mm; and u_*/u_τ= 0.03742). These values give a roughness Reynold's Number of;

$$u_*.z_0/\nu = 0.75$$

where:

ν = kinematic viscosity (0.015)

This value is low compared to the generally accepted value of 2 taken as indicative of fully rough flow. Teunissen *et al.* (1987) stated that when $u_*.z_0/\nu$ lies between 3 (fully rough) and 0.2

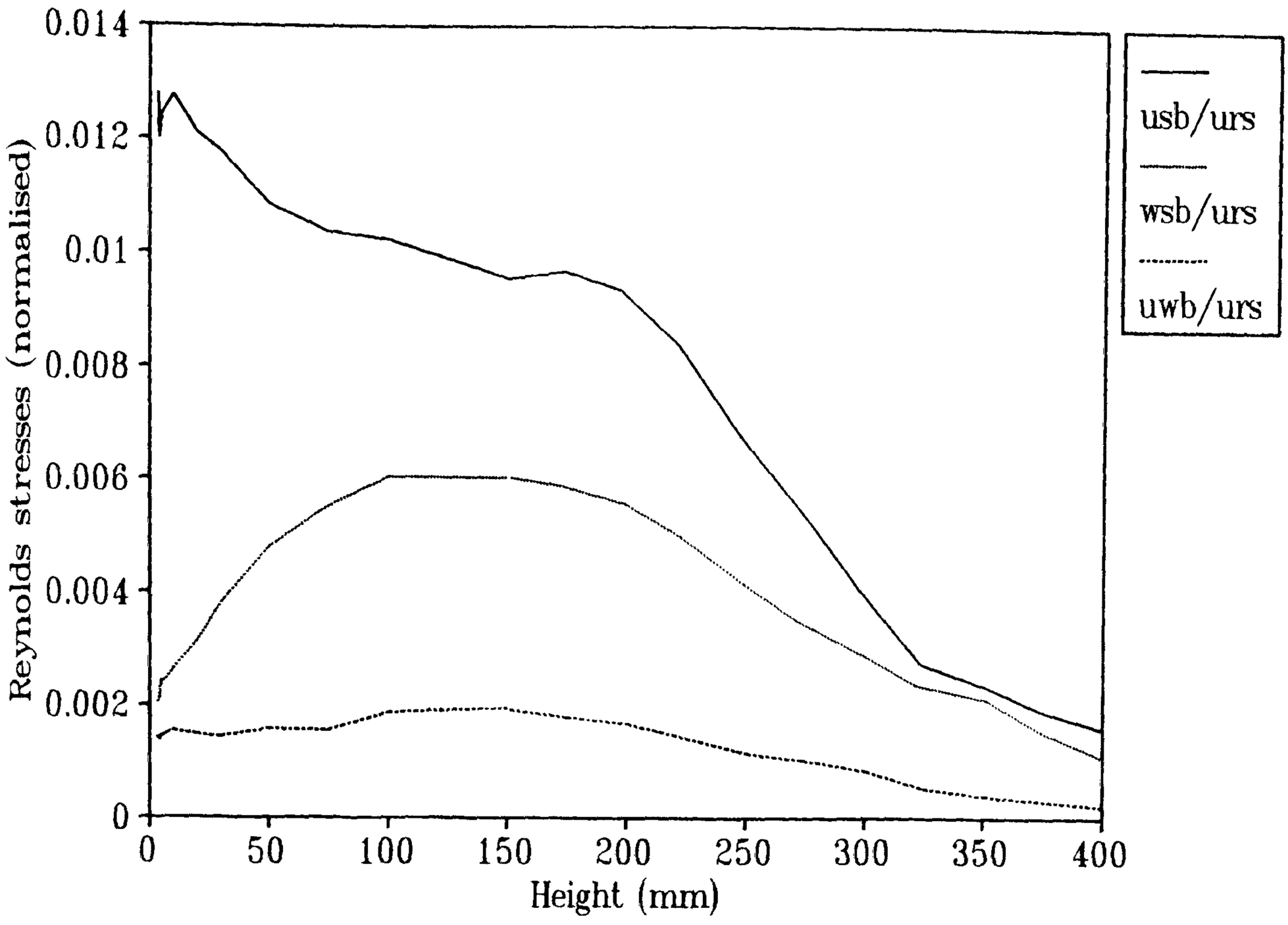

Figure 4.14 Vertical profiles of Reynold's stress in the simulated atmospheric boundary layer.

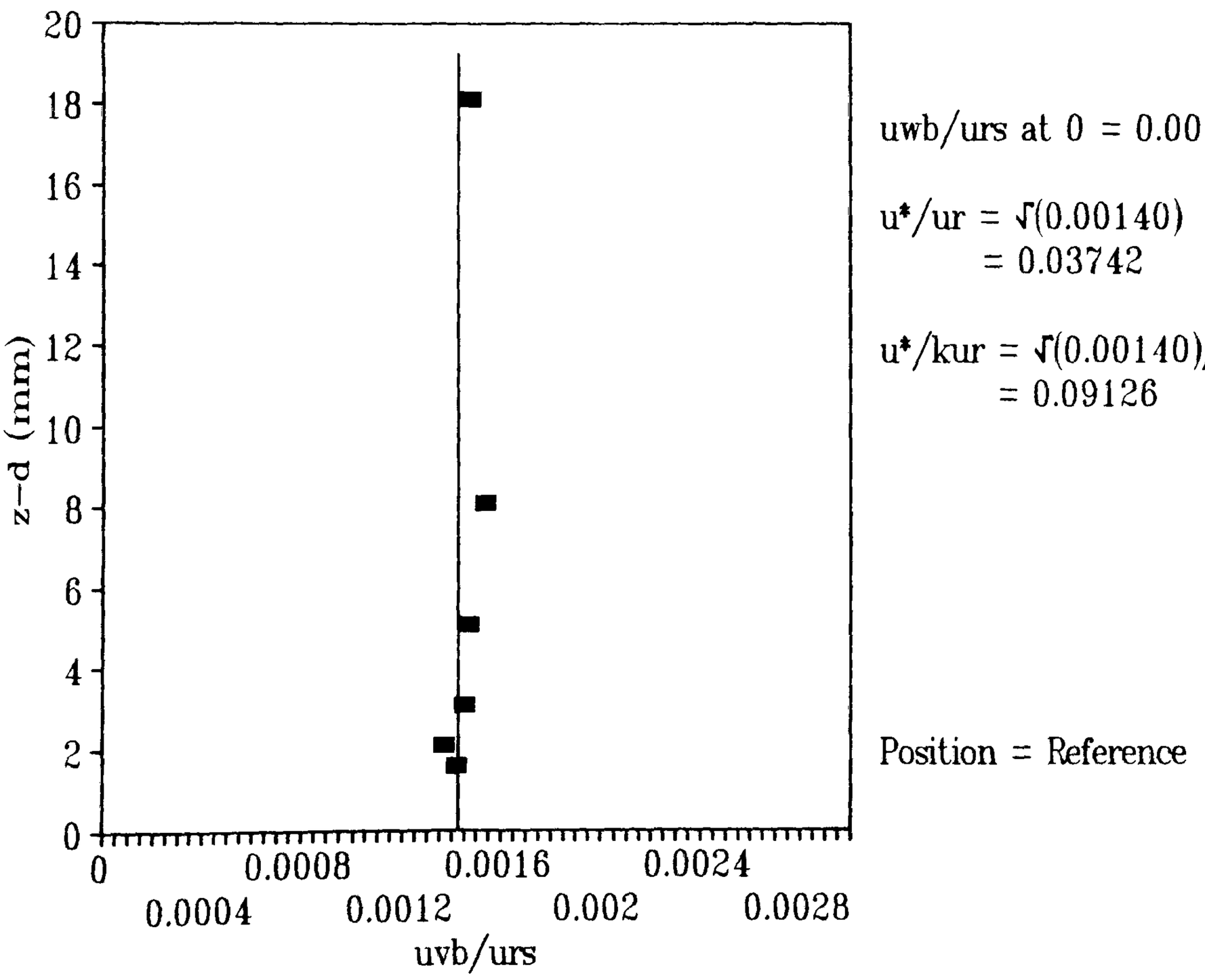

Figure 4.15 Extrapolating shear stress to the surface to calculate surface shear velocity.

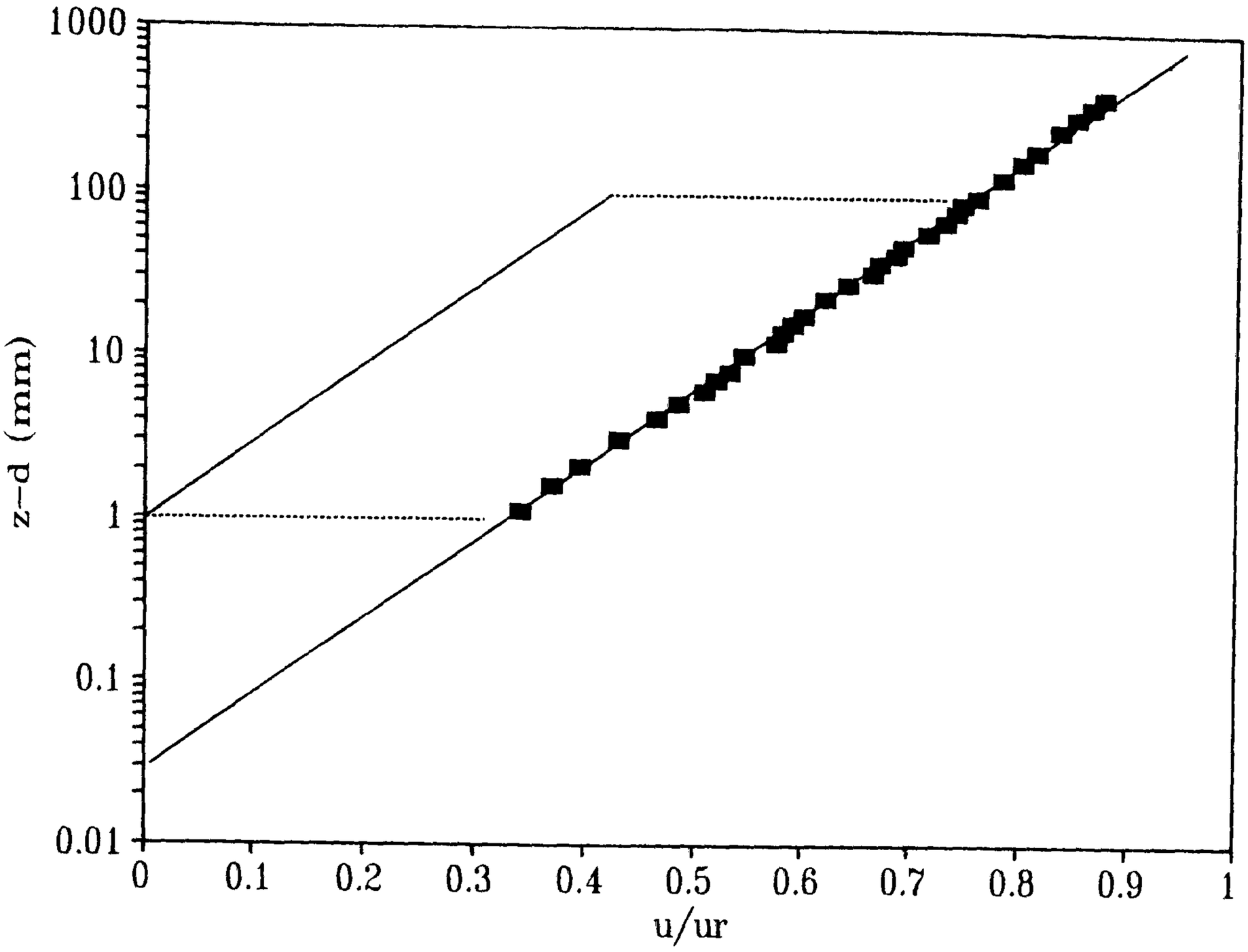

Figure 4.16 Superimposing the extrapolated shear velocity gradient onto the vertical velocity profile.

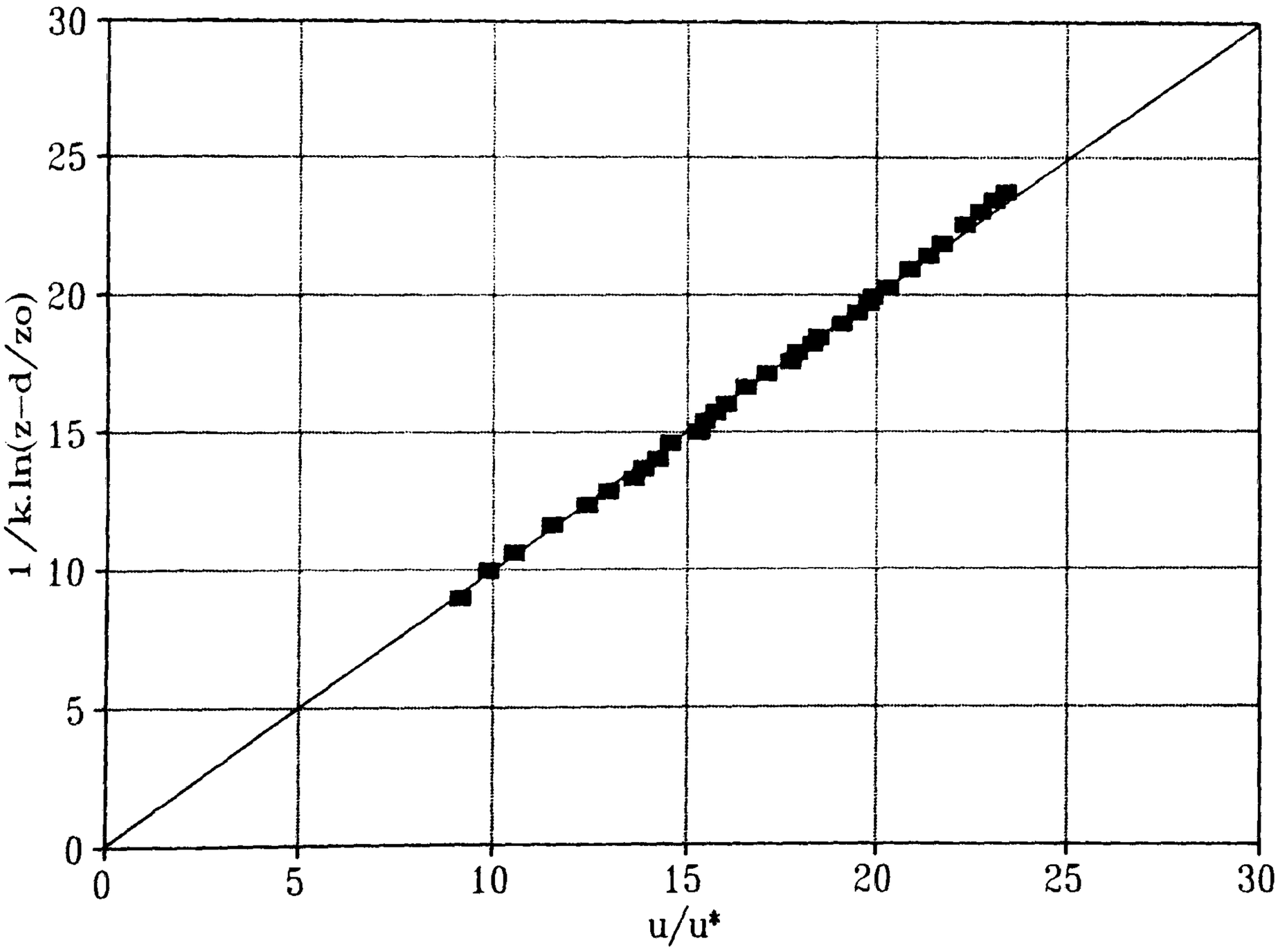

Figure 4.17 Plot showing the satisfaction of Equation 4.4.

(fully smooth) then the viscous forces may become significant to the flow field. However, they also noted that aerodynamic roughness criterion for topographic modelling can be less stringent than for pipe flow and cite Goh (1981) who found that a minimum value of $u_*.z_0/\nu$ of between 0.41 and 0.84 was adequate for minimising adverse viscous effects. This is particularly valid when the roughness elements are bluff (sharp-edged), as in this case. Measurements by Teunissen *et al.* (1987) showed that the relaxation of the criterion of aerodynamic roughness only affected flow in the lee of their hill where separation occurred. In the present study it was considered that a roughness Reynold's number of 0.75 allowed sufficient leeway for viscous effects to be negligible.

Therefore, Figure 4.16 represents a satisfactory reconstruction of a near-fully-turbulent ABL in terms of the time-averaged velocity profile, roughness length, zero-plane displacement, shear stress and roughness Reynold's Number.

The length-scale of the turbulence in the tunnel at different heights was measured using standard auto-correlation and power spectral density techniques. Auto-correlation requires the measurement of the same fluctuating quantity at two different points in space (Bradshaw, 1971). This was undertaken in the tunnel by gradually increasing the distance (l) between two hot-wire probes, placed parallel to the flow, until no correlation could be found between the fluctuating velocities. Typical ranges for l were between 50 mm and 500 mm. By integrating the correlation co-efficient with l, values of turbulence length scales were derived.

The power spectral density is a measure of the amount of energy contained in turbulence structures of differing wavelength. By plotting output voltage against a hot-wire signal passed through a variable band-pass filter, the frequency spectrum was discovered. For an atmospheric boundary layer the data should be defined by;

$$\Sigma_{(k)} \approx A\varepsilon^{2/3} k^{-5/3} \qquad \textbf{(4.6)}$$

where:

Σ = spectral density
k = wavenumber
A = constant (0.53)
ε = turbulence dissipation rate.

The log-log plot of frequency against spectral density at 20 mm height is shown in Figure 4.18. This plot shows adequate correspondence with the -5/3 law (Equation 4.6) and distinctly defines the three energy ranges, namely;

1. Energy-containing range, representing the frequencies containing the most energy.

2. Inertial sub-range, which corresponds to the -5/3 law.

3. The dissipation sub-range, which represents those high frequencies where energy is dissipated as heat.

The integral length scale of the energy-containing eddies (which are the most important in the transfer of turbulent kinetic energy) can be deduced from;

$$L_x = \tfrac{1}{4} U_c . \Sigma_{(f=0)}$$

where:

L_x= integral length scale
U_c= local flow velocity
Σ = measured spectral density at peak.

The length scales of the turbulent energy as measured by the methods discussed above are shown in Table 4.3 below;

Table 4.3 The Turbulent energy length scales as measured by Auto-correlation and Spectral Density.

Height (mm)	Auto-correlation Length Scale (mm)	Spectral Density Length Scale (mm)
405	90	88
300	135	133
200	150	148
100	150	154
50	155	160
20	155	160

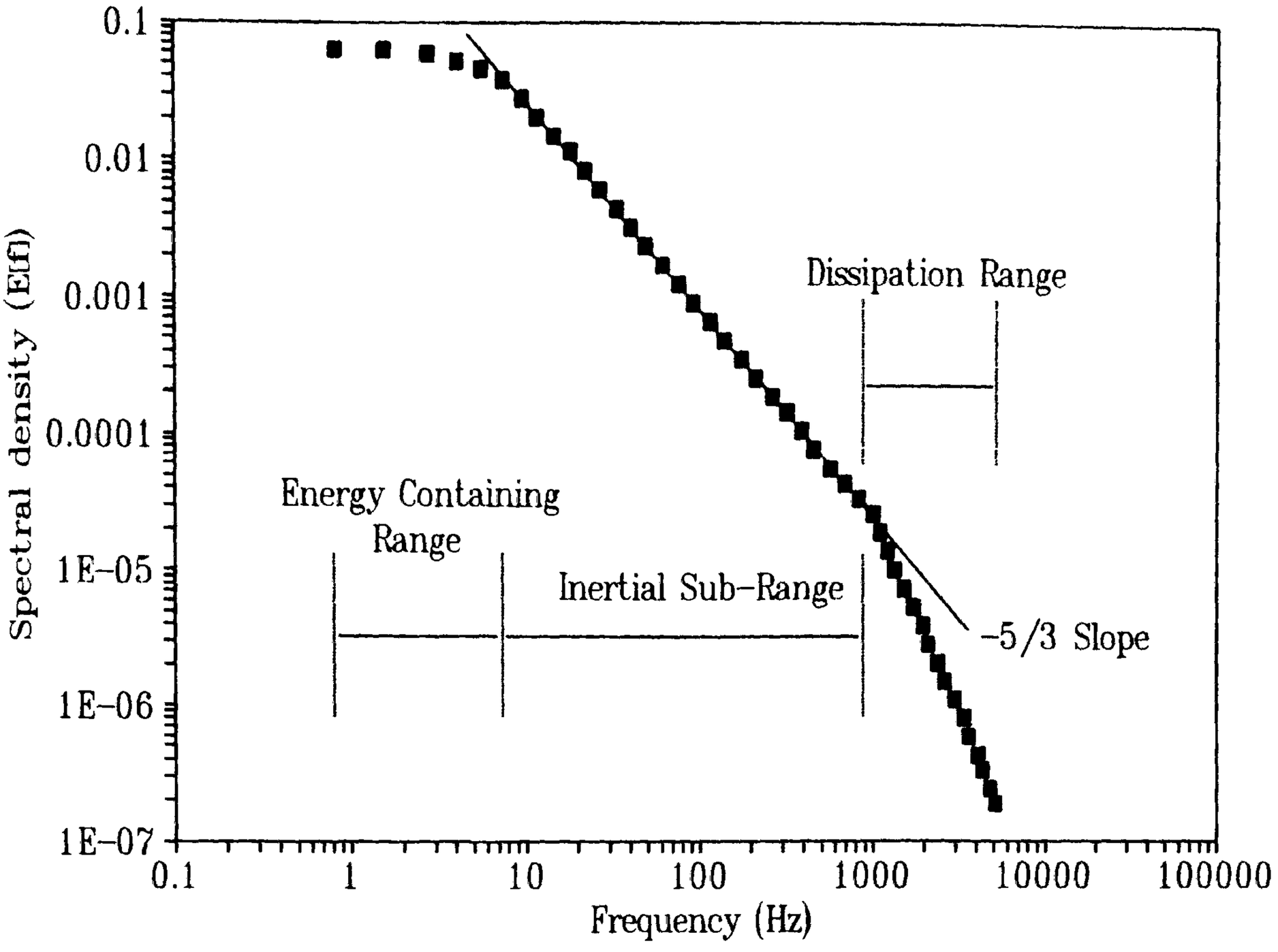

Figure 4.18 Spectral density and frequency at 20 mm height showing the characteristic -5/3 gradient.

The length scales calculated with the two methods correspond very well and represent full-scale values close to the surface of ≈ 30 m (at ≈1:200 scale). This is comparable to measurements and deductions of full-scale integral length scales which are of the order of 10 m to 100 m (Blackader, 1962; Panofsky & Dutton, 1984; Wyngaard, 1990).

The exhaustive procedure described in this section resulted in an accurate reconstruction of the atmospheric boundary layer. Turbulence scales, shear stress, and roughness length are all favourably comparable to the field prototypes, so reliable analogous measurements could be taken.

Tunnel Blockage

The size of the dune model was dictated by the size of the wind tunnel and the minimum size over which accurate measurements could be taken. The model was constructed by the technical staff at the University of Surrey at ≈1:200 scale by photo-reducing a detailed contour map of the dune produced from the field data. The model was built up gradually with separate contour segments cut from polyurethane plastic and the "steps" between contours smoothed over with modelling plastic. The dimensions of the model and prototype dune were therefore geometrically similar, although some distortion was introduced when a roughness covering of 2 mm high Lego board was added (see Chapter 4.3.2).

Introducing a model into the tunnel immediately places a restriction on the tunnel flow, possibly causing tunnel blockage and velocity speed-up. With a model crest height of 45.5 mm the maximum possible cross-sectional blockage was only 3.9%, well within the generally accepted limit of ≈ 5% (Goh, 1981). Furthermore, Teunissen *et al.* (1987) cited Jackson (1979) who stated that the height of the tunnel (H_t) should be equal to or greater than 3L (where L = half length of the hill). In this case $H_t/L = 3.0$, so tunnel blockage effects have been assumed to be negligible.

At this scale, however, the wings of the model dune reach the tunnel walls. No measurements were required within 250 mm of the tunnel walls (well outside the boundary layer thickness of 170 mm identified on Figure 4.19). Nonetheless, it was thought that the proximity of flow perturbations induced by the terrain so close to the wall might introduce irregularities into the flow and so effect the measurement areas.

To test this possibility, velocity measurements were carried out over a dune model based on the Howard *et al.* (1977) survey at 1:200 scale. This model only extended over half the width of the

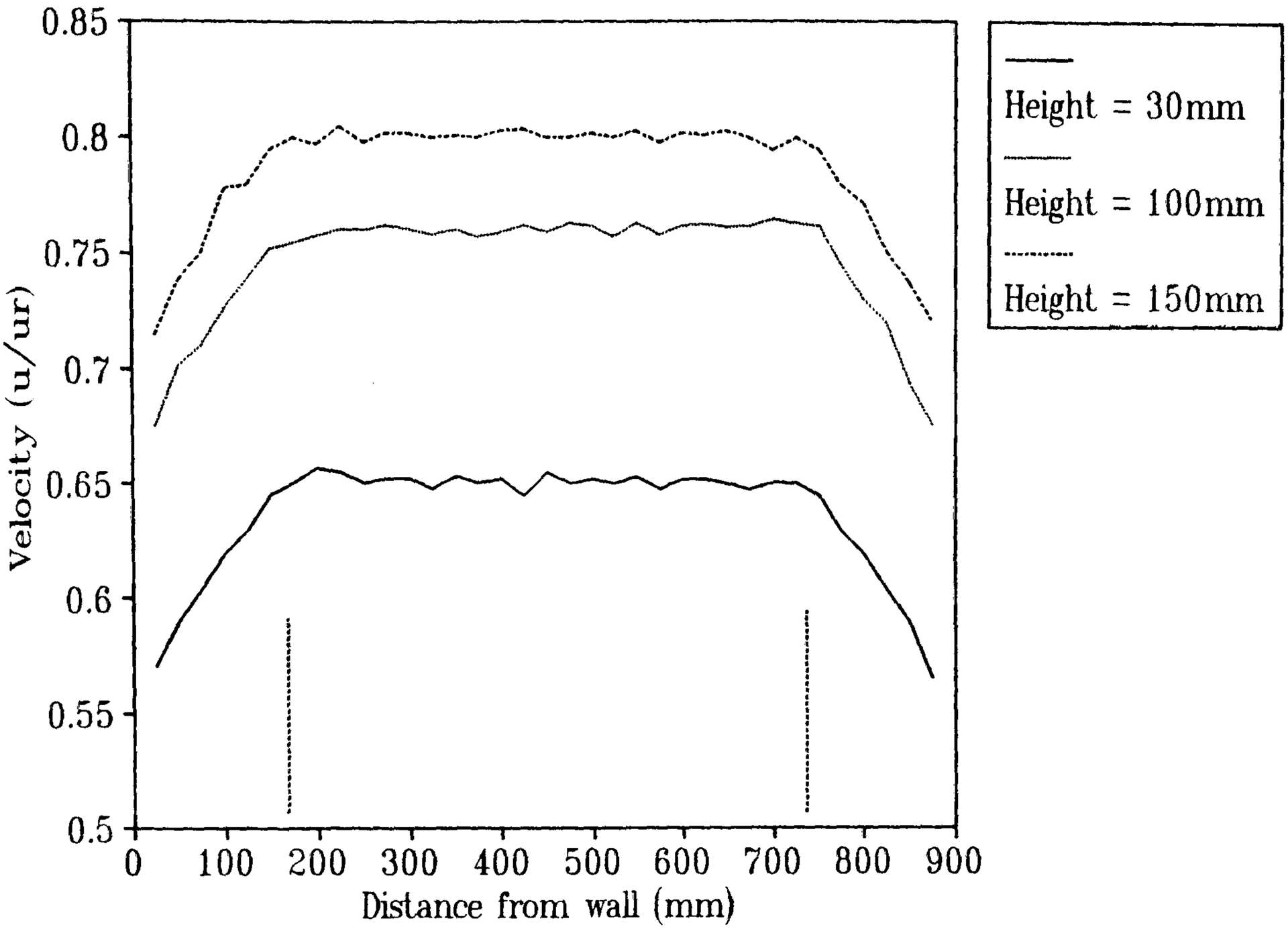

Figure 4.19 The thickness of the side-wall boundary layer 3500 mm from the mixing mesh.

tunnel, so the wings were one-half the dune width away from the walls. Velocity measurements were taken on the dune centre-line and wings and compared with similar measurements over the same model but with false tunnel walls positioned along both wings. The design of these walls is shown in Figures 4.20 and 4.21. As shown in Figure 4.22a+b, the deviation in flow velocity caused by the close proximity of the false tunnel walls to the dune terrain is less than 2%, with no systematic error evident. It was therefore concluded that the proximity of the wings of the experimental model dune to the tunnel walls would have negligible effect on the measurements on the three section lines.

Dimensionless Constants and Other Parameters

A comparison of a number of parameters and dimensionless constants between the field and laboratory which have not already been discussed is given in Table 4.4 below;

Table 4.4 Comparison of field and laboratory similarity parameters

Parameter	Field Value	Laboratory Value
Reynold's Number Re= u.H/ν	$4.4*10^6$	$3.2*10^3$
Maximum dune height, H (m)	9.46	0.0455
Half length, L (m)	40.6	0.2
Inner-layer depth, l (m) (Jackson & Hunt, 1975)	2.0	0.01
H/l	20	20
H/L	0.23	0.24
H/z_0	1890	1580

The above Table shows that the geometric similarity parameters are highly comparable (*e.g.* H/L and H/z_0). The Reynold's Numbers, however, differ by an order of magnitude. Nevertheless, because the boundary layer is near-fully-rough the preservation of Reynold's Number between the field and laboratory is not necessary for dynamic similarity (Howard *et al.*, 1977; Knott, 1979). From Table 4.4 it is clear that not only has the inner-layer depth in the wind tunnel been preserved whilst also maintaining z_0, but it is also sufficiently large to enable the insertion of a hot-wire probe.

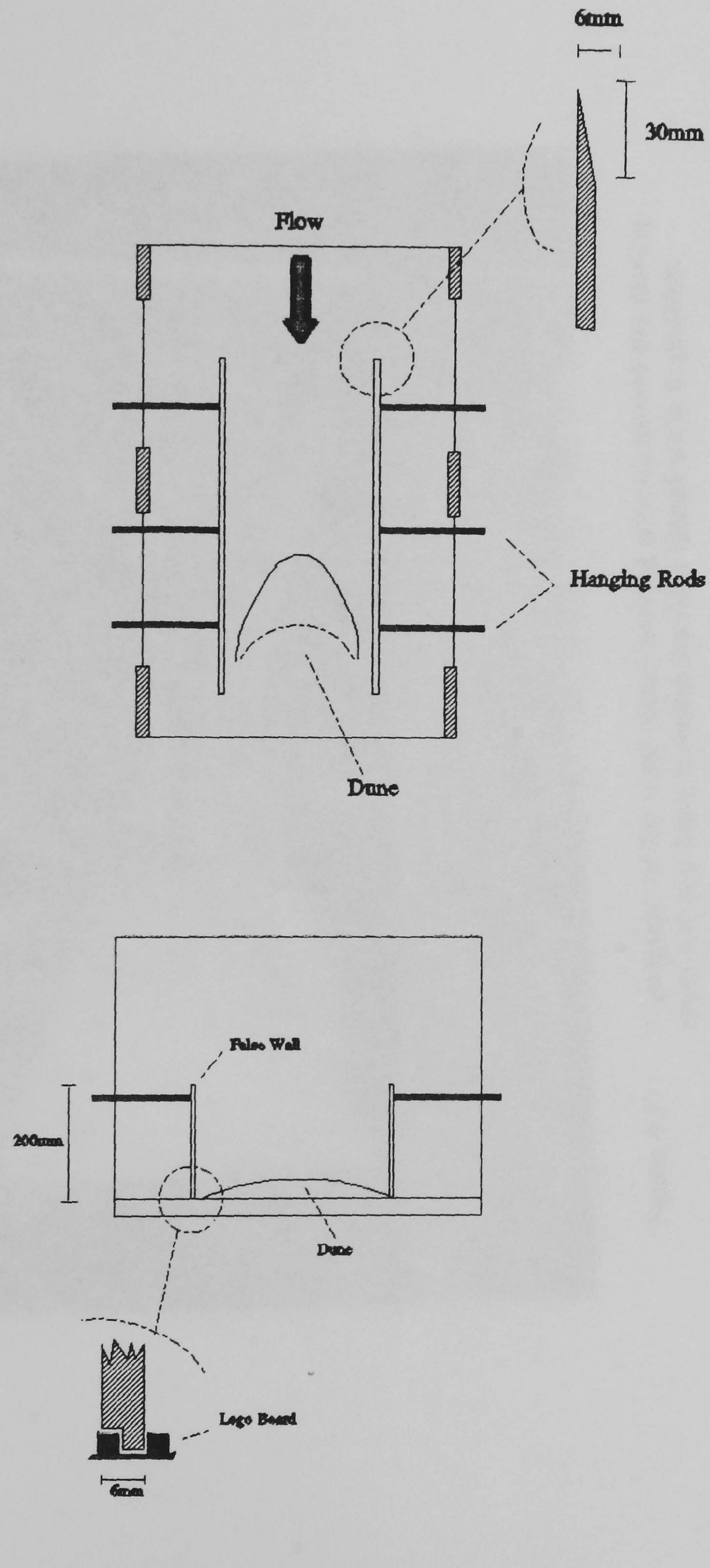

Figure 4.20 Design of the false tunnel walls to test for tunnel blockage.

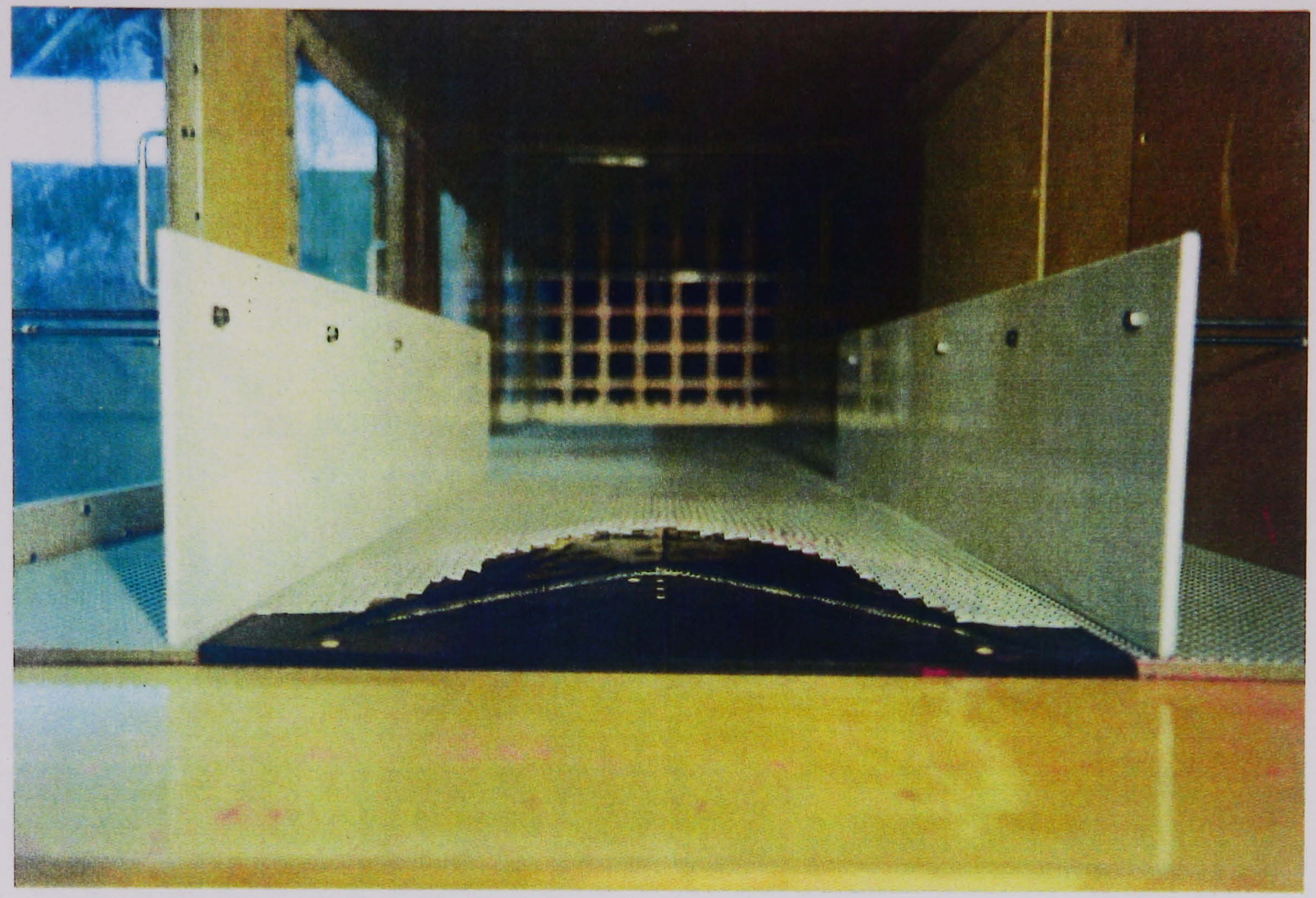

Figure 4.21 Photograph of the wind tunnel looking upwind toward the mixing mesh and trip fence showing the false tunnel walls in position.

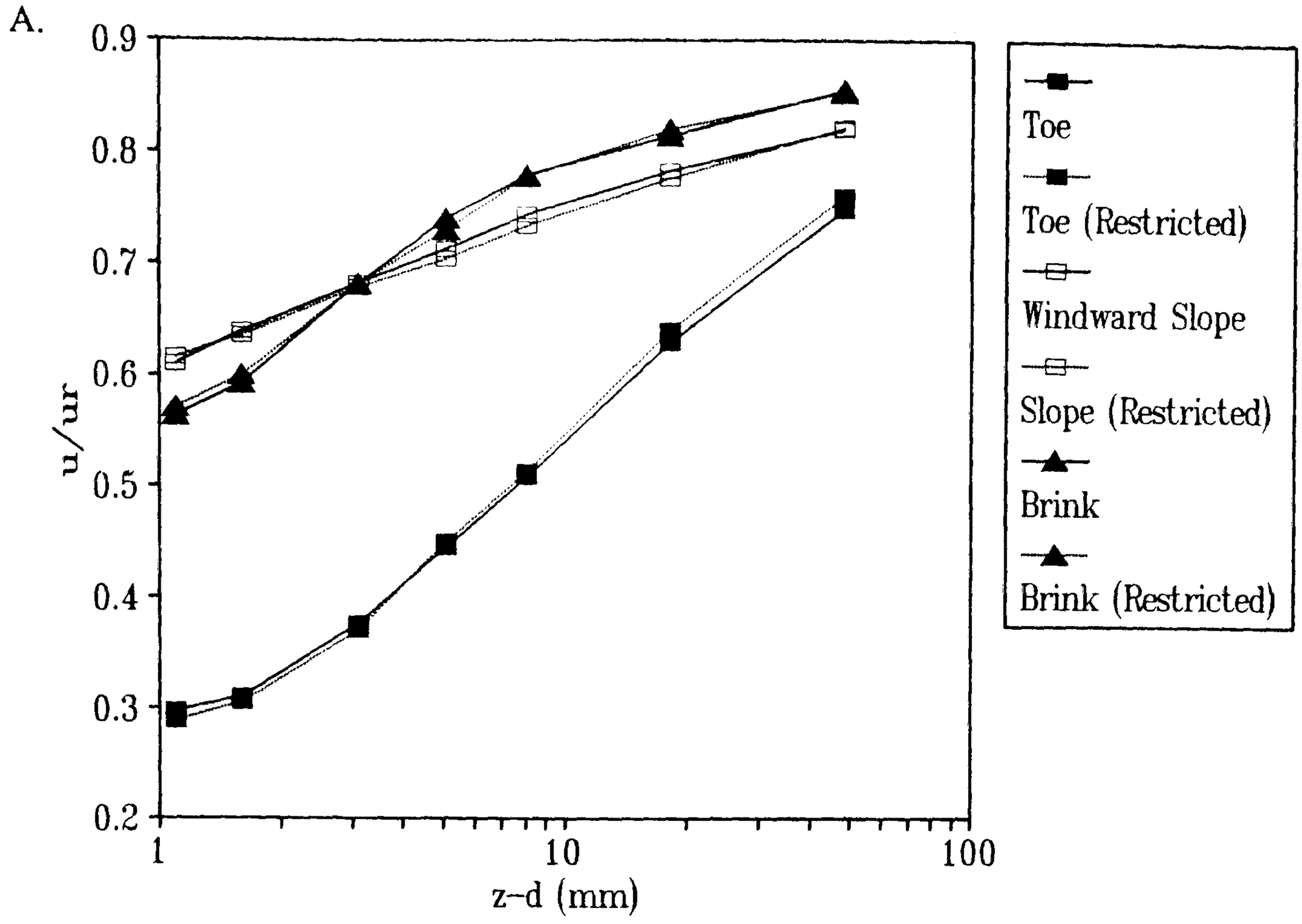

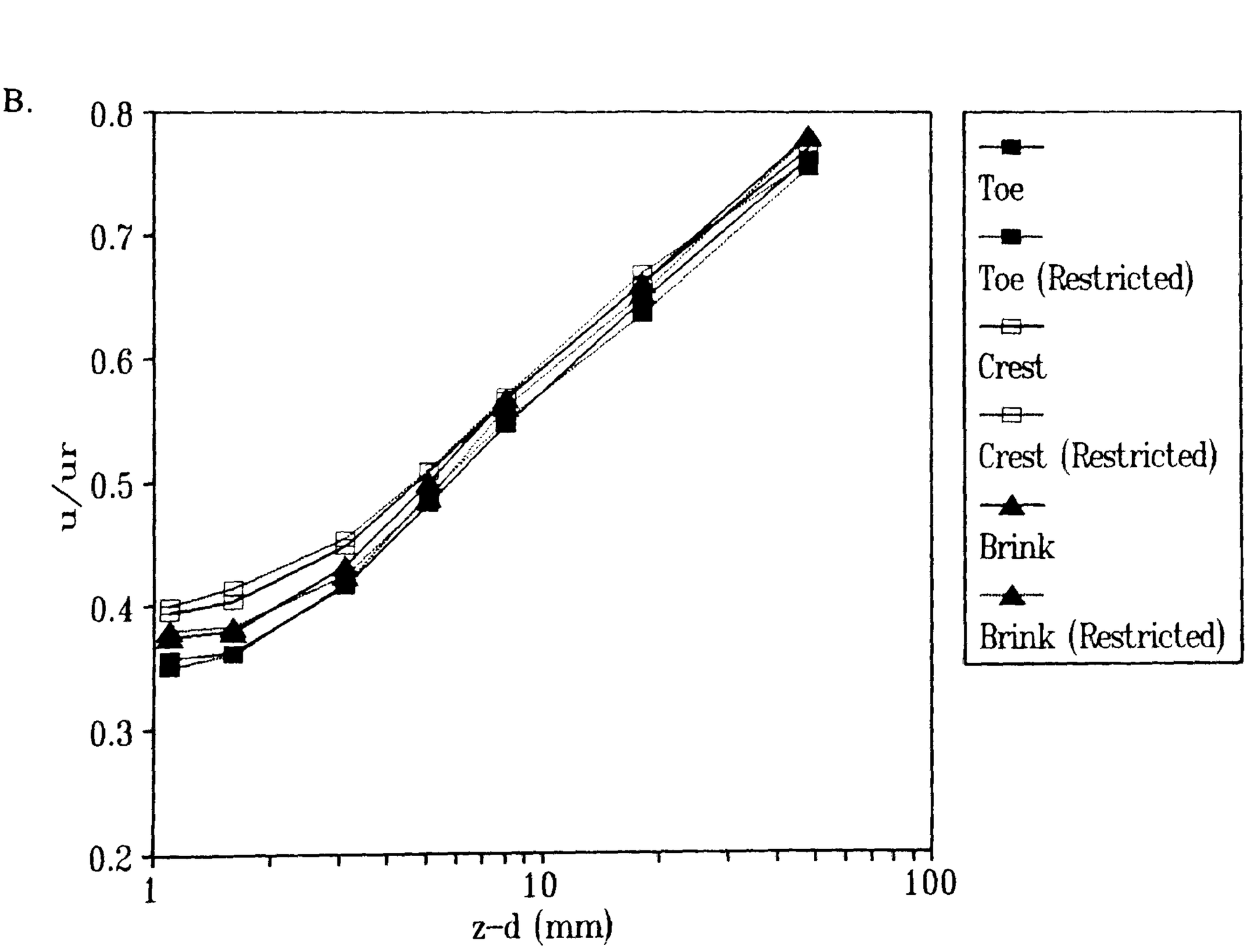

Figure 4.22 Comparison between unimpeded flow (*ie.* without false walls) and restricted flow (*ie.* with false tunnel walls) over the test dune. A = along the dune centre-line; B = along the dune edge.

Conclusion

By reconstructing a near-fully-rough boundary layer which satisfies the "law-of-the-wall" parameters and turbulence length scales of a fully-rough boundary layer, a situation has been reached whereby measurements within the inner-layer are possible. The necessary similarity requirements for geometric and dynamic similarity have been satisfied. The thorough presentation and examination of the methods involved in setting up the tunnel also allows a confident comparison of subsequent experiments with the field measurements and mathematical modelling.

4.3 Experimental Observations

4.3.1 Flow Direction Measurements

There have been very few studies of wind direction on barchan dune models in wind tunnels. Many studies have been concerned only with the two-dimensional case and hence have not measured flow patterns (*e.g.* Lai & Wu, 1978; Tsoar, 1985). Only Allen (1968), Howard *et al.* (1977) and Knott (1979) have attempted to measure flow around a 3-D model. Knott (1979) measured mean streamline angles using micro-yaw and hinge vanes, whilst Howard et al. (1977) inferred flow angle from a cross-wire probe measuring the u- and v- (horizontal) components of flow. Both of these methods failed to achieve direction measurements at the surface of the dune model because of the large size of their sensors. Measurements taken above the surface in a wind tunnel tend to lose their significance when the measuring height is scaled up to full-size. Allen (1968) successfully measured flow directions at the surface of a barchan dune by using smooth plaster models which developed surface flute marks when immersed into in a flume.

A method for obtaining the direction of surface shear in wind tunnels has been frequently used by engineers involved in research on recirculating turbulent flows (McCluskey pers. comm.) and a similar method was successfully used by Tsoar *et al.* (1985). The procedure they adopted was to coat the surface of a model with wet oil-paint. The subsequent streaks of oil after the tunnel had been switched on could be photographed and traced. Similar techniques were used in the experiments reported here.

Paraffin Paint.

The method in this experiment was essentially the same as that of Tsoar *et al.* (1985). The smooth dune model (*i.e.* no roughness attached) was carefully coated with a mixture of paraffin and powder paint (ratio 5:1). The tunnel was then switched to its running speed (10 ms^{-1}). As

the paraffin mixture flowed, it also dried, leaving a streak of red paint powder (Figure 4.23). This streak pattern was then traced.

Ink-Dot Method.

In this case a sheet of tracing paper was cut and arranged so that it could be stuck to the model and conform to the contours (Figure 4.24). On the paper a grid of non-permanent ink dots had been established on top of a grid of permanent ink-dots. The whole paper was sprayed with a thin coating of paraffin and the tunnel switched on. As the paraffin flowed it left streaks of non-permanent ink which later dried onto the paper. The origin of these streaks could be determined from the positions of the permanent ink-dots which had not been dispersed by the paraffin. In this way the path of streamlines could be followed. The advantage of this technique over the paraffin paint method is that the resulting streak pattern is less confused and easier to analyse. This is because the density of streaks depends upon the density of dots, which can be altered as required. Furthermore, the length of the ink-dot streak represents the velocity of flow along the streamline.

Surface Streamlines over the Model Dune.

Figures 4.25 and 4.26 show the surface flow directions measured by the paraffin paint and ink-dot methods respectively. They both exhibit almost exactly similar results with divergence of flow around the flanks of the dune and some convergence at the brink. In a similar manner to the field and FLOWSTAR assessments of flow direction (Chapters 2.4.1 and 3.4 respectively) the greatest magnitude of flow divergence is in the basal region of the dune adjacent to the centre-line and along the basal regions of the flanks. The maximum recorded deviation in this region is ≈15°. These results are comparable to those of Allen (1968) and Howard *et al.* (1977). Unfortunately, in the present study, no measurements were made upwind of the dune. Such an experiment might have revealed interesting results concerning the effect of the intrusion of the dune on upwind flow. In contrast to the field assessments, the wind tunnel data show some convergence of flow at the brink of the dune (3-8°). This result is also in accordance with the measurements of Allen (1968) and Howard *et al.* (1977), although it is less than that predicted by FLOWSTAR. As discussed in Chapter 3.4, the magnitude of flow divergence on the windward slope of the dune is not enough to have a significant effect on the measured flow variables (*i.e.* velocity and shear stress) which were recorded with probes oriented parallel to the free stream and not parallel to the local flow direction. The maximum flow divergence in the wind tunnel experiments of 15° results in ≈3% error for the surface shear stress measurements.

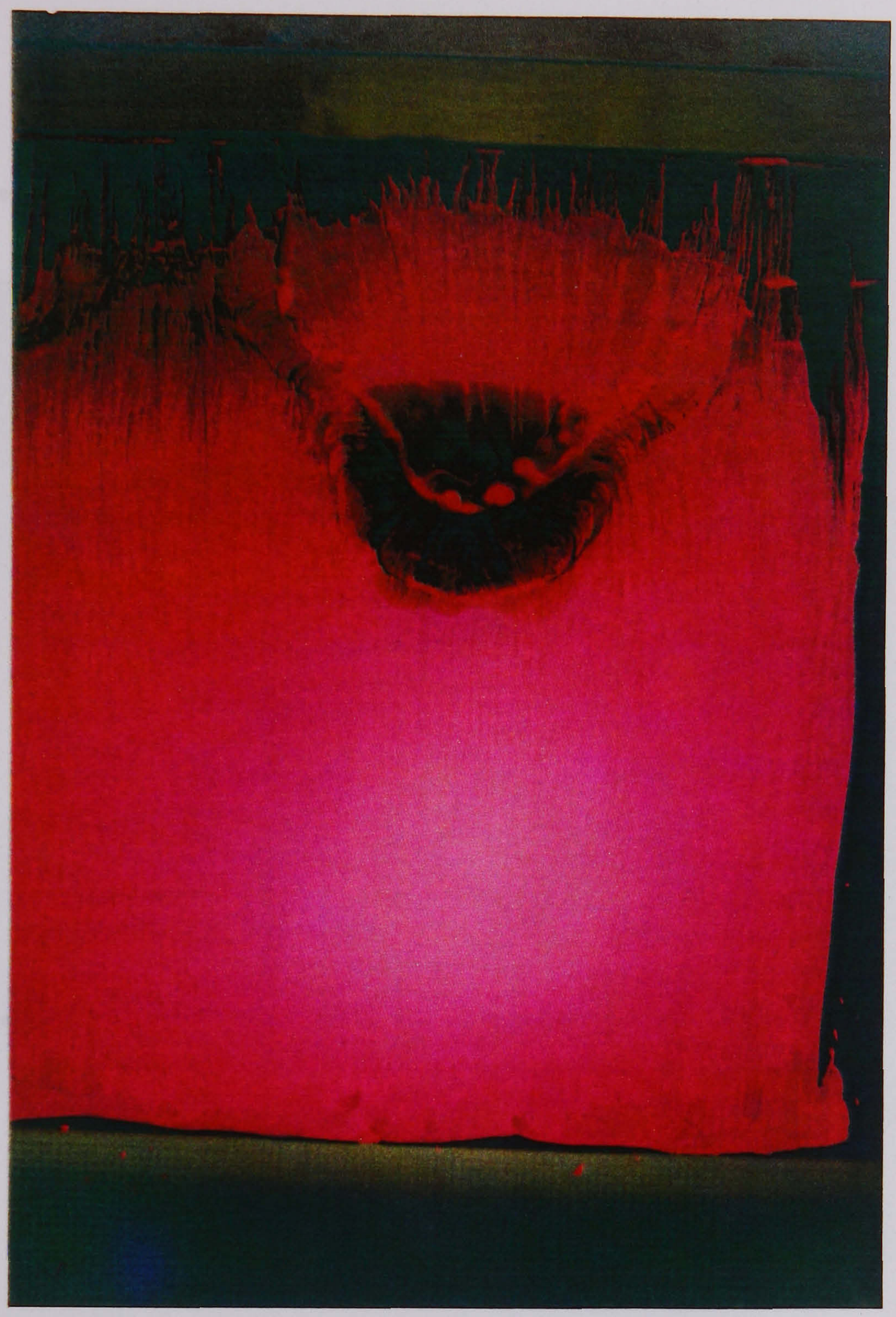

Figure 4.23 Plan view of the streak pattern observed from paraffin paint flow direction measurements. Flow direction from bottom of picture.

Figure 4.24 Tracing paper fixed to the model dune prior to the 'ink-dot' flow direction measurements. Flow direction is from the right.

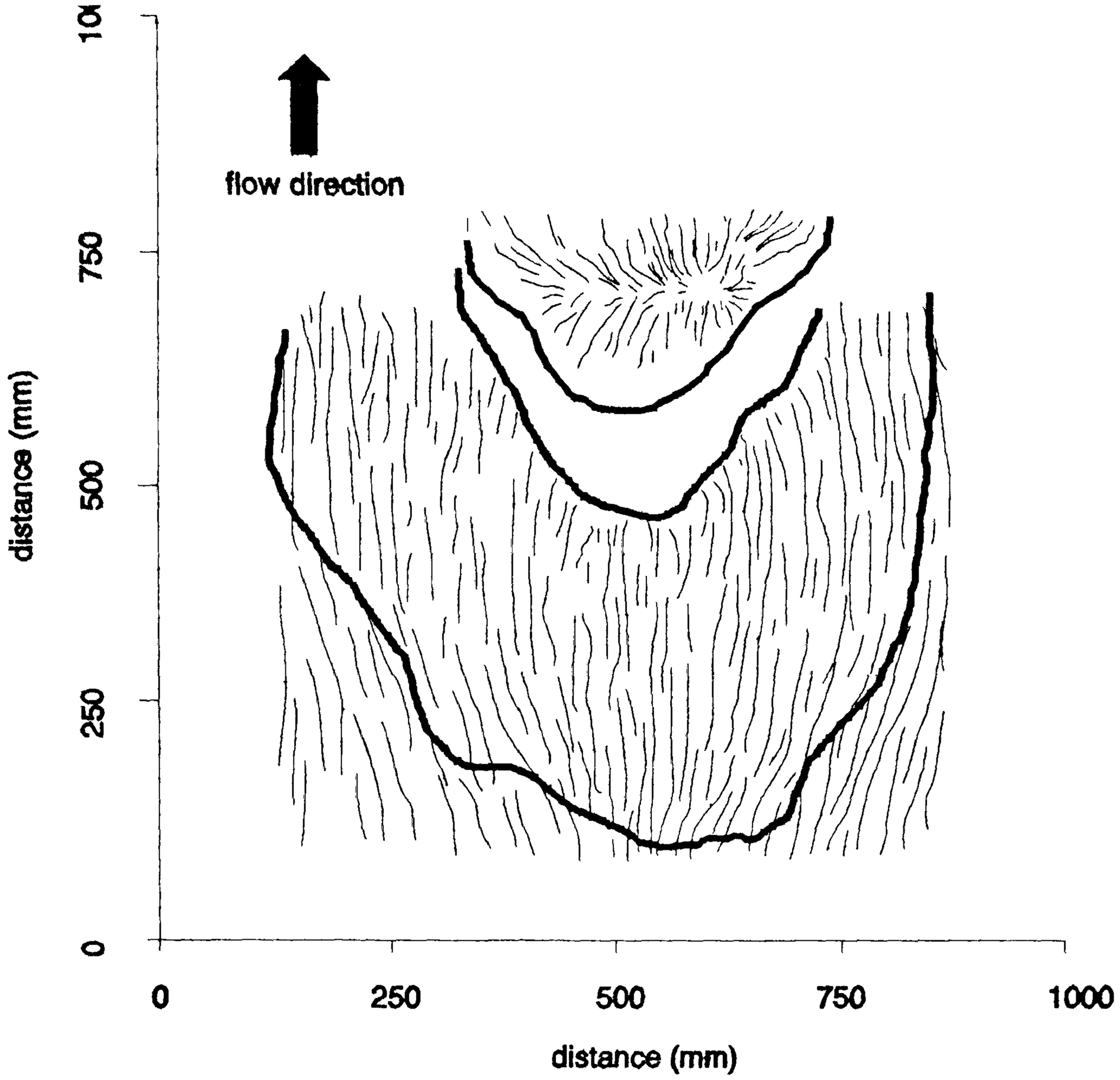

Figure 4.25 Streamline pattern over the model dune evident from paraffin paint experiments.

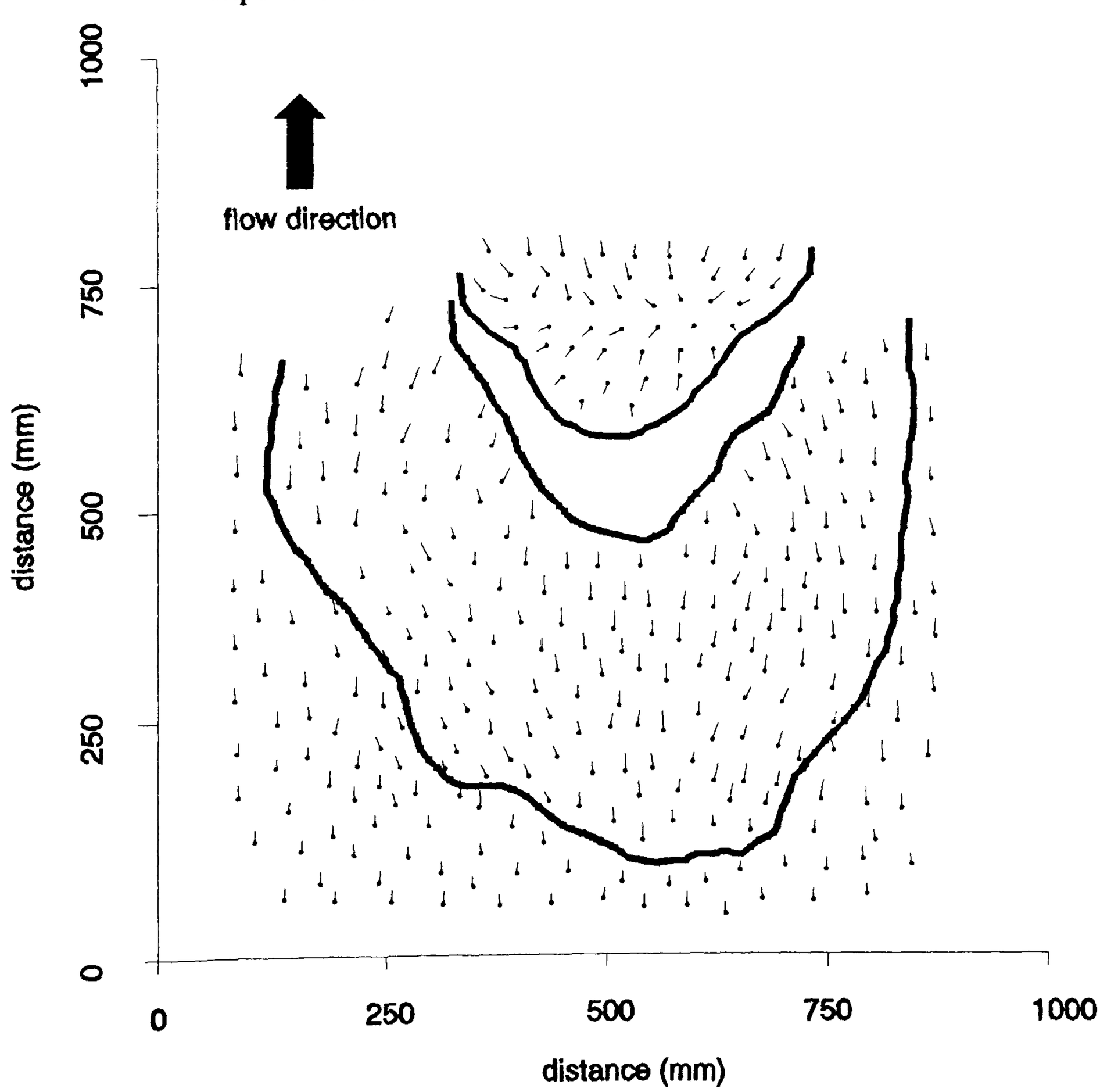

Figure 4.26 Streamline pattern over the model dune evident from 'ink-dot' experiments. Tails indicate flow direction.

The majority of the windward slope experiences <5° of flow divergence and this corresponds to <0.5% error in the surface shear stress measurements (presented in Chapter 4.3.4).

Figures 4.25 and 4.26 also show flow direction measurements in the lee of the dune. Both Figures clearly represent the region of reverse flow and zone of re-attachment. Due to the non-symmetrical nature of the dune the zone of re-circulation is off-centre, toward the left flank. This is typical of asymmetrical dunes (Allen, 1968). The zone of re-attachment is located at about x = 650 mm to 670 mm. This is comparable to the field measurements of lee-flow velocity (Chapter 2.4.3).

4.3.2. Co-ordinate System, Data Normalisation and Roughness Similitude

Co-ordinate system

Velocity and turbulence measurements were carried out on the three section lines studied in Chapters 2 and 3, namely, the centre-line and left and right flanks of the dune. The model dune was constructed on a moveable board. The x and y co-ordinates for each measurement point originated from the right upwind corner of the board, as shown in Figure 4.27. Any measurements taken upwind of the base line are given as negative. The z co-ordinate was measured using the measuring convention shown in Figure 4.13, taking the zero-plane-displacement (d) into account.

Velocity measurements were taken as vertical profiles above a point on the surface of the dune. The number of points in each profile and the proximity of profiles varied depending upon their position on the section lines. Hence, profiles at the toe, crest and brink were more closely spaced and had more measured points in each profile.

Normalising the Data

The measurements from both single and cross-wires were normalised by a reference velocity taken at 200 mm from the roof of the tunnel immediately above the model (u_r). In the analysis presented here, the change in any element (*e.g.* δu) is defined as its difference from the value measured at the same height in the absence of the dune (*i.e.* a value taken from the simulated atmospheric boundary layer profile shown in Figure 4.12).

For ease of discussion the values taken in the absence of the dune will be referred to as the upstream values. Therefore;

$$\delta u = u_{xyz} - u_{\infty}$$

Where:

δu = change in velocity
u_{xyz} = measured velocity with dune in place at co-ordinates x,y,z
u_{∞} = measured velocity at height z in absence of dune (upstream value).

The perturbation of any element is defined as its change from the upstream value, divided by the upstream value. Hence the perturbation of a parameter at any point is given by Equation 2.3.

Owing to the size of the model, velocity profiles had to be measured 900 mm upwind of the dune before the effect of the dune on the upwind flow proved insignificant. The values z_o, d, and u_* are all fetch-dependent and this far upstream (900 mm upwind of the toe) the velocity profile was not log-linear because the simulated boundary layer was not fully developed. The under-developed boundary layer velocity profile at this point is compared to the fully-developed profile in Figure 4.28 and the difference in velocity at specified heights is shown in Figure 4.29. As can be seen from these two Figures the undeveloped boundary layer at -780 mm can differ from the fully-developed boundary layer by up to about 8%. The boundary layer only becomes fully developed at about -380 mm. Therefore, the perturbations of the measured values were calculated using the respective underdeveloped profiles for all measurements taken upwind of -380 mm and the fully developed log-layer (shown in Figure 4.12) was used for all measurements downwind of, and including, -380 mm. Care should be taken with the results from this procedure as it assumes that the "law-of-the-wall" parameters remain constant, which is not necessarily correct.

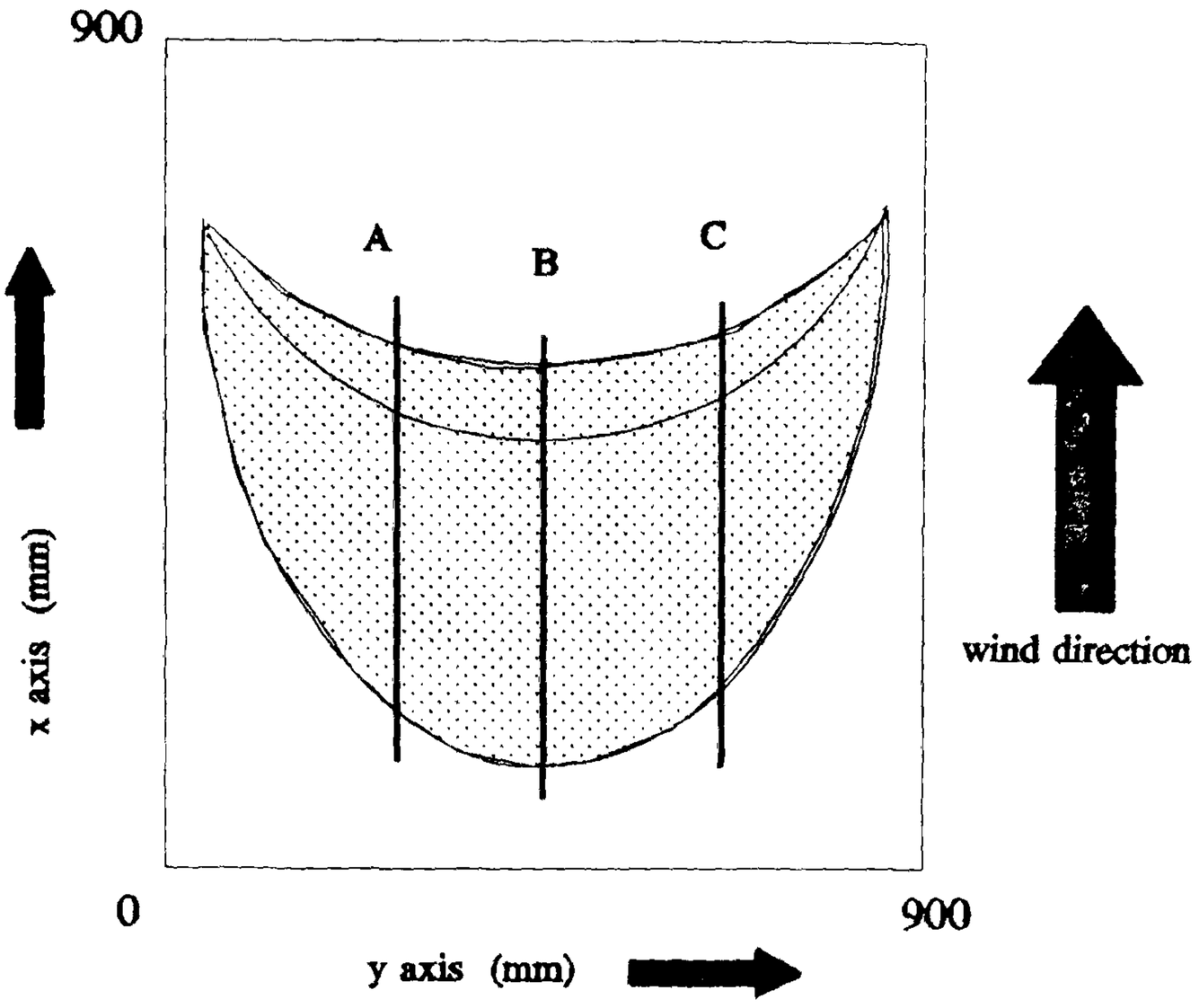

	TOE		CREST		BRINK	
	x	y	x	y	x	y
A. Right Flank	375,	188	375,	550	375,	615
B. Centre-line	523,	107	523,	480	523,	480
C. Left Flank	645,	99	645,	501	645,	595

Figure 4.27 Co-ordinate convention.

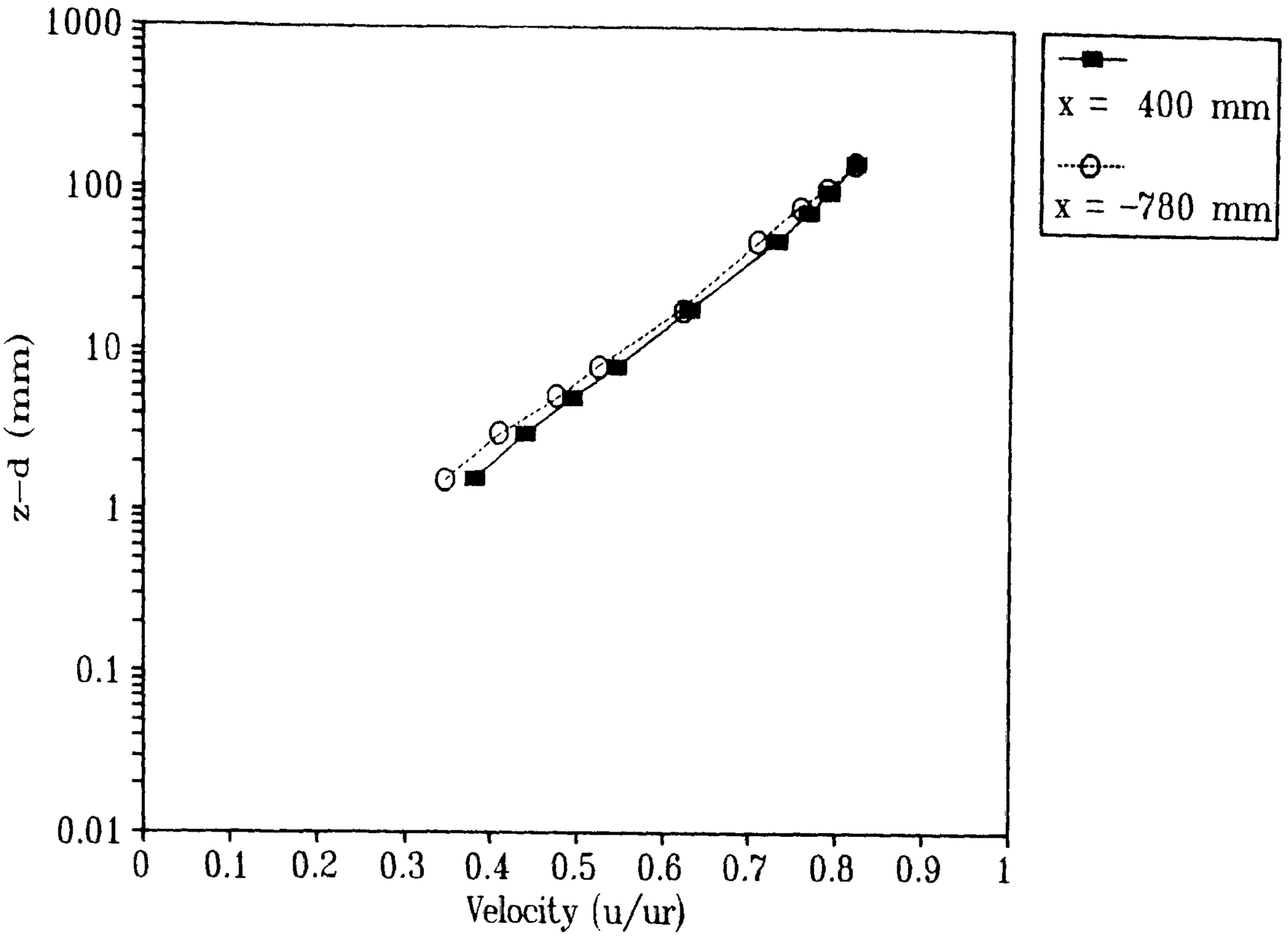

Figure 4.28 Comparison of velocity profiles at two points in the tunnel without inclusion of dune model.

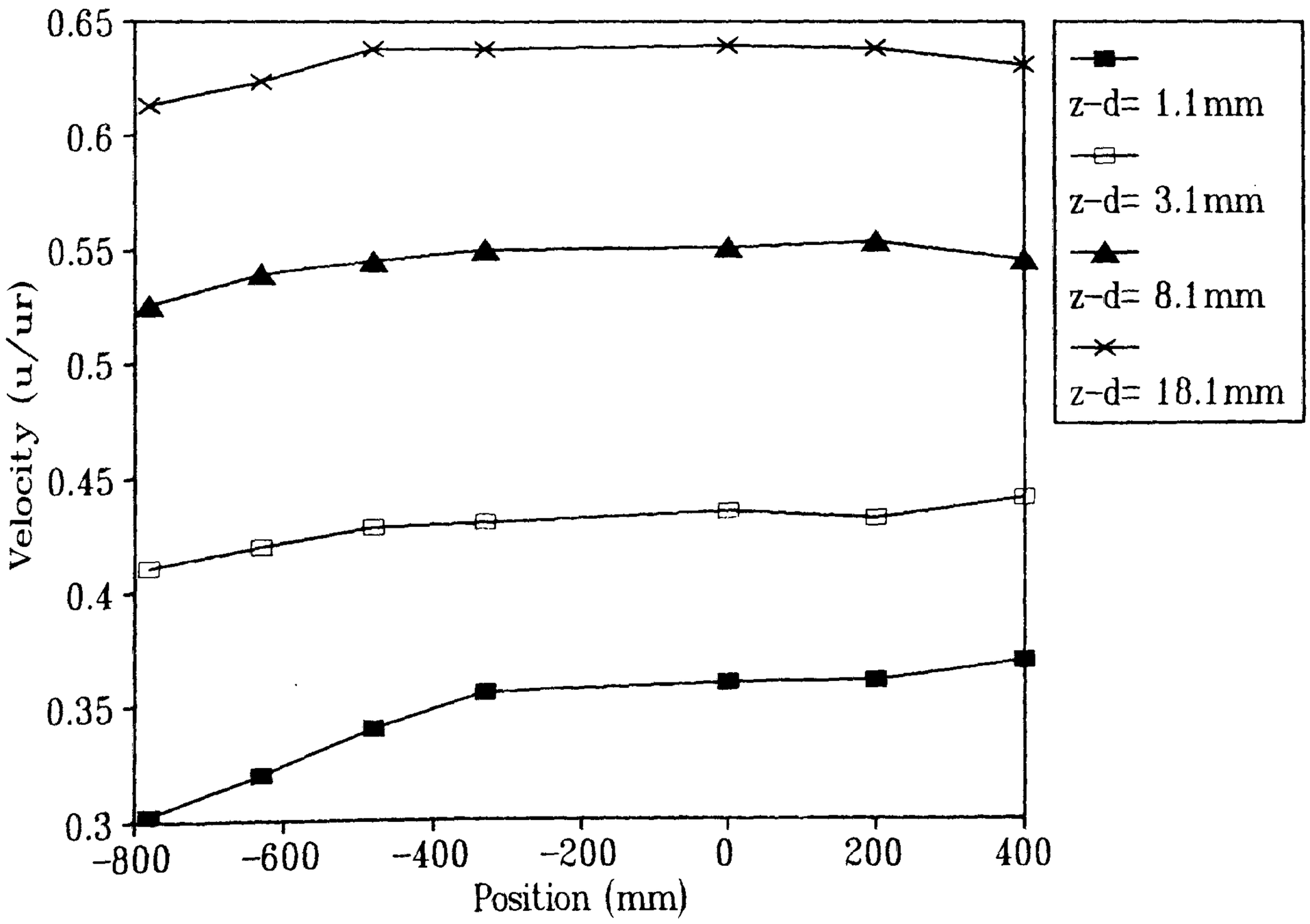

Figure 4.29 The velocity profile along the tunnel cross-section. Flow direction is left to right.

The Aerodynamic Roughness of the Dune Surface

A difference in aerodynamic roughness between the upwind surface and the dune model should result in changes in near-surface velocity owing to the growth of an internal boundary layer. This was tested in the laboratory by measuring a velocity profile firstly at the crest of the smooth dune model and then with the surface roughened using strips of *Lego* baseboard, cut to mirror the contours of the dune. A comparison of the two profiles is shown in Figure 4.30a. The internal boundary layer grown with an aerodynamically smooth dune results in an increase in near-surface velocities of nearly 25%. Similar results were noted by Howard *et al.* (1977).

It was therefore necessary to roughen the surface of the dune. The field measurements of surface roughness on the upwind gravel surface and on the dune showed no clear difference between the two (Chapter 2). It was therefore decided that a best approximation for the roughness of the dune model in the wind tunnel would be to use the same roughness as for the upwind surface. *Lego* base-board was therefore cut into squares around each roughness element (size $\approx$ 2 mm^2) and stuck onto the model surface with double-sided tape (Figure 4.30b).

4.3.3 Observations of Mean and Turbulent Velocity

Most wind tunnel studies of flow over low hills and sand dunes present the mean velocity (u) either as a velocity profile at the crest compared to upwind conditions (*e.g.* Britter *et al.*, 1981; Jensen & Zeman, 1985), or as a single line of velocity at a constant height above the surface (*e.g.* Tsoar, 1985; Tsoar *et al.*, 1985; both on two-dimensional cross sections). Few studies (except Gong & Ibbetson, 1989; Finnigan *et al.*, 1990; both on low hills) have documented the detailed development of the mean velocity up a windward slope. No study has presented such data on the windward slope of a sand dune.

In this section the velocity measurements are presented both as profiles above specified points on the dune surface, and as a function of distance across the windward slope along a line of constant height.

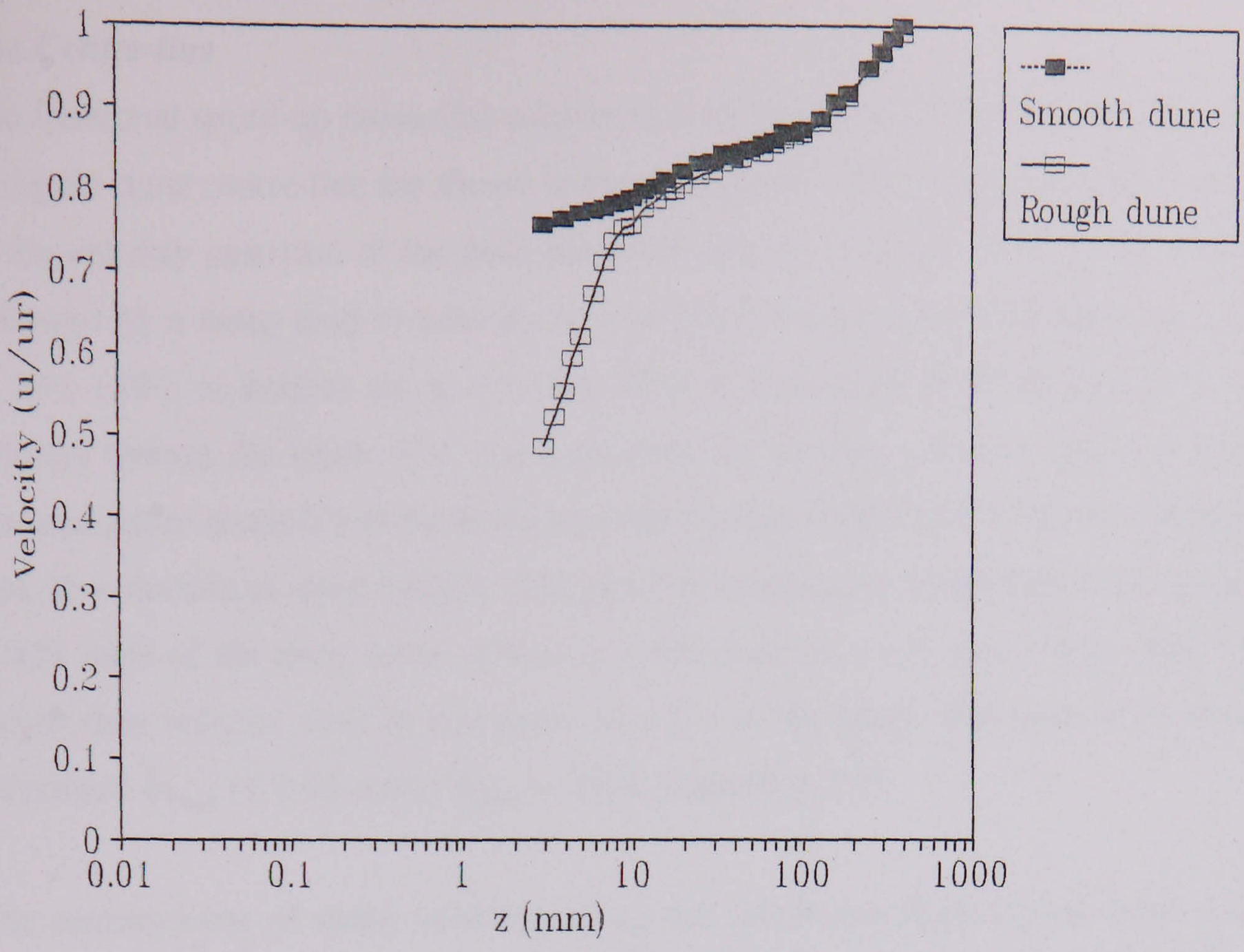

Figure 4.30a The effect of roughness addition on the velocity profile at the crest of the centre-line.

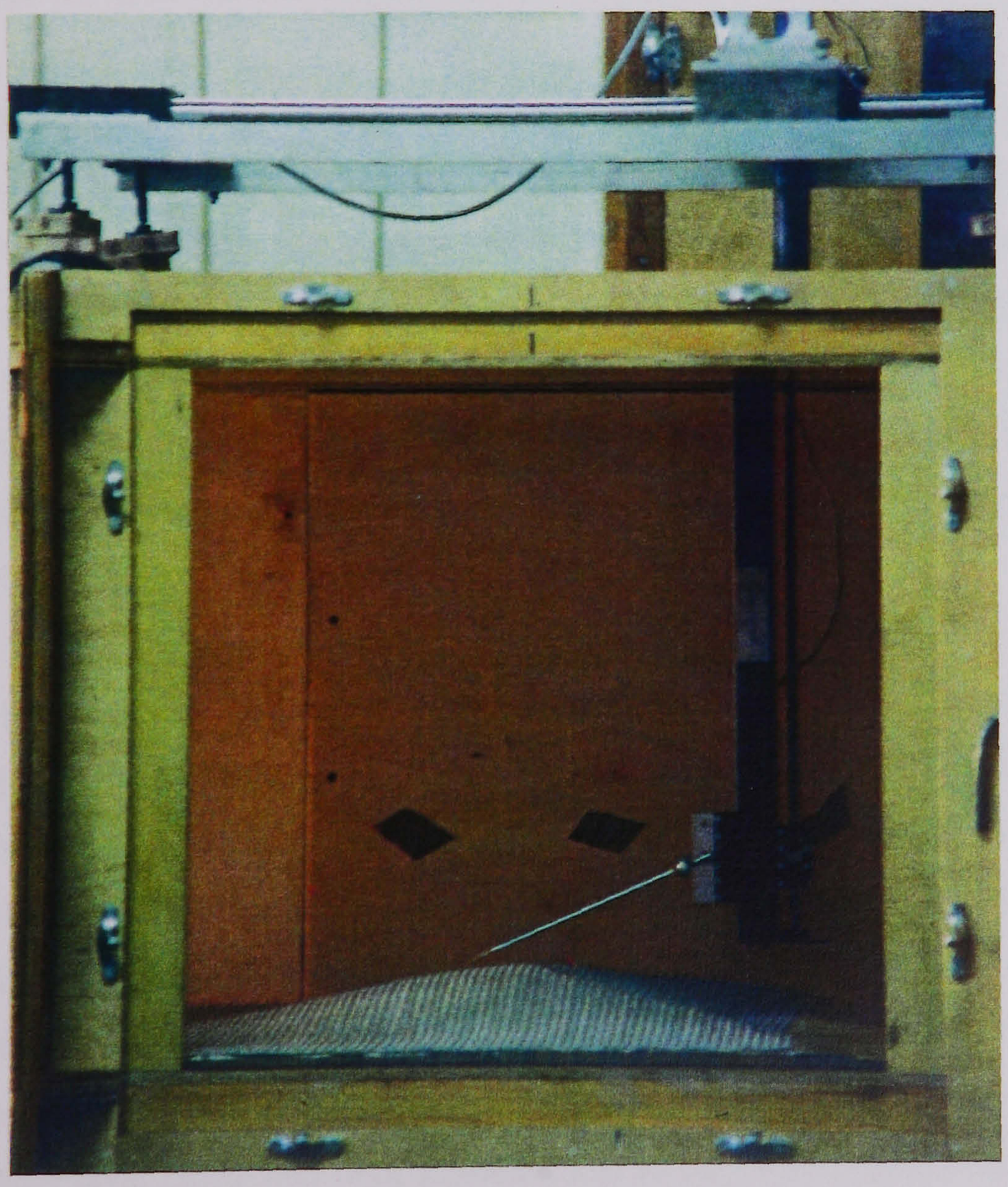

Figure 4.30b The model dune with roughness attached positioned in the wind tunnel. Direction of flow is from the left.

The Centre-line

The fractional speed-up ratios (δs) calculated from Equation 2.3 for a variety of constant heights along the dune centre-line are shown in Figure 4.31a+b. This Figure indicates a gentle reduction in the velocity upstream of the dune toe at all heights from x = -800 mm to +100 mm. This is followed by a sharp drop in velocity downwind of the toe itself to a minimum of around δS = -0.13 (-13%), at heights up to 5.1 mm. This is succeeded at all heights by a steady rise in velocity toward the brink. The speed-up does not become positive until x = 260 mm, which corresponds to about 0.3 of the maximum dune height (h/H = 0.3; where h = local surface height and, H = maximum dune height). The peak in speed-up is 0.496 which occurs just upwind (x = 429 mm) of the dune brink (where x = 480 mm) at a z-d of 1.1 mm. The velocity at that height then reduces, only to rise again to ≈ 0.4 at the brink. The peak in δs concurs with the calculated δs_{max} of 0.44 using $\delta s_{max} = 2H/L$ (Equation 2.8).

The development of mean velocity (u) up the windward slope of the dune conforms to the expected pressure gradient (discussed in Chapter 2.4.3). Similar measurements from wind-tunnel studies have been presented by Howard *et al.* (1977), Lai & Wu (1978), Tsoar (1985), Tsoar *et al.* (1985), Gong & Ibbetson (1989) and Finnigan *et al.* (1990).

A detailed picture of the variation of δs with height is shown in Figure 4.32, where vertical profiles of δs are shown as a function of distance along the windward slope. From this Figure it is clear that the δs is not constant with height in the inner-layer (below ≈ 10 mm). The minimum values of δs in profiles A, B, C and D (Figure 4.32) are all at heights of between 1.6 and 2.1 mm. The maximum values of δs in profiles F and G, occur at a height of 3.1 mm, corresponding with the second maximum in profile H. The first being at a height of 1.1 mm (and the maximum speed-up on the dune). Between profiles H and J the maximum δs gradually rises in height from 3.1 mm to 8.1 mm at the brink.

Several previous wind tunnel and field experiments have also shown that the observed maximum speed-up is at a height lower than the Jackson & Hunt (1975) prediction (see discussion in Chapters 2.4.3 and 3.4). The detailed profiles measured by Gong & Ibbetson (1989) of flow over a low three-dimensional hill show an almost identical relationship to the one presented here, and the vertical velocity profiles measured over Askervein Hill (Taylor *et al.*, 1987; Teunissen *et al.*, 1987; Mickle *et al.*, 1988) and Nyland Hill (Mason, 1986) suggest that the maximum speed-up is at about l/3 (where l = the JH inner-layer height, Equation 2.1), corresponding with the depth of the inner-layer calculated from Equation 2.2. In the present study, the inner-layer depth

A.

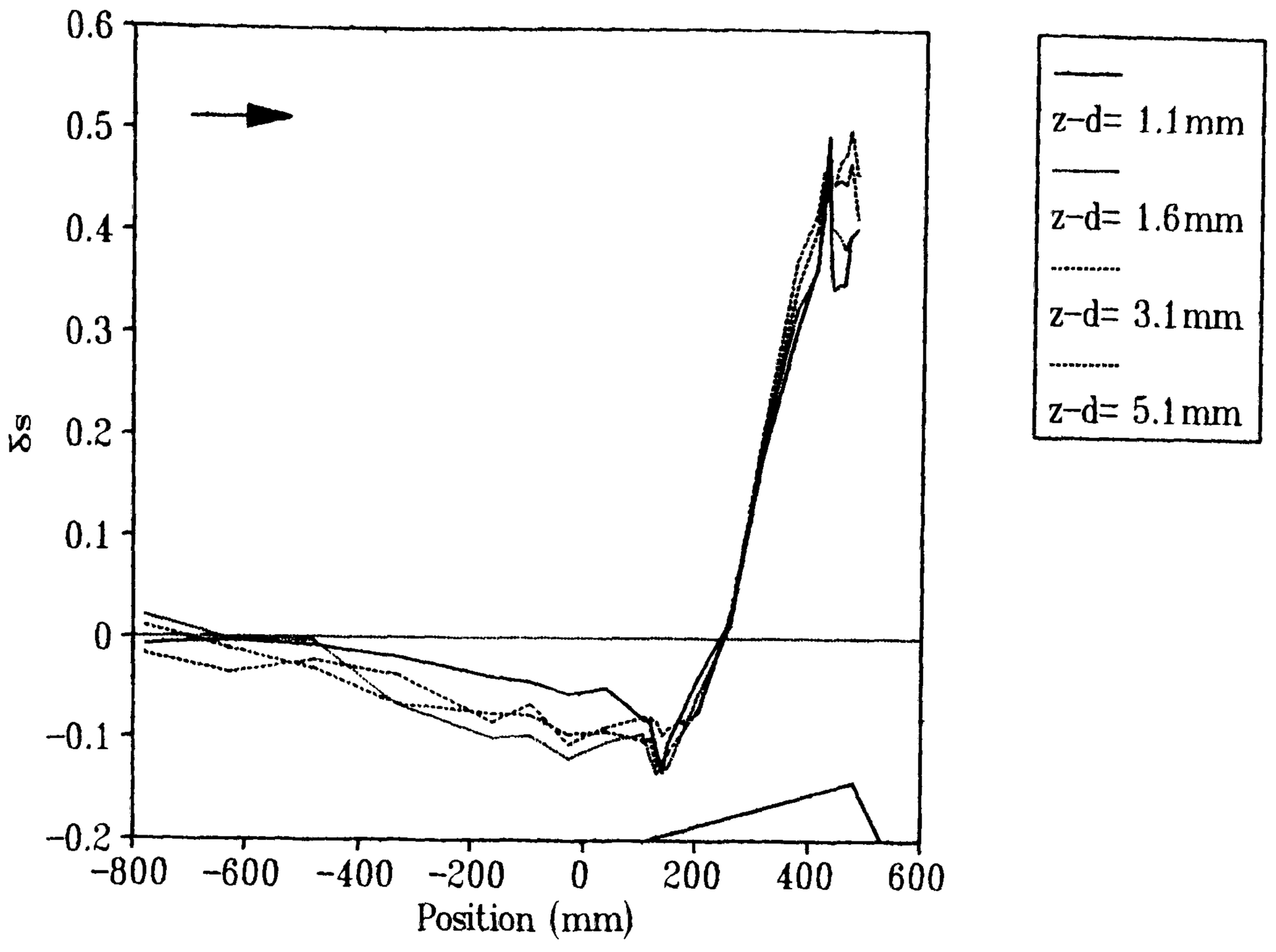

B.

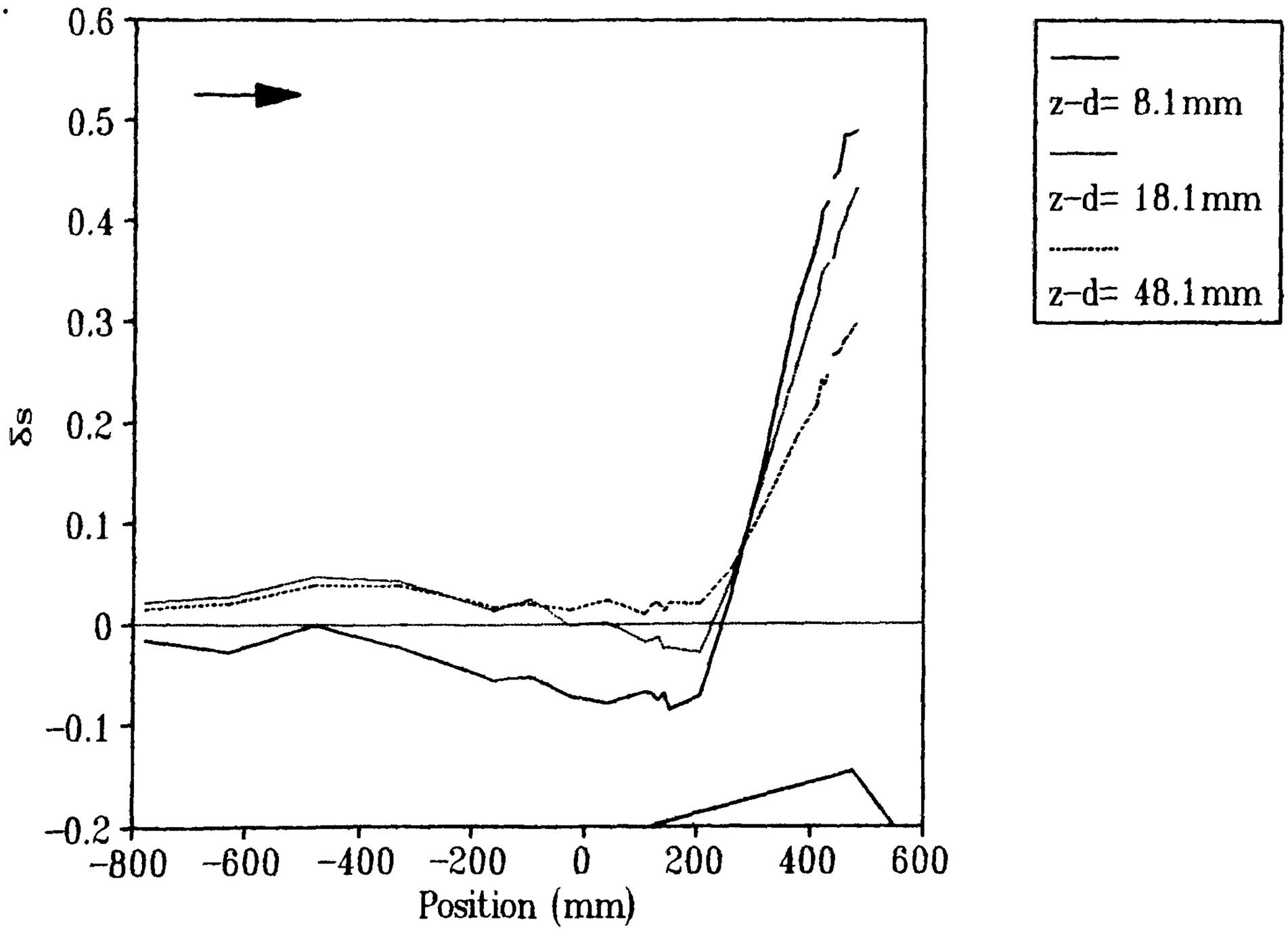

Figure 4.31 Fractional speed-up ratio (δs) on the centre-line of the model dune. A = near-surface heights; B = distant heights.

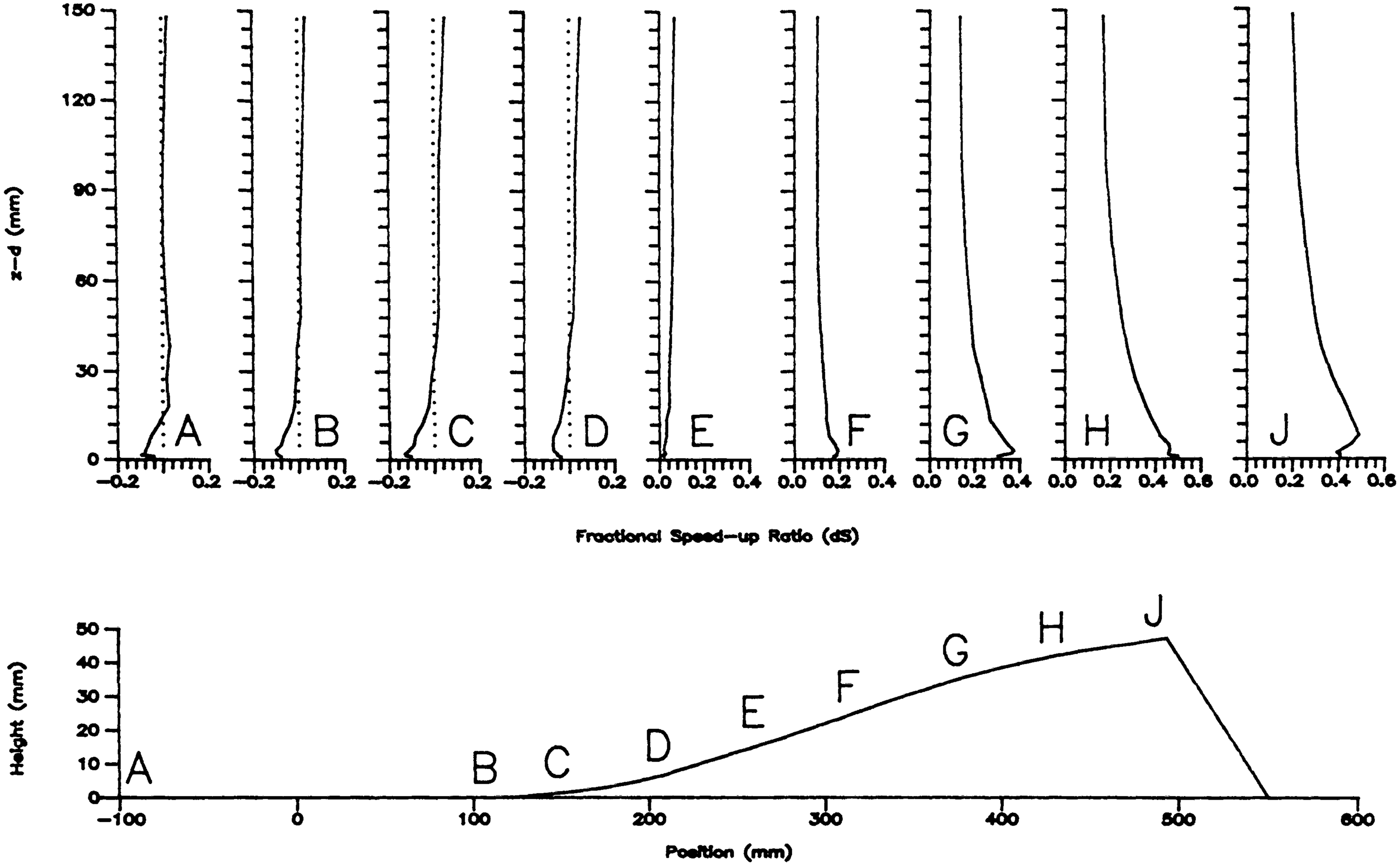

Figure 4.32 Vertical profiles of fractional speed-up ratio on the centre-line of the dune model.

calculated from Equation 2.2 was 3 mm, and that from Equation 2.1 was 10 mm. The variation in velocity speed-up between 3 mm and 10 mm therefore appears reasonable.

The Flanks

The velocity measurements on the left and right flanks of the dune are similar to those described on the centre-line. Figures 4.33a and 4.33b show the δs along lines of constant height on the left flank. As the flow approaches the dune, the δs is reduced to a minimum of -0.19 on the windward slope at x = 189 mm. Again, a sharp upwind reduction in δs is noticeable at heights up to 5.1 mm. There follows an increase in δs up the windward slope, with the values becoming positive where $h/H \approx 0.3$. The greatest δs for all measured heights occurs at the crest (x = 501 mm), and this maximum is 0.4 at a height of 8.1 mm (relatively consistent with $2H/L = 0.33$). Beyond the crest there is a sharp reduction in δs, with values at heights of 5.1 mm and below becoming negative. The lowest value in this region is -0.2, at a height of 1.6 mm.

The vertical profiles of δs on the left flank (Figure 4.34) show a reduction in velocity upwind of the dune to profile C with the maximum speed-up at profile F, the crest. The height of the maximum speed-up along the windward face rises from 2.1 mm at profile D to 8.1 mm at profile F. In the region between the crest and brink a sharp reduction in near-surface velocity can be seen. This is coupled with the height of maximum speed-up ($\delta s = 0.3$) rising to 18.1 mm at profile J. This is consistent with the maximum δs staying at a fairly constant height in relative space, while the airstream below diffuses its energy into turbulent eddies as a result of the sudden imposition of an adverse pressure gradient and streamline expansion. This turbulent momentum deficit zone appears to have no effect on the velocity above 18.1 mm.

The evolution of the mean velocity over the right flank of the dune, shown in Figures 4.35a and 4.35b, demonstrates an almost exactly similar response to that of the left flank. The minimum δs of -0.15 occurs at the toe (x = 188 mm) at a height of 1.6 mm. The speed-up values become positive at x = 260 mm (where $h/H = 0.3$), and the maximum ($\delta s = 0.39$) is at the crest (x = 549 mm) at a height of 8.1 mm (compare with $2H/L = 0.34$). The reduction in speed-up between the crest and brink results in a minimum of 0.09 at 1.1 mm at the brink.

The vertical profiles of flow acceleration on the right flank (Figure 4.36) show the rise in height of the maximum δs from 1.6 mm at profile D to 8.1 mm at the crest (profile G). At the brink, the maximum δs is at 18.1 mm and, as with the left flank, this corresponds with a fixing in relative height of a "jet" from the crest. The reduction in δs only close to the surface is

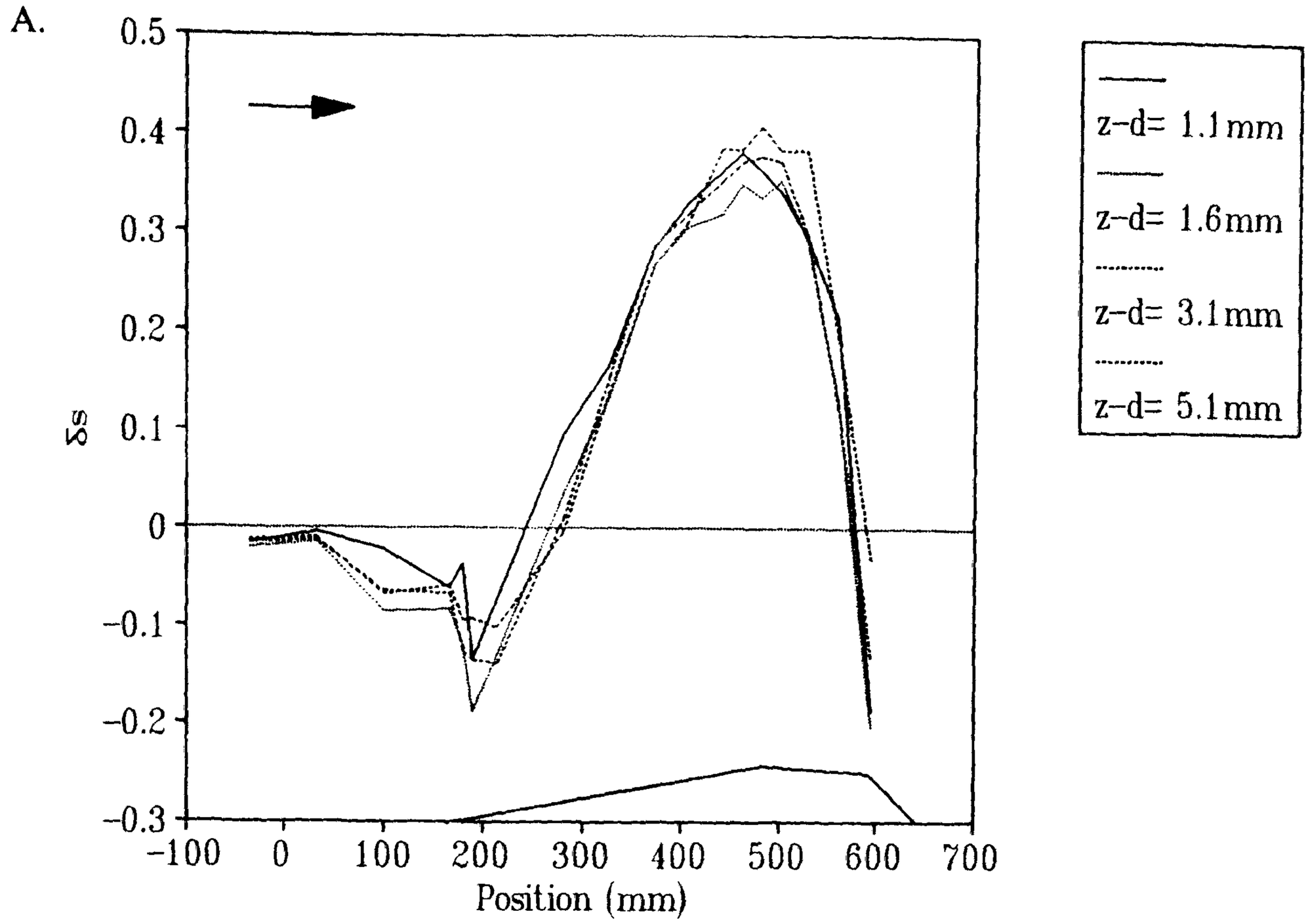

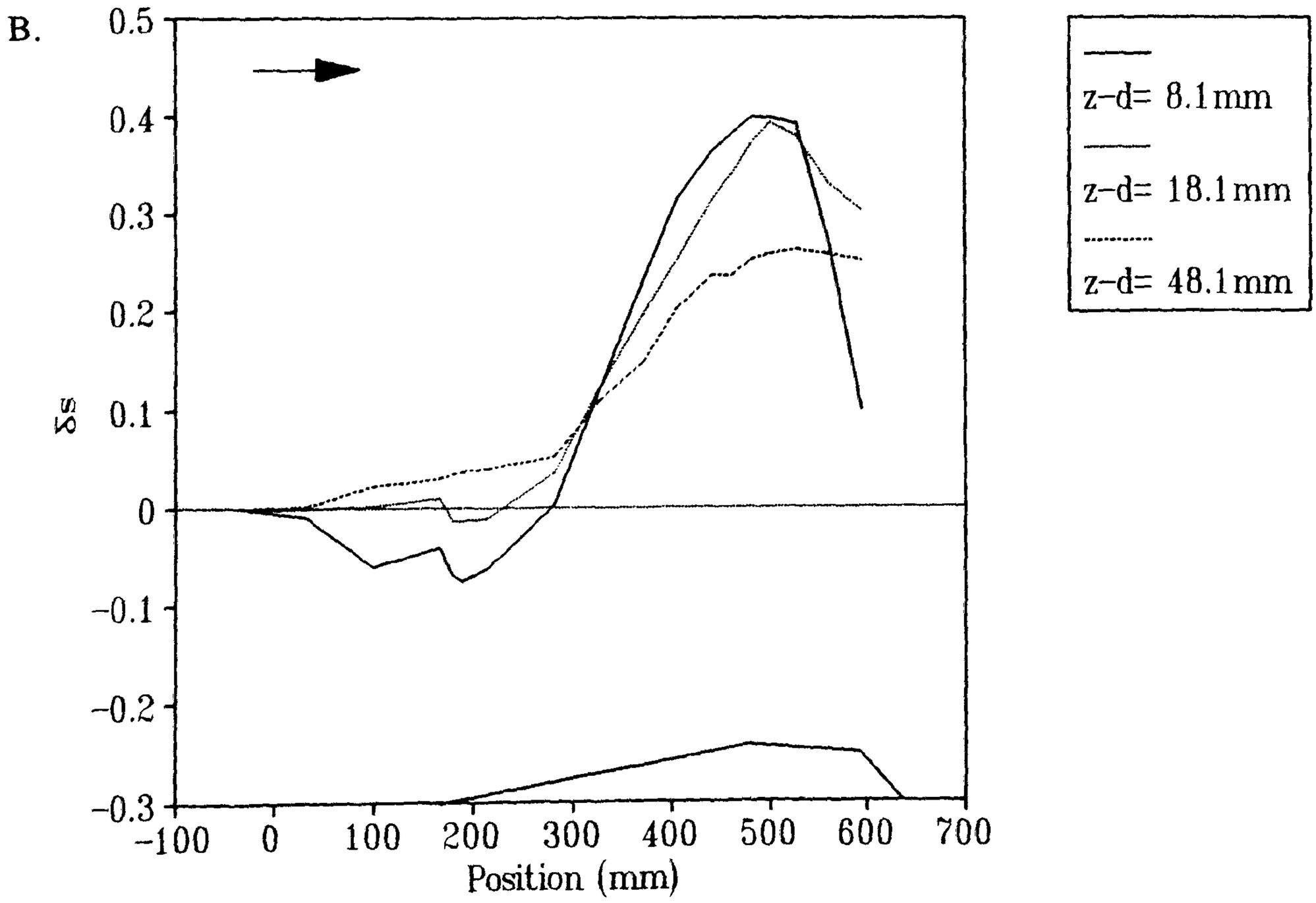

Figure 4.33 Fractional speed-up ratio (δs) on the left flank of the model dune. A = near-surface heights; B = distant heights.

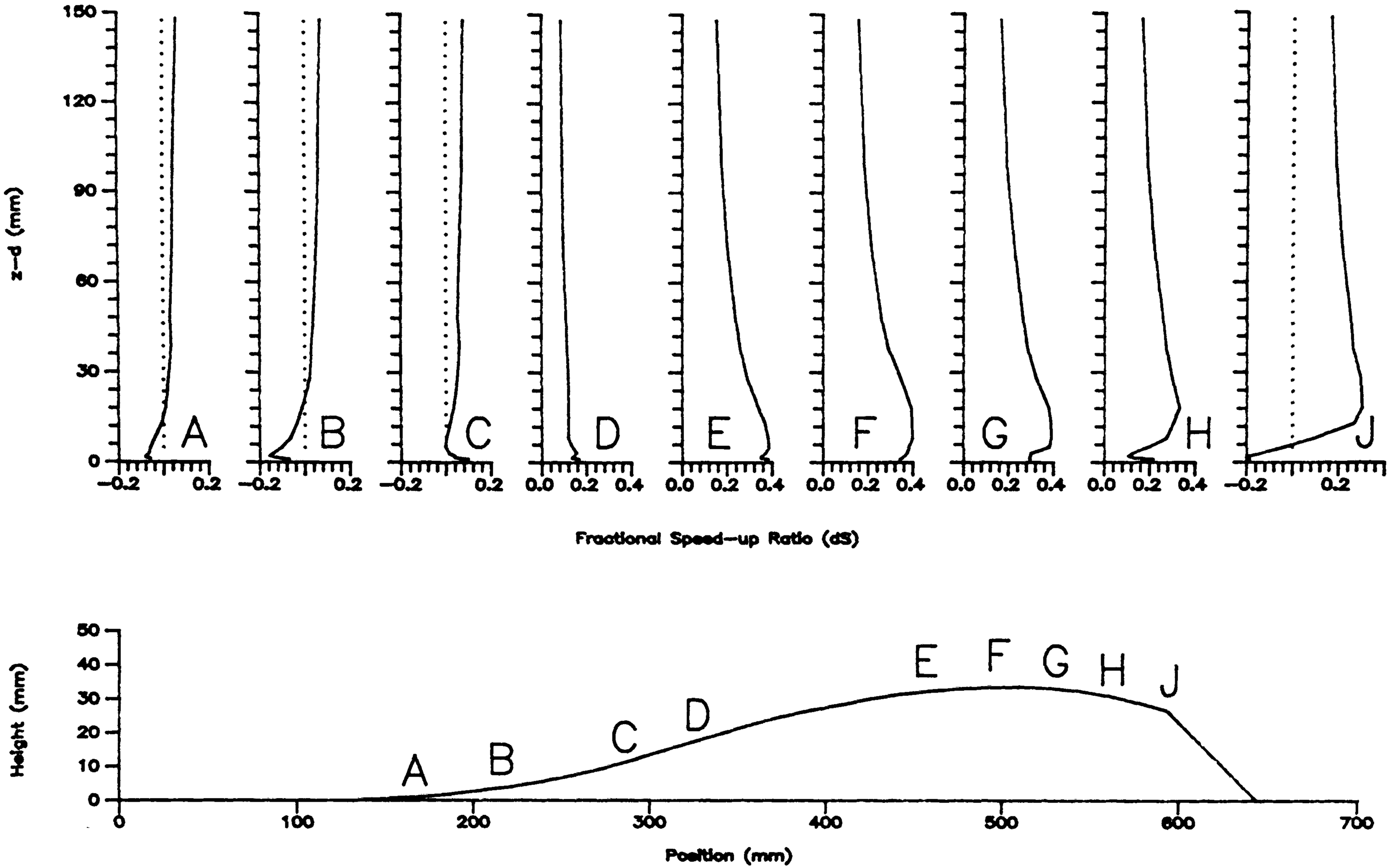

Figure 4.34 Vertical profiles of fractional speed-up ratio on the left flank of the dune model.

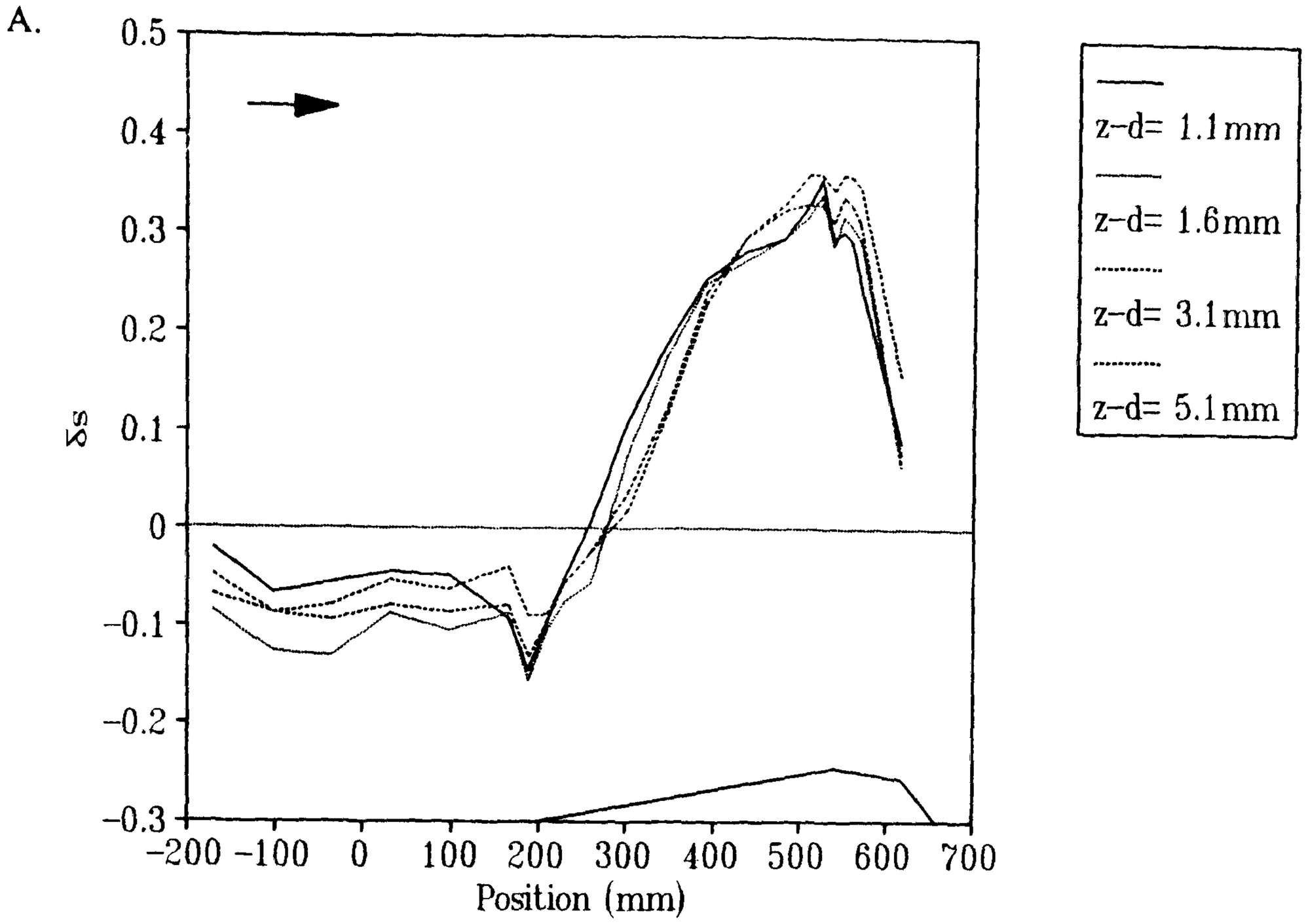

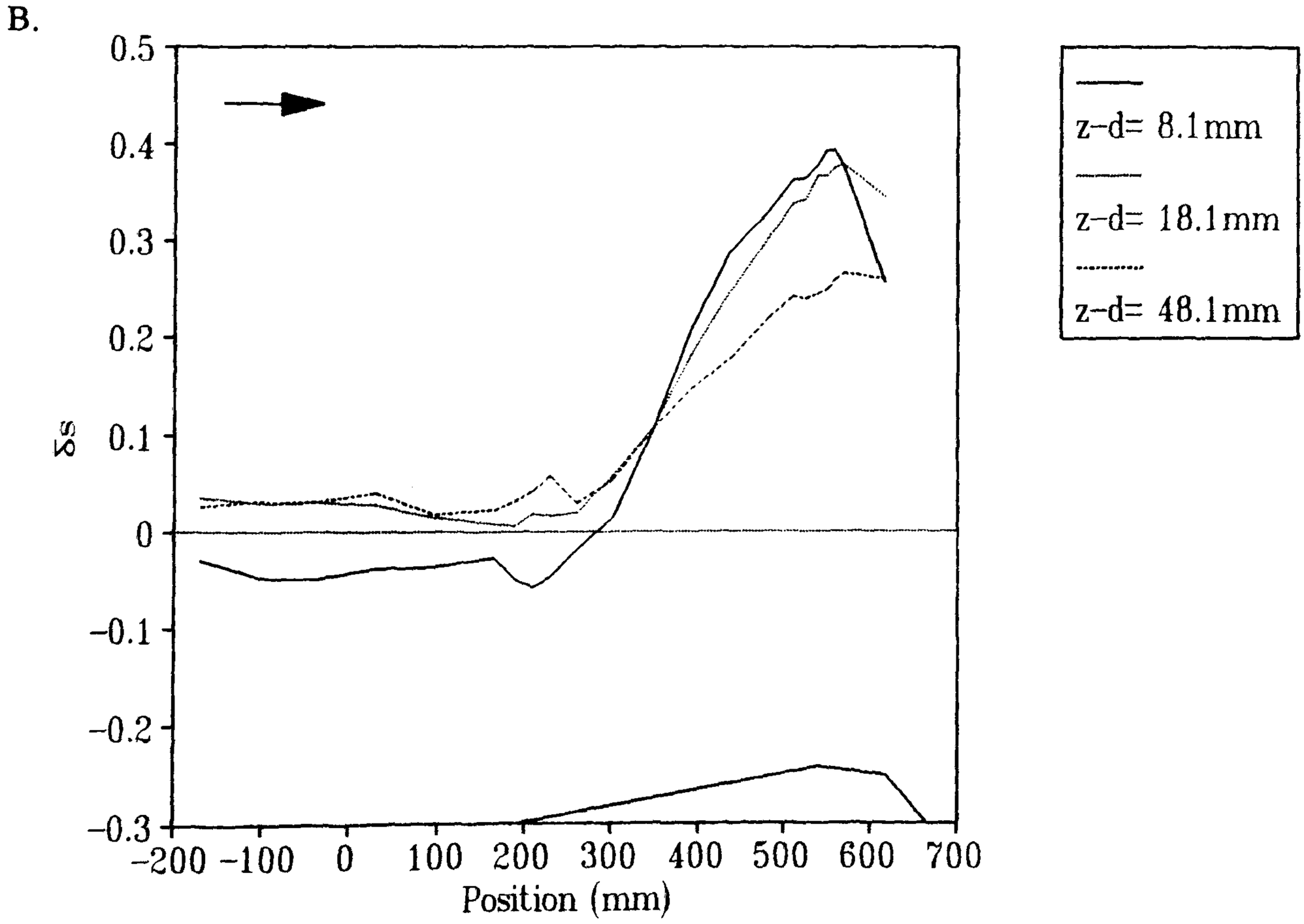

Figure 4.35 Fractional speed-up ratio (δs) on the right flank of the model dune. A = near-surface heights; B = distant heights.

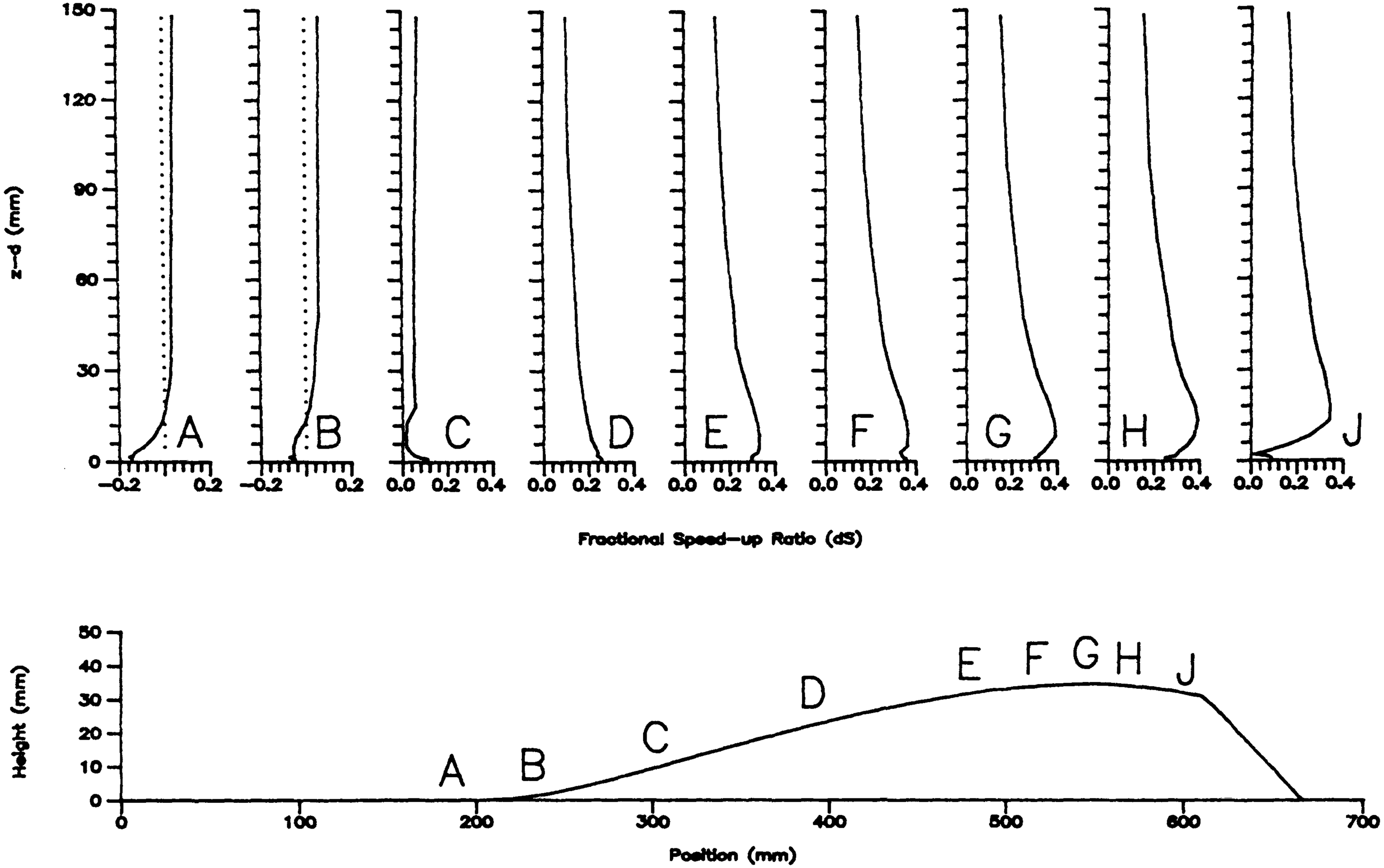

Figure 4.36 Vertical profiles of fractional speed-up ratio on the right flank of the dune model.

characteristic of wake regions in the lee of low hills (Gong & Ibbetson, 1989; Finnigan *et al.*, 1990).

Comparison of the Velocity Section Lines

A comparison of the three velocity section lines described here reveals the expected contrast between the centre-line and the flanks in the crestal region. The flow acceleration on the centre-line is significantly higher than the flanks, corresponding with its increased height and concurring with the 2H/L rule, with the half-lengths of each of the section lines being the same. However, of more interest is the reduction in velocity in the toe region of the flanks being greater than that at the centre-line. The respective minimum δs values in the toe regions of the centre-line and left and right flanks are -0.13, -0.19 and -0.15 respectively. One might have expected that the flanks would have much less of a reduction in velocity compared to the centre-line in these areas because the adverse pressure gradient due to the height of the dune is reduced.

A possible explanation for this peculiarity is that at the centre-line proper the flow does not diverge laterally. Hence, the adverse pressure gradient induced by the dune blockage tends to extend vertically. This is coupled with an increase in turbulent mixing which blends in higher velocity flows from above. In contrast, on the flanks, the tendency is for the pressure gradient to extend laterally, with the increased turbulent mixing blending in airflows of a similar velocity. Evidence for this would be negative values of δs occurring at higher levels on the centre-line than on the flanks. Reference to Figures 4.32, 4.34 and 4.36 show that this is the case. On the centre-line, negative speed-up values occur at heights of between 30 mm and 35 mm. On the flanks, the maximum height at which negative values of speed-up occur is just 15 mm to 20 mm.

Further evidence is the greater amount of turbulent mixing evident at the toe on the centre-line (Figure 4.37a, b and c). These turbulence intensities were calculated from single-wire velocity profiles using;

$$\alpha = u'/u$$

where:

α = turbulence intensity
u' = local fluctuating horizontal component of velocity
u = local mean velocity.

The maximum turbulent intensity on the centre-line is nearly 31%, compared to 28% and 29% for the two flanks. This increased intensity occurs at all measured heights.

Another notable feature in comparing the velocity sections is that the velocity deficit in the crest-brink region on the left flank is much more pronounced than that on the right flank (Figures 4.34 and 4.36). This is because the drop in height from crest to brink on the left flank (1.4 m) is almost double that of the right flank (0.8 m). The right flank also has slightly more turbulent mixing in this region (Figure 4.37) possibly because of a greater degree of deflection of high velocity flows from the centre-line (see Chapter 4.3.1), hence increasing the mean u.

The peaks in δs at all measured heights upwind of the brink on the centre-line (Figure 4.31) are also peculiar. Other wind tunnel studies of flow over low hills (*e.g.* Gong & Ibbetson, 1989; Finnigan *et al.*, 1990) have measured peak velocities at the hill crests. This point is discussed further in Chapter 4.3.4.

4.3.4 Observations of Reynold's Stress and Surface Stress

Correction Factors

The components of Reynold's stress were measured by a cross-wire at points coinciding with the single-wire velocity traverses. In order to achieve reliable shear stress measurements with a cross-wire probe in highly turbulent flows (rms. >15%) it is necessary to correct the data for turbulent fluctuations in the airflow (Castro, 1986). Some studies (*e.g.* Finnigan *et al.*, 1990) have avoided this necessity by using triple wires, hence increasing the angle of acceptability of the probe. However, calibration and use of such probes is complex (Castro, 1986). One of the more useful correction techniques was devised by Tutu and Chevray (1975). They derived total errors in measurement due to high turbulence acting on a cross-wire probe and presented their data as errors in measured quantities. A re-working of their data (from Castro, 1986) is shown in Figure 4.38. The relationships shown in Figure 4.38 were used in this study to correct the usb, wsb and uwb components for the turbulent intensities shown in Figure 4.37.

A further correction that is required is that for streamline angle. During measurement traverses the cross-wire was positioned horizontally, not parallel with the surface of the dune. The streamlines over a hill have been shown to be displaced vertically at an angle dependent upon the distance above and the inclination of the surface (Gong & Ibbetson, 1989).

A.

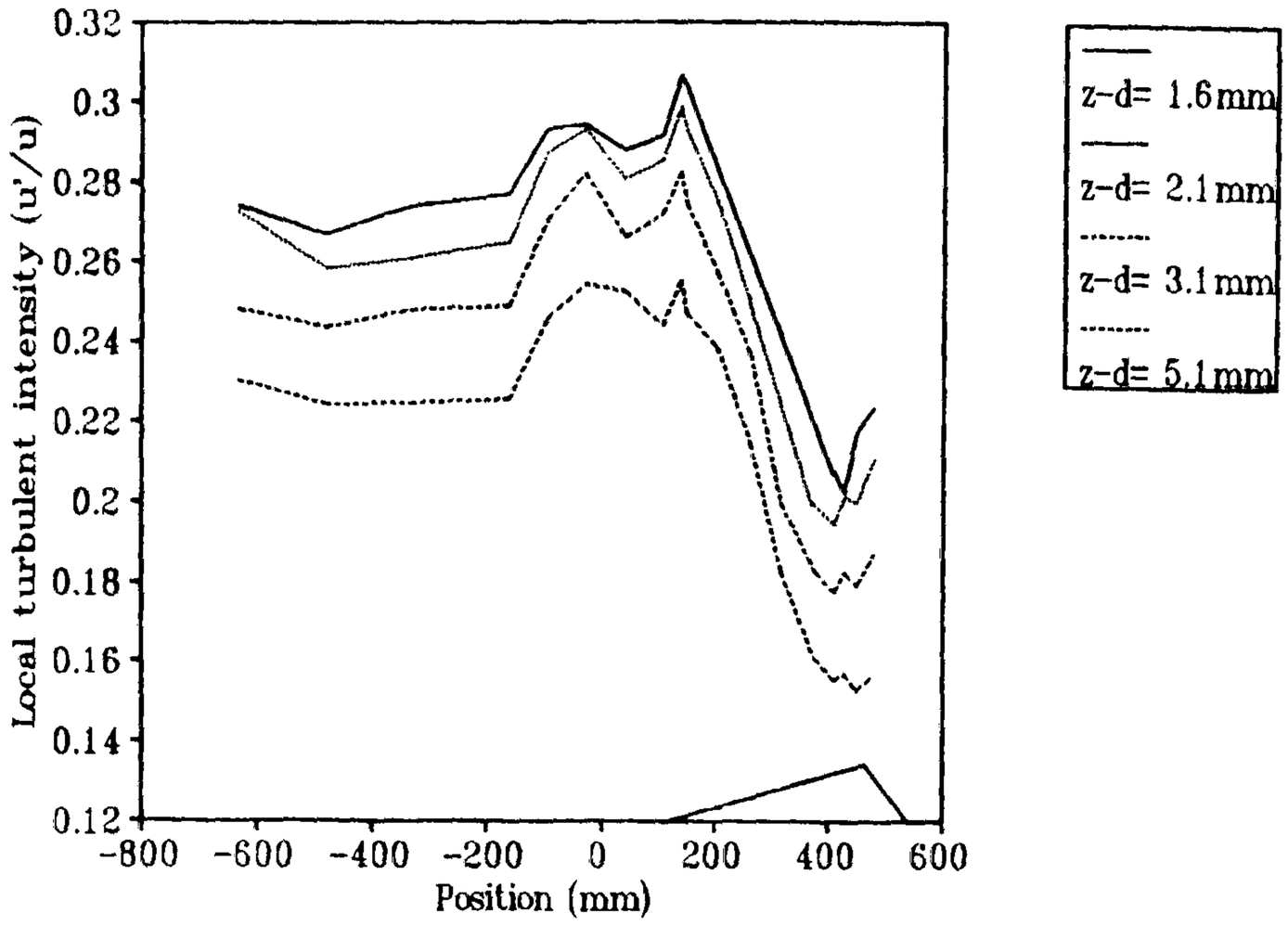

B.

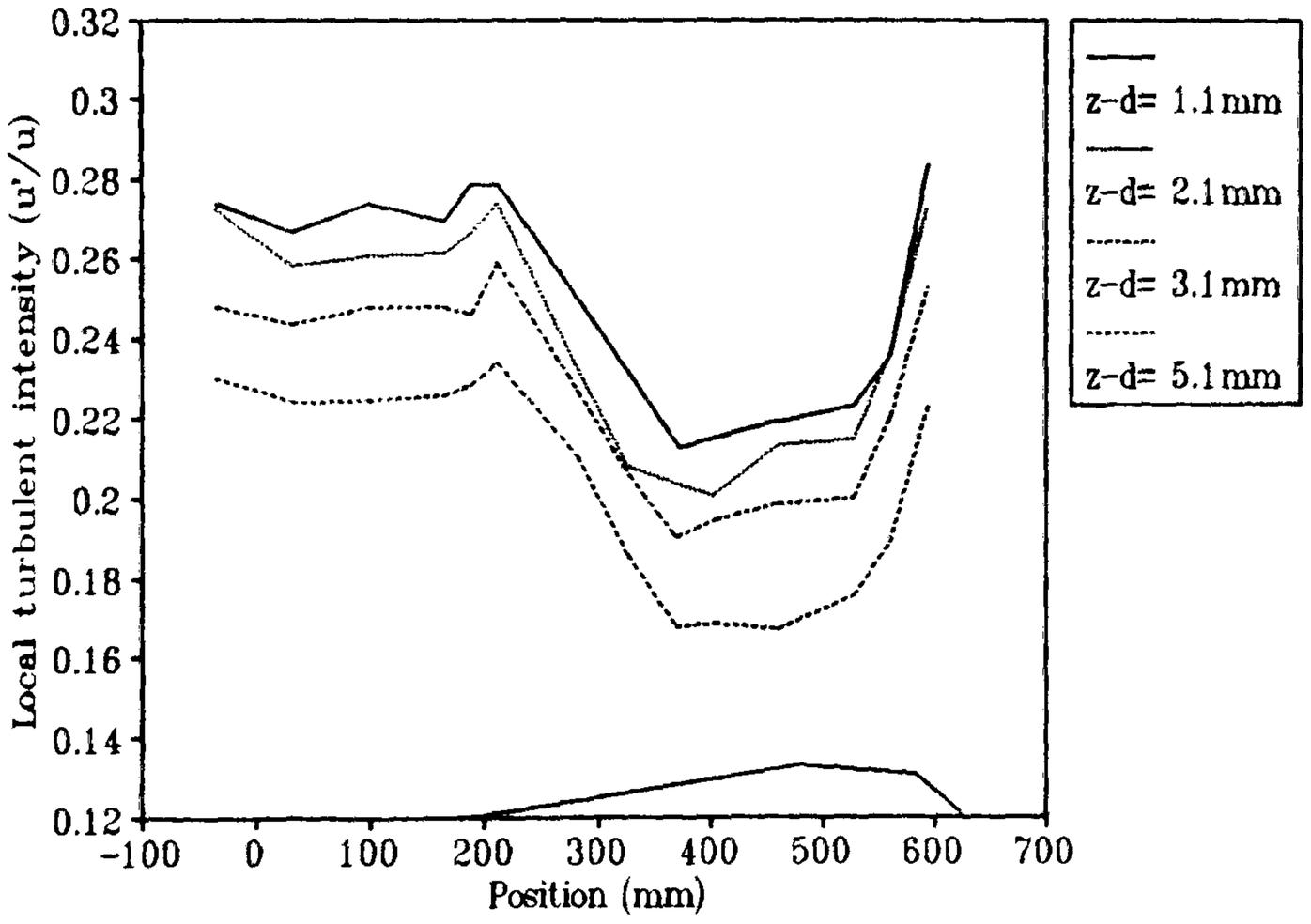

C.

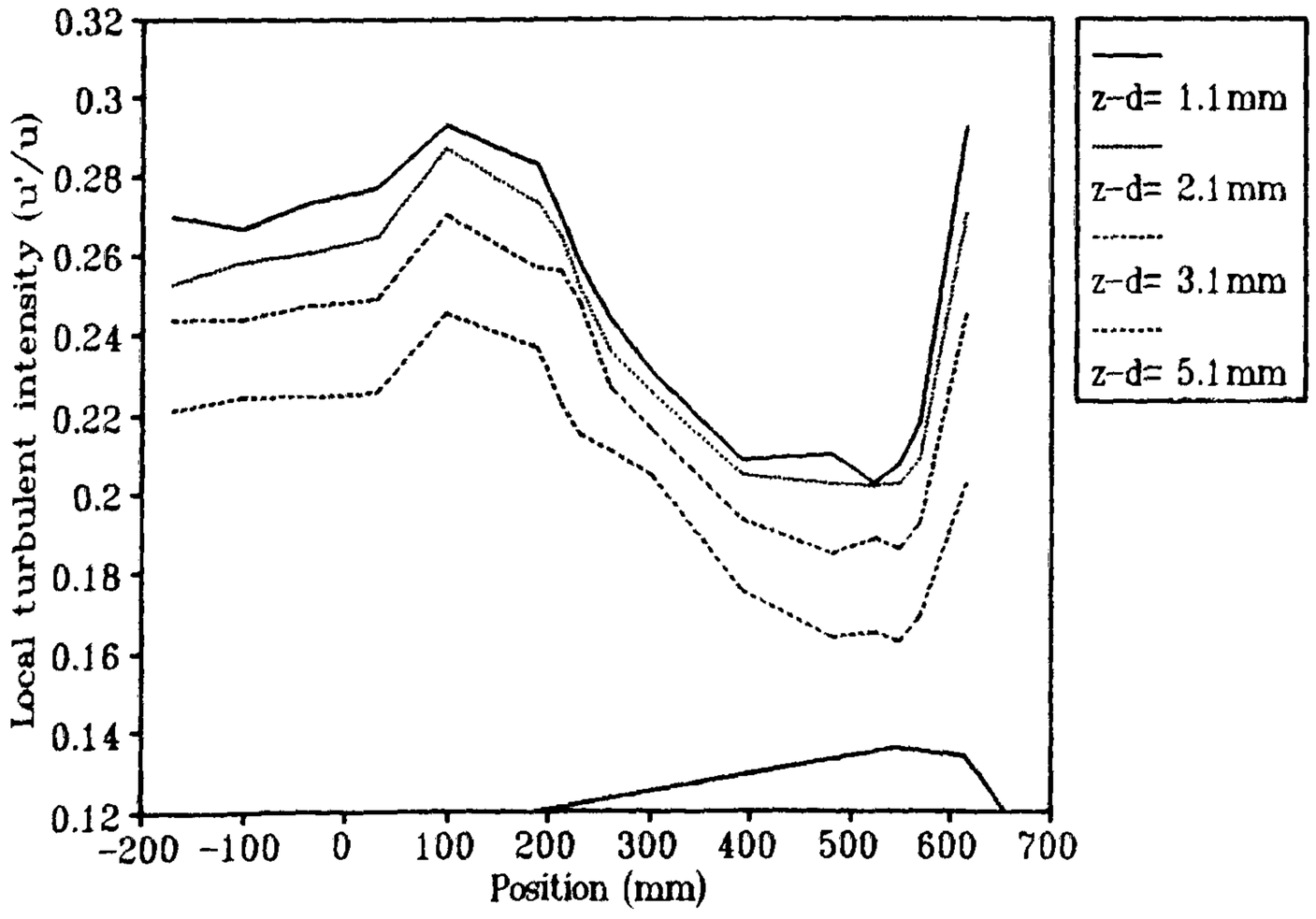

Figure 4.37 Turbulence intensities over the model dune. A = centre-line; B = left flank; C = right flank.

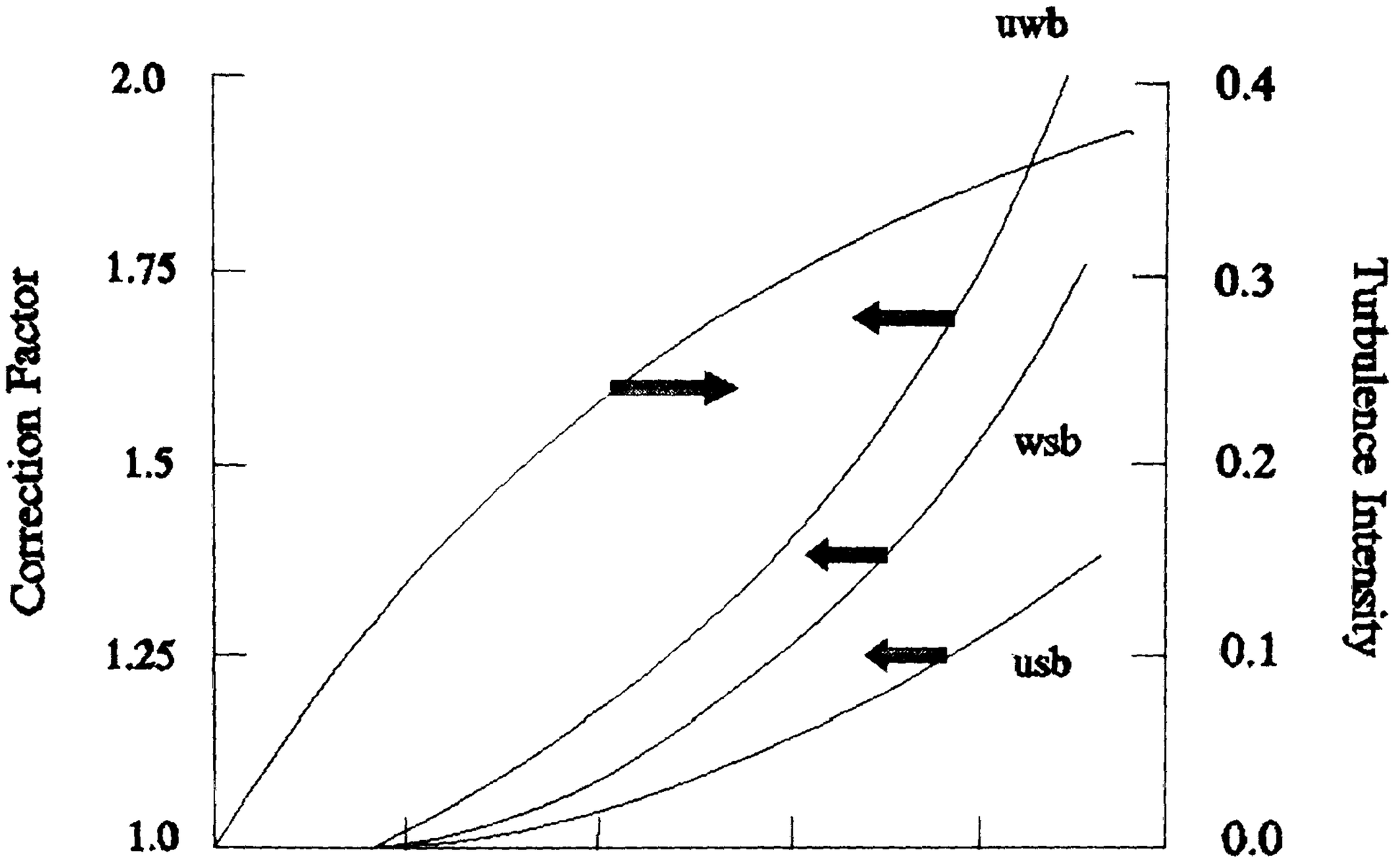

Figure 4.38 Correcting Reynold's stress components for turbulence intensities. Arrows signify axes relevant to each line.

This means that all the results in the present study were subject to error because of the angle of inclination between the cross-wires and the angle of the local streamline. The streamline angle can be calculated from;

$$\tan \phi = (w/u)$$

The corrected Reynold's stress component can then be calculated from the following equations;

$$-uwb_s = \cos 2\phi + (usb - wsb).(\tfrac{1}{2} \sin 2\phi) \quad (4.7)$$

$$usb_s = usb \cos 2\phi + wsb \sin 2\phi + uwb \sin 2\phi \quad (4.8)$$

$$wsb_s = wsb \cos 2\phi + usb \sin 2\phi - uwb \sin 2\phi \quad (4.9)$$

where:

x_s = component adjusted for streamline angle
ϕ = calculated streamline angle.

The profiles of streamline angle for the three section lines (determined from cross-wire measurements in the wind tunnel) are shown in Figure 4.39a, b and c. The values plotted at z-d = 0 are the surface slope angles of the dune. As expected, the profiles show that the deviation of streamline angle is height-dependent, with a maximum near the surface. In each case the upwind profile (at x = -200 mm) shows almost no deviation. However, at the toe, an angle is evident at nearly all heights despite the surface slope being zero. This is probably because the streamlines are responding to surface slope effects further downwind. Near the surface at the toe, the streamline angles reach nearly 3 °. In each of the profiles the maximum streamline angle is on the windward slope. From there to the crest the angles decrease, in response to the surface slope convexity. On the flanks, with crest/brink separation, the streamline angles become negative at the brink.

The streamline angle cross-sections (Figure 4.40a, b and c) show how the streamline angles at lower heights (in this case 3.1 mm) strongly reflect the surface slope. On the flanks downwind of the maximum streamline angle, however, a delay between the change in slope and the change in angle can be identified (particularly noticeable on the right flank, Figure 4.40c). This is a result of the change in streamline angle being less responsive to negative than positive surface slope changes, also noted by Gong & Ibbetson (1989). It is also notable that the streamline angles on each section line become positive upwind of the dune. On the centre-line (Figure 4.40) this occurs at x = -300 mm, more than 400 mm upwind of the toe.

A.

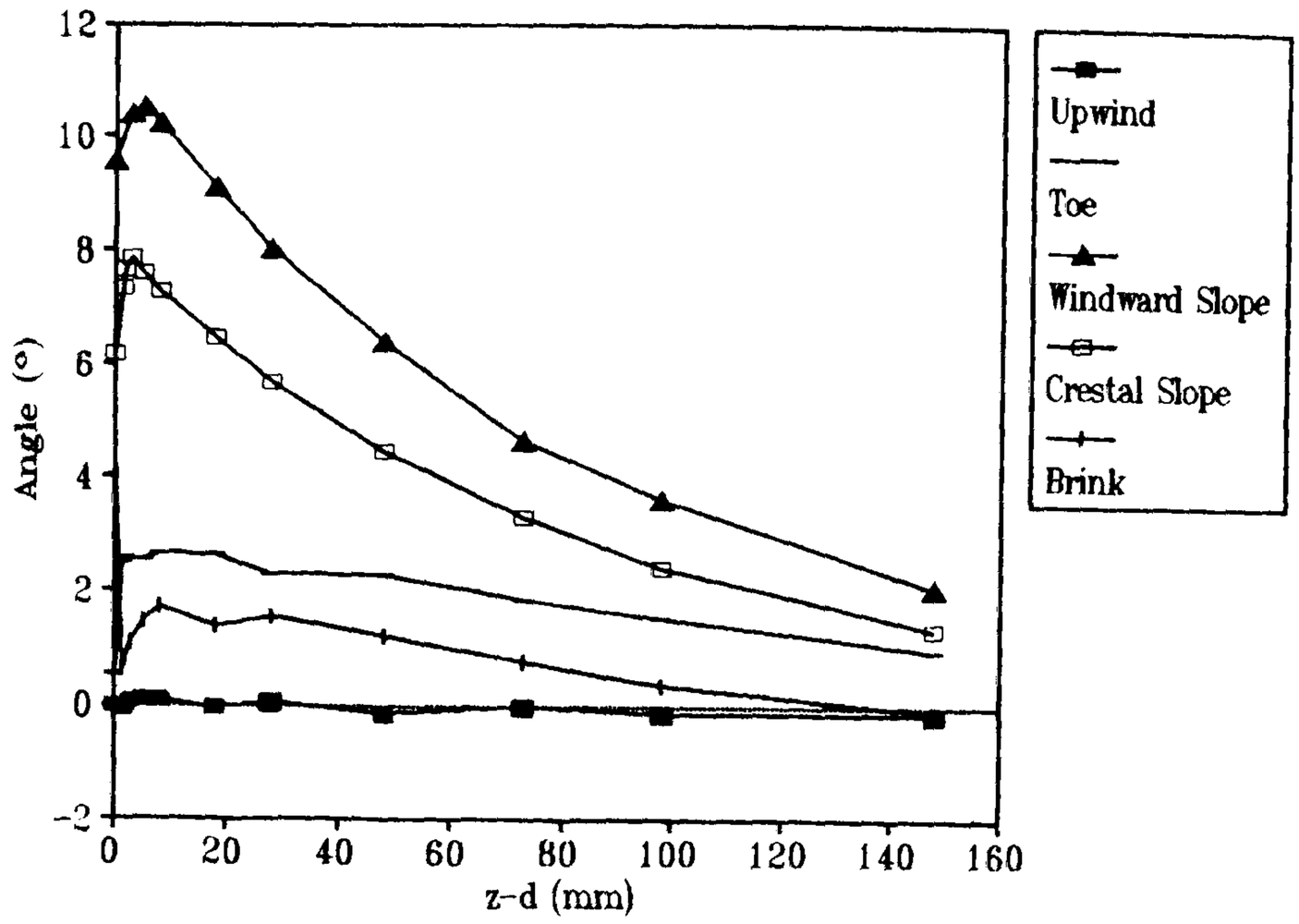

B.

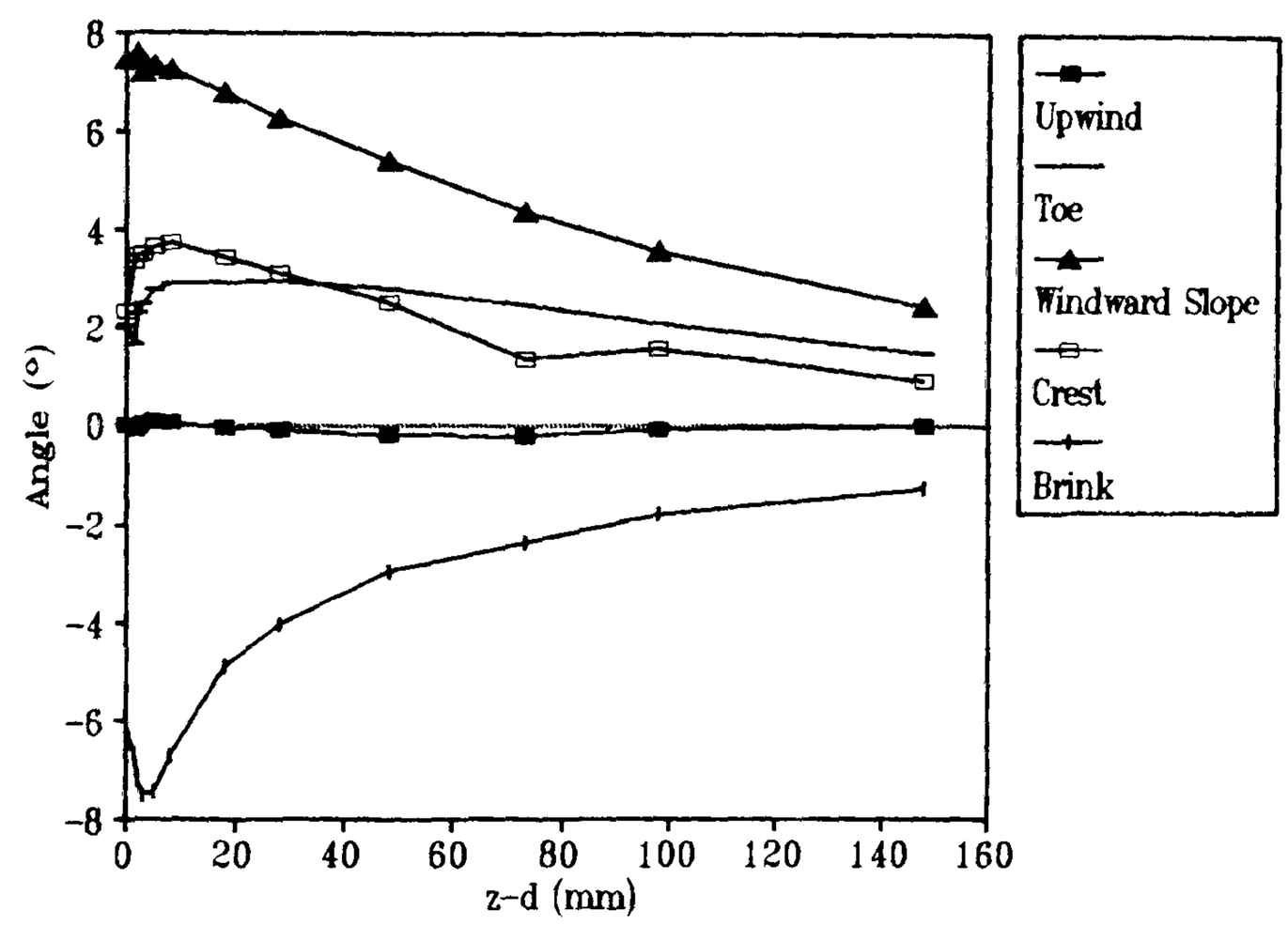

C.

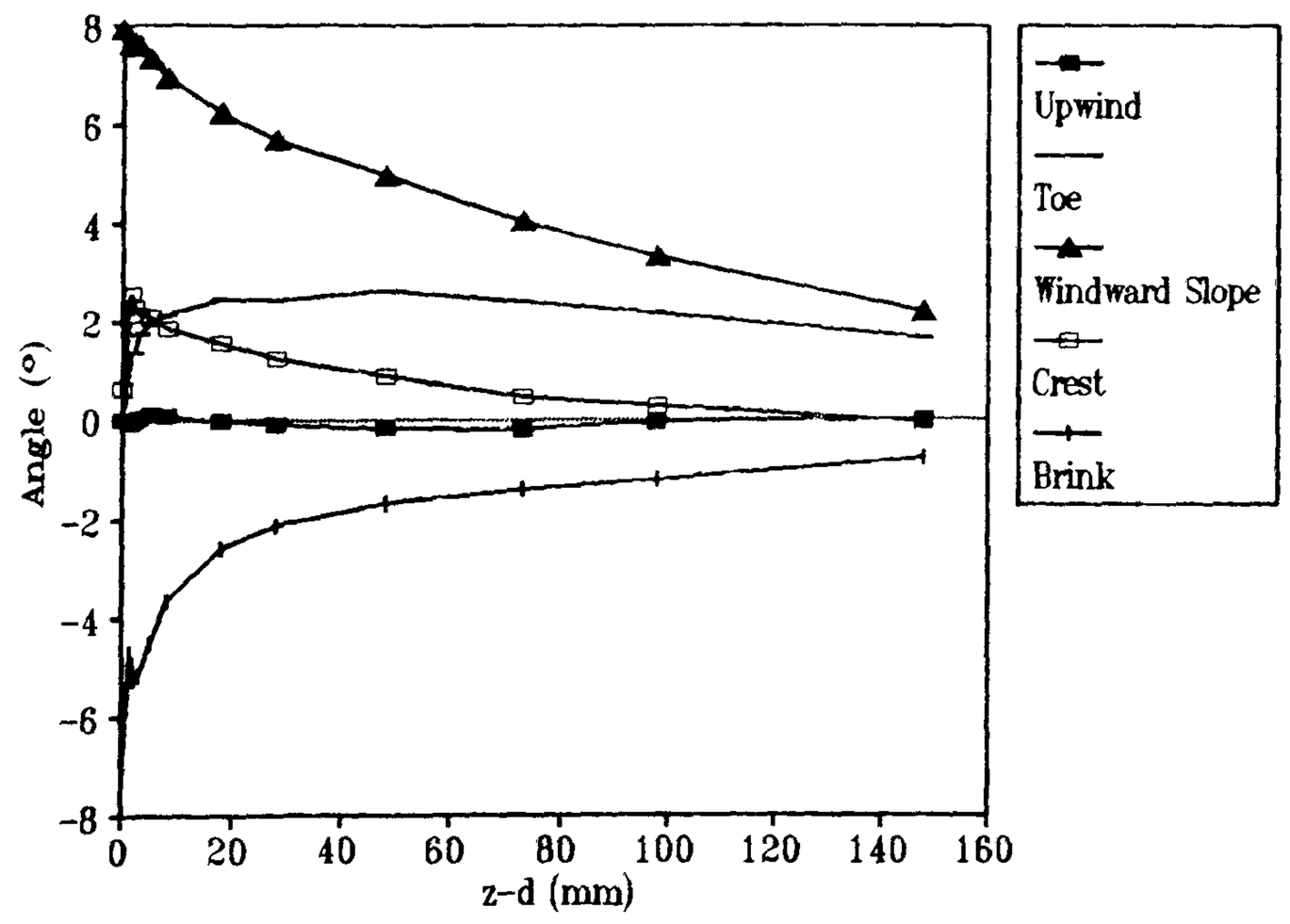

Figure 4.39 Vertical profiles of streamline angle over the dune model. A = centre-line; B = left flank; C = right flank.

A.

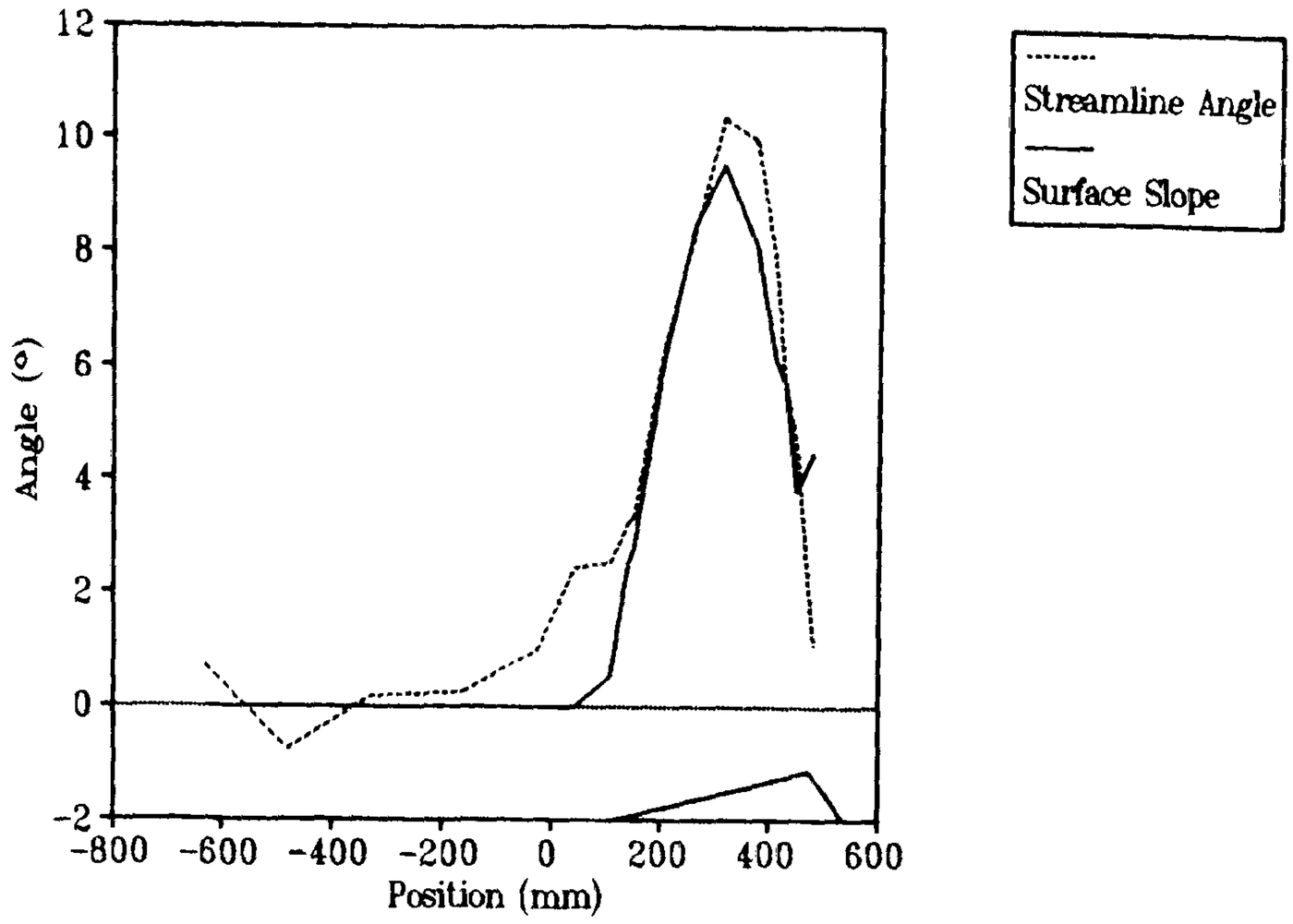

B.

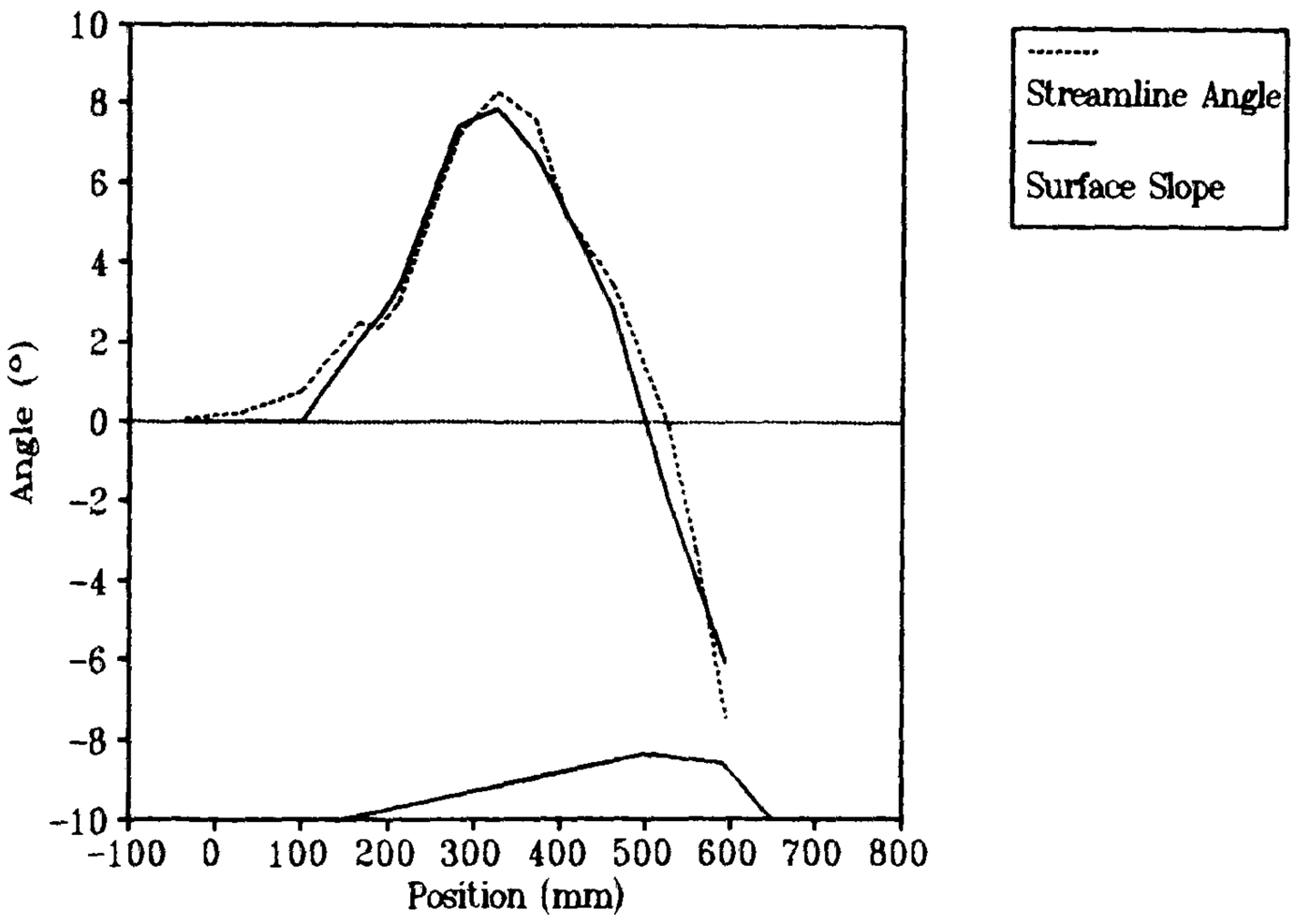

C.

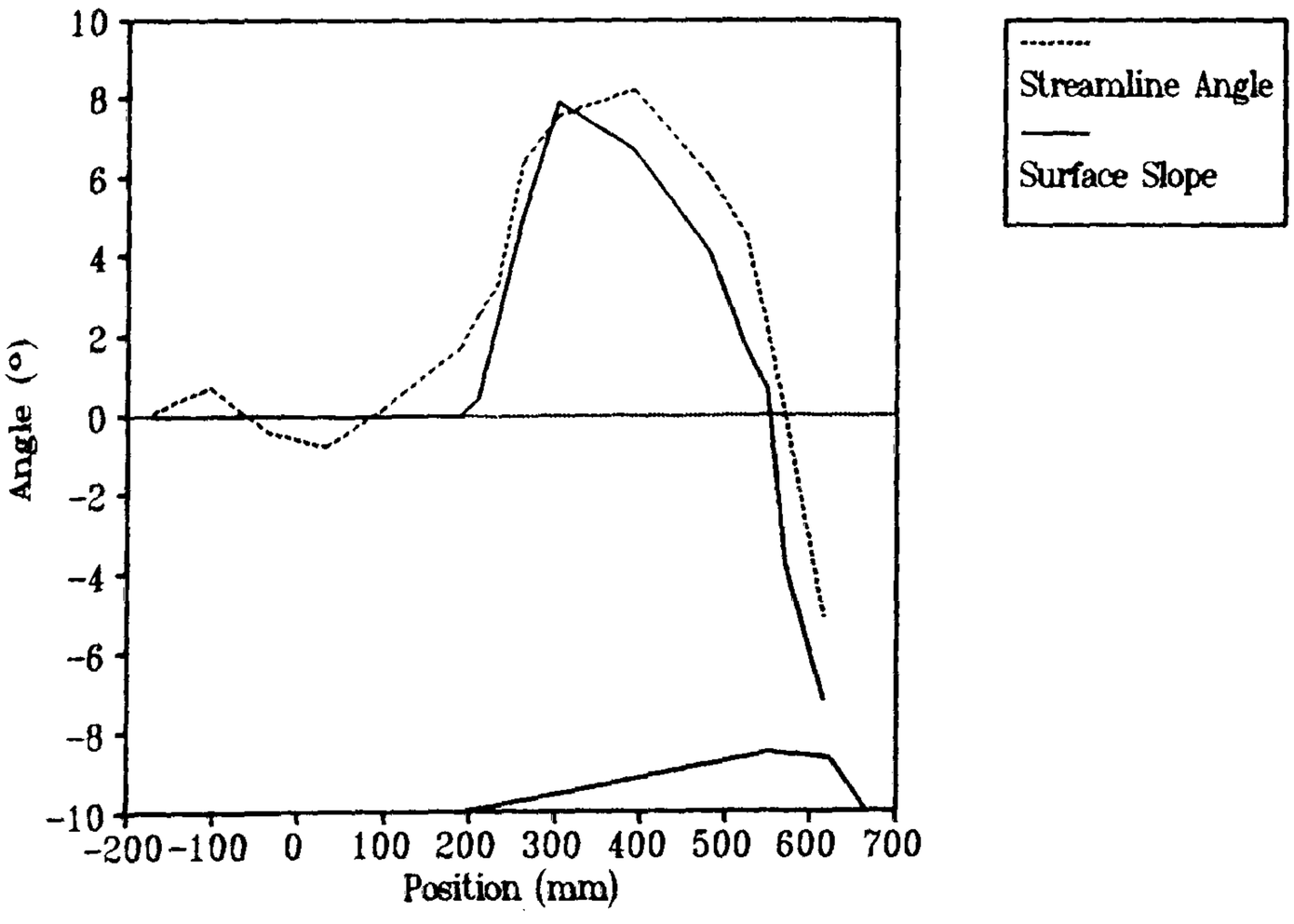

Figure 4.40 Streamline angles measured in the wind tunnel at z-d = 3.1 mm compared to surface slope angles. A = centre-line; B = left flank; C = right flank.

Using the calculated streamline angles, the measured Reynold's stress components were corrected by applying Equations 4.7 to 4.9. The influence that the adjustments have on the shear stress measurements (-uwb) is quite considerable and is demonstrated in Figure 4.41 which shows the difference between adjusted and un-adjusted normalised shear stress (at z-d = 3.1 mm) along the centre-line. It is of particular note that the most dramatic effect of applying the turbulence corrections is apparent at the toe of the dune.

Reynold's Stress Measurements

The Centre-line

The measured and corrected Reynold's stress components closely resemble results from other studies. A plot of usb at four constant heights along the centre-line is shown in Figure 4.42a. The values increase at the toe of the dune, after a small upwind reduction, and then reduce along the windward slope. However, just upwind of the brink, they increase sharply to a peak. Very close to the surface (z-d = 1.6 mm) usb increases up the windward slope. This relationship is typical of the evolution of usb over low hills (Teunissen *et al.*, 1987; Finnigan *et al.*, 1990), except that in these studies the sharp rise to a peak tends to occur later, in the wake region, whilst the minimum is at the brink. The earlier rise in usb in this study, with a peak at the crest, is more typical of measurements in an inner turbulent region close to the surface, recognised by Teunissen *et al.* (1987) and Britter *et al.* (1981). The height of this region is thought to be of the order of the height of the inner-layer. Figure 4.42b demonstrates that far from the surface the evolution of usb is opposite to that measured within the inner-layer. This pattern being comparable with the measurements of Teunissen *et al.* (1987) and Finnigan *et al.* (1990).

The fact that measurements were taken within the turbulent inner-layer may also explain the progression of wsb over the centre-line. Figure 4.43 shows values of wsb at constant heights. The development of wsb along the windward slope is similar to that of usb, but with no increase at the toe. The values rise steadily from about x = 300 mm to peak at the crest. Measurements by Finnigan *et al.* (1990) in the rapid distortion region of the flow (above the inner-layer) show a rise at the toe and a minimum at the crest. The difference between the measurements might be explained by the presence of the turbulent inner-layer in this study.

In their review of boundary layer flow over low hills, Taylor *et al.* (1987) noted that the horizontal evolution of turbulence components had not been verified. The data they examined from previous studies showed that the progression of usb, wsb and uwb appeared to be

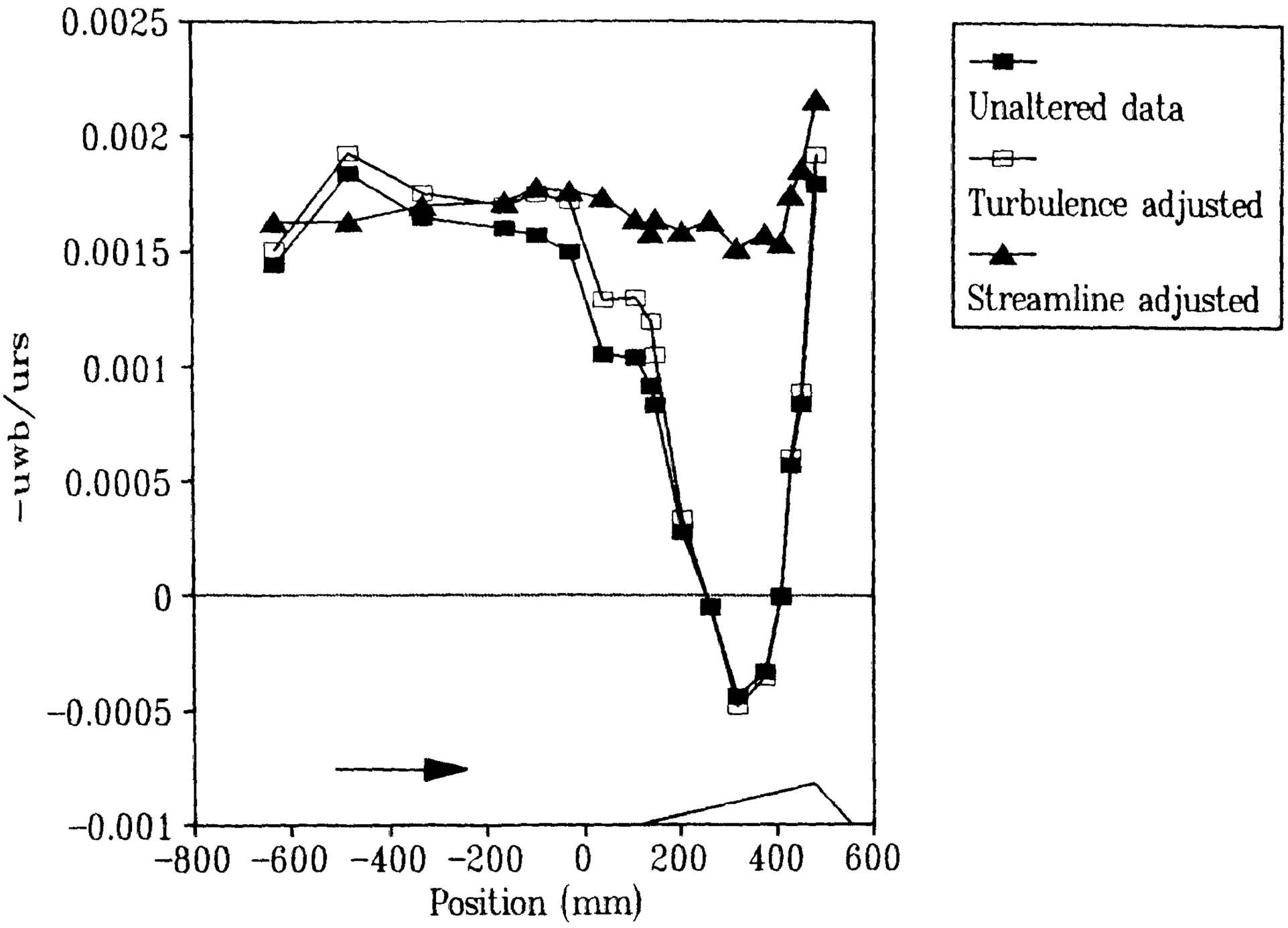

Figure 4.41 The effect of streamline and turbulence corrections on the measurements of Reynold's stress. Streamline adjusted includes the turbulence adjustment.

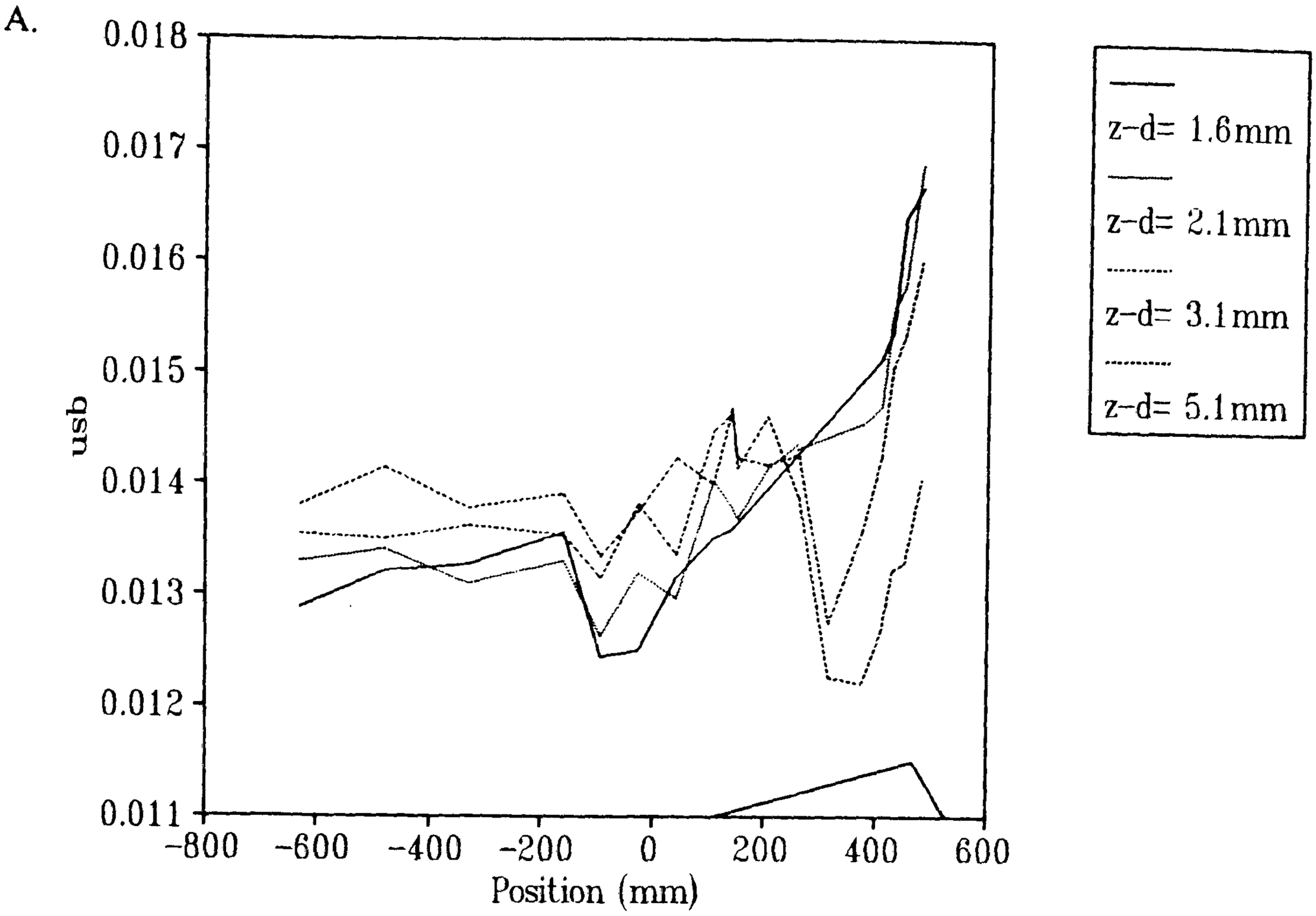

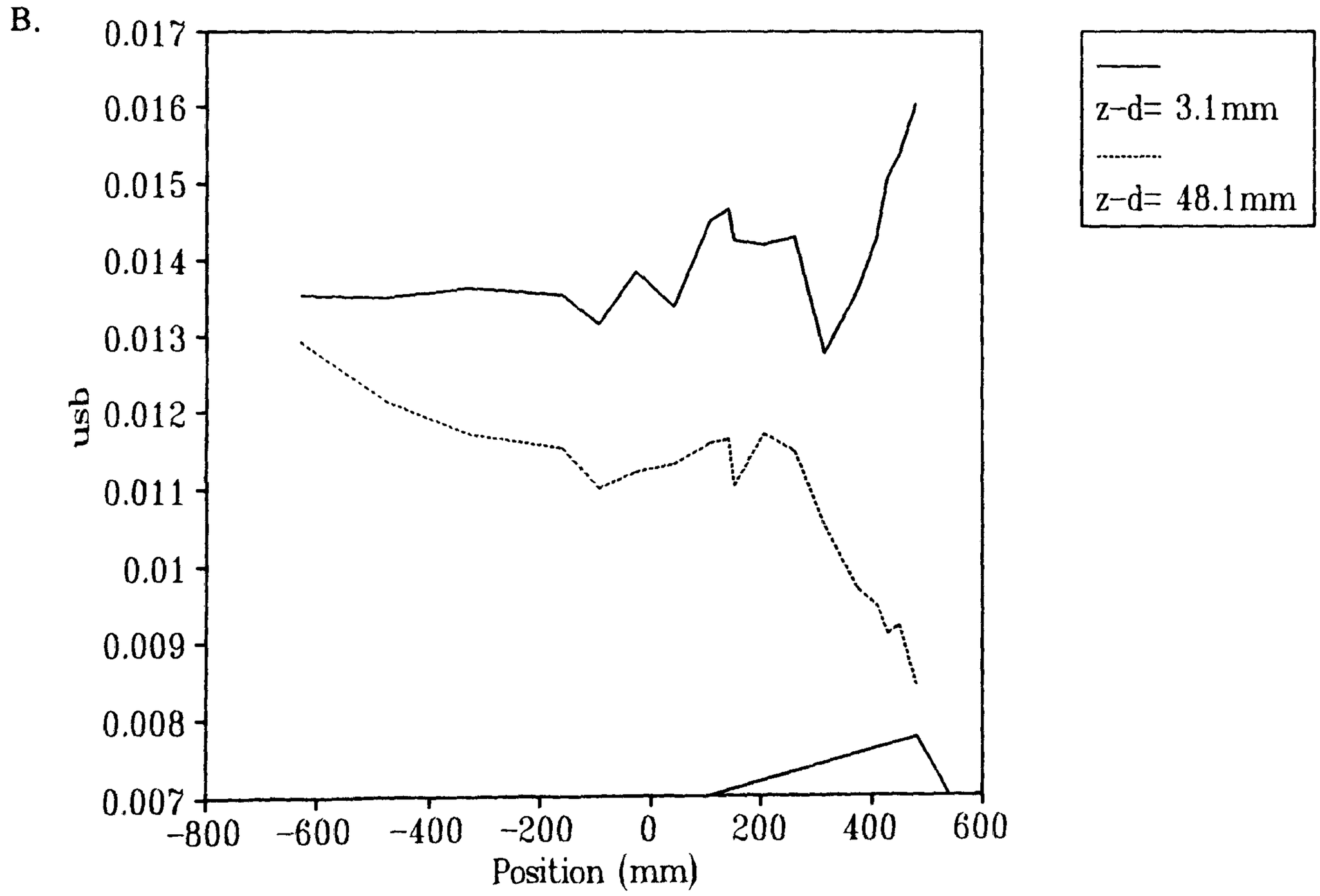

Figure 4.42 Measurements of usb on the centre-line of the model dune. A = near-surface heights; B = comparison between near-surface and distant heights.

dependant upon the scale of the study, three dimensionality and several non-dimensional parameters (such as H/L and L/z_0). These ideas have yet to be confirmed but, in conjunction with the probable existence of the turbulent inner-layer in this study, they help to explain the differences in the turbulent components between these results and others like them (*e.g.* Finnigan *et al.*, 1990).

The uwb component of Reynold's stress is plotted as -uwb (*i.e.* τ, as $\tau = -\rho uwb$) in Figure 4.44. Finnigan *et al.* (1990) described the progression of -uwb over a low hill with an increasing stress from the toe to half way up the windward slope, and a minimum at the crest. This relationship held at all heights above the surface down to their closest measurement height at ≈ 10 mm. The present data conform to this relationship at the 5.1 mm level (Figure 4.44). However, at lower heights (within the turbulent inner-layer) the relationship appears to become inverse with a slight dip in -uwb at the toe and a sharp rise to a maximum at the crest.

The surface shear velocity (u_*) was derived from the -uwb (shear stress) profiles by extrapolating them to the surface (as described in Chapter 4.2.2) The profiles showing the extrapolation and calculation of u_* along the centre-line are shown in Figure 4.45a-r. The extrapolation to the surface in each case results in a minimum and a maximum surface shear velocity, with two lines being continued to the surface. One line continuing the apparent trend and the other assuming a vertical reduction to the surface from the last measured point.

Profiles a, b and c in Figure 4.45 show an almost constant shear stress in a region close to the surface. Profiles d to m indicate a retardation in shear stress near the surface, succeeded in profiles n to r by a strongly positive shear stress gradient between the surface and 6 mm height.

The shape of the shear stress profiles shown in Figure 4.45, with a switch from a negative to a positive gradient, can be explained with reference to the changing pressure gradient over the dune. Using the axial momentum equation, it can be shown that at the surface u = w = 0, and that ignoring the viscous terms and additional stress terms;

$$\delta uwb/\delta z = -1/e.\delta p/\delta y \qquad \textbf{(4.10)}$$

where:

$\delta uwb/\delta z$ = change of uwb with height
$\delta p/\delta x$ = horizontal pressure gradient.

Hence, if pressure is increasing with height, then;

$$\delta uwb/\delta z < 0 \quad \text{or} \quad \delta\text{-}uwb/\delta z > 0$$

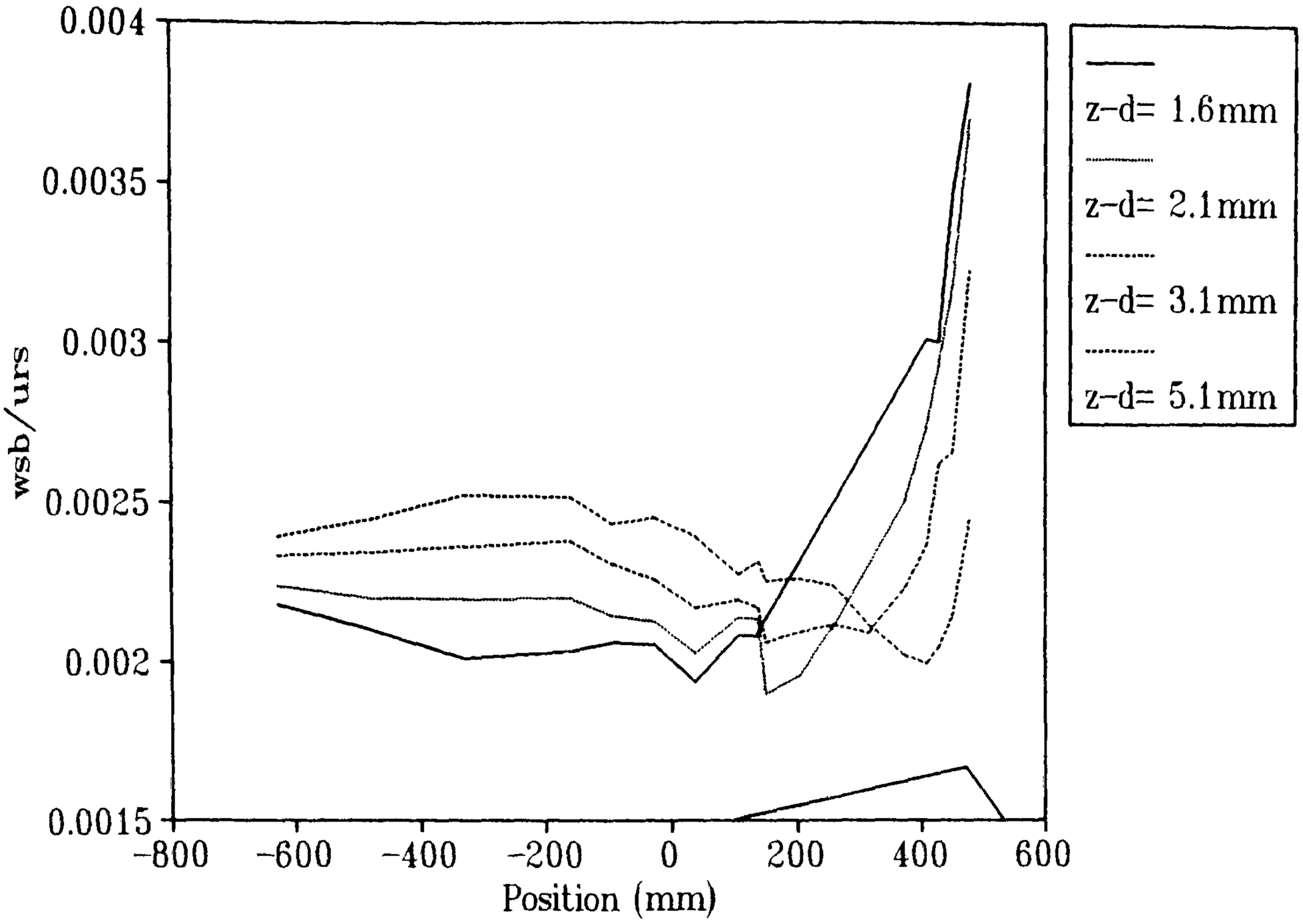

Figure 4.43 Measurements of wsb on the centre-line of the model dune.

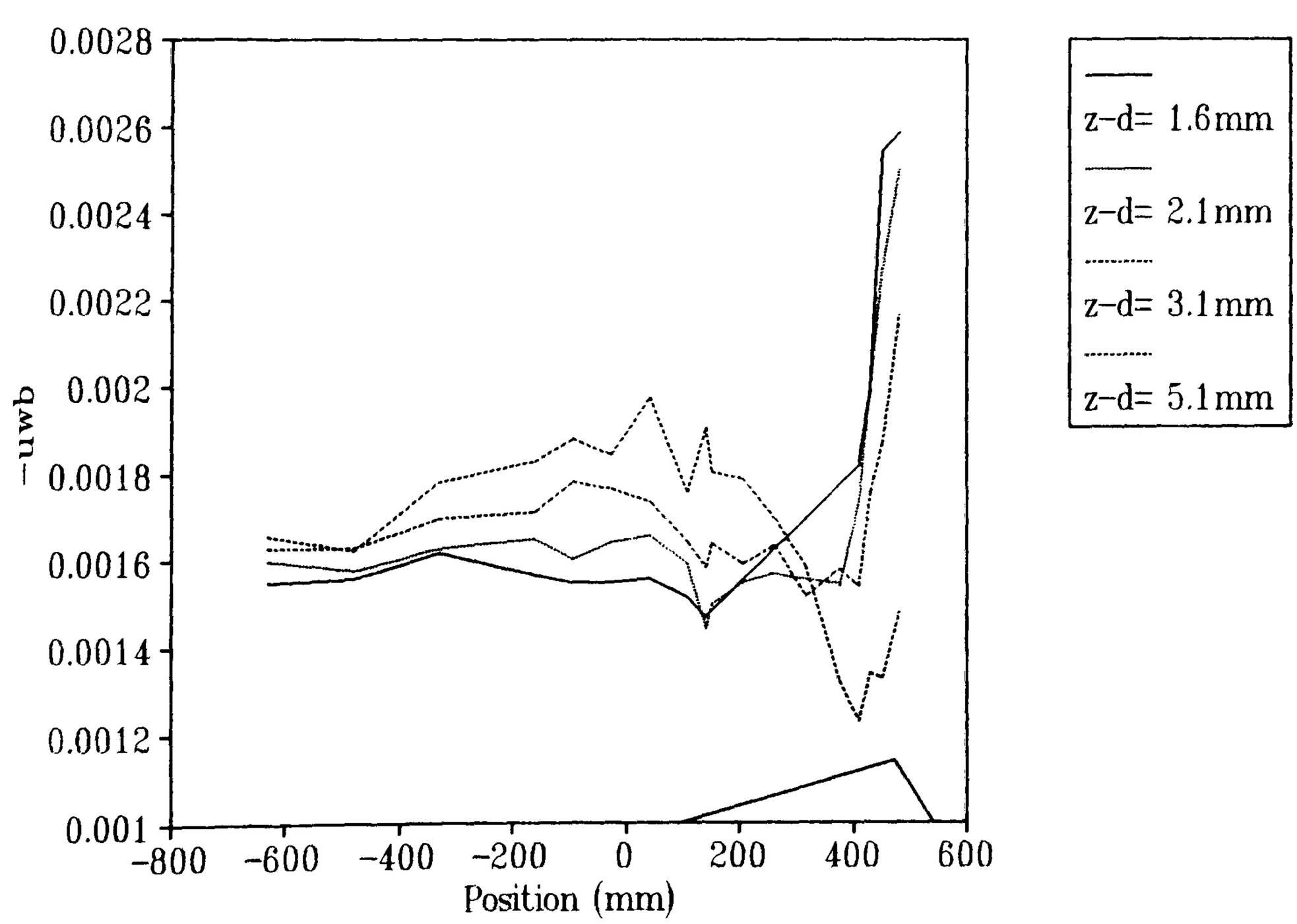

Figure 4.44 Measurements of -uwb on the centre-line of the model dune.

A.

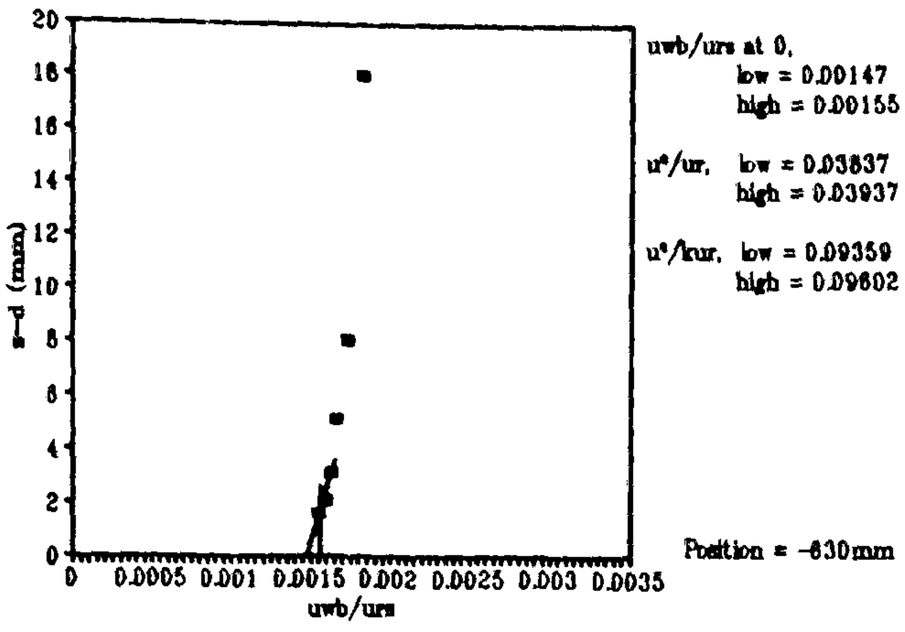

B.

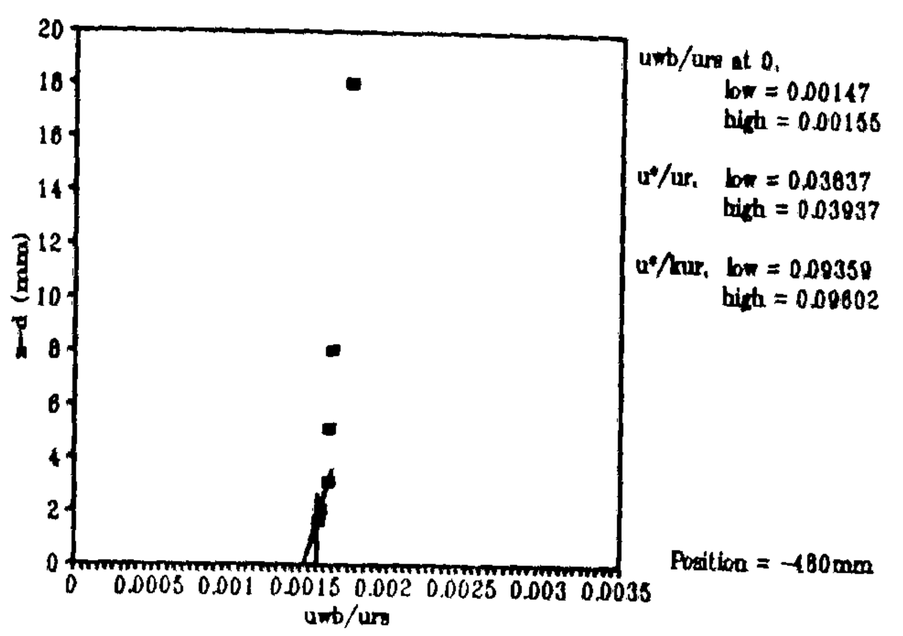

C.

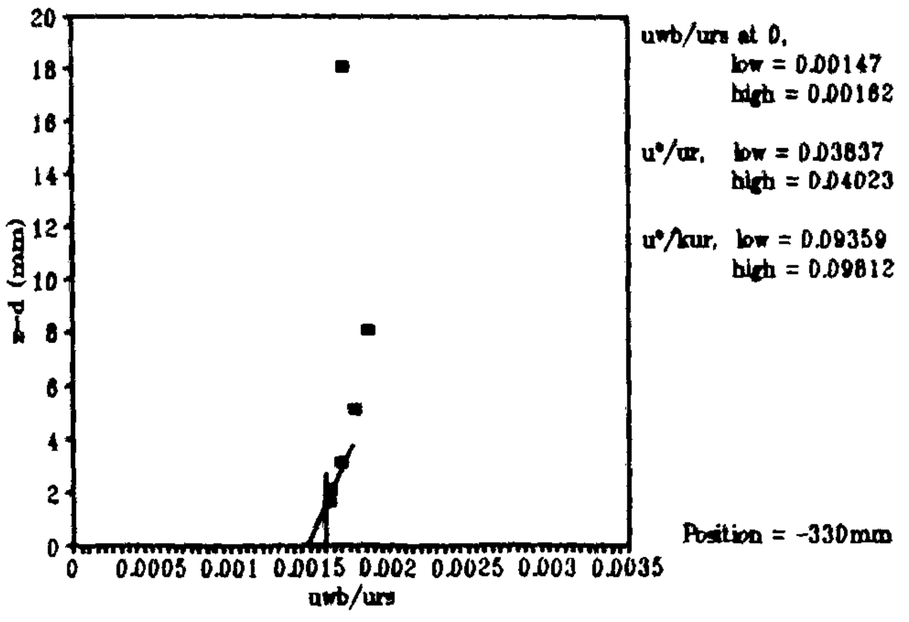

D.

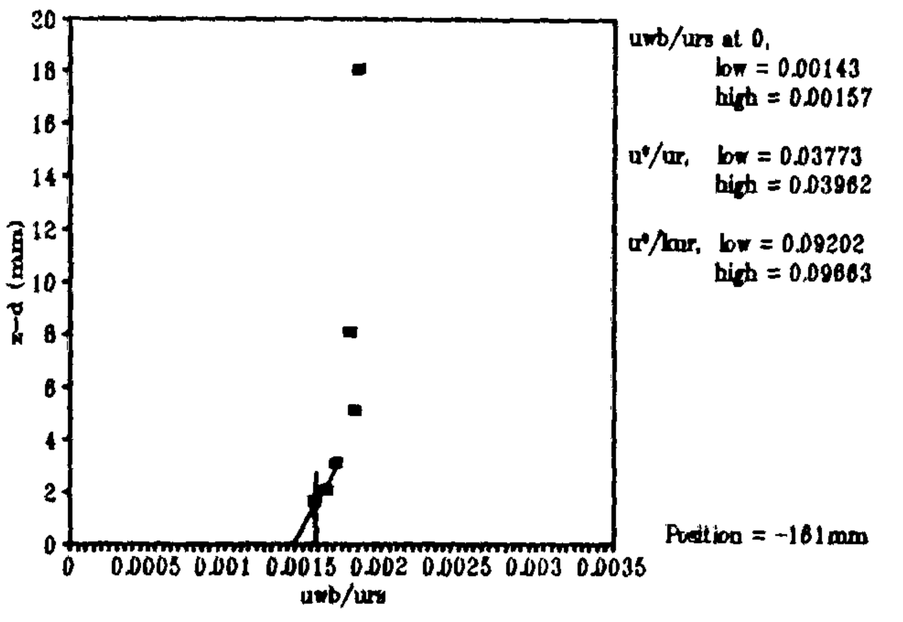

E.

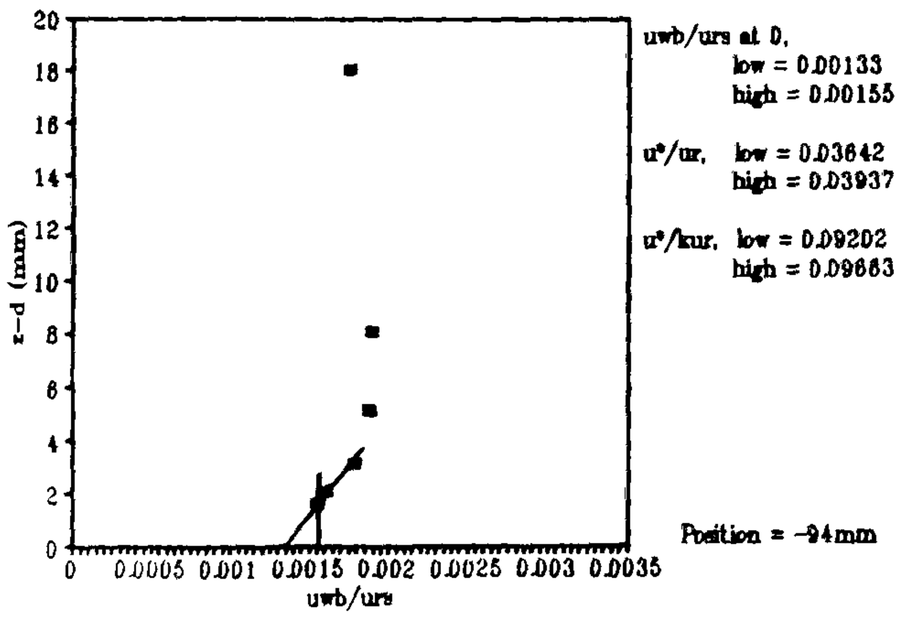

F.

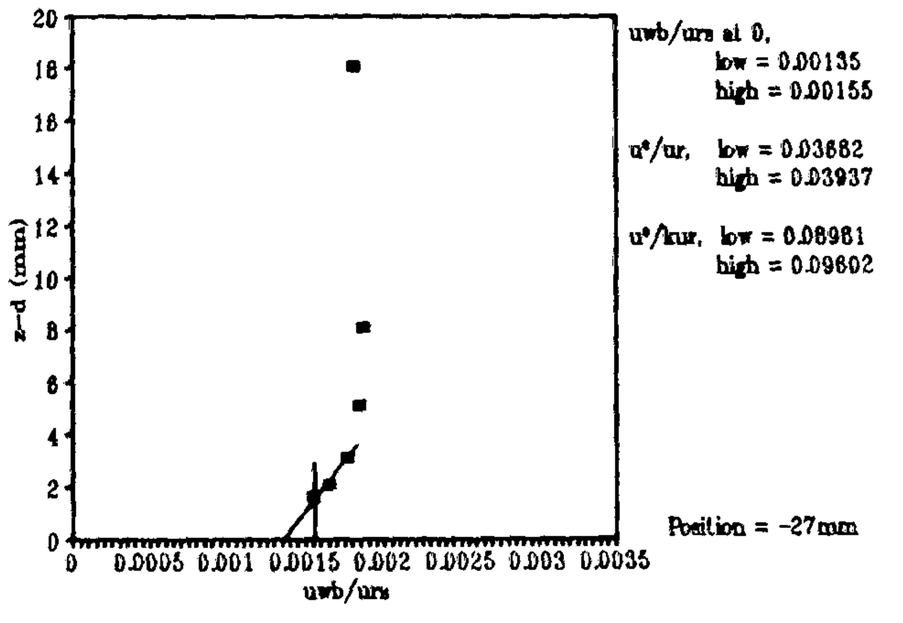

G.

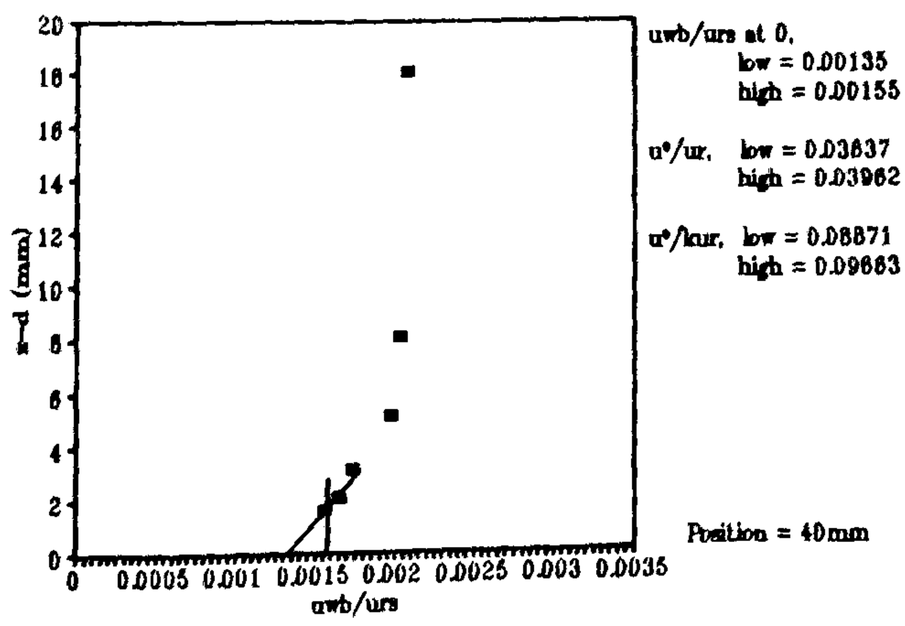

H.

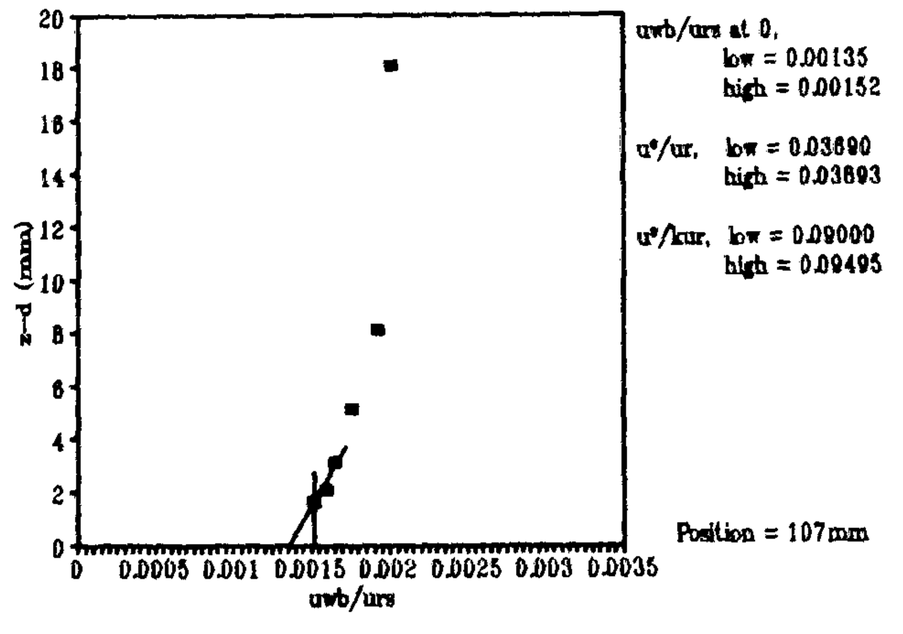

Figure 4.45 Extrapolating shear stress to the surface to calculate surface shear velocity on the centre-line of the model dune. A = upwind; R = crest.

I.

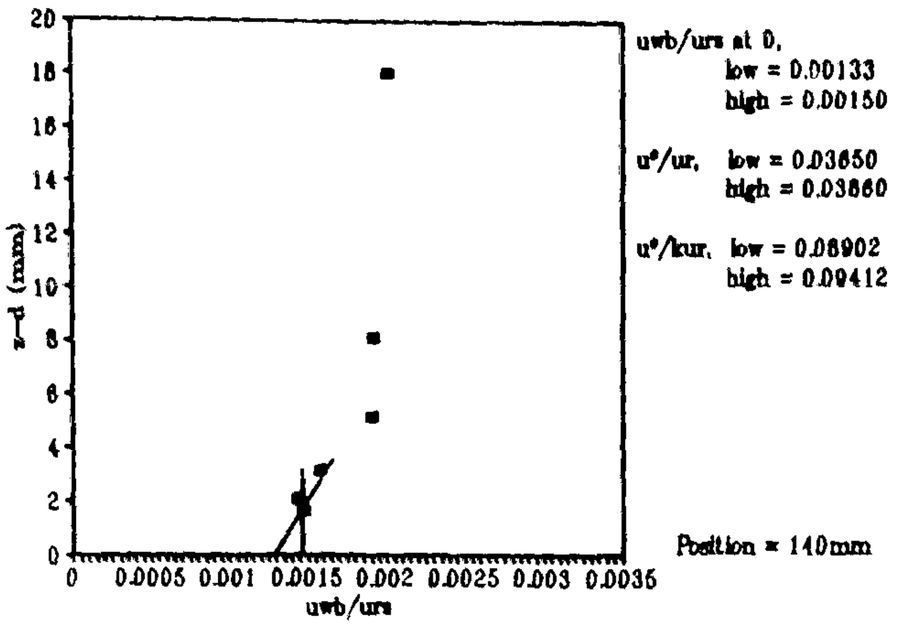
z-d (mm)
uwb/urs
0 0.0005 0.001 0.0015 0.002 0.0025 0.003 0.0035
0 2 4 6 8 10 12 14 16 18 20
uwb/urs at 0,
low = 0.00133
high = 0.00150
u*/ur, low = 0.03650
high = 0.03860
u*/kur, low = 0.08902
high = 0.09412
Position = 140mm

J.

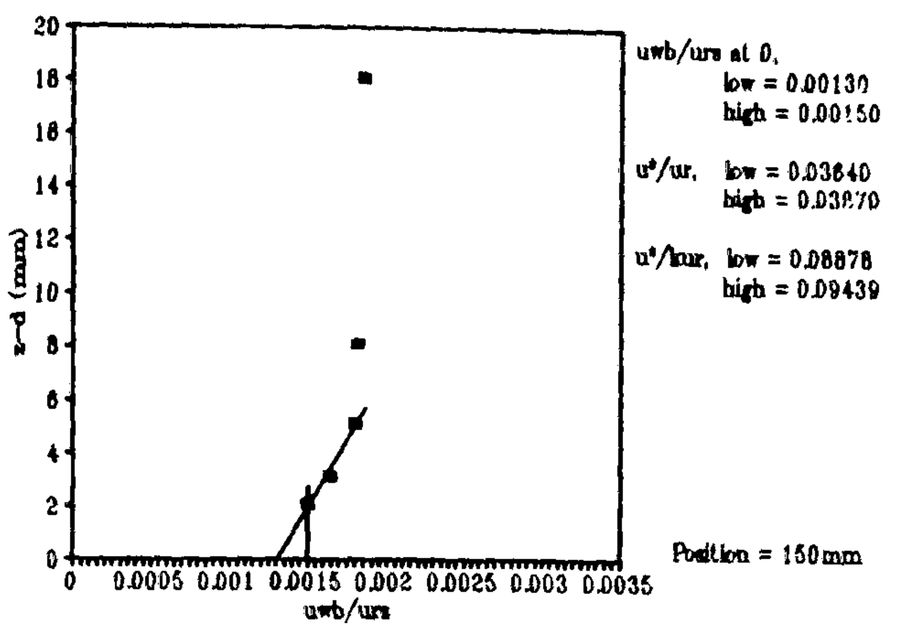
z-d (mm)
uwb/urs
0 0.0005 0.001 0.0015 0.002 0.0025 0.003 0.0035
0 2 4 6 8 10 12 14 16 18 20
uwb/urs at 0,
low = 0.00130
high = 0.00150
u*/ur, low = 0.03640
high = 0.03870
u*/kur, low = 0.08878
high = 0.09439
Position = 150mm

K.

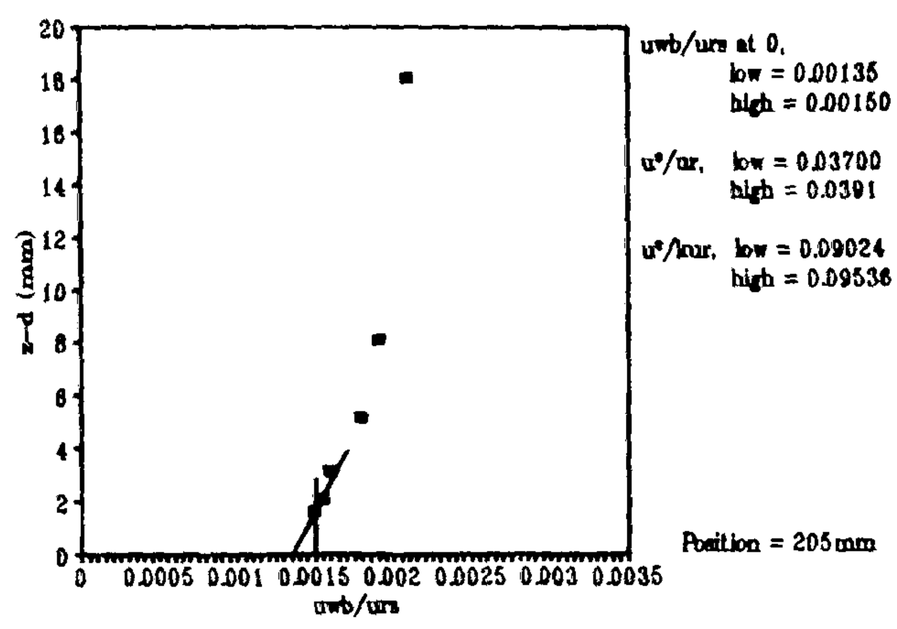
z-d (mm)
uwb/urs
0 0.0005 0.001 0.0015 0.002 0.0025 0.003 0.0035
0 2 4 6 8 10 12 14 16 18 20
uwb/urs at 0,
low = 0.00135
high = 0.00150
u*/ur, low = 0.03700
high = 0.0391
u*/kur, low = 0.09024
high = 0.09536
Position = 205mm

L.

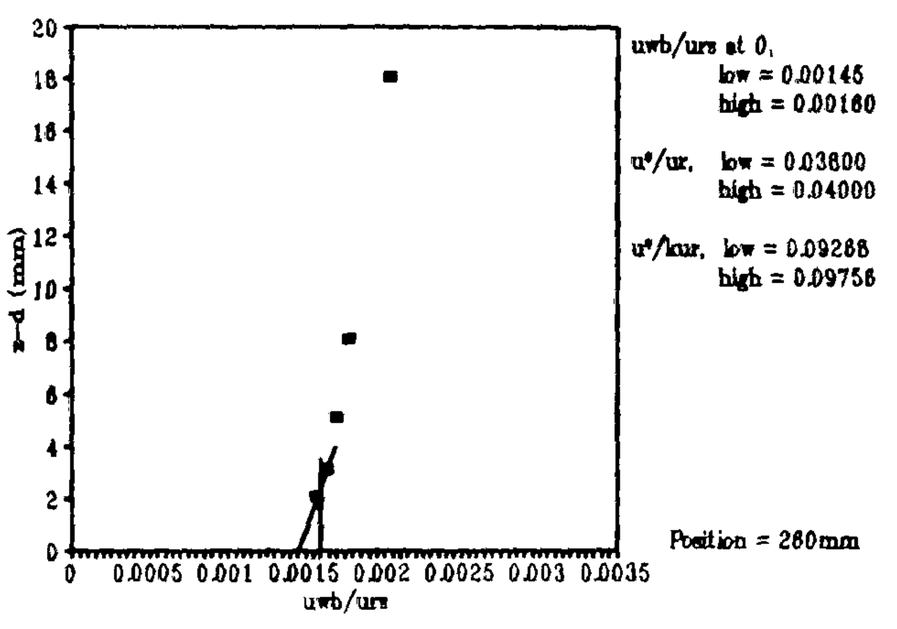
z-d (mm)
uwb/urs
0 0.0005 0.001 0.0015 0.002 0.0025 0.003 0.0035
0 2 4 6 8 10 12 14 16 18 20
uwb/urs at 0,
low = 0.00145
high = 0.00160
u*/ur, low = 0.03600
high = 0.04000
u*/kur, low = 0.09288
high = 0.09756
Position = 260mm

M.

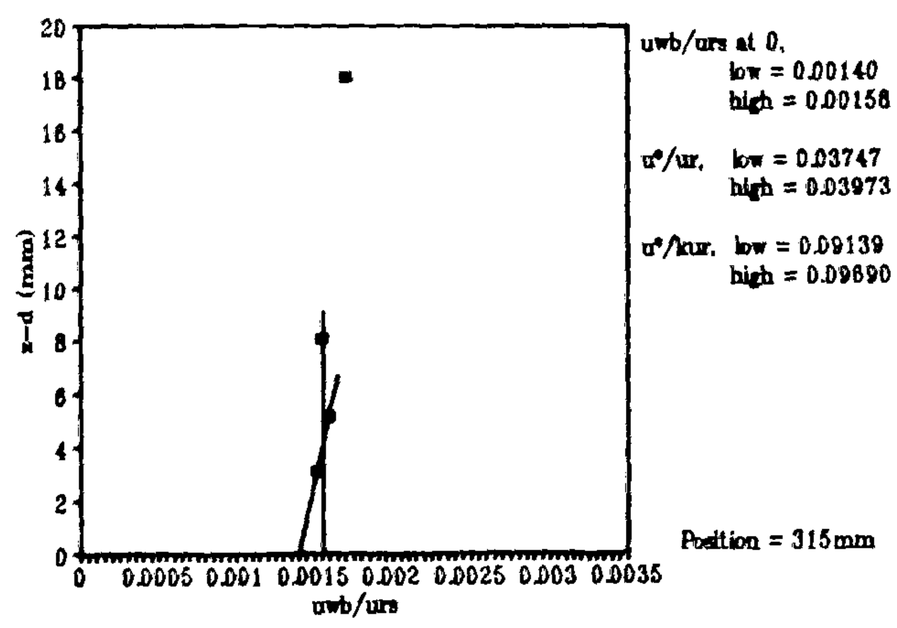
z-d (mm)
uwb/urs
0 0.0005 0.001 0.0015 0.002 0.0025 0.003 0.0035
0 2 4 6 8 10 12 14 16 18 20
uwb/urs at 0,
low = 0.00140
high = 0.00158
u*/ur, low = 0.03747
high = 0.03973
u*/kur, low = 0.09139
high = 0.09690
Position = 315mm

N.

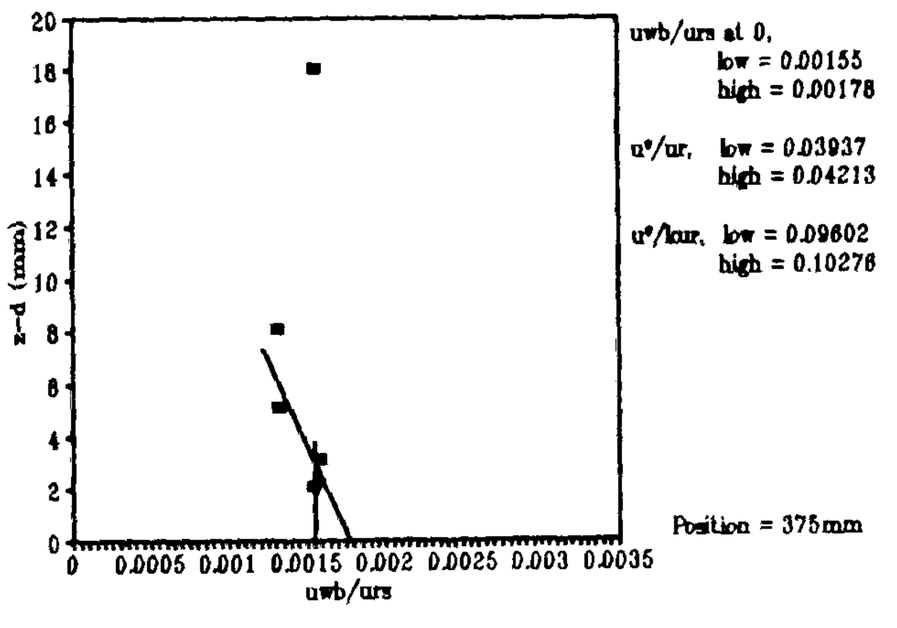
z-d (mm)
uwb/urs
0 0.0005 0.001 0.0015 0.002 0.0025 0.003 0.0035
0 2 4 6 8 10 12 14 16 18 20
uwb/urs at 0,
low = 0.00155
high = 0.00178
u*/ur, low = 0.03937
high = 0.04213
u*/kur, low = 0.09602
high = 0.10276
Position = 375mm

O.

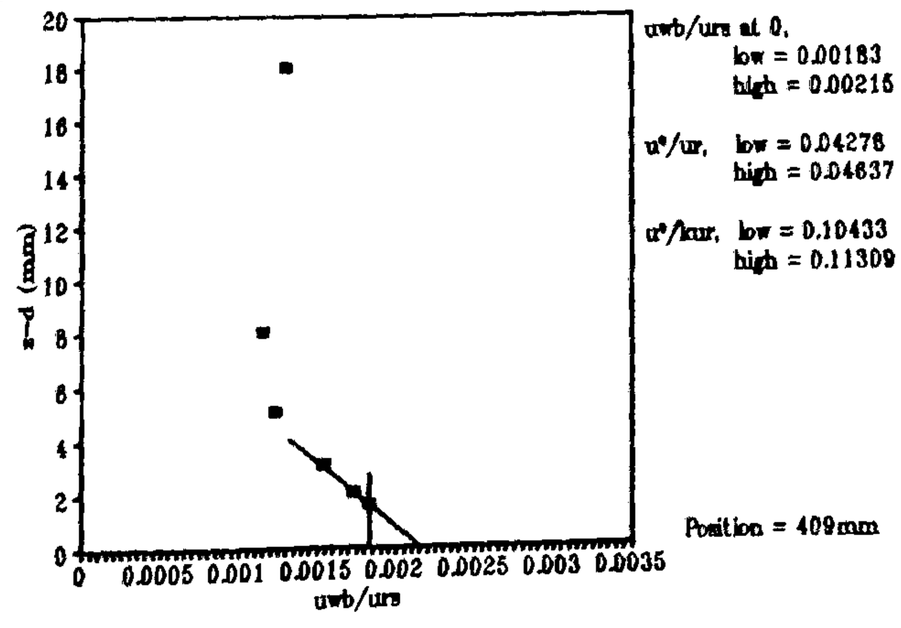
z-d (mm)
uwb/urs
0 0.0005 0.001 0.0015 0.002 0.0025 0.003 0.0035
0 2 4 6 8 10 12 14 16 18 20
uwb/urs at 0,
low = 0.00183
high = 0.00215
u*/ur, low = 0.04276
high = 0.04637
u*/kur, low = 0.10433
high = 0.11309
Position = 409mm

P.

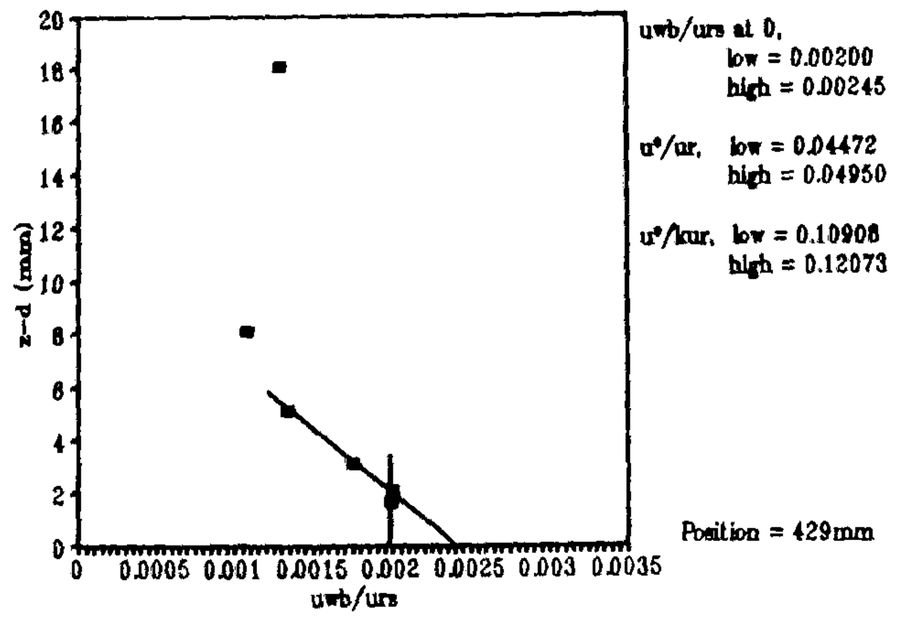
z-d (mm)
uwb/urs
0 0.0005 0.001 0.0015 0.002 0.0025 0.003 0.0035
0 2 4 6 8 10 12 14 16 18 20
uwb/urs at 0,
low = 0.00200
high = 0.00245
u*/ur, low = 0.04472
high = 0.04950
u*/kur, low = 0.10908
high = 0.12073
Position = 429mm

Q.

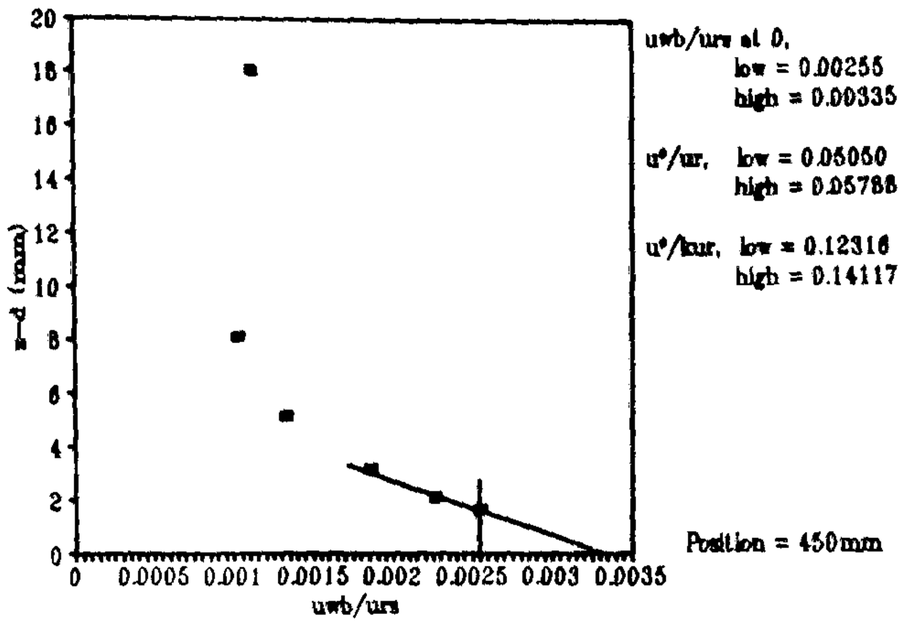
uwb/urs at 0,
low = 0.00255
high = 0.00335
u*/ur, low = 0.05050
high = 0.05788
u*/kur, low = 0.12316
high = 0.14117
Position = 450mm
s-d (mm)
uwb/urs
0 0.0005 0.001 0.0015 0.002 0.0025 0.003 0.0035
0 2 4 6 8 10 12 14 16 18 20

R.

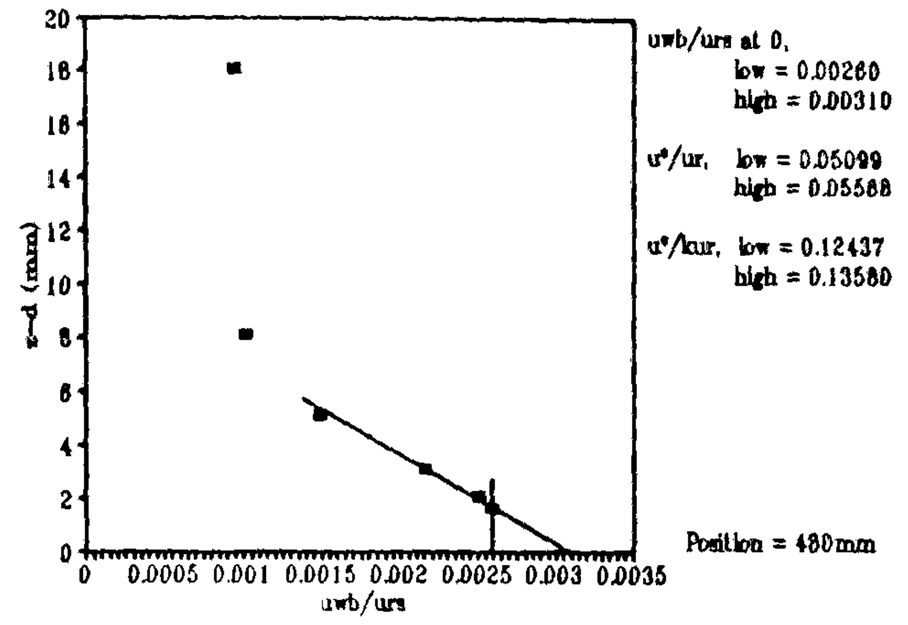
uwb/urs at 0,
low = 0.00260
high = 0.00310
u*/ur, low = 0.05099
high = 0.05588
u*/kur, low = 0.12437
high = 0.13580
Position = 480mm
s-d (mm)
uwb/urs
0 0.0005 0.001 0.0015 0.002 0.0025 0.003 0.0035
0 2 4 6 8 10 12 14 16 18 20

Therefore, shear stress increases with height near the surface. The negative gradient profiles in Figure 4.45d-m therefore correspond to an adverse pressure gradient, while profiles n-r correspond to a decreasing pressure gradient.

The inflection point from negative to positive gradient occurs at x = 315 mm. This matches the point on the dune surface where the concave profile is succeeded by a convex one (Figure 4.40a). Figure 4.45 also indicates that the decreasing pressure gradient has far greater influence on the shear stress profiles than the adverse pressure gradient.

Figure 4.46 shows the surface shear velocities derived from the -uwb profiles plotted as a function of x (downwind distance). The commonly observed reduction in shear velocity at the toe (Chapter 1) is not so evident in this case. However, the zone of shear velocity (offered by the minimum and maximum estimates) does allow for a reduction in shear velocity at the toe of about 7%. The surface shear velocity becomes greater than its upwind value at about x = 260 mm (approximately corresponding with $h/H \approx 0.3$), it then proceeds to rise to a maximum peak value of 0.0575 (u/u_*) in the region of the crest. This corresponds to an increase from the upwind value of about 47%.

The gradients of the velocity profiles suggested by the surface shear values were calculated using Equation 4.5. The results of these calculations are shown as $u_*/\kappa u_r$ on the respective profiles in Figure 4.45. Figures 4.47a-h show the calculated velocity profile gradients ($u_*/\kappa u_r$) plotted with the logarithmic velocity profiles measured by the single-wire probe. A comparison of the calculated (from the shear stress extrapolations and Equation 4.5) and actual velocity gradients (as measured by the single-wire) reveals a close association. The upwind profiles (a and b, Figure 4.45) show that the velocity profile is little changed from its logarithmic relationship. The whole profile fits the shear velocity gradient. At the toe (profile c), the reduction in velocity at lower heights causes a bend in the profile. This results in only the lowest six velocity measurements (< 10 mm high) fitting the shear stress gradient. This is not surprising considering that the shear gradient is derived from only the lowest few cross-wire measurements. Profile d is similar to that of profile c, but profile e (at x = 260 mm) indicates a return to a logarithmic relationship as the velocity at lower heights becomes subject to a positive speed-up. Profiles f, g and h show progressively severe bending as flow acceleration becomes more intense. The shear velocity gradients in these profiles only fit the lowest two or three velocity measurements, as would be expected.

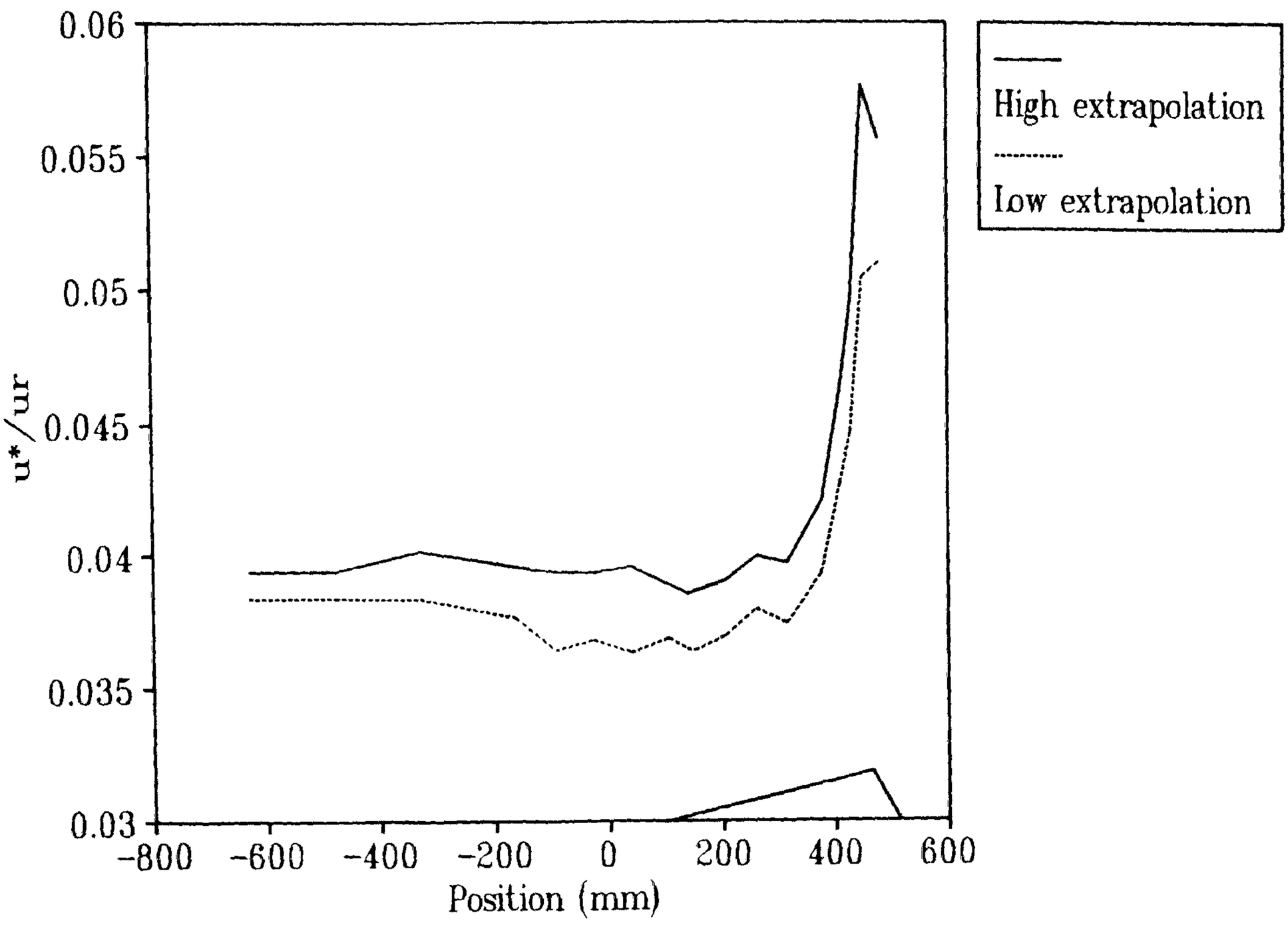

Figure 4.46 Low and high extrapolations of surface shear velocity on the centre-line of the model dune.

A.

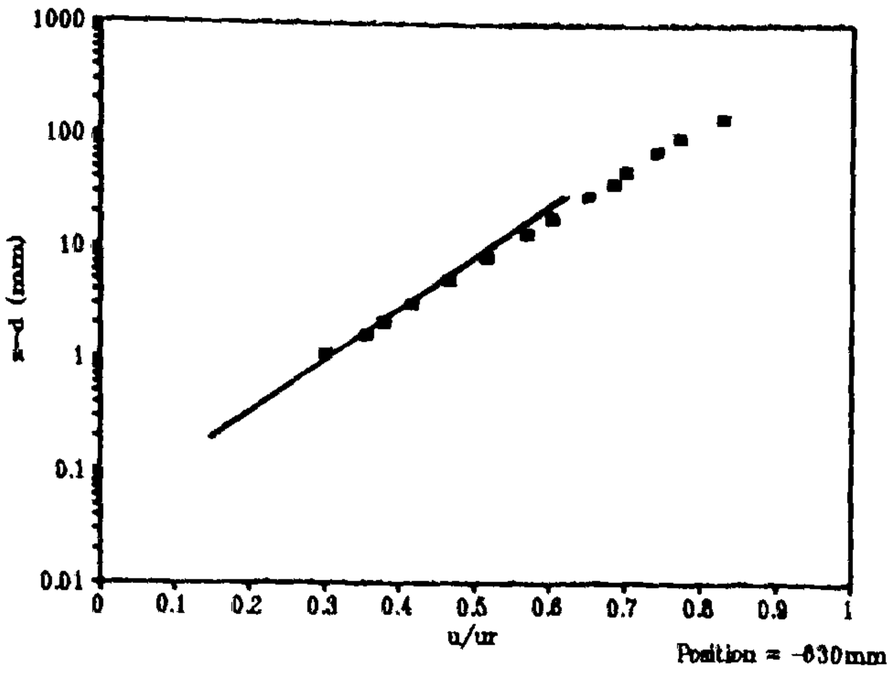

B.

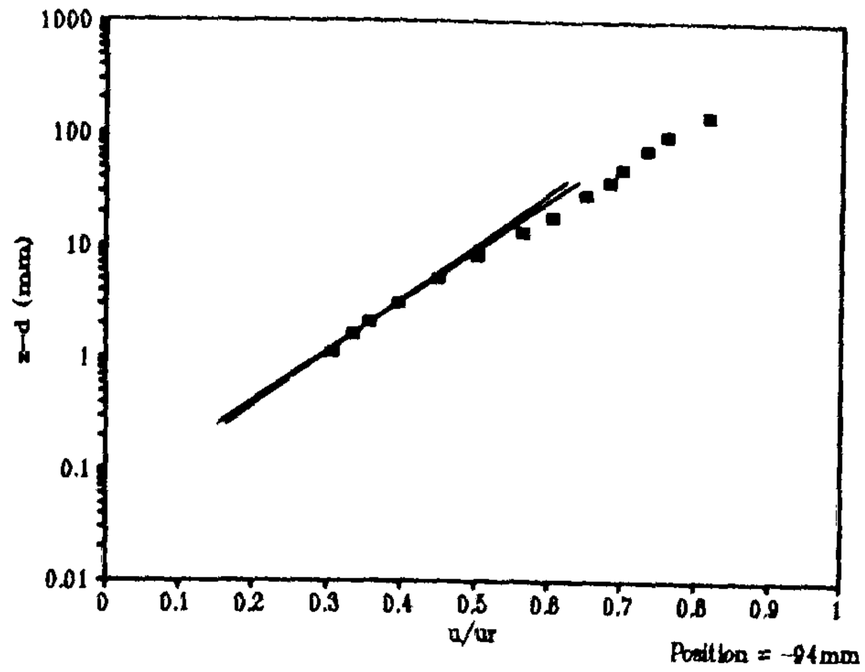

C.

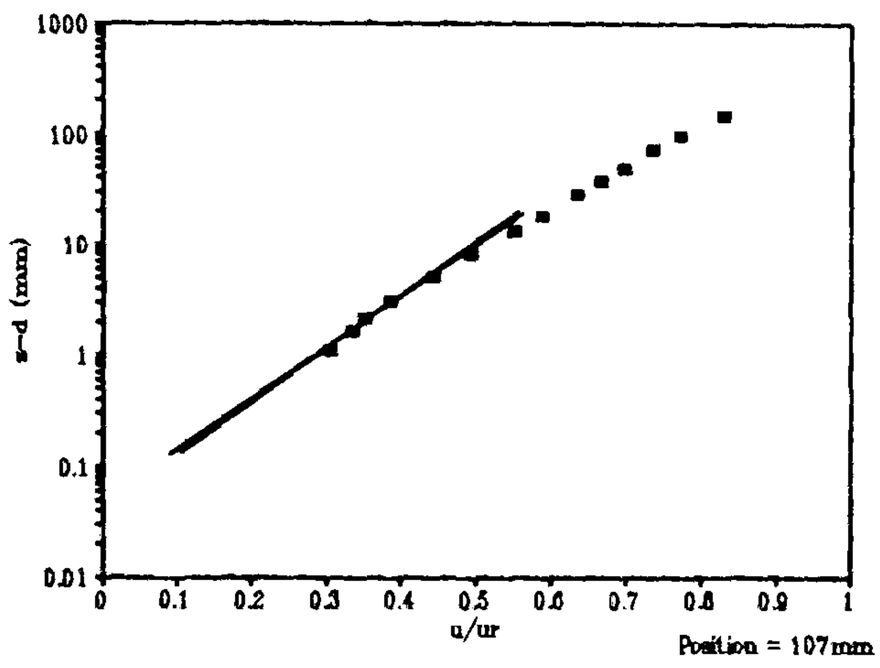

D.

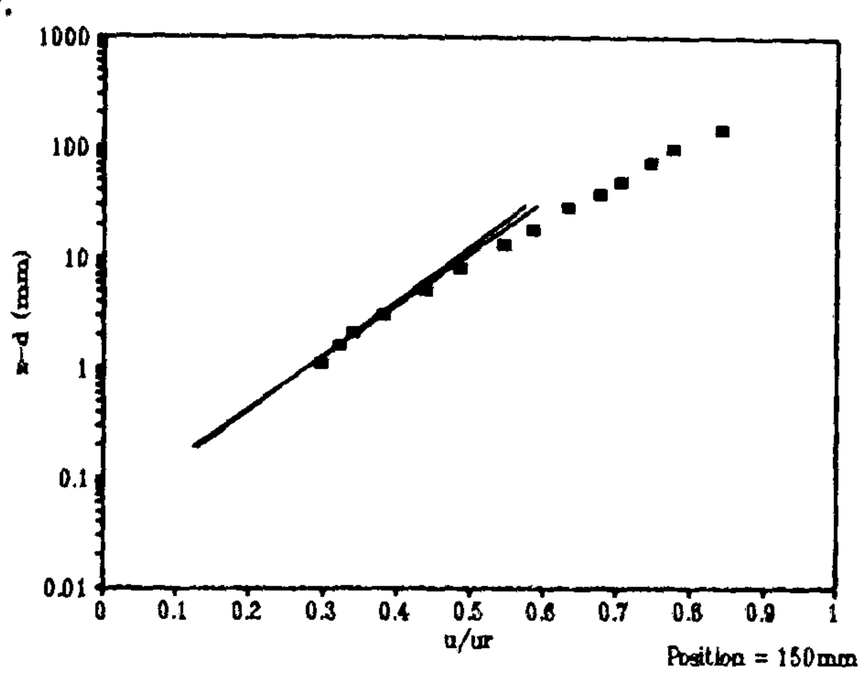

E.

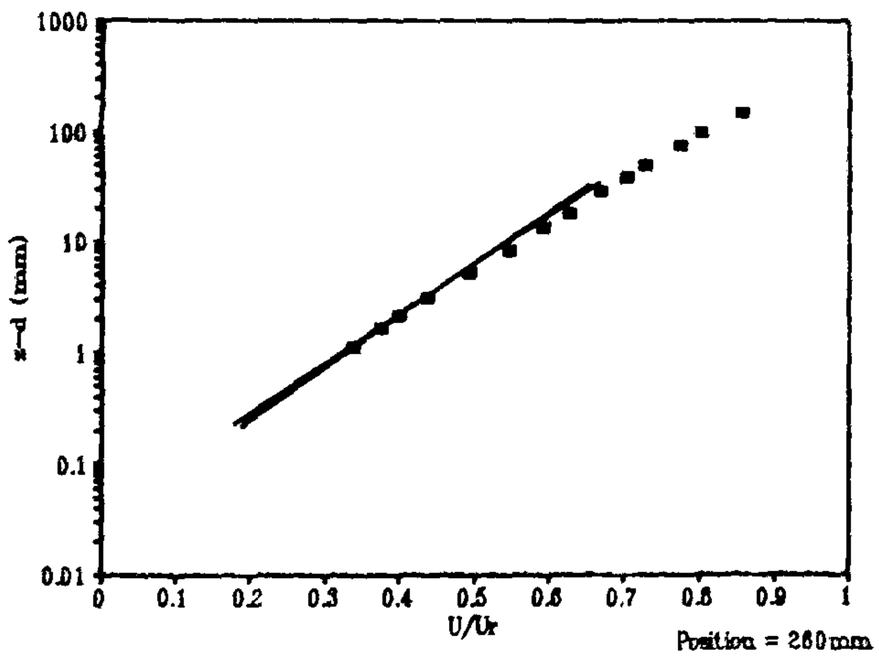

F.

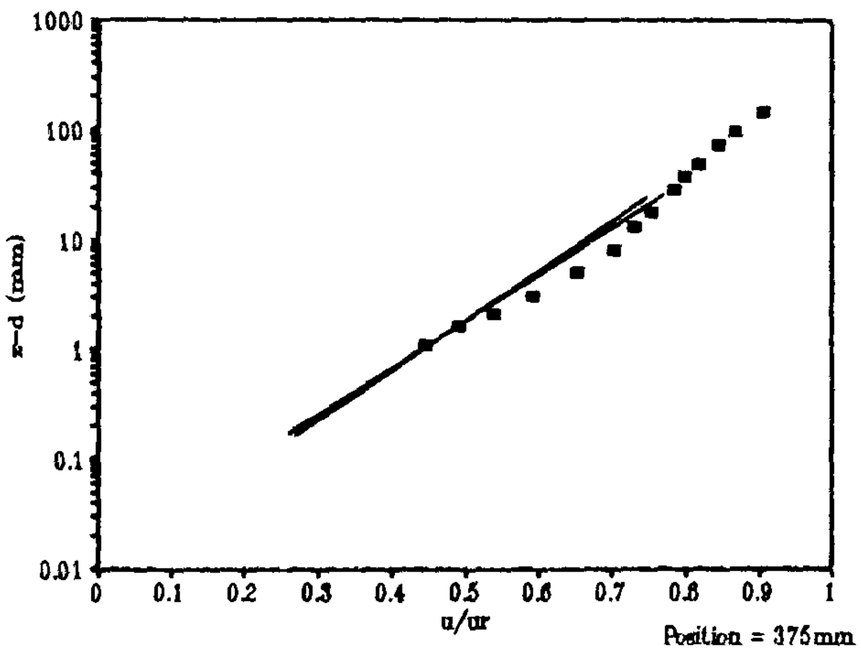

G.

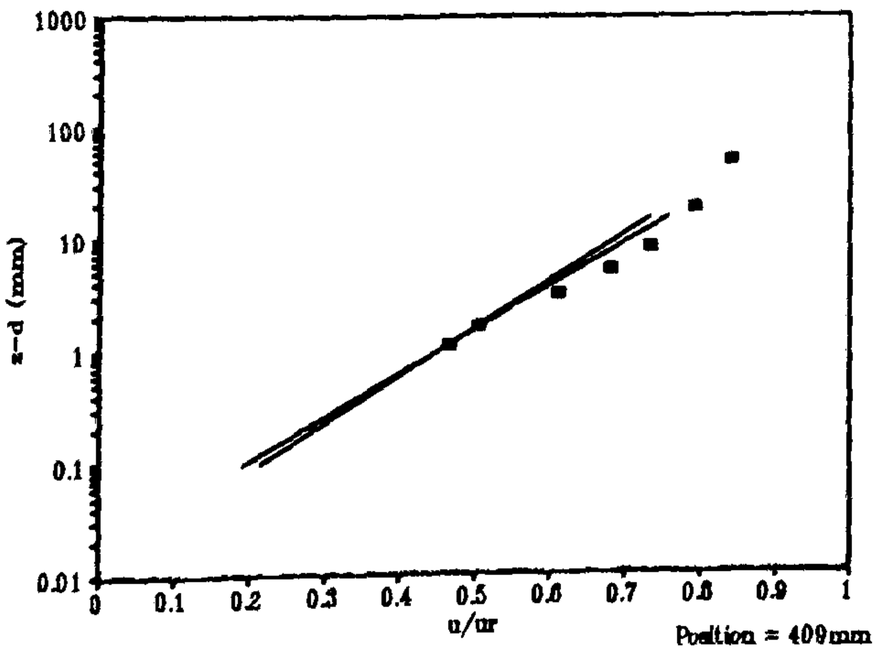

H.

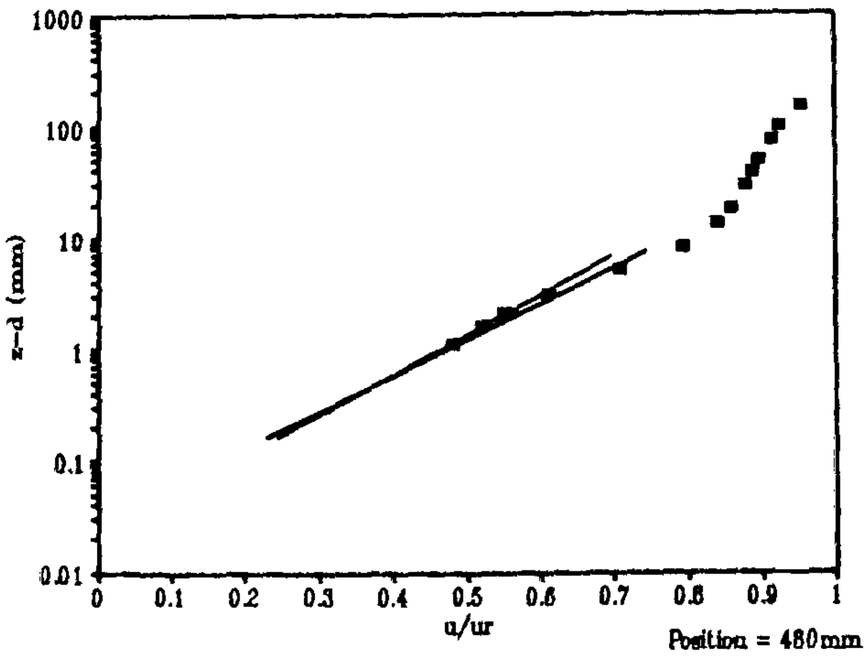

Figure 4.47 Superimposing the extrapolated shear velocity gradients onto the vertical velocity profiles at selected points on the centre-line of the model dune. A = upwind; H = crest.

The good agreement between derived shear velocity gradients and velocity measurements suggest that the methods employed in determining the surface shear stress are not subject to significant error. The fitting of the shear velocity gradients to only the lowest few measured velocities also demonstrates the possible errors involved in calculating shear velocity from velocity profile measurements, as undertaken with the field data (see Chapter 6 for these calculations).

The Flanks

The Reynold's stress relationships for both flanks are similar to those described for the centre-line. However, the results on the flanks are of particular interest because the measurements taken between the crest and brink may loosely be compared with previous studies which have taken measurements in the wakes of low hills (*e.g.* Gong & Ibbetson, 1989; Finnigan *at al.*, 1990).

Figures 4.48 and 4.49 show the progression for usb along the left and right flanks respectively. They follow the characteristic increase at the toe and reduction along the windward slope, although in both cases this reduction is less severe than along the centre-line. The left flank then shows a rise to a peak at the crest, and then a sudden drop almost to upwind values at the brink. In contrast, the right flank shows a peak at the crest, but then displays a greater peak at the brink. This is more in line with the measurements undertaken by Finnigan *et al.* (1990) in the wake of a low hill.

Figures 4.50 and 4.51 show the wsb progression along the left and right flanks respectively. Neither of these Figures display a rise at the toe (as suggested by Finnigan *et al.*, 1990). However, they both rise toward the crest, as with the centre-line measurements. Between the crest and brink they rise at a faster rate to peak finally at the brink. These peaks in wsb at the brink on both flanks are significantly higher than the peak along the centre-line at the crest. This is expected, considering the rise in turbulent intensity found in these regions (Figure 4.37). Comparable results are described by Finnigan *et al.* (1990).

The lowermost measurements of -uwb for the left and right flanks, shown in Figure 4.52 and 4.53 respectively, follow the same development as along the centre-line (Figure 4.44). That is, a slight reduction in shear stress at the toe coupled with a rise toward the crest. The peak in -uwb at the crest for the left and right flanks respectively are 56% and 43% more than their upwind values. This compares with slightly less than 62% for the centre-line. Between the crest and brink on the flanks the shear stress is reduced. In the case of the left flank this reduction is

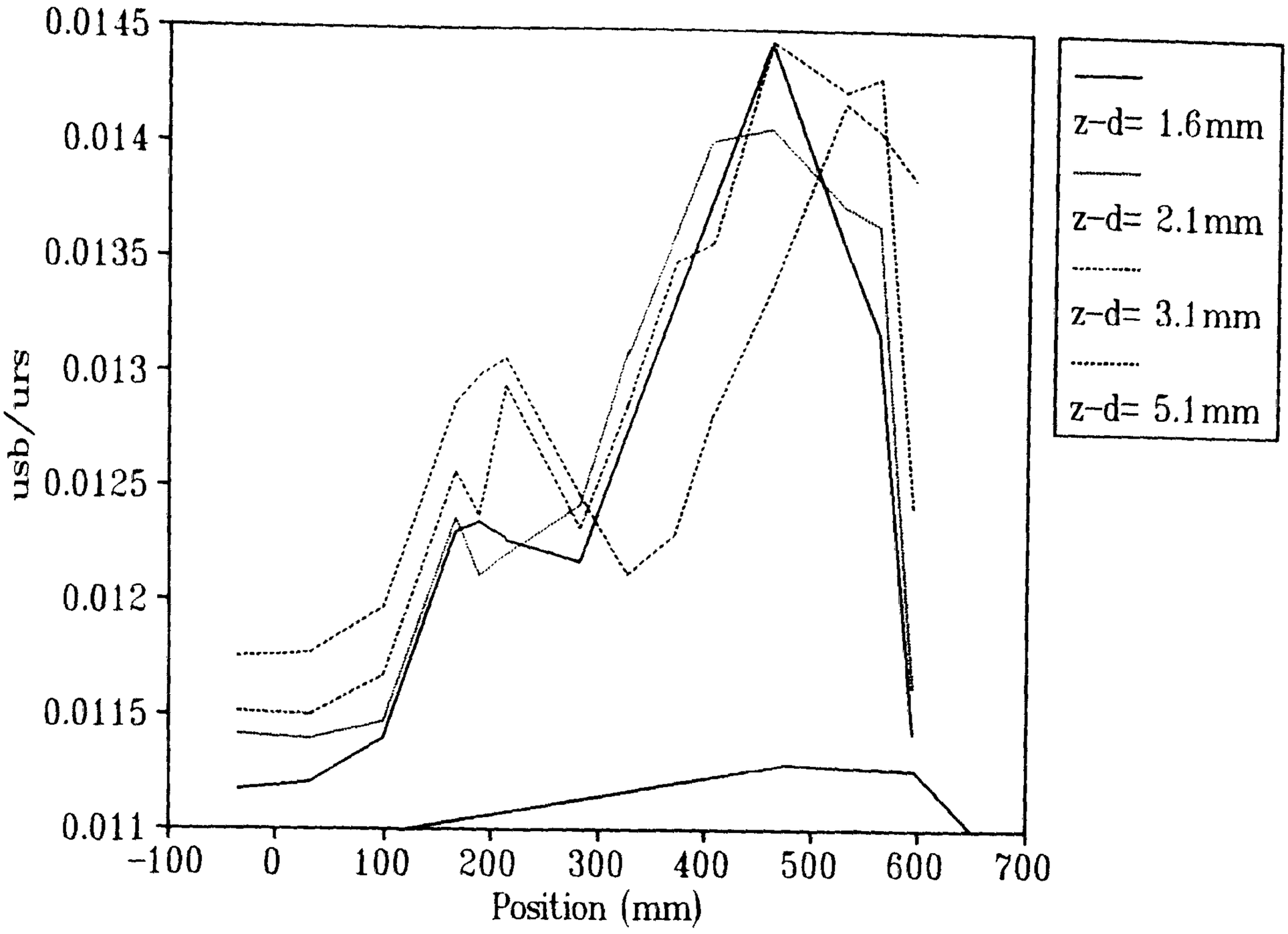

Figure 4.48 Measurements of usb on the left flank of the model dune.

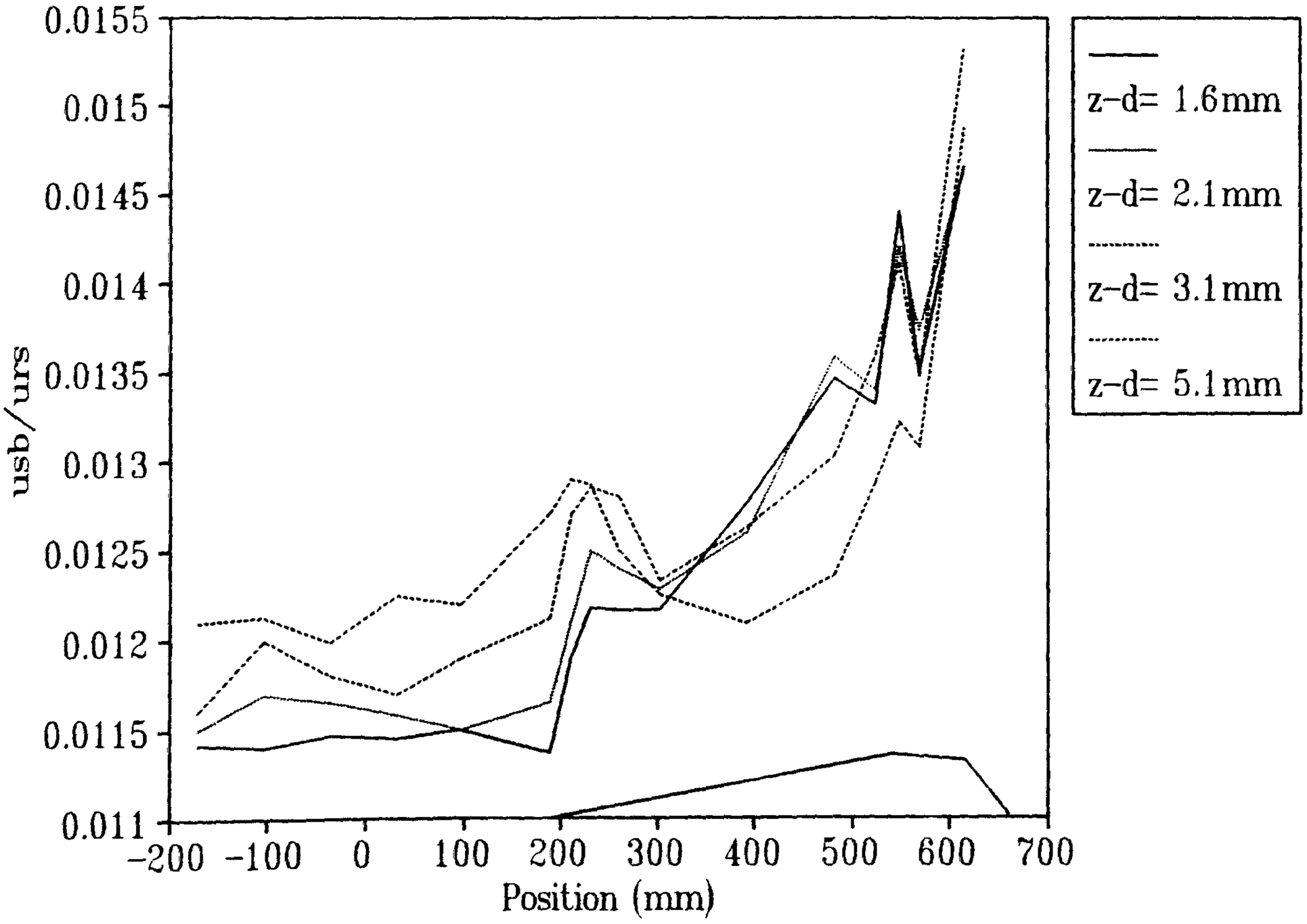

Figure 4.49 Measurements of usb on the right flank of the model dune.

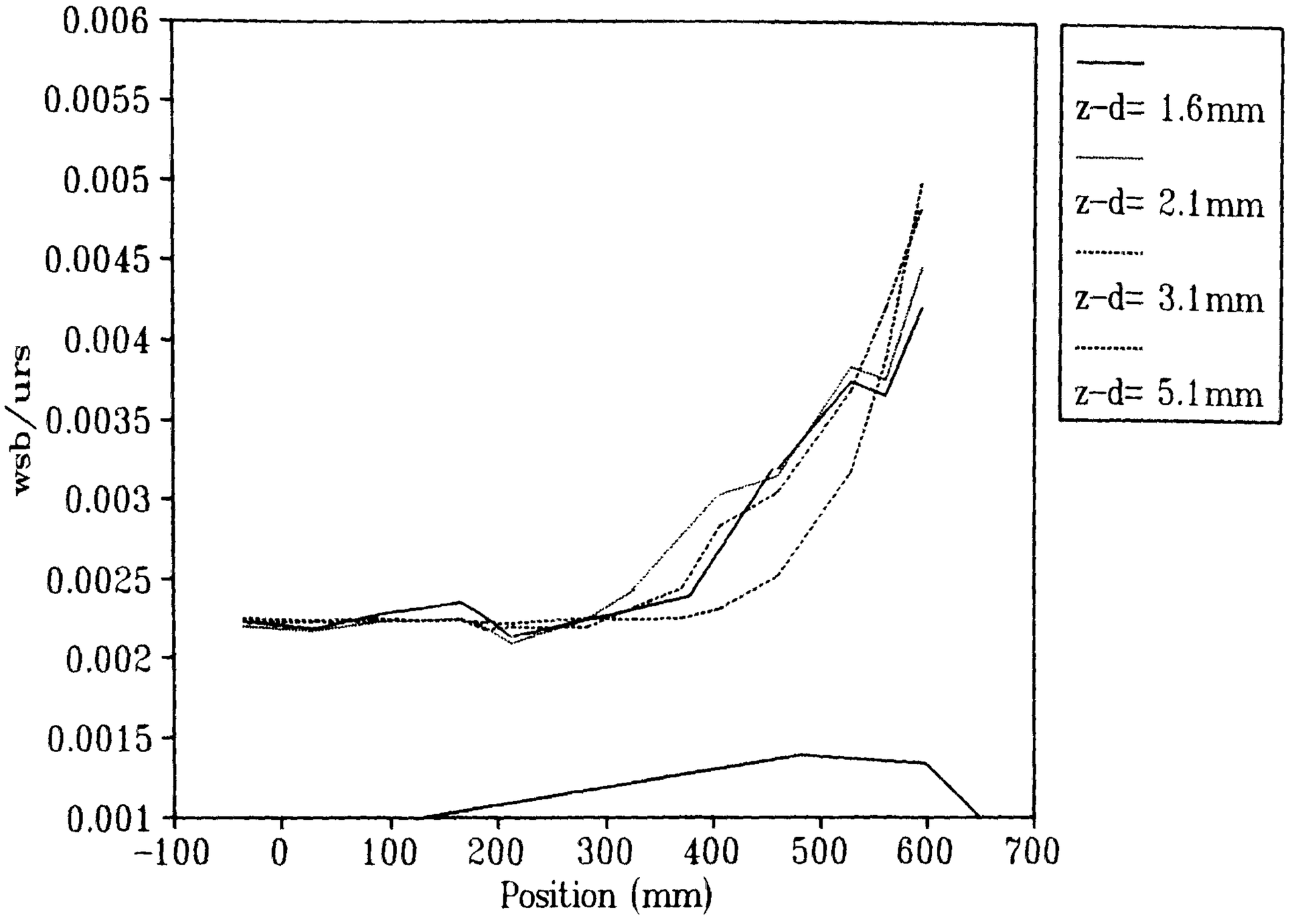

Figure 4.50 Measurements of wsb on the left flank of the model dune.

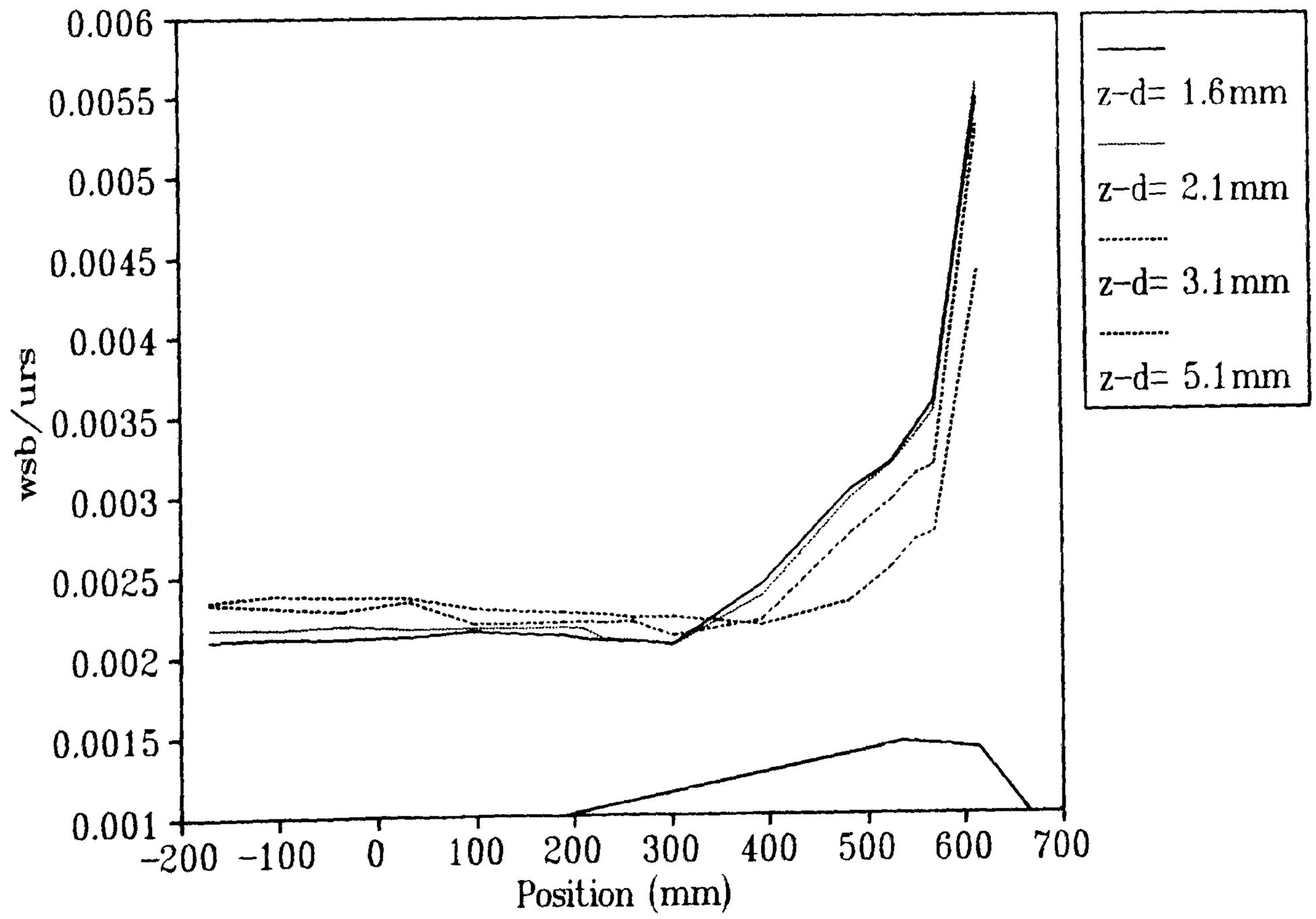

Figure 4.51 Measurements of wsb on the right flank of the model dune.

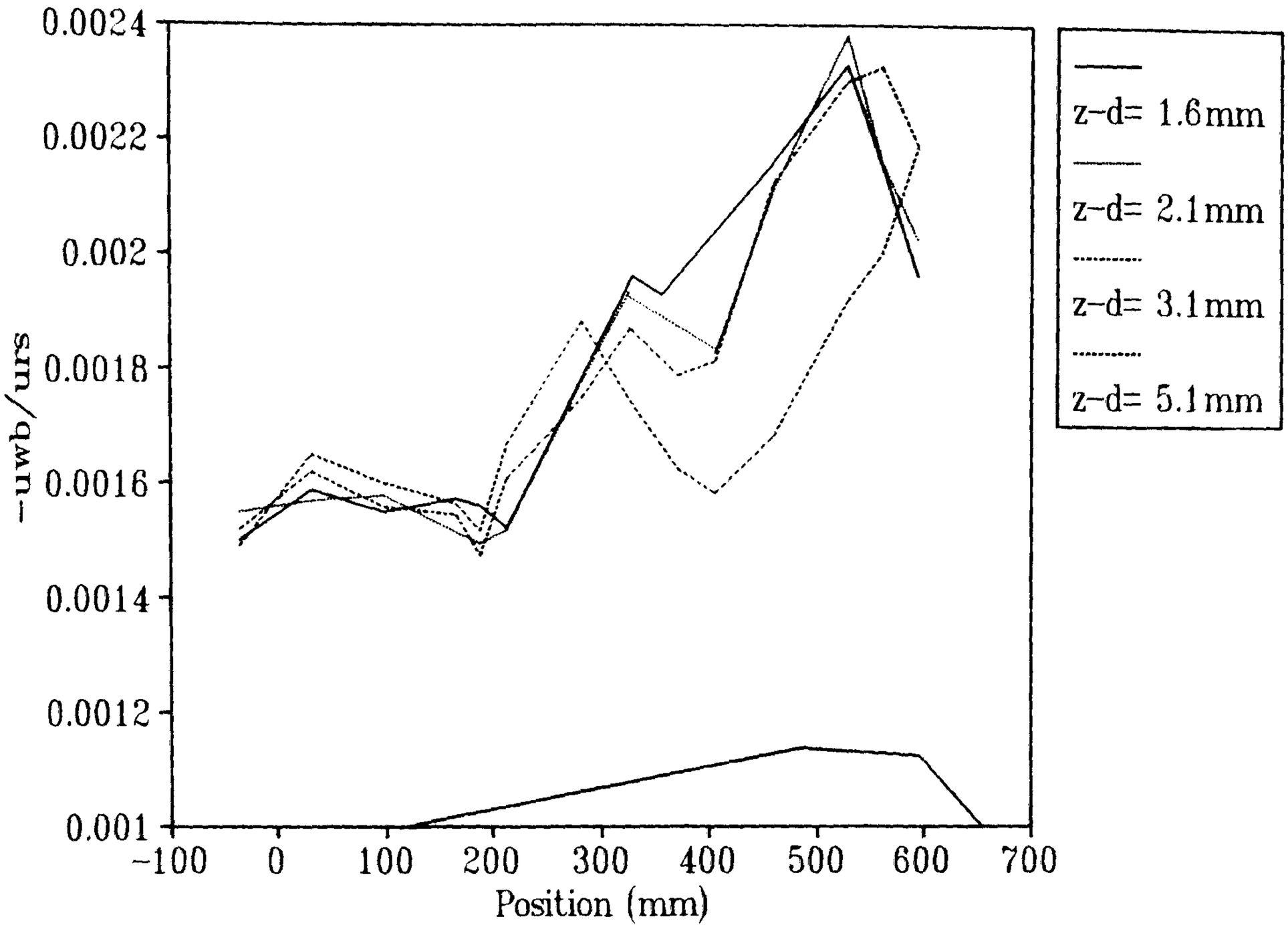

Figure 4.52 Measurements of -uwb on the left flank of the model dune.

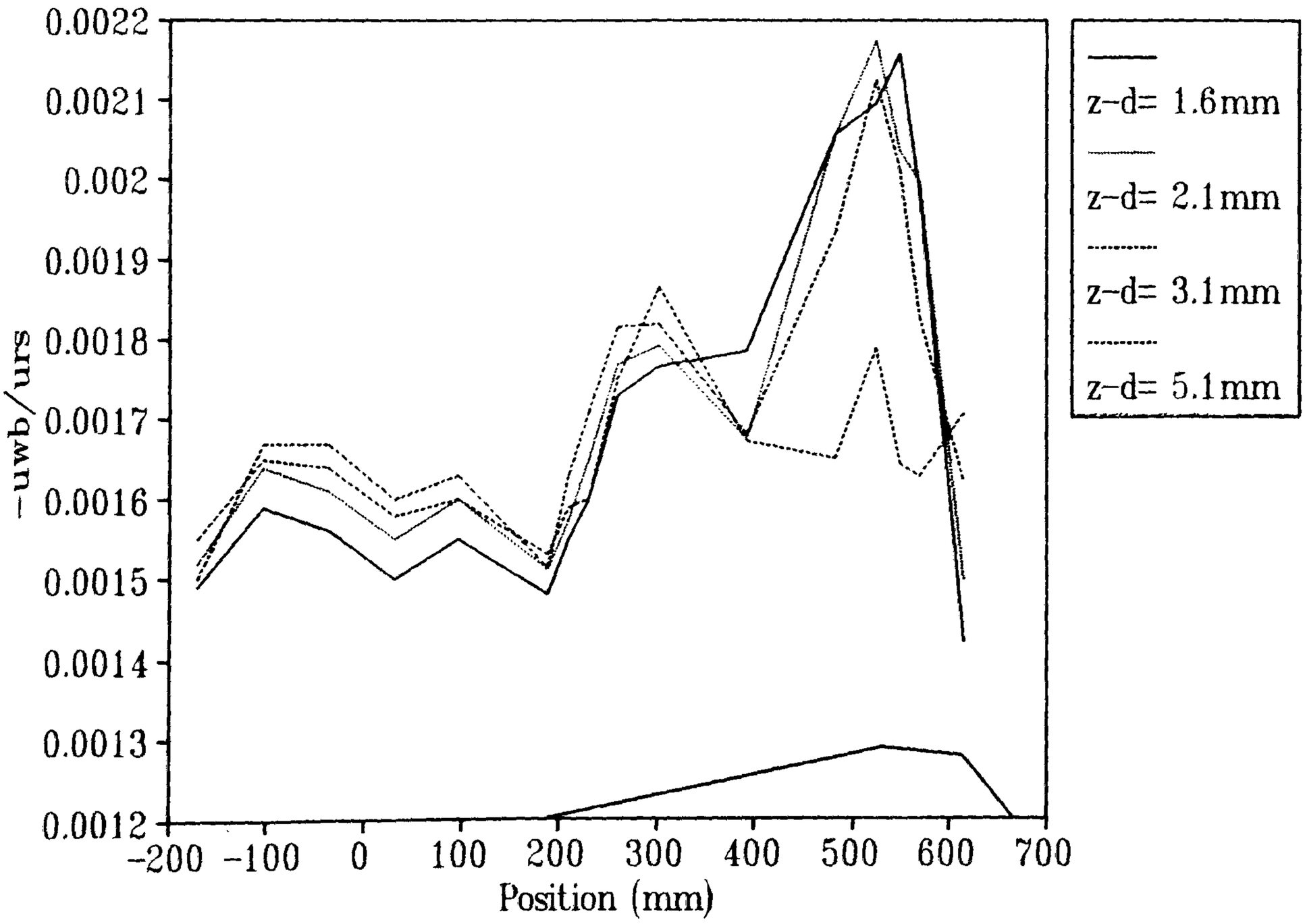

Figure 4.53 Measurements of -uwb on the right flank of the model dune.

only by about 15% of the crest value. However, the stress on the right flank drops to just below its upwind value.

At higher levels the progression of -uwb is similar to that measured by Finnigan *et al.* (1990). The plots at z-d = 5.1 mm (Figures 4.52 and 4.53) show a rise in value just after the toe, followed by a minimum in the crest region, rising again toward the brink.

A peculiarity of Figures 4.52 and 4.53 is the secondary peak in the shear stress term at about x = 300 mm. This peak is not recognisable on the centre-line (Figure 4.44). This anomaly is discussed further in the next section.

The surface shear velocity (u_*) was calculated in the same way as for the centre-line, by extrapolating the -uwb profiles to the surface. The evolution of the profiles is similar to that described above. For comparison, Figures 4.54a and b show the vertical shear stress profiles at the brink for the left and right flanks respectively. These can be compared to the centre-line profile in Figure 4.45r. The sharp reduction in -uwb near the surface on both flanks is indicative of the growth of an adverse pressure gradient in the turbulent wake, in accordance with Equation 4.9.

The derived surface shear velocities are shown in Figures 4.55 and 4.56. Both show similar results in that they rise from the toe to the crest, peaking at about 23% higher than their upwind values. From the crest to the brink u_* decreases on both flanks. These results are comparable with the centre-line derivations presented in Figure 4.46. The centre-line shows a peak in u_* (47% higher than upwind) more than double that for the flanks and it also allows for a possible reduction in shear stress at the toe. In contrast, little reduction in shear stress can be identified at the toe on either of the flanks.

The vertical gradients in velocity suggested by the derived surface shear velocities were plotted against the measured velocity profiles. The profiles for the brinks on the left and right flanks are shown in Figures 4.57a and b. Both of the profiles show a sharp deviation from a logarithmic profile below z-d = 10 mm due to flow deceleration. The derived shear velocity gradients fit the velocity measurements only below z-d = 3 mm. The other profiles for the flanks are not presented here but show similar relationships to those shown in Figure 4.57 and the profiles for the centre-line (Figure 4.47).

A.

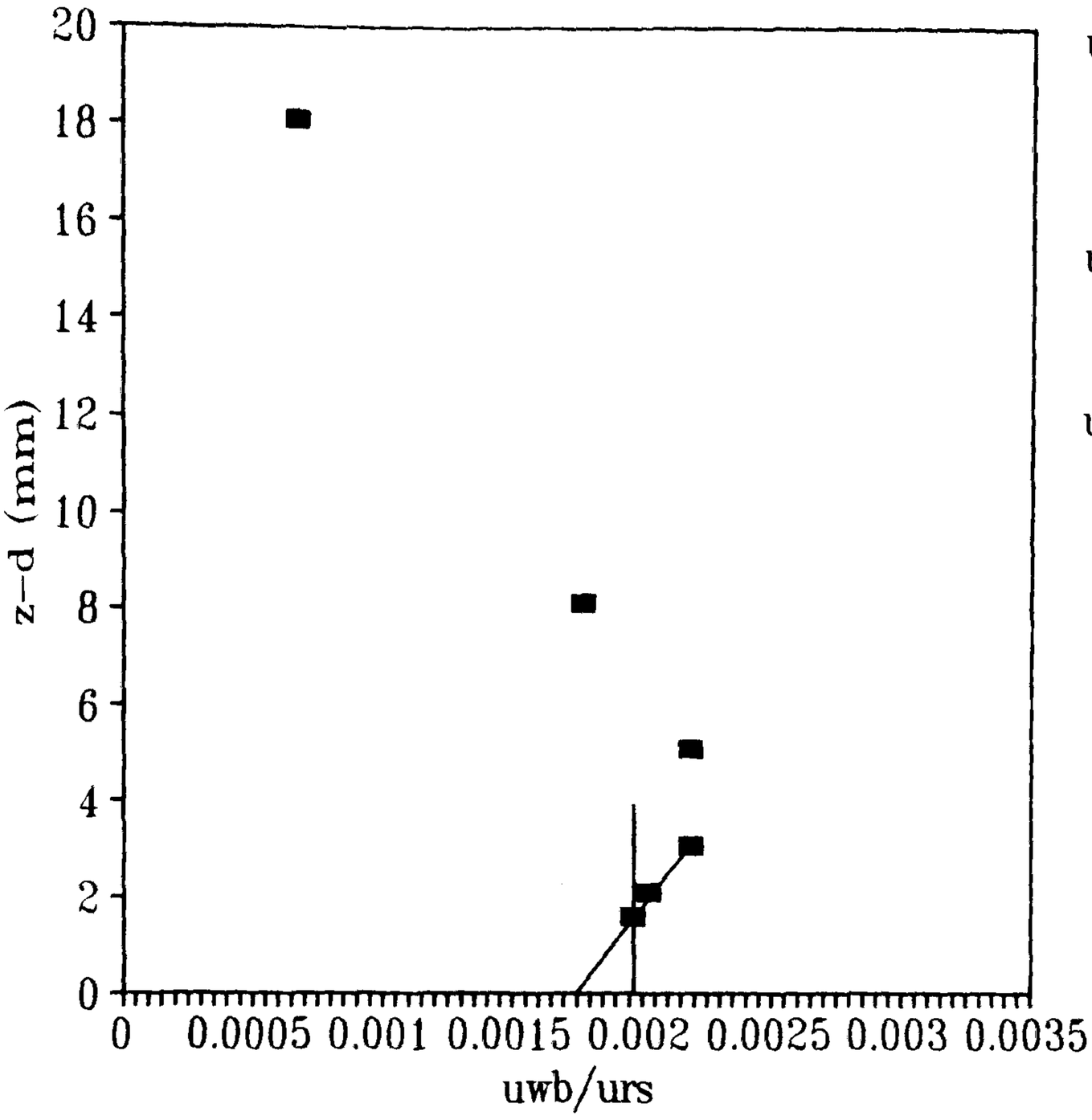

uwb/urs at 0,
low = 0.00175
high = 0.00198

u*/ur, low = 0.04183
high = 0.04444

u*/kur, low = 0.10203
high = 0.10839

Position = 595mm

B.

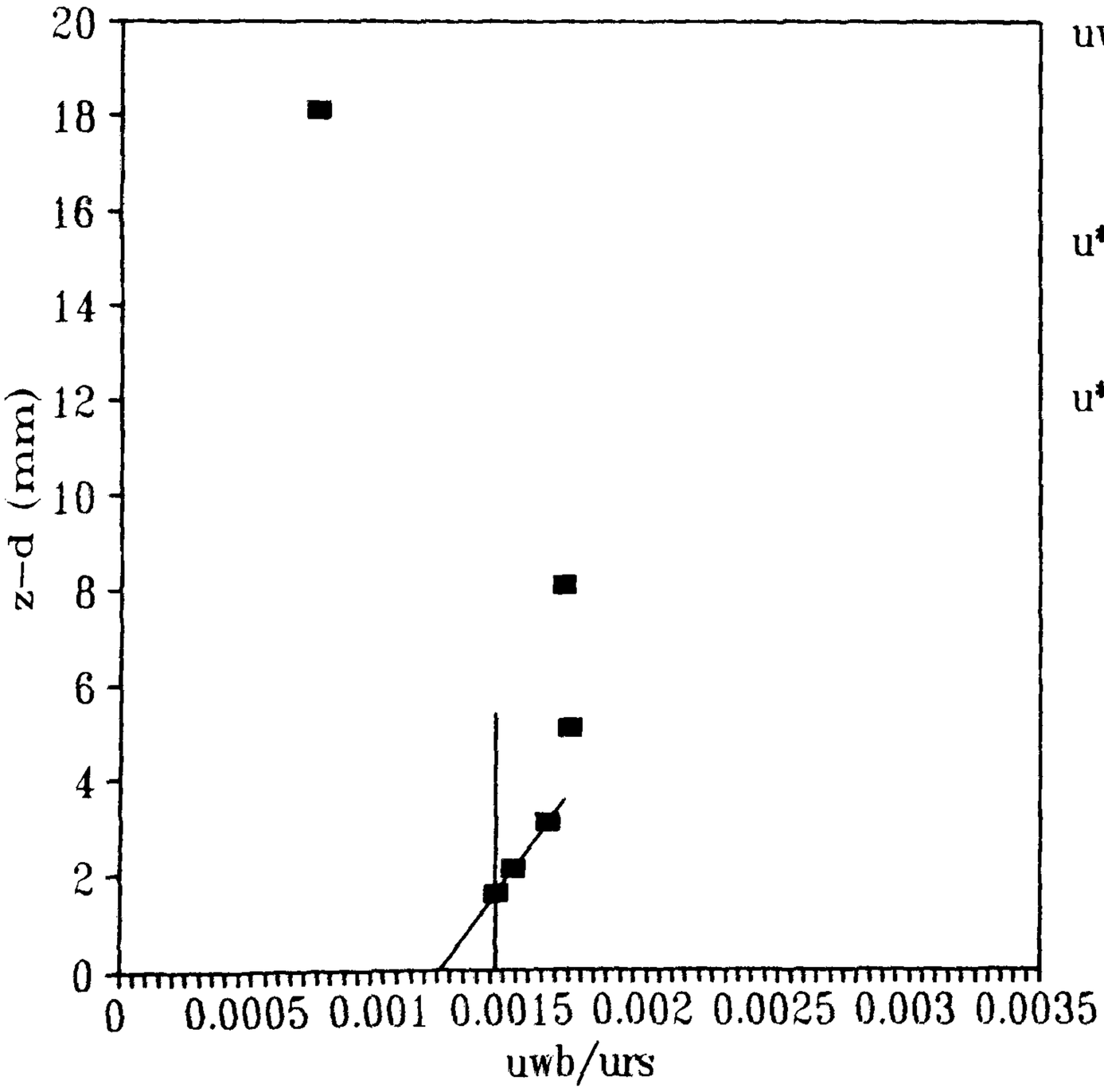

uwb/urs at 0,
low = 0.00123
high = 0.00143

u*/ur, low = 0.03500
high = 0.03775

u*/kur, low = 0.08536
high = 0.09207

Position = 616mm

Figure 4.54 Extrapolating shear stress to the surface to calculate surface shear velocity at the brinks of the left (A) and right (B) flanks.

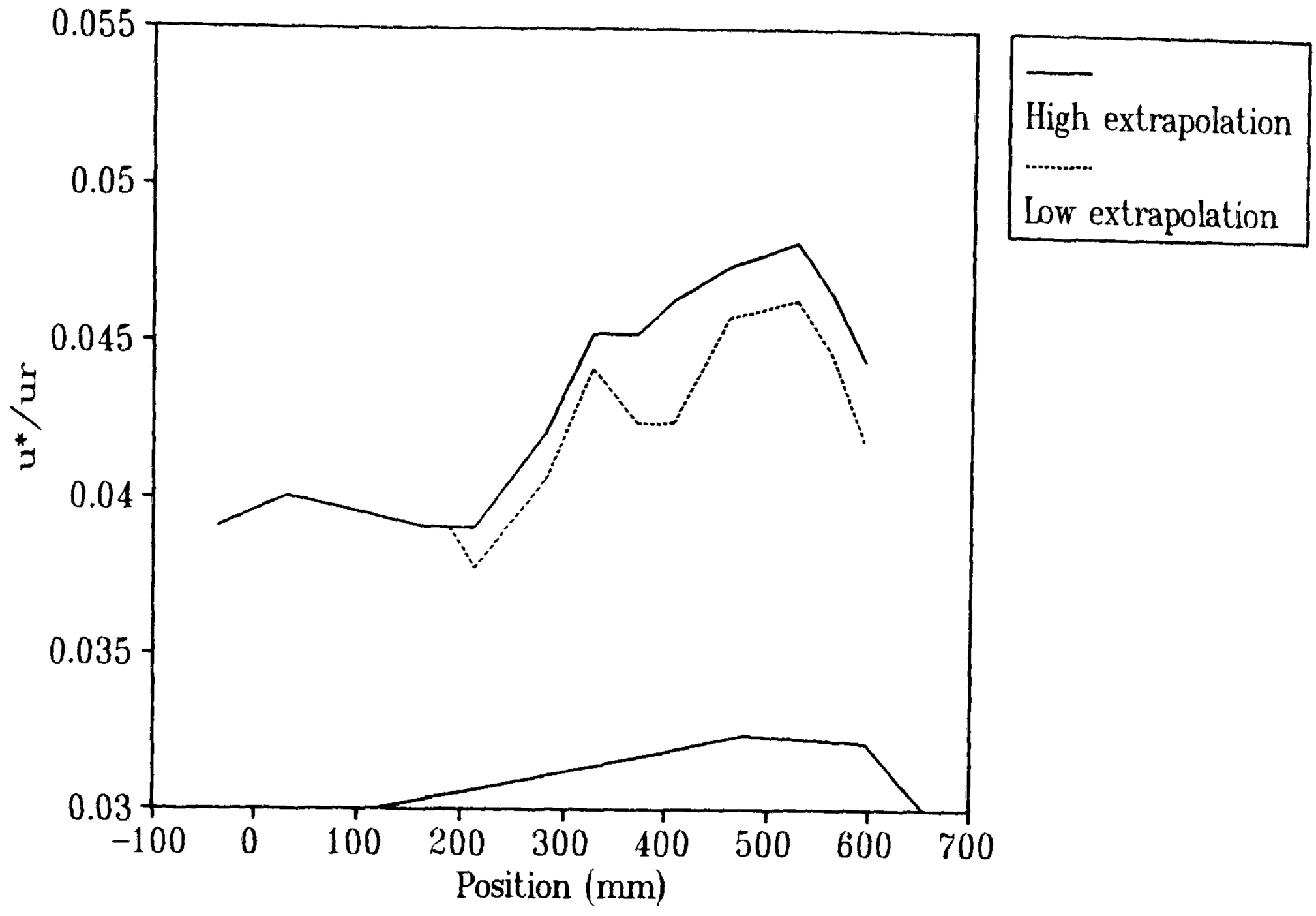

Figure 4.55 Low and high extrapolations of surface shear velocity on the left flank of the model dune.

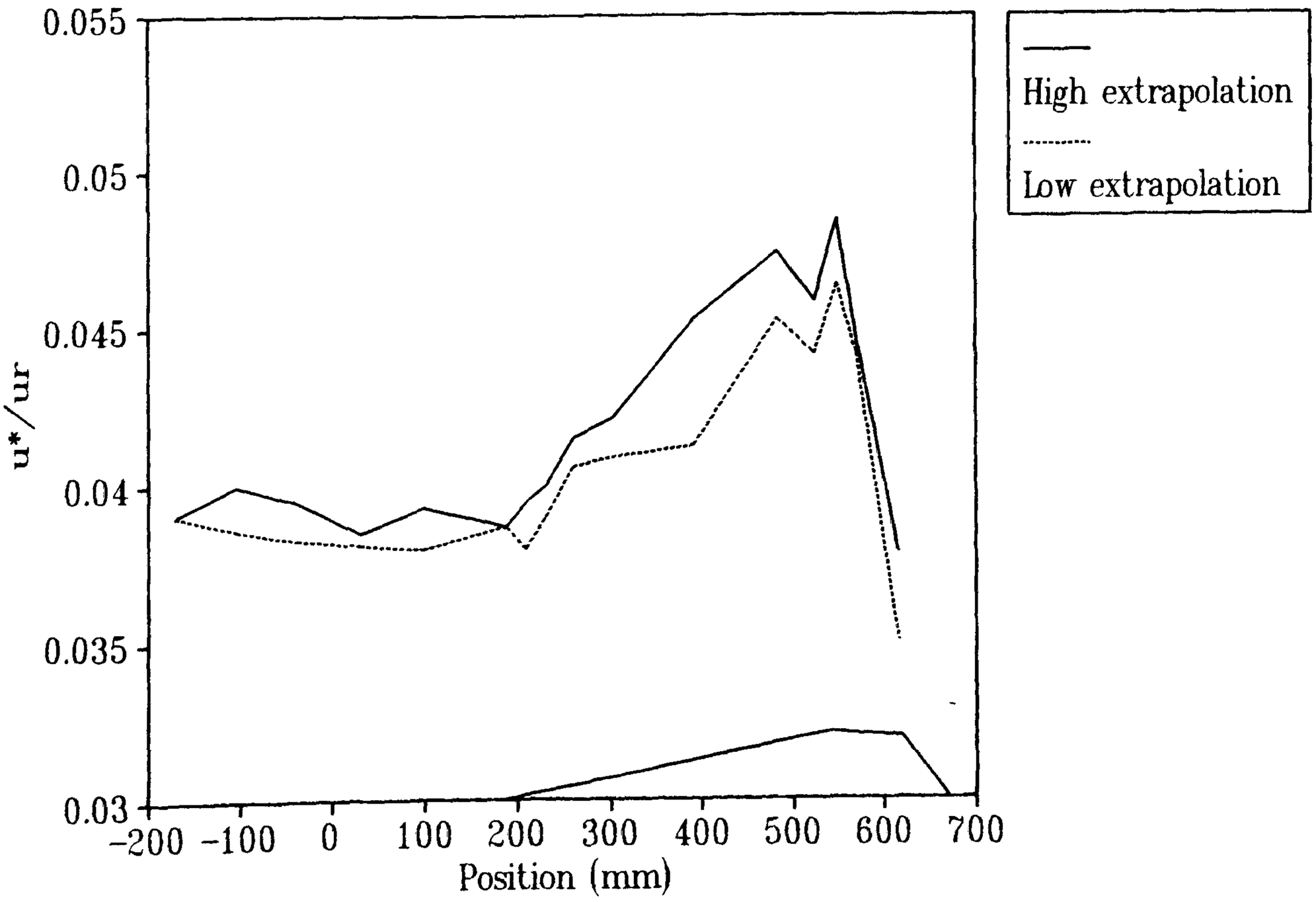

Figure 4.56 Low and high extrapolations of surface shear velocity on the right flank of the model dune.

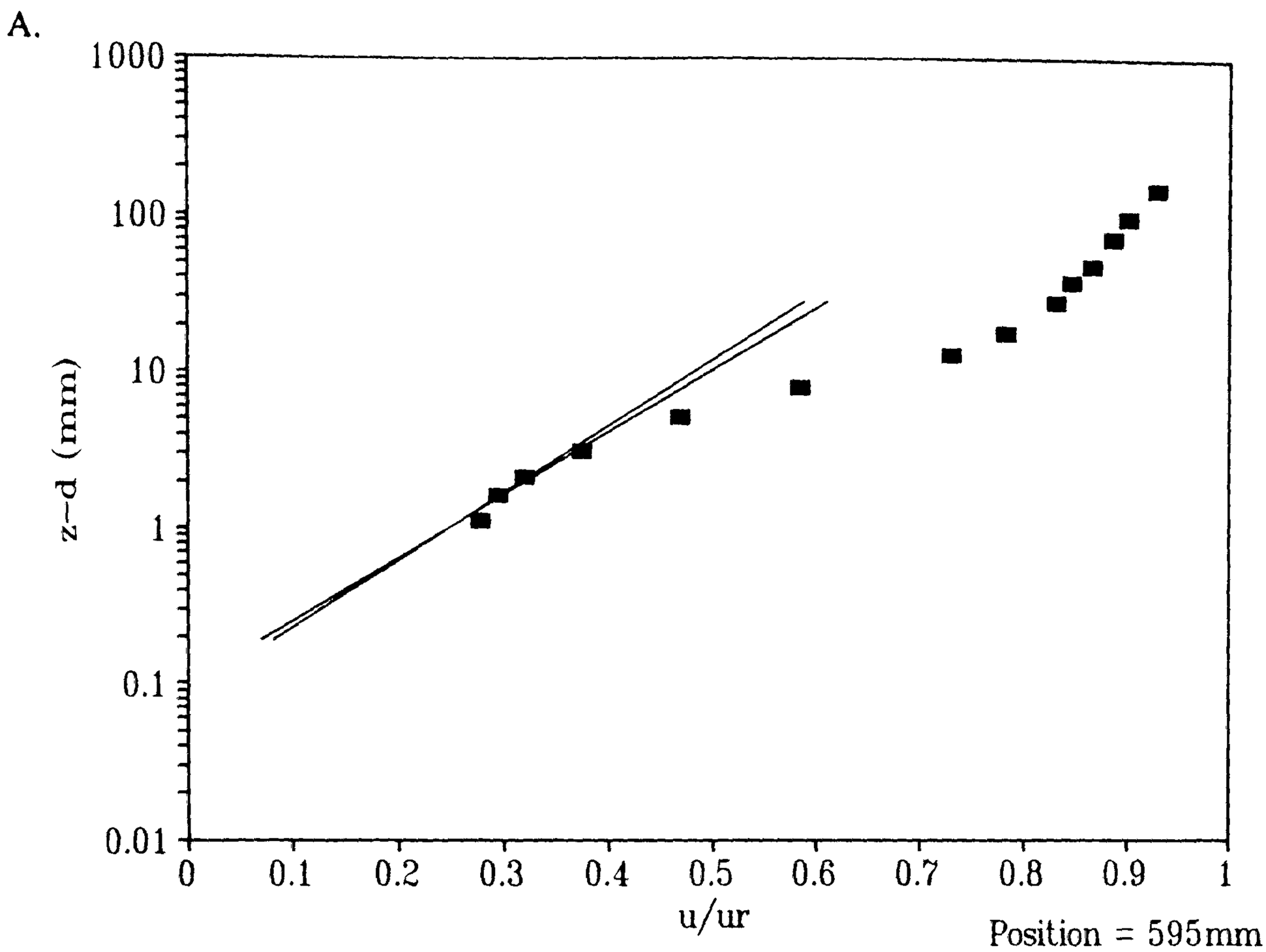

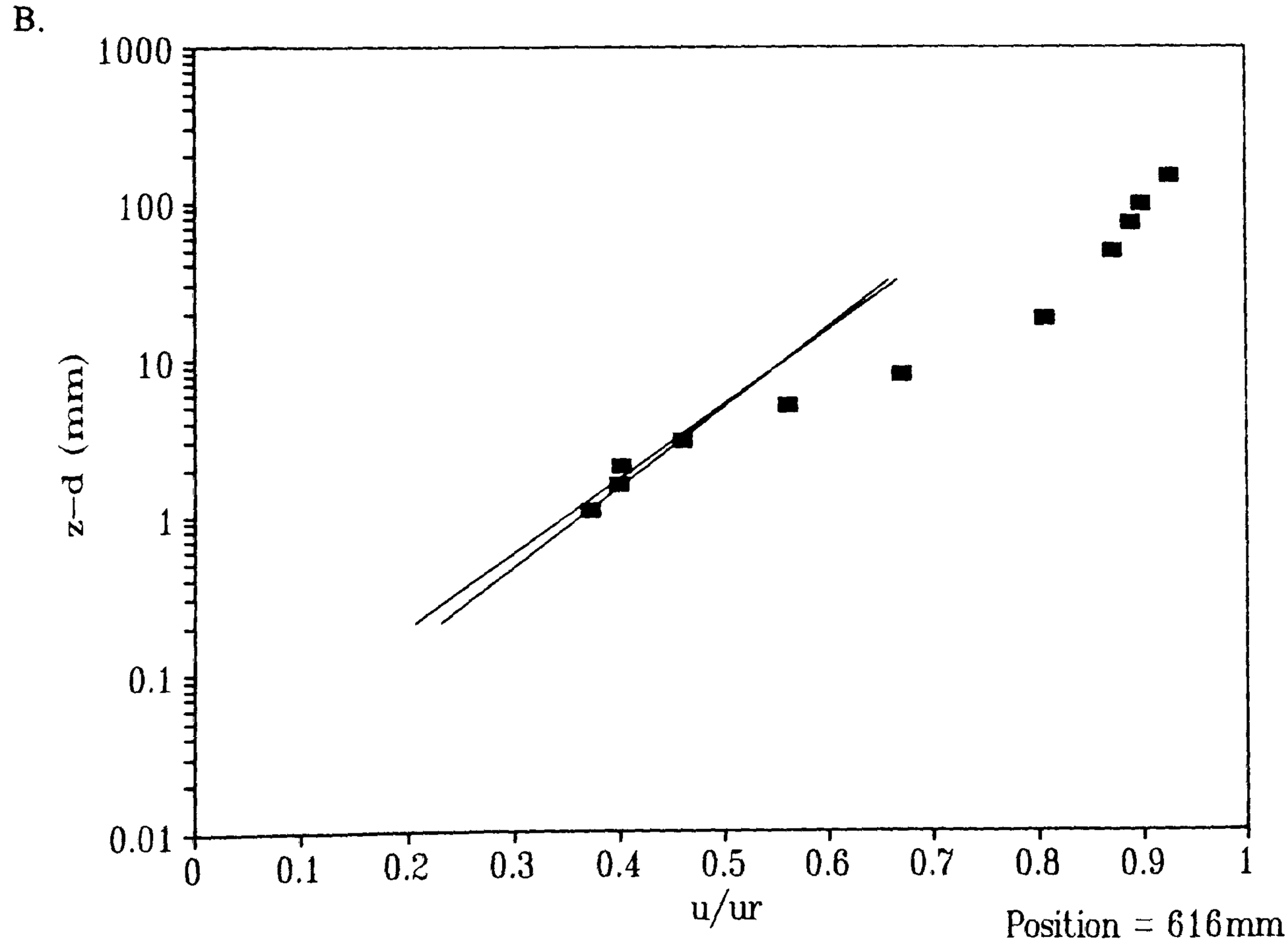

Figure 4.57 Superimposing the extrapolated shear velocity gradients onto the vertical velocity profiles at the brinks of the left (A) and right (B) flanks.

Surface Shear Stress

Surface shear stress measurements were undertaken at various points on the windward slope and in the re-circulation zone to the lee, with the pulse-wire probe described in Chapter 4.2.1. To carry out these measurements the probe was inserted through the tunnel floor into the flow so that the probe head was parallel with the dune surface and at the same height (k) as the roughness elements (Figure 4.58a+c). Holes were drilled through the tunnel floor and dune model at the required angles so that the probe head was at the required position. In order to achieve a satisfactory relationship with the probe calibration, the sensor had to be positioned between two roughness elements, as shown in Figure 4.58b+c (Castro pers. comm.). Measurements were taken along the centre-line on the windward slope and in the leeside region, and at three points on each flank (toe, crest and brink).

Figure 4.59 shows the measured shear velocity (*i.e.* the square-root of the measured shear stress) along the centre-line normalised by the reference wind velocity. The upwind value of 0.0354 at x = -300 mm corresponds reasonably well with that for the undisturbed ABL derived from the cross-wire measurements of 0.037 (see Chapter 4.2.2). Figure 4.59 shows a steady rise in u_* toward the brink and then a sharp drop to negative (*i.e.* re-circulating flow) in the lee. The return to positive values occurs between x = 700 mm and 800 mm. This signifies the zone of re-attachment of airflow after separation at the brink. This measured zone is somewhat downwind of that inferred from the flow visualisation experiments (Chapter 4.3.1). This can be explained by the difference in roughness between the two experiments. The flow visualisation was carried out on a smooth dune with relatively faster near surface velocities, hence separation on the flanks would occur later, resulting in a smaller zone of re-circulation (Castro & Snyder, 1982; Teunissen *et al.*, 1987).

No reduction in surface shear velocity at the toe can be distinguished on Figure 4.59. A clearer picture of this region can be obtained by plotting the values as perturbations calculated from Equation 2.3. The shear velocity perturbations for all the centre-line measurements are shown in Figure 4.60, indicating that the peak in shear velocity at the brink is about 50% higher than the upwind value. Figure 4.61 shows the same data but without the leeside region. This larger scale graph displays no reduction in shear velocity at the toe of the dune. At the toe (x = 107 mm) the shear stress had increased in magnitude by ≈ 3%.

The surface shear velocity measured by the pulse-wire probe is compared to that derived from the cross-wire measurements in Figure 4.62. There is a large discrepancy upwind of the toe, where the pulse-wire probe measurements are lower than their cross-wire counterparts, and also

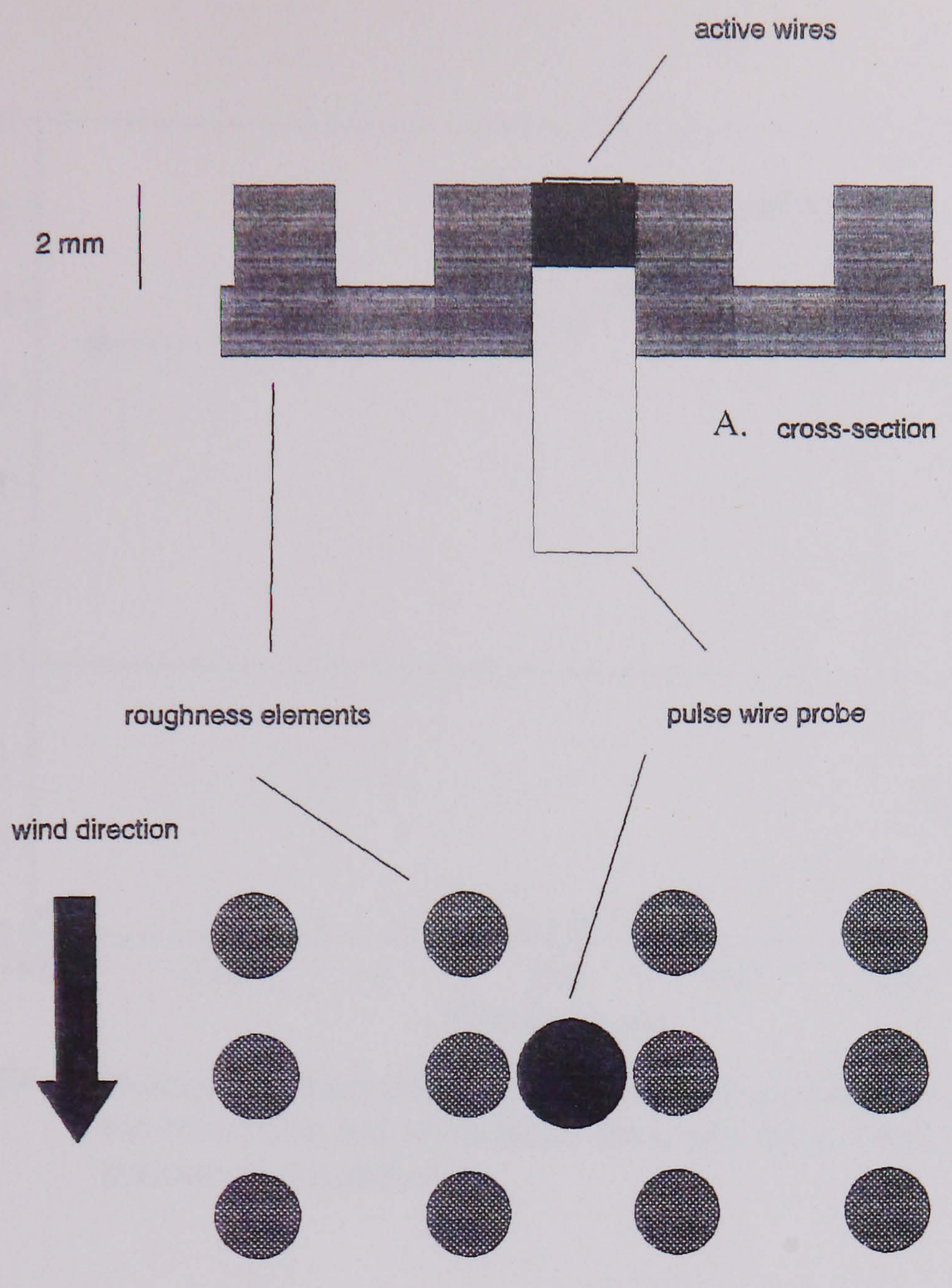

Figure 4.58 The configuration and positioning of the pulse-wire probe in relation to the roughness elements. A = cross-section; B = plan view; C = photograph of pulse-wire probe head (mid-picture) inserted through the tunnel floor, direction of flow is from the left.

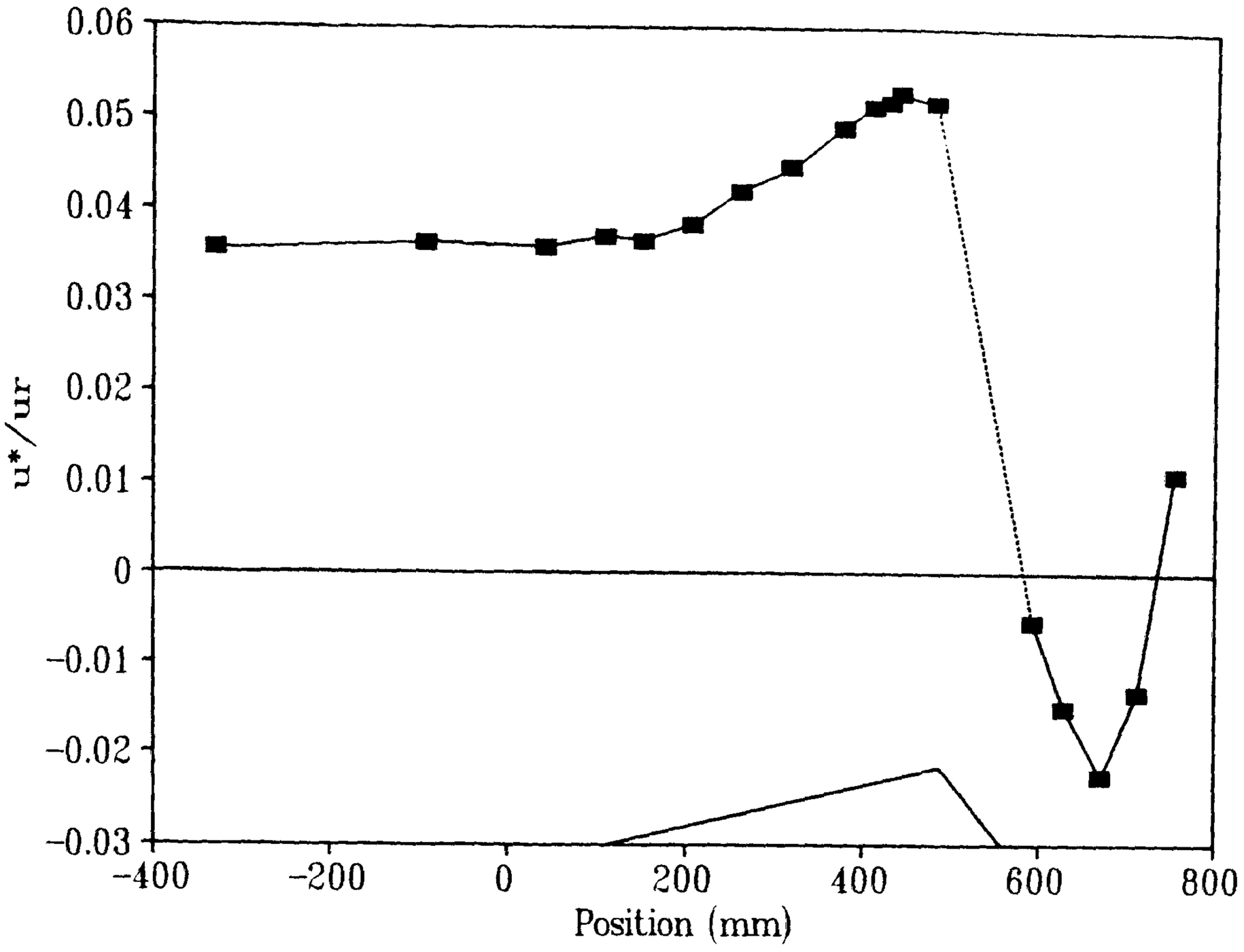

Figure 4.59 Normalised shear velocity measured by the pulse-wire probe along the centre-line and in the lee of the model dune. Negative numbers indicate re-circulation.

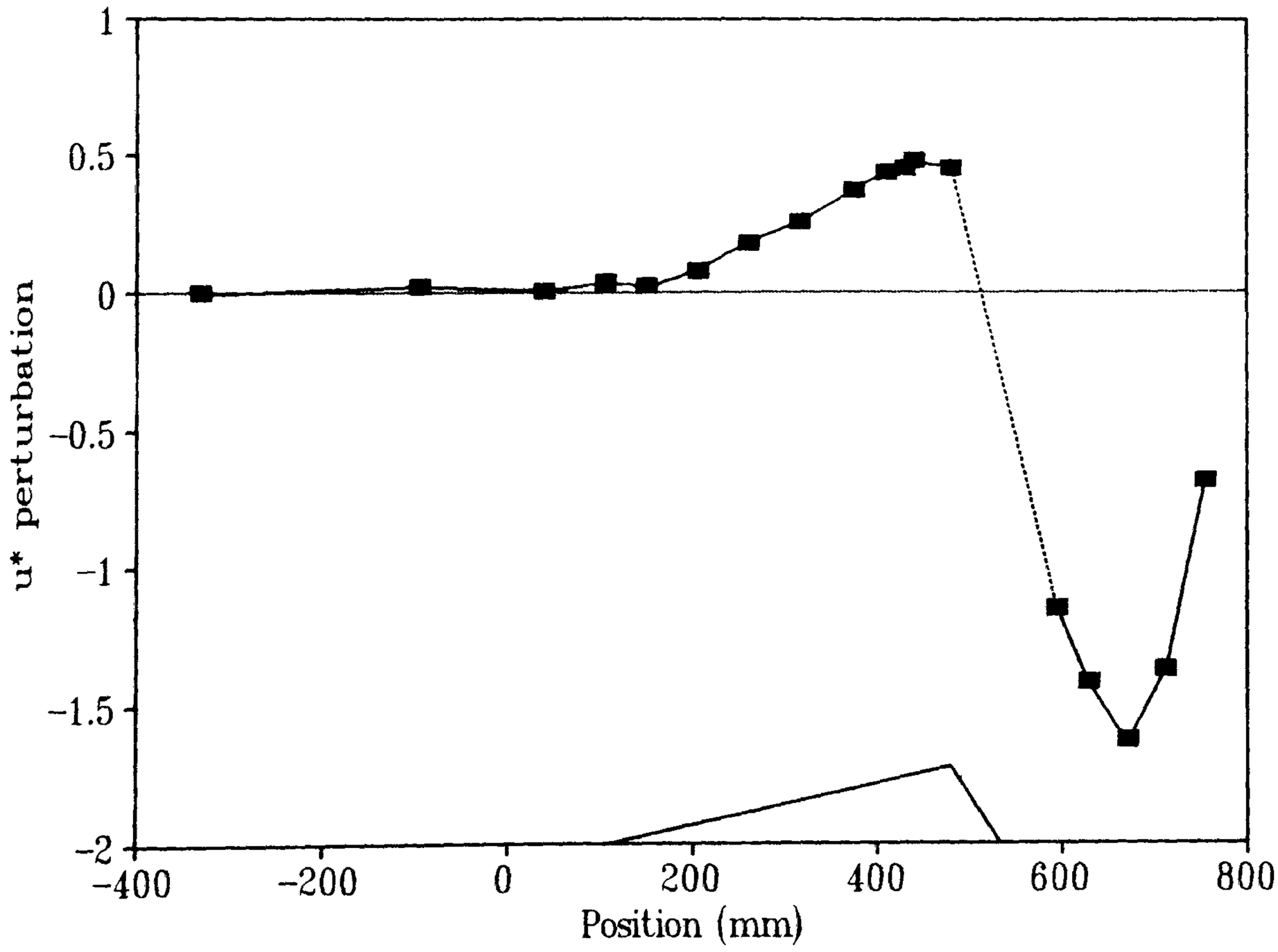

Figure 4.60 Shear velocity perturbation measured by the pulse-wire probe along the centre-line and in the lee of the model dune.

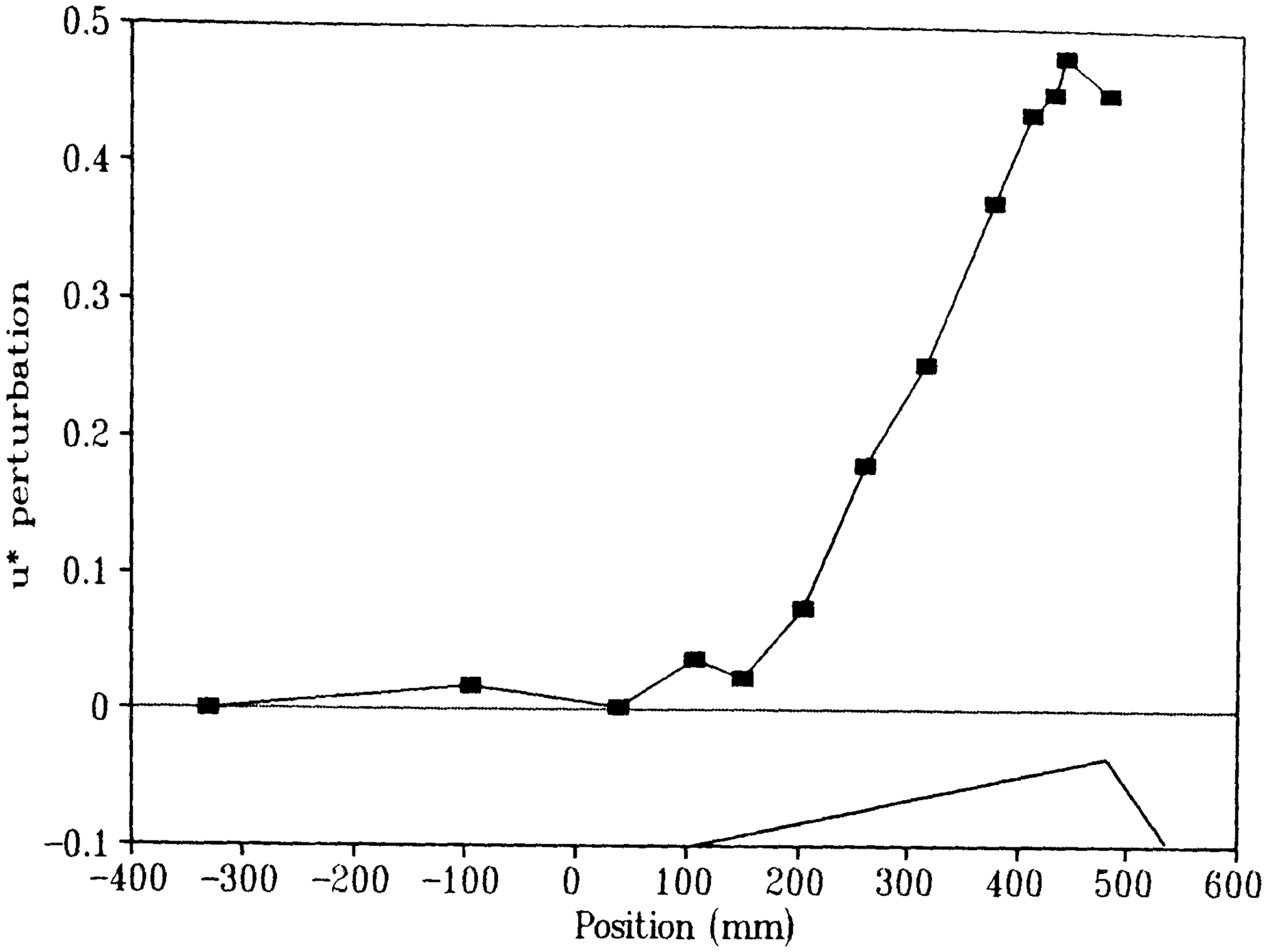

Figure 4.61 Shear velocity perturbation measured by the pulse-wire probe along the centre-line of the model dune.

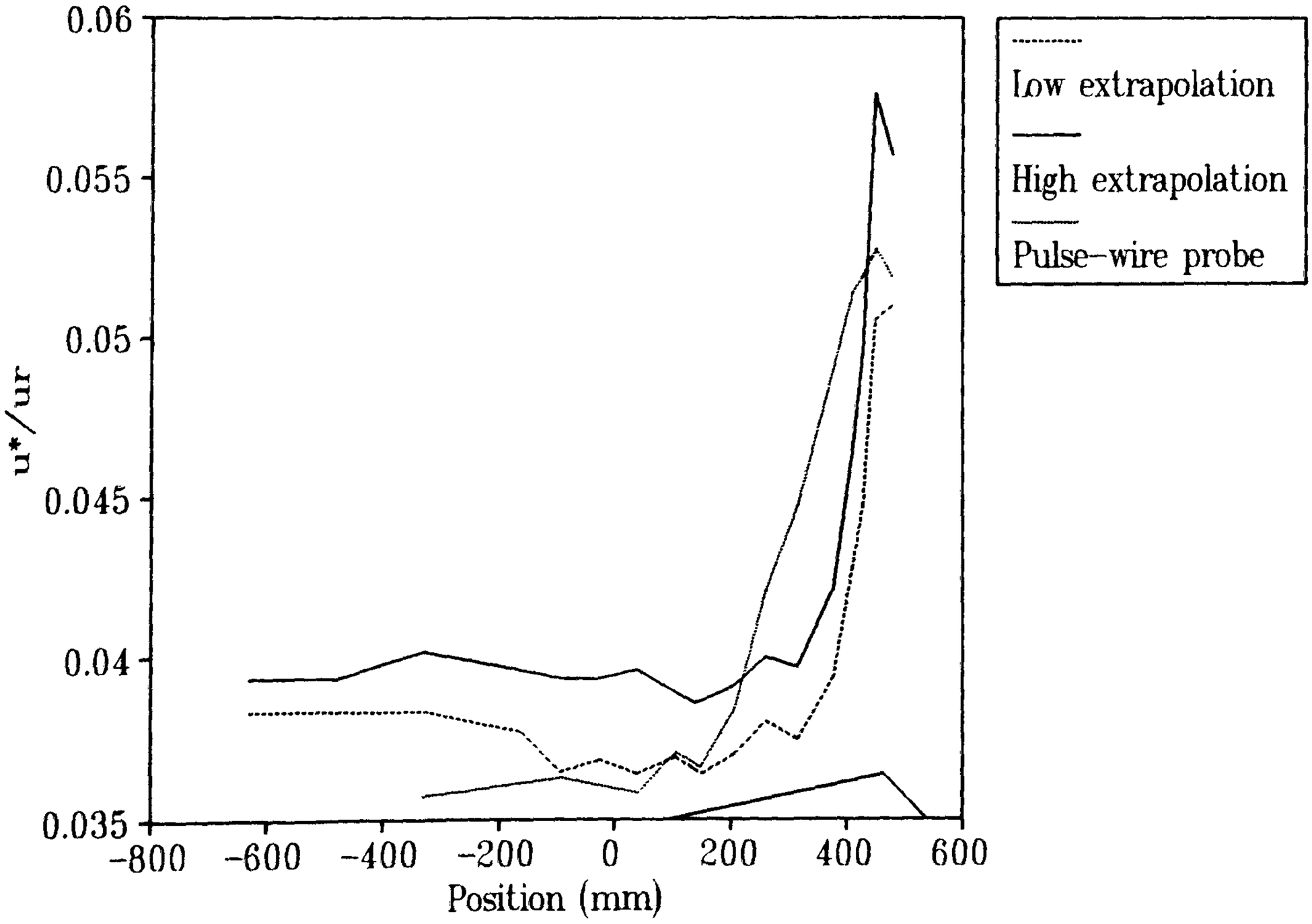

Figure 4.62 Comparison between the pulse-wire probe measurements of shear velocity and that extrapolated from the cross-wire measurements along the centre-line of the model dune.

on the windward slope, where the pulse-wire measurements are higher. These contrasts cannot adequately be explained. Similar relationships between the two methods can be seen in Figures 4.63 and 4.64 which show a comparison on the left and right flanks respectively.

No reduction in shear velocity is recognisable from the pulse-wire probe results along the centre-line, but a reduction of maximum 7% is possible with the cross-wire derivations if both the maximum and minimum estimates are taken into account. It seems likely, considering the effect of height on the shear stress profiles shown in Figure 4.45, that this slight anomaly is a result of the height above the surface of the cross-wire measurements. Owing to the design of the cross-wire probe, and configuration of the roughness elements, the lowest measured values were at z = 3.5 mm (z-d = 1.6 mm). However, the general trends in shear velocity determined by the two methods seem comparable, and with the evidence of the pulse-wire probe it would appear that there is no reduction in surface shear velocity in the toe region of the dune.

4.4 The Effects of Streamline Curvature on Shear Stress and Turbulence Measurements

The sensitivity of airflow over hills to streamline curvature has been stressed by Zeman & Jensen (1987), Gong and Ibbetson (1989) and Finnigan *et al.* (1990). However, no attempt has been made to investigate the effects of streamline curvature on airflow over sand dunes. Analysis of the measured turbulence components in the present study reveals that streamline curvature may have an important influence on surface shear stress. Streamlines close to the surface tend to reflect terrain contours on the windward slope of the dune (Figure 4.40). In the present study, therefore, concave curvature is likely to be found at the toe of the dune and up the lower half of the windward slope whilst convex curvature is probable on the upper half of the windward slope and over the crest. The delineation between the two can be seen on the streamline angle cross-sections in Figure 4.40. Up to the peak in streamline angle on the windward slope concave curvature is likely to prevail and beyond this it is likely to be convex.

Concave curvature has a de-stabilising effect on the airflow structure (Figure 4.65a) with turbulence structures of high velocity being conveyed into regions of low velocity. Convex curvature (Figure 4.65b) has the opposite effect, stabilising the structure.

As discussed by Zeman & Jensen (1987) and Finnigan *et al.* (1990), the three components of turbulence are affected differently by the two curvature types. Concave curvature tends to

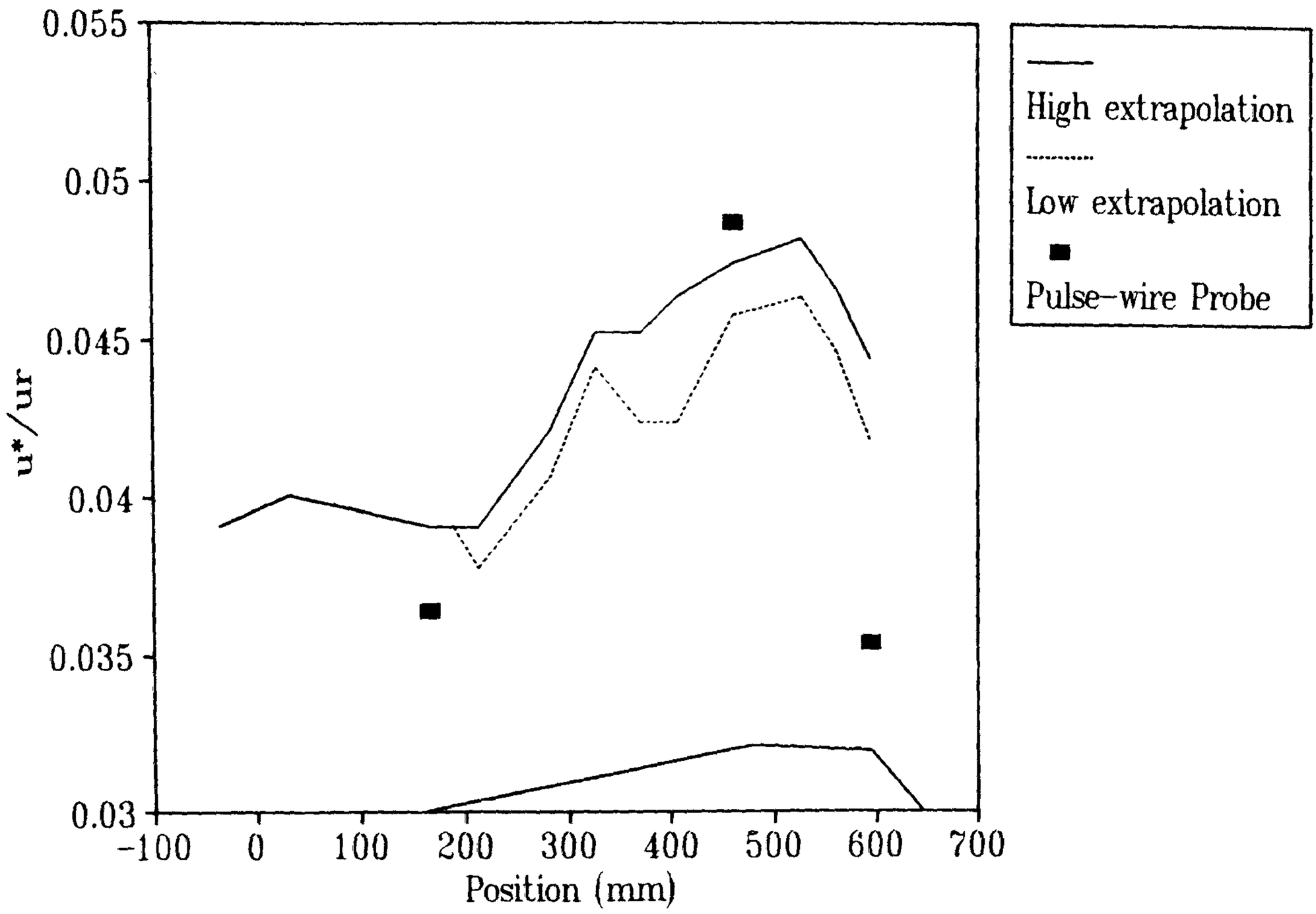

Figure 4.63 Comparison between the pulse-wire probe measurements of shear velocity and that extrapolated from the cross-wire measurements along the left flank of the model dune.

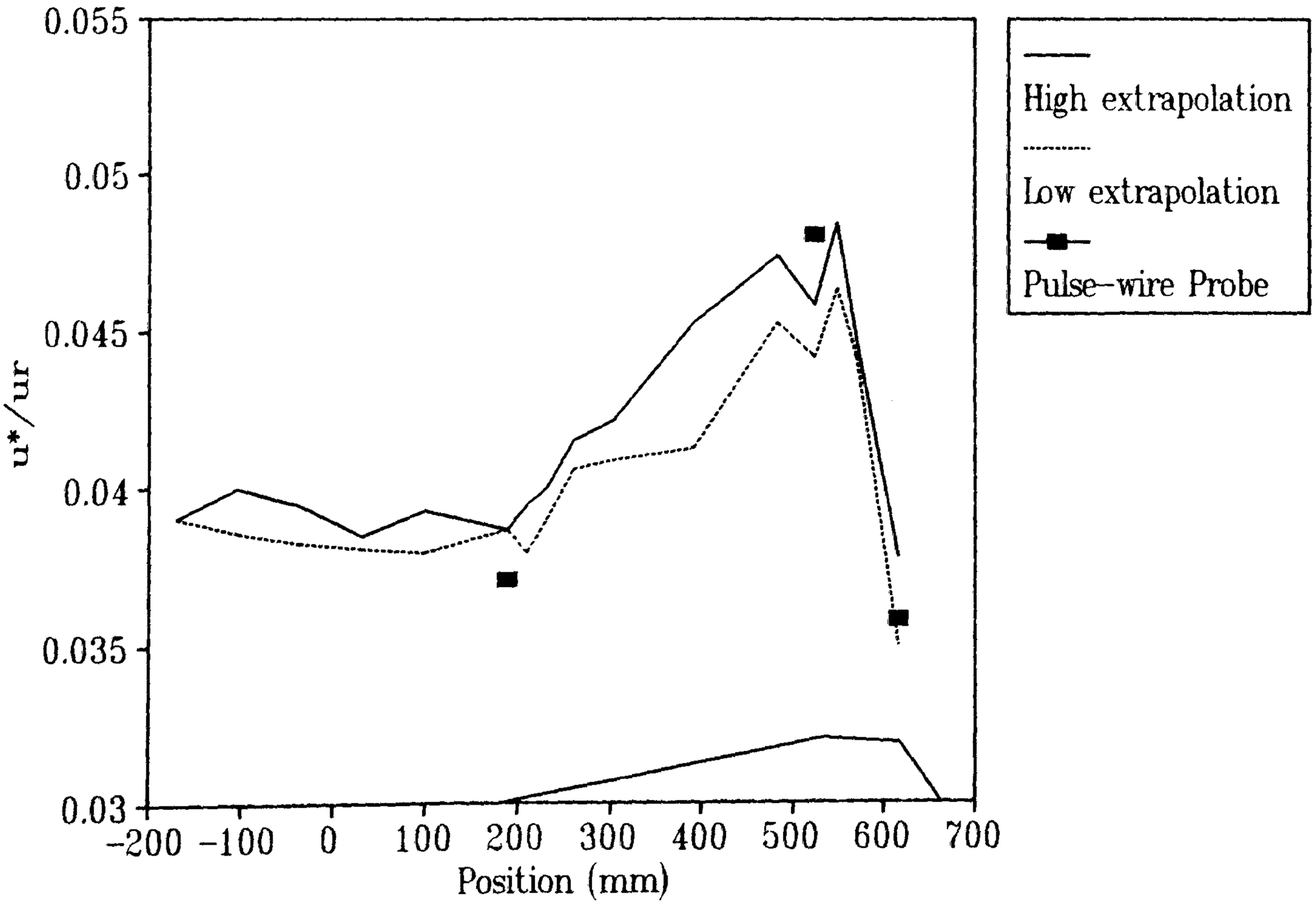

Figure 4.64 Comparison between the pulse-wire probe measurements of shear velocity and that extrapolated from the cross-wire measurements along the right flank of the model dune.

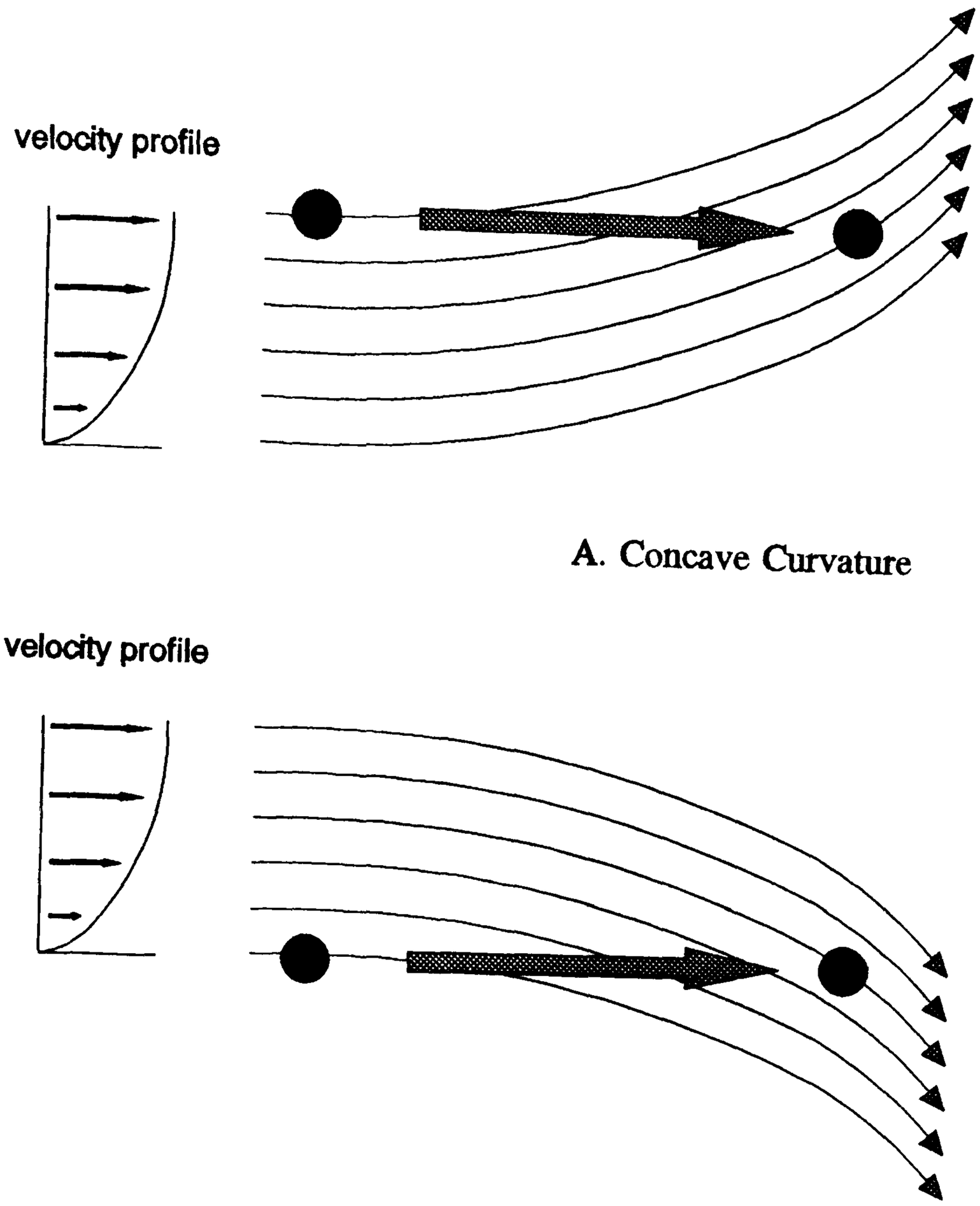

Figure 4.65 Concave (A) and convex (B) streamline curvature. Black circles represent turbulent eddies and their relative movement in the velocity profile is indicated by the arrows.

increase both the wsb and -uwb components of turbulence, whilst convex curvature decreases them. Neither type of curvature has a dramatic effect upon usb as this is controlled more by plane-strain (acceleration) than curvature. Furthermore, the effects of concave curvature take time to influence the airflow structure, whilst those of plane strain and convex curvature are almost immediate. Figures 4.49 and 4.53 show a small phase difference between the peak in usb at the toe, and the peak in -uwb on the right flank of the study dune. The peak in usb is a result of the deceleration of the flow and is almost immediate. In contrast, the later peak in -uwb is a delayed response to the onset of concave curvature. A similar lag between usb and -uwb can also be seen on the left flank (Figures 4.48 and 4.52).

The secondary peaks in -uwb half-way up the windward slope of the flanks were described previously (Chapter 4.3.2). Their existence may be due to the effects of concave curvature and streamwise acceleration acting in concert for a restricted period. Hence, when the positive curvature effects are removed (and convexity prevails) then only the acceleration of flow increases the shearing stress. This results in a small drop in -uwb at the point where the convex curvature takes effect. For example, on the right flank this point is at x = 350 mm (from Figure 4.40c). This corresponds to the point on Figure 4.53 where the small reduction in shear stress begins. It is postulated that no secondary peak is developed along the centre-line (Figure 4.44) because the cessation of concave curvature coincides with an area of maximum flow acceleration. This over-riding of curvature effects by acceleration effects was also found by Mickle *et al.* (1988).

Of particular importance in this discussion is the notion that concave streamline curvature induces an increase in shear stress (-uwb). This suggests that at the toe, instead of a drop in u_* caused by flow deceleration, it may remain steady or even rise because of the positive effects of curvature. The vertical -uwb profiles shown in Figure 4.45 show no evidence of an increase at the toe, but without curvature effects the reduction might be more severe. Furthermore, the most important impact of flow curvature may occur within the inner-surface-layer (see Figure 2.3) which, in the wind tunnel, is of a size of the order of the roughness elements and hence cannot be measured by cross-wire probes, although the pulse-wire probe measurements may lie within this region. This postulated increase in surface shear at the toe of the dune would occur only if the curvature effects dominated the generation of shear stress and if the lag between the onset of curvature and its effects on the shear were small (as has been demonstrated). One may then expect an unstable flow to be exhibited at the toe, increasing surface shear stress in the low velocity zone. The low velocity zone upwind of the dune may also be counter-acted by the effects of concave streamline curvature. As shown in Figure 4.40, the streamline angles

calculated from the cross-wire measurements become positive (indicating concave curvature) at approximately the same upwind point that the approach flow is decelerated.

Evidence in conflict with the arguments above (concerning the effects of streamline curvature) is provided by the development of the wsb component of turbulence on the windward slope of the dune (Figures 4.43, 4.50 and 4.51). Following the arguments of Zeman & Jensen (1987) and Finnigan *et al.* (1990), concave curvature (found in the toe region of the dune) should be associated with an increase in wsb and convex curvature (on the upper windward slope) with a decrease in wsb. However, Figures 4.43, 4.50 and 4.51 show no evidence of this.

The usb and -uwb components of turbulence on the windward slope of the model reflect those of other studies where streamline curvature has been shown to have a significant effect on the structure of the flow (Zeman & Jensen, 1987; Gong & Ibbetson, 1989; Finnigan *et al.*, 1990). The lack of evidence for a significant drop in surface shear stress demonstrated in the present study (Figures 4.62, 4.63 and 4.64) implies that curvature effects are dominating the generation of shear stress in the toe region.

4.5 Relationship of Velocity and Shear Stress Measurements to Terrain Features

It has been suggested (Tsoar, 1985) that the progression of the fractional speed-up ratio closely follows the shape of the dune terrain. Figure 4.66 shows that in the present study the δs on the windward slopes of each of the section lines reflects the dune terrain. The exception to this is at the toe, where deceleration occurs, and near the crest, where there is a tendency for the δs to peak quite sharply. The peak in δs at lower heights on the centre-line (*e.g.* at 1.1 mm in Figure 4.66a) occurs earlier than those at greater height (*e.g.* at 8.1 mm in Figure 4.66b). This may be an extreme reaction to the small positive change in slope angle evident at about x = 420 mm (Figure 4.66a). This relationship becomes clearer in Figure 4.67a which shows δs plotted against the rate-of-change of slope angle ($\delta\theta/\delta x$). The peaks in δs in the crestal region (x = 400 mm to 480 mm) show a close association with the rate-of-change of slope.

By plotting the rate-of-change of the fractional speed-up ratio ($\Delta s/\delta x$) together with the rate-of-change of the slope ($\delta\theta/\delta x$) (Figure 4.68) it is evident that the two are closely tied. In all cases there appears to be a phase difference, with the response of $\Delta s/\delta x$ lagging that of $\delta\theta/\delta x$, particularly at the toe. On the centre-line (Figure 4.68a), $\Delta s/\delta x$ is decreased in the zone of deceleration at the toe, where $\delta\theta/\delta x$ is increasing rapidly. This is followed by an increase in

A.

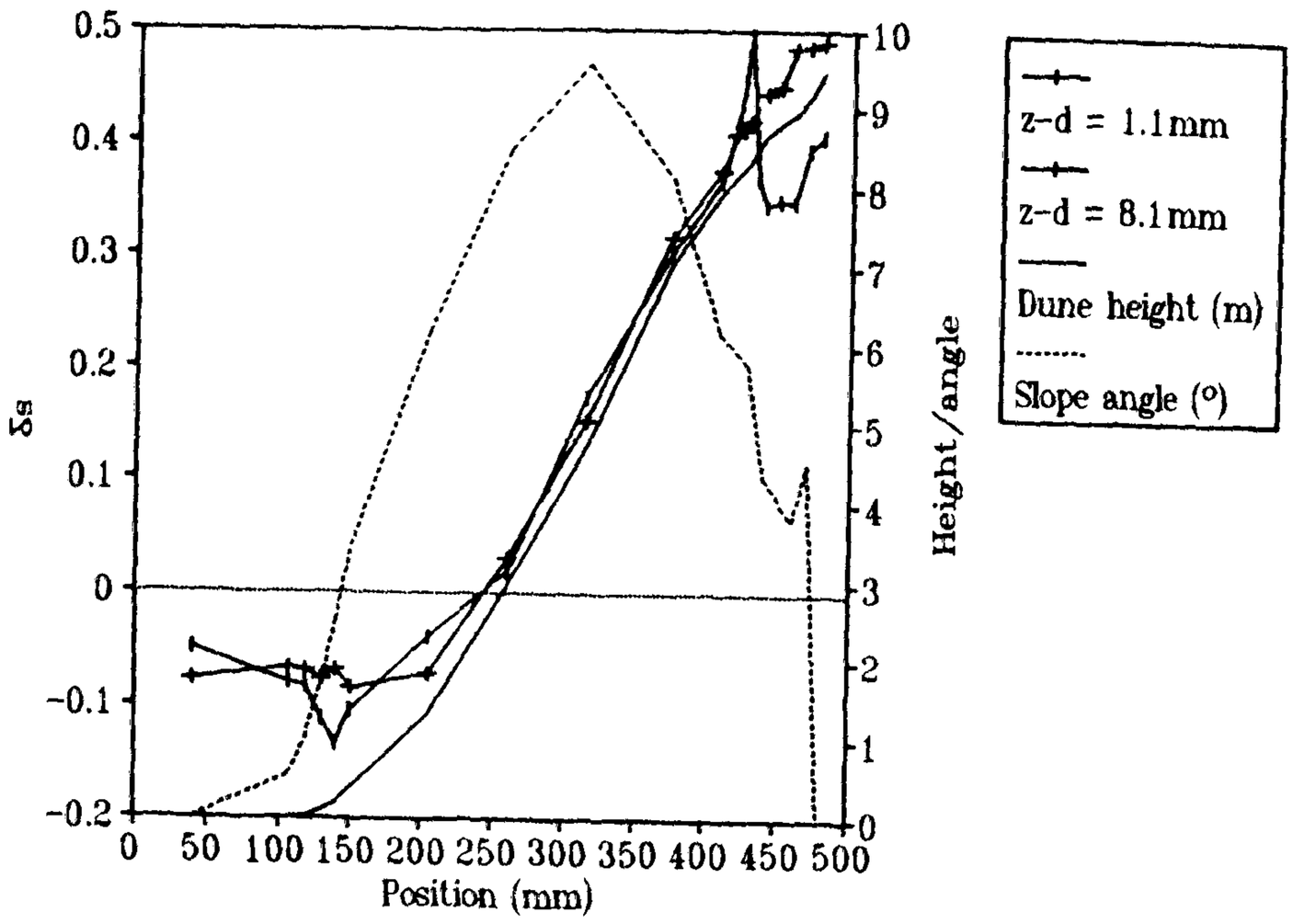

B.

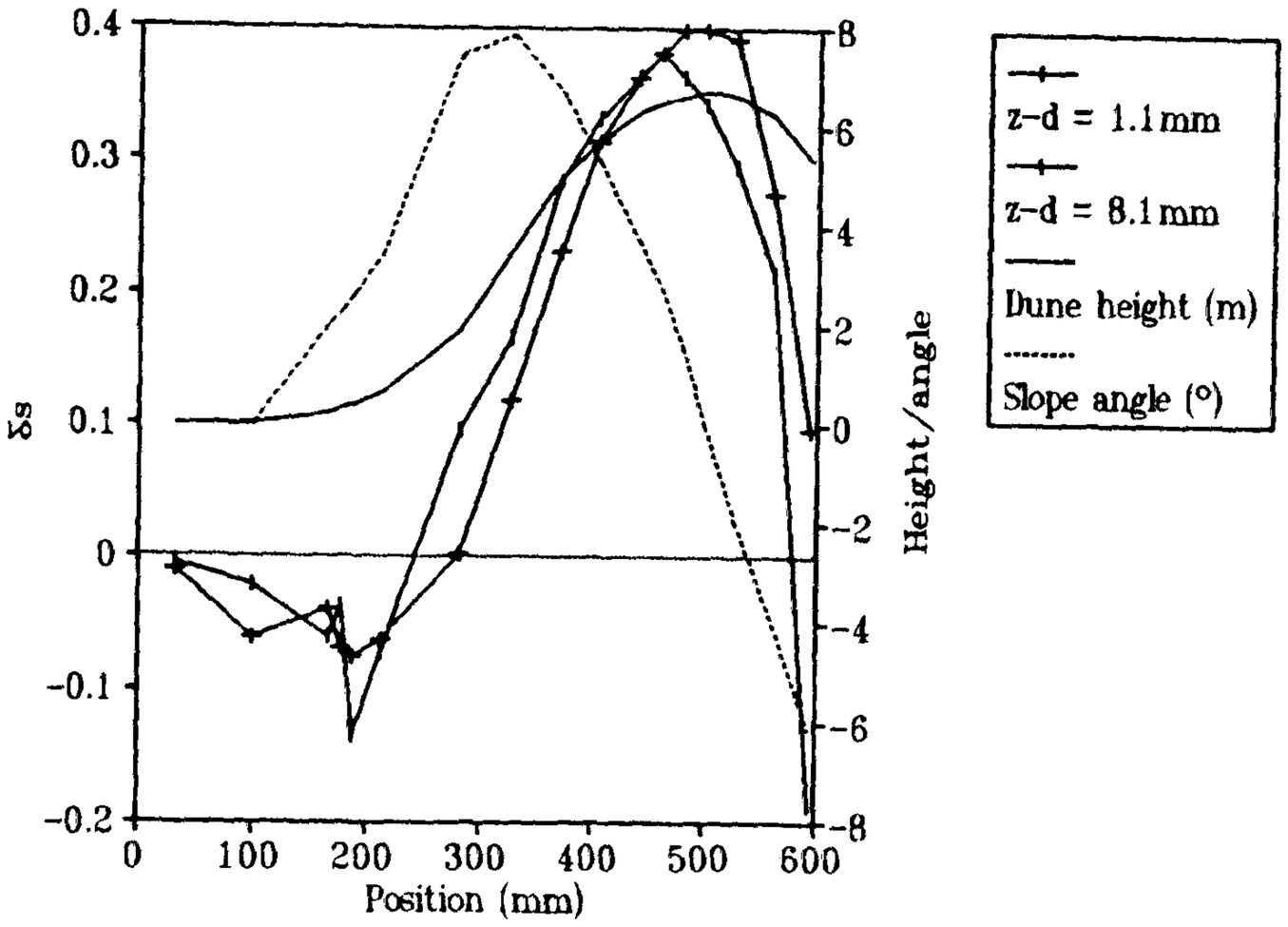

C.

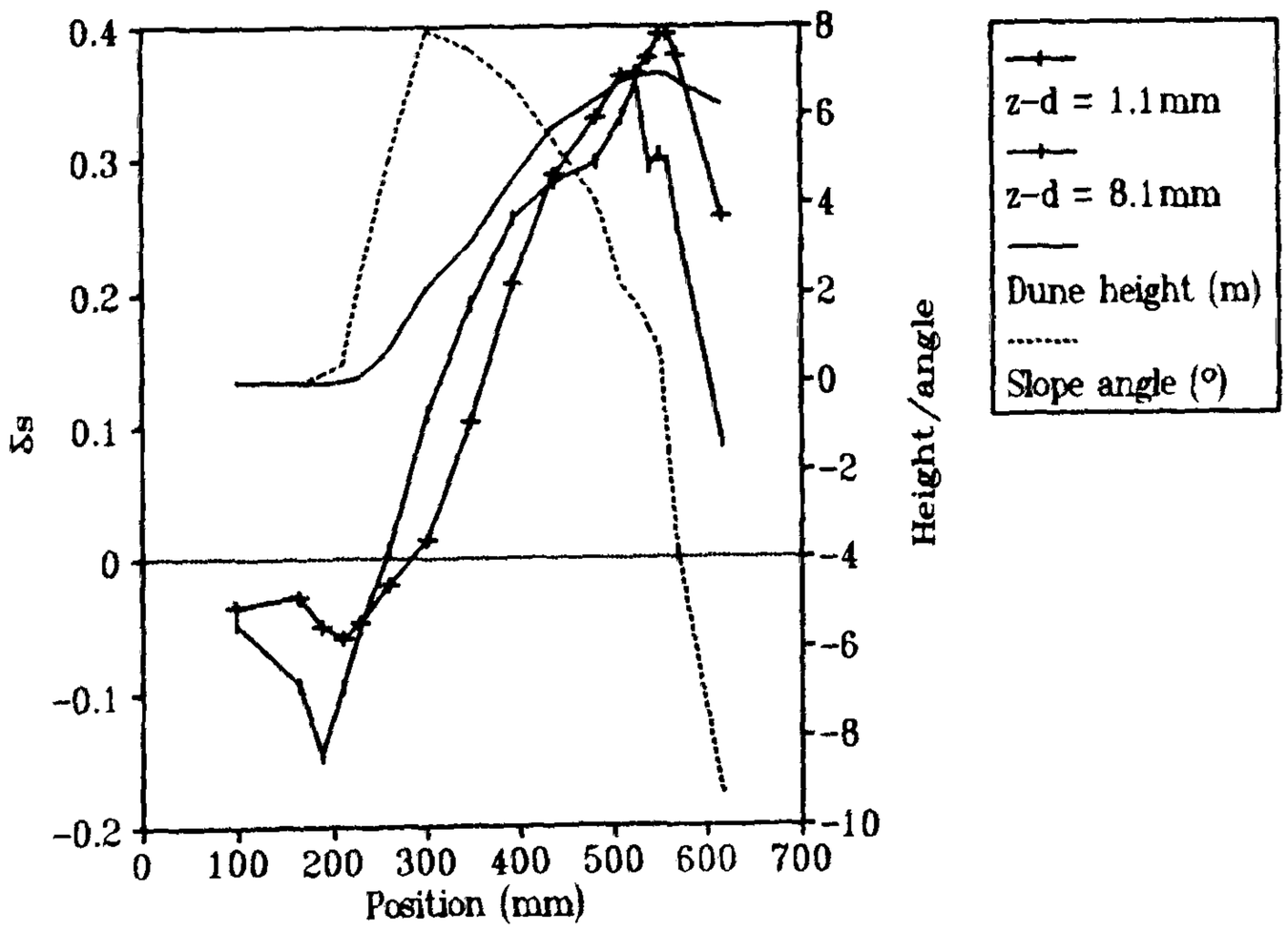

Figure 4.66 Relationship between surface height, slope angle and measured fractional speed-up ratio (δs) along the measurement section lines. A = centre-line; B = left flank; C = right flank.

A.

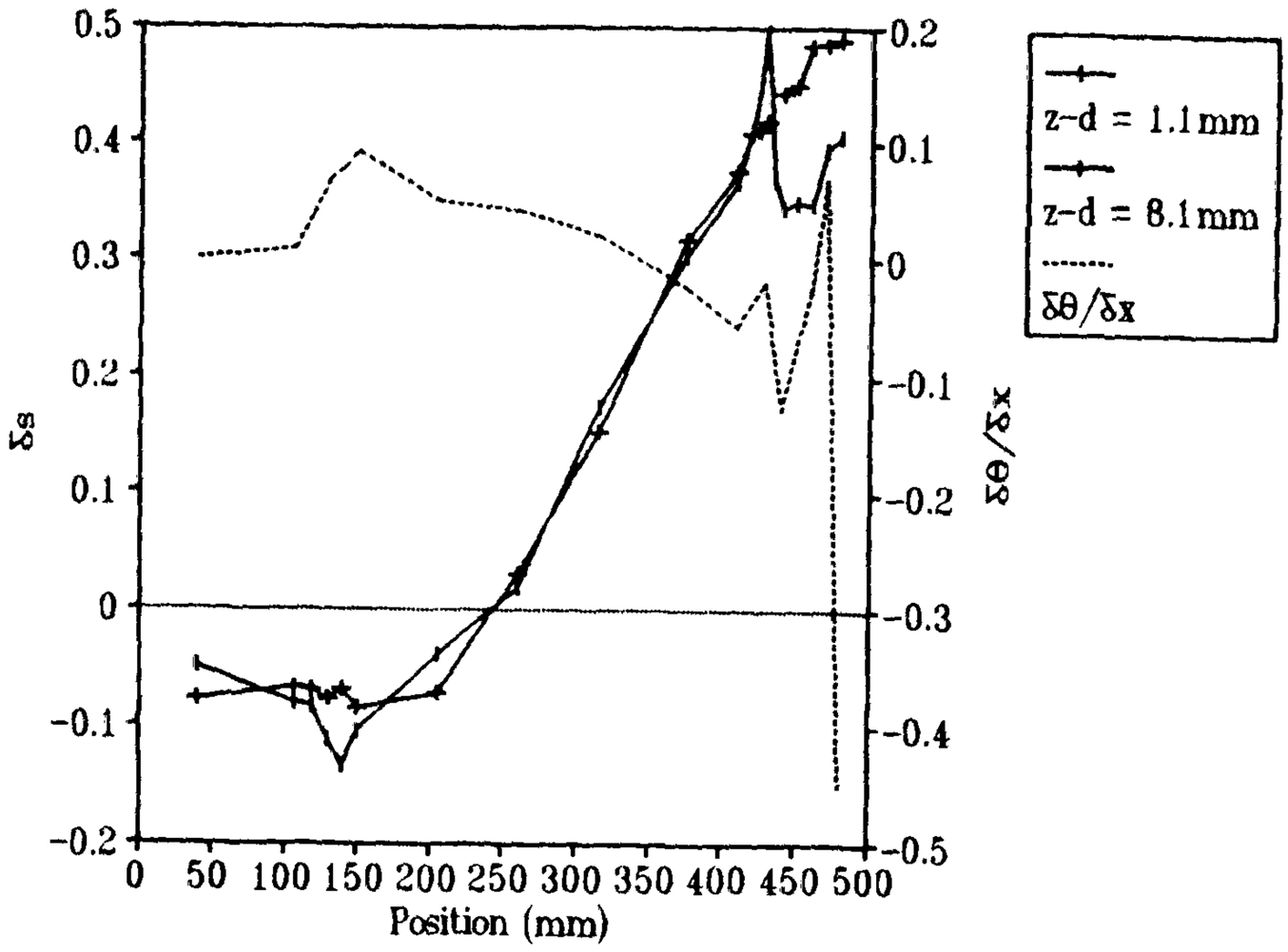

B.

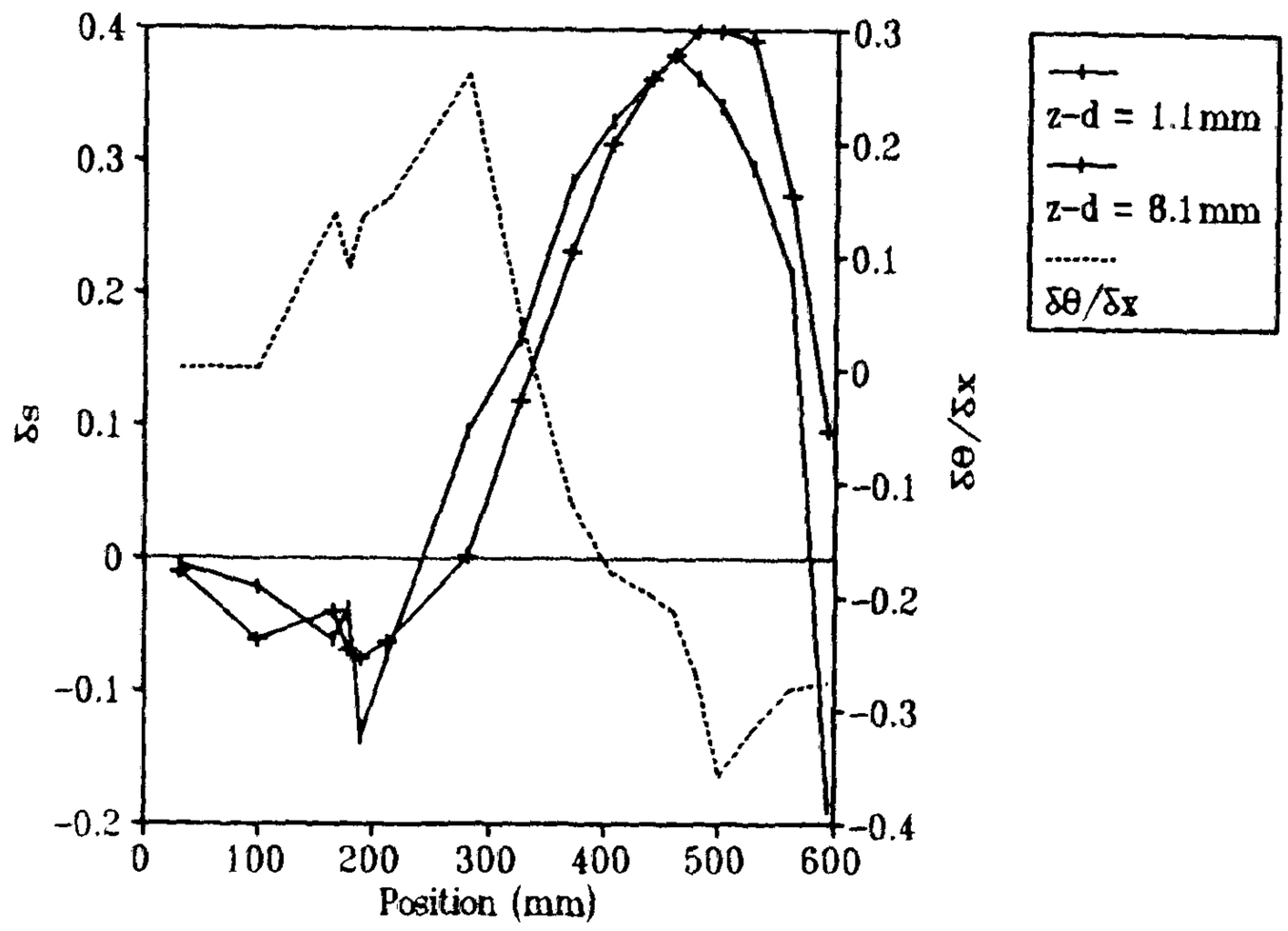

C.

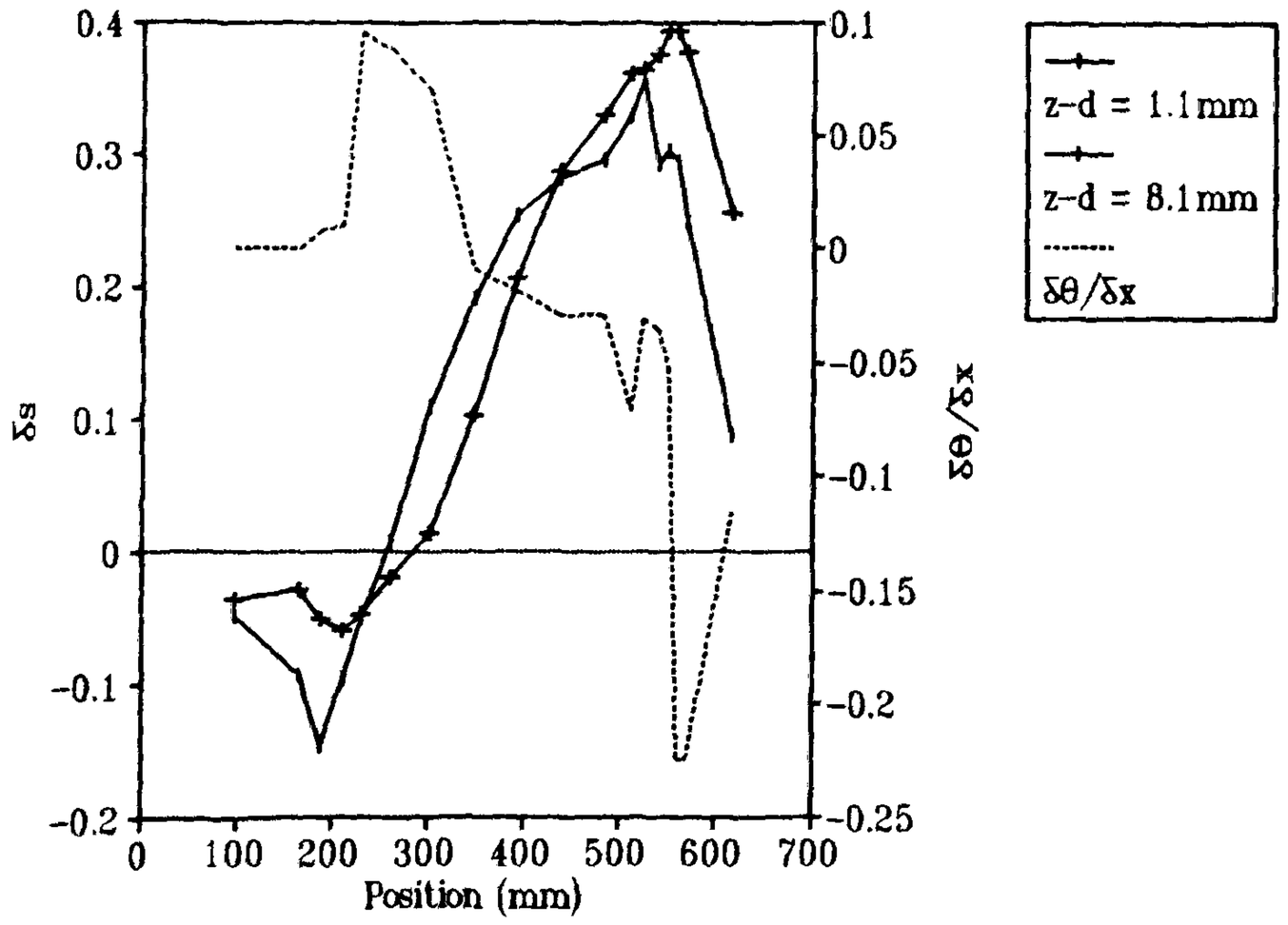

Figure 4.67 Relationship between surface height, rate-of-change of slope angle ($\delta\theta/\delta x$) and measured fractional speed-up ratio (δs) along the measurement section lines. A = centre-line; B = left flank; C = right flank.

A.

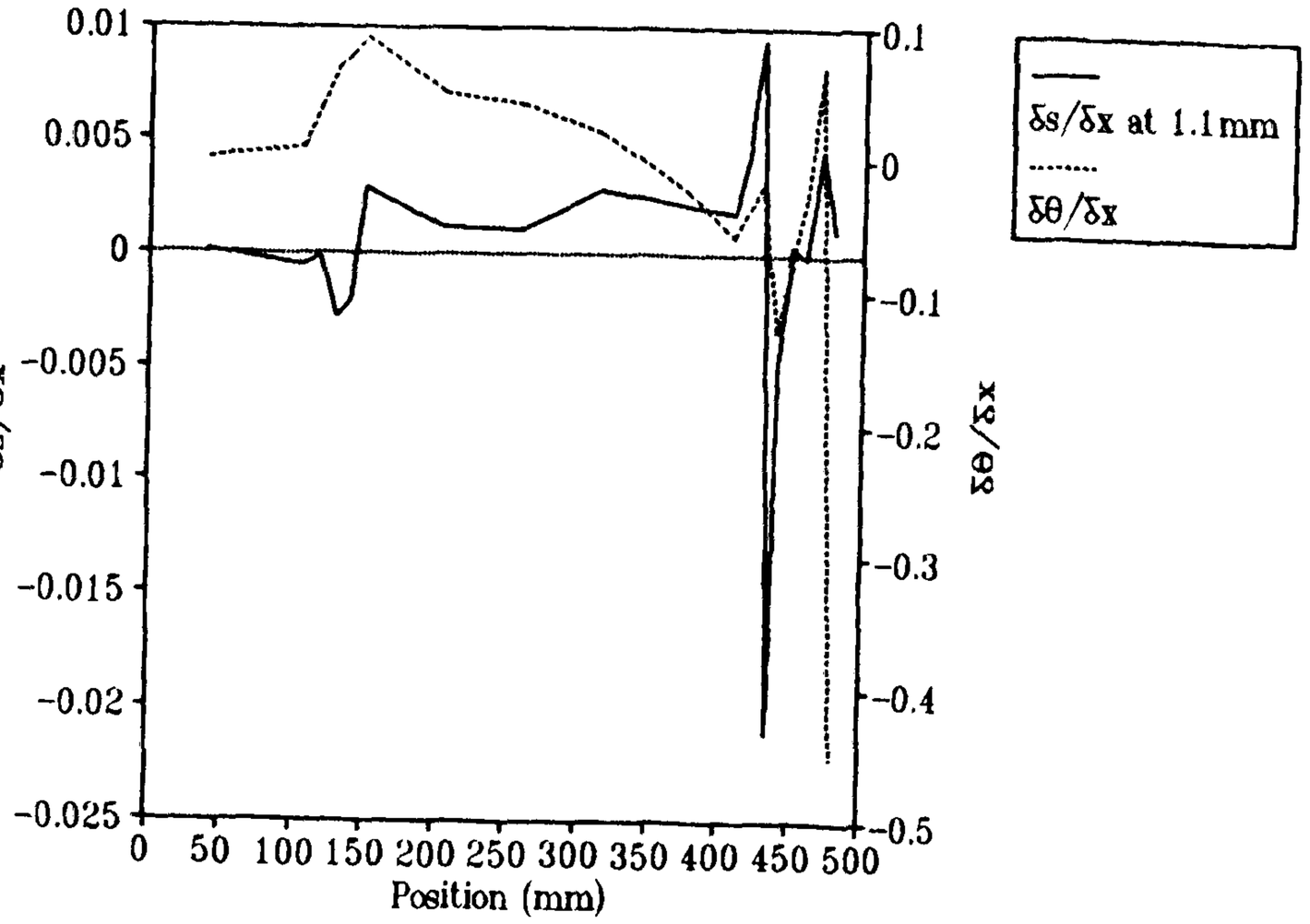

B.

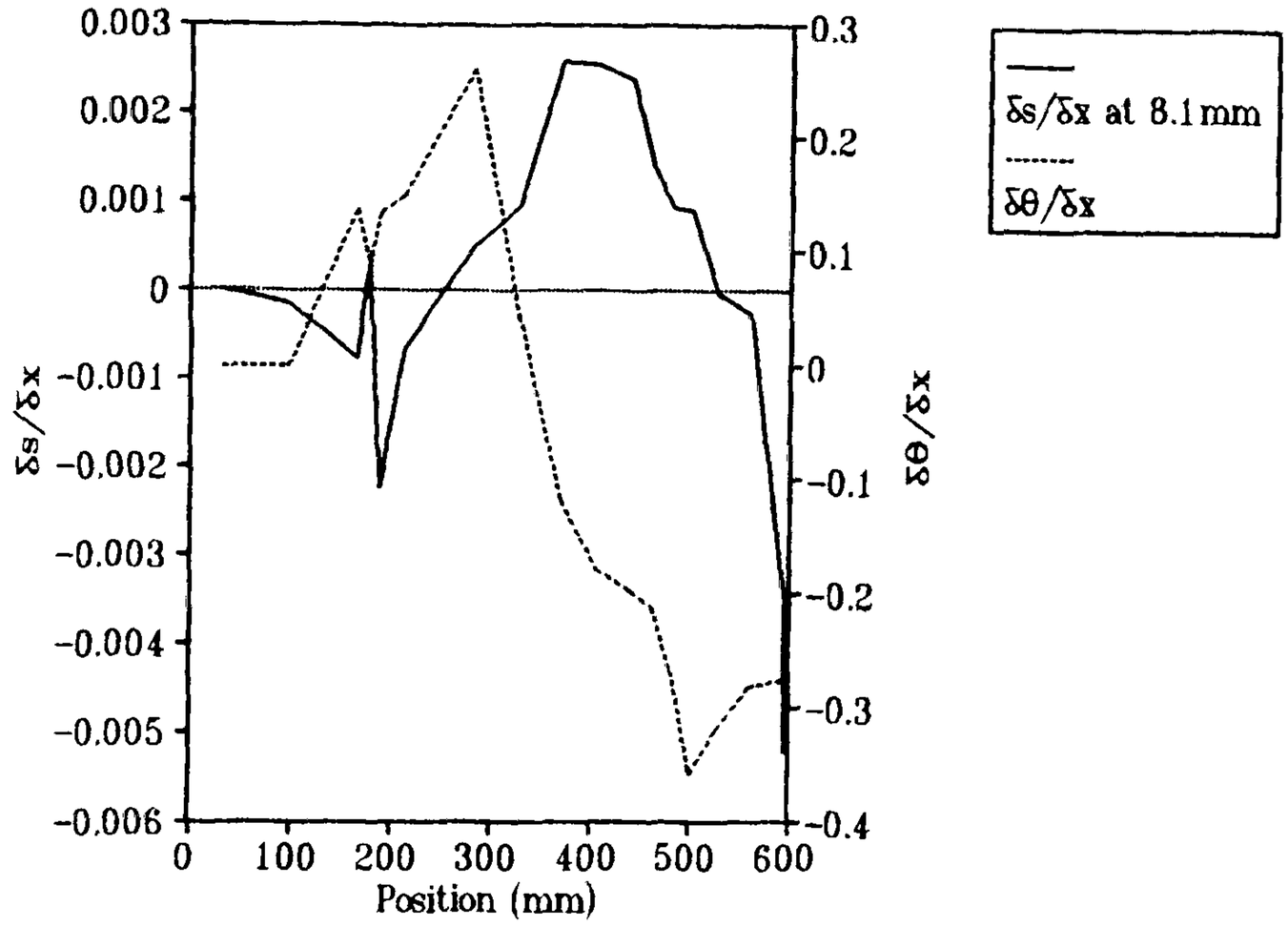

C.

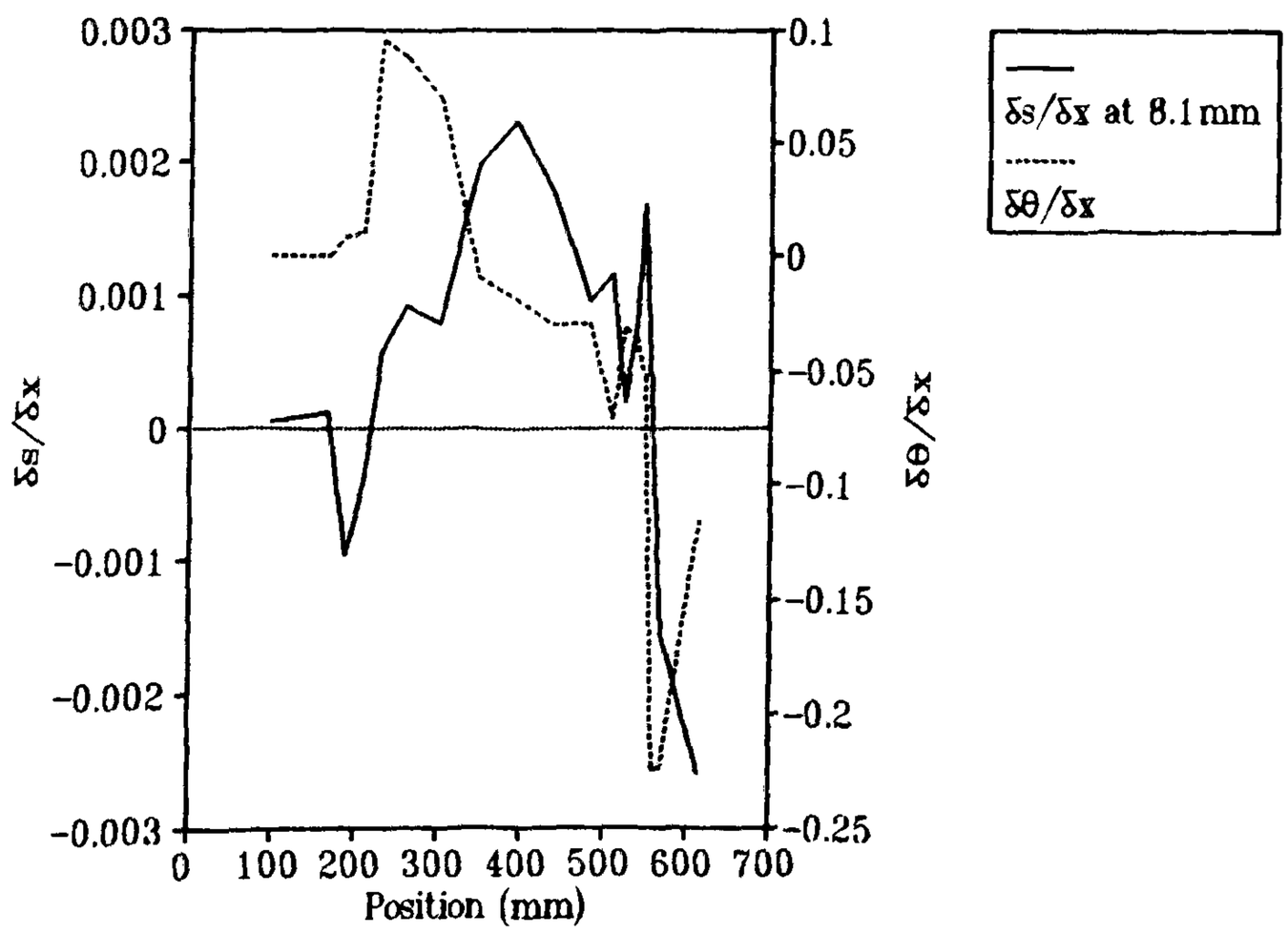

Figure 4.68 Relationship between surface height, rate-of-change of slope angle ($\delta\theta/\delta x$) and rate-of-change of fractional speed-up ratio ($\delta s/\delta x$) along the measurement section lines. A = centre-line; B = left flank; C = right flank.

$\Delta s/\delta x$, coinciding with a peak in $\delta\theta/\delta x$ at x = 150 mm. Up to x = 400 mm $\Delta s/\delta x$ is fairly constant, despite a reducing $\delta\theta/\delta x$. It is also within this region that the shape of the dune changes from concave to convex (*i.e.* $\delta\theta/\delta x$ becomes negative). Once the dune shape becomes convex then $\Delta s/\delta x$ appears to be more sensitive to changes in $\delta\theta/\delta x$. This is shown by the sharp increases and decreases in the rate-of-change of the fractional speed-up ratio between x = 400 to 480 mm (Figure 4.68a), despite only small changes in $\delta\theta/\delta x$. This increased sensitivity in the convex part of the slope is not exhibited on the left flank (Figure 4.68b) but is evident on the right flank (Figure 4.68c).

Also shown in Figure 4.68b and c is that the maximum rate-of-change of speed-up occurs where $\delta\theta/\delta x$ becomes negative (*i.e.* when the slope changes from concave to convex at its steepest part). This agrees with previous studies (Nørstrud, 1982; Walmsley *et al.*, 1982; Tsoar, 1985) which found a decline in the rate of increase of speed-up on convex hills, and an accelerated rate of increase on concave hills (Pearse *et al.*, 1981). The fact that such a relationship is not exhibited along the centre-line is probably because the effect is swamped in scale by the peak due to the sudden increase in $\delta\theta/\delta x$ at x = 420 mm (Note the differences in scale on the primary y-axes in Figure 4.68a, b and c).

The development of the rate-of-change of surface shear velocity ($\Delta u_*/\delta x$) to the shape of the dune is somewhat different. Figure 4.69 shows $\Delta u_*/\delta x$ derived from the cross-wire measurements, plotted with the dune height and slope angle on each of the section lines. For clear presentation, only the high extrapolation of surface shear velocity has been used here. The low extrapolation exhibited similar relationships.

The centre-line and right flank (Figure 4.69a and b) both indicate a peak in $\Delta u_*/\delta x$ at, or close to, the crest in each case. In contrast, the left flank (Figure 4.69c) shows a peak at the point of maximum slope angle. The differences in the scale of the primary y-axis of the three graphs should be noted. The contrast found between the left flank and the centre-line and right flank may stem from the substantial contrast in $\delta\theta/\delta x$. The rates-of-change of slope on the left flank are much more severe, particularly in the concave region immediately downwind of the toe (Figure 4.69). This sudden increase in the rate-of-change of slope may precipitate an earlier peak in the rate-of-change of shear stress.

Plotting the rate-of-change of slope ($\delta\theta/\delta x$) with $\Delta u_*/\delta x$ (Figure 4.70) reveals a close relationship between the two. The left flank (Figure 4.70b) shows a lag between the peak in

A.

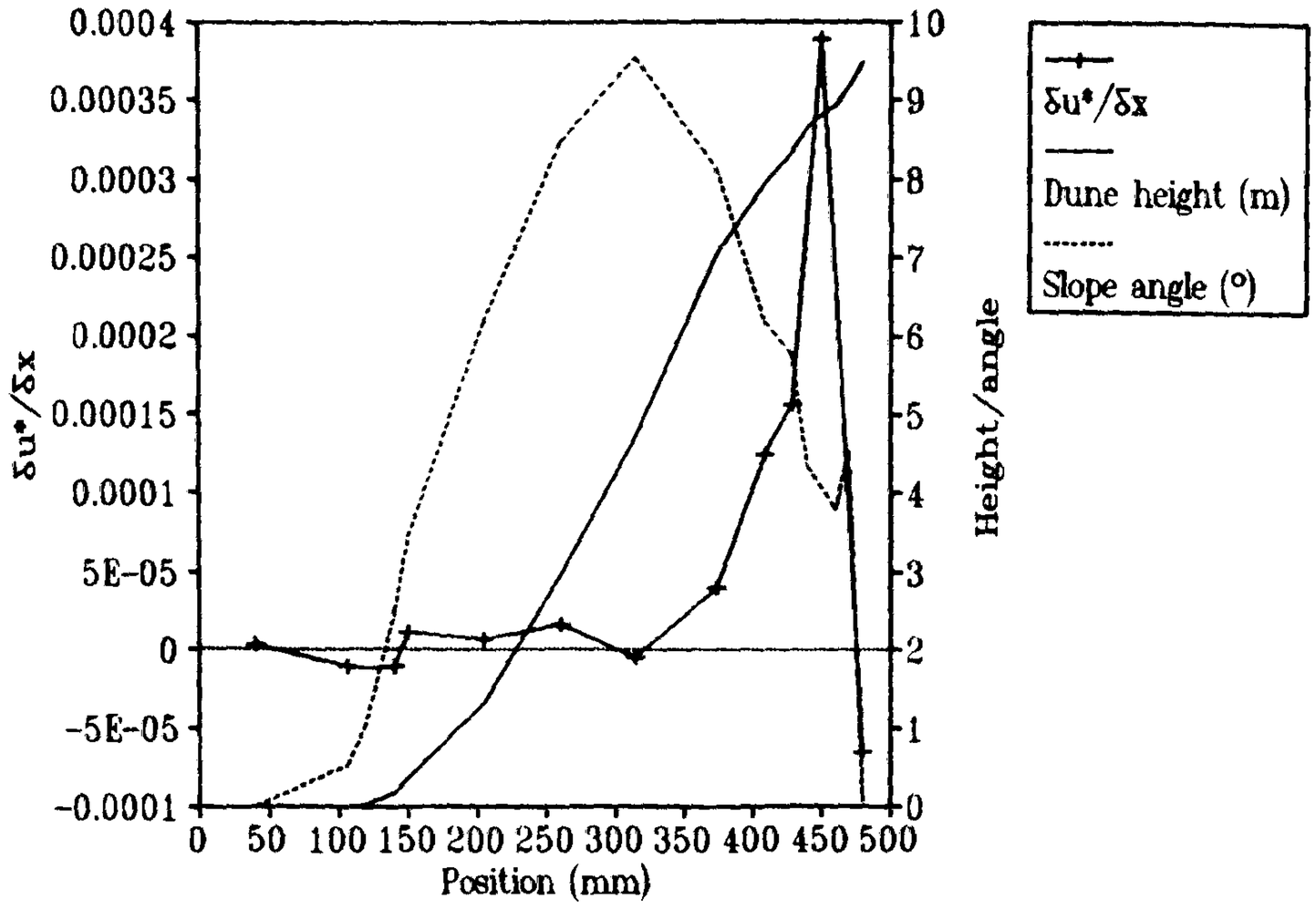

B.

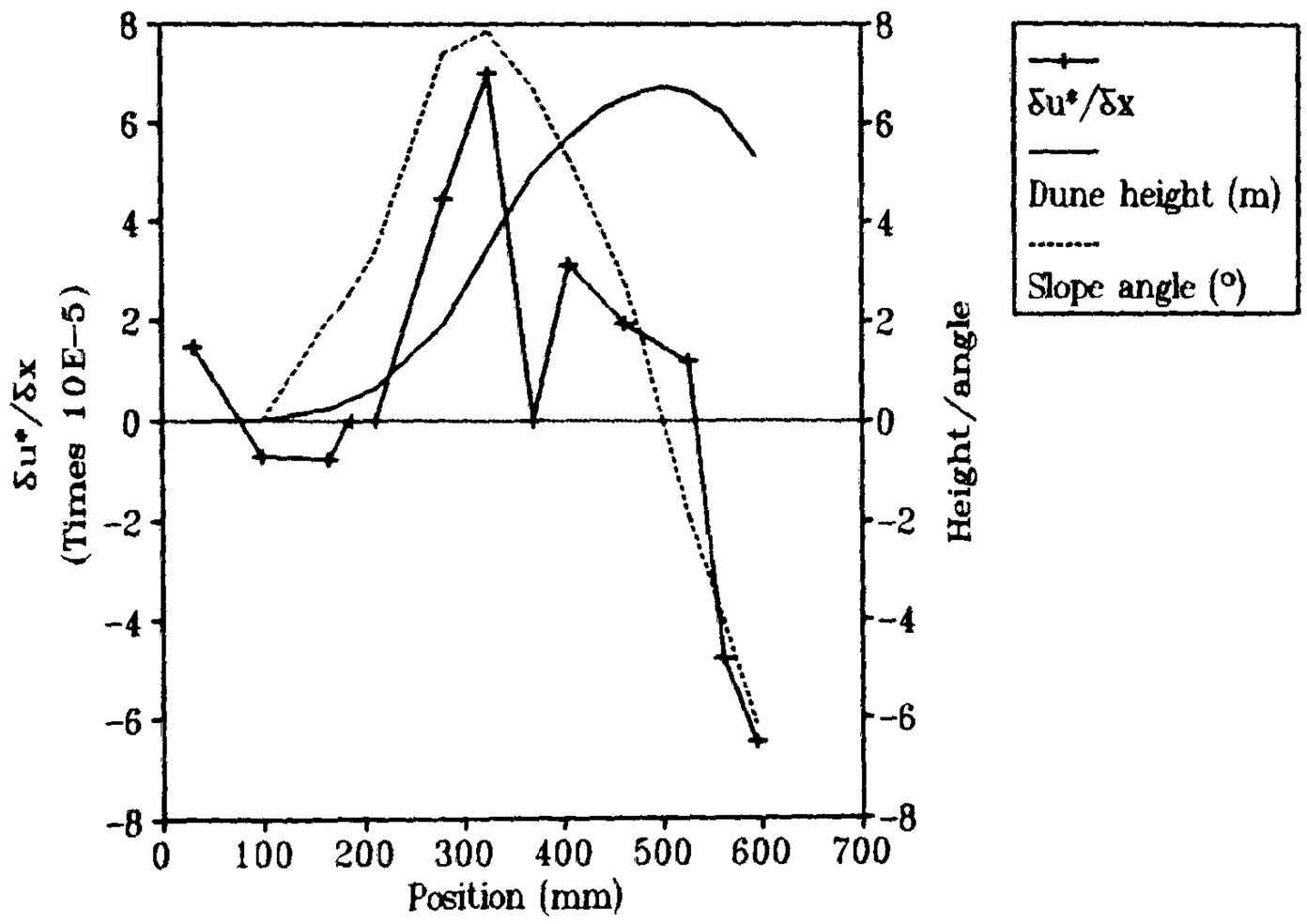

C.

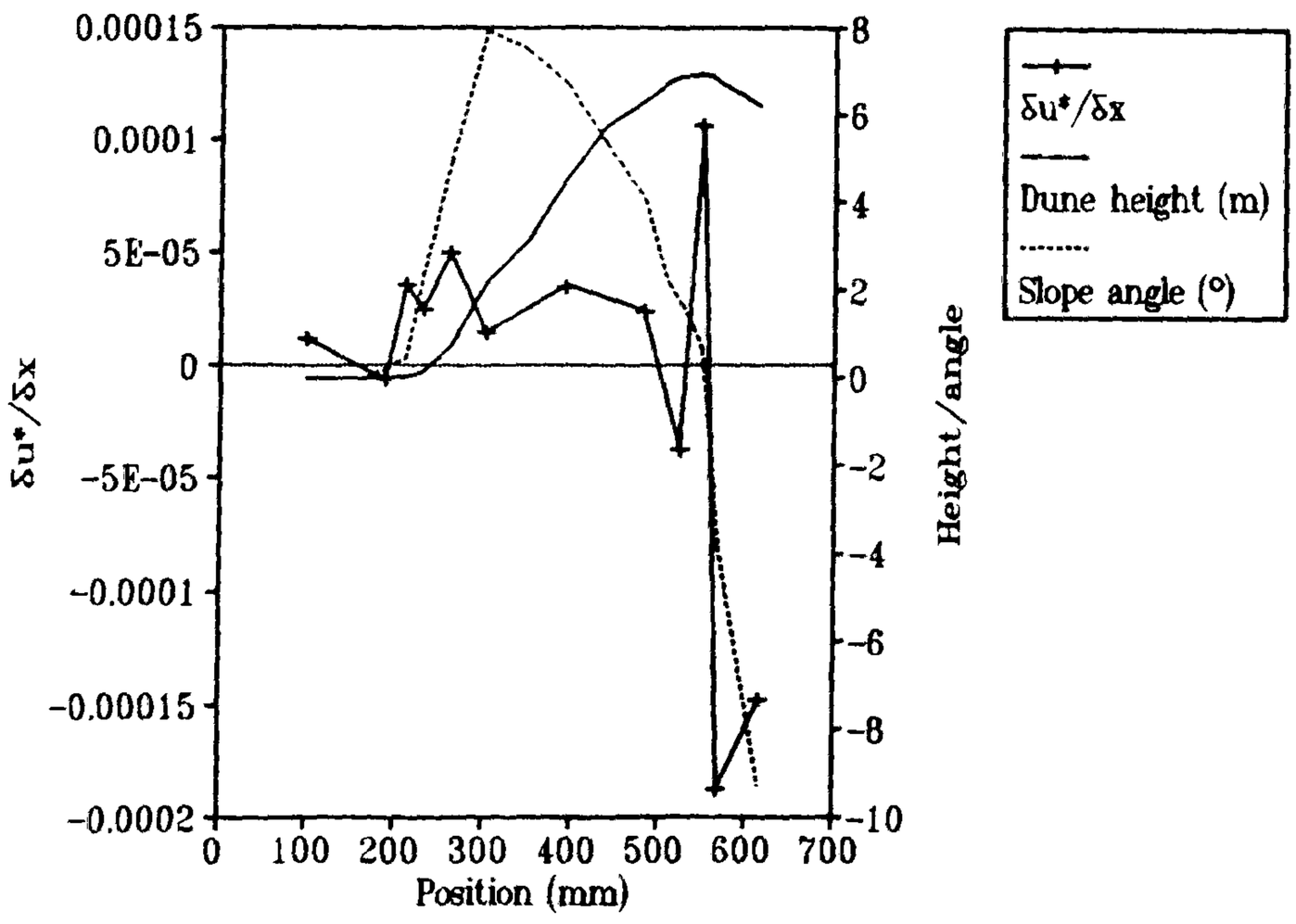

Figure 4.69 Relationship between surface height, slope angle and rate-of-change of surface shear velocity ($\delta u_*/\delta x$) along the measurement section lines. A = centre-line; B = left flank; C = right flank.

A.

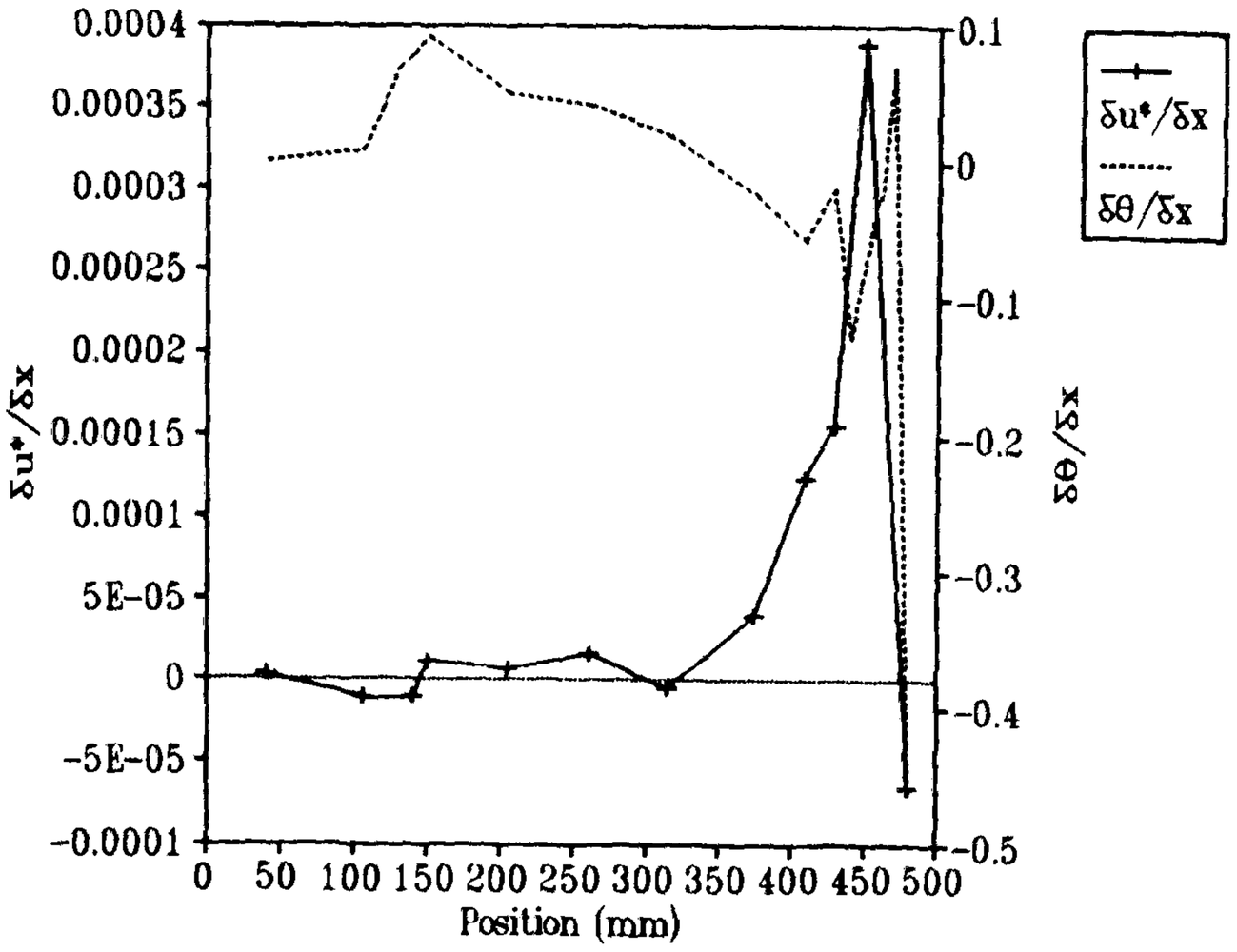

B.

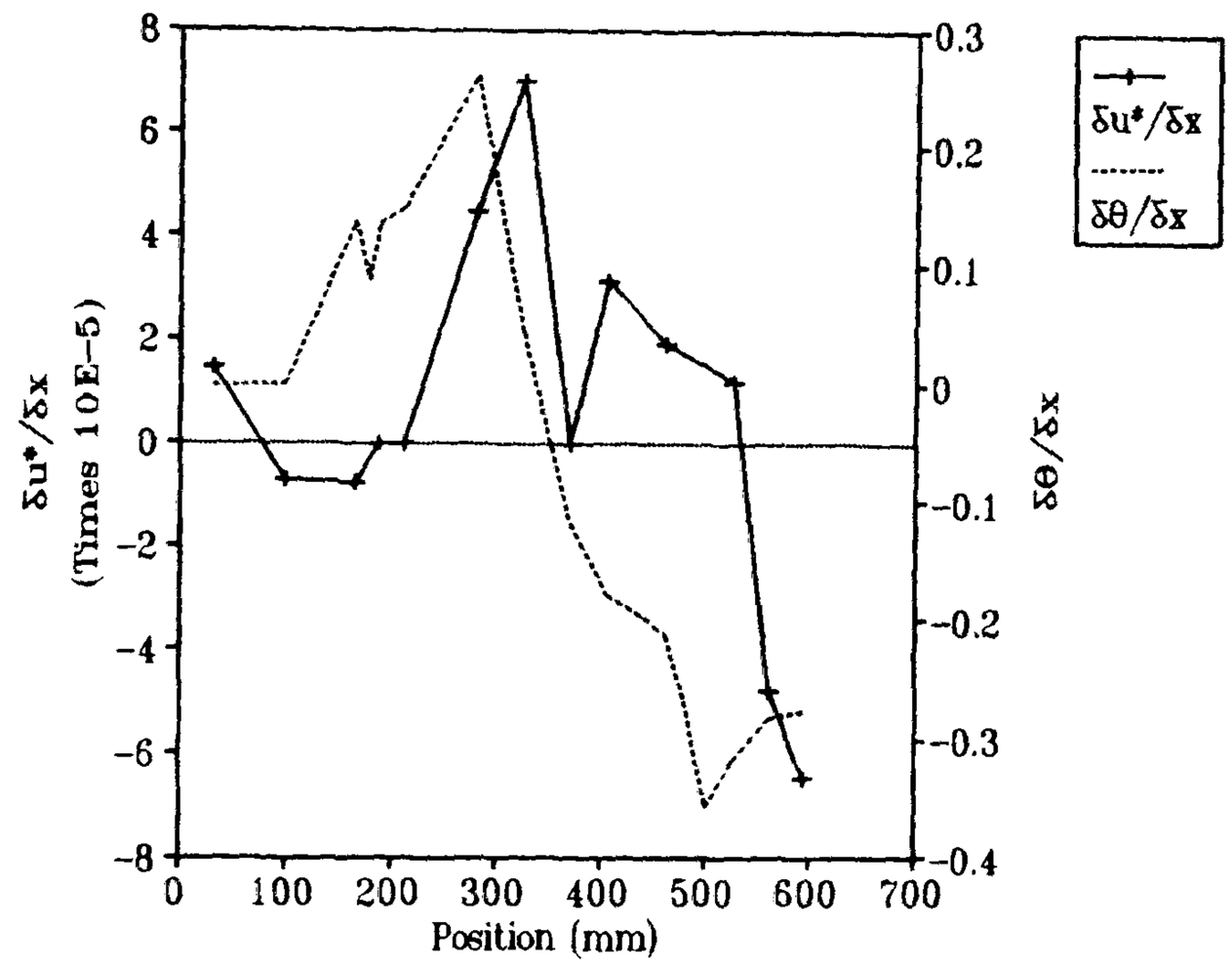

C.

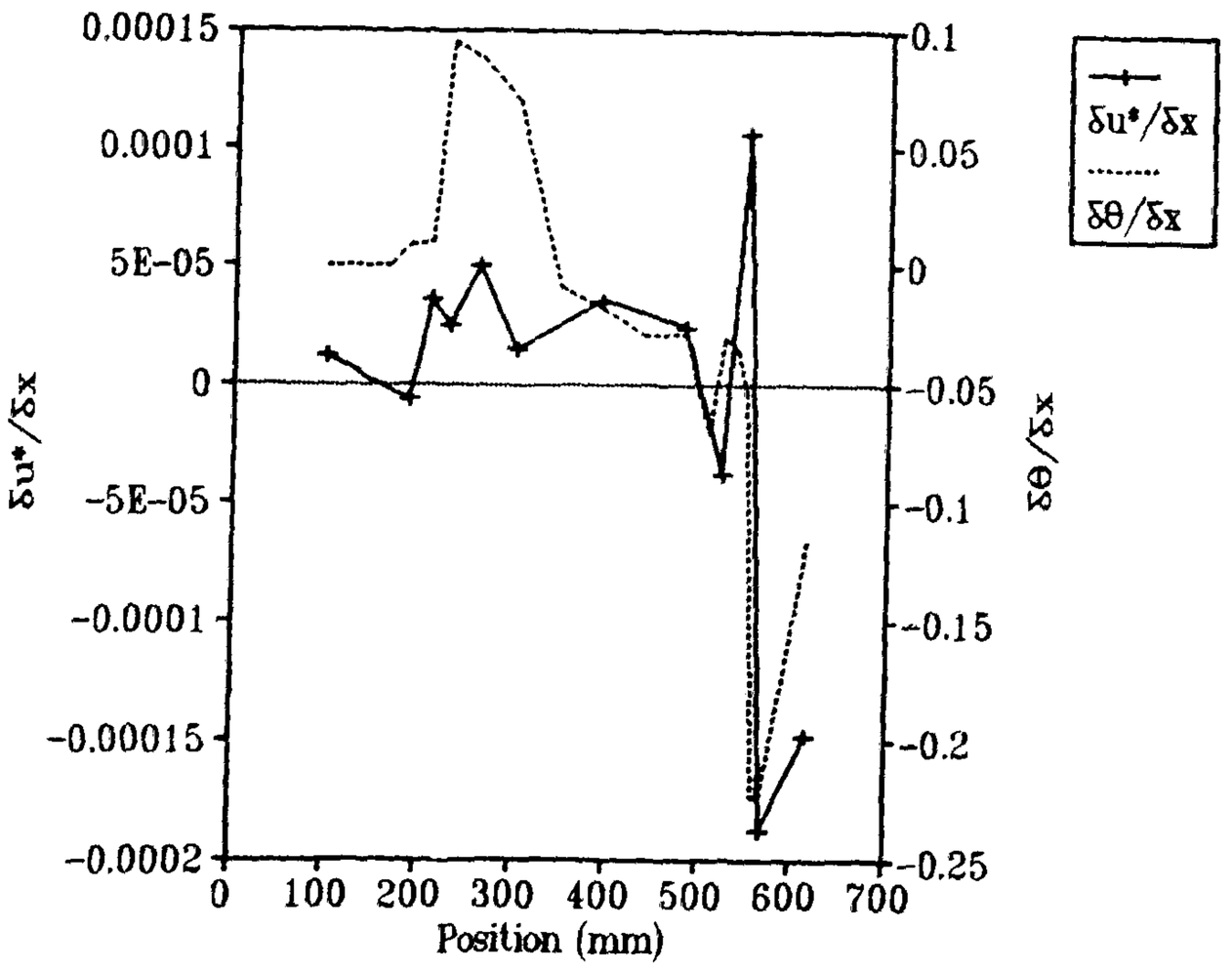

Figure 4.70 Relationship between surface height, rate-of-change of slope angle ($\delta\theta/\delta x$) and rate-of-change of surface shear velocity ($\delta u_*/\delta x$) along the measurement section lines. A = centre-line; B = left flank; C = right flank.

$\delta\theta/\delta x$ and that of $\Delta u_*/\delta x$. A similar magnitude rise in $\Delta u_*/\delta x$ just after the peak of $\delta\theta/\delta x$ is shown on the right flank (Figure 4.70c), but the peak in $\Delta u_*/\delta x$ occurs much later in the convex region of slope in response to a sudden change in $\delta\theta/\delta x$, where x = 520 mm. The centre-line (Figure 4.70a) also shows a rise in $\Delta u_*/\delta x$ near the peak in $\delta\theta/\delta x$, but as for the right flank, the maximum $\Delta u_*/\delta x$ occurs in the convex region of slope in response to the same change in slope as effected the speed-up ratio. It should be noted that the maximum $\Delta u_*/\delta x$ on the centre-line is considerably greater than that on either of the flanks.

A comparison of the rate-of-change of surface shear velocity derived from the pulse-wire probe ($\Delta u_{*_1}/\delta x$) with the surface slope angle is shown in Figure 4.71. A close association can be seen with the maximum values of $\Delta u_{*_1}/\delta x$ coinciding with the region of maximum slope angle. This relationship is in contrast to that described for the centre-line cross-wire measurements (Figure 4.69a), although it is in close agreement to the relationship found on the left flank (Figure 4.69c).

A complex relationship exists between the height of the dune and the rates-of-change of velocity, shear velocity and slope. However, it appears that the dune can be divided into two surface regions. The downslope concave zone, and the upslope convex zone. The trends of the rate-of-change of the fractional speed-up ratio ($\Delta s/\delta x$) and the surface shear velocity ($\Delta u_*/\delta x$) are fairly similar in each of the zones. Both parameters increase in the concave zone, possibly to peak at the point of change between the concave and convex zones, although they show some streamwise lag from the point of maximum rate-of-change of slope ($\delta\theta/\delta x$). Similar results have been described by Zeman & Jensen (1987) who noted the largest enhancement in -uwb on the upwind slope of a hill at the point where curvature changed from concave to convex, a result of the accumulation of concave effects from upstream. Once entering the convex zone in the present study, the rates-of-change of both velocity and shear velocity become susceptible to even small rates-of-change in slope. The peak in both parameters may then occur in the convex zone in response to these abrupt rates-of-change of slope.

4.6 Conclusion

The velocity and turbulence components measured along three section lines of the dune compare favourably with results from previous studies over low hills. By not strictly regarding the necessity for a fully-rough boundary layer, measurements have been possible within the turbulent inner-layer.

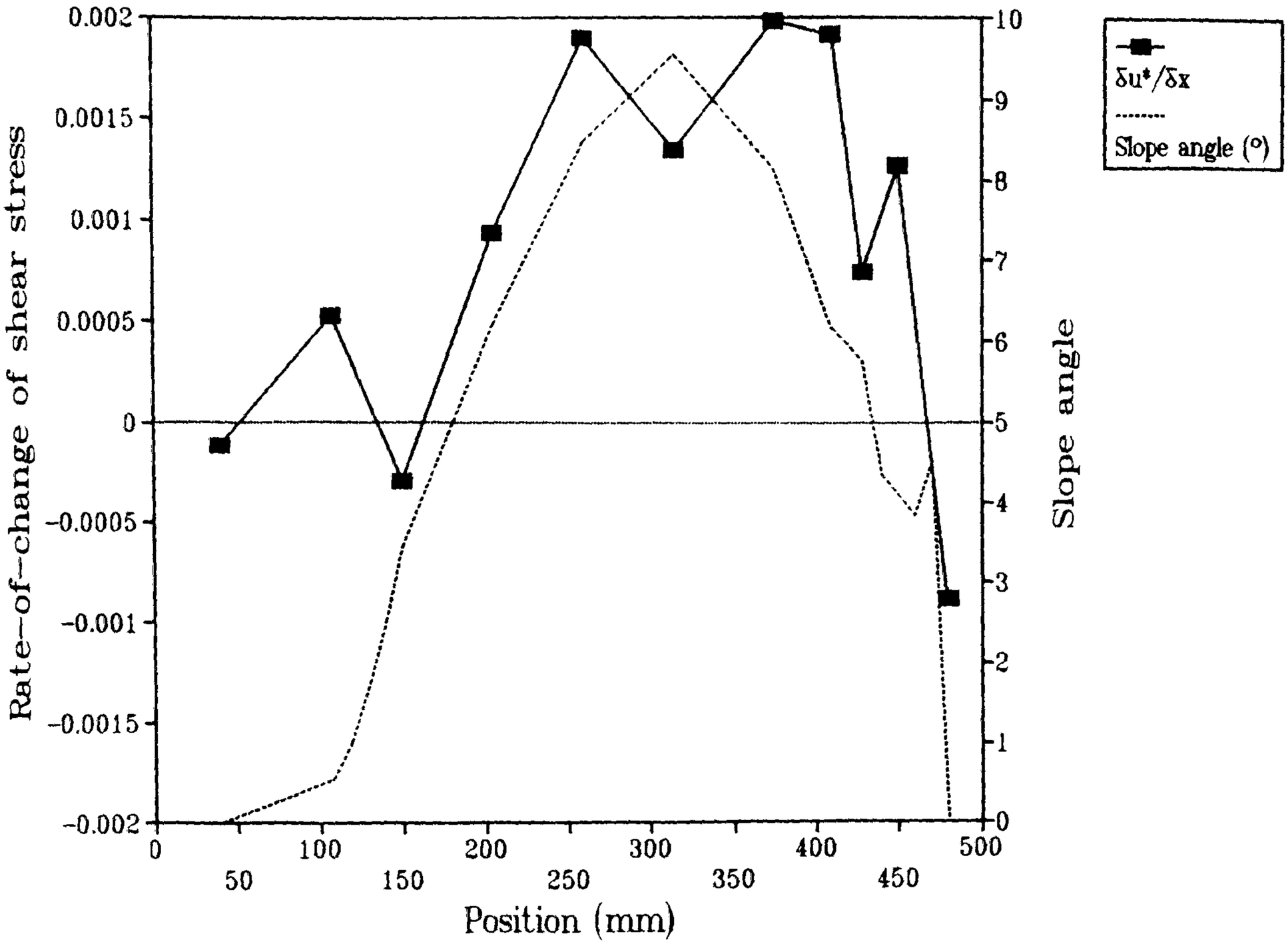

Figure 4.71 Relationship between slope angle and rate-of-change of surface shear velocity ($\delta u_{*_1}/\delta x$) measured by the pulse-wire probe along the centre-line of the model dune.

Surface flow direction measurements revealed similar results to the field and mathematical modelling results. Flow divergence existed at the base of the windward slope on the flanks and a small degree of convergence was noted at the brink. Fractional speed-up ratios show a reduction in velocity at the toe of the dune and an increase toward the crest. In crest-brink separated regions on the flanks, large areas of turbulence and momentum deficit exist, dramatically reducing the velocity.

Derivations of surface shear velocity from cross-wire measurements, and measurements with a near-wall pulse-wire sensor were carried out along all three section lines. They displayed an increase in surface shear stress from the toe to a peak at the crest, with a reduction toward the brink. No significant reduction in surface shear velocity was recognised at the toe. A heuristic explanation for this was presented involving the instability of the airflow in the toe region caused by streamline curvature.

The complex relationship between the height of the dune and the rates-of-change of velocity, shear stress and slope was discussed. It appeared that an important point on the surface was where the slope trend changed from concave to convex, precipitating peaks in both rates-of-change of velocity and shear velocity. The maximum values of the two parameters may occur later in the convex region of the dune if large rates-of-change of slope are encountered.

CHAPTER 5 TECHNIQUE COMPARISON

5.1 Introduction

Chapters 2, 3 and 4 showed that the results of the field measurement, mathematical modelling and wind tunnel modelling gathered in the present study were reasonably consistent with results from investigations of airflow over low hills and sand dunes. It is the purpose of this Chapter to compare the results gained from the three techniques used in the present study.

The discussion presented in this Chapter focuses on the detailed comparisons of the flow field parameters (*i.e.* velocity, shear velocity and shear stress) between the field, mathematical modelling and wind tunnel techniques. This approach is comparable to that common in the engineering investigations of flow over low hills where comparisons are made between field-measured and mathematical or wind tunnel-modelled data (Bradley, 1980; Britter *et al.*, 1981; Mason & King, 1985; Finnigan *et al.*, 1990). The approach is in contrast to that preferred in the geomorphological studies of sand dune dynamics Howard *et al.*, 1977; Tsoar, 1985; Wippermann & Gross, 1986). These geomorphological investigations rely more on comparisons between measured surface change on a study dune and that predicted by the airflow assessments from either mathematical or wind tunnel modelling. The latter approach is the logical conclusion for the geomorphological based studies for it is the modification of the dune's form which is of interest. However, such an approach constrains analysis because it inhibits a detailed investigation of the airflow structure which is responsible for the morphological modifications. The advantage of the latter approach, however, is that predictions of morphological change can be compared with measured change, which is easily assessed in the field and entails little error. This is not the case where comparisons between airflow parameters are undertaken because field measurements of these parameters also include a substantial degree of error (see Chapter 2). For this reason, Chapter 7 is concerned with the comparisons between measured surface change in the field and that predicted by the field evaluation, mathematical modelling and wind tunnel modelling.

Consideration should be made of how best to compare the measured and predicted airflow parameters. Engineering investigations of flow over hills consider agreement between measured and predicted numerical values to be "good" if they are within about ±20% of each other (Britter *et al.*, 1981; Walmsley *et al.*, 1982; Teunissen *et al.*, 1987; Weng *et al.*, 1991). Although further consideration is also given to general trends and tendencies. Similar levels of comparability were also utilised by Tsoar (1985) who noted only similarities in trends. A different approach was

used by Howard *et al.* (1977) and Howard & Walmsley (1985). Howard and Walmsley used correlation coefficients to determine the association between measured and predicted values and Howard *et al.* employed a detailed statistical examination of the bias, variance and correlation between predicted and measured dune surface change. A similar approach to this statistical analysis is carried out in the present study in Chapter 7, where a nominal set of conditions (*i.e.* the measured values of surface change) is available against which predictions can be compared. In the comparisons of the airflow parameters undertaken in this Chapter only correlations (to determine trend associations) and brief statistical descriptions (*e.g.* mean and standard deviations) are presented. This is because the errors and uncertainties involved in the field evaluations of the airflow parameters (particularly shear stress) reduce their competence as nominal 'right-answers' against which predictions from the other techniques can be statistically tested.

5.2 Velocity Relationships

5.2.1 The Centre-line

Figures 5.1 to 5.4 show the variations in fractional speed-up ratio along the centre-line of the dune obtained from each of the techniques at four different heights. For the purposes of this comparison the wind tunnel co-ordinates have been converted into metres. Owing to the different scales of measurement and reduction of the wind tunnel data by the zero-plane displacement (1.9 mm), the data presented in these Figures for the different methods are not all at exactly the same height. The field and FLOWSTAR measurement heights are the same, but those of the wind tunnel vary by as much as ±15% near the surface. However, at the lowest measurement height in the field of 0.25 m this represents a difference of only ±0.035 m. Considering the accuracy of the vertical placement of the anemometers in the field of ±0.005 m and the accuracy in the velocity measurements of ±6%, the differences in the heights of measurement between the methods was not considered significant.

The Figures for the centre-line (5.1 to 5.4) show the same general progression in speed-up along the windward slope for each of the methods. Figures 5.3 and 5.4 do not include field measurements because none were obtained above 1.5 m. The near-surface (0.25 m) measurements (Figure 5.1) suggest that the effect of the intrusion of the dune on the flow velocity is negligible between 50 m and 60 m upwind of the toe (5-6 times the dune height). However, this contrasts with the wind tunnel measurements presented in Chapter 4 and in Figure 5.2. In this Figure it can be seen that 50 m upwind of the dune (at x = -20 m) the tunnel measurements show a speed-up of between -0.8 and -0.1 at a height of 1 m. Reference to

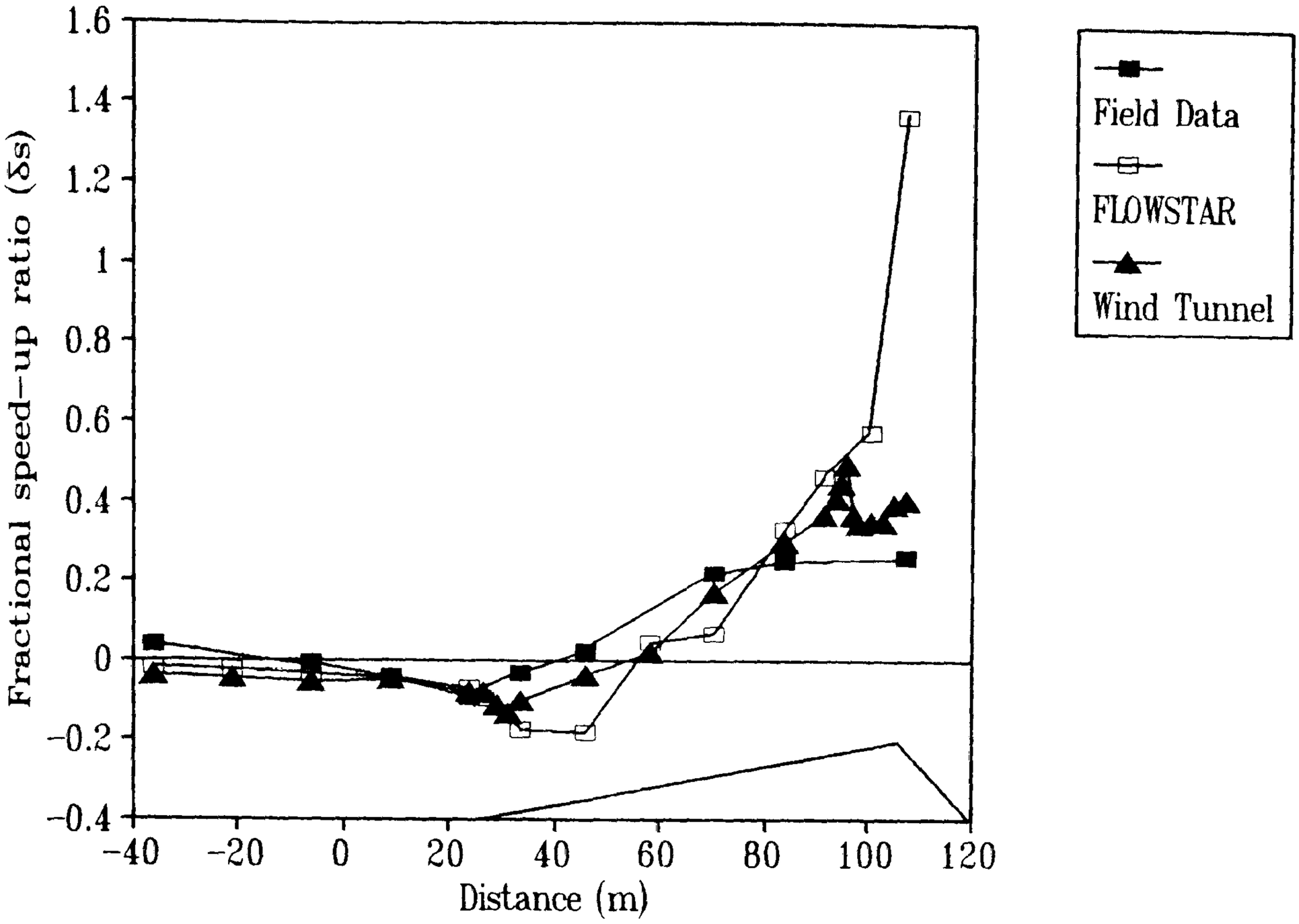

Figure 5.1 Fractional speed-up ratio on the centre-line of the dune at 0.25 m.

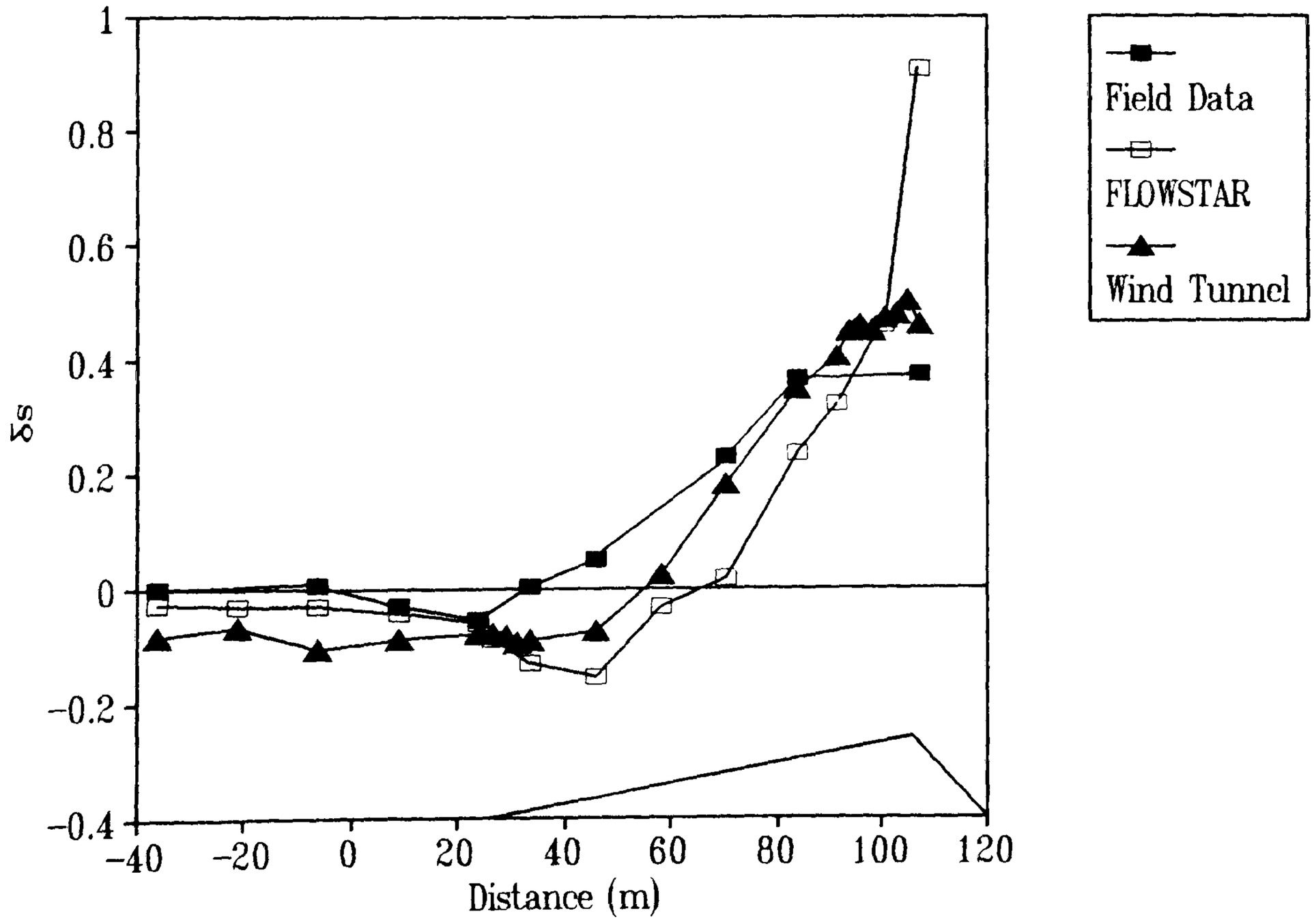

Figure 5.2 Fractional speed-up ratio on the centre-line of the dune at 1.0 m.

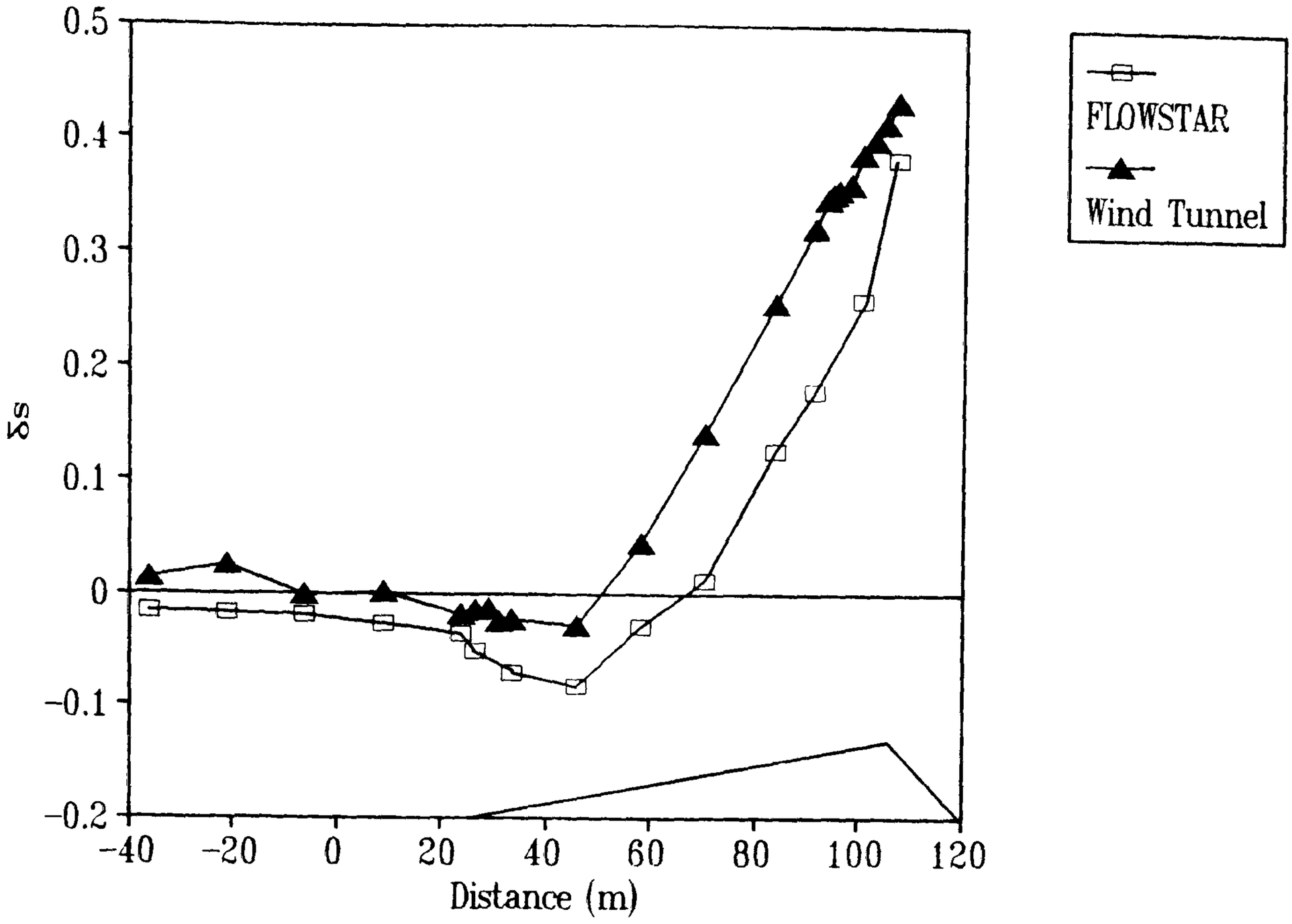

Figure 5.3 Fractional speed-up ratio on the centre-line of the dune at 4.0 m.

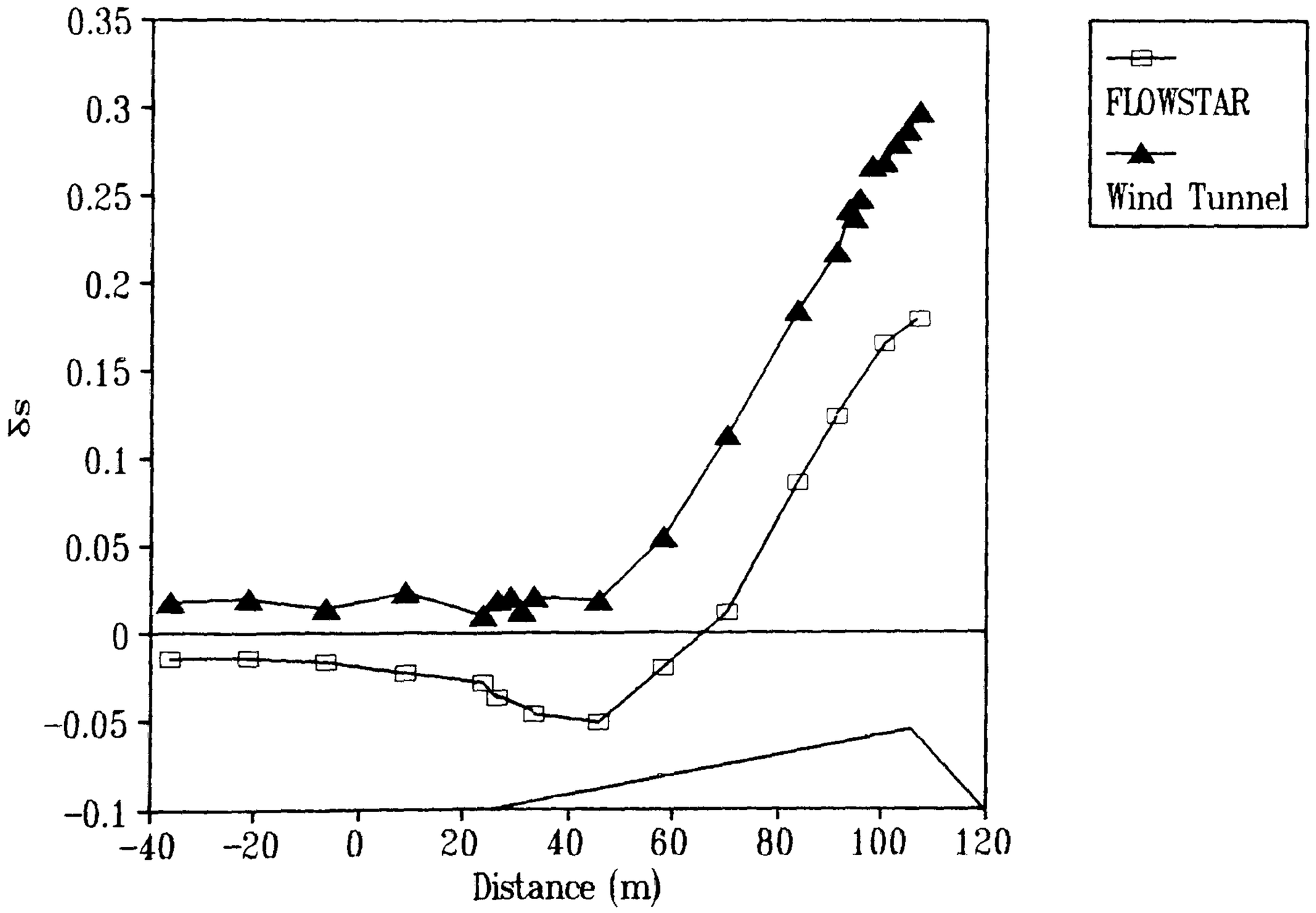

Figure 5.4 Fractional speed-up ratio on the centre-line of the dune at 10.0 m.

Chapter 4 indicates that the wind tunnel measurements only exhibit a negligible velocity perturbation close to the surface 100 m upwind of the toe, almost double the distances shown by the field measurements and FLOWSTAR predictions.

There are two possible explanations for this difference. First, if one assumes that the flow is reduced as much as 100 m upwind, then the placement of the reference station in the field at 50 m upwind of the toe would result in an inaccurate assessment of both the degree and extent of the low velocity zone. Secondly, it should be noted that the simulated atmospheric boundary layer in the wind tunnel did not become fully-developed until x= 0 m, although it had similar properties from about x= -40 m. The measured velocity deficit upwind of 0 m in the wind tunnel may therefore be incorrect. Considering that the FLOWSTAR predictions agree with the field measurements in this zone and that on the flanks (where the toe positions are downwind of x= 0 m), the results upwind of the toe for tunnel, field and FLOWSTAR are consistent (Figures 5.7 to 5.14), the latter explanation seems more likely. However, in future field experiments it is suggested that the reference velocities for data normalisation should be measured either at dune crests or on a flat plain to one side of the dune. Since transverse dunes are constantly moving the latter may be more appropriate.

Figures 5.1 and 5.2 demonstrate that in the toe region there is some variation between the methods in the degree of near-surface velocity deceleration and the horizontal position of the minimum δs. These differences are summarised in Table 5.1 which shows the extreme values of δs along the centre-line and the height at which they occur. At 0.25 m and 1 m heights (Figures 5.1 and 5.2) it is noticeable that the field measurements demonstrate a minimum δs exactly at the position of the toe. The wind tunnel measurements and FLOWSTAR predictions show progressively later (*i.e.* downwind) minima respectively. The FLOWSTAR predictions reach a minimum nearly 25 m downwind of the leading edge. However, as shown in Table 5.1, the extreme values of deceleration in this area are in quite good agreement, at between 10-20%.

As a result of these variations in the horizontal position of the maximum deceleration, large contrasts in the horizontal progression of δs downwind of the toe are evident. At 0.25 m (Figure 5.1) the deceleration measured in the field between x= 30 m and 40 m is only half that measured in the tunnel and predicted by FLOWSTAR. Furthermore, at x= 45 m, where the field measurements exhibit a positive perturbation, the FLOWSTAR prediction is still decreasing. The higher-velocity field measurements in this region should be treated with scepticism on account of the high degree of turbulence measured in the wind tunnel in this region (Chapter 4.3). These measurements of streamwise turbulence suggested that at the toe and up to 50 m upwind, the

turbulence intensity along the centre-line rose by as much as 15%. If this were true in the field, significant inaccuracies in the anemometer measurements might be expected. As discussed in Chapter 2.3.1, a hysteresis effect is evident with cup-anemometers (Kagnov and Yalom, 1976) where their response to an increase in windspeed is faster than to a decrease. The inertia of the cup-anemometers in this experiment, coupled with the existence of a zone of high turbulence around the toe may have resulted in an overestimation of windspeed by the cup-anemometers, possibly by as much as 15% (Knott & Warren, 1981).

The large negative speed-up values predicted by FLOWSTAR in the toe region and their delay in development to positive perturbations, compared to the other techniques of study, is less easy to explain. The sizeable velocity deceleration predicted by FLOWSTAR is noticeable even at 10 m from the surface (Figure 5.4), where it predicts a speed-up of about -0.05. No reduction is evident from the wind tunnel data. A similar under-prediction of velocity in this region by linear theory is described by Gong and Ibbetson (1989) in comparison with wind tunnel measurements. They recognise, however, that the proximity of the side-walls of their wind tunnel may have increased the measurements of velocity at the toe of the model in the wind tunnel, hence causing the linear model predictions to appear as under-estimations. The experiments reported in Chapter 4 to test for the influence of the tunnel walls suggest that this explanation is unlikely to be applicable in the present study. It seems more likely that FLOWSTAR over-predicts the positive gradient of surface pressure at the foot of the dune. This has led to an over-estimation of flow deceleration. Similar variations in measured and predicted near-surface speed-up in this region have been described by Howard & Walmsley (1985) and Weng *et al.* (1991). In the present study, although the differences between the wind tunnel measurements and the FLOWSTAR predictions of fractional speed-up ratios in the toe region at x= 45 m appear large (100%), it should be remembered that in terms of prediction of absolute velocity it is, on average, only a 20% variation.

The vertical profiles of fractional speed-up ratio at the toe are shown in Figure 5.5. The profiles for all three methods show a progressive reduction in δs toward the surface. At any height, the difference between the field and tunnel measurements and the FLOWSTAR predictions is never more than 5%. However, at a height of 0.6 m (ln -0.5 m) the wind tunnel measurements exhibit an increasing δs toward the surface. This 'kink' in the profile in the region of the inner-layer is not recognisable in either of the other methods of study, although the FLOWSTAR predictions do show a reduction in the rate-of-change of δs originating at about the same height. It is uncertain whether the near-surface increase in speed-up recognisable in the wind tunnel measurements represents an actual response by the flow to pressure gradients within the inner-

layer or whether it is merely an anomaly caused by the proximity of the hot-wire probe to the roughness elements in the tunnel. The height of the 'kink' (0.6 m) corresponds with a height of 3 mm above the zero-plane displacement (d) in the tunnel. This distance is enough to make the effect of the intrusion of the hot-wire probe into the tunnel flow negligible (Castro & Dianat, 1990). Furthermore, similar wind tunnel measurements of δs by Teunissen *et al* (1987) and Gong & Ibbetson (1989) also display 'kinks' at this location at heights consistent with the inner-layer depth. Lack of comparable data in the literature makes it difficult to be conclusive, but it appears that the height of the δs minimum in profiles near the toe of the dune might be expected to be at a height consistent with the inner-layer depth. Table 5.1 shows that the values of maximum deceleration in the toe region using each of the methods occur at heights between 0.25 m and 0.6 m, and this is compatible with the range of inner-layer heights calculated in Chapter 2. The fact that the change in δs caused by the 'kink' shown by the wind tunnel measurements in Figure 5.5 amounts to only 2% may explain why it is not recognisable in the field measurements which are unable to interpret such small changes. Despite these differences the agreement between the three methods at the toe is quite good.

On the windward slope between x= 45 m and x= 90 m the near-surface speed-up ratios (Figures 5.1 and 5.2) from each of the methods are within 15-20% of each other. At heights of 4 m and 10 m (Figures 5.3 and 5.4) the agreement between the tunnel measurements and FLOWSTAR predictions is even better, within 10-15% and with very similar rates of change. However, it is noticeable that in each of the Figures it is generally the field measurements which demonstrate the highest δs at any particular point along the windward slope, and the FLOWSTAR values which exhibit the lowest.

Within the crestal region of the centre-line (x= 90 m to x= 110 m) more significant differences between the results of the three techniques are observed. Table 5.1 indicates that the δs_{max} recorded by each method occurs at different horizontal positions and has different values. At heights of 0.25 m and 1 m (Figures 5.1 and 5.2) the rate-of-change of δs for the field data is reduced to almost zero. This is in contrast to that for the FLOWSTAR predictions which rapidly rise to a maximum at the crest. However, as described in Chapter 3, the values predicted by the model at the brink of the dune cannot be relied upon because of the neighbouring region of highly turbulent, separated flow. The wind tunnel measurements also demonstrate a general reduction in the rate-of-change of speed-up. However, the wind tunnel measurements are disrupted by a sharp peak in δs upwind of the crest. As noted in Chapter 4.3, the near-surface peak in speed-up upwind of the crest on the centre-line in the wind tunnel measurements appears to be a response to an uncharacteristic peak in the surface slope angle of the dune model. The

upwind velocity peak is therefore probably a result of inaccuracy in the interpolation of the co-ordinates for the model dune and not a realistic assessment of the pattern of windflow. Ignoring this peak means that the field and tunnel values of speed-up in the crestal region of the centre-line are within a 5-10% agreement. At 4 m and 10 m heights (Figures 5.3 and 5.4) the FLOWSTAR predictions of δs are less than the tunnel measurements. However, the actual values of speed-up are within 10% agreement and in the absence of anomalous peaks in either assessment, their rates of change are similar.

The vertical profiles of δs at the crest of the centre-line are shown in Figure 5.6. Above 1.5 m (ln 0.5 m) the tunnel measurements and FLOWSTAR predictions are in good agreement. Below 1.5 m, however, the δs values predicted by FLOWSTAR continue to increase to the surface, whilst the tunnel measurements reduce from 0.5 to 0.4. The wind tunnel profile of δs below 1.5 m is comparable to the field measurements which decrease from 0.4 to 0.2 at the surface. The unsatisfactory prediction by FLOWSTAR in this region has previously been explained (Chapter 3) and the difference between the measurements of the tunnel and field is small.

Tables 5.2 and 5.3 show the associations between the horizontal and vertical profiles using each method calculated as correlation coefficients (Pearson's product-moment). The horizontal profile correlations between similar heights (Table 5.2) all show strong positive correlations (accentuated in bold). It is noticeable that the correlations of the field measurements at 0.25 m and 1.0 m heights with the wind tunnel measurements (0.977 and 0.983 respectively) are stronger than with the FLOWSTAR predictions (0.838 and 0.890 respectively), although the correlations between the wind tunnel and FLOWSTAR are also very high (0.863 to 0.983). There also appears to be a propensity for the correlations at lower elevations to be less strong than those further from the surface. This might be expected, considering that the fluctuations in flow close to the surface are greater. This is suggested by the turbulence measurements in the wind tunnel (Chapter 4) and reinforced by the standard deviations of δs at different heights presented in Table 5.4. The statistical description of the horizontal profile data shown in Table 5.4 (means, medians and standard deviations) also reveal a closer association between the field and wind tunnel measurements than between the field measurements and FLOWSTAR predictions.

The vertical profile correlations (Table 5.3) tend to be lower than for the horizontal correlations. At the toe there is a strong positive correlation between the field and FLOWSTAR data (0.895), but not between the field and tunnel data (0.358). At the crest the situation is reversed where a strong negative correlation is evident between the field measurements and FLOWSTAR predictions. The correlations between the wind tunnel measurements and FLOWSTAR are

Table 5.1 Centre-line velocity comparison summary. Maximum and minimum fractional speed-up ratios and the heights at which they occur. Position represents distance from toe or crest (+ is downwind, - is upwind). All distances in metres.

	Field			FLOWSTAR			Tunnel		
	Height	Position	δs	Height	Position	δs	Height	Position	δs
Toe	0.25	0	-0.11	0.25	+25	-0.19	0.6	+7	-0.13
Crest	1.0	0	0.39	0.25	-10	0.57	1.5	-11	0.49
Calculated δs_{max}	0.44								

Table 5.2 Centre-line, horizontal velocity profile correlations

		Field		FLOWSTAR				Wind Tunnel		
	Height	0.25	1.0	0.25	1.0	4.0	10.0	0.25	1.0	4.0
Field	1.0	0.994								
FLOWSTAR	0.25	**0.838**	0.887							
	1.0	0.842	**0.890**	0.996						
	4.0	0.874	0.917	0.974	0.989					
	10.0	0.927	0.96	0.923	0.947	0.984				
Wind Tunnel	0.25	**0.977**	0.992	**0.863**	0.877	0.920	0.958			
	1.0	0.964	**0.983**	0.854	**0.874**	0.922	0.963	0.985		
	4.0	0.952	0.980	0.915	0.934	**0.970**	0.991	0.976	0.993	
	10.0	0.952	0.979	0.913	0.930	0.964	**0.983**	0.969	0.992	0.996

Table 5.3 Centre-line, vertical velocity profile correlations

		Field		FLOWSTAR		Wind Tunnel
		Toe	Crest	Toe	Crest	Toe
Field	Crest	0.970				
FLOWSTAR	Toe	**0.895**	0.880			
	Crest	-0.928	**-0.914**	-0.985		
Wind Tunnel	Toe	**0.358**	0.254	**0.976**	-0.962	
	Crest	0.845	**0.800**	-0.789	**0.688**	-0.778

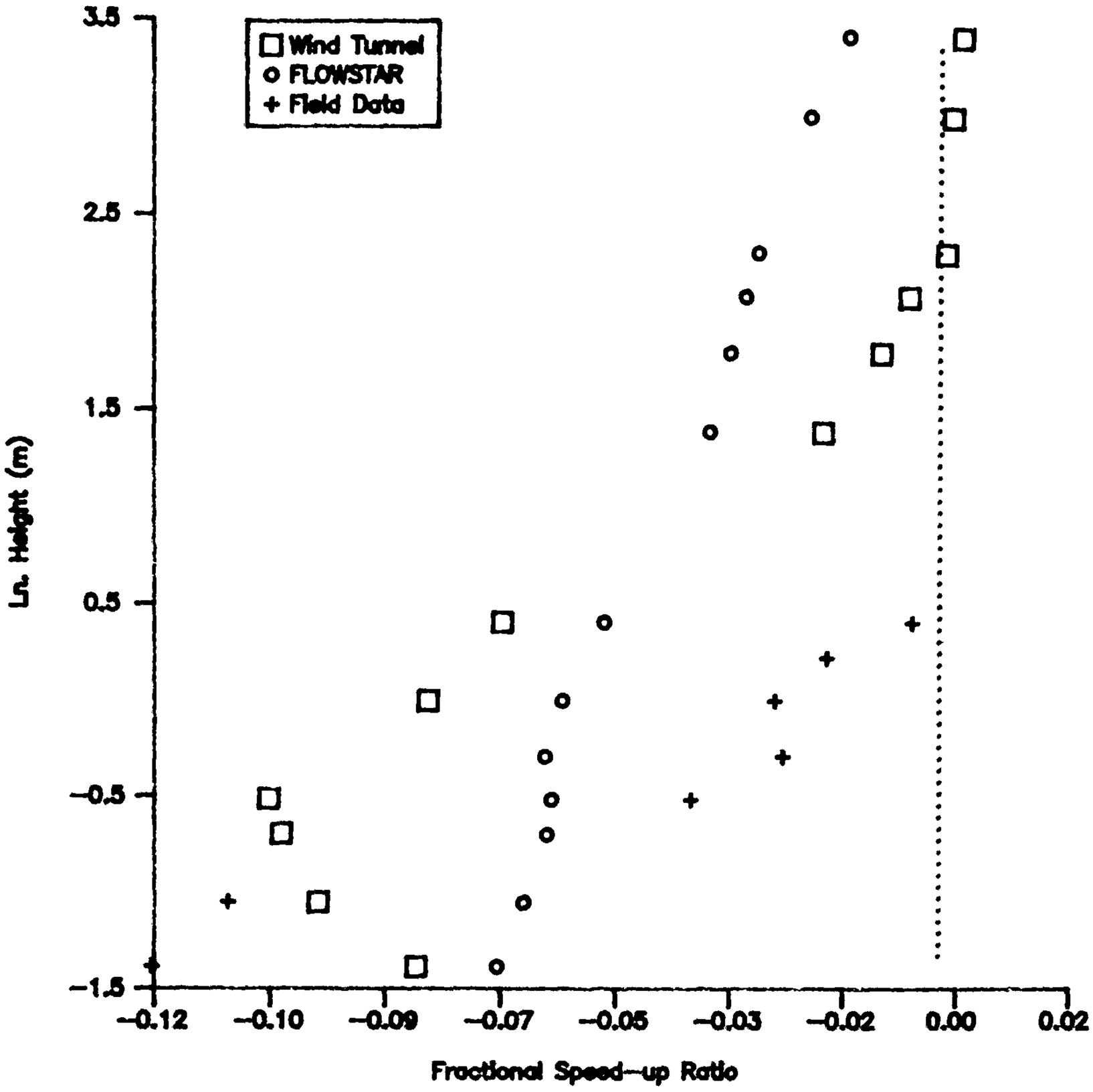

Figure 5.5 Vertical profiles of fractional speed-up ratio at the toe of the centre-line.

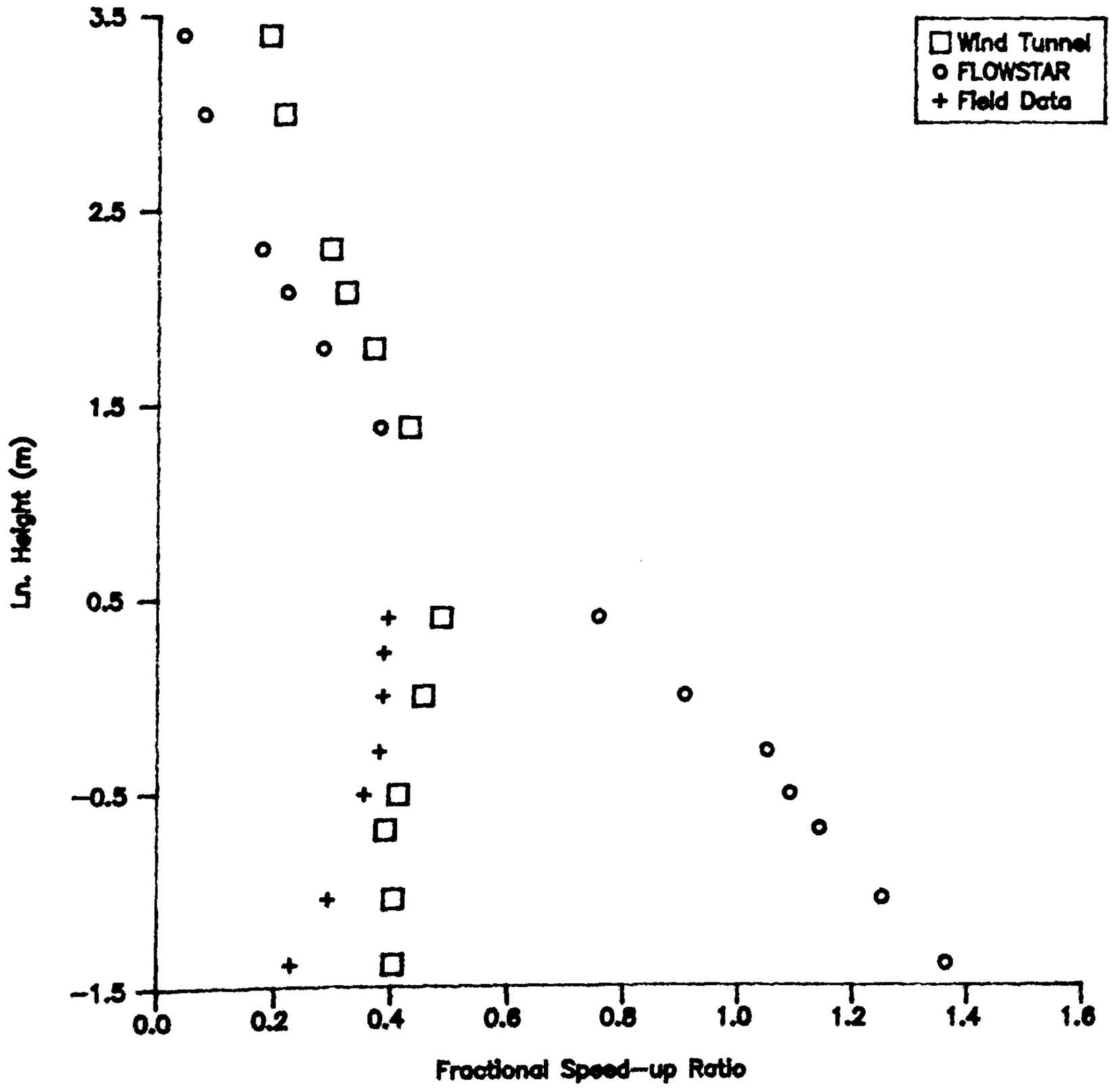

Figure 5.6 Vertical profiles of fractional speed-up ratio at the crest of the centre-line.

strongly positive at both the toe (0.976) and crest (0.688). The statistical descriptions of the vertical profiles (Table 5.5) reveal similar results for all three methods at the toe. At this position the means and medians for all three methods are negative (indicating flow deceleration) and of reasonably similar amplitude. At the crest, however, the FLOWSTAR predictions have a much higher mean, median and standard deviation than the field and tunnel profiles. This is clearly a result of the over-prediction of wind velocity at the crest/brink by the mathematical model.

Table 5.4 Centre-line, horizontal velocity profile description

	0.25 m Height			1.0 m Height			4.0 m Height		10 m Height	
	Field	FLOW*	Tunnel	Field	FLOW*	Tunnel	FLOW*	Tunnel	FLOW*	Tunnel
Number	9	14	27	9	14	26	14	26	14	26
Mean	0.039	0.158	0.136	0.139	0.096	0.143	0.044	0.149	0.023	0.115
Median	-0.003	-0.021	-0.003	0.077	-0.030	-0.020	-0.018	0.044	-0.015	0.038
Std.	0.137	0.417	0.220	0.165	0.294	0.252	0.140	0.179	0.080	0.115

Table 5.5 Centre-line, vertical velocity profile description

	Toe			Crest		
	Field	FLOW*	Tunnel	Field	FLOW*	Tunnel
Number	7	13	12	7	13	12
Mean	-0.048	-0.045	-0.041	0.346	0.674	0.3667
Median	-0.026	-0.052	-0.043	0.381	0.759	0.3991
Std.	0.047	0.019	0.051	0.063	0.487	0.0921

It should be noted, however, that the correlations and statistical descriptions presented in these Tables (and the following Tables) for the field data are a result of only seven or nine observations (Tables 5.4 and 5.5). Much less than the number of wind tunnel observations or FLOWSTAR predictions. There is therefore a lot of scope for error. Moreover, the vertical profiles of the wind tunnel measurements and FLOWSTAR predictions extend to much higher levels (30 m) than do the field measurements (1.5 m). A further concern is the applicability of correlation coefficients of this type to the testing of similarities between velocity profiles over dunes. First, it is noticeable that correlations between relatively isolated data-sets can be stronger than between supposedly connected data. For example, in Table 5.2 the correlation between the FLOWSTAR prediction at 0.25 m and the field measurement at 0.25 m (0.838) is less than between the field measurement at 0.25 m and the prediction at 10.0 m.

Secondly, the strong positive correlations identified in Tables 5.2 and 5.3 which suggest close associations between variables, hide

important differences in the development of speed-up across the dune. For example, the correlations between the horizontal profiles of δs at 0.25 m (Table 5.2) of 0.838 and 0.977, combined with the similar means, medians and standard deviations of the vertical profiles at the toe (Table 5.5) might suggest that all the measurements and predictions, particularly at the toe, are essentially identical. This masks the large differences in the horizontal position and magnitude of the maximum deceleration identified in Figures 5.1 and 5.2, which may have a very important bearing on the resultant morphological changes at the toe predicted from each technique (Chapter 7). The use of correlation statistics in this situation (commonly used by Lancaster, 1983; 1985; 1987; 1988) is therefore considered to be of limited value.

5.2.2 The Flanks

The progression of δs along the left and right flanks of the dune resembles that along the centre-line. Figures 5.7. and 5.8 show the calculated speed-up at 0.25 m along each of the flanks. The general relationships between the methods of study on each flank are very similar. There is a reduction in speed-up in the toe region, a progressive increase to a maximum towards the crest and a reduction toward the brink.

Upwind of both flanks the three methods all show similar results with no indication that the deceleration in the wind tunnel begins further upwind than either the field measurements or FLOWSTAR predictions. On both flanks the deceleration seems to occur between 20-40 m upwind of the toe, which is 5-7 times the local dune height. On the left flank (Figure 5.7) both the wind tunnel measurements and FLOWSTAR predictions show a minimum δs of similar value 5 m and 15 m respectively downwind of the toe (Table 5.6).

Table 5.6 Left flank velocity comparison summary. Maximum and minimum fractional speed-up ratios and the heights at which they occur. Position represents distance from toe, crest or brink (+ is downwind, - is upwind). All distances in metres.

	Field			FLOWSTAR			Tunnel		
	Height	Position	δs	Height	Position	δs	Height	Position	δs
Toe	1.0	0	-0.04	0.25	+15	-0.18	1.0	+5	-0.19
Crest	1.0	0	0.43	0.25	0	0.34	1.6	0	0.4
Brink	All	0	0.15	0.25	-9	0.11	0.25	0	-0.2
Calculated δs_{max}	0.33								

The agreement between the tunnel measurements and the FLOWSTAR predictions in the toe region of the left flank is very strong at all heights. Figures 5.9 to 5.11 show δs on the left flank at 1 m, 4 m and 10 m heights. Even at a height of 10 m (Figure 5.11), where the divergence between the results is greatest, the agreement is within 10%. However, the field measurements on both the left and right flanks do not show such an agreement. The near-surface field measurements on the left flank (Figure 5.7) show little reduction in the toe region, whilst those at 1 m height (Figure 5.9) indicate only a small (<4%) reduction. On the right flank (Figures 5.8 and 5.12) the field measurements also show only a modest (4%) reduction in windspeed at 0.25 m and 1 m. However, these measurements should be seen with respect to the errors involved. On both flanks the agreement in the toe region between all of the methods is within 15%. The field measurements are only accurate within ±6% and in the toe region they are subject to further error due to the increased turbulence intensities (as discussed above and in Chapter 4.3). The lack of a significant drop in δs in the field at the toe should therefore not be surprising.

The agreement between the tunnel measurements and FLOWSTAR predictions at the toe of the right flank is not as good as along the left flank. At lower heights (Figures 5.8 and 5.12) the FLOWSTAR predictions of minimum δs are both further downwind (13 m) and greater in extent than the tunnel measurements. At 4 m and 10 m heights (Figures 5.13 and 5.14) FLOWSTAR predicts a 5% drop in velocity, whilst none is shown in the tunnel. In this case the FLOWSTAR predictions are more consistent because they show the minimum δs to be downwind of the toe on the centre-line, left flank and right flank. The wind tunnel measurements, however, show this to occur only on the left flank.

Vertical profiles of δs at the toes of each flank are shown in Figures 5.15 and 5.16. From both Figures it is clear that the deviation between the results is never more than 10%. It is also noticeable that the field measurements exhibit the least deceleration. The field profiles in these Figures appear to be inconsistent. On the right flank (Figure 5.16) they show an increasing negative perturbation toward the surface (except at the lowest measurement level), whilst on the left flank (Figure 5.15) they show a decreasing perturbation toward the surface. As discussed above, the closeness of the measured field perturbations to the accuracy of the cup-anemometers, means that conclusions regarding the field data in this region are difficult to draw.

The progression of δs along the windward slopes of both the left and right flanks is similar. Figures 5.7, 5.8, 5.9 and 5.12 show that at 0.25 m and 1 m the results from the three techniques agree to within 15-20%. The degree of divergence is larger at the bottom of the windward slope, near the toe, principally because the field measurements show only a small reduction at the toe

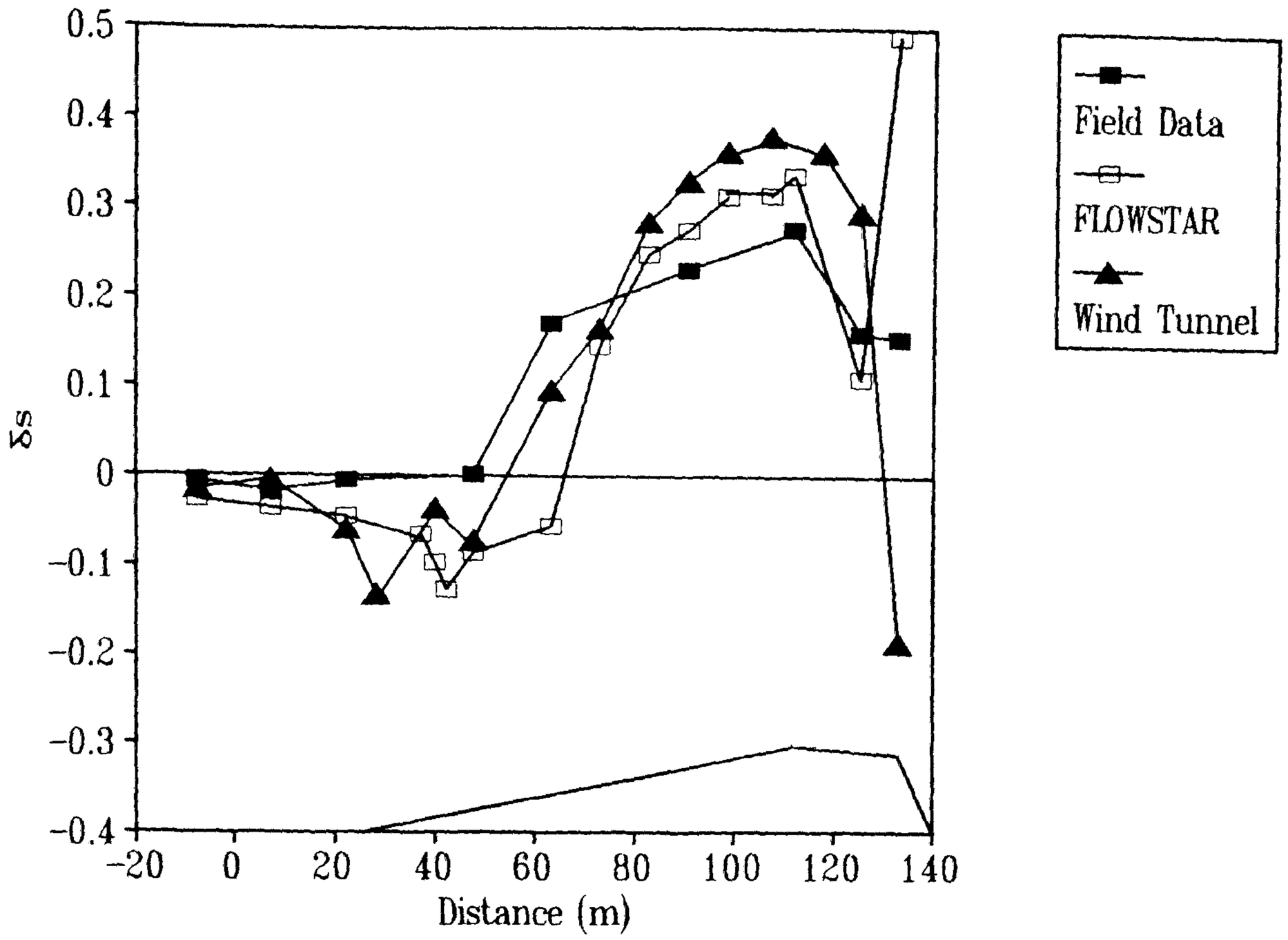

Figure 5.7 Fractional speed-up ratio on the left flank of the dune at 0.25 m.

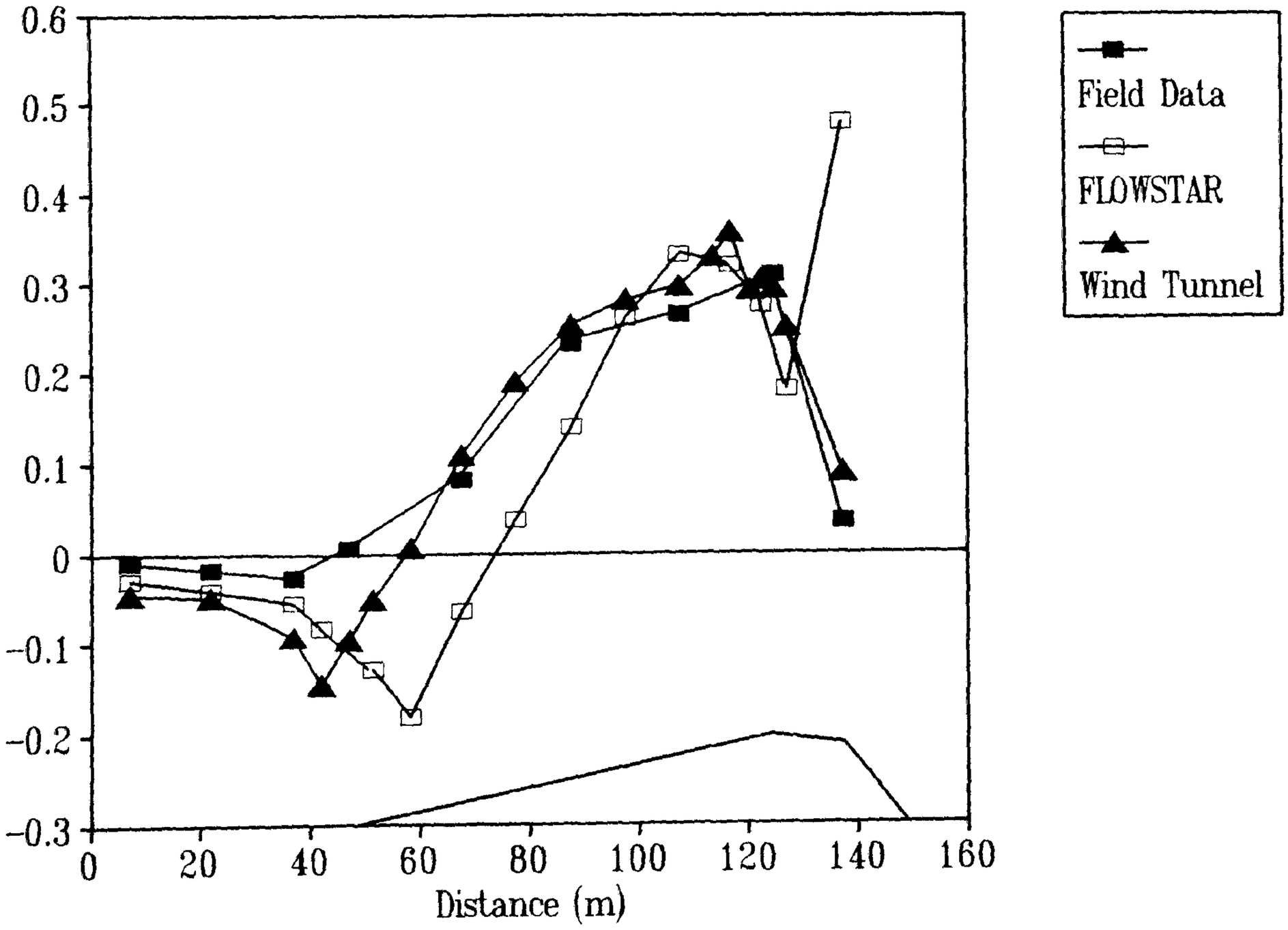

Figure 5.8 Fractional speed-up ratio on the right flank of the dune at 0.25 m.

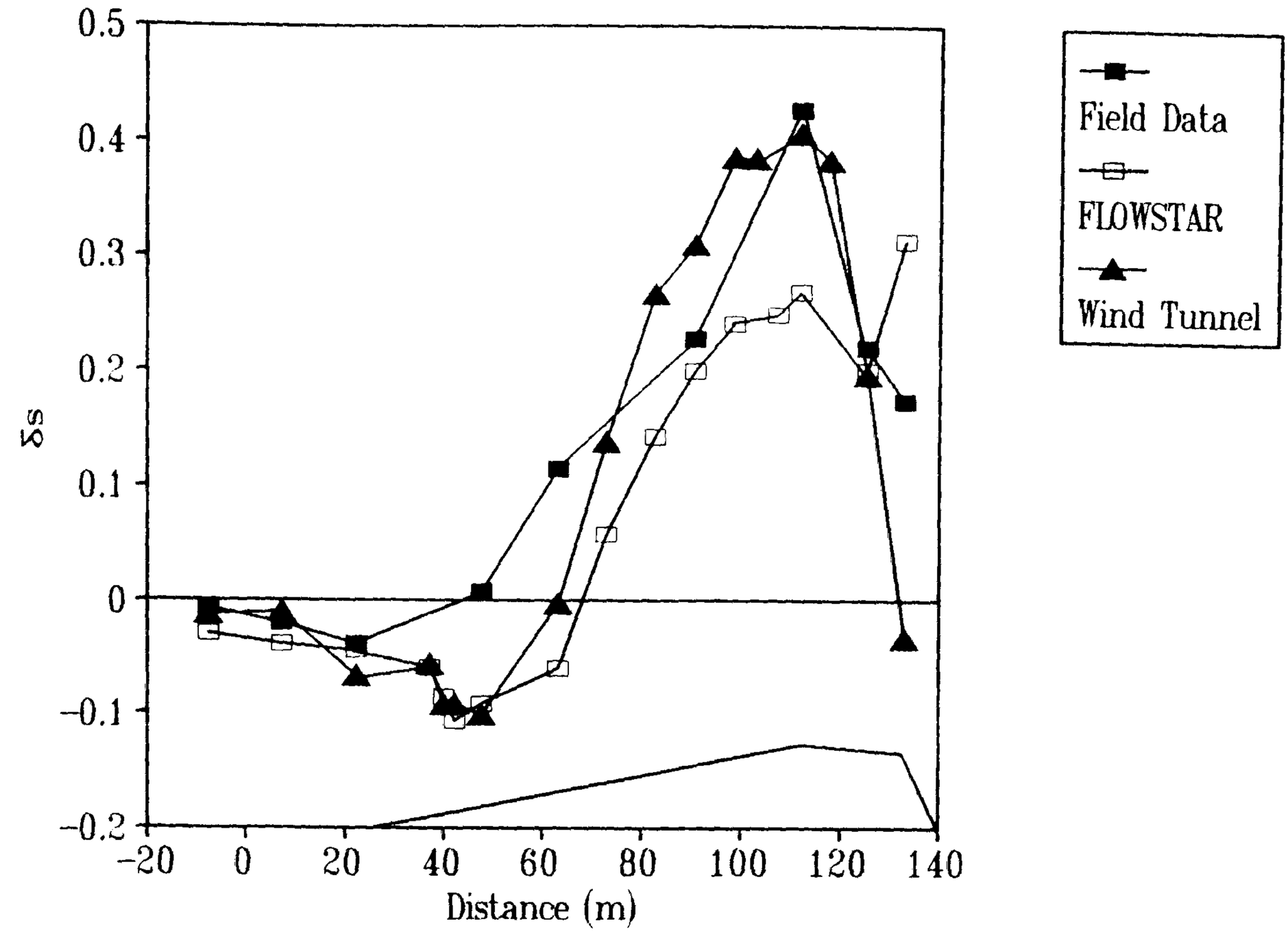

Figure 5.9 Fractional speed-up ratio on the left flank of the dune at 1.0 m.

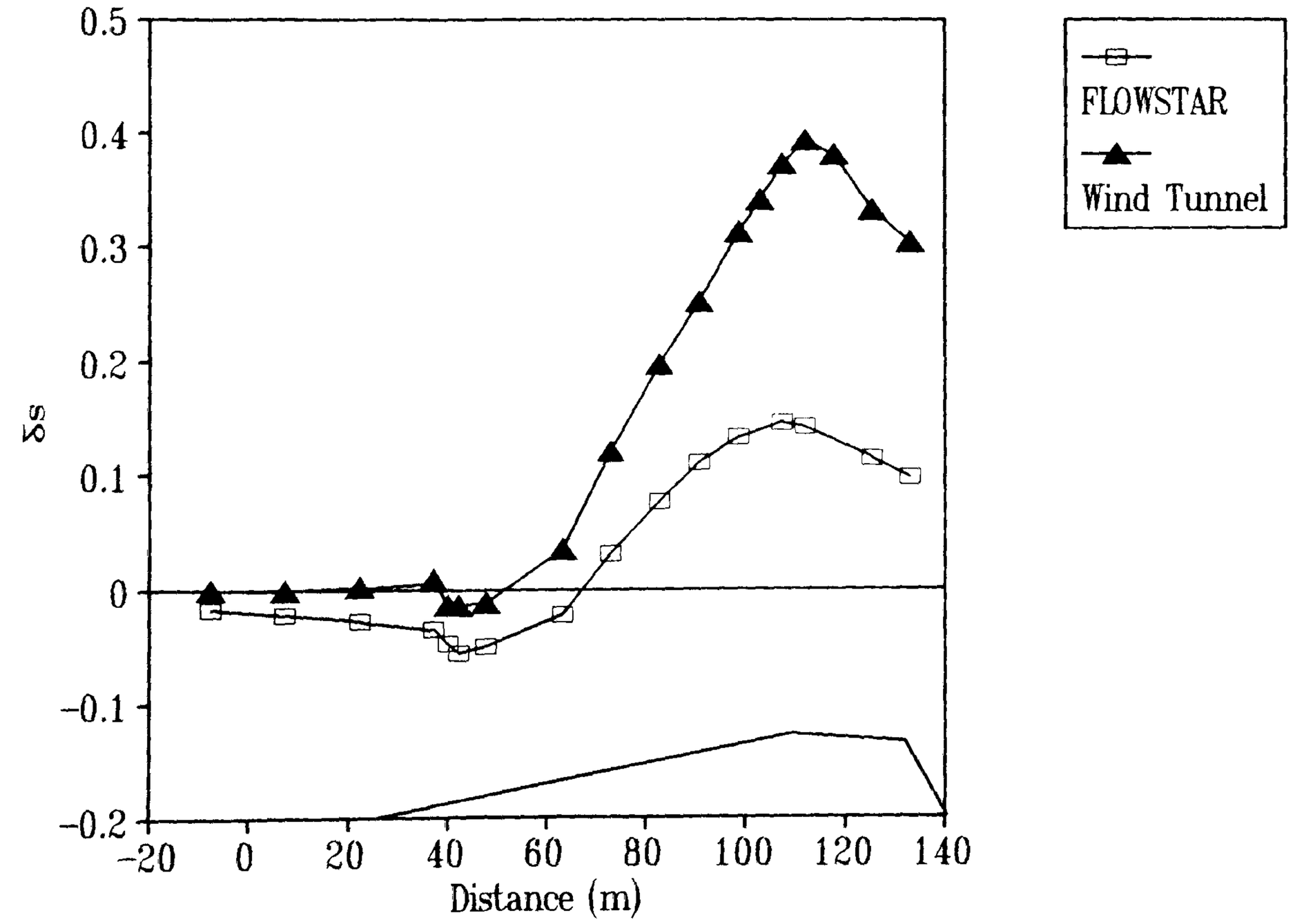

Figure 5.10 Fractional speed-up ratio on the left flank of the dune at 4.0 m.

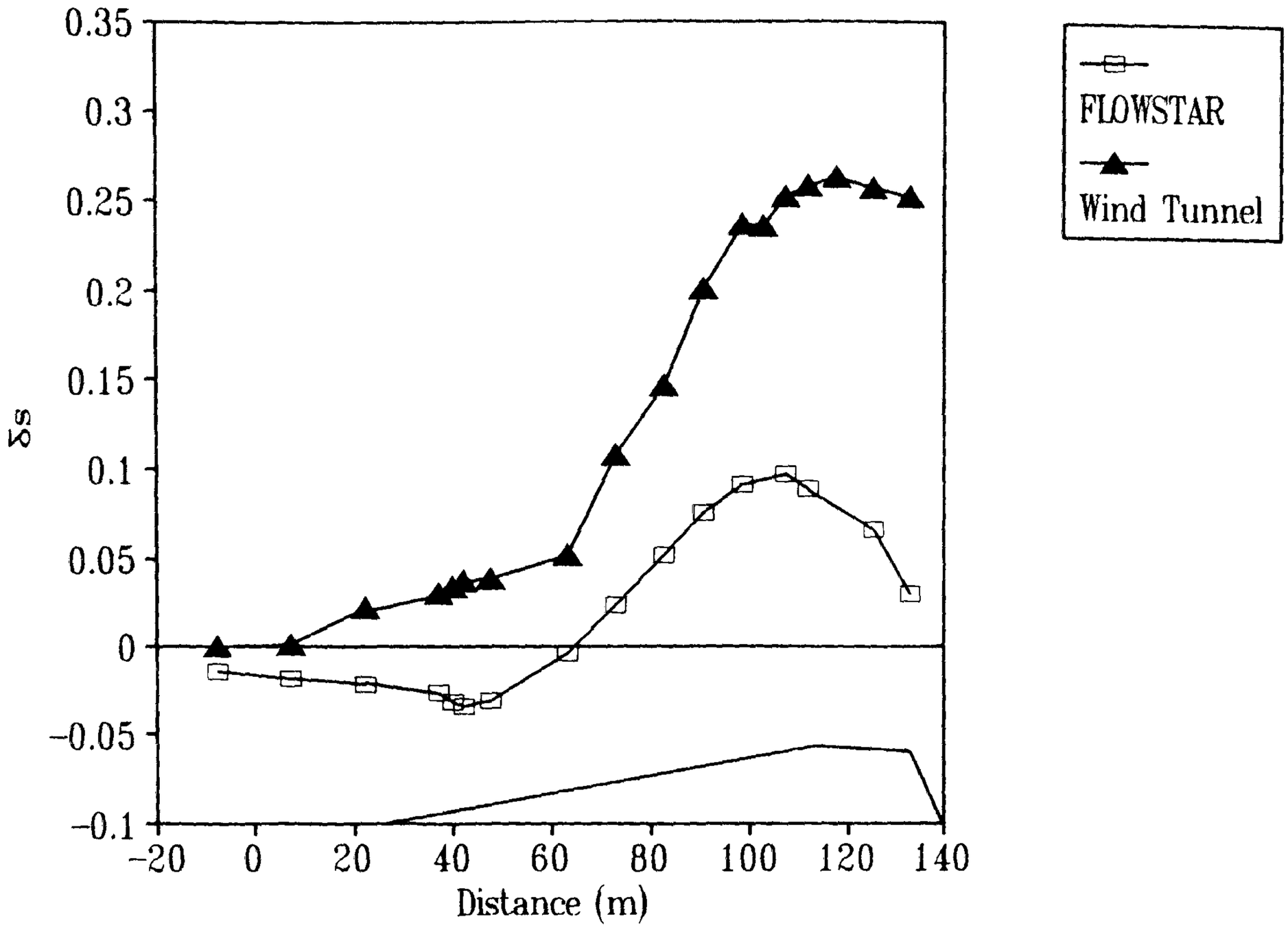

Figure 5.11 Fractional speed-up ratio on the left flank of the dune at 10.0 m.

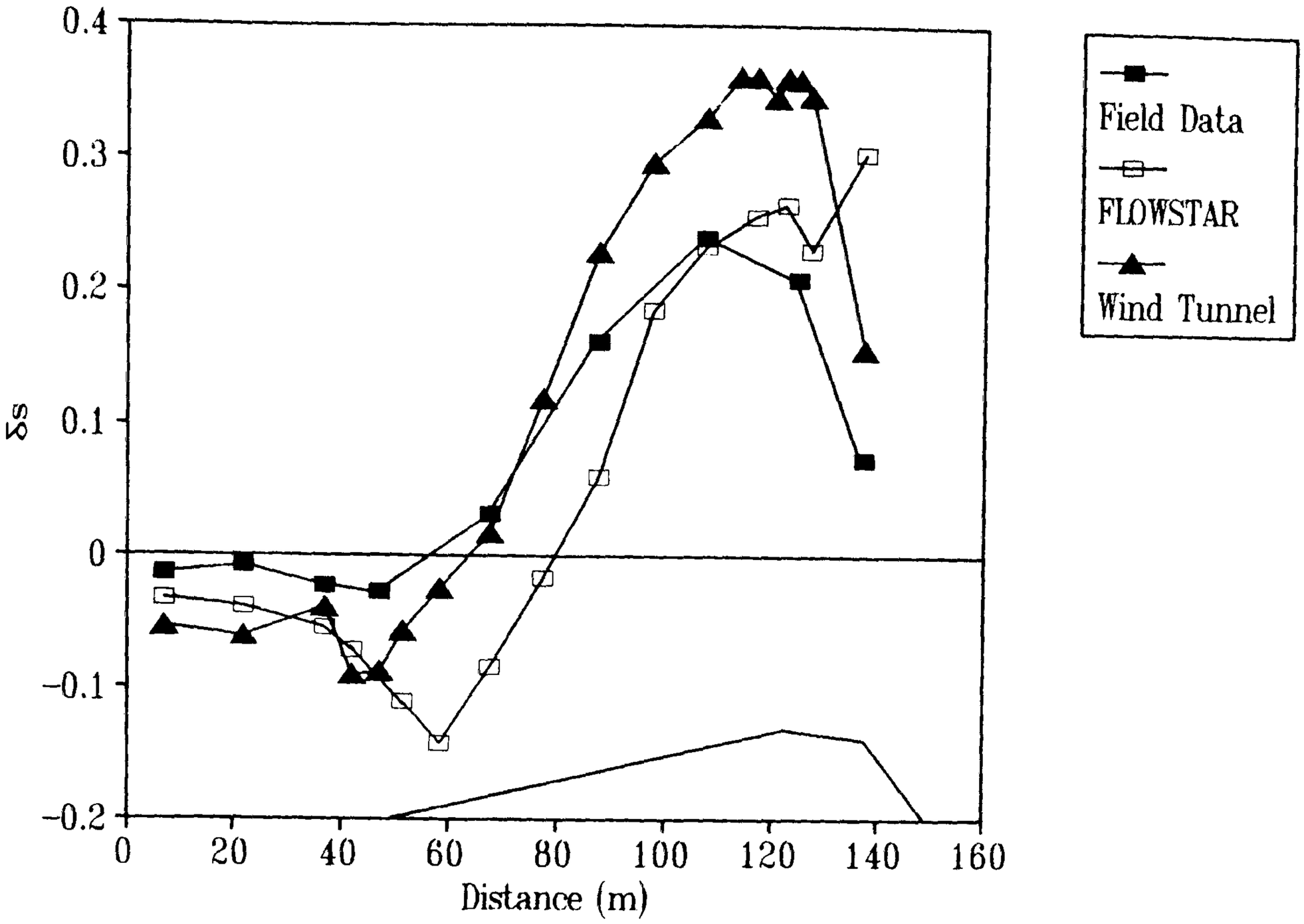

Figure 5.12 Fractional speed-up ratio on the right flank of the dune at 1.0 m.

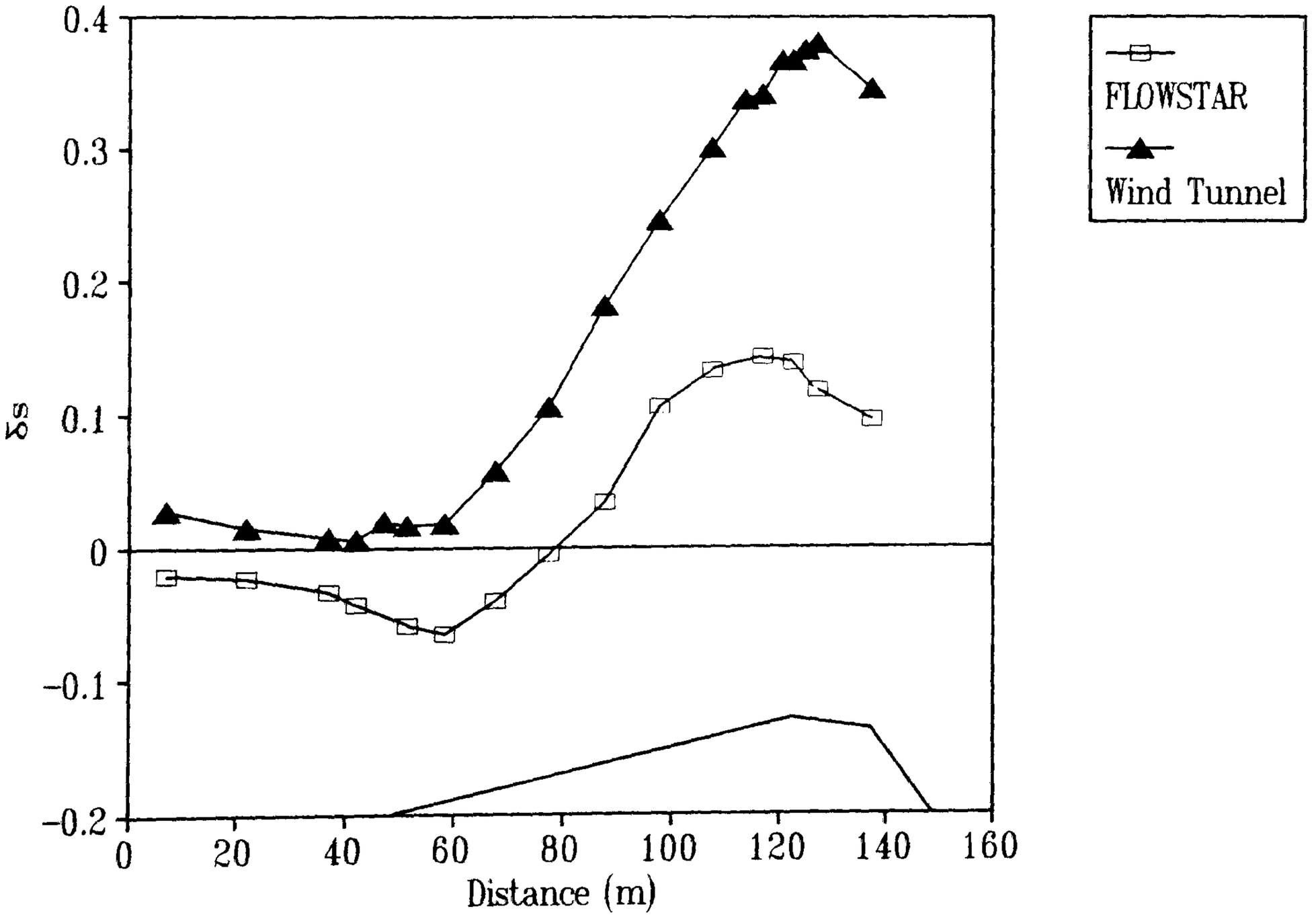

Figure 5.13 Fractional speed-up ratio on the right flank of the dune at 4.0 m.

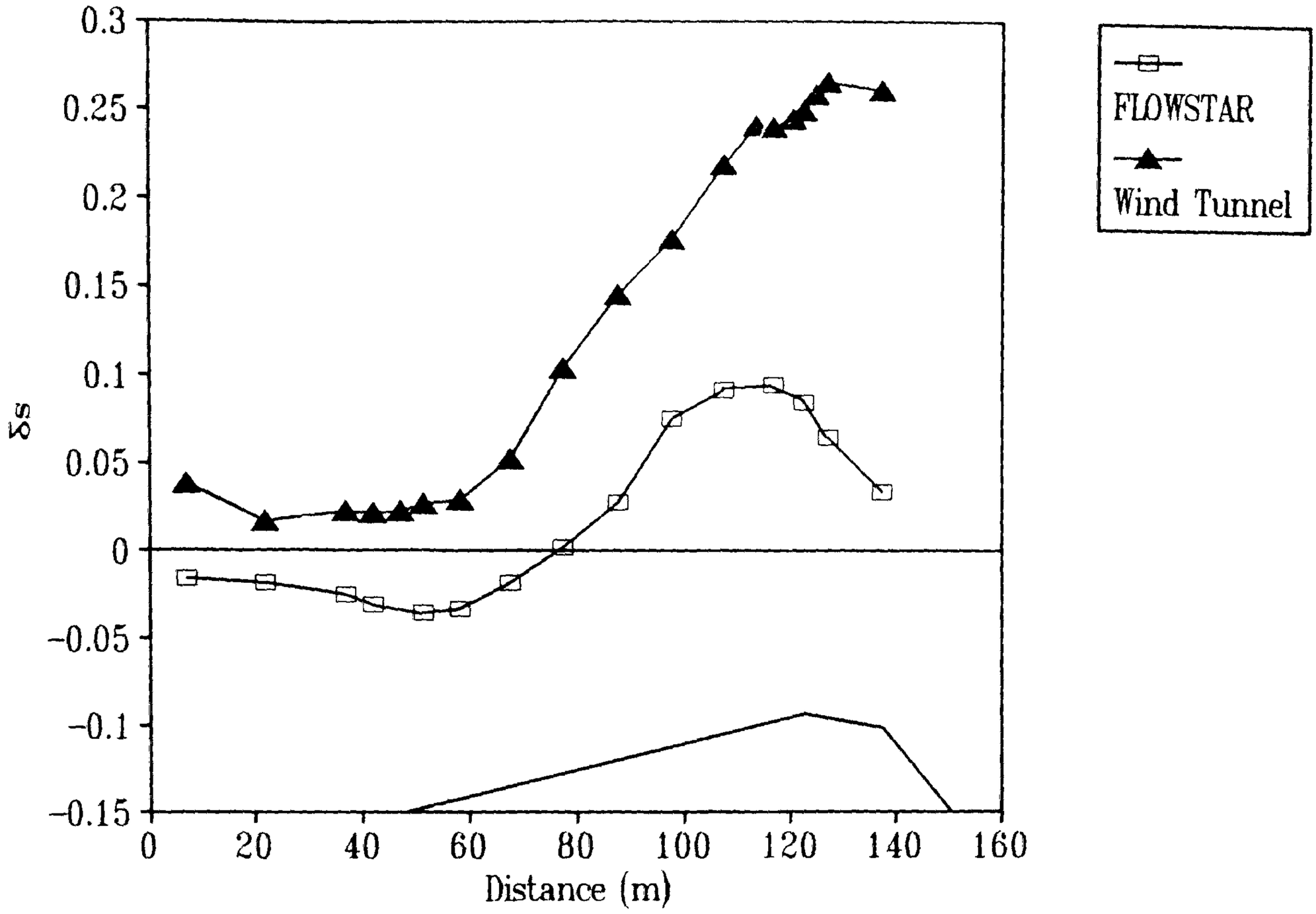

Figure 5.14 Fractional speed-up ratio on the right flank of the dune at 10.0 m.

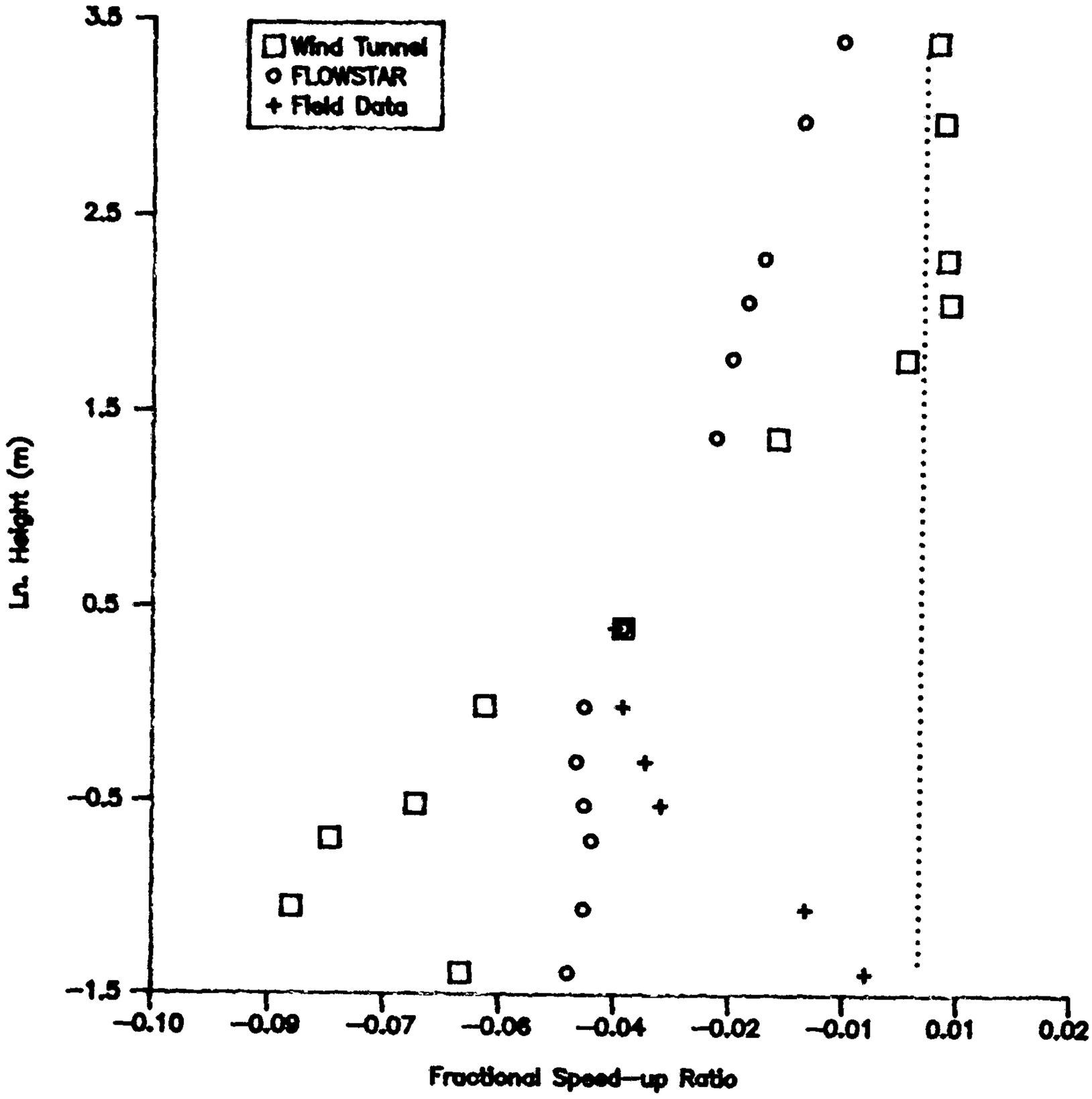

Figure 5.15 Vertical profiles of fractional speed-up ratio at the toe of the left flank.

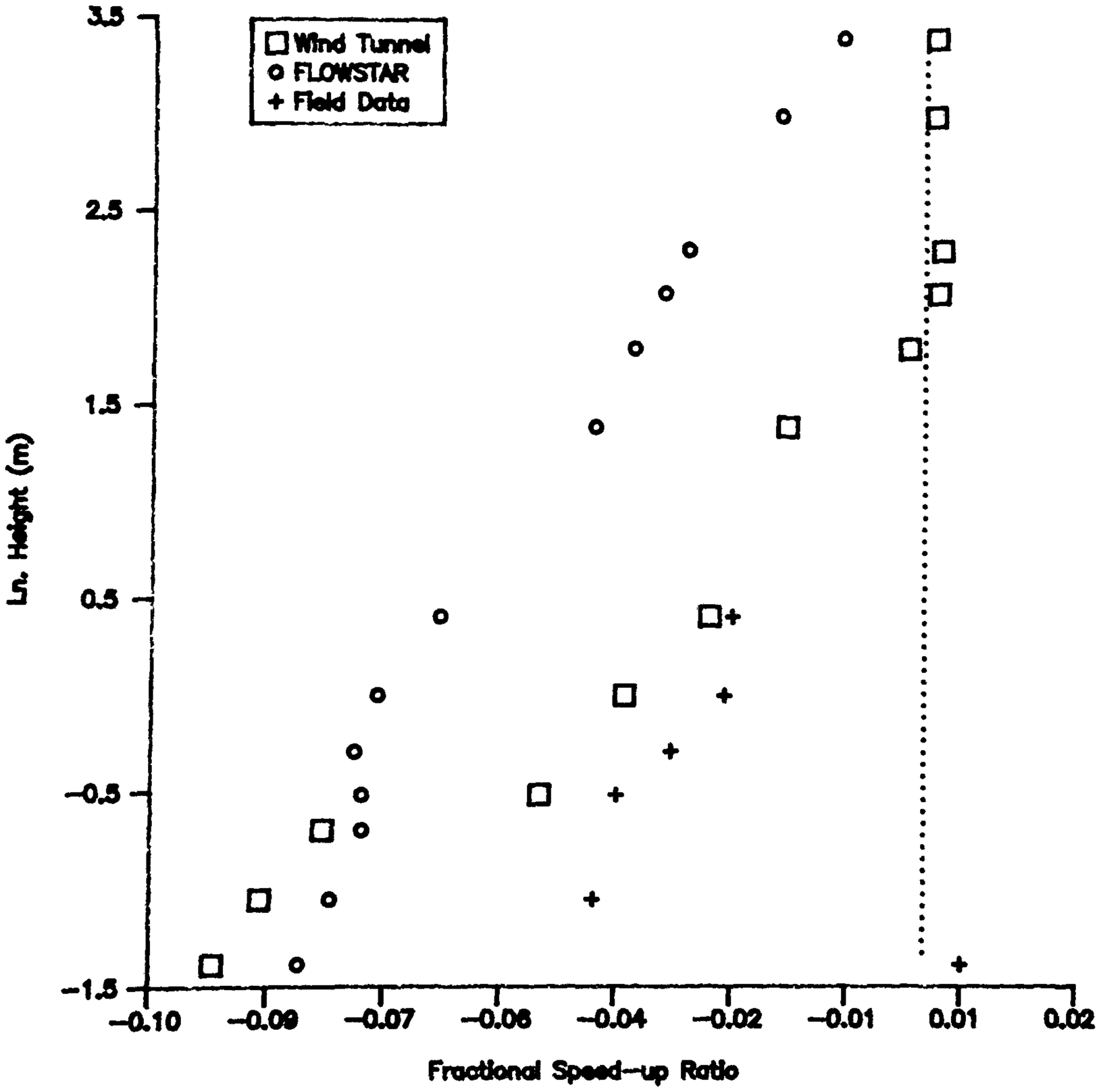

Figure 5.16 Vertical profiles of fractional speed-up ratio at the toe of the right flank.

and the FLOWSTAR predictions tend to have a delay in the onset of positive perturbations. These two factors combine at x = 60 m to x = 70 m on both flanks to produce agreement between the two to within only 20-30%. Further from the surface at heights of 4 m and 10 m the agreement between the tunnel and FLOWSTAR up the windward slopes of the flanks is better, to within about 10% (Figures 5.10, 5.11 and 5.13, 5.14). In most near-surface conditions, the agreement between the wind tunnel and field data is good. The FLOWSTAR predictions seem to consistently undercut the tunnel and field measurements on the windward slopes and do not have such good agreement with the other two techniques.

The horizontal locations of the peak in δs for each of the techniques tends to be quite variable with height, although the actual position of δs_{max} for each technique occurs at the crest itself (Tables 5.6 and 5.7). On the left flank, all three techniques show a peak in δs at the crest except close to the surface at 0.25 m height (Figure 5.7). At this height the wind tunnel measurements show a 5 m upwind shift in the location of the peak. A similar upwind shift is also evident on the right flank at 0.25 m height (Figure 5.8) in both the wind tunnel data (5 m upwind) and the FLOWSTAR predictions (15 m upwind). At 1 m height on the right flank (Figure 5.12) both the tunnel and FLOWSTAR data show peaks at the crest, but the field data exhibit a 15 m upwind shift in position. At heights of 4 m and 10 m (Figures 5.13 and 5.14), the wind tunnel measurements and FLOWSTAR predictions show peaks in δs 5 m downwind and 5 m upwind respectively. There appears to be no systematic pattern in these differences in the measured and predicted horizontal location of δs_{max} using the different methods. They may be considered to be a consequence of "noise" in the measurements. In every case the difference between the measured or predicted δs_{max} and the δs_{max} at the crest is within 4% and more normally within 2%. It is probable that the actual horizontal location of δs_{max} is at the crest. The actual values of δs_{max} at the crest from the different methods are within 15-20% agreement. It should be noted that at most heights it is the wind tunnel measurements which exhibit the highest values and the FLOWSTAR predictions the lowest.

Table 5.7 Right flank velocity comparison summary. Maximum and minimum fractional speed-up ratios and the heights at which they occur. Position represents distance from toe, crest or brink (+ is downwind, - is upwind). All distances in metres.

	Field			FLOWSTAR			Tunnel		
	Height	Position	δs	Height	Position	δs	Height	Position	δs
Toe	0.35	0	-0.04	0.25	+13	-0.18	0.25	0	-0.15
Crest	0.35	0	0.35	1.0	0	0.33	1.6	0	0.39
Brink	All	0	-0.05	0.25	-9	0.18	0.25	0	0.09
Calculated δs_{max}	0.34								

Vertical profiles of δs at the crest for each flank are shown in Figures 5.17 and 5.18. Despite the profiles for the different techniques having different shapes, the measured and predicted speed-ups near the surface agree to within 5-7% on both flanks. On the left flank (Figure 5.17) FLOWSTAR predicts a continuously increasing δs toward the surface. This is in contrast to the field and tunnel measurements which both show a 'kink' in their profiles at about 1.5 m height (ln. 0.5 m) where the δs changes from increasing toward the surface to decreasing. Similar 'kinks' are noticeable at the crest of the right flank (Figure 5.18). At this position the measured and predicted speed-ups near the surface given by the three techniques agree to within 3%. However, above the surface there is a divergence, reaching a maximum at 1.5 m height where the agreement is only within 20%. Figure 5.18 shows that although the shapes of the profiles for the three techniques are essentially the same, with 'kinks' evident between 0.6 m and 1.5 m, the better agreement is between the FLOWSTAR predictions and the field measurements.

At all heights at the brink the tunnel and field measurements exhibit a reduction in wind velocity (Figures 5.7 to 5.14). This is only true of the FLOWSTAR predictions at a greater distance from the surface, as shown at 4 m and 10 m heights in Figures 5.10, 5.11, 5.13 and 5.14 on the left and right flanks respectively. Nearer the surface at 0.25 m and 1 m heights, the FLOWSTAR predictions largely over-predict the windspeed (Figures 5.7, 5.8, 5.9 and 5.14). At these near-surface heights it can be seen that the agreement between the field and tunnel measurements is much closer (within 10%) on the right flank (Figures 5.8 and 5.12) than on the left flank (Figures 5.7 and 5.9), where it is only within about 30-40%. The principal reason for this large difference on the left flank is that the wind tunnel measurements show a rapid reduction in δs into negative perturbations due to the larger reduction in dune height between the crest and brink on this flank. The field data do not appear to be as affected by this height reduction and they retain positive perturbations. Turbulence measurements in the wind tunnel (Chapter 4) indicated more turbulent mixing between the crest and brink on the flanks than along the windward slope. This might explain an over-prediction of velocity by the cup-anemometers in the field. However, if this were the case then the agreement between the field and tunnel results on the right flank would also be expected to be small. A further possibility is that, owing to the non-sharp nature of the boundary between the windward slope and the slip-face on the flanks of the wind tunnel model (caused by the presence of the roughness elements), the airflow may have separated from the surface further upwind than expected. This would have the effect of reducing the near-surface wind velocity quite rapidly. This possibility, in combination with the fact that the definition of the brink itself was not simple (hence making the precise positioning of the hot-wire more difficult), may explain the unexpected reduction in δs between the crest and brink on the left flank.

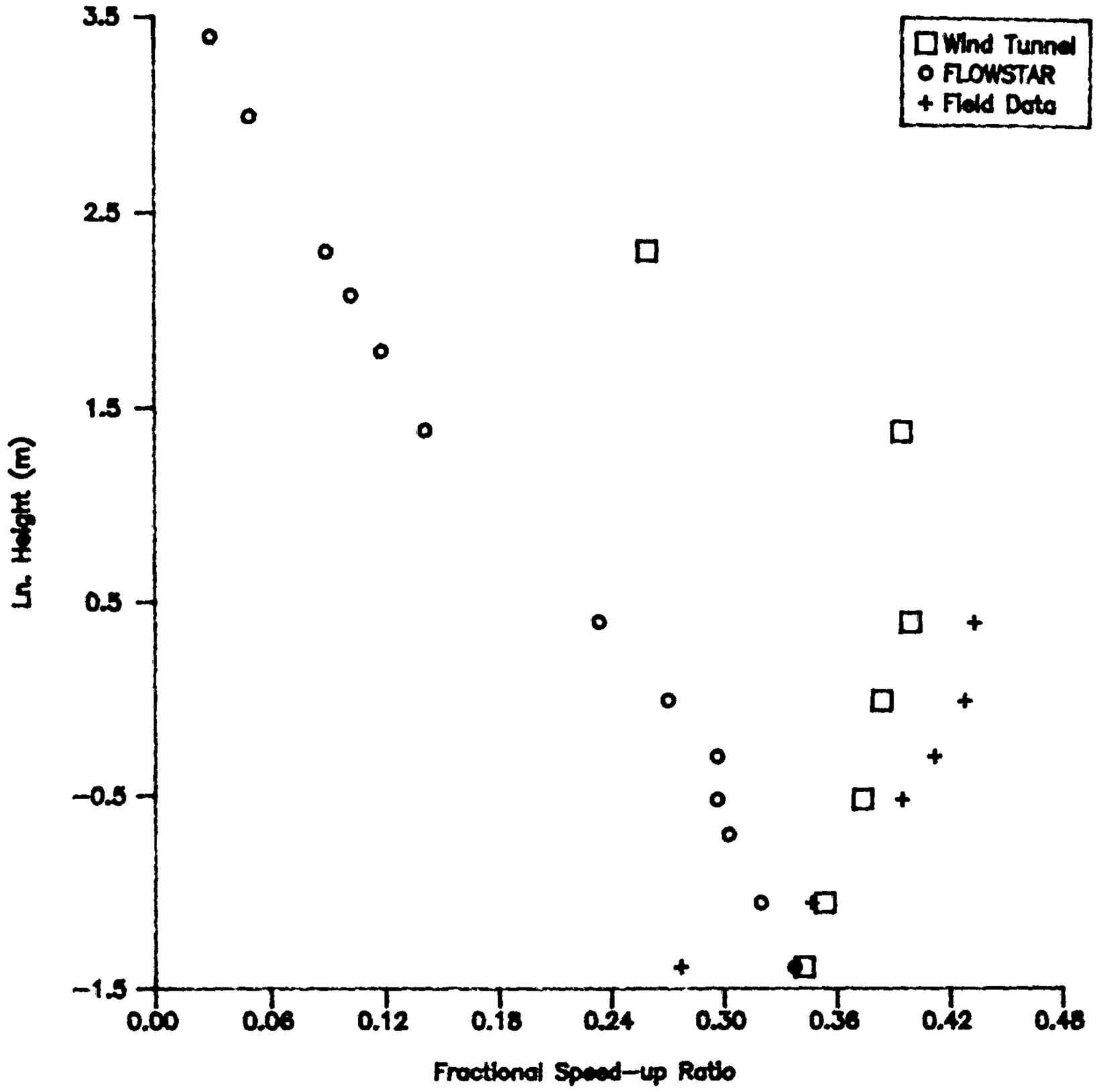

Figure 5.17 Vertical profiles of fractional speed-up ratio at the crest of the left flank.

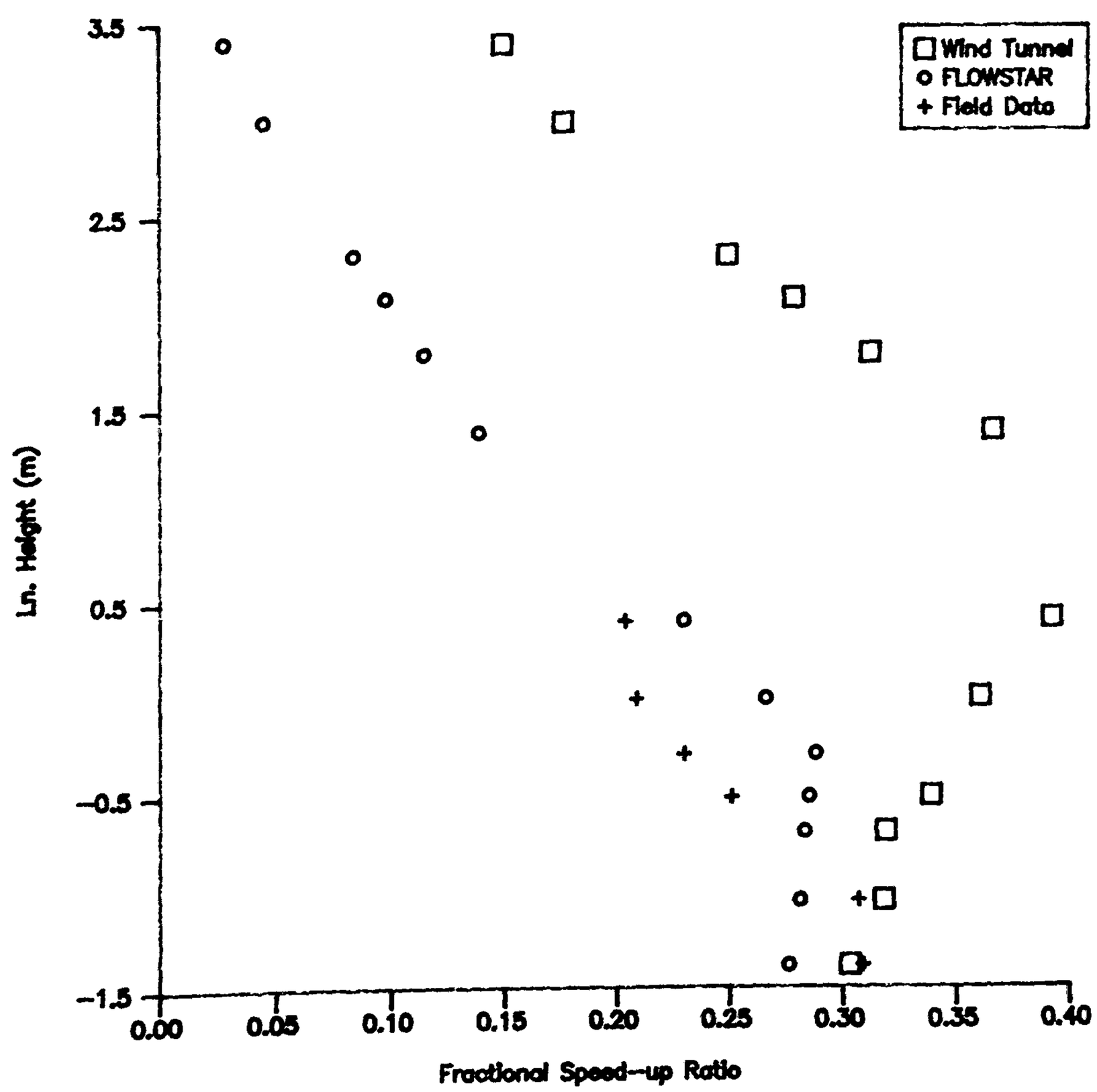

Figure 5.18 Vertical profiles of fractional speed-up ratio at the crest of the right flank.

These differences are highlighted in the speed-up profiles for the brinks shown in Figures 5.19 and 5.20. The right flank (Figure 5.20) shows excellent correspondence between the field and tunnel results, but little accordance with the FLOWSTAR predictions. The left flank (Figure 5.19), however, demonstrates a wide disparity between results. Whilst the over-prediction by the FLOWSTAR model can be explained in terms of the vicinity of separated flow, no such interpretation can explain the differences between the field and tunnel measurements.

Tables 5.8 to 5.11 show the horizontal and vertical profile correlation coefficients for the three methods on the left and right flanks respectively. The horizontal profile correlations on both flanks (Tables 5.8 an 5.9) generally reveal a stronger association between the field and wind tunnel data near to the surface than between any other two techniques. Analysis of the FLOWSTAR and wind tunnel correlations also uncovers increasingly strong correlations with increasing height, although the strongest associations occur at 4.0 m height and not 10.0 m. The relationships between the methods at different heights are also shown in Tables 5.12 and 5.13 in which basic statistical parameters are described. On each of the flanks FLOWSTAR appears to generally under-estimate the degree of flow acceleration. This is indicated by the consistently lower means and medians than either the wind tunnel or field measurements in Tables 5.12 and 5.13. At the lower heights of 0.25 m and 1.0 m the standard deviations between all three methods are consistent. At 4.0 m and 10.0 m however, the standard deviations of the FLOWSTAR predictions are less than half of the wind tunnel measurements. This is a result of the larger perturbations over the flanks measured in the wind tunnel. The differences in the number of observations should be noted.

The vertical profile correlations (Tables 5.10 and 5.11) show generally less strong associations than the horizontal profile correlations, although the relationship at the toe between the wind tunnel and FLOWSTAR predictions and also that at the brinks between the wind tunnel and field measurements are good. Many of the correlations are strongly negative. The statistical descriptions of the vertical profile data shown in Tables 5.14 and 5.15 reveal consistency at the toe. At this position on both flanks all the techniques exhibit means and medians which are negative (indicating flow deceleration) and of similar value. At the crest on both flanks the means and medians of the methods are again very similar, although the FLOWSTAR predictions are lower and the standard deviations are quite different, revealing an increased degree of variation in the mathematical model predictions. However, at the brink, the FLOWSTAR predictions for the means and medians are much higher than the field or tunnel measurements and the field and tunnel measurements are not in good agreement with each other, despite the high correlations indicated in Tables 5.12 and 5.13.

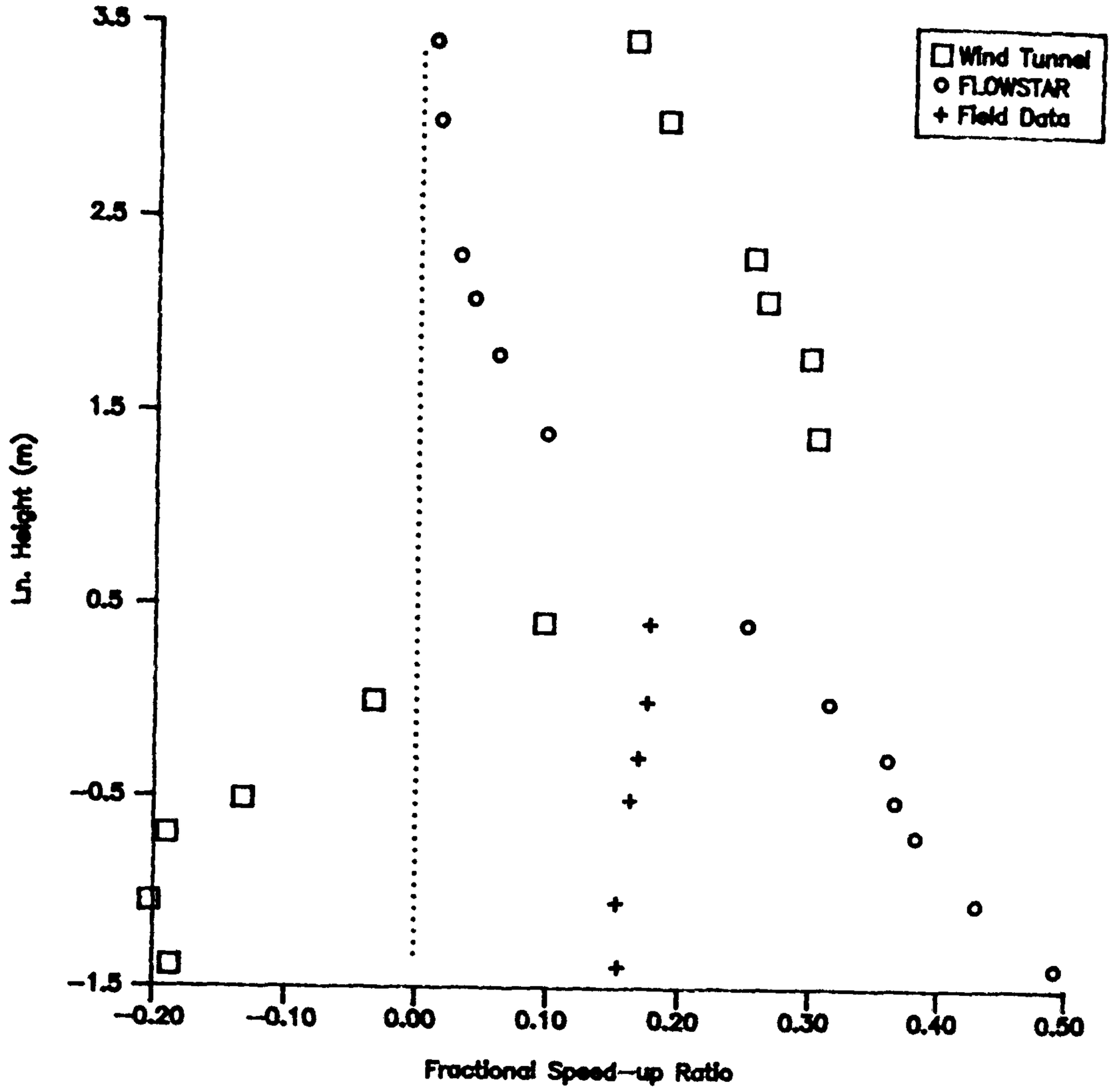

Figure 5.19 Vertical profiles of fractional speed-up ratio at the brink of the left flank.

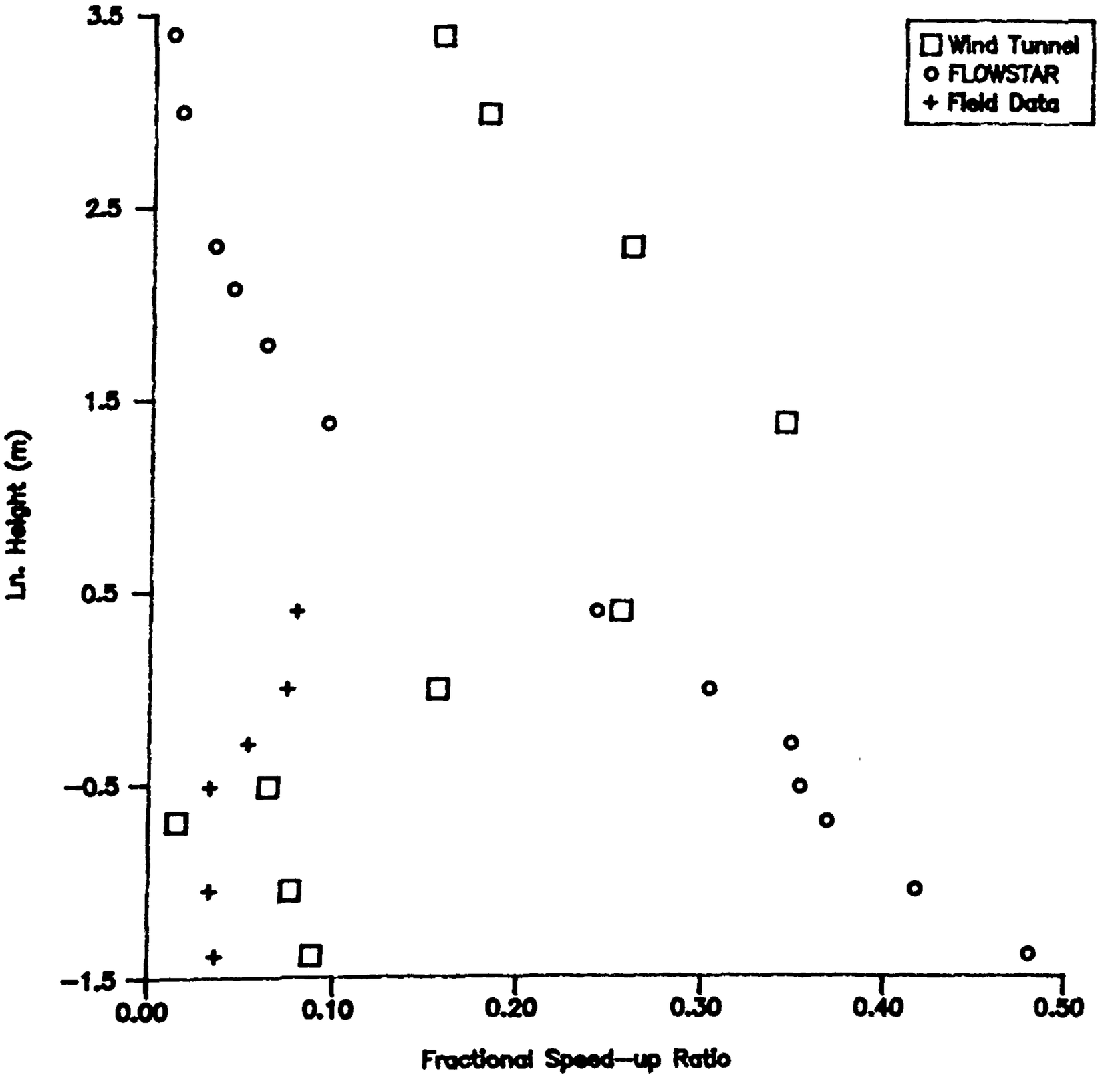

Figure 5.20 Vertical profiles of fractional speed-up ratio at the brink of the right flank.

Table 5.8 Left Flank, horizontal velocity profile correlations

		Field		FLOWSTAR				Wind Tunnel		
	Height	0.25	1.0	0.25	1.0	4.0	10.0	0.25	1.0	4.0
Field	1.0	0.946								
FLOWSTAR	0.25	**0.716**	0.742							
	1.0	0.773	**0.827**	0.967						
	4.0	0.849	0.905	0.911	0.974					
	10.0	0.898	0.937	0.850	0.919	0.983				
Wind Tunnel	0.25	**0.711**	0.719	**0.554**	0.630	0.781	0.878			
	1.0	0.821	**0.878**	0.733	**0.796**	0.904	0.962	0.960		
	4.0	0.851	0.921	0.900	0.973	**0.986**	0.956	0.757	0.881	
	10.0	0.839	0.881	0.894	0.963	0.961	**0.923**	0.701	0.830	0.988

Table 5.9 Right Flank, horizontal velocity profile correlations

		Field		FLOWSTAR				Wind Tunnel		
	Height	0.25	1.0	0.25	1.0	4.0	10.0	0.25	1.0	4.0
Field	1.0	0.963								
FLOWSTAR	0.25	**0.462**	0.661							
	1.0	0.459	**0.669**	0.972						
	4.0	0.656	0.835	0.931	0.979					
	10.0	0.815	0.941	0.883	0.931	0.984				
Wind Tunnel	0.25	**0.963**	0.971	**0.748**	0.774	0.850	0.907			
	1.0	0.938	**0.983**	0.829	**0.880**	0.936	0.961	0.971		
	4.0	0.753	0.847	0.918	0.968	**0.965**	0.935	0.890	0.958	
	10.0	0.730	0.829	0.917	0.955	0.945	**0.914**	0.882	0.951	0.995

Table 5.10 Left Flank, vertical velocity profile correlations

		Field			FLOWSTAR			Wind Tunnel	
		Toe	**Crest**	**Brink**	**Toe**	**Crest**	**Brink**	**Toe**	**Crest**
Field	**Crest**	-0.979							
	Brink	-0.909	0.874						
FLOWSTAR	**Toe**	**-0.493**	0.556	0.511					
	Crest	0.847	**-0.862**	-0.911	-0.988				
	Brink	0.924	-0.940	**-0.924**	-0.952	0.985			
Wind Tunnel	**Toe**	**-0.569**	0.473	0.804	**0.979**	-0.986	-0.964		
	Crest	-0.959	**0.951**	0.943	-0.506	**0.405**	0.312	-0.460	
	Brink	-0.811	0.792	**0.939**	0.820	-0.883	**-0.937**	0.886	-0.156

Table 5.11 Right flank, vertical velocity profile correlations

		Field			FLOWSTAR			Wind Tunnel	
		Toe	**Crest**	**Brink**	**Toe**	**Crest**	**Brink**	**Toe**	**Crest**
Field	**Crest**	0.246							
	Brink	0.050	-0.861						
FLOWSTAR	**Toe**	**-0.330**	-0.847	0.804					
	Crest	-0.205	**0.520**	-0.764	-0.992				
	Brink	0.393	0.941	**-0.837**	-0.964	0.958			
Wind Tunnel	**Toe**	**-0.132**	-0.944	0.973	**0.943**	-0.939	-0.986		
	Crest	-0.268	**-0.942**	0.881	-0.739	**0.730**	0.546	-0.518	
	Brink	0.106	-0.766	**0.926**	0.528	-0.564	**-0.682**	0.679	0.071

Table 5.12 Left flank, horizontal velocity profile description

	0.25 m Height			1.0 m Height			4.0 m Height		10 m Height	
	Field	FLOW*	Tunnel	Field	FLOW*	Tunnel	FLOW*	Tunnel	FLOW*	Tunnel
Number	9	16	18	9	16	18	16	18	16	18
Mean	0.107	0.106	0.128	0.123	0.073	0.133	0.035	0.167	0.022	0.135
Median	0.154	0.041	0.131	0.115	0.014	0.068	0.007	0.158	0.010	0.127
Std.	0.115	0.198	0.196	0.155	0.153	0.203	0.077	0.166	0.050	0.107

Table 5.13 Right flank, horizontal velocity profile description

	0.25 m Height			1.0 m Height			4.0 m Height		10 m Height	
	Field	FLOW*	Tunnel	Field	FLOW*	Tunnel	FLOW*	Tunnel	FLOW*	Tunnel
Number	9	18	22	9	18	22	18	22	18	22
Mean	0.097	0.077	0.111	0.072	0.050	0.121	0.024	0.164	0.014	0.127
Median	0.036	-0.020	0.099	0.032	-0.027	0.068	-0.017	0.082	-0.013	0.080
Std.	0.134	0.188	0.174	0.106	0.150	0.192	0.075	0.157	0.047	0.102

Table 5.14 Left flank, vertical velocity profile description

	Toe			Crest			Brink		
	Field	FLOW*	Tunnel	Field	FLOW*	Tunnel	Field	FLOW*	Tunnel
Number	6	13	12	6	13	7	6	13	12
Mean	-0.028	-0.033	-0.015	0.381	0.198	0.357	0.165	0.219	0.068
Median	-0.035	-0.040	-0.015	0.40	0.233	0.373	0.165	0.251	0.130
Std.	0.014	0.013	0.053	0.059	0.112	0.048	0.010	0.180	0.204

Table 5.15 Right flank, vertical velocity profile description

	Toe			Crest			Brink		
	Field	FLOW*	Tunnel	Field	FLOW*	Tunnel	Field	FLOW*	Tunnel
Number	6	13	12	6	13	12	6	13	10
Mean	-0.027	-0.053	-0.021	0.252	0.186	0.297	0.051	0.214	0.161
Median	-0.030	-0.063	-0.010	0.241	0.230	0.315	0.045	0.243	0.157
Std.	0.017	0.024	0.047	0.047	0.102	0.074	0.210	0.174	0.103

5.2.3 Discussion and Conclusion

The three techniques of study have produced results which are generally comparable in their evaluation of fractional speed-up ratio upwind of and across the study dune. All three techniques exhibit a reduction in wind velocity around the upwind base of the dune, an acceleration up the windward slope and, where crest-brink separation is evident, a deceleration toward the brink. This confirms previous empirical measurements of flow over hills and dunes and substantiates the use of Jackson & Hunt techniques for predicting the general development of such flows.

The agreement between the techniques appears to be stronger in the horizontal plane than in the vertical. This is demonstrated in Tables 5.16 and 5.17 where correlation coefficients for the total data-set (at limited height values) are given for both the horizontal and vertical profiles. In each case the horizontal correlations are more powerful than the vertical. However, the limitations of this type of analysis have been discussed. Despite such high correlations between the methods, substantial contrasts are evident when a more detailed investigation is undertaken of the development of δs at particular points on the windward slope. In the toe region the FLOWSTAR predictions of δs are typically lower than the wind tunnel and field measurements. The minimum δs predicted by FLOWSTAR also exists further downwind and occurs on the windward slope, not at the toe. This is evident from Figures 5.21 to 5.24 which plot the FLOWSTAR and field speed-up ratios against the wind tunnel ratios at four different heights. At the near-surface heights of 0.25 m and 1.0 m (Figures 5.21 and 5.22), but particularly at 1.0 m height, the negative perturbations predicted by FLOWSTAR are consistently lower than the line of equality for the tunnel data and are grouped below the field data. Indeed, at nearly all positions on the windward slope of the dune, the FLOWSTAR predictions of δs are generally lower than the tunnel and field measurements.

At the brinks on all three section lines, the FLOWSTAR predictions are consistently too large, with no agreement with the tunnel and field measurements. This is probably a result of the inability of the mathematical model to take changes in the flow structure caused by the downwind separated flow region into account. This over-prediction of δs is evident in Figures 5.21 and 5.22, where very large positive values of δs occur above the line of equality. No such over-prediction is exhibited further from the surface at heights of 4.0 m and 10.0 m (Figures 5.23 and 5.24 respectively). This feature is therefore only apparent close to the surface. However, it is at heights such as these where sand transport takes place, so it is important to be able adequately to predict flow velocity at these heights.

Table 5.16 Total data, horizontal velocity profile correlations

		Field		FLOWSTAR				Wind Tunnel		
	Height	0.25	1.0	0.25	1.0	4.0	10.0	0.25	1.0	4.0
Field	1.0	0.871								
FLOWSTAR	0.25	**0.589**	0.737							
	1.0	0.627	**0.783**	0.984						
	4.0	0.713	0.853	0.950	0.984					
	10.0	0.815	0.917	0.890	0.934	0.982				
Wind Tunnel	0.25	**0.844**	0.845	**0.701**	0.744	0.828	0.897			
	1.0	0.872	**0.903**	0.781	**0.830**	0.899	0.951	0.974		
	4.0	0.831	0.878	0.841	0.900	**0.928**	0.936	0.892	0.950	
	10.0	0.818	0.855	0.828	0.844	0.906	**0.910**	0.870	0.932	0.993

Table 5.17 Total data, vertical velocity profile correlations

		Field			FLOWSTAR			Wind Tunnel	
		Toe	Crest	Brink	Toe	Crest	Brink	Toe	Crest
Field	Crest	0.247							
	Brink	-0.105	0.742						
FLOWSTAR	Toe	**0.143**	0.685	0.982					
	Crest	-0.601	**0.012**	0.179	-0.561				
	Brink	0.624	-0.016	**-0.141**	-0.796	0.971			
Wind Tunnel	Toe	**0.248**	-0.116	0.345	**0.852**	-0.728	-0.971		
	Crest	-0.177	**0.355**	0.656	-0.548	**0.633**	0.520	-0.653	
	Brink	-0.218	-0.459	**-0.590**	0.313	-0.732	**-0.771**	0.725	-0.203

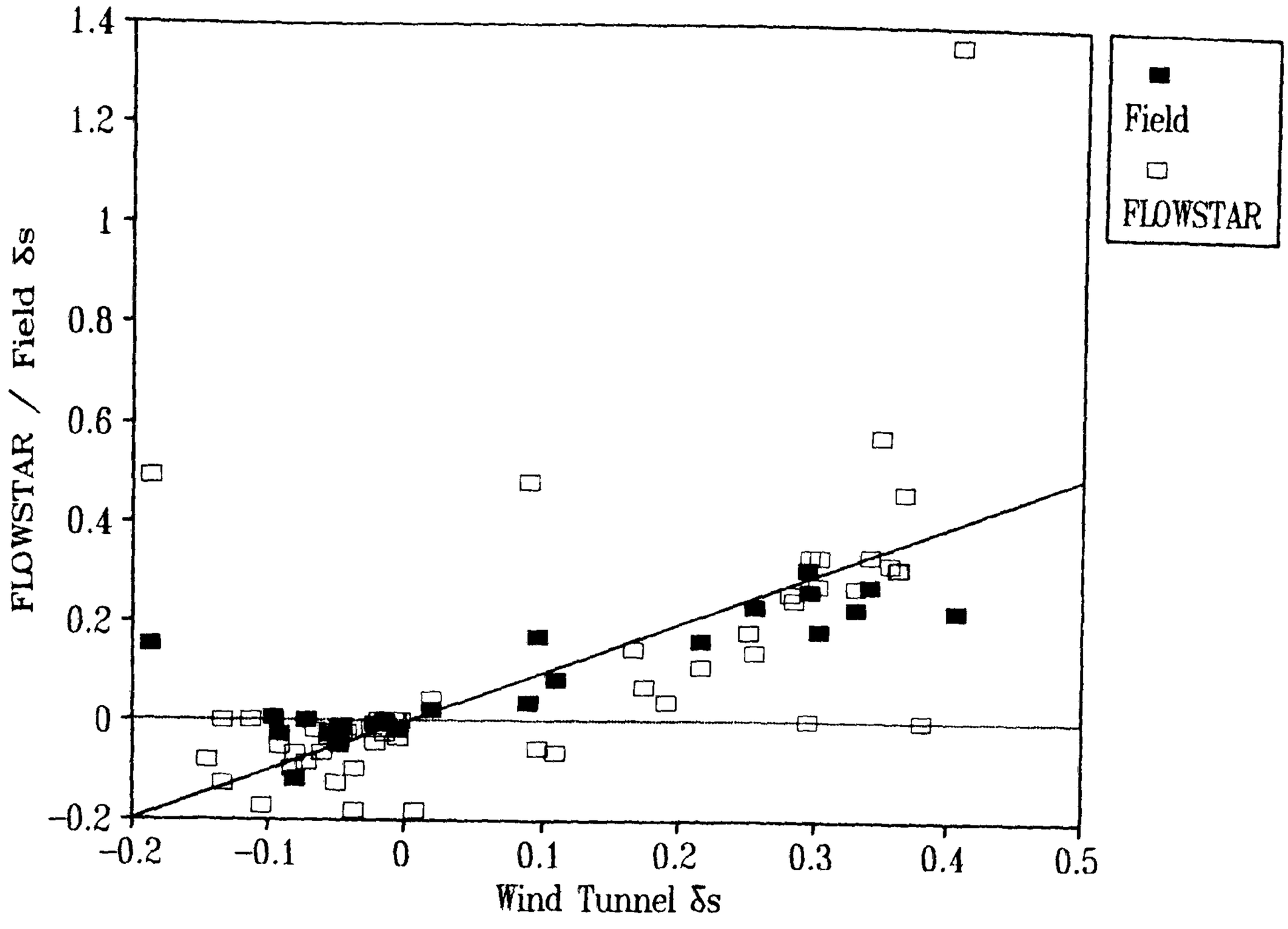

Figure 5.21 Comparison between the techniques of fractional speed-up ratio at 0.25 m.

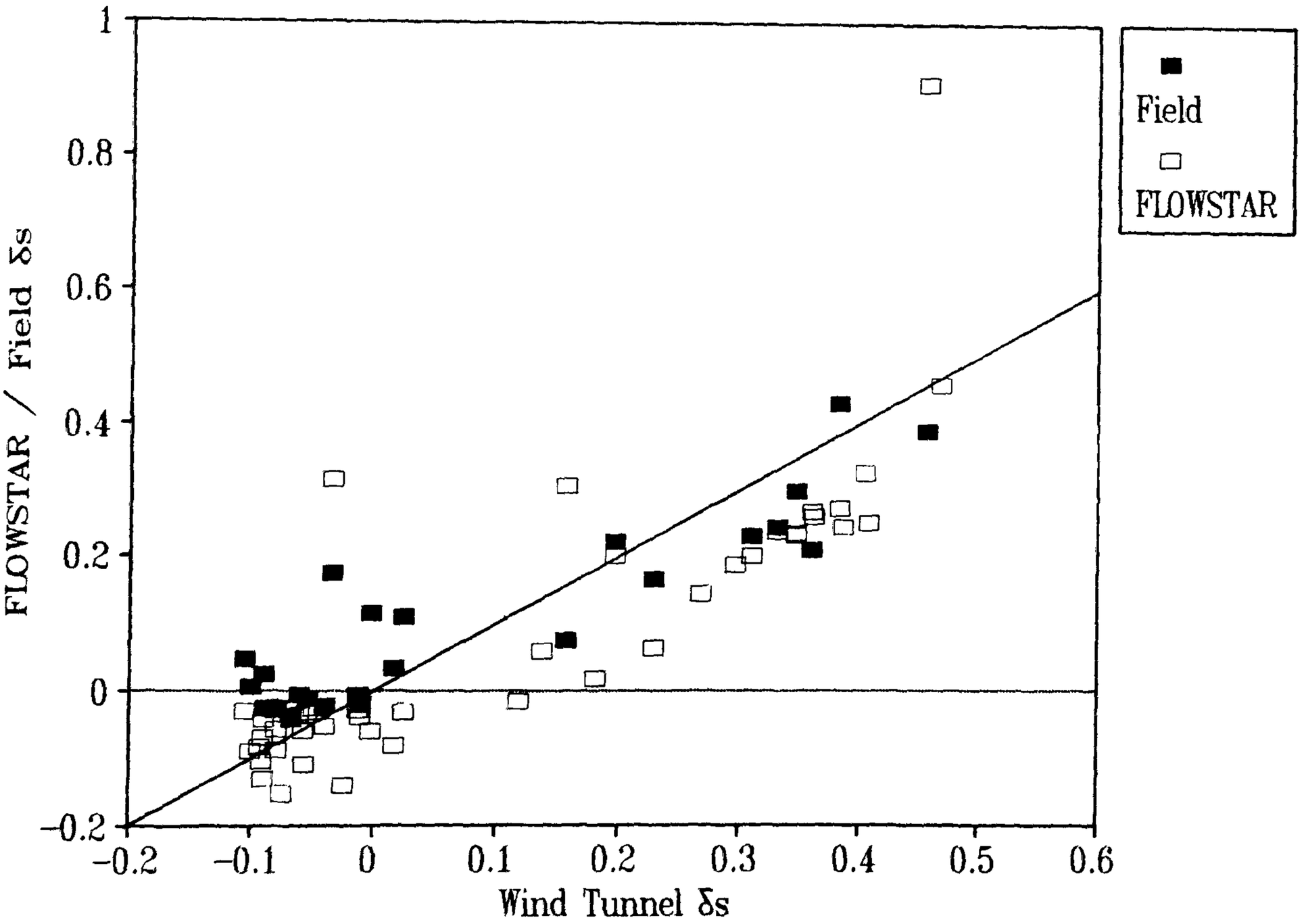

Figure 5.22 Comparison between the techniques of fractional speed-up ratio at 1.0 m.

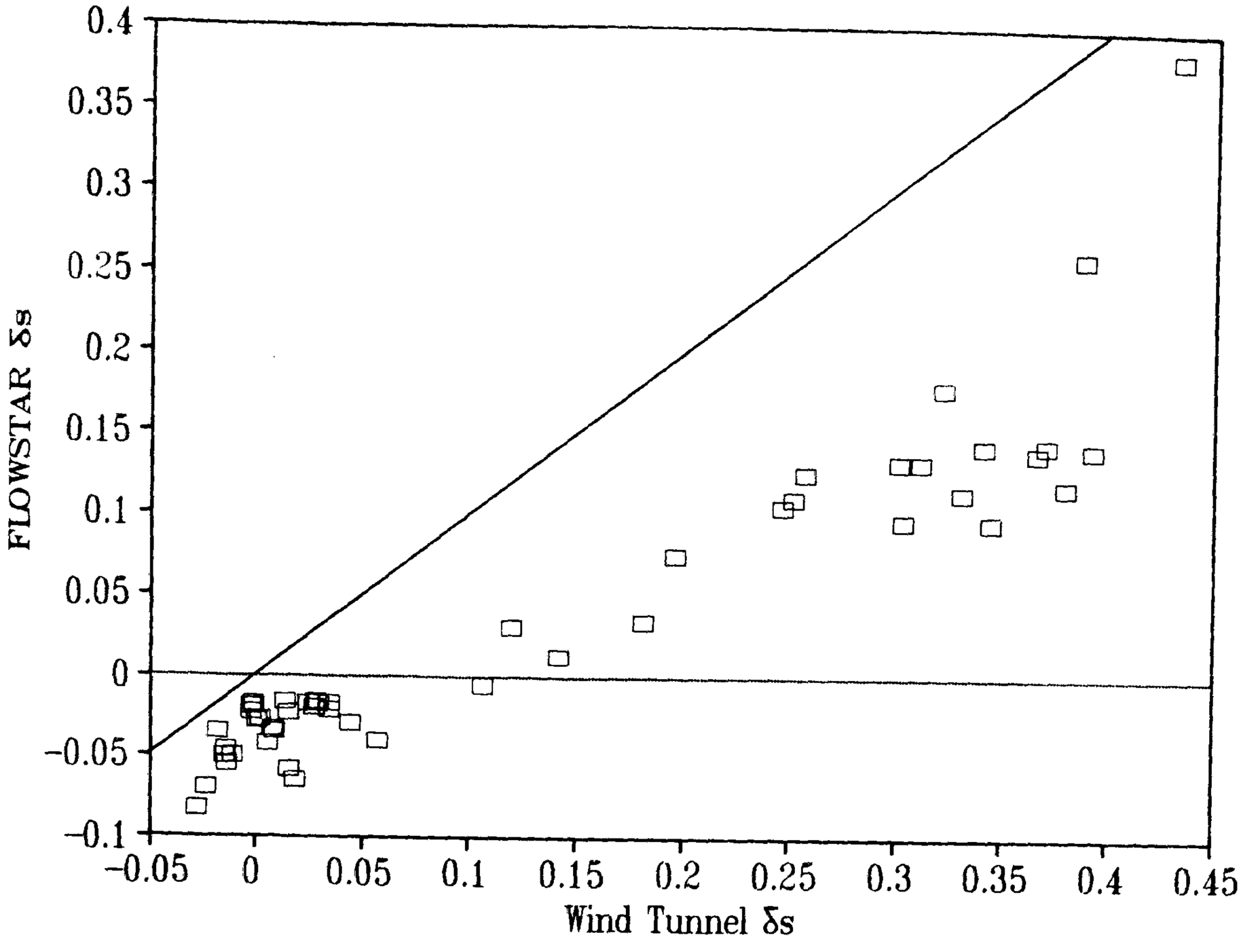

Figure 5.23 Comparison between the techniques of fractional speed-up ratio at 4.0 m.

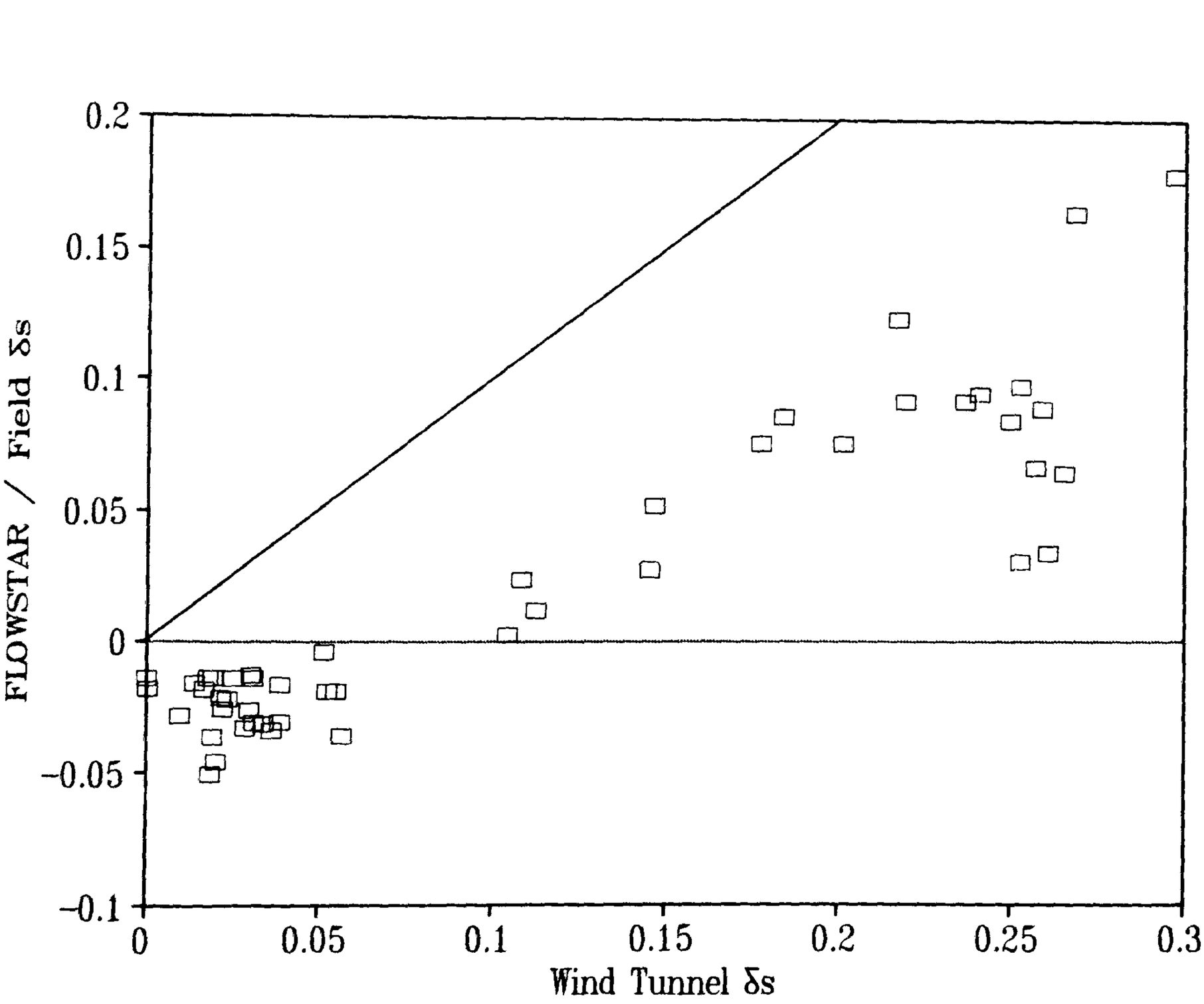

Figure 5.24 Comparison between the techniques of fractional speed-up ratio at 10.0 m.

Regression analysis on the total data-set at selected heights revealed a stronger association between the tunnel and field measurements than with the FLOWSTAR predictions. At 0.25 m and 1.0 m heights the r^2 values for the regressions between the tunnel and field data-sets were 0.7 and 0.8 respectively. Those between FLOWSTAR and the wind tunnel were 0.47 and 0.68 respectively and those between FLOWSTAR and the field data were 0.47 and 0.59. At greater distance from the surface, however, the agreement between the tunnel and FLOWSTAR results was good, with r^2 values at 4.0 m and 10.0 m of 0.86 and 0.82 respectively.

Although general agreement between the methods has been found for the horizontal profiles of fractional speed-up ratio, the distinct differences which have been noted may have important effects on the predicted morphological changes. These contrasts are discussed in Chapter 7.

The vertical profiles of δs presented for the different methods are ambivalent in their depiction of an inner-layer depth. Along the windward slope the height of the maximum δs is highly variable between 0.25 m and 2.0 m. The inner-layer heights calculated for the study dune in this investigation, using the available formulae, are given below:

Jackson & Hunt (1975) approximate formula: 1.90 m

Jensen *et al.* (1984) approximate formula: 0.55 m
(cited in Rasmussen *et al.*, 1985)

Hunt *et al.* (1988a) revised equilibrium formula: 0.68 m

The height of δs_{max} in this study may therefore be expected to lie somewhere between 0.22 m (*i.e.* 0.68/3) and 1.9 m. As discussed by Finnigan *et al.* (1990), all of the above equations rely on extending to hill-flows the parameterisations of turbulent shear stress strictly appropriate to equilibrium, horizontally homogeneous conditions. Hence, they can only provide order-of-magnitude estimates. Furthermore, some observations of flow at the crests of low hills have demonstrated contradictory evidence on the height of δs_{max}. Mickle *et al.* (1988) cite evidence of the maximum speed-up on Askervein Hill being within 1 m of the surface, whilst the measurements of Bradley (1980) confirmed the original JH theory. There is clearly scope for interpretation. It should also be noted that previous tests of the above equations have been carried out on hills with large inner-layer depths (10-20 m). In the present study the inner-layer is much smaller, and errors in the estimates of its depth are likely to be compounded. It is

suggested that a better delineation of the inner-layer height may be evident from shear stress profiles rather than velocity profiles, as discussed in the next section.

The variations of δs with height significantly disturb the log-linear nature of the velocity profile across the windward slope. Figures 5.25 to 5.27 show the velocity profiles evident from each of the techniques at the toe and crest on the centre-line and at the brink of the right flank. At the toe (Figure 5.25) the disruption of the log-linear profile due to flow deceleration is slight and is only noticeable below about 5.0 m. At the crest and brink (Figures 5.26 & 5.27), flow acceleration causes considerable disruption to the profile, observable even at 30 m height. On the crest, a constant log-linear profile is only observed below about 0.7 m. At the brink this is reduced to below about 0.5 m. This confirms previous measurements by Mulligan (1988) and Butterfield (1991), although neither of these studies investigated the profile structure at the toe of a dune. The non-log-linear nature of these velocity profiles is likely to have considerable effect on the calculation of shear velocity from velocity profiles in the field. This is particularly important in the field where no other method of shear velocity determination is currently available (see Chapter 6).

5.3 Shear Stress Comparisons

Both the wind tunnel measurements using cross-wire probes and the FLOWSTAR predictions furnish data on the perturbation of Reynold's stresses (-uwb component) at heights above the dune surface. In this section the measured and predicted stresses acquired from these two techniques are compared. Measurements of Reynold's stress were not undertaken in the field, but field shear velocity (u_*) calculations are compared to the assessments of Reynold's stress (converted to u_*) from the wind tunnel and FLOWSTAR data in Chapter 6.

The results discussed in this section refer to both horizontal and vertical profiles of shear stress (-uwb). They indicate significant changes in the value of shear stress above the surface of the dune, particularly close to the surface (< 1 m). Comparison between the techniques reveals generally similar relationships, although the FLOWSTAR predictions are anomalous in the lower half of the windward slope and at the brink.

In order directly to compare the wind tunnel measurements and FLOWSTAR predictions of shear stress it was first necessary to convert them to a similar format. Direct measurements of shear stress were made in the wind tunnel using the cross-wire probe (Chapter 4). These

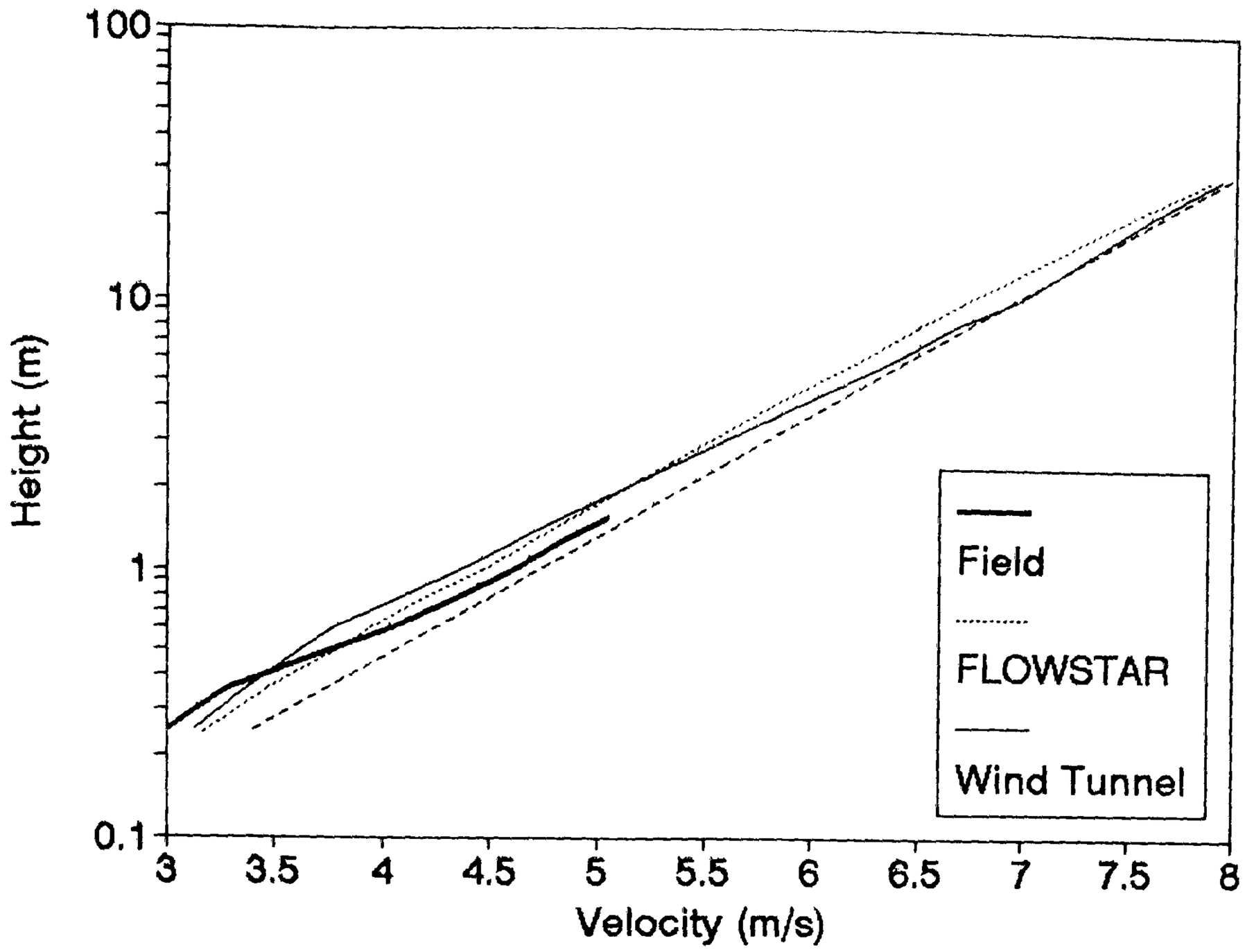

Figure 5.25 Vertical velocity profiles at the toe of the centre-line compared to the upwind log-linear profile.

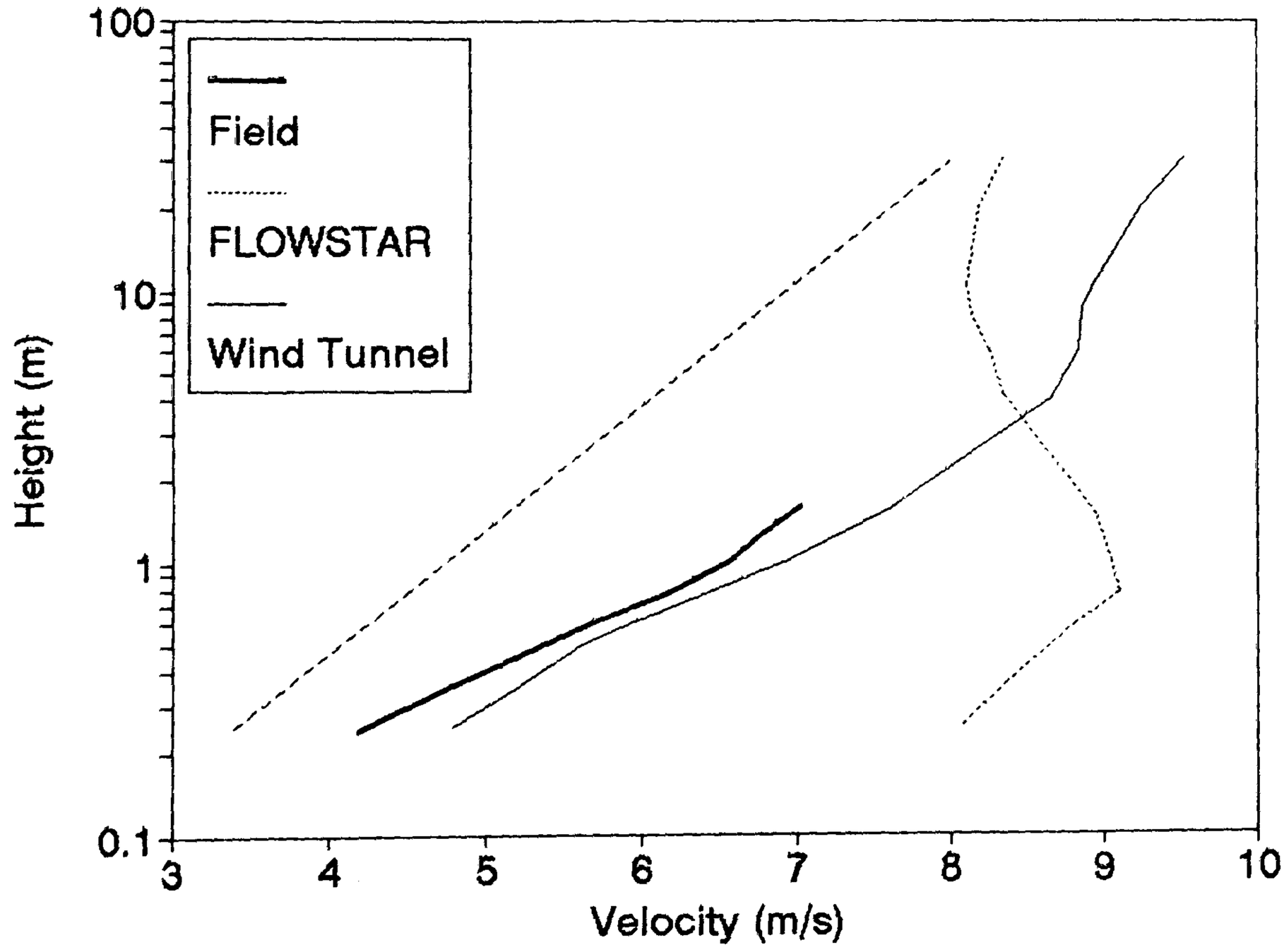

Figure 5.26 Vertical velocity profiles at the crest of the centre-line compared to the upwind log-linear profile.

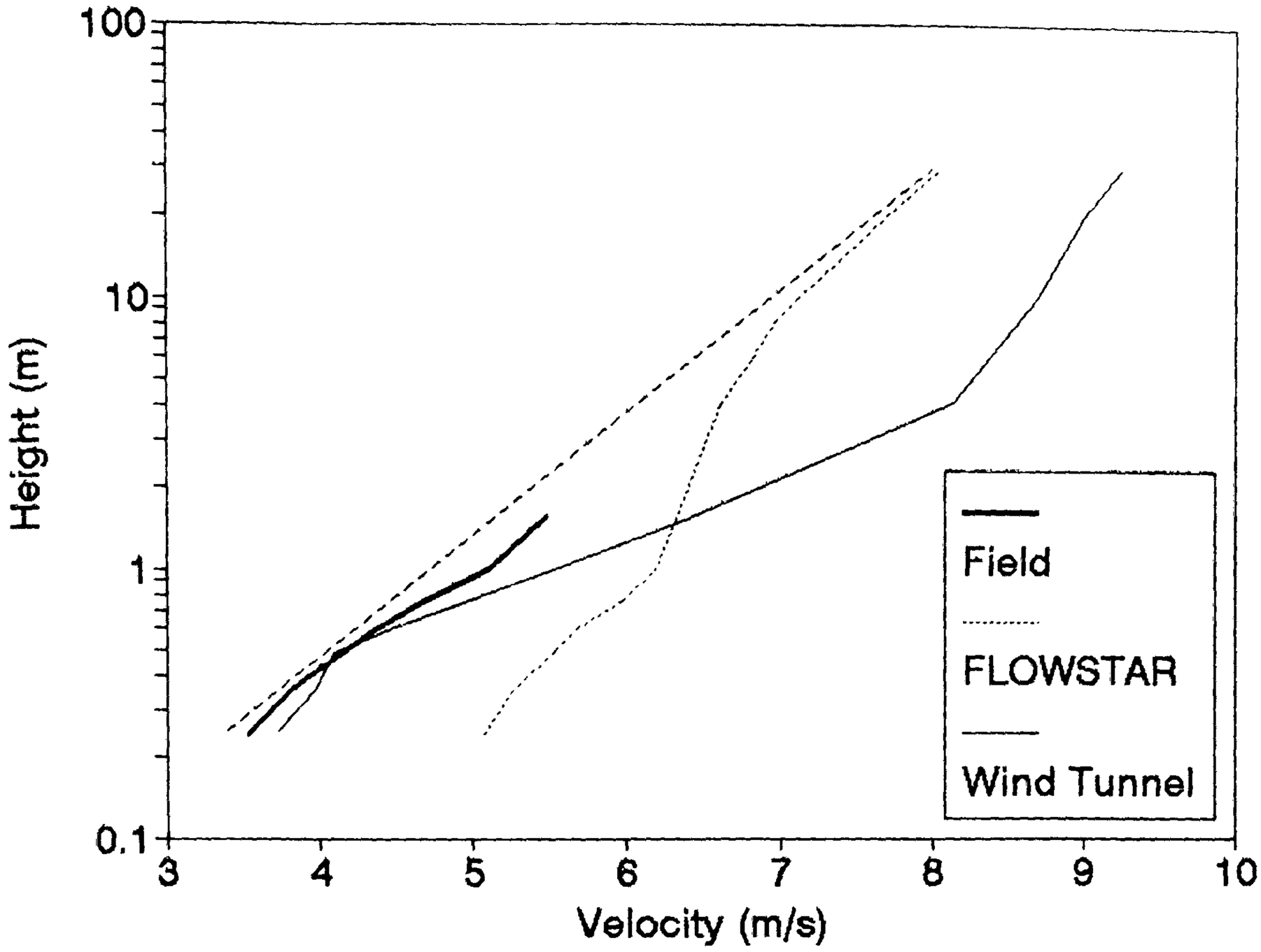

Figure 5.27 Vertical velocity profiles at the brink of the right flank compared to the upwind log-linear profile.

measurements were corrected for streamline angle and turbulence intensity and normalised by U_r^2 (the square of the mean reference velocity). They were converted to perturbations using the following equation:

$$-uwb_{pert} = ((-uwb/U_r^2)-(-uwb/U_{r\,up}^2)) / (-uwb/U_{r\,up}^2)$$

where:

$-uwb_{pert}$ = perturbation shear stress
$-uwb/U_r^2$ = local measured shear stress (normalised)
$-uwb/U_{r\,up}^2$ = upwind reference shear stress (normalised)

The FLOWSTAR predictions of shear stress (Chapter 3) were presented with the upwind (reference) shear stress subtracted. Conversion to a format analogous to the wind tunnel perturbations of shear stress was achieved in the following manner:

$$-uwb_{pert} = (-uwb_{local}) / u^{*2}$$

where:

$-uwb_{local}$= predicted local shear stress ((-)uwb - u_*^2)
u_* = upwind reference shear velocity (0.375 ms^{-1})

5.3.1 Centre-line

Figures 5.28 and 5.29 show the values of measured and predicted shear stress along the centre-line of the dune at two heights. The trends in the values from the two different methods are fairly similar. At 0.35 m height (Figure 5.28) the wind tunnel data show a fairly constant stress up to x = 50 m (although a small reduction in stress (-5%) may be visible between the toe and x = 50 m). Along the windward slope (between x = 50 m and x = 90 m) the data capture is scarce because of difficulties involved in positioning the cross-wire probe close to a steeply sloping surface. However, at x = 90 m (near the crest) the shear stress has risen by nearly 20% and this continues to a maximum at the crest (x= 110 m) where it attains a 70% increase over upwind values. The FLOWSTAR predictions are similar to the tunnel measurements in the upwind section (up to x= 50 m), although the variation in the predictions is much larger. Between the toe and x= 60 m, FLOWSTAR predicts a declining shear stress which is followed downwind (up to x= 80 m) by a rise of nearly 20% above upwind values. Downwind of this point, however, the similarity between the FLOWSTAR predictions and wind tunnel measurements is reduced. Between x = 90 m and x = 110 m (the crest) the predictions are highly

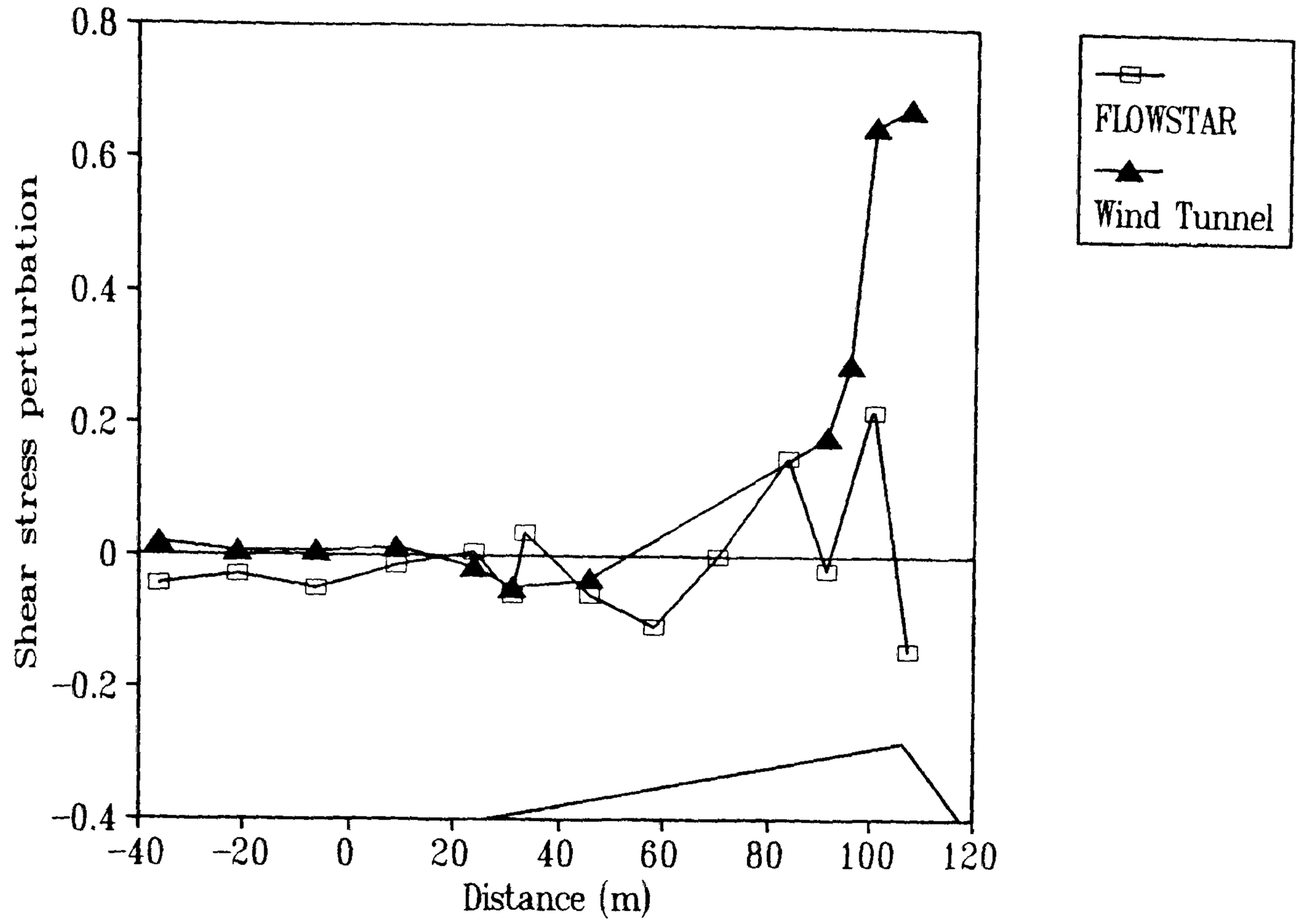

Figure 5.28 Shear stress (-uwb) perturbations at 0.35 m on the centre-line.

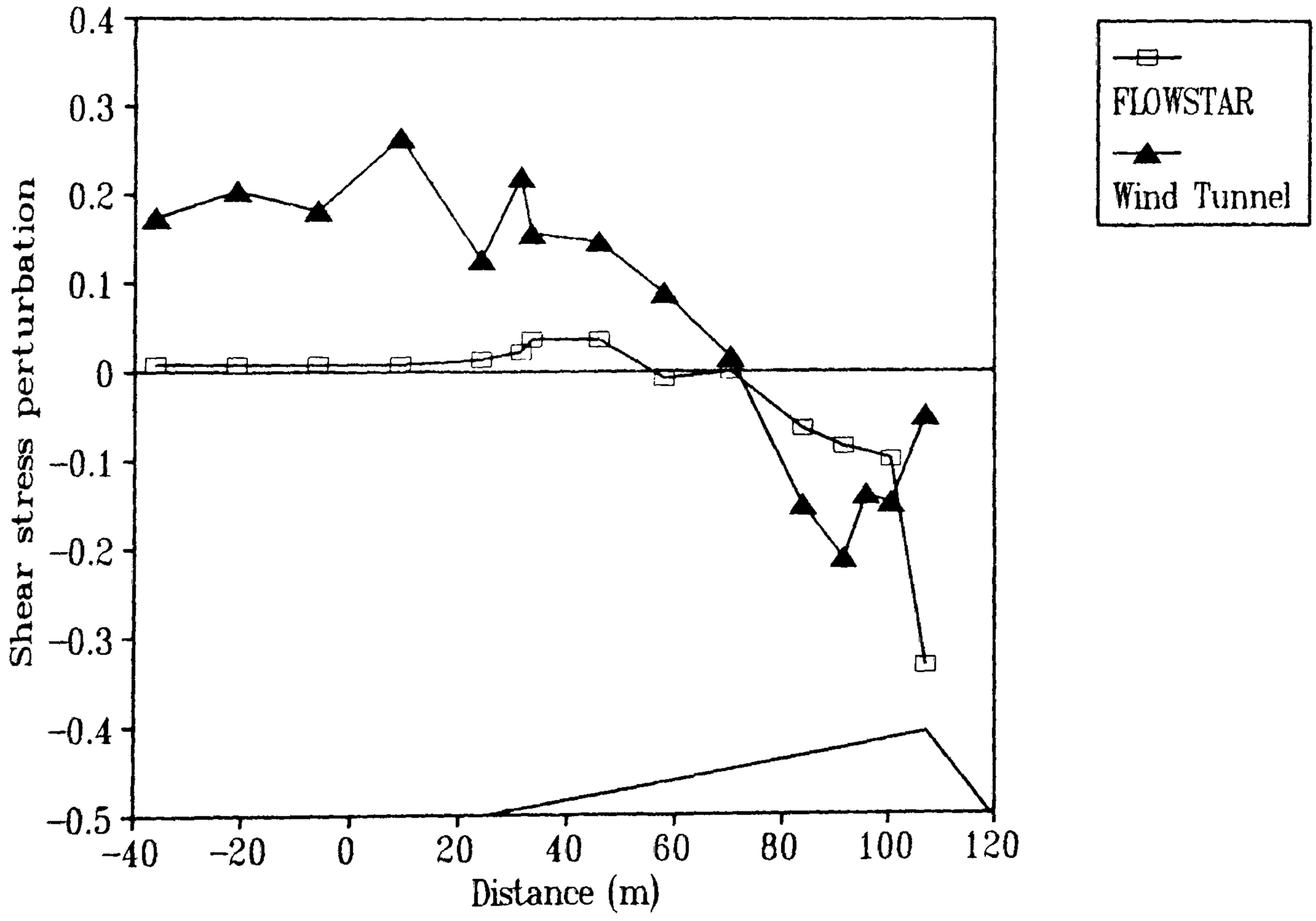

Figure 5.29 Shear stress (-uwb) perturbations at 1.0 m on the centre-line.

variable ranging from +0.2 to -0.2 in no discernible relationship. The minimum (-0.2) is at the crest.

The results at 1.0 m height (Figure 5.29) are in contrast to those near the surface (Figure 5.28). The wind tunnel measurements in Figure 5.29 show large positive perturbations of between 10% and 20% even 60 m upwind of the toe of the dune. The results presented in Chapter 4 suggested that this perturbation was initiated about 120 m upwind and was probably due to the non-representative nature of the simulated atmospheric boundary layer upwind of x= 0 m (Chapter 4.2). At the toe of the dune a steady decline in shear stress is evident to a minimum of -0.23 at x = 90 m. A downwind rise in shear stress is then apparent to a value of -0.05 at the crest. FLOWSTAR shows no positive perturbation upwind of the toe of the dune and only a small perturbation (+0.05) at the toe itself. A steady decline is then apparent to just upwind of the dune crest where the shear stress perturbation reaches a value of -0.1. This is followed by a perturbation minimum of -0.35 at the crest itself.

The trend in both sets of results seems to be of a rise in shear stress toward the crest of the dune near the surface (0.35 m), as shown in Figure 5.28, and a decline in shear stress toward the crest at a height of 1.0 m (Figure 5.29). The differences in the development of shear stress at different heights is exemplified by the vertical stress profiles at the toe and crest of the centre-line shown in Figures 5.30 and 5.31.

At the toe (Figure 5.30) both the FLOWSTAR and wind tunnel data show a generally decreasing shear stress toward the surface. In the case of the wind tunnel profile this decrease begins at 5 m height. The FLOWSTAR predictions are less variable in the vertical profile than the wind tunnel measurements and show no discernible perturbation above 1 m. However, between 1.0 m and 0.5 m the perturbations become slightly positive before decreasing to a minimum of -0.15 at 0.25 m. Shear stress gradients are therefore evident in the toe profile below 1 m.

At the crest (Figure 5.31) the shear stress gradients are more dramatic. Between 12 m and about 1.5 m the wind tunnel data demonstrate decreasing perturbations to a minimum of about -0.45 between 4.5 m and 2.0 m height. Below 1.5 m, this trend is reversed with an increasing perturbation to a maximum at 0.35 m of 0.75. The perturbations become positive at a height of about 1.0 m. This trend is mirrored by the FLOWSTAR predictions to some extent, although here the perturbations tend to occur lower in the profile. The FLOWSTAR data demonstrate decreasing and negative perturbations from below about 4.5 m, which is where the wind tunnel data is close to exhibiting a minimum shear stress perturbation. The FLOWSTAR predictions

attain a minimum perturbation at about 0.6 m. Below this height the perturbations increase to a maximum at 0.25 m of 0.15. The FLOWSTAR data demonstrate positive perturbations only below about 0.3 m to 0.4 m.

5.3.2 The Flanks

The shear stress perturbations over the flanks of the dune are very similar to those over the centre-line (Figures 5.28 and 5.29). The perturbations in the wind tunnel data along the left and right flanks at 0.35 m (Figures 5.32 and 5.33) both demonstrate a rise in shear stress toward the crest and then a decline toward the brink. Only a few data points are presented for the left flank (Figure 5.32) because the slope of the surface and the distribution of roughness elements created difficulties with the positioning of the probe along the windward slope. Nevertheless, a trend in stress perturbation can be identified. The comparable FLOWSTAR predictions shown in Figures 5.32 and 5.33 are more variable and a trend is less apparent. However, a tendency for higher shear stress perturbations at or near the crest and a decline at the brink can be distinguished.

At 1.0 m height (Figures 5.34 and 5.35) the trends are reversed. On both flanks the wind tunnel data demonstrate a rise in positive shear stress perturbations around the toe and the concave regions of the windward slope, followed by a reduction in stress to near upwind values toward the windward slope convexity and crest. Between the crest and brink of the left flank this minimum in stress is succeeded by an increasing positive perturbation. This trend is not so easily identifiable on the right flank (Figure 5.35). The FLOWSTAR predictions show similar general trends to the wind tunnel measurements but do not demonstrate the same degree of perturbation. On both the left and right flank the FLOWSTAR data exhibit a small positive perturbation in shear stress (+5%) around the toe followed by a decrease to negative values (of about -10%) toward the crest and just downwind. On both flanks the penultimate data points show an increase in perturbation between the crest and brink (similar to the tunnel data), although this is succeeded by a sharp drop to a perturbation of about -0.17 at the brinks.

The vertical profiles of shear stress at the toe of the flanks are also similar to the centre-line data. The wind tunnel results at the toes of the left and right flanks (Figures 5.36 and 5.37) demonstrate positive perturbations at about 12 m height which dwindle to zero close to the surface (below about 1.5 m). There appears to be little or no perturbation in the wind tunnel data below this height although on the right flank a small near-surface negative perturbation may be distinguished. The FLOWSTAR predictions show no perturbation above 0.5 m in height. Below

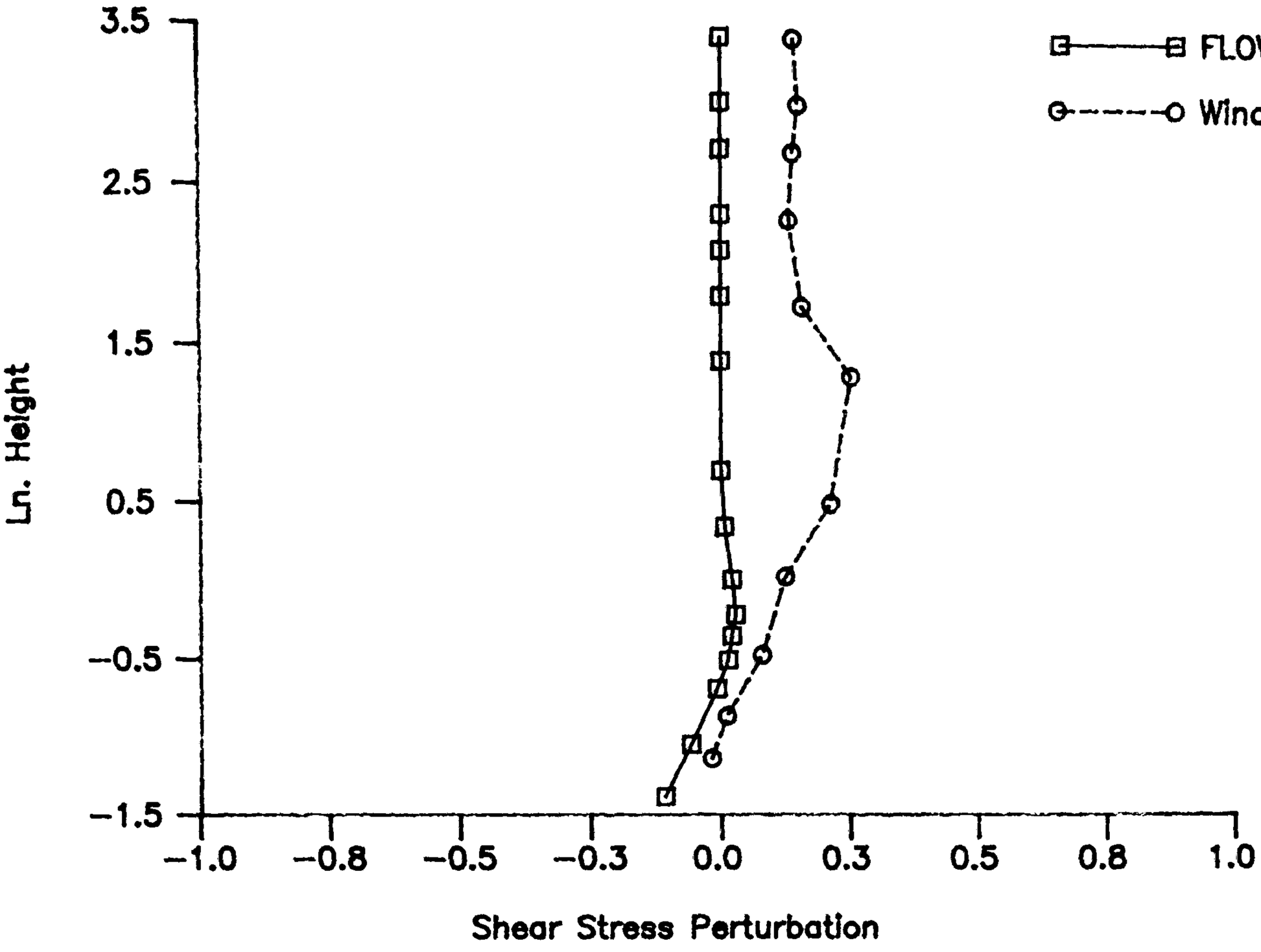

Figure 5.30 Vertical profiles of shear stress at the toe of the centre-line.

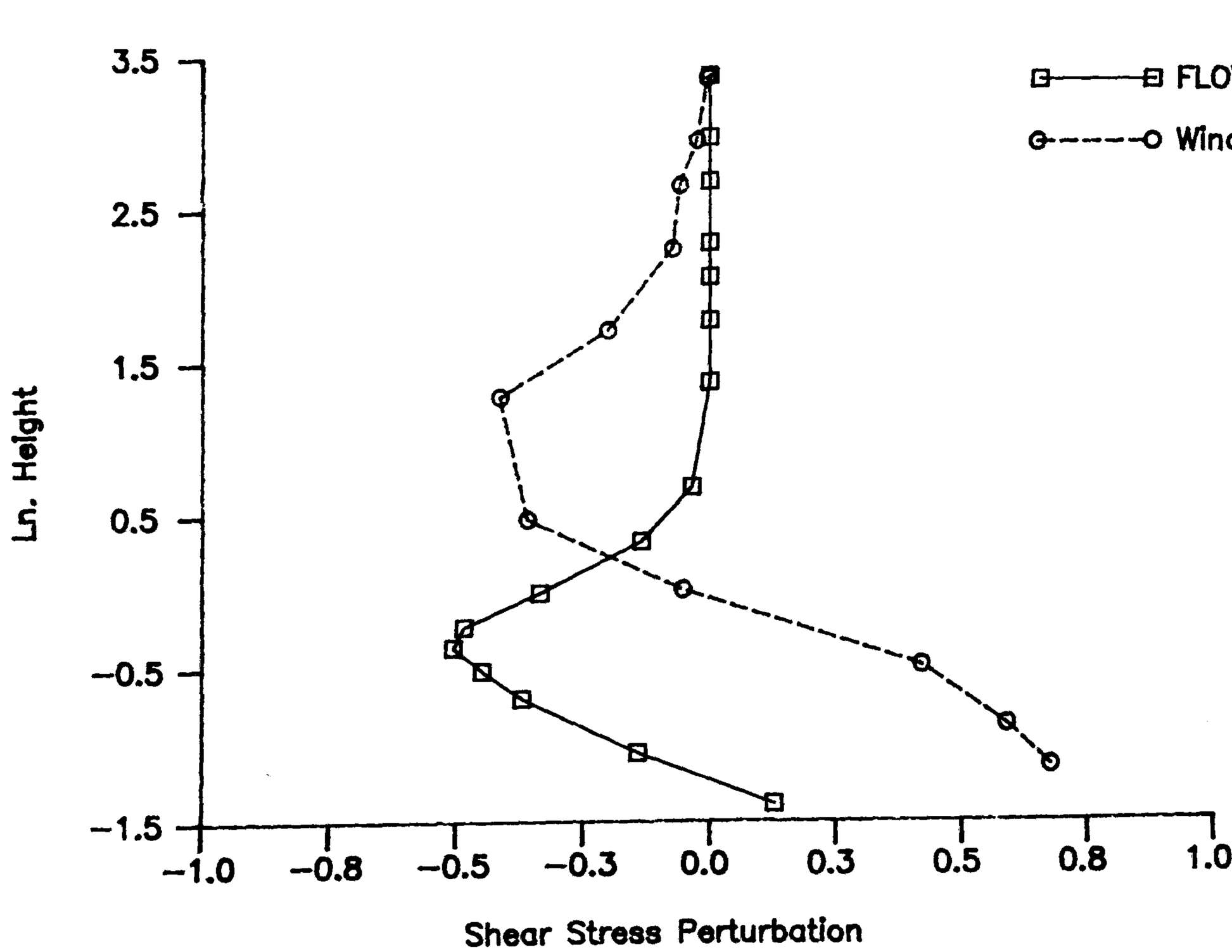

Figure 5.31 Vertical profiles of shear stress at the crest of the centre-line.

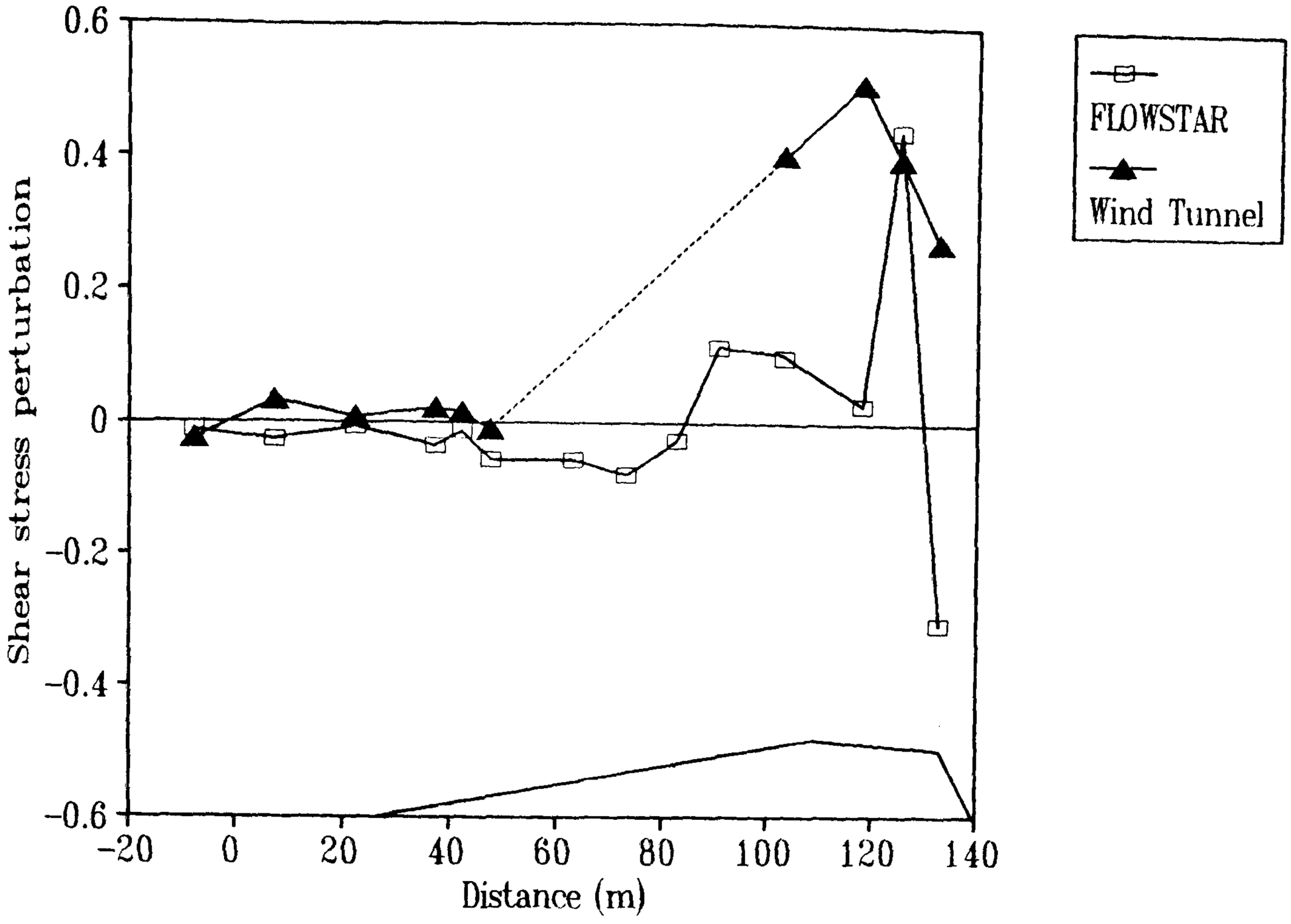

Figure 5.32 Shear stress (-uwb) perturbations at 0.35 m on the left flank.

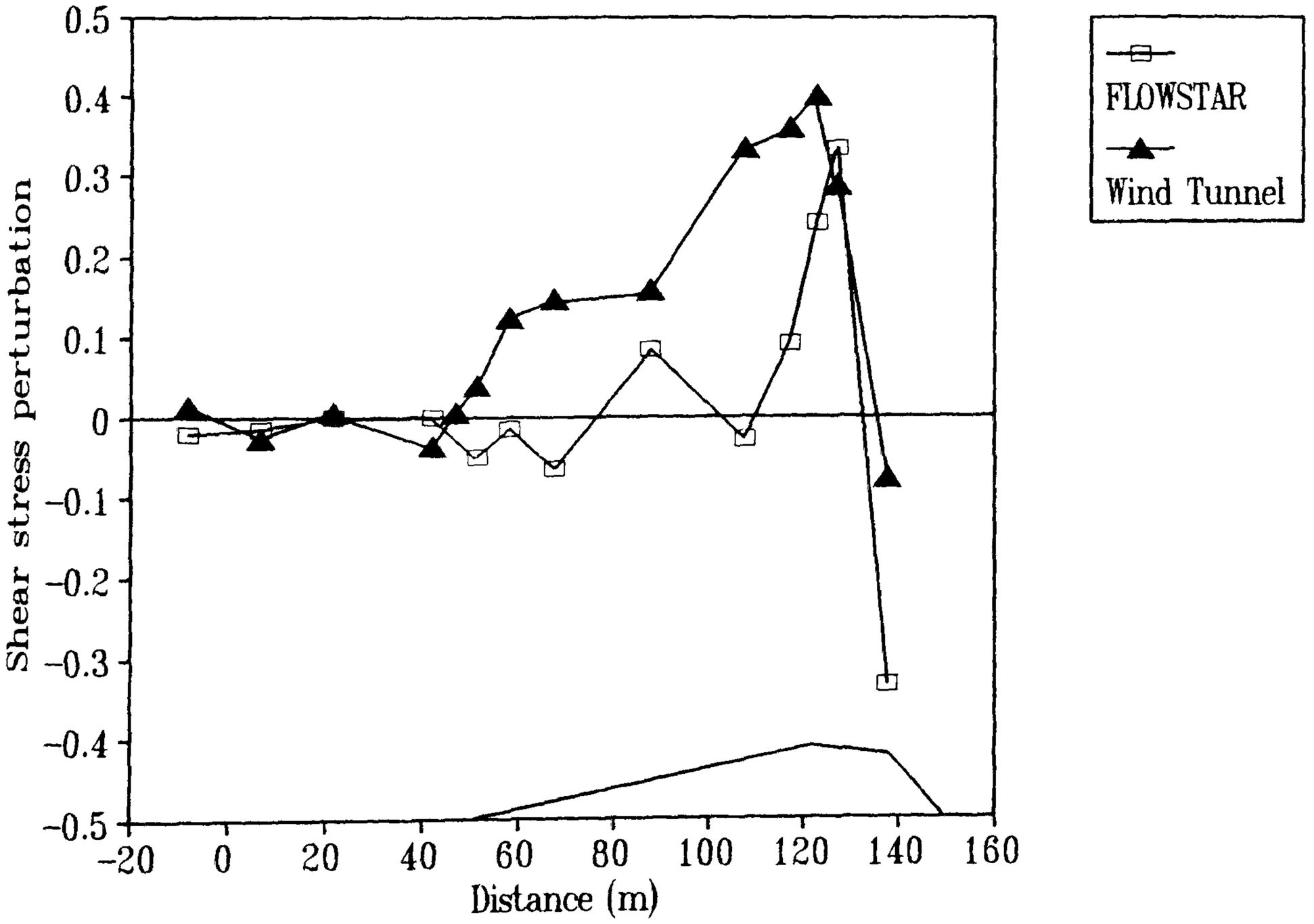

Figure 5.33 Shear stress (-uwb) perturbations at 0.35 m on the right flank.

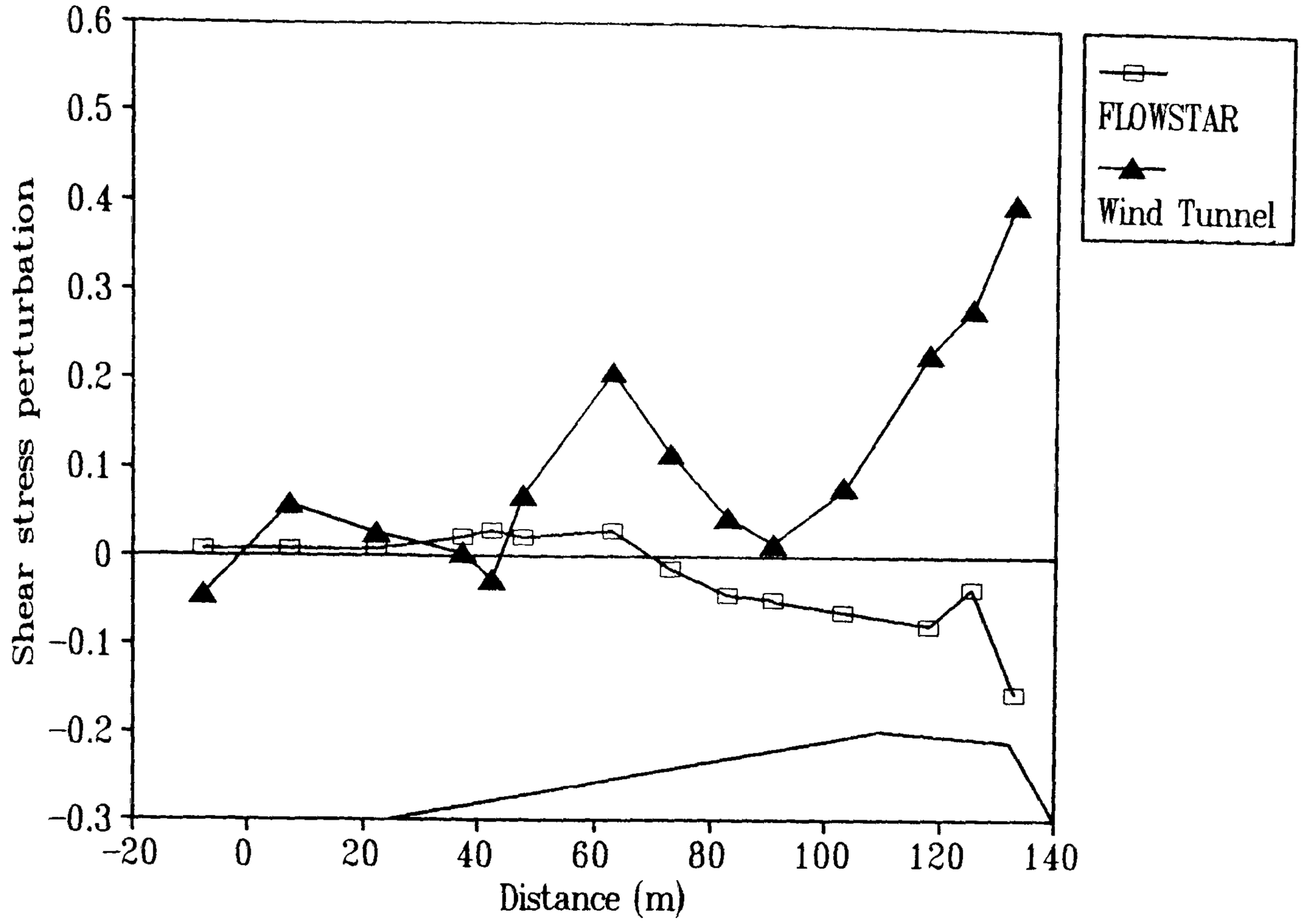

Figure 5.34 Shear stress (-uwb) perturbations at 1.0 m on the left flank.

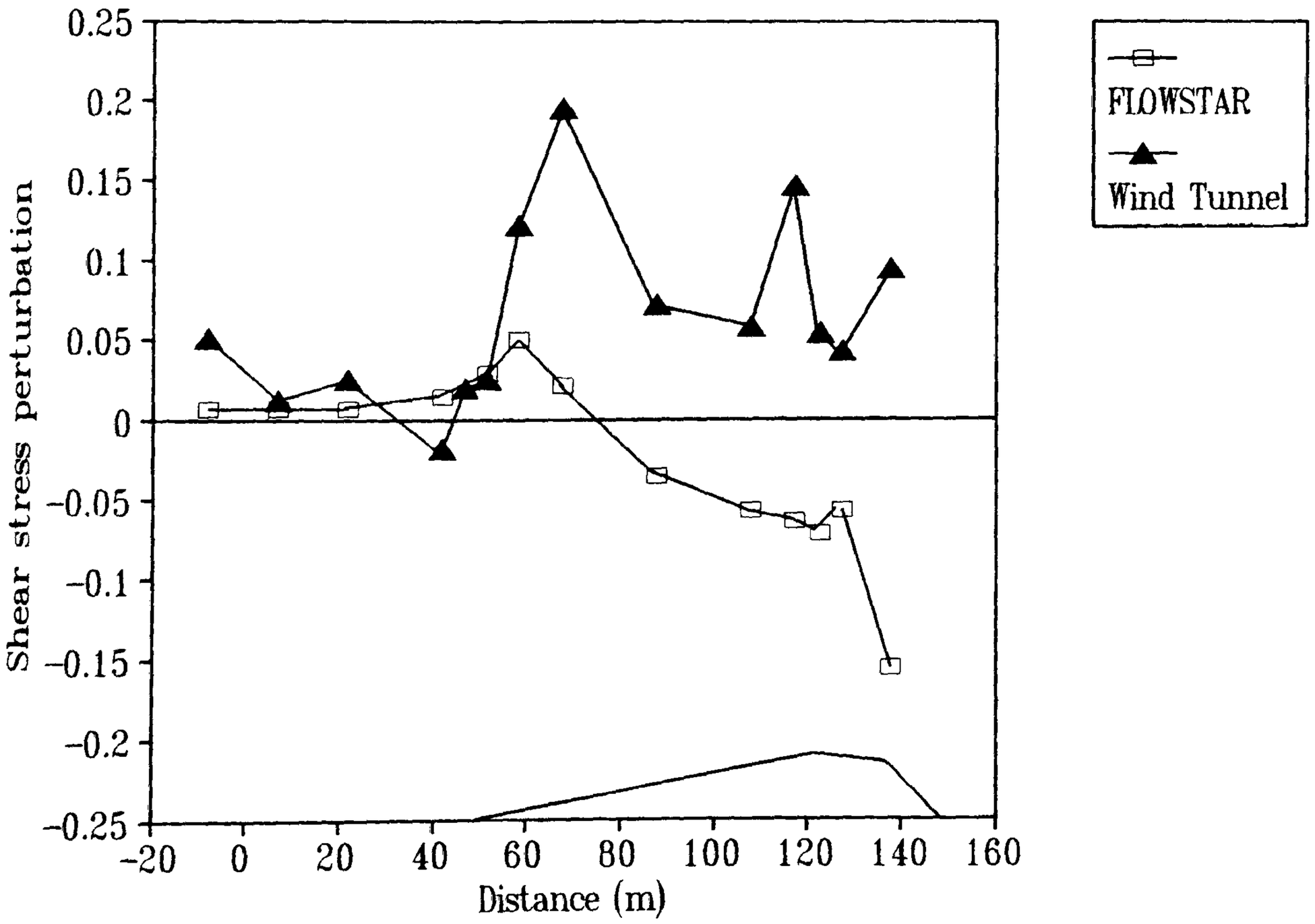

Figure 5.35 Shear stress (-uwb) perturbations at 1.0 m on the right flank.

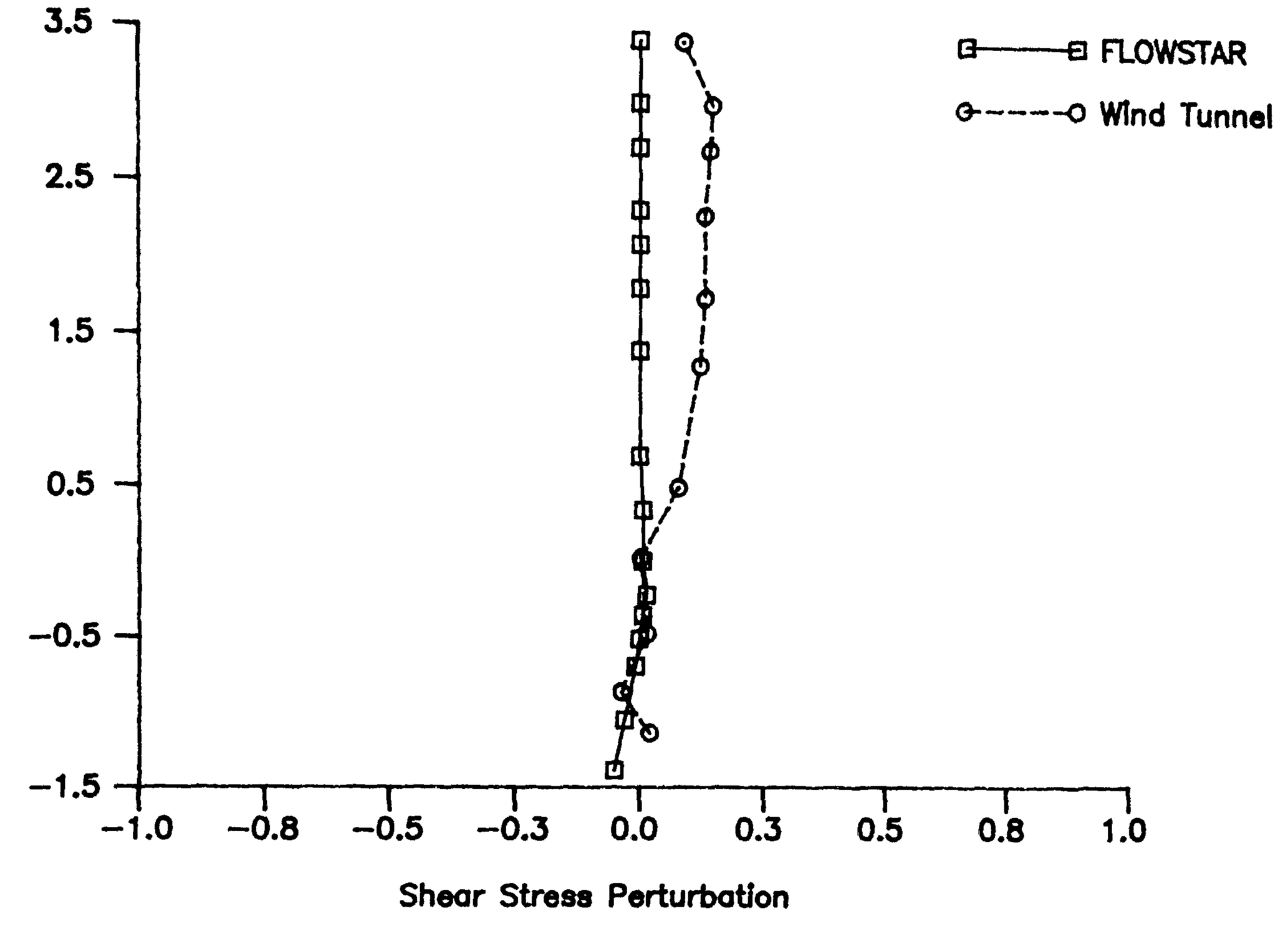

Figure 5.36 Vertical profiles of shear stress at the toe of the left flank.

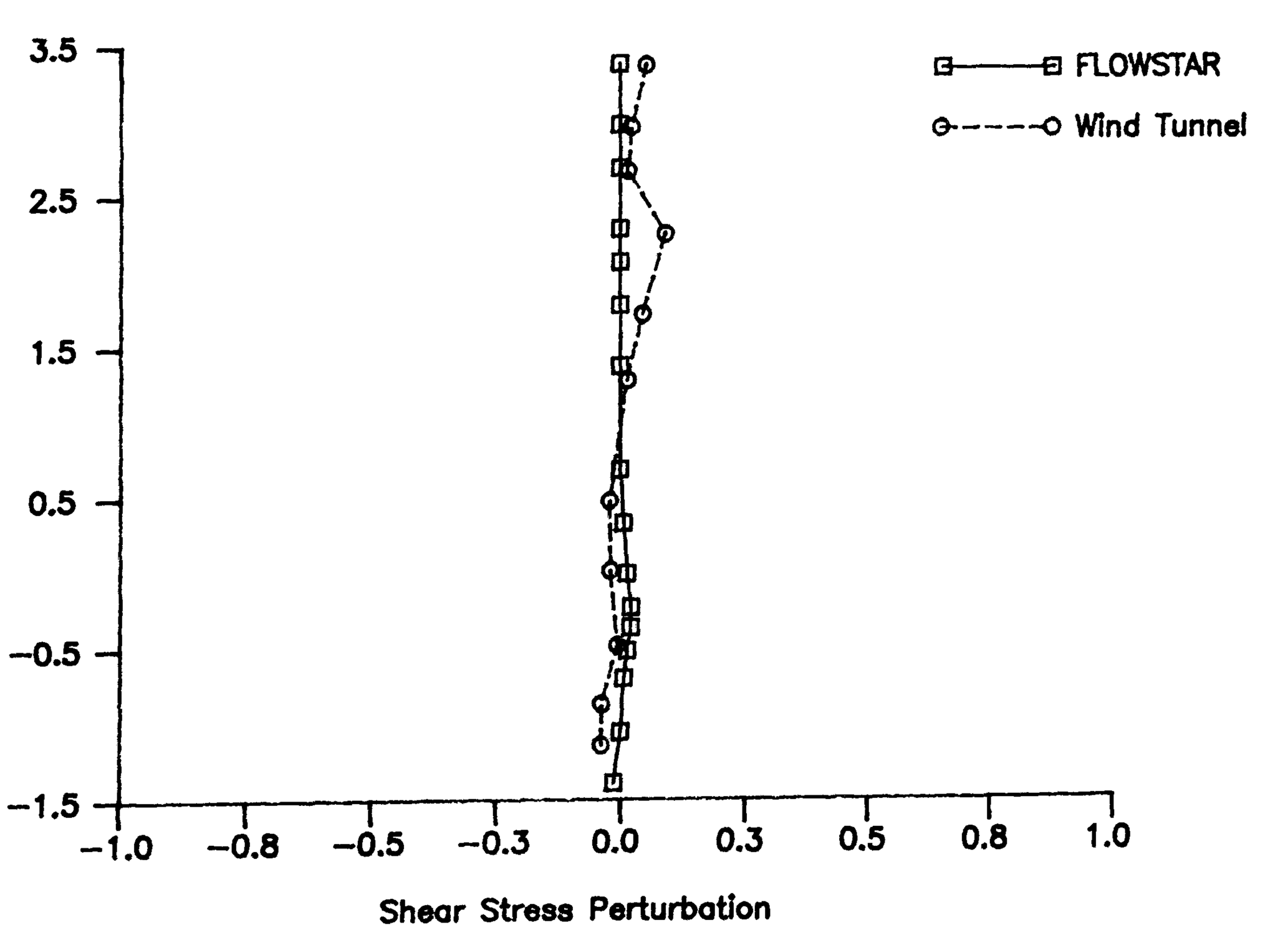

Figure 5.37 Vertical profiles of shear stress at the toe of the right flank.

this height very small (<-5%) negative perturbations may be identified, decreasing toward the surface.

At the crests of the flanks (Figures 5.38 and 5.39), the vertical profiles of shear stress for the wind tunnel data are almost identical to the centre-line tunnel data. At about 3 m in height the data for both flanks demonstrate minima in shear stress perturbations of about -0.45. Below this there is an increase in shear stress toward the surface with maxima (of +0.5) at the lowest measurement height of 0.25 m. As with the centre-line data, the perturbations are positive only below a height of about 1.0 m. The FLOWSTAR predictions at the crest of each flank (Figures 5.38 and 5.39) show similar vertical-profile shapes as the wind tunnel perturbations. However, the minimum perturbations of the predicted values occur closer to the surface (0.6 m) than the wind tunnel measurements. Below this height there is an increase in the values of predicted shear stress, with maximum positive perturbations occurring close to the surface at 0.25 m. As on the centre-line, the FLOWSTAR data at the crests of the flanks demonstrate positive perturbations in shear stress only below about 0.4 m.

At the brinks of the flanks, the vertical profiles of shear stress (Figures 5.40 and 5.41) show near-surface reductions with both the wind tunnel measurements and FLOWSTAR predictions. Above 1.6 m, the profiles in Figures 5.40 and 5.41 duplicate the profiles at the crests (Figures 5.38 and 5.39). However, below this height the wind tunnel data show a reduced increase in stress toward the surface, reaching maximum positive perturbations on both flanks at about 0.5 m. The shear stress is then reduced toward the surface. On the right flank, this involves a shift to negative perturbations in shear stress below 0.4 m. The FLOWSTAR predictions are also reduced below about 1.6 m at the brinks. However, the FLOWSTAR data shown in Figures 5.40 and 5.41 reveal no increase in stress below its minimum value at 0.6 m. At this height at the brinks there is only a reduction in the rate of shear stress decline. Below 0.6 m on both flanks there is an increasing negative perturbation toward the surface.

5.3.3 Discussion and Conclusion

One of the more noticeable aspects of both the measurements and predictions of shear stress perturbations is the strong stress gradient near the surface below about 1 m in height. This gradient is less noticeable at the toe of the dune on the centre-line or flanks, but it is very marked at the crest and brink. The wind tunnel measurements and FLOWSTAR predictions vary in their representation of this stress gradient, particularly in terms of the depth of flow in which

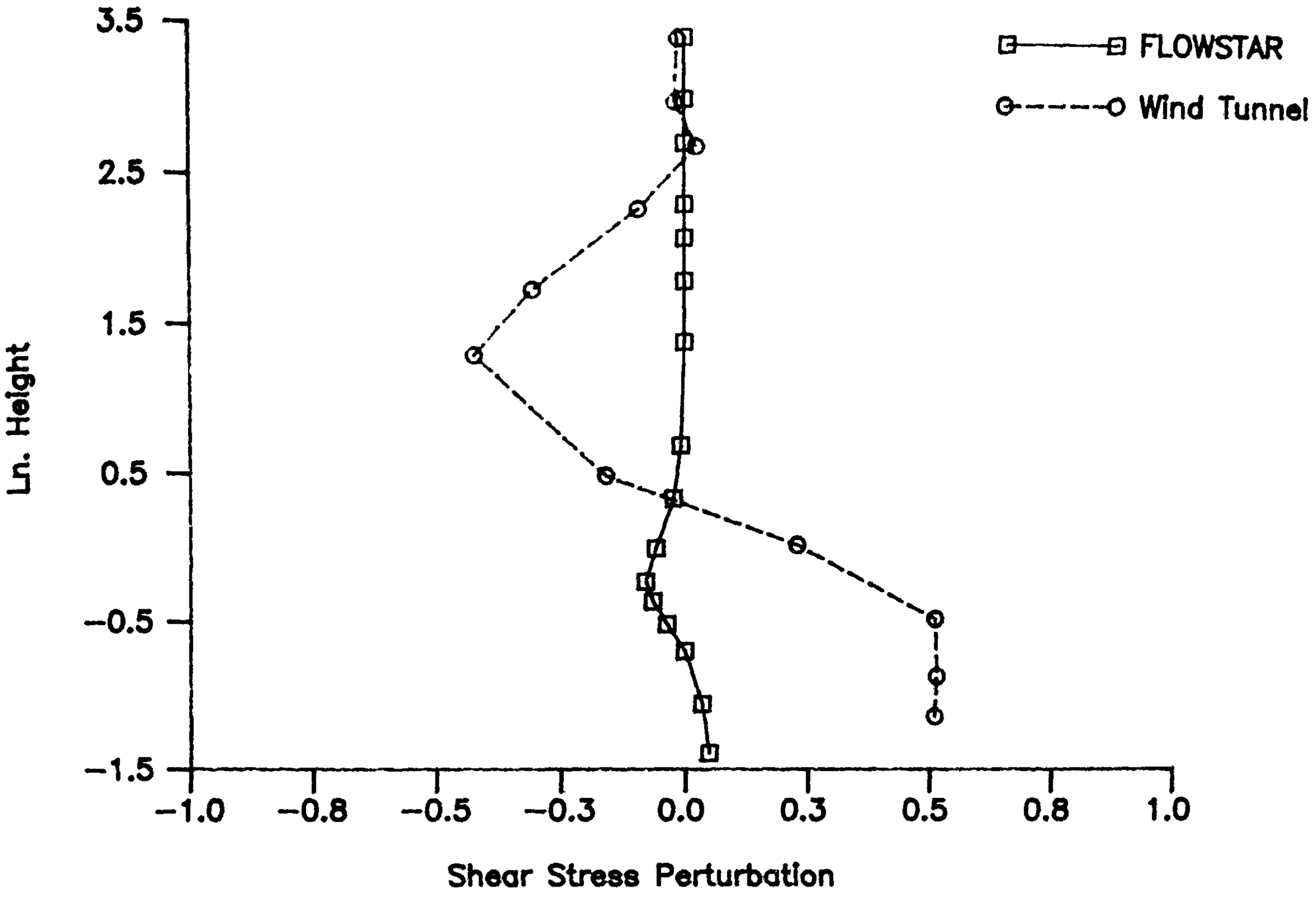

Figure 5.38 Vertical profiles of shear stress at the crest of the left flank.

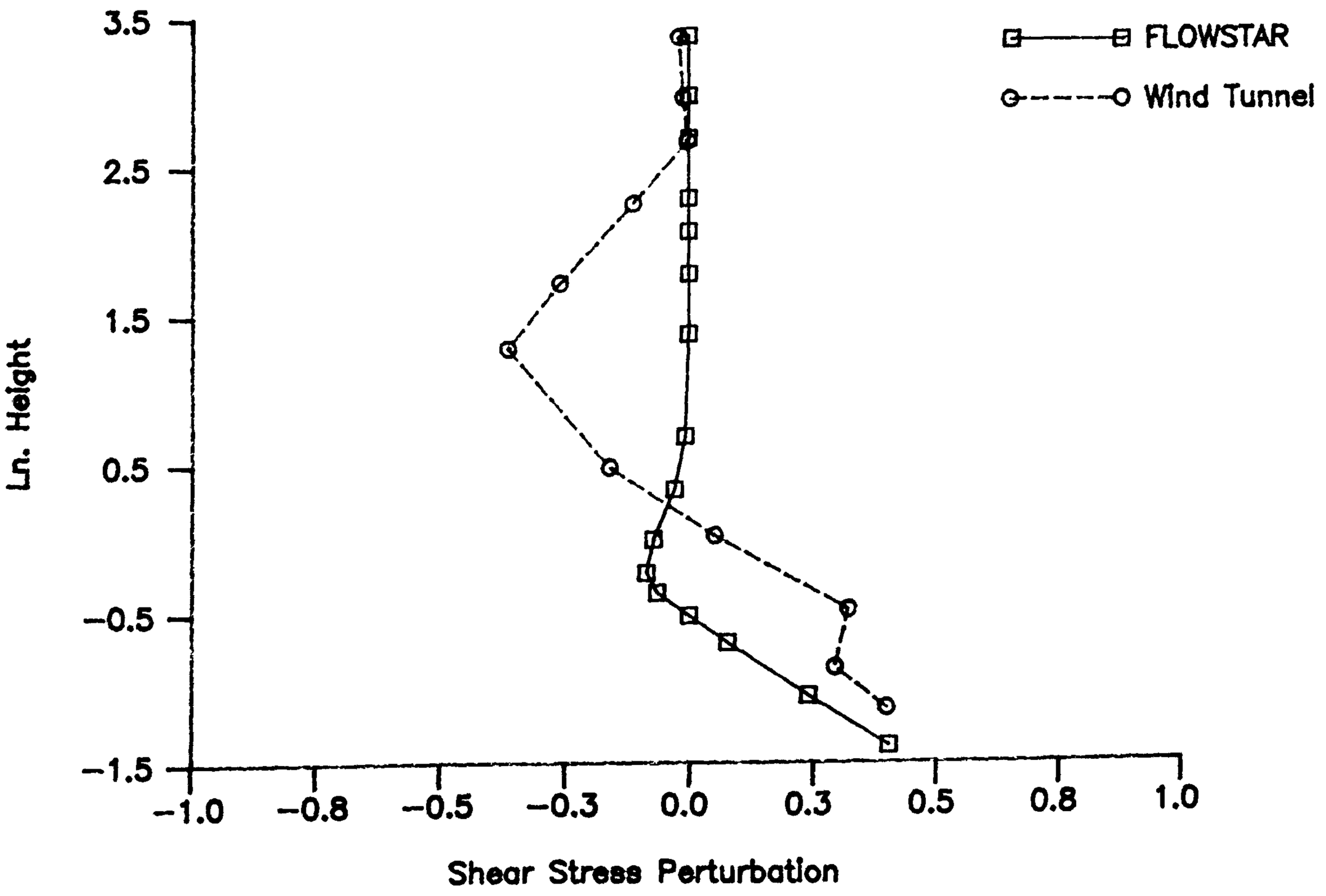

Figure 5.39 Vertical profiles of shear stress at the crest of the right flank.

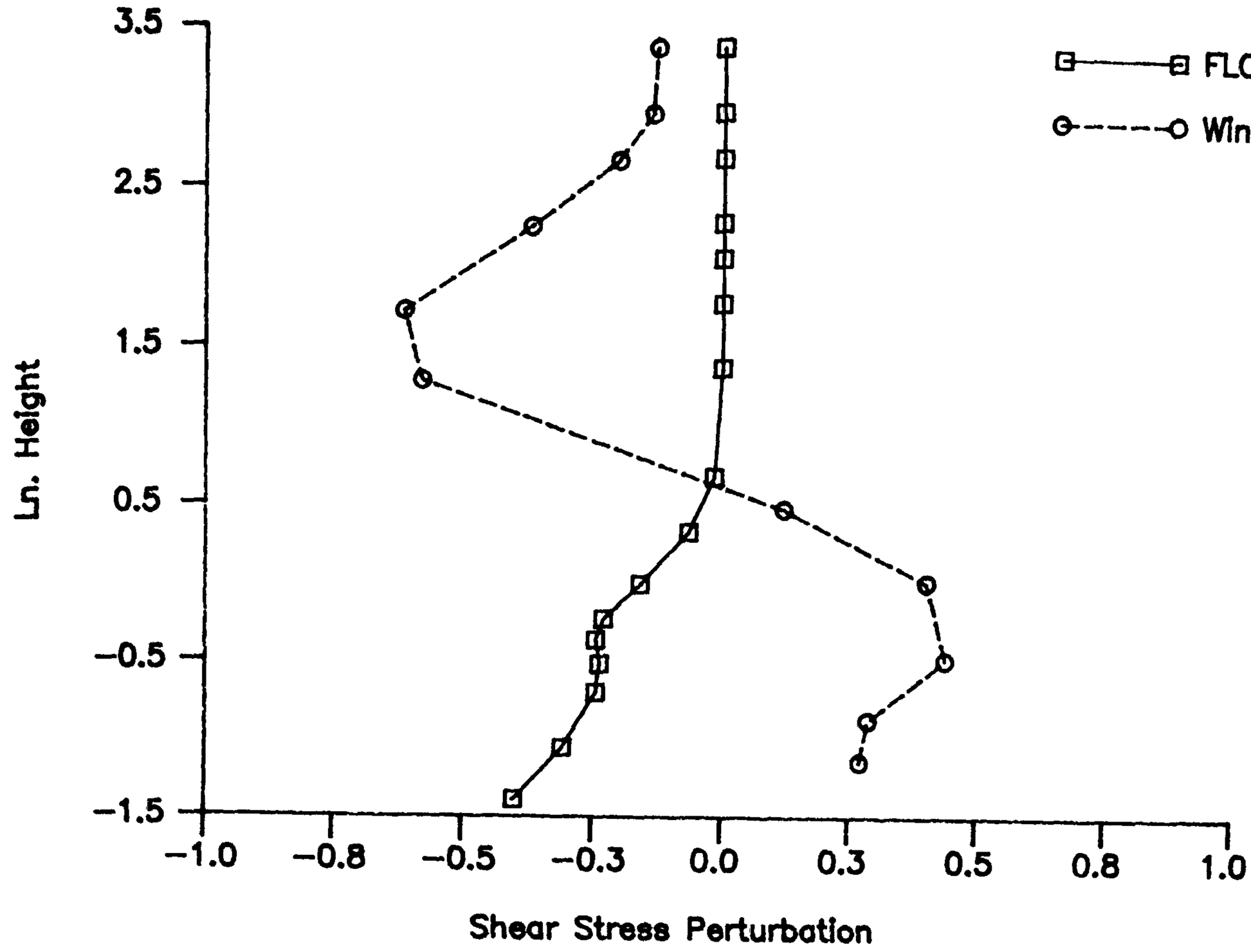

Figure 5.40 Vertical profiles of shear stress at the brink of the left flank.

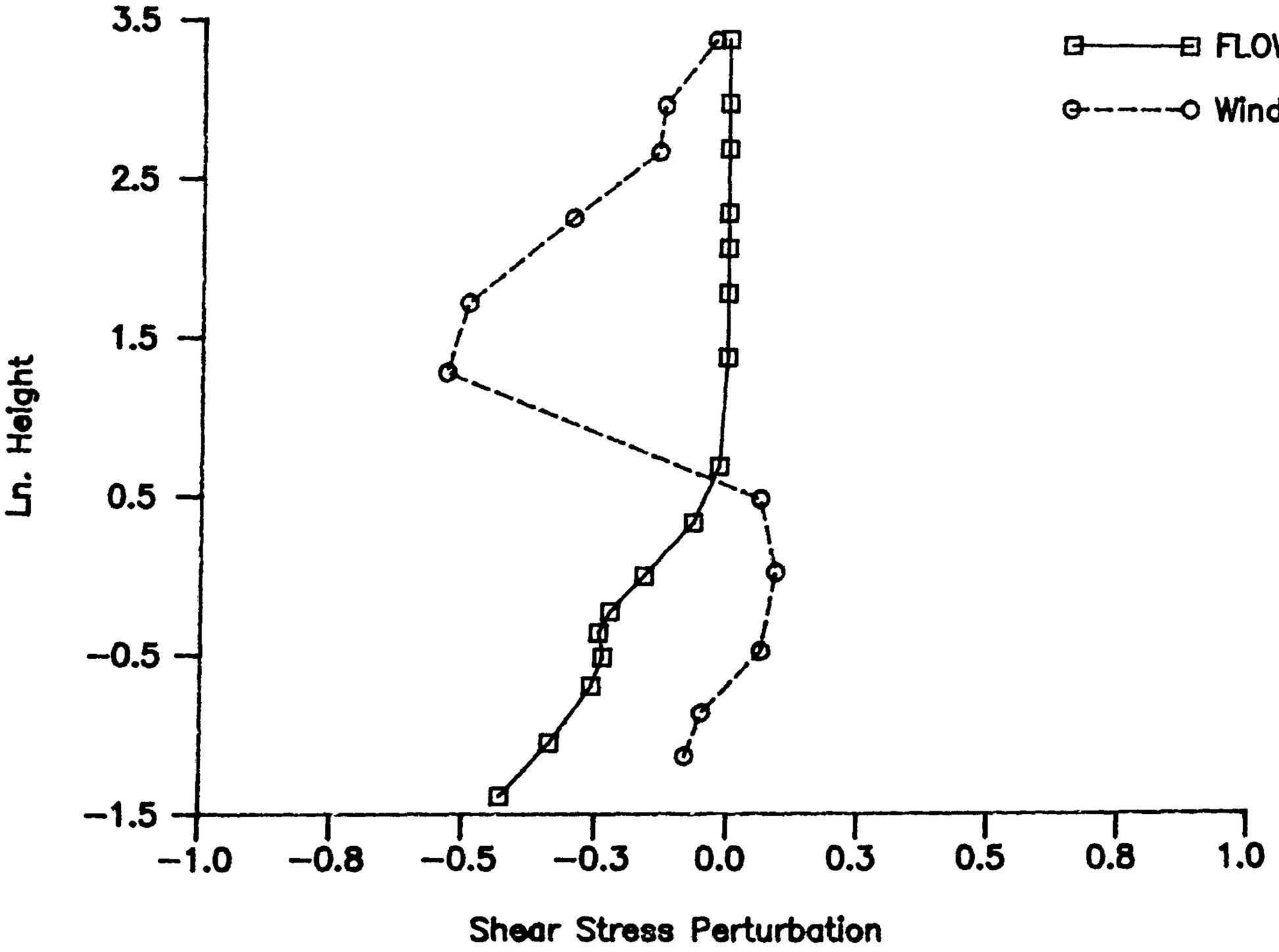

Figure 5.41 Vertical profiles of shear stress at the brink of the right flank.

it is apparent and the degree of gradient. However, it is noticeable in both sets of results and is associated with the vertical variations in fractional speed-up ratio identified in Chapter 5.2.

In Chapter 5.2 it was noted that the height of the inner-layer (l) was difficult to identify from values of fractional speed-up (δs) alone. This was because it was assumed (after Jackson & Hunt, 1975) that the limit of the inner-layer was characterised by maximum values of δs (δs_{max}). The data presented in Chapter 5.2 showed that the height of δs_{max} varied considerably up the windward slope of the dune. However, a re-analysis of the JH theory by Hunt *et al.* (1988a) resulted in a re-evaluation of the profiles of both u and τ (shear stress) within the inner-layer. The revised analysis of the JH theory involved the introduction of an inner-surface-layer (l_s), of order of magnitude z_0, and a shear stress layer within the inner-layer. Within the shear stress layer the horizontal velocity perturbation was not affected by the shear stresses to the first approximation. However, in the second approximation a balance was achieved between the gradients of shear stress and acceleration. This resulted in the height of $\delta s_{max} \approx l/3$. Within the shear stress layer the perturbations in shear stress were modified from maximum positive values at the surface to negative values of comparable magnitude at the top of the inner-layer. The inner-surface-layer was simply defined as the height below which the shear stress analysis could not be applied. The revised analysis of Hunt *et al.* (1988a) therefore re-established the definition of the inner-layer as the depth within which shear stress perturbations become important and it satisfies the experimental evidence which suggests that $\delta s_{max} \approx l/3$ (Jensen *et al.*, 1984).

The re-evaluation of the inner-layer in terms of shear stresses (and not merely flow acceleration) accords with the shear stress gradients measured in the present study. The FLOWSTAR predictions and wind tunnel measurements generally agree as to the shape of the shear stress gradients below 1 m height. Each technique suggests that the perturbations in shear stress are modified from maximum positive values at the surface to negative values at a height approximately consistent with the top of the inner-layer. The FLOWSTAR predictions suggest $l \approx 0.6$ m whilst the wind tunnel measurements suggest $l \approx 1.0$ m.

Evidence for the effect of streamline curvature on the turbulence components of flow over the dune were presented in Chapter 4. Further evidence is contributed from a comparison of the shear stress profiles provided by the wind tunnel measurements and FLOWSTAR predictions. The wind tunnel measurements exhibit a much larger negative perturbation at the crest than their FLOWSTAR equivalents. It has been noted (Chapter 4) that convex streamline curvature is likely to control the generation of stresses in this crest zone and, hence, a decrease in shear stress is probable. FLOWSTAR takes no account of curvature terms in its calculation of the flow field

so it might be expected to predict higher shear stresses in the crest-brink zone than the wind tunnel measurements, as shown above 0.5 m in height in Figures 5.38 and 5.39. Close to the surface (< 0.5 m) where the tunnel measured shear stresses exceed their upwind values, the effect of convex curvature reducing stress at the crest appears to be outweighed by increases in stress caused by flow acceleration. The characteristic "S" shape of the shear stress profile at the crest of the dune has also been observed at the crest of large hills (Teunissen *et al.*, 1982; Mason & King, 1985; Finnigan *et al.*, 1990).

A further important consideration in relation to the strong vertical shear stress gradients identified in the measurements is the impact these gradients might have on the field calculations of u_*. Nearly all the commonly-used field methods for calculating u_* rely on the measurement of velocity at two or more heights above the surface in order to determine the velocity gradient ($\delta u/\delta z$), which is assumed to relate to shear stress ($u_*^2 = -uwb$). However, as shown by the vertical stress profiles presented in this Chapter, shear stress changes rapidly close to the surface. The determination of u_* in the field is thus highly dependent upon the positioning of the anemometers within the strong near-surface shear stress gradient. This point has also been noted by Jensen & Zeman (1985) and is discussed further in Chapter 6.

The horizontal profiles of shear stress presented for the wind tunnel measurements and FLOWSTAR predictions generally follow the same pattern on the centre-line and flanks for the two heights examined, although the FLOWSTAR data tend to have more moderate perturbations. However, on all three section lines at 0.35 m height, the FLOWSTAR predictions appear liable to large variation and scatter. This makes direct comparison with the wind tunnel measurements much more difficult. This "noise" in the predicted values is likely to be caused by over-sensitivity of the program to small-scale variations in terrain features (as noted in Chapter 3). In a similar manner to the velocity predicted by FLOWSTAR, the predicted shear stress values are unlikely to be correct at the brink of the dune. However, in contrast to the velocity results, shear stress at the brink appears to be under-predicted by FLOWSTAR in each case, always dropping to negative perturbations.

Despite these difficulties, a general trend in shear stress development at different heights across the windward slope of the dune has been demonstrated. At heights above the inner-layer (> ≈1.0 m) the horizontal shear stress profile is characterised by a rising positive perturbation from the toe to half-way up the windward slope (in the concave slope region), succeeded by a declining perturbation toward the dune crest. On the crest-brink separated flanks there is evidence of a renewed increase in shear stress perturbation toward the brink.

Close to the surface (< ≈1.0 m) this trend is generally reversed and shear stress either maintains upwind levels or shows some small reduction around the toe and lower slope regions. Along the windward slope, the near-surface values of shear stress increase toward a maximum at the crest. On the crest-brink separated flanks this is followed by a reduction toward the brink.

There is a large divergence between the wind tunnel and FLOWSTAR stress perturbation values at the toe and crest. In Chapter 4 it was stated that the development of -uwb (above 1.0 m equivalent in height) in the wind tunnel was consistent with similar measurements undertaken by Finnigan *et al.* (1990), and that they agreed with theories of flow curvature. This was argued with reference not only to the -uwb measurements, but also to the usb component of Reynold's stress which showed similar curvature characteristics. There is no facility in the FLOWSTAR code to take account of the effects of flow curvature, and this is evident in the predicted data. Around the toe region, the wind tunnel measurements indicate an increase in shear stress above 1 m height which might be due to the effects of destabilising concave curvature. The FLOWSTAR predictions show only a very small rise in shear stress perturbation (≈ +0.04) at this point, much smaller than the wind tunnel measurements, where the perturbation is about +0.2. Similarly at the crest, the wind tunnel measurements exhibit a large (40%) drop in shear stress in relation to the toe region peak which may be caused by stabilising convex curvature which reduces shear stress. The FLOWSTAR predictions show only a modest (10%) reduction in shear stress when compared to the toe region perturbations.

The inability of FLOWSTAR to take account of flow curvature effects may have a significant effect on the validity of its predictions of shear stress perturbation. Coupled with this difficulty is the assumption by FLOWSTAR that the other Reynold's stress parameters (usb and wsb) are constant throughout the flow profile, even over the dune. The measurements of usb and wsb in the wind tunnel (Chapter 4) show that this is not correct. All the Reynold's stress parameters (-uwb, usb and wsb) are altered as the flow proceeds up the windward slope and some of this alteration may be due to the effects of flow curvature. By neglecting to take account of this the FLOWSTAR predictions avoid calculation of the significant extra stresses which might be induced by streamline curvature.

From this discussion, the following conclusions can be made:

1. The depth of the inner-layer (l) is best described by the height of the shear stress minimum in the vertical profile, not by the height of the maximum value of δs.

2. The vertical shear stress profiles show a strong gradient in stress close to the surface within the inner-layer. The existence of this region of rapidly changing shear stress is likely to make field assessments of u_* very difficult.

3. Differences between the measured shear stress in the wind tunnel and the FLOWSTAR predicted shear stress might be explained by the inability of the mathematical model to take into account changes in flow structure caused by streamline curvature.

CHAPTER 6 SHEAR VELOCITY CALCULATIONS AND COMPARISONS

6.1 Introduction

The preceding Chapters have dealt with measurements and calculations of airflow parameters over the dune. No attempt has yet been made to relate the measured and calculated airflow structures gained from the three different methods to changes in dune morphology. The characterisation of the relationships between airflow and dune dynamics is necessary successfully to model sand dune behaviour.

The change in dune morphology is a function of the relative erosion and deposition. This, in turn, is defined by the spatial variability of the sand transport rate. In order to determine changes in dune morphology it is therefore necessary to ascertain sand transport rates (q) at different points on the dune surface. This is commonly achieved with reference to airflow parameters such as the shear velocity (u_*) which can be related to sand transport rates using the cubic relationship derived by Bagnold (1941):

$$q \propto u_*^3$$

In this Chapter, field values of u_* are calculated and compared to values predicted by the FLOWSTAR model and measured in the wind tunnel. It will be shown that the derivation of u_* from field velocity measurements is very difficult using contemporary methods and knowledge. Furthermore, it is shown that the complex and poorly understood physics of the interaction between the sand bed and airflow restricts the usefulness of both the wind tunnel modelling and numerical modelling in the prediction of changes in dune morphology, which is determined in Chapter 7.

6.2 Methods of Shear Velocity (u_*) Calculation

Under conditions of neutral stability on a horizontal surface and in the absence of sand movement, the velocity profile gradient can be described by the Karman-Prandtl logarithmic

velocity profile law (Equation 2.7 and expressed below):

$$U/u_* = 1/\kappa . \ln (z/k)$$

where:

U = mean wind velocity
u_*= shear velocity
κ = von Karman's constant ($\approx$0.4)
z = measurement height
k = surface roughness length.

The shear velocity (u_*) is directly related to the momentum transfer between the flow and surface, and hence to the sand transport rate (q), by the following expression:

$$u_*^2 = \tau/\nu$$

where:

τ = surface shear stress
ν = kinematic viscosity

Shear velocity is therefore a parameter which is commonly used in aeolian studies where sand transport rates need to be determined. The surface roughness length (k) can be determined by measuring a series of velocity profiles which should converge at a focus above the surface. The height of the focus depends only on the roughness of the surface (Bagnold, 1941). An alternative method is to use the relationship determined by Prandtl between the average surface grain size and k, whereby k = d/30 (where d = the average grain size). However, Bagnold (1936) showed that when sand is in motion, the value of k is increased by an amount dependent on the height of saltation (Figure 6.1). Equation 2.7 can then be re-written as:

$$U/u_* = 1/\kappa \ln (z/z_0) + u_z \quad \textbf{(6.1)}$$

where:

z_0 = aerodynamic roughness
u_z = mean wind velocity at height z

The shifting of the focus of velocity lines resulting from saltation describes the aerodynamic roughness (z_0) and a velocity (u_t), which is defined as the threshold for grain movement (Bagnold, 1941) (Figure 6.1). The gradient of the line described by Equation 6.1 is proportional to the shear velocity (u_*). Therefore, u_* and z_0 are commonly calculated from velocity profiles measured above the surface. The shear velocity should be able to be determined from log-linear regression and z_0 from the intersection of differing shear velocity plots. These parameters should then be able to be used to calculate the potential sand transport rate of the wind by the methods reviewed in Chapter 7.

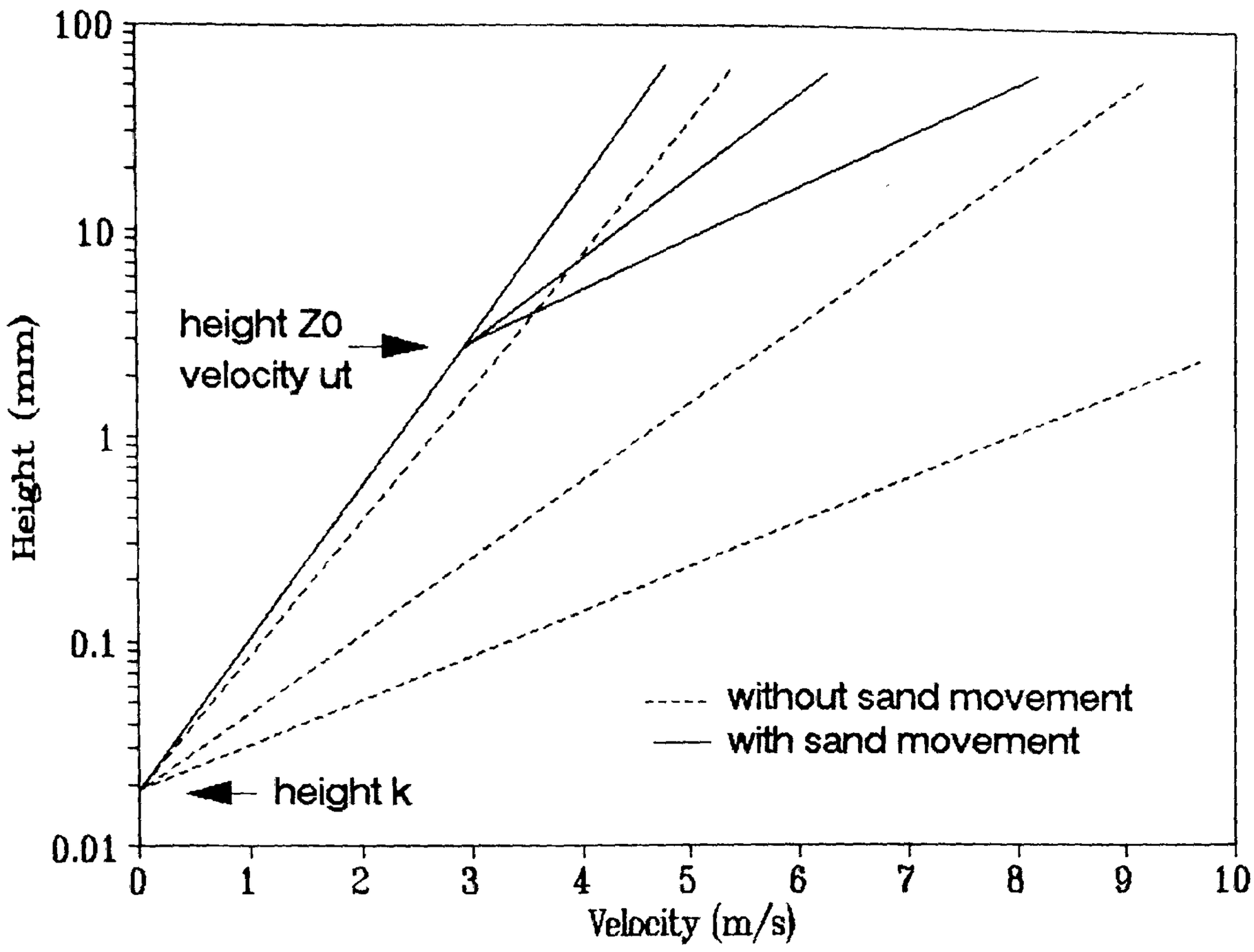

Figure 6.1 The focus of velocity lines at different shear velocities (u_*) during saltation describing the aerodynamic roughness (z_0) and threshold of grain movement (u_t). From Bagnold (1941).

In the present study the shear velocities for the wind tunnel are provided by the pulse-wire probe measurements (Chapter 4) and FLOWSTAR calculates the surface shear stress (as discussed in Chapter 3) which can then be converted to u_* by square-rooting. Therefore, the only shear velocity which needs to be calculated in order for comparisons to be made and sand transport rates to be determined, is that from the field data.

The classic regression method of determining u_* (as described above) was used in Chapter 2 on the reference station velocity measurements in order to gain an "average" shear velocity value which was then used in the wind tunnel and numerical modelling. The method has been widely used by aeolian geomorphologists to determine shear velocities over sand dunes. However, questions remain as to the statistical reliability of the method and its relevance to the dune circumstance. Rasmussen & Mikkelsen (1988) noted that u_* data from different authors were highly variable. They reasoned that this might be because of inaccurate wind data and also the fact that estimating z_0 accurately from velocity profiles was very difficult, particularly as it is often necessary to extrapolate over several decades of the logarithmic scale. Using regression analysis on velocity data, Lancaster *et al.* (1991) recorded orders of magnitude variation in z_0 at a single site.

In aeolian geomorphology u_* has frequently been calculated from velocity measurements at only two or three heights. The correlation coefficients (r^2) associated with the regressions give some idea of the fit of the data to the "best-fit" line but give no indication of the errors associated with the estimations of u_* and z_0. Following the analysis of Wilkinson (1983/84), the statistical errors involved with and reliability of the regression carried out on the reference station data in Chapter 2 were determined. Figure 2.34 showed that neither u_* nor z_0 can be estimated with confidence. Wilkinson noted that the statistical error was proportional to $t/\sqrt{(N-2)}$, where t is the students t parameter and N is the number of observations. He recognised that the reduction in error slackened off above N = 5 and hence suggested a minimum of six observation heights in order to estimate u_* with the greatest efficiency (considering the likelihood of equipment failure).

It is difficult to insert 6 anemometers within the inner-layer of airflow over a dune. As discussed in Chapters 2 and 5, it is only within the inner-layer that changes in shear stress (and hence shear velocity) are significant. As recognised by Rasmussen *et al.* (1985), an inaccurate assessment of u_* will result if inner- and outer- layer velocity measurements are combined in a calculation. In Chapter 5 it was concluded that the height of the inner-layer was both difficult to determine and spatially variable (between 0.4 m and 1.5 m) thus making decisions as to which velocity data were usable in calculations of u_* very difficult.

This problem could be overcome by using only that velocity data which are concordant with a log-linear profile. However, as discussed in Chapter 5, the effect of flow acceleration resulted in the velocity profiles over the dune being distinctly non-logarithmic. The non-linear velocity profiles, particularly over the upper windward slope and crest of the dune, negate the possibility of using regression analysis to determine the shear velocity. Similar conclusions were reached by Mulligan (1988) and Butterfield (1991) in their studies of airflow structure over sand dunes. The use of regression analysis might therefore be restricted to flat interdune and beach areas. However, as recognised in Chapter 5, even on the interdune upwind of the toe of the dune flow deceleration disturbs the velocity profile so that it becomes non-logarithmic.

Mulligan (1988) suggested that the problem could be overcome by calculating u_* from single velocity measurements close to the surface. He recommended a measurement height of 0.2 m. Using this technique a u_* value can be evaluated by calculating the height of the Bagnold "focus" from grain size analysis. The slope of the line between the calculated focus and the velocity measurement when plotted semi-logarithmically is proportional to u_*. Mulligan stated that this method of analysis prevented significant errors in the calculation of u_* (and hence q) which occur if measurements from higher in the non-logarithmic velocity profile were used in the calculation. The conclusion that more accurate estimates of sand transport result where velocity measurements are taken close to the surface seems reasonable. However, Mulligan (1988) did not undertake measurements of actual sand flux so this hypothesis remains untested.

Mulligan's recommendations entail making several broad assumptions and generates some difficulties. At the practical level, there is the problem of using an anemometer close to a sand surface. At 0.2 m height, the anemometer is likely to be barely outside the zone of vigorous saltation. A cup-anemometer operating under such conditions would be unlikely to provide accurate estimates of wind velocity due to the effects of the impact of sand grains on the cups and the infiltration of sand into the bearings. For this reason it is more reasonable to suggest a minimum anemometer height of between 0.3 m and 0.4 m. Also, considering the arguments of Wilkinson (1983/1984) questions arise as to the statistical significance of u_* evaluations calculated from only one velocity measurement.

At a more theoretical level, the Mulligan method assumes first that a velocity focus exists and is associated with the aerodynamic roughness height, and secondly that the height of this focus remains constant across the whole of the dune surface. Wind tunnel measurements by Gerety (1985) and her re-analysis of the measurements of others (Chepil, 1945; Belly, 1964; Kadib, 1965; Chiu, 1972) suggested that during saltation no velocity focus could clearly be defined. She

noted that in some cases a "zone" of focus could be observed, but that the determination of a focal height was largely arbitrary. As recognised by Gerety (1985), the velocity profiles presented by Bagnold (1941) show a distinct kink near the surface (≈ 2 cm). Bagnold stated that the height of this kink was a measure of the fixed roughness of the surface, although he admitted that it increased with an increase in u_*. Gerety (1985) suggested that the kink was more likely to be due to the extraction of momentum from the air caused by the process of saltation, the grain-borne shear stress. Hence, an increase in u_* resulted in an increase in the height of saltation and a commensurate rise in the height of the kink. Gerety (1985) therefore remarked that a rise in u_* must be associated with a parallel growth in z_0.

In her review of u_* determination methods Gerety (1985) commented that most workers fitted log-linear regressions to data above an assumed focus, while others fitted a regression to the data immediately above the kink, despite the fact that the position of the kink was not always obvious. Using the upper flow (outside the saltation layer) to calculate u_* assumes that the upper flow momentum is coupled to the lower flow, where transport is occurring. In her conclusions she inquired whether the log-law was applicable at all in cases where saltation was occurring, because the action of saltation and grain-borne shear stress might affect the whole of the velocity profile, making it curved and variable with height. This disruption of the profile near the surface caused by saltation has also been recognised by Anderson (1991) who stated that it had caused many incorrect assessments of u_* in the past. Gerety (1985) suggested that if the law was applicable then it may only be in a certain part of the profile, perhaps only in the lowest 2 cm where the kink occurs. Her final conclusions were that a focal point should not be used to define the roughness height and that Bagnold's method of determining u_* was unjustified and conceptually unacceptable. This view is supported by McEwen (1992) who stated that there was no sound physical basis for assuming a velocity focus.

In order to satisfy the concept of an increasing z_0 with increasing u_* when saltation is occurring, several workers (Rasmussen *et al.*, 1985; Anderson & Haff, 1991; McEwen, 1992) have turned their attention to an alternative method of u_* determination based on the work of Charnock (1955). In his work on roughness changes between the sea and land, Charnock developed the following expression:

$$z_{0\ sea} = Cu_*^2/2g$$

where:

$z_{0\ sea}$ = aerodynamic roughness of sea surface
C = constant (≈0.015)
g = gravity

Owen (1964) applied this relationship to the saltating sand surface. In this case the depth of saltation (associated with the aerodynamic roughness height) is related to the lift-off velocity of the individual sand grains, which in turn is governed by the shear velocity (u_*) and the force of gravity. Hence, Equation 6.2 predicts an increase in z_0 when there is a rise in u_*:

$$z_0 = C_0 u_*^2/2g \qquad \textbf{(6.2)}$$

where:

z_0 = aerodynamic roughness height during saltation
C_o = constant (≈0.02)

As discussed by McEwen (1992), the value of C_o is well constrained in wind tunnel studies at about 0.02, but it is unverified in the field. Field experiments by Rasmussen *et al.* (1985) found values for C_o of 0.14 and 0.18, ten times the wind tunnel assessments. McEwen (1992) suggested that it was inadvisable to use this method for the determination of u_* until C_o was adequately constrained for field data. In addition, Raupach (1991) used an analytic argument to show that C_o was not a constant and that it was strongly dependent upon u_*. He cited this as one reason why there was such a large difference between wind tunnel and field assessments of C_o. Furthermore, he argued that the wind tunnel evaluations of C_o were likely to be inaccurate because measurements in short wind tunnels could not hope to achieve equilibrium saltation. Also, Pye & Tsoar (1990) found that $u_*^2/2g$ was not a good predictor of saltation height and was not easily determined for a natural sand showing a variation in grain size. A significant problem is that the Owen relationship assumes a constant grain trajectory height which, in field conditions, is not readily applicable. There is therefore some controversy as to the applicability of the Owen method of u_* determination.

Butterfield (1991) also noted the difficulties of calculating u_*. Using single hot-wire probes within 2-20 cm of the surface he calculated u_* from short log-linear sections of the profile using regression analysis. However, his study revealed an inverse relationship between u_* and q near the surface under conditions of near-constant free stream velocity. He explained this by noting that reductions in velocity adjacent to the saltation layer were accompanied by a reduction in sand transport. This near-surface velocity reduction induced an increase in u_* measured immediately above the saltation layer because of the increased velocity gradient. Butterfield (1991) recorded a closer relationship between the wind velocity measured immediately above the saltation layer and sand transport than between the shear velocity measured above the saltation layer and sand transport. Furthermore, Butterfield's measurements showed that the region of flow which demonstrated a log-linear profile (*i.e.* constant stress) varied considerably

across the dune. On the stoss slope it was between 6 and 20 cm deep and at the crest it was between 2 and 20 cm deep. The lack of a region of constant shear stress near the surface in the present study was highlighted by the shear stress profiles presented in Chapter 5.3. Questions therefore arise as to where regression should be applied in order to calculate a u_* which is associated with the sand transport rate. Perhaps more useful results could be obtained by concentrating on near-surface velocity measurements rather than shear velocity.

It is within this domain of uncertainty that the field shear velocities in the present study were calculated. The techniques described above were applied to the data and compared with each other and to the wind tunnel measurements and FLOWSTAR predictions. The results and comparisons are described in the next section.

6.3 Calculation of Field Shear Velocity

The Bagnold / Mulligan approach

The following calculation of u_* combines the technique described by Bagnold (1941), which involves the calculation of a velocity ray focus, and the procedure developed by Mulligan (1988) which concerns the use of near-surface velocity data in order to overcome the non-logarithmic nature of the velocity profile (see discussion above).

With sand in saltation Bagnold (1941) developed the following relationship for the expression of u_*:

$$u_* = \kappa / \ln z/z_0 \, (u_z - u_t) \qquad (6.3)$$

where:

z = velocity measurement height
z_0= aerodynamic roughness during saltation
u_z= velocity at height z
u_t= impact threshold velocity

The values of z_0 and u_t define the focus of the velocity profile under sand driving conditions. Supporting the findings of Gerety (1985) no focus of velocity rays could be confidently determined from the field data (Figure 2.33). Therefore, to ascertain the focus determined by z_0 and u_t in Equation 6.3, z_0 was assumed to be equal to the average aerodynamic roughness (an average determined from the intercept of velocity rays at zero velocity in Chapter 2.4.3, Figure

2.33) and the value of u_t was calculated from the following expression (Bagnold, 1941):

$$u_t = 5.75\ A\ \sqrt{((\sigma-\rho)/\rho)\ g.d}\ \ln(z_0/k) \qquad \textbf{(6.4)}$$

where:

A = constant (0.08)
σ = grain density (2.65 gcm^{-3})
ρ = fluid density (0.00122 gcm^{-3})
d = average grain size
z_0= effective aerodynamic roughness with saltation
k = aerodynamic roughness without saltation

The constant (A) in Equation 6.4 was found by Bagnold (1941) to be ≈0.08 although Chepil (1945) found a value of 0.085 to be more appropriate for grains larger than (0.1 mm)(see Greeley & Iversen, 1985 for a full discussion of the value of A). The difference in the calculated value of u_t consequent on the value of A used in Equation 6.4 is minimal when compared to other errors such as the derived value for z_0. For this reason the original value for A of 0.08 was used in this study.

The expression $\ln(z_0/k)$ in Equation 6.4 can be calculated using the value of z_0 derived in Chapter 2.4.3 (*i.e.* 0.5 cm) and a value for k calculated using the relationship derived by Prandtl whereby the roughness is related to 1/30 of the average grain size (k = d/30). The average grain size (d) was determined from laser granulometry (Chapter 2.2) and found to be 0.24 mm. This is a common method of surface roughness determination (Greeley & Iversen, 1985). However, recent investigations by Lancaster *et al.* (1991) suggest that particle size is not a good measure of surface roughness and that roughness element spacing and micro-topography are also important. They found a poor relationship between k and d varying from d/4 to d/48. This magnitude of variation casts doubt on the applicability of the Prandtl relationship in determining surface roughness and reservations should be held on the accuracy of the calculation of k in the present study.

Using Equation 6.4 the velocity threshold for grain movement was found to be 2.866 ms^{-1} at a height (z_0) of 0.5 cm. This value compares well with other values of u_t calculated for dune sand (Bagnold 1941; Mulligan, 1988).

Equation 6.3 was applied to the same velocity profile data along the centre-line as was discussed in Chapters 2 & 5. Figure 6.2 shows the velocity profile at the crest of the centre-line and the subsequent determinations of u_* using the data at different heights (z), assuming the focus to be at z_0 and u_t. Owing to the non-logarithmic nature of the velocity profile at the crest (recognised

in Chapters 2 & 5) the calculated values of u_* from velocity data at different heights are very different. Table 6.1 shows the perturbations in u_* calculated from the data shown in Figure 6.2.

Table 6.1 Values of u_* perturbation calculated from velocity data at different heights above the dune crest.

Anemometer Height (m)	u_* Perturbation
1.5	0.609
1.25	0.602
1.0	0.605
0.75	0.602
0.6	0.566
0.35	0.483
0.25	0.386

The shape of the velocity profile at the crest results in the u_* perturbation calculated from the velocity data at 0.25 m being only 63% of the value calculated from the data at 1.5 m. Further evidence of the height dependency of the u_* calculations using this method is shown in Figure 6.3 which demonstrates how the non-logarithmic nature of the velocity profile at the toe of the dune also effects the u_* calculations. Figure 6.3 shows a 20% difference in calculated u_* perturbation between 0.25 m and 1.5 m at the toe.

Similar results were found by Mulligan (1988), although his analysis demonstrated a decreasing value of u_* with increasing height of anemometer. This difference between the data-sets is not surprising because the nature of the relationship depends upon the shape of the profile which is, in turn, dependent upon the height of maximum speed-up which would be expected to vary between dunes of different size. One of Mulligan's profiles does in fact show the same relationship as outlined in this study (*i.e.* increasing u_* with increasing anemometer height).

The reasons for the height dependence of u_* using this method of calculation are that there is no constant stress region in the profile between 0.25 m and 1.0 m. This fact was highlighted in the near-surface wind tunnel measurements of Reynold's stress described in Chapter 5. Butterfield (1991) found constant stress regions of varying length in his dune profiles only below 0.2 m, within the saltation layer.

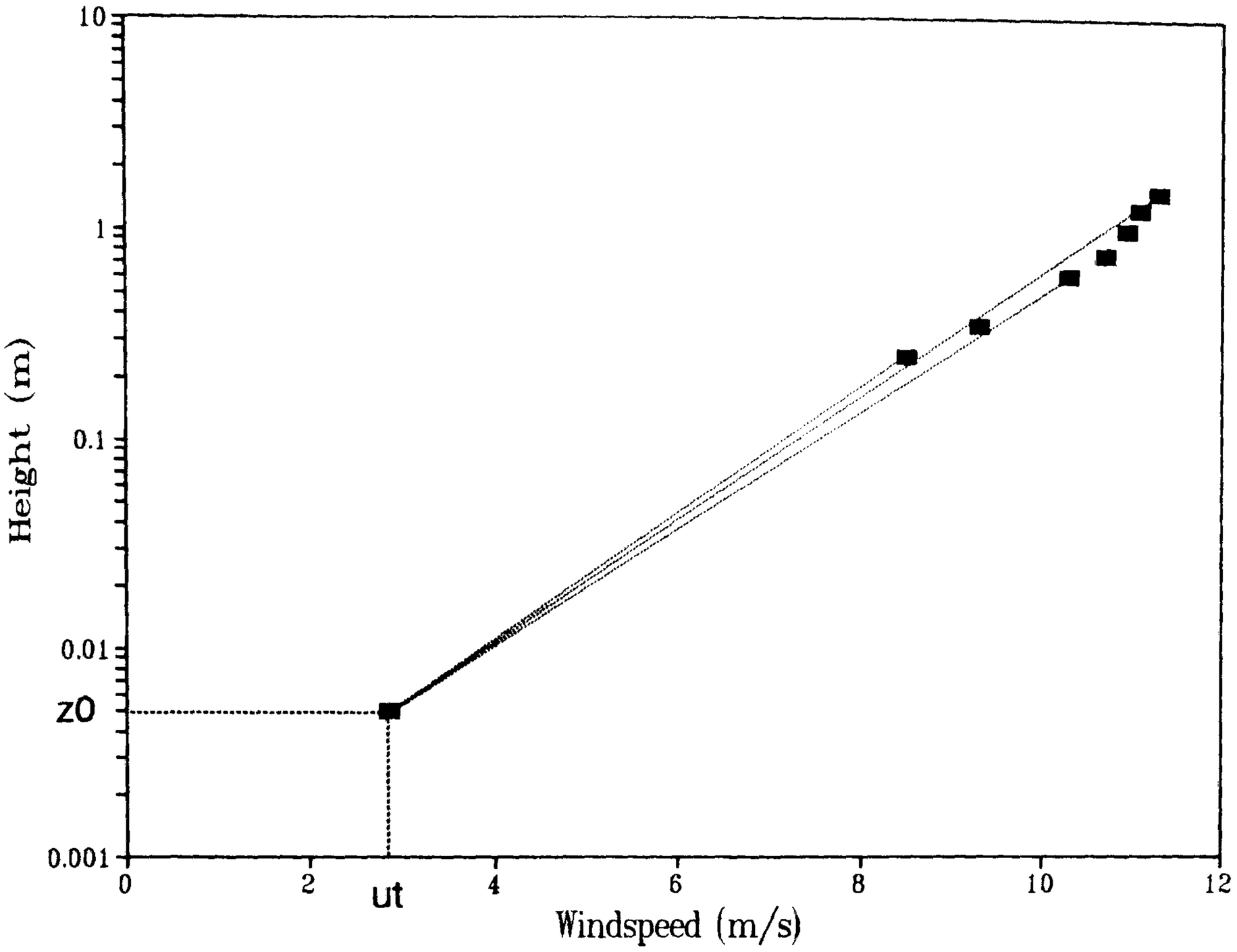

Figure 6.2 The field velocity profile at the crest of the centre-line and the shear velocity gradients at different heights assuming $z_0 = 0.05$ m and $u_t = 2.866$ ms^{-1}.

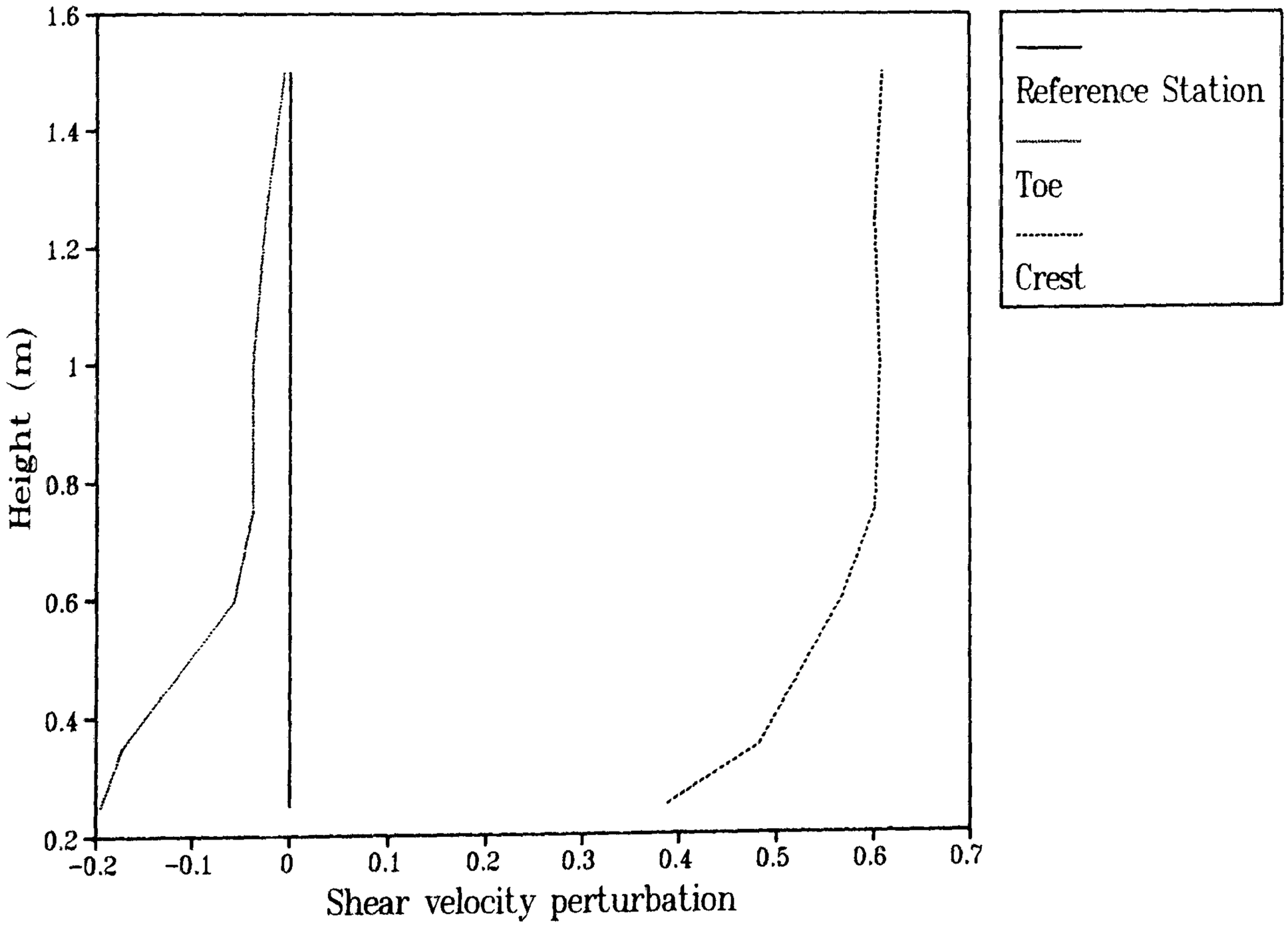

Figure 6.3 Shear velocity perturbations at the toe and crest of the centre-line calculated using the Bagnold/Mulligan approach (Equation 6.3).

It is for these reasons that Mulligan (1988) suggested that only velocity data from 0.2 m or below should be used in this method of u_* calculation, assuming that measurements closer to the surface were more likely to be representative of the moving sand. In this study it was considered that the lowest velocity measurement height (0.25 m) may have been disturbed by the saltation layer, so in the following analysis, u_* was calculated using velocity data at the next lowest measurement height of 0.35 m.

The regression analysis approach

Least-squares regression analysis was carried out on the velocity profiles along the centre-line where seven anemometers were employed. Three regressions were undertaken on each of the profiles, as follows:

a. using all of the data in the profile (*i.e.* seven velocity measurements between 0.25 m and 1.5 m),

b. using the highest four data points only (0.75 - 1.5 m),

c. using the lowest four data points only (0.25 - 1.5 m).

The reasoning behind using the highest four and lowest four velocity measurements in the regression analysis is that at about 0.6 - 0.75 m most of the velocity profiles demonstrate a kink in their generally non-log-linear profile, associated with the height of maximum speed-up (Figure 6.2). The two separate segments therefore both represent the closest approximation to a log-linear profile. However, considering that these segments represent only four velocity readings each, it is likely that the statistical errors associated with the calculations of u_* and z_0 will be large. However, larger profile segments resembling log-linearity could not be found.

The velocity data were regressed against the natural logarithm of height. For each equation the values of u_* and z_0 were determined from the following:

$$u_* = \kappa.m$$

$$z_0 = \exp(-c/m)$$

where:

κ = von Karman's constant
m = x-coefficient from regression equation
c = intercept constant from regression equation.

Figure 6.4 shows the derived values of u_* for each of the profiles along the dune centre-line using the three regression techniques (a, b and c above). Upwind of the dune the maximum difference in derived u_* between the techniques is 20%. This steadily increases to 58% at the dune crest. On each profile the u_* calculated from the lowest four velocity measurements is greater than that calculated from the highest four velocity measurements. This is as one would expect considering the nature of speed-up over the dune. As the height of maximum speed-up (δs_{max}) lies approximately in the middle of the vertical velocity profile, then as the flow passes over the dune the gradient of the velocity profile below the point of δs_{max} must increase and that above the height of δs_{max} must decrease. Hence, u_* calculated from regression analysis on the lowest four measurement heights will always be greater than that calculated from the highest four.

The development of z_0 calculated from regression analysis along the centre-line is shown in Figure 6.5. As one would expect, the z_0 derived form the regressions involving the lowest four measurement heights show a steady increase up the windward slope whilst that derived from the highest four measurements generally show a decline. With no artificially imposed "focus" on the data an increase in u_* will almost certainly result in an increase in derived z_0.

The calculation of u_* based on regression analysis is therefore strongly height-dependent. This occurs for the same reasons as described for the Bagnold / Mulligan approach above, namely the lack of a constant shear stress layer and the non-logarithmic nature of the velocity profiles over the dune. It is therefore important to use velocity data which is close to the surface for the calculation of u_*. In the following analysis the u_* values calculated from regression analysis are all derived from velocity data below 1 m in height at four heights (0.25 m, 0.35 m, 0.6 m and 1.0 m).

The Owen approach

Using Equation 6.2 an estimate of u_* can be gained from only one velocity measurement, using the argument below:

$$u_z = u_*/\kappa \ln (z/z_0) \quad [\text{where } z_0 = u_*^2/2g]$$

$$\therefore \quad \kappa u_z = \ln (z/Bu_*^2)^{u^*} \quad [\text{where } B = C_o/2g]$$

$$\therefore \quad \exp(\kappa u_z) = (z/Bu_*^2)^{u^*} \qquad \textbf{(6.5)}$$

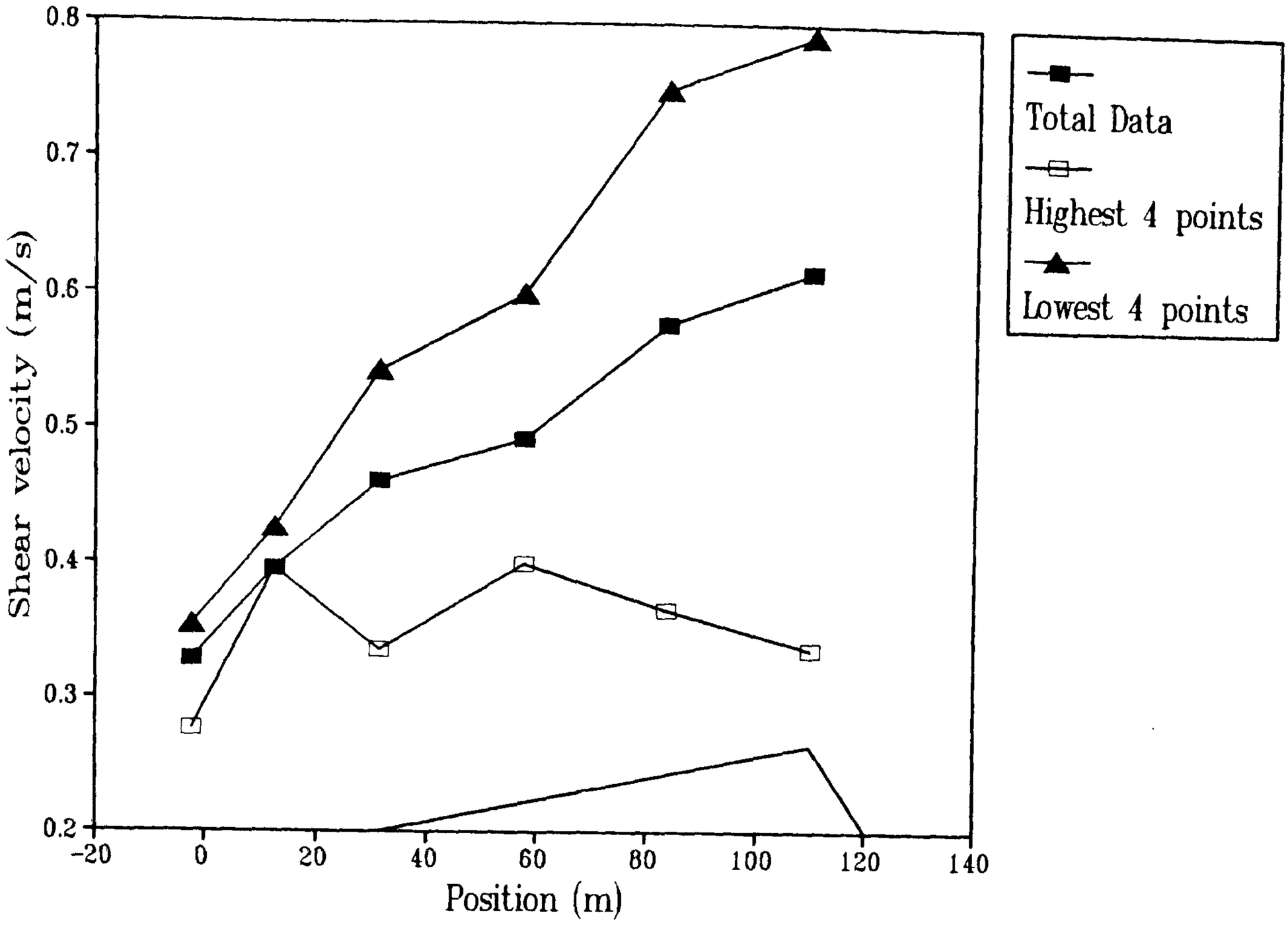

Figure 6.4 Derived values of u_* on the centre-line of the dune using the regression analysis approach.

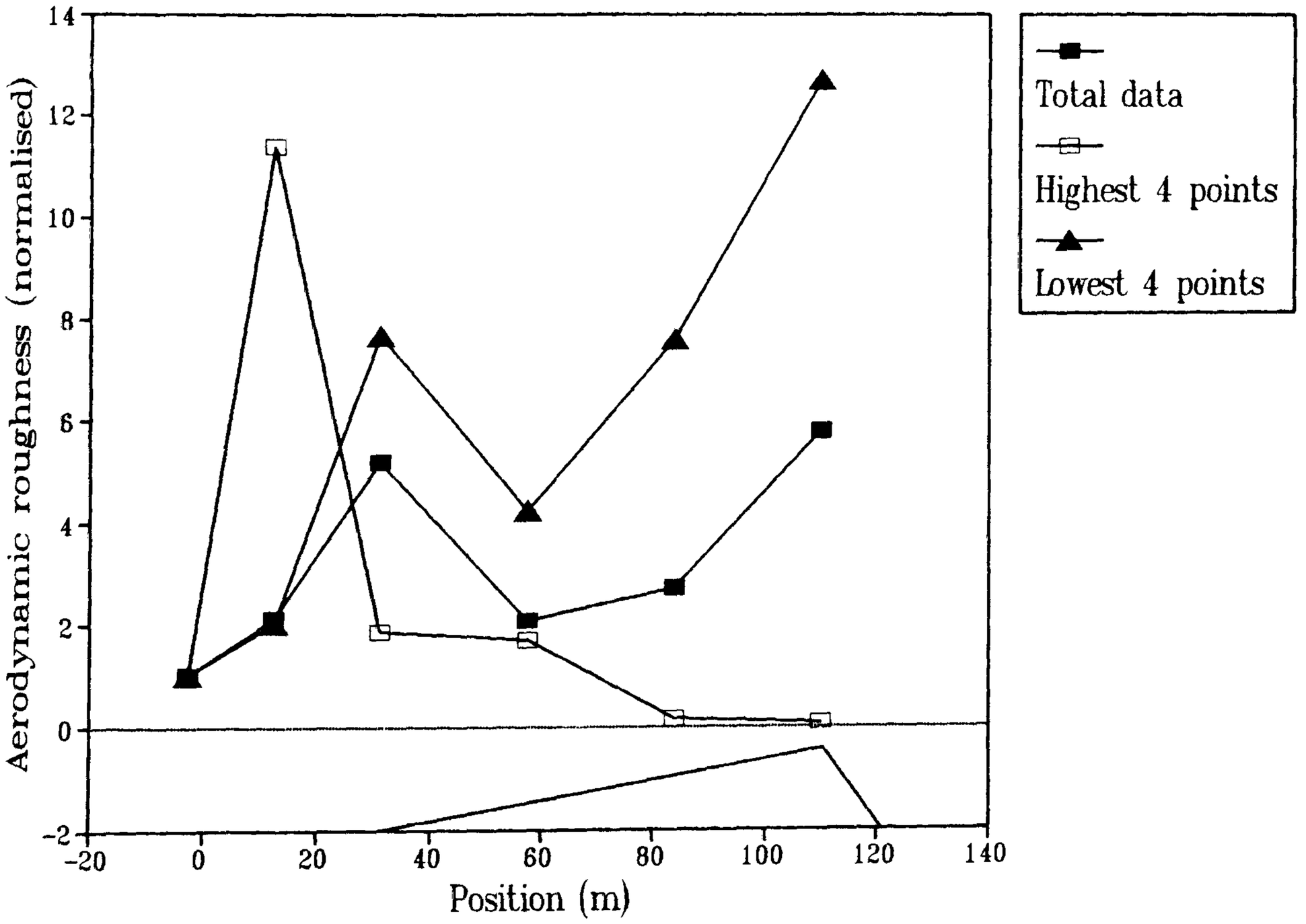

Figure 6.5 Derived values of z_0 on the centre-line of the dune using the regression analysis approach to shear velocity calculation.

The left hand side of Equation 6.5 can be calculated from the velocity data, and on the right hand side u_* is the only unknown. This is because the constant B (which is equal to $C_d/2g$) can be found from the y-axis intercept of velocity profile rays on a semi-logarithmic graph, as shown in Figure 6.6. The correct value of u_* to fit Equation 6.5 can then be determined by trial-and-error.

Individual analysis of 350 one-minute velocity averages at the reference station site gave average values for B of 0.0123 and C_o of 0.242. This value for C_o is larger than the range found by Rasmussen *et al.* (1985) in field conditions (0.14 to 0.18) and that of 0.02 which is considered to be the value in wind tunnels (McEwen, 1992). As discussed in Chapter 6.2, the value of C_o in field conditions is unknown and the values derived from wind tunnel experiments are of uncertain accuracy. The C_o calculated in this study is therefore not inconsistent with those found by Rasmussen *et al.* (1985). One probable reason for the deviation from the Rasmussen *et al.* figures is that the C_o in the present study is derived from velocity data well above the top of the saltation layer (>0.25 m). Furthermore, the derivation of C_o is dependent upon the correct determination of z_0 (as $z_0 = Bu_*^2$ and $B = C_d/2g$). In this study the variation in calculated z_0 from the 350 one minute velocity averages (calculated as the y-axis intercept on semi-logarithmic velocity profiles) ranged from 0.0005 m to 0.015 m. The difficulties involved in the correct determination of z_0 cast doubt on the accuracy of the assessment of C_o. The range in C_o apparent from the variation in z_0 is from 0.84 to 0.015. The value of 0.242 chosen for the subsequent analysis in this study is an integration of all the values calculated from the 350 individual samples. However, the large variance in calculations of z_0 in field situations may account for a wide variety in field calculations of C_o in future studies.

Using Equation 6.5 and the derived values of B and C_o, estimates of u_* were determined from velocity data measured at a height of 0.35 m.

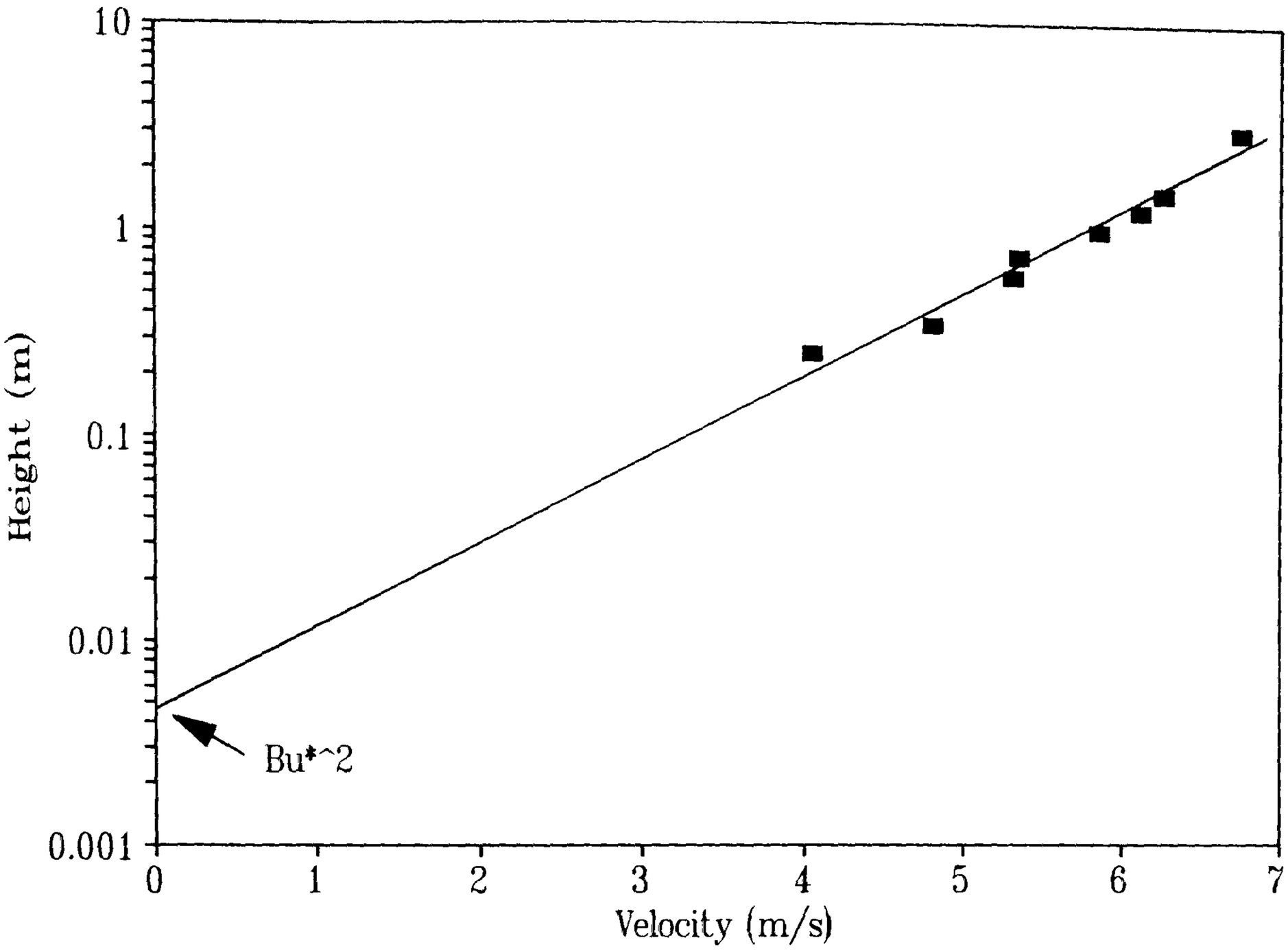

Figure 6.6 The derivation of constant B in Equation 6.5 from velocity profile rays.

6.4 Comparison of the Field Shear Velocity Calculation Techniques

The field velocity measurements used in the following analysis were acquired from profiles of four anemometers at heights of 0.25 m, 0.35 m, 0.6 m and 1.0 m. The advantage of a four-profile configuration over the seven-profile configuration (as previously described) was that with the limited number of anemometers available it allowed the whole of a section-line to be instrumented in two anemometer runs of one hour each, rather than six runs of twenty minutes each. This procedure was adopted where measurements of sand transport were undertaken (see Chapter 7) in order to increase the accuracy of the results and reduce the necessity for data normalisation which is more suspect when values of high variance (*i.e.* sand transport) are to be compared.

Figure 6.7 shows the u_* perturbations calculated along the centre-line of the dune using all of the techniques outlined above (Chapter 6.3). Figure 6.7 demonstrates a close association between the Mulligan and Owen methods of calculation. Both show a reduction in u_* of about 15-20% at the toe of the dune and then a sharp rise up the windward slope to maxima perturbations at the crest of 0.72 for the Owen calculation and 0.62 for the Mulligan calculation. In contrast, the regression analysis shows an increase in u_* toward the toe where there is a perturbation of 0.35. This is followed by an abrupt decrease to a perturbation of -0.35 along the windward slope and a further rise to 0.35 at the crest. Comparable results are shown for the left and right flanks in Figures 6.8 and 6.9. The left flank (Figure 6.8) shows a similar development for the Mulligan and Owen methods to just downwind of the toe, both decreasing in value between 3-5%. The regression analysis in this region shows very unstable results varying between zero and -20%. However, downwind of x= 45 m the Mulligan and Owen methods display a divergence in u_* perturbation with the Owen results reaching a maximum perturbation at the crest of 0.9 whilst the Mulligan results reach a perturbation of only 0.35 at this point. The results gained by the Owen method at the crest are in fact much more comparable to the regression analysis than the Mulligan results. Between the crest and the brink on the left flank (Figure 6.8) all the results show a reduction in u_* perturbation to between 0.18 and 0.32.

On the right flank (Figure 6.9) all three methods are in good agreement upwind of and at the toe. All show negative u_* perturbations of between 5-10% at the toe. However, along the windward slope the results differ markedly. The regression analysis is again very unstable showing irregular variations in perturbation between -0.18 and +0.14. Both the Mulligan and Owen results display maxima at the crest but of highly different value. The Mulligan results show a steady increase up the windward slope to a maximum of 0.35 whilst the Owen results

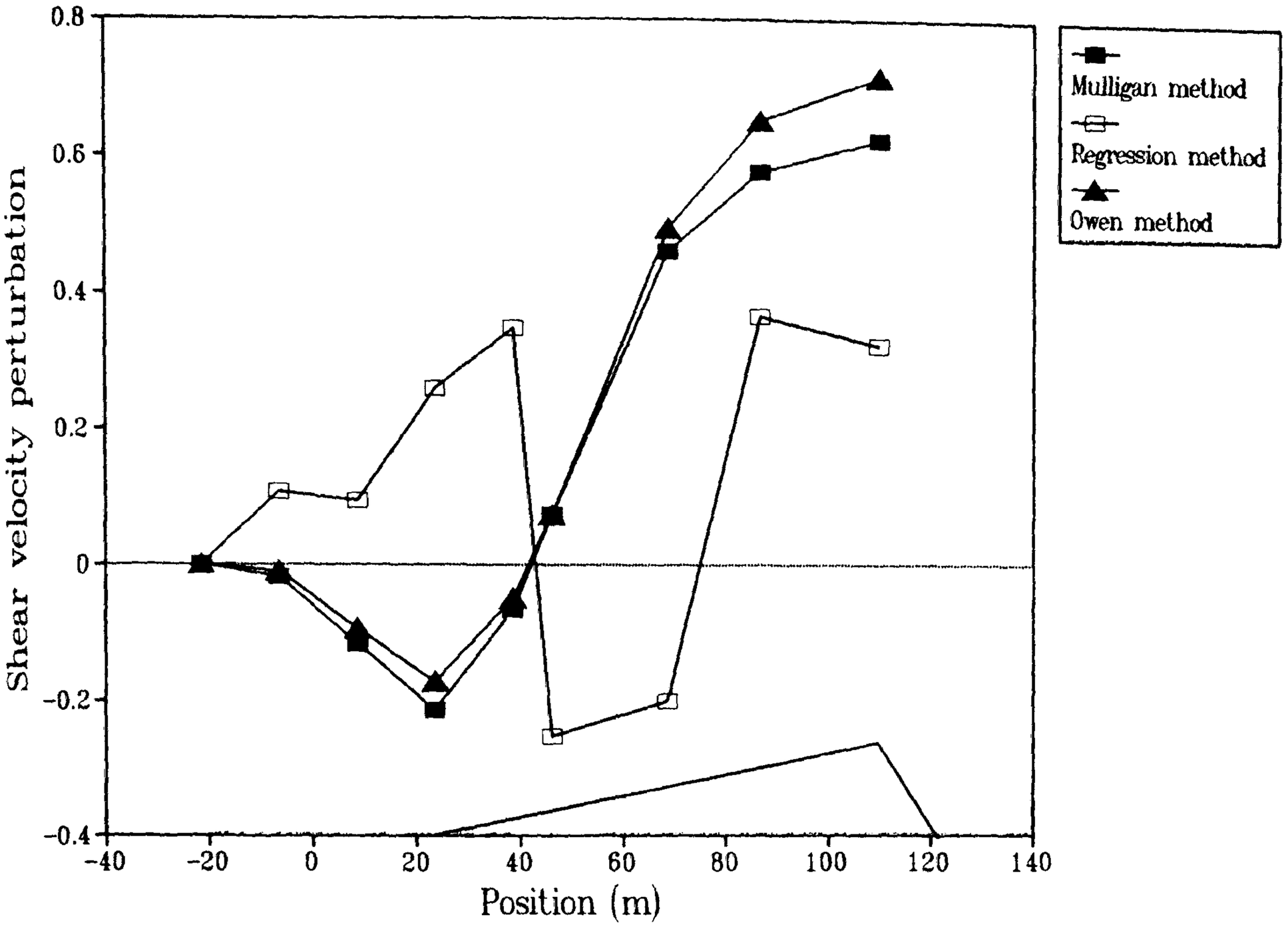

Figure 6.7 Derived values of shear velocity perturbation on the centre-line of the dune calculated using the different approaches on field measurements of velocity.

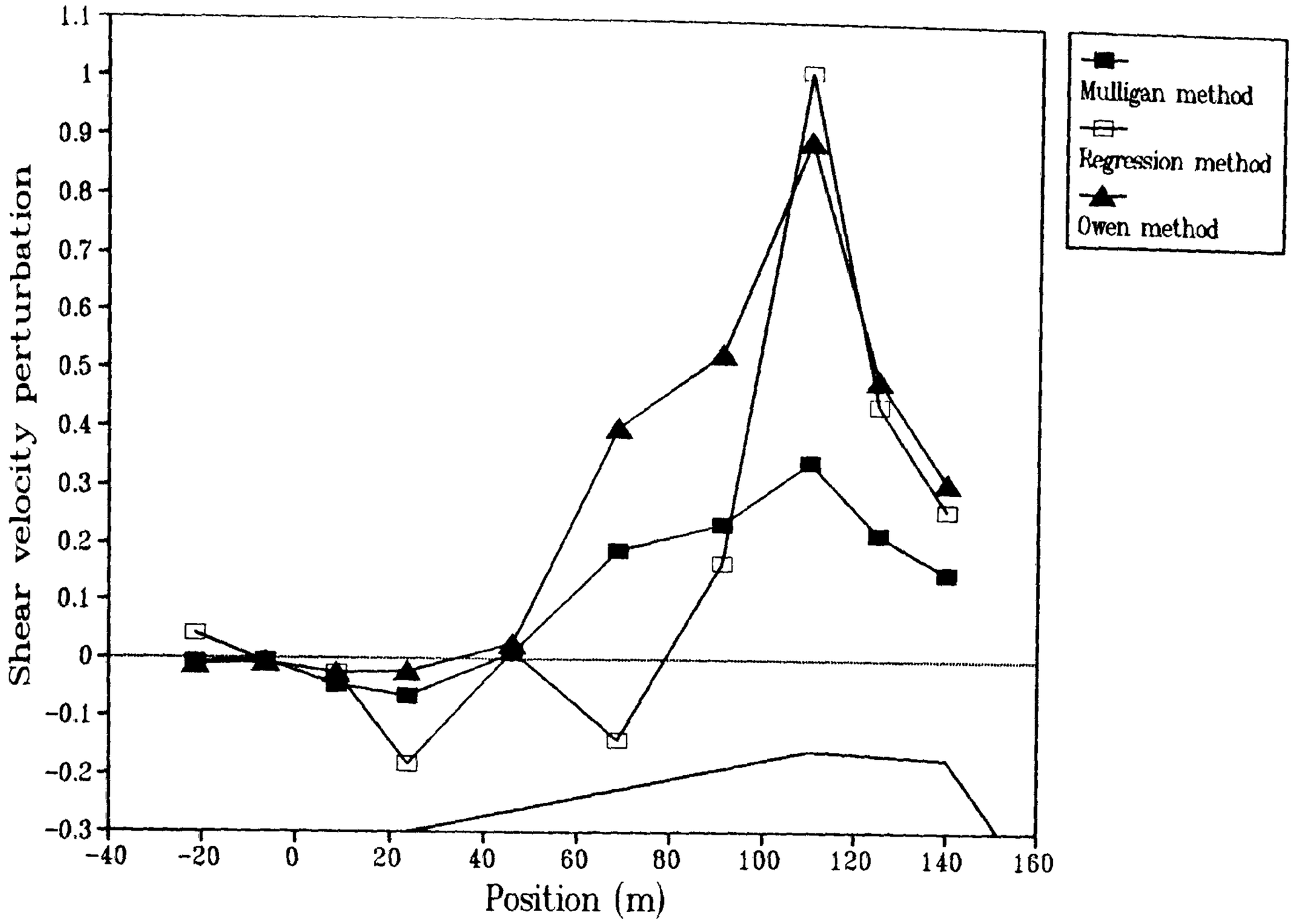

Figure 6.8 Derived values of shear velocity perturbation on the left flank of the dune calculated using the different approaches on field measurements of velocity.

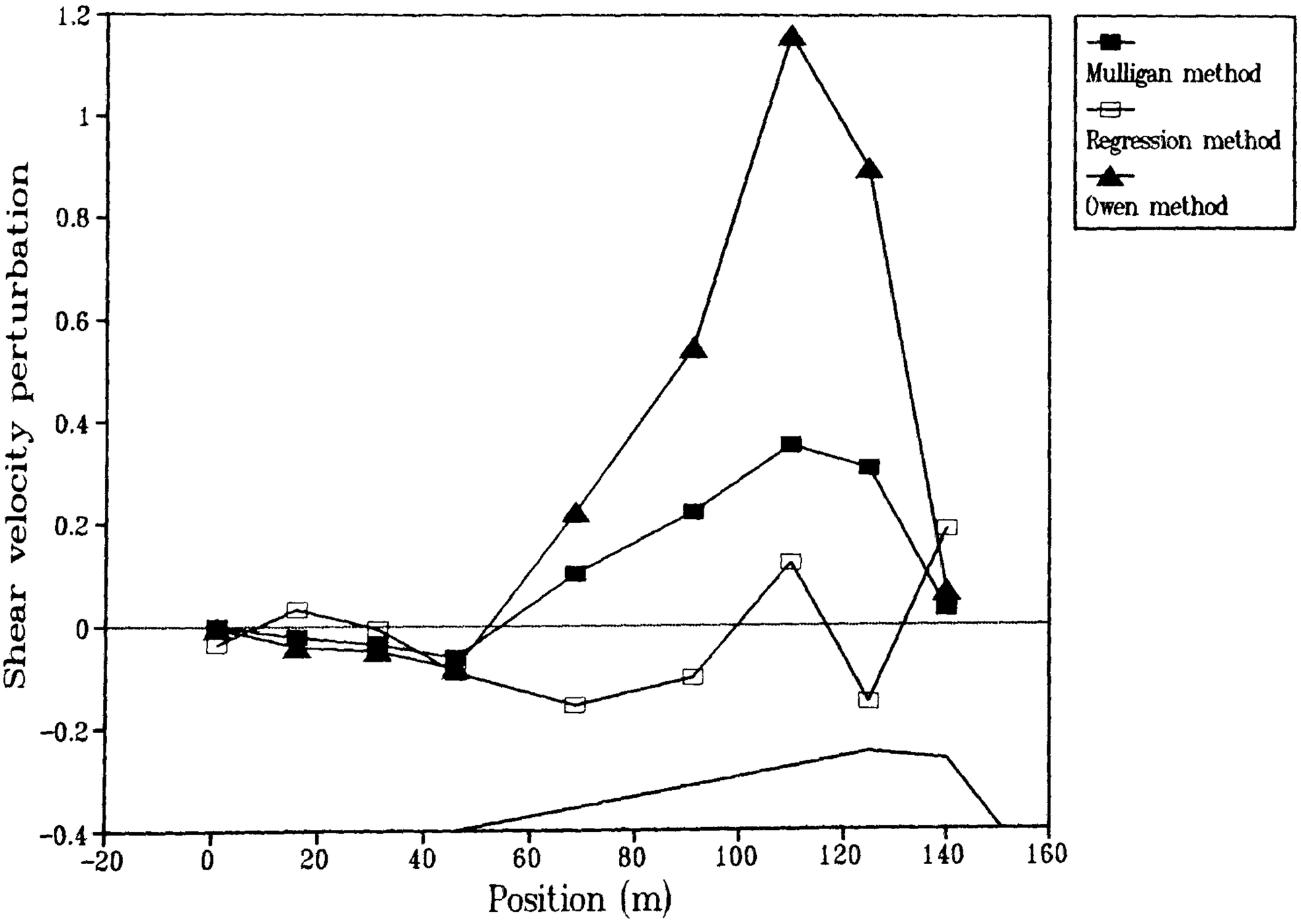

Figure 6.9 Derived values of shear velocity perturbation on the right flank of the dune calculated using the different approaches on field measurements of velocity.

show an increasing rate of growth to a maximum perturbation of nearly 1.2. In a similar manner to the left flank (Figure 6.8) the perturbations calculated by the Owen and Mulligan methods between the crest and brink on the right flank both show a similar reduction to perturbation values between 0.3 and 0.5. The regression analysis in this zone is still highly variable showing perturbations between -0.18 and +0.18.

In each of the Figures (6.7, 6.8 and 6.9) the regression analysis shows highly unstable and varying results with little systematic change. This is in contrast to the results gained from the Owen and Mulligan methods which display similar forms of development over the three section lines, although the perturbations using the Owen method are larger in each case and considerably so over the flanks. Following the arguments presented above, these results might be expected. Considering the disruption of the airflow caused by the intrusion of the dune into the boundary layer and the lack of a significant portion of log-linear profile at any point on the windward slope of the dune (see Chapter 5) it is not surprising that the regression analysis produces results of high variance and little meaning. Upwind of the toe along the centre-line (Figure 6.7), the regression analysis shows an increasing u_* perturbation. This is because as the flow approaches the dune, the reduction in near-surface velocity causes a steepening of the vertical velocity gradient. This effect is less noticeable upwind of the flanks because the deceleration of flow is less severe. On the windward slope of the dune itself the uniform nature of the vertical speed-up profile results in a slackening of the velocity gradient and a reduction in u_* as calculated by regression analysis. This effect is particularly noticeable on the right flank (Figure 6.9) and centre-line (Figure 6.7) and also along the base of the windward slope on the left flank (Figure 6.8). Likewise, the results from the Owen method tend to give perturbation values larger than the Mulligan method of calculation because no restriction on roughness height is imposed. This allows the calculated velocity gradient to become steeper (hence increasing z_0). Furthermore, the Owen and Mulligan methods are likely to produce broadly similar results (*i.e.* a reduction in u_* perturbation at the toe rising to a maximum at the crest) because they both rely on single measurements of wind velocity which have been shown to follow the same pattern (Chapter 5).

Despite the similarities between the Mulligan and Owen methods of u_* calculation there are also some distinct contrasts worthy of note. Using the methods of Mulligan, it can be seen from Figures 6.7, 6.8 and 6.9 that the maximum u_* perturbation at the crest of the centre-line (Figure 6.7), is at least 50% higher than the maximum at the crests of the flanks. This is a situation which might be expected considering the larger mass of the dune at the centre-line than at the flanks. It is also at the crest of the centre-line that the maximum velocity speed-up was recorded (Chapter 5). This is in contrast to the results obtained using the Owen method of u_* calculation.

In this case the maximum perturbation is seen to be at the crests of the flanks (Figures 6.8 and 6.9) with large perturbations of nearly 1.2 and 1.0 along the right and left flanks respectively. This compares to the smaller centre-line perturbation which only reaches a value of 0.7 at the crest. As a consequence, the two methods which produce very similar results along the centre-line, are quite divergent along the flanks. No explanation can be found for this outcome.

In an attempt to assess which of the methods of calculation was the more appropriate, each calculation technique was applied to the centre-line wind tunnel velocity data-set and compared to the pulse-wire probe measurements of u_*. The results of this comparative procedure (Figure 6.10) show a very close relationship between the Mulligan and Owen methods of u_* calculation. Both sets of results display a reduction in u_* upwind of the toe of between 10-15% and a rise to a maximum near the crest. The regression analysis demonstrates a smaller reduction in u_* upwind of the dune but these results do show a large amount of variation. At the crest, the regression analysis reveals a very sharp peak in u_* just upwind of the brink. This peak is also recognisable with the Owen and Mulligan methods but it is of a smaller degree. None of the techniques provide an exact parallel to the pulse-wire probe measurements of u_* (discussed in Chapter 4). The principal differences are at the toe and crest of the dune model. At the toe all three of the field methods of u_* determination show a reduction to negative perturbations. The pulse-wire probe measurements remain relatively constant. Near the crest, all three of the field methods of u_* determination show a sharp peak in perturbation upwind of the brink. The pulse-wire probe measurements show a relatively constant u_* in the crest region with no peak. Reasons for these contrasts are discussed fully in the next section. At this stage it is clear that the comparison shown in Figure 6.10 does not allow discrimination between the methods of field calculation of u_* in terms of their representativeness of actual u_*. Assuming that the pulse-wire measurements represent actual u_*, it is clear that none of the field methods of calculation is entirely satisfactory.

Figures 6.7, 6.8 and 6.9 suggest that using regression analysis is not a satisfactory method of determining u_* on the windward slopes of dunes. Only on the flat surface upwind of the dune does the regression analysis appear to give sensible results (concordant at least with the other two methods) where flow deceleration is not too severe (*i.e.* upwind of the two flanks). On the centre-line (Figure 6.7) where flow deceleration is much in evidence, the regression analysis suggests a rapidly increasing u_* merely because of the near-surface flow deceleration. This result is not compatible with the development of sand transport at the surface (see Chapter 7) and it is discordant with the wind tunnel measurements of shear velocity and the two alternative field methods. It is considered that meaningful values of u_* cannot be gained from this method of

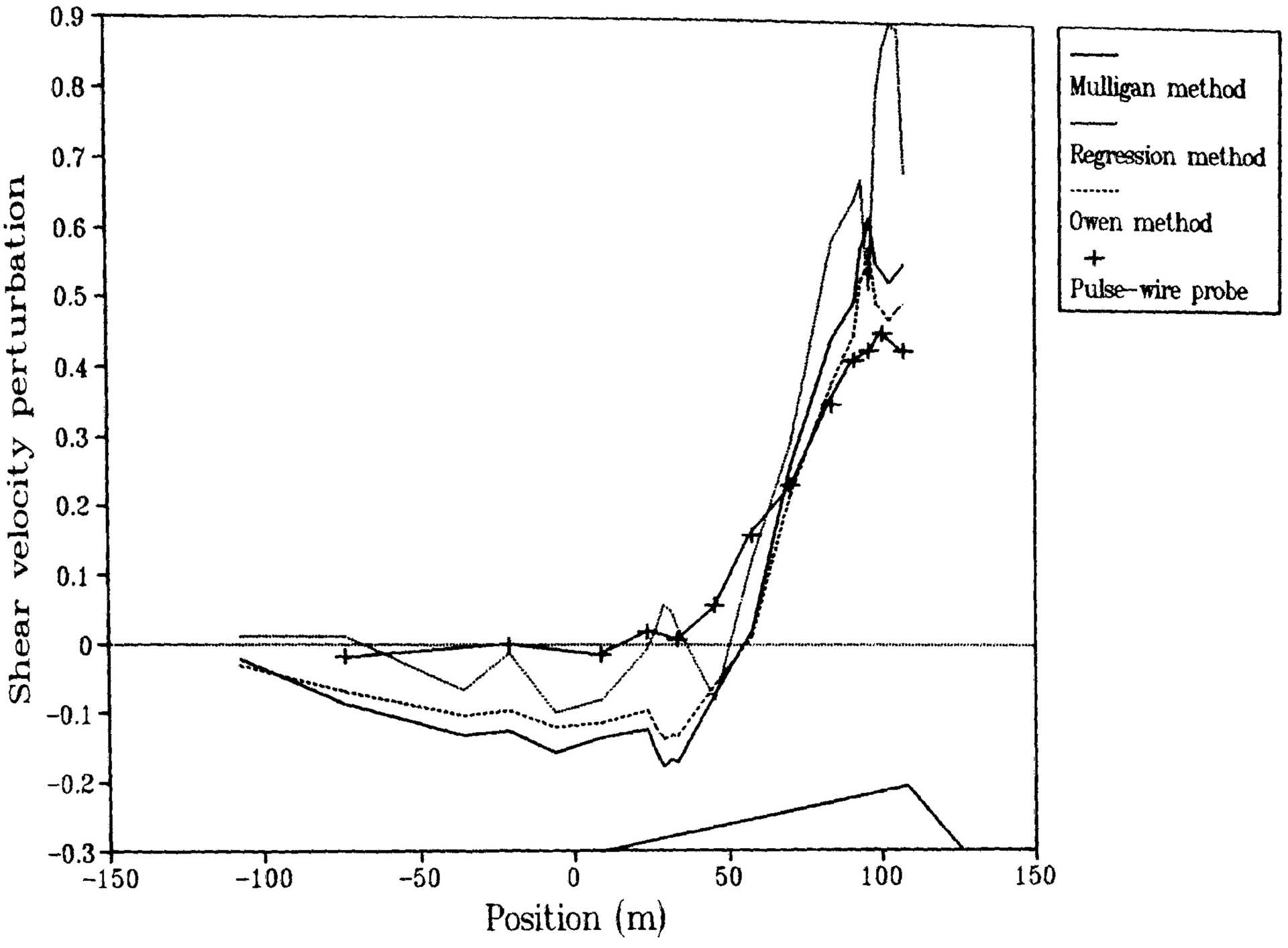

Figure 6.10 Derived values of shear velocity perturbation on the centre-line of the dune calculated using the different approaches on wind tunnel measurements of velocity and compared to the pulse-wire probe shear velocity measurements.

calculation using velocity data more than 0.25 m from the surface. For regression analysis to provide correct results velocity measurements must be made within the saltation layer and log-linear segments recognised in the near-surface profile. However, as discussed by Butterfield (1991) and McEwen (1992), even velocity measurements at 2 cm from the surface fail to provide adequate results. The high variance in calculated u_* apparent from the regression analysis may also be a function of the statistical errors associated with using just four velocity measurements for the calculation. Using the technique of Wilkinson (1983/1984) the 95% confidence limits for the calculated u_* at the crest of the centre line (Figure 6.7) were determined. It was found that $u_* = 0.46\ ms^{-1} \pm 57\%$. A 57% margin of error covers the maximum calculated perturbation (37%). Therefore, no conclusions concerning the development of u_* calculated by regression analysis can be made.

The Owen technique of calculation seems to give results at the crest of the dune which are probably too high. It is unlikely that the u_* at the crest would be more than twice that upwind. The distrust of these results stems from the fact that the derived u_* perturbations at the crests of the flanks are larger than that for the crest of the centre-line. The inability of the Owen technique to provide adequate results is shown in Figure 6.11 which shows the u_* perturbations calculated using the different techniques along the right flank of the dune during a 4-minute sand trapping run. Similar to the results presented above for the 1 hour recording sequences, the Mulligan technique results in Figure 6.11 show a reduction in u_* at the toe and a rise to a maximum at the crest. The regression analysis results show their typically highly variable nature and the Owen technique results are similar to the Mulligan results until they reach the windward slope. At this point the Owen results show a sharp rise in u_* perturbation reaching a flat-topped maximum at the crest before reducing toward the brink. However, this flat-top does not reflect the true results. As discussed in Chapter 6.3, the value of u_* using the Owen technique involves balancing the two sides of Equation 6.5 by inserting values of u_* on a trial-and-error basis. However, it was found that this was only possible up to a certain value of u_* beyond which the resulting value of $(z/Bu_*^2)^{u^*}$ was reduced. This is clearly shown in Figure 6.12 which demonstrates the effect of increasing u_* at various values of C_o (which is included in the y-axis term as $B = C_o/2g$). With $C_o = 0.24$ (see Chapter 6.3) the value of u_* which results in the largest computation of $(z/Bu_*^2)^{u^*}$ is 1.975. This is too small to balance Equation 6.5 when using the data at the crest of the right flank during the sand trap run. This results in the maximum possible perturbation being 1.32, hence resulting in the flat-topped graph shown in Figure 6.11. The flat-top represents the highest value of u_* which can be calculated, although it does not represent a correct satisfaction of Equation 6.5.

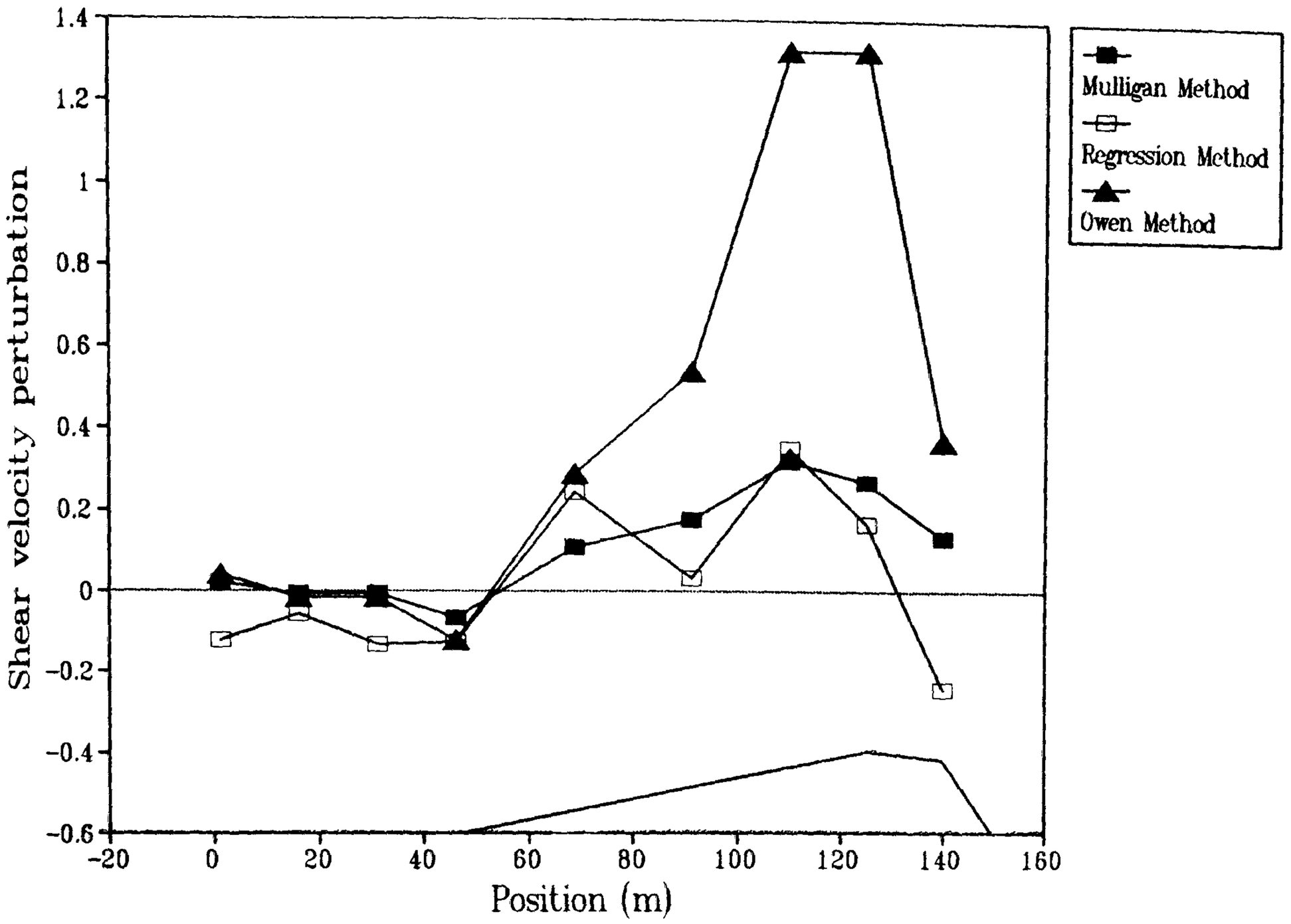

Figure 6.11 Derived values of shear velocity perturbation on the right flank of the dune calculated using the different approaches on field measurements of velocity during a four-minute sand trapping run.

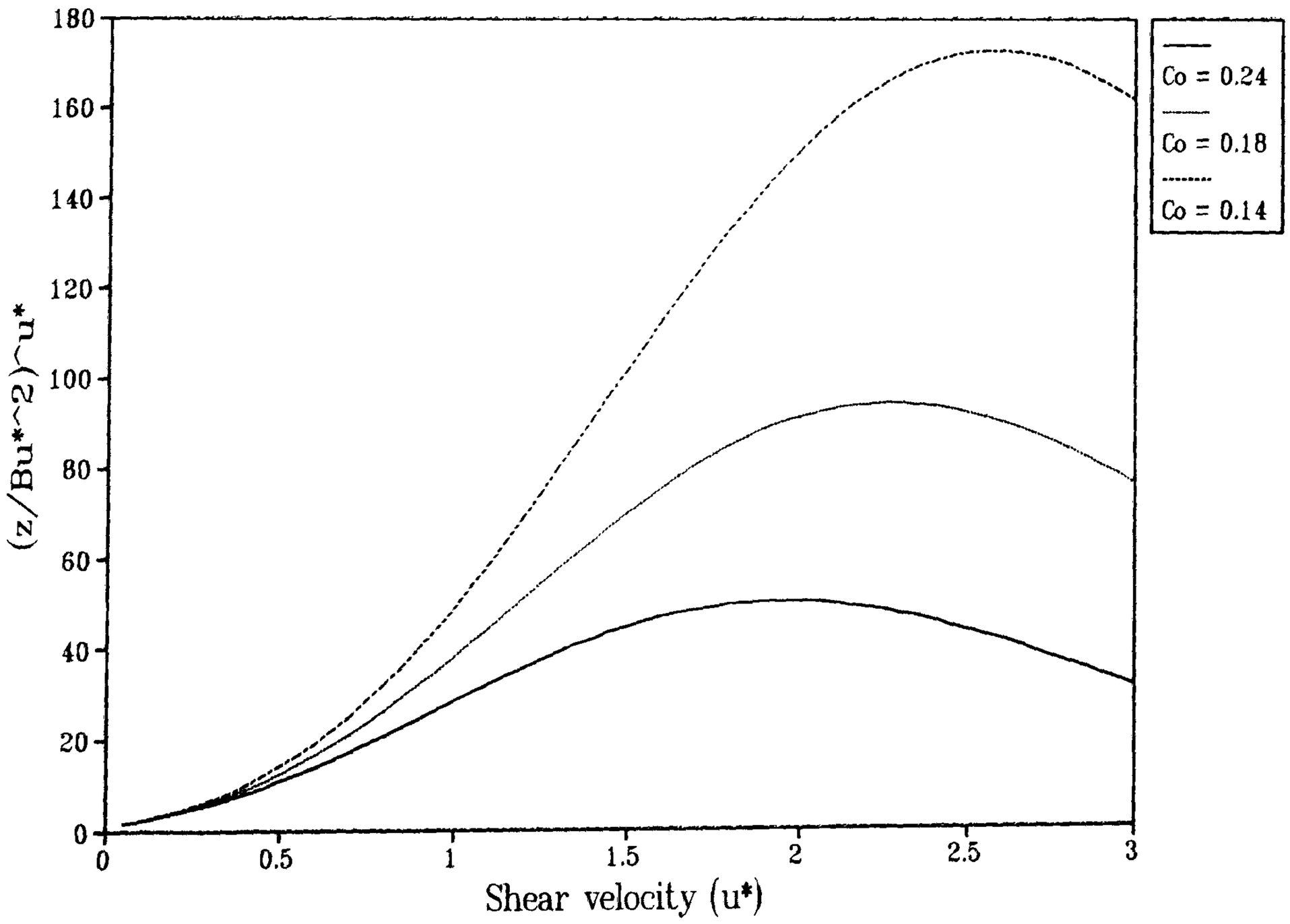

Figure 6.12 The relationship between terms in Equation 6.5 at different values of C_o.

It was decided not to use the Owen method of u_* determination in the following analysis of sand transport rates (Chapter 7) for the following reasons:

1. The derived shear velocities using the technique seemed unreasonably high on the windward slopes and crestal regions of the dune. One reason for this may be that the calculated value of C_o (0.242) was inaccurate. This is a likely explanation considering that it was derived from wind velocity data measured outside of the saltation layer. Previous studies (Rasmussen *et al.*, 1985; McEwen, 1991) have derived the value of C_o from velocity measurements within or very close to the saltation layer. A further possible explanation for the unreasonably high calculation of u_* at the crest of the dune is that the value of C_o may not be a constant. Raupach (1991) stated that the value of C_o was dependent upon the value of u_*, which increases along the windward slope of the dune. The value in the present study may therefore be unrepresentative across the whole of the windward slope.

2. Very few field studies of the technique have been carried out (excepting Rasmussen *et al.*, 1985) and the value of C_o is not well constrained in the field. The uncertainty in the use of the technique in the field combined with the probable unrepresentative nature of the calculations presented in this study make it unwise to use in this instance.

3. Windspeeds during the short sand trapping runs were quite high and, as shown in Figure 6.11, sensible values for u_* could not be determined at the crest of the dune in many instances due to the curved nature of the relationship shown in Figure 6.12. More detailed analysis of the nature of C_o in the field must be carried out before this technique can be used to determine u_* on sand dunes in a field situation

The Mulligan method of u_* calculation appears to provide the most reasonable results. The maximum calculated shear velocities at the crests are not unduly large and the centre-line shear velocities show larger perturbations than the flanks. Despite all the theoretical difficulties associated with this approach, discussed in Chapter 6.3, it contributes the most appropriate answers. It was concluded that this technique was the most pragmatic and should be used in the calculation of sand transport rates and in the comparative discussion of shear velocities between the wind tunnel, FLOWSTAR and field techniques.

Concluding Statement

The above discussion highlights some of the problems involved with measuring u_* over sand dunes from field velocity profiles. Principal difficulties arise because flow acceleration produces a strong shear stress gradient above the surface and the cup-anemometers are unable to operate within the saltation layer. From the analysis of Gerety (1985) and Butterfield (1991) it seems likely that adequate assessments of u_* (*i.e.* assessments applicable to sand transport rate measurements) can only be acquired from careful near-surface measurements (<0.2 m) within the saltation layer. However, even at this level the relationships between sand transport rate and shear velocity calculations are not clear (Butterfield, 1991). None of the methods described above is satisfactory. Regression analysis, as used in this study, cannot be applied on the windward slope of the dune due to flow acceleration and it cannot be applied on the flat upwind inter-dune surface because of flow deceleration. The Owen method of calculation suffers from a lack of empirical testing in the field. The results using this technique appear unreasonably high and, in some cases, the magnitude of u_* required to balance the governing equation cannot be gained. This negates the use of the Owen technique in the present study. The Mulligan method of calculation provides the most meaningful results in terms of sensible values of u_* but it suffers from conceptual criticism. It allows for no increase in z_0 with increasing u_* and it assumes a velocity profile focus which is unlikely to exist. Furthermore, it assumes a log-linear velocity profile below 0.35 m, an unlikely occurrence (Butterfield, 1991). However, having discarded the other two methods as being inappropriate in a practical sense and having no alternative options for evaluating u_* it was decided to continue the analysis using the Mulligan technique of calculation in order to determine how appropriate it is for sand transport rate modelling in comparison to the results gained from the wind tunnel and FLOWSTAR techniques.

6.5 Shear Velocity Evaluations: comparison between the techniques

Figures 6.13 to 6.15 show the shear velocity perturbations for the field, wind tunnel and FLOWSTAR data along the centre-line and left & right flanks respectively. The field values of u_* presented in these Figures are those calculated by the Mulligan technique (as described above) employing wind velocity measurements at a height of 0.35 m. The wind tunnel shear velocities (on the centre-line) are those gained from the pulse-wire probe (as described in Chapter 4) and the FLOWSTAR predictions of are the square-root of the calculated surface shear stresses (see Chapters 3 & 5). All the data shown in these Figures are therefore in a similar format and capable of comparison as shear velocities (u_*).

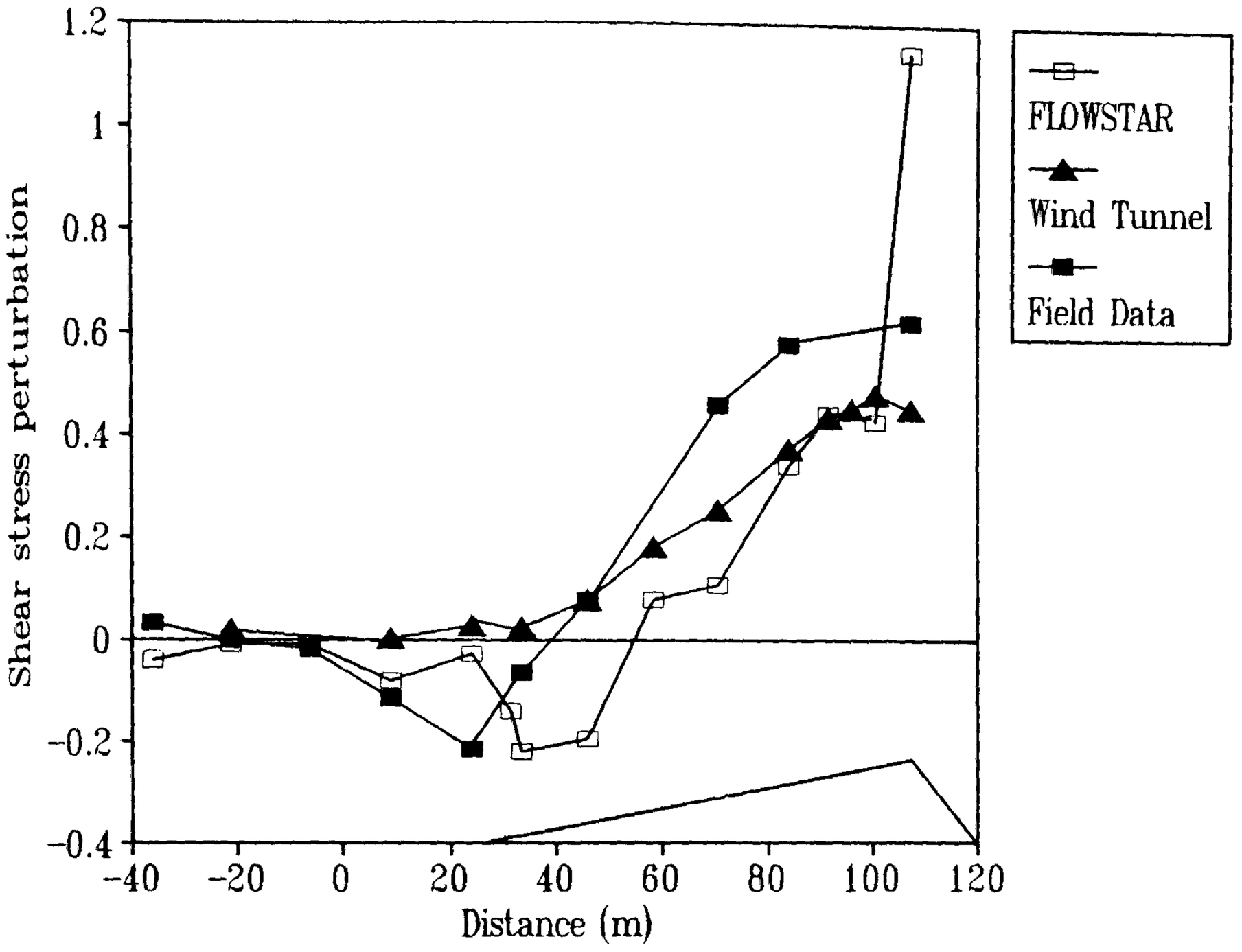

Figure 6.13 Shear velocity perturbation comparisons between the three techniques on the centre-line of the dune. Wind tunnel results are derived from the pulse-wire probe measurements.

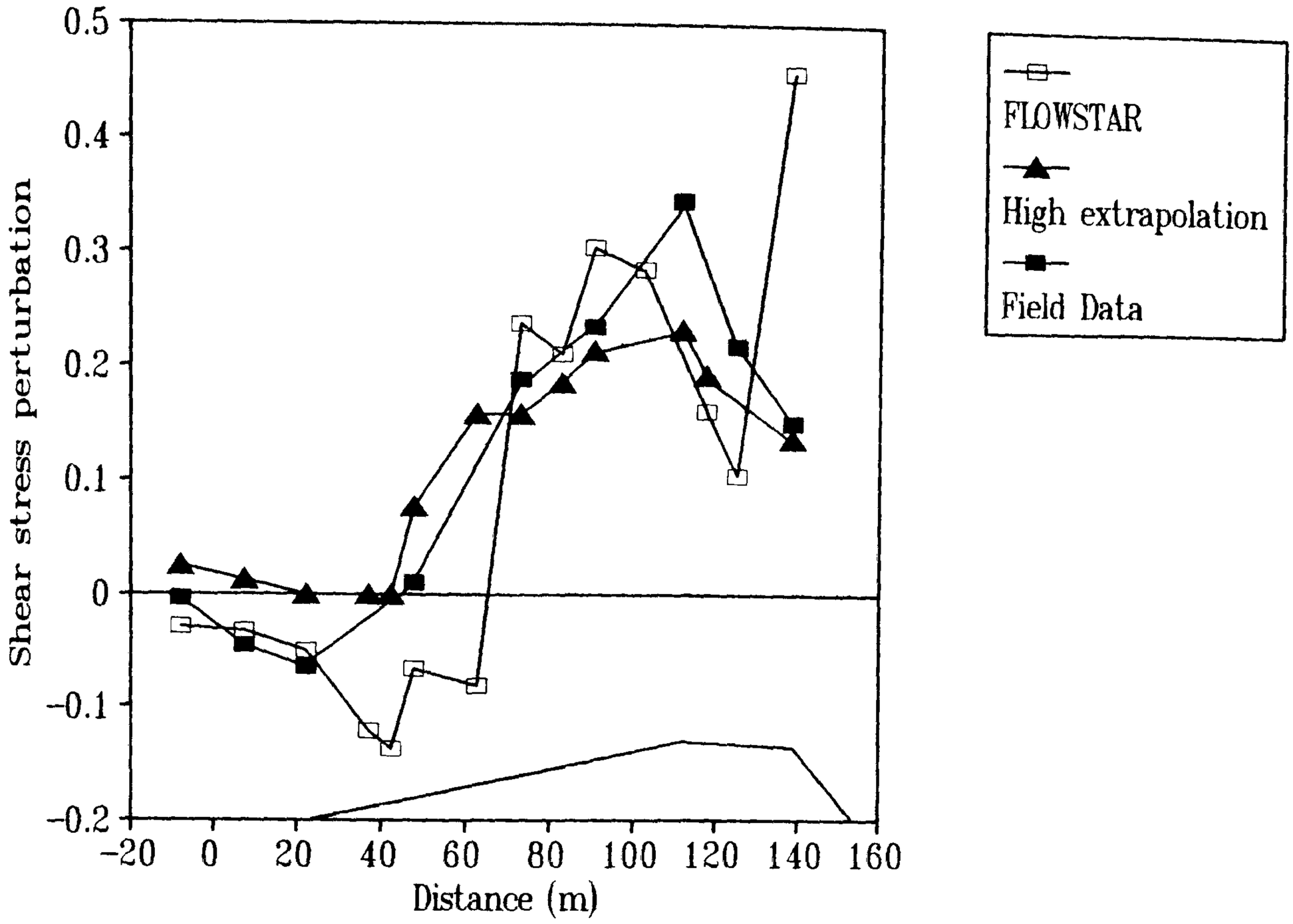

Figure 6.14 Shear velocity perturbation comparisons between the three techniques on the left flank of the dune. High extrapolation represents the u_* derived from the wind tunnel cross-wire measurements.

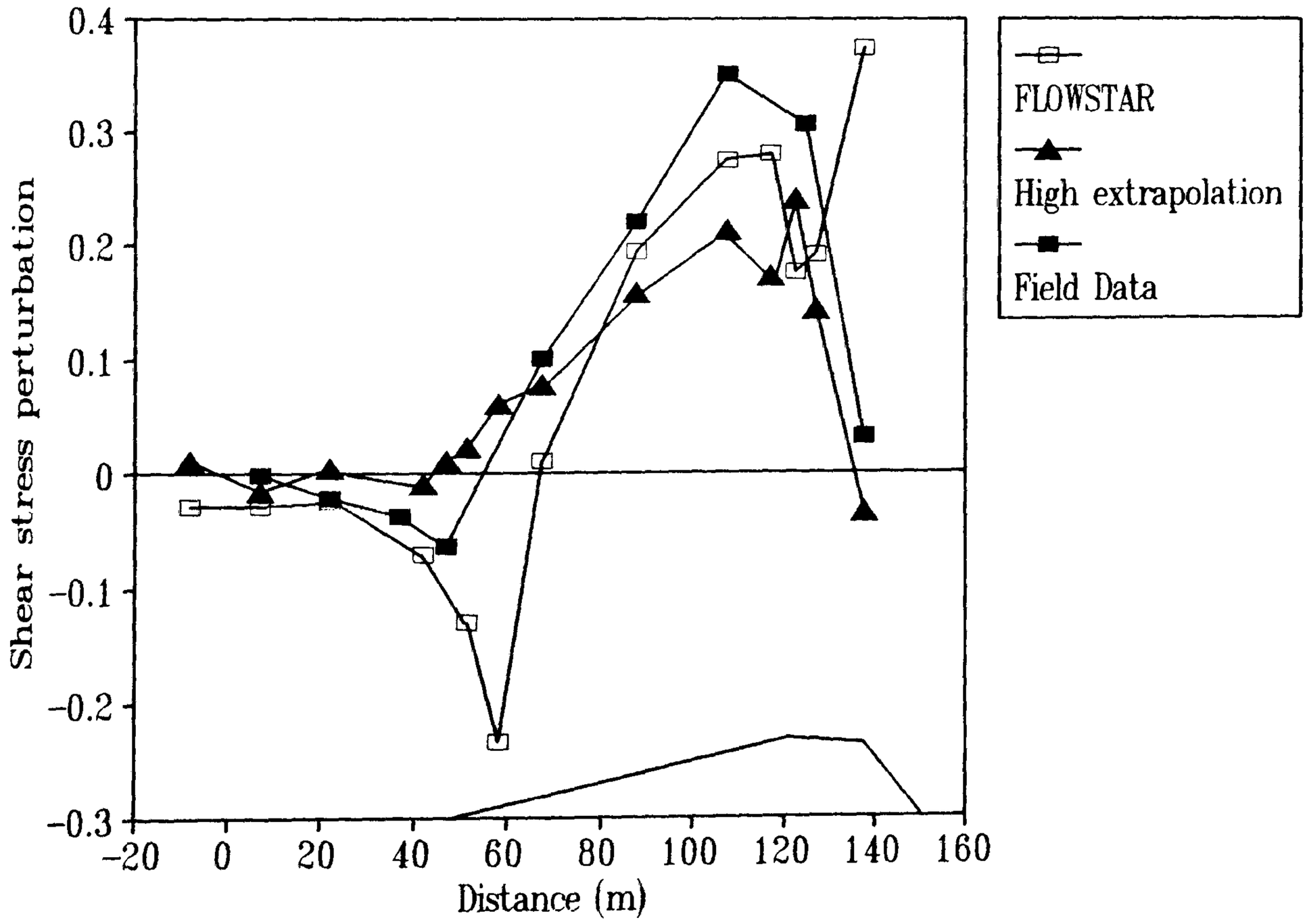

Figure 6.15 Shear velocity perturbation comparisons between the three techniques on the right flank of the dune. High extrapolation represents the u_* derived from the wind tunnel cross-wire measurements.

On the centre-line (Figure 6.13), all three techniques demonstrate a similar progression in u_* perturbation along the windward slope with maxima at the crest. However, several disagreements between the results can be identified particularly near the toe of the dune. Upwind and at the toe of the centre-line (between x = -5 m and +25 m) both the field and FLOWSTAR u_* perturbations show a reduction of upto 20%. The FLOWSTAR model predicts this reduction to continue until x ≈ 45 m before a recovery occurs, whilst at this point the field calculations are already showing positive perturbations. The FLOWSTAR perturbations do not become positive again until x ≈ 55 m. The development of this fall in u_* up to 30 m upwind of the dune with the FLOWSTAR and field measurements is distinct and well defined. This is in sharp contrast to the wind tunnel measurements which show no reduction in u_* in this region and maintain a level similar to upwind values until positive perturbations are evident downwind of the toe.

Along the windward slope from x = 60 m to x = 100 m the wind tunnel measurements and FLOWSTAR predictions are in good agreement. Although the field measurements show a similar rate of increase of u_* to the wind tunnel and FLOWSTAR values along the windward slope, the magnitude of the perturbations is larger. The maximum value of u_* perturbation for the field measurements (0.6) is therefore larger than that for the wind tunnel measurements (0.45). The FLOWSTAR prediction of u_* perturbation at the crest is very high at 1.15, significantly larger than with the other two techniques. This peak in u_* is likely to be caused for the same reasons that a peak in wind velocity was predicted in the region of the brink (Chapter 3), namely, the proximity of the reverse flow region downwind of the brink.

The left and right flanks (Figures 6.14 and 6.15) show broadly similar relationships. On both flanks only three pulse-wire probe measurements were taken so, in order to give an impression of the development of u_* along the windward slopes, the high extrapolations of surface shear velocity derived from the cross-wire measurements have also been plotted on Figures 6.14 and 6.15. The method of derivation of u_* from cross-wire measurements is fully discussed in Chapter 4.2.2. The FLOWSTAR predictions on both flanks show a very sharp drop in u_* perturbation upwind of the toe of the dune. On both flanks the reductions are of similar magnitude and form as on the centre-line. The reductions begin 15-20 m upwind of the toe and regain positive perturbations 30-40 m downwind of the toe. The field calculated values of u_* do not show such a marked reduction in this region as on the centre-line (Figure 6.13). On both flanks (Figures 6.14 and 6.15), the reductions in u_* at the toe result in negative perturbations of between -0.05 and -0.07. The shear velocities derived from the cross-wire measurements maintain a relatively constant level in these regions although small reductions in u_* may be identified. The single pulse-wire probe measurements at the toe of each flank show no evidence of a reduction in u_*

from upwind values (see Chapter 4.3.4). Along the windward slopes of the flanks the field-calculated shear velocities and the wind tunnel values show similar increases in perturbation toward respective crests. However, the rate of increase of the field perturbations becomes higher than the wind tunnel on the upper part of the windward slopes and so in the crestal regions of both flanks (Figures 6.14 and 6.15) the field perturbations are generally higher than their wind tunnel equivalents. This effect is not due to an increase in the rate-of-change of the field calculations but more to a decrease in the rate of increase of the wind tunnel results on the upper convex windward slopes. The FLOWSTAR predictions rise very sharply up the windward slopes of both flanks, principally as a result of the recovery from the severe negative perturbations apparent around the toe regions.

Both Figures 6.14 and 6.15 show a wide range of u_* perturbations apparent from each of the techniques in the crestal regions of the flanks. On each flank it is the field calculations which show the largest perturbations in the crest zone and the wind tunnel cross-wire derivations which show the smallest. For all three techniques the magnitude of u_* at the crests of the flanks is smaller than that apparent along the centre-line. The position of the maximum perturbation is also slightly different for each of the techniques. On the left flank (Figure 6.14) the position of the FLOWSTAR maximum is nearly 15 m upwind of the field-calculated maximum. However, this magnitude of discrepancy is not remarkable and may be partly attributable to errors in the demarcation of the crest in the field and failures in the processes of modelling the dune from the survey data in both the wind tunnel and mathematical model. Generally, however, all three techniques demonstrate maximum u_* perturbations in the crest region of the flanks.

Between the crest and brink on the flanks the wind tunnel and field techniques show a reduction in u_* to a similar final value. The FLOWSTAR results, however, show their typical peak in values at the brink due to the proximity of the region of reverse flow. On both flanks the shape of the u_* perturbation cross-sections are convex, indicating an increasing rate of reduction toward the brink. On the right flank (Figure 6.15) the u_* perturbations at the brink for the wind tunnel and field results are in good agreement, both being at or near zero. On the left flank (Figure 6.14) the reduction at the brink is less than on the right flank with both the wind tunnel and field data showing positive perturbations near to 0.1. This more severe reduction in u_* on the right flank is in contrast to the wind tunnel velocity measurements which showed a more severe reduction at the brink on the left flank (Chapter 4.3.3).

6.6 Discussion and Conclusion

Some trends in the measurements and predictions of u_* can be identified from Figures 6.13 to 6.15. The field and FLOWSTAR u_* perturbations tend to show a reduction upwind of and at the toe of the dune. This is not apparent with the wind tunnel measurements. On the windward slope of the dune the FLOWSTAR predictions take time to recover to positive values whilst the field measurements show an almost immediate reaction to the sloping surface and rise sharply. The wind tunnel measurements also show an immediate increase in u_* with the onset of the slope of the windward face. On the upper part of the windward slope the wind tunnel measurements and FLOWSTAR predictions are in good agreement although the field calculations tend to show a larger perturbation on the upper windward slope. All three techniques show a maximum shear velocity perturbation at or very near the crest. The peaks apparent at the crest are also larger than those found on the flanks. All three methods show similar reductions in u_* toward the brink on the crest-brink separated section lines (ignoring the peak in u_* predicted by FLOWSTAR at the brinks).

A further tendency is for the field calculations and FLOWSTAR predictions of u_* perturbation to be more extreme than the wind tunnel measurements. Upwind of the dune the wind tunnel measurements show no apparent decrease in u_* whilst the other two techniques do. On the upper windward slopes of the dune and at the crest, the wind tunnel measurements consistently show a smaller u_* perturbation than either the field calculations or FLOWSTAR predictions.

The literature concerned with the development of u_* over sand dunes is very small. Watson (1987), Lancaster (1987) and Livingstone (1990) have debated the subject, but none of them present data concerning u_*. Most of the research concerning sand dune dynamics has concentrated on the development of wind velocity (Tsoar, 1985; Lancaster, 1985). Both Mulligan (1989) and Butterfield (1991) present data on u_* on the windward slopes of dunes but their measurements are at a point (the crest) and their discussions are concerned with the intricacies of calculation rather than the development and change in shear velocity across the dune. The engineering literature contains several examples of wind tunnel and field measurements of shear stress over low hills (reviewed in Taylor *et al.*, 1987) and the wind tunnel results in this study have been shown to be in broad agreement with them (Chapter 4).

One study which presented data on the development of u_* up the windward slope of a dune is that of Lai & Wu (1978). In their wind tunnel studies of flow over a coastal dune, Lai & Wu derived "shear stress" from velocity profiles measured with a single hot-wire probe. This method,

in fact, gives values for shear velocity. In comparison to the data presented in Figures 6.13 to 6.15, the results of Lai & Wu show some contrast. Watson (1987) claimed that Lai & Wu (1978) found the maximum shear velocity on the steep windward slope of the dune upwind of the crest, whilst the wind velocity maximum was at the crest. This conclusion is similar to that of Burkinshaw & Rust (1992) who calculated shear velocity over a reversing transverse coastal dune in South Africa. Burkinshaw & Rust (1992) also found the maximum shear velocity on the steepest part of the dune. This is in contrast to the results shown in Figures 6.13 to 6.15, all of which suggest that the maximum shear velocity is at the crest. This finding is concordant with a decreasing pressure gradient caused by streamline compression at the crest of the dune. Careful re-analysis of the Lai & Wu (1978) data revealed that the maximum shear velocity, as defined by the velocity gradient, actually reached a maximum at the crest, not on the steepest part of the windward slope. This highlights the difficulties involved in fitting a straight line to essentially curved velocity profiles, as applied by Watson (1987) on the Lai & Wu (1978) data-set, in order to determine shear velocity.

The Burkinshaw & Rust (1992) results are also somewhat questionable. Their values for u_* were determined from assessments of wind velocity at a height of 6 cm using a similar method to the Bagnold / Mulligan technique described in Chapter 6.2.

$$u_* = (u - u_t) / 5.75 \text{ ln. } z/z_0$$

where:

u = velocity at height z
u_t= threshold velocity for sand movement
z_0= surface roughness

However, measurements of velocity using cup-anemometers this close to the surface and deep within the saltation layer are highly suspect. Also, the windspeed at 6 cm height (from which u_* was calculated) was frequently interpolated from measurements of velocity further from the surface. There is no mandate for this procedure and it is questionable whether windspeeds within a saltation layer can be accurately predicted from windspeeds above the saltation layer.

Burkinshaw & Rust (1992) stated that:

> *"shear stress will be enhanced by increased compression which is related directly to the inclination of the surface"*

This is no explanation for the apparent maximum in u_* on the steepest part of the slope because the technique used for calculating u_* only allows for the effects of compression in an indirect manner, from the windspeed. The maximum compression of streamlines should also occur at the crest of the dune, although the maximum *rate-of-change* may be apparent on the steepest part of the slope. In order for Burkinshaw & Rust (1992) to calculate a maximum u_* on the steepest part of the windward slope they also had to measure the maximum windspeed at this point. If the maximum compression of streamlines is assumed to occur at the crest of the dune, then the maximum windspeed should also occur there. Considering that Burkinshaw & Rust (1992) were working on a steeply sloping reversing dune with the probability of very high turbulence intensities and also interpolating windspeeds and shear velocities within the saltation layer, their results remain questionable.

In the discussion concerning the probable development of u_* over the windward slopes of sand dunes (Watson, 1987; Lancaster, 1987; Livingstone, 1990, Burkinshaw & Rust, 1992) much of the argument concerns the position of the point of maximum u_*. However, much more important to questions concerning sand dune dynamics is the rate-of-change of u_*. This is important because it governs the rate-of-change of sand transport and, hence, the spatial variability of erosion and deposition. In order to discuss the relative merits of the determinations of u_* from each of the three techniques (in relation to sand dune dynamics) it is first necessary to calculate sand transport rates.

CHAPTER 7 DUNE DYNAMICS

7.1 Introduction

To compare rates of erosion and deposition apparent from the three study techniques used here it was first necessary to evaluate the rates of sand transport predicted by each. There have been many attempts to characterise the rate of sand transport as a function of the shear velocity (as reviewed by Hsu 1971, 1973; Sarre 1987, 1988). In this Chapter some of the more common of the sand transport rate expressions are compared to the actual rates of sand transport as measured by sand traps (Chapter 2). The expression which described the actual sand flux best is then applied to the wind tunnel and FLOWSTAR shear velocity data-sets. This enables a comparison to be made between the predicted sand transport rates from the three techniques and the actual transport rates measured in the field.

The spatial variation of predicted sand transport rate determined for each of the three techniques is then used to evaluate rates of erosion and deposition. These predicted rates of surface change are compared to the actual rates as determined from the erosion pin measurements in the field (Chapter 2). One of the reasons for the discrepancies between the prediction of morphological changes between the three methods may be the absence of flow curvature terms in the numerical modelling and field techniques. In consideration of this fact a new model of dune dynamics is formulated which is based on an equilibrium between flow velocity changes and flow curvature modifications.

7.2 Sand Transport Rate Calculations

7.2.1 Review of Sand Transport Rate Formulae

Most of the expressions used to calculate sand transport rate (q) from wind velocity data are derived from theoretical and wind tunnel experimental work. They all tend to be of the form;

$$q = Au_*^b$$

There has been very little empirical testing of the relationships in the field (Sarre, 1987; Sherman, 1990). The empirical testing that has been accomplished (Sarre, 1987) has shown a great deal of variation between the observed rates and those predicted as a function of u_*.

The two types of relationship frequently used to calculate sand transport rate are typified by the expressions of Bagnold (1941) and Kawamura (1951):

$$q = C(d/D)^{0.5}\, u_*^3\, \rho/g \qquad \text{(Bagnold, 1941)} \qquad \textbf{(7.1)}$$

$$q = K_k(u_* - u_{*_t})(u_* + u_{*_t})^2\, \rho/g \qquad \text{(Kawamura, 1951)}$$

where:

q = sand transport rate ($gm^{-1}s^{-1}$)
C = constant (1.8 for naturally graded dune sand)
d = grain diameter
D = standard grain diameter (0.25 mm)
ρ = air density
g = gravity
K_k= constant (2.78)
u_{*_t}=threshold shear velocity for grain entrainment

The Bagnold (1941) expression works from the basis of calculating the loss of momentum from air to the saltating grains. The Kawamura (1951) calculation partitions the shear stress into that provided by the velocity gradient and that provided by the impact of falling grains. Well known problems with the Bagnold (1941) expression include the fact that it predicts sand movement below the threshold of entrainment and it commonly predicts rates which are considered too low at high values of shear velocity (Sarre, 1987). Owing to the inclusion of a threshold term in the Kawamura (1951) calculation it should be more accurate at low values of shear velocity. However, this expression only incorporates the effect of grain size in the threshold term (u_{*_t}) despite the fact that it is also likely to have an important effect on the transfer of momentum on grain impact.

Zingg (1953) followed a similar argument to Bagnold (1941) but used a 3/4 power function:

$$q = C_2(d/D)^{3/4} u_*^3\, \rho/g \qquad \textbf{(7.2)}$$

where:

C_2= constant (0.83)

Owen (1964) found that this expression was more accurate over a wider range of particle sizes than the Bagnold (1941) formula. A similar expression has been derived by Horikawa & Shen (1964).

In later analyses Bagnold (1956) included a threshold term in his expression. This was refined by Lettau & Lettau (1978):

$$q = C_1(d/D)^{0.5}(u_* - u_{*_t})u_*^2\rho/g \qquad (7.3)$$

where:

C_1= constant (4.2)
$u_{*_t} = A[(\rho'-\rho/\rho)gd]^{0.5}$
A = constant (0.8 for impact threshold)
ρ'= grain density

There are many different expressions for calculating u_{*_t} some of which take lift and inter-particle attraction into account (Chepil, 1959; Chepil & Woodruff, 1963; Allen, 1970). However, Howard *et al.*, (1977) stated that the Bagnold formula is adequate for dune sands and the scope of this study is not sufficient to allow an examination of the more complicated formulae (see Greeley and Iversen (1985) for a full discussion of these).

It was decided to test three commonly used sand transport rate expressions which characterised the three different approaches taken in the literature and reflected the mainstream concepts described above. The formulae used were:

1. Bagnold (1941), Equation 7.1
2. Zingg (1953), Equation 7.2
3. Lettau & Lettau (1978), Equation 7.3

The three formulae were each derived from theoretical and experimental work which assumed a flat bed. However, a sloping dune surface affects both the motion of saltating grains and the threshold of motion. Sand transport is inhibited on windward slopes and enhanced by a downslope gradient (Howard *et al.*, 1977). There has been much discussion as to the effect of bedslope on sand transport rate (Hunt & Nalpanis, 1985; Nalpanis, 1985; Hardisty & Whitehouse, 1988; Whitehouse & Hardisty, 1988). Bagnold (1941) derived a simple geometric relationship to describe the effect of bedslope on sand transport rate:

$$q_s = q/\cos\theta\ (\tan\alpha + \tan\theta) \qquad (7.4)$$

where:

q_s= sand transport rate on a sloping surface
q = sand transport rate on a flat surface
θ = bedslope angle
α = angle of repose of sand (32°)

Howard *et al.* (1977) studied the operation of Equation 7.4 and found that it had only a small effect on sand transport rate predictions and characterised actual sand transport rate no better than if bedslope was not taken into account. However, Hardisty & Whitehouse (1988), using a portable wind tunnel on Saharan dunes, found that bedslope had a significant effect on sand transport rate. They showed that on a sloping surface the sand transport rate could be defined from:

$$j_b = A.k(u^2-B^2.u_t^2)u$$

where:

j_b = mass transport rate per unit width on a sloping surface
k = coefficient of proportionality
u_t = threshold velocity for sediment movement
A = k_b/k_0, ratio of sloping to flat-bed value of coefficient
B = u_{*tb}/u_{*to}, ratio of sloping to flat-bed value of critical velocity threshold

From their analysis they found that the function B (the effect of bedslope on the threshold of movement) was accurately described by the theoretical analysis of Dyer (1986):

$$B=\frac{\sqrt{\tan i-\tan b}}{\tan i}\cos b \qquad (7.5)$$

and the effect of bedslope on the transport rate was found to be:

$$A=\left(\frac{\tan i}{\tan i-\tan b}\right)^7 \qquad (7.6)$$

Equation 7.6, derived from empirical measurements, suggests that sand transport rate is much more dependent on surface slope than predicted by the theoretically derived relationship of Bagnold (Equation 7.4). Hardisty & Whitehouse (1988) explained this discrepancy by suggesting a gravity flow effect caused by vibration which had not previously been recognised.

In order to examine the effect of surface slope on sand transport rate in the present study, both of the above relationships (Bagnold, 1941 [Equation 7.4] and Hardisty & Whitehouse, 1988 [Equations 7.5 and 7.6]) were applied to the u_* data derived from the field velocity measurements and tested against the simultaneously measured transport rates.

7.2.2 Comparison of Sand Transport Rate Formulae

Figure 7.1 shows the predictions of sand transport rate using the Bagnold (1941) [Equation 7.1], Zingg (1953) [Equation 7.2] and Lettau & Lettau (1978) [Equation 7.3] formulae (as applied to the field u_* derivations) compared to the measured rate of transport. None of these calculations has been modified for surface slope. The data plotted in Figure 7.1 are the result of 88 measurements of u_* and sand transport rate across the centre-line and both flanks of the dune. The three expressions predict widely divergent transport rates particularly at high values of u_*. From Figure 7.1 it is not possible to determine which of the formulae best predicts actual sand transport. However, it is clear that the Zingg (1953) expression consistently under-predicts q.

When plotted on logarithmic axes (Figure 7.2) the differences between the formulae are more distinguishable. The under-prediction by the Zingg (1953) expression is quite distinct and it appears that the Bagnold (1941) formula over-predicts sand transport rate below $u_* = 0.35$ ms^{-1}. The Lettau & Lettau (1978) formula which includes an expression for the threshold of grain movement in the calculation (u_{*_t}) predicts the actual transport rate at low values of u_* better than the Bagnold (1941) calculation. The result of the inclusion of u_{*_t} in the Lettau & Lettau (1978) calculation is a curved relationship with u_* in contrast to the straight lines of the Bagnold (1941) and Zingg (1953) expressions. It is not clear from Figure 7.2 whether the measured sand transport rates follow a similar curved pattern. The measured rates do appear to fall away at low values of u_*, but a lack of data in this region of the graph makes it difficult to draw conclusions. However, the sand transport rate measurements of Sarre (1988), across a beach, covered a much wider range of u_* (between 0.14 ms^{-1} and 1.15 ms^{-1}) and displayed a distinctly curved relationship.

Figures 7.3 and 7.4 show the actual sand transport rates compared to the calculated rates modified for surface slope (using Equations 7.4 and 7.5 & 7.6 respectively). Both Figures show that despite correcting for surface slope the predicted transport rates may be up to ten times more than the actual rates. Both the Bagnold and Lettau & Lettau formulae considerably over-predict transport rates after correction for slope whilst the Zingg formula still under-predicts rates. The degree to which each of the combinations of formulae describe the actual sand transport rate can be provided by statistically analysing the regression equations between actual and calculated flux. Table 7.1 shows selected statistical parameters which describe the linear regressions of predicted flux against observed flux. A perfect prediction of observed flux would be shown by a correlation coefficient of 1.0, an x-coefficient of 1.0 and a constant of zero.

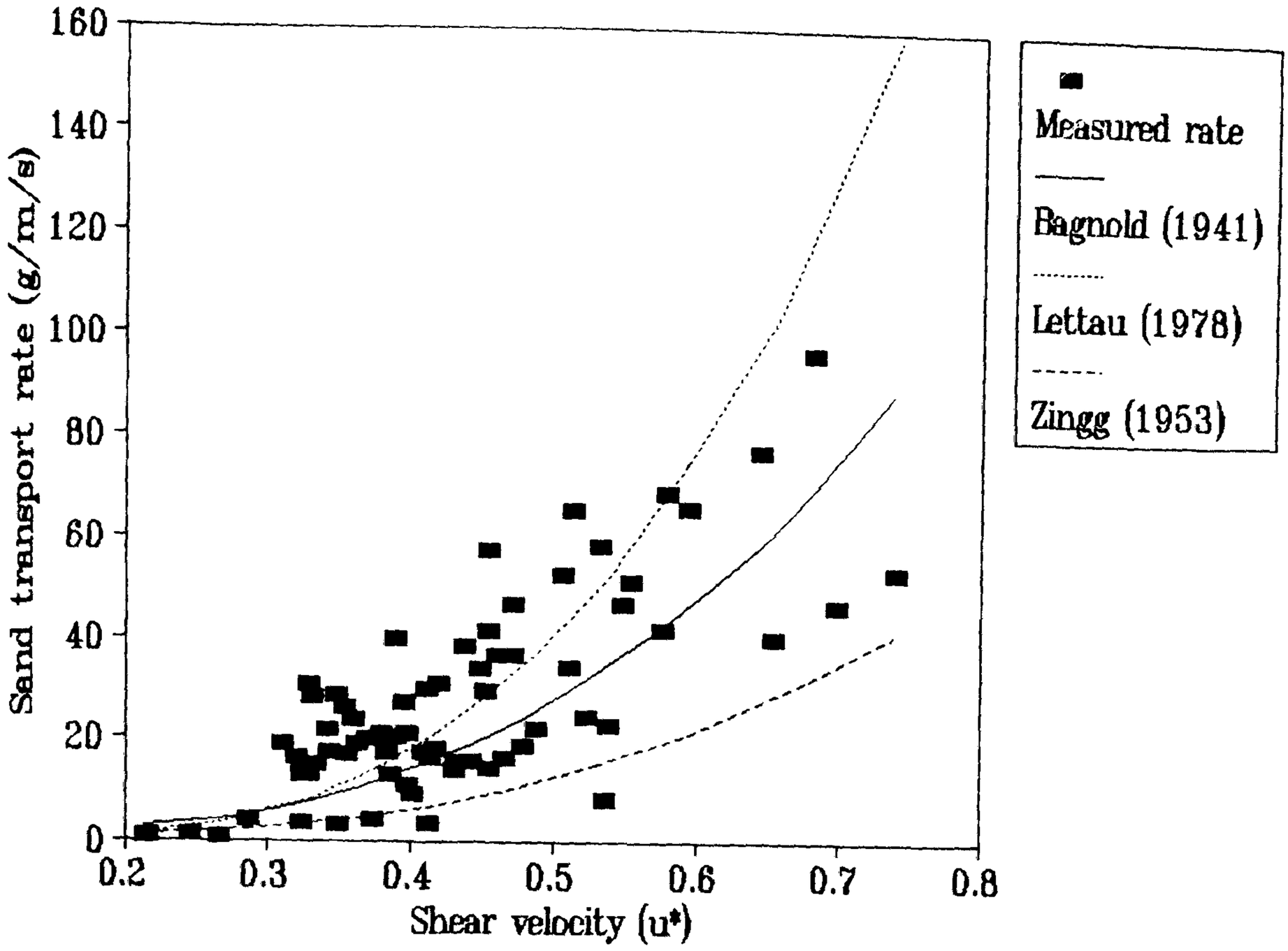

Figure 7.1 Relationship between shear velocity, measured sand transport rate and that calculated from three sand transport rate formulae (normal axes).

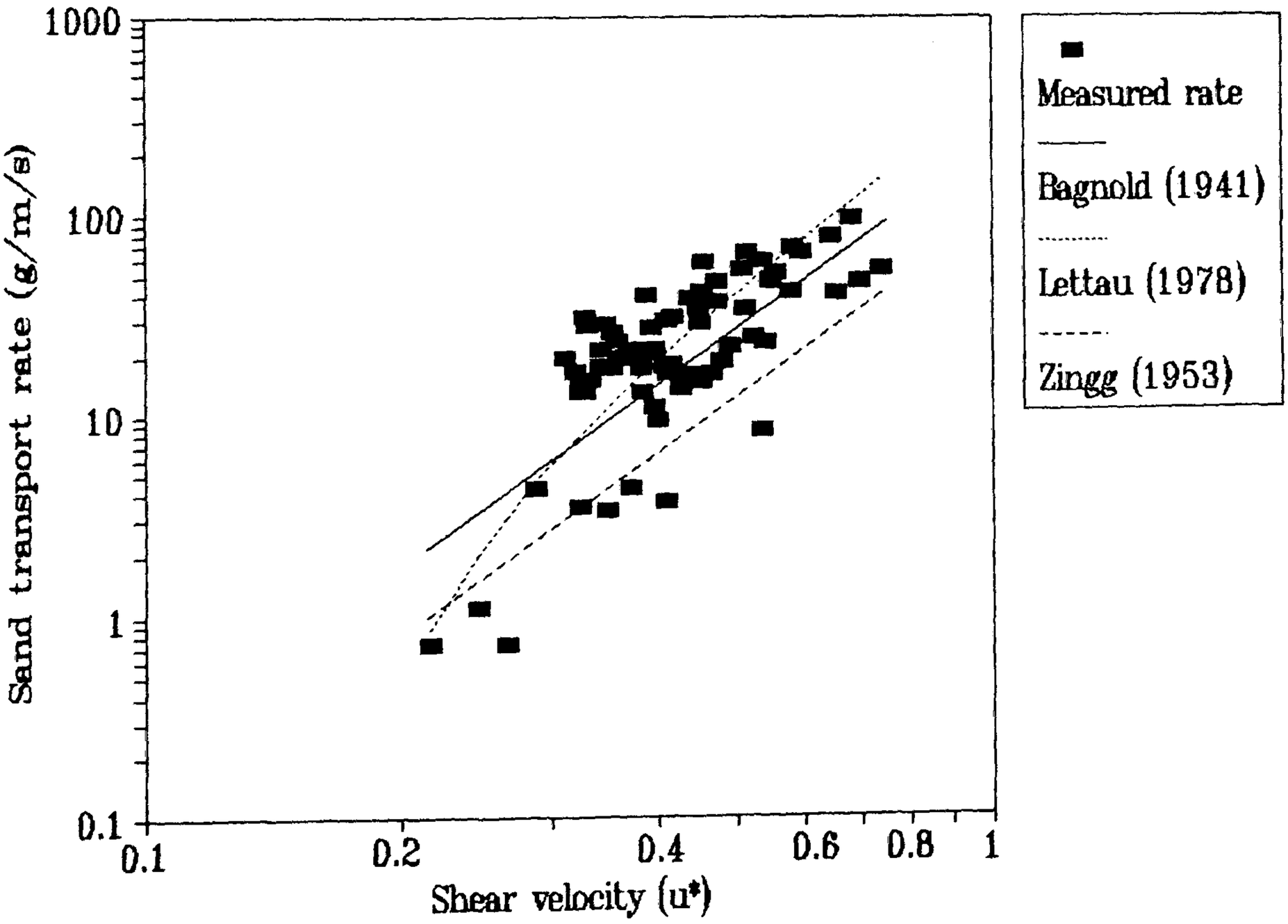

Figure 7.2 Relationship between shear velocity, measured sand transport rate and that calculated from three sand transport rate formulae (logarithmic axes).

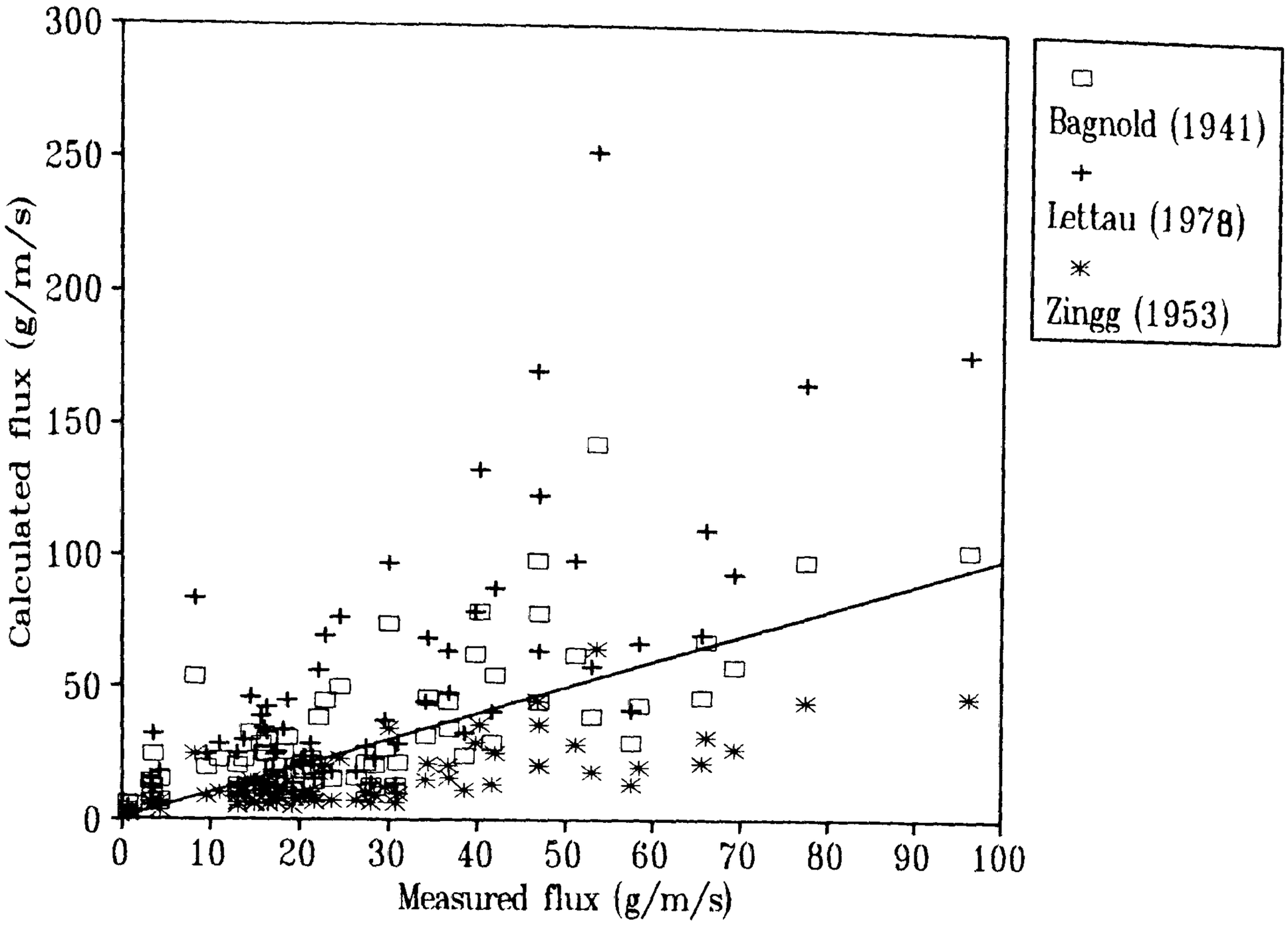

Figure 7.3 Relationship between measured sand transport rate and calculated sand transport rate modified for surface slope by Equation 7.4.

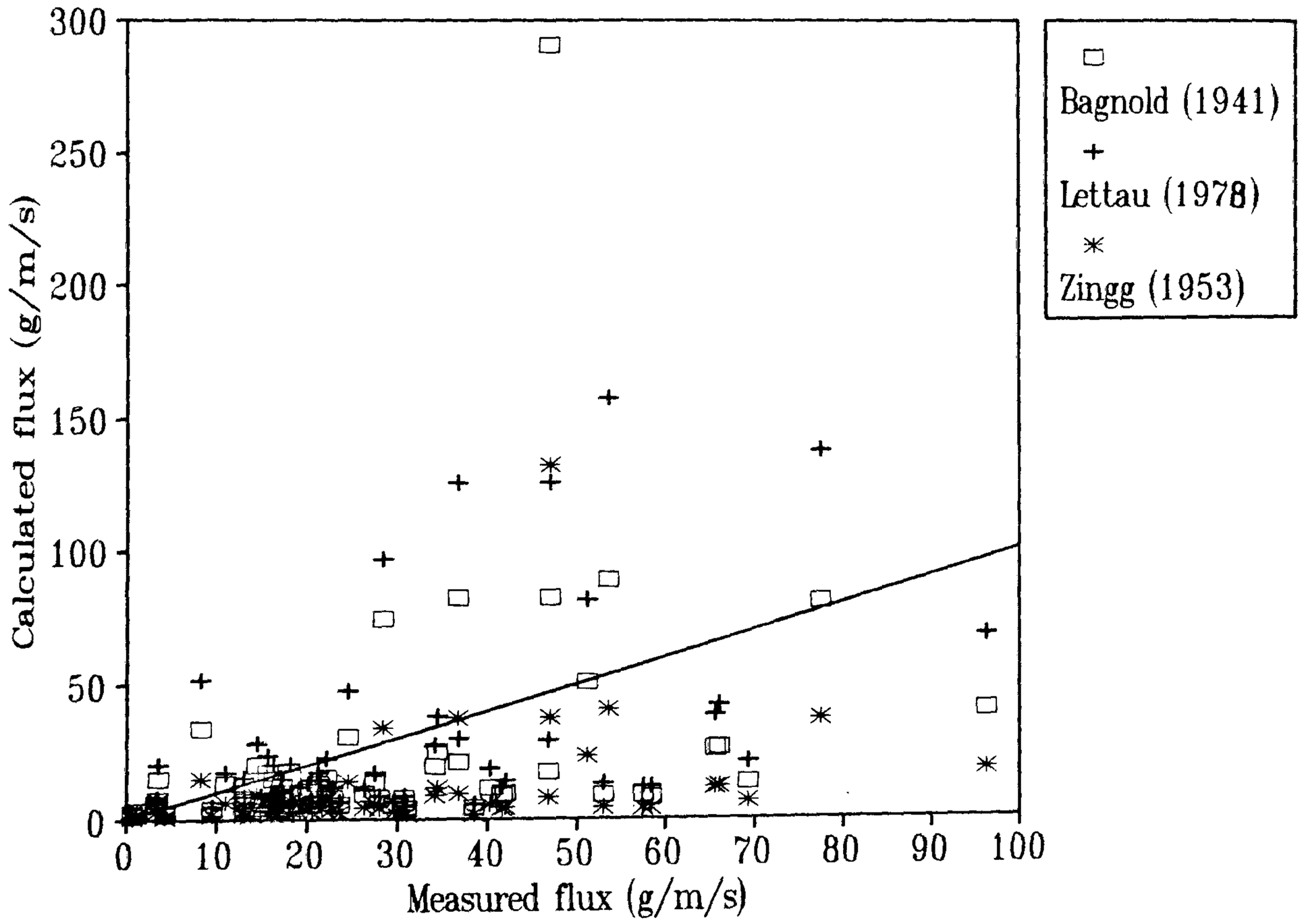

Figure 7.4 Relationship between measured sand transport rate and calculated sand transport rate modified for surface slope by Equations 7.5 and 7.6.

Table 7.1 Regression analysis of predicted and observed sand transport rate using different predictive equations

A. Equations not slope modified	Bagnold (1941) Equation 7.1	Lettau & Lettau (1978) Equation 7.3	Zingg (1953) Equation 7.2
r^2	0.52	0.51	0.53
Pearson's r	0.73	0.72	0.73
x-coefficient	0.63	1.12	0.29
constant	3.49	-0.02	0.31
B. Modified for slope by Equation 7.4			
r^2	0.54	0.53	0.54
Pearson's r	0.74	0.73	0.74
x-coefficient	0.99	1.74	0.46
constant	5.73	0.40	2.61
C. Modified for slope by Eq. 7.5 & 7.6			
r^2	0.24	0.28	0.24
Pearson's r	0.49	0.53	0.49
x-coefficient	0.51	0.88	0.23
constant	3.31	0.64	1.51

Case A

Where there has been no adjustment for the effects of surface slope (Case A in Table 7.1) the Table shows that there is little difference between the three sand transport rate formulae in terms of data scatter about the regression lines (shown by their similar r^2 values). However, the Lettau & Lettau (1978) formula gives an x-coefficient for the regression line of 1.12 which is much closer to unity than either of the other two expressions. The x-coefficient for the Zingg (1953) expression is very low at only 0.29. The Lettau & Lettau equation also provides an intercept on the y-axis closer to zero than either of the other two formulae. This is in contrast to the Bagnold (1941) formula which predicts a sand transport rate of 3.49 $gm^{-1}s^{-1}$ when the measured rate is

zero. Analysis of the x-coefficients and intercept constants gained from regression analysis between observed and predicted sand transport rates therefore suggests that the Lettau & Lettau (1978) expression (Equation 7.3) provides the best agreement when no account is made of surface slope. Figure 7.5 shows the observed sand transport rate along the centre-line of the dune during a four-minute trapping run compared to the rates predicted by the three formulae. From this Figure it can be seen that the three formulae all estimate a similar development in q across the dune. In each case a reduction in q upwind and at the toe is predicted with an increase in q up the windward slope toward a maximum near the crest. In this study, where the identification of zones of erosion and deposition is important, predicting the actual value of sand transport rate is less significant than predicting the 'shape' of the sand transport rate curve across the dune. The choice of which transport equation to use (where no account is made for surface slope) in this instance is therefore fairly arbitrary as they all show a similar 'shape' from upwind to the crest of the centre-line.

Case B

With Case B in Table 7.1 (where the sand transport rate has been modified in accordance with Equation 7.4) it can be seen that there is little or no improvement on the unadjusted results. For each of the formulae in case B the r^2 values and correlation coefficients are marginally improved and the x-coefficients and constants are all increased. This increase brings the x-coefficients for the Bagnold and Zingg expressions closer to unity but raises the Lettau & Lettau x-coefficient further from unity to a much larger value of 1.74. The inflation of the constants takes the values for each of the equations further from zero than with case A. This enlargement of the constants in the regression equations is unsurprising as the geometric relationship described by Equation 7.4 always predicts a higher sand transport rate on a surface of zero slope than the unmodified (Case A) formulae. For Equation 7.4 to predict an unmodified sand transport rate on a surface of zero slope (as would be expected), the denominator [$\cos \theta (\tan \alpha + \tan \theta)$] must equal 1. However, because $\tan \alpha$ (the angle of repose of sand) is 0.62 and $\cos \theta$ (the surface slope angle) is 1 (when $a = 0$), the predicted sand transport rate on a flat surface is actually 62% higher than that predicted by the formulae which do not take bedslope into account. This is a fundamental error in the formula and is a result of its reliance on purely geometric relationships. For this reason, and due to the fact that no significant improvement was made in the prediction of actual sand transport rates, it was decided that modifying the sand transport rate calculations for surface slope angle by using Equation 7.4 was inappropriate.

Case C

The regression analysis results for the Hardisty & Whitehouse (1985) modification for surface slope (Equations 7.5 & 7.6 and Case C in Table 7.1) show that it also fails to improve the prediction of observed transport rates. For each of the predictive formulae the correlation coefficient is halved and the x-coefficients of the regression lines are further from unity than with either Case A or Case B. There is also no improvement in the value of the regression line constants. For each formula the constants are the same or further from zero than in Case A, where no adjustment was made for surface slope angle.

Modifying the calculated sand transport rates for surface slope angle does not improve their prediction of observed sand transport rates. A similar conclusion was reached by Howard *et al.* (1977) with their analysis of the Bagnold (1941) formula (Equation 7.4). For this reason no account was made for surface slope angle in subsequent analysis. The best agreement between predicted and observed sand transport rates is provided by the Lettau & Lettau (1978) formula (Equation 7.3) unadjusted for surface slope angle. The calculation of sand transport rates for the field, wind tunnel and FLOWSTAR derivations of u_* was therefore achieved by utilising Equation 7.3.

7.3 Comparison between Field-Predicted and Observed Sand Transport Rates

Notable differences can be observed between the actual sand transport rate (as measured with sand traps) and that predicted by Equation 7.3 from u_* derived from field wind velocity measurements. These differences are most marked upwind of and at the toe of the dune where a progressive and distinct dissimilarity can be distinguished. In the crest and brink regions of the dune it is less simple to define a pattern or relationship between the measured and calculated sand transport rates.

The Toe Region and Upwind of the Dune

A comparison between observed and field-predicted sand transport rates across the centre-line of the dune is shown in Figure 7.6. These data were collected in two four-minute periods on 27.7.90 in two separate runs. The first run was on the downwind section of the dune (toe - crest) and the second run was on the upwind interdune flat. However, because the u_* at the reference site (at x = -21.25 m) was the same during each run, it was possible to combine the two measurement sequences without normalising the data. It can be seen from Figure 7.6 that the

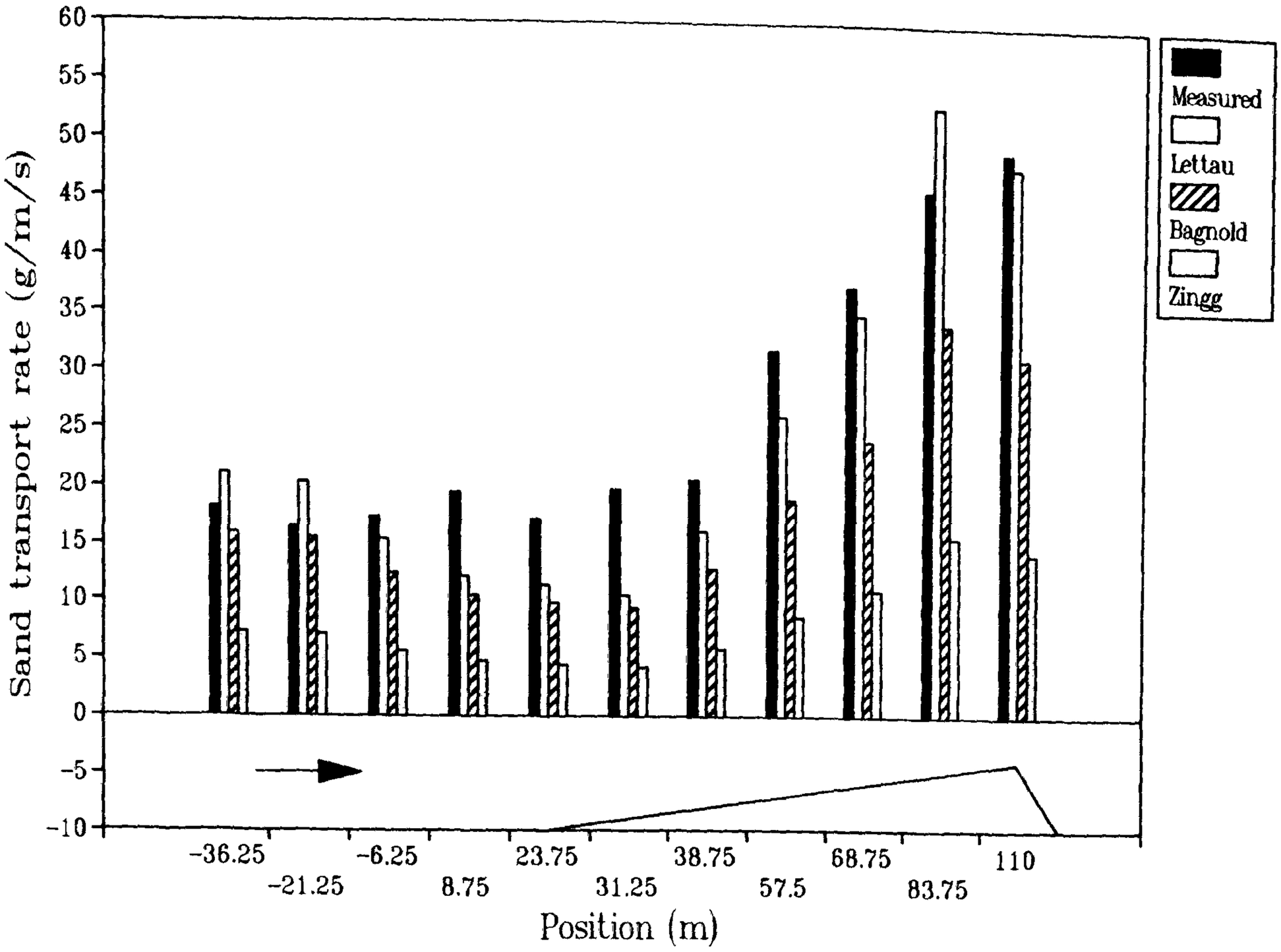

Figure 7.5 Comparison between measured sand transport rate on the centre-line of the dune during a sand trapping run and that predicted from Equations 7.1, 7.2 and 7.3 using field velocity data to calculate u_*.

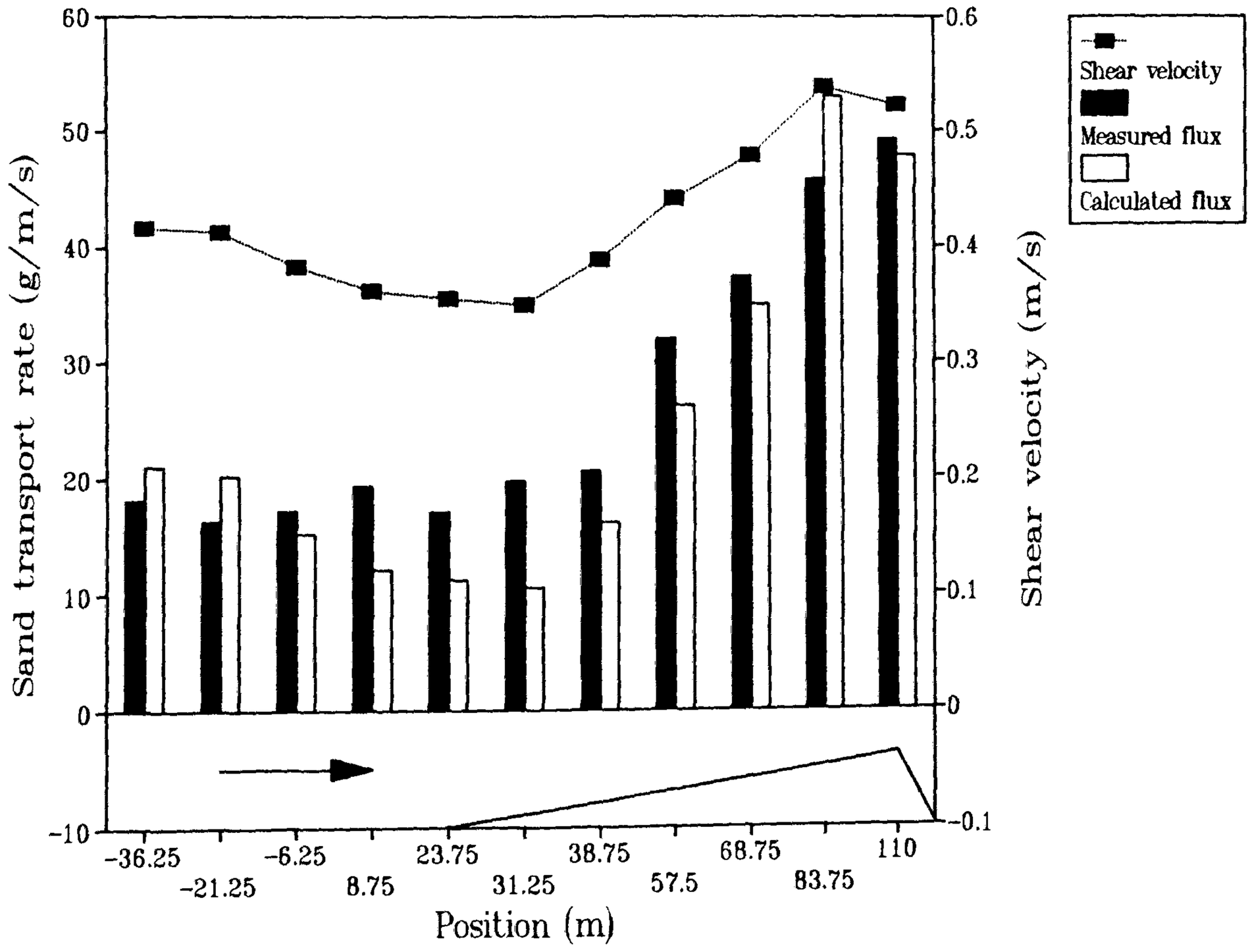

Figure 7.6 Observed and field-predicted sand transport rate on the centre-line of the dune (run 1).

predicted potential sand transport rate (calculated flux) fell to a minimum of 12 $gm^{-1}s^{-1}$ at the toe of the dune (from an upwind value of 23 $gm^{-1}s^{-1}$), coincident with a fall in calculated u_* from 0.43 ms^{-1} to 0.36 ms^{-1}. In contrast, the measured transport rate (measured flux) remained fairly constant. This difference is highlighted in Figure 7.7 which shows the perturbations in u_*, measured and predicted flux. The reduction in u_* at the toe of 15% resulted in a reduction in potential sand transport of nearly 50%, although the measured transport rate remained within ±9% of the upwind value with no progressive reduction.

Similar relationships to those shown in Figure 7.7 are displayed in Figure 7.8 which also shows measured and predicted sand transport rate perturbations across the centre-line of the dune. The data for this Figure were collected in a repeat experiment to that described above consisting of two four-minute sand trapping runs on 27.7.90. Again, there is a progressive reduction in calculated transport rate upwind of and at the toe of the dune to a minimum rate of 50% of the upwind flux. This is consistent with a reduction in derived u_* of about 17% and is in contrast to the uniformity of the measured transport rate upwind of the dune which is maintained at a fairly constant level.

The dissimilarity between predicted and observed transport rate around the toe of the dune is not restricted to the centre-line. Figures 7.9 to 7.12 show a comparison between predicted and observed transport rates along the left and right flanks respectively. These Figures represent the data from two trapping periods of between two and five minutes each. The left flank measurements (Figures 7.9 and 7.10) were carried out on 28.7.90 and the right flank (Figures 7.11 and 7.12) on 29.7.90. The measurements on both flanks demonstrate less of a dissimilarity between observed and predicted sand transport rates around the toe region than on the centre-line. Considering the modest u_* perturbation on the flanks, this is expected. Both runs on the left flank (Figures 7.9 and 7.10) show a reduction in u_* at the toe of the dune of between 5% and 10%, resulting in a reduction in calculated potential sand transport rate of between 20% and 32%. The measured transport rates at the toe of the left flank remain relatively constant. Very similar relationships are observed on the right flank. In Figures 7.11 and 7.12 at the toe of the right flank the reduction in u_* is about 10% for each trap run. This has resulted in the calculated sand transport rate dropping by as much as 40%, a reduction not mirrored by the measured sand transport rate.

The Crest and Brink Regions

There is no definite relationship between measured and predicted sand transport rates in the crestal region of the dune. On the centre-line (Figures 7.7 & 7.8) the calculated flux perturbations during both runs on the windward slope and at the crest are less (by about 50%) than the measured flux perturbations. In the first run (Figure 7.7) the maximum measured flux perturbation of 2.1 is at the crest while that of the calculated flux (1.6) is 25 m upwind of the crest. In the second run (Figure 7.8) the maximum measured and calculated flux perturbations are both 25 m upwind of the crest with values of 3.6 and 2.9 respectively.

On the left flank (Figures 7.9 and 7.10) the position is the reverse of that found on the centre-line. Here, the calculated transport rates generally demonstrate larger perturbations in the crestal region than their measured counterparts. In the first run (Figure 7.9) the maximum calculated flux occurs at the crest with a perturbation of 4.7. This compares with the measured perturbation (also at a maximum at the crest) of only 1.8. Similarly, in the second run (Figure 7.10) both the measured and calculated flux perturbations reach maxima at the crest. Again, the calculated perturbation is larger (at 4.1) than the measured perturbation (at 3.3).

The right flank (Figures 7.11 and 7.12) demonstrates conflicting findings. In the first run (Figure 7.11) the calculated flux maximum perturbation (of 6.5) which occurs at the crest is more than double that of the measured flux perturbation of 2.8 (which also occurs at the crest). However, in the second run (Figure 7.12) both flux perturbations reach maxima at the crest but the measured flux maximum perturbation (of 5.7) is larger than the calculated perturbation (of 3.2).

Discussion

In the crest regions and on the windward slope there appears to be no consistent relationship between the calculated and measured flux perturbations. In some instances the measured transport rate perturbations on the windward slope are larger than the calculated perturbations, whilst in others the opposite is true. One would expect that in equivalent conditions the results might be more consistent. In the toe region the calculated flux perturbations are invariably lower (and more negative) than the measured flux perturbations. At the crest one might expect the measured flux perturbations on the centre-line to be larger than those on the flanks. However, when comparing Figure 7.7 with Figure 7.12 it can be seen that the maximum perturbation at the crest on the right flank of 5.7 is more than double that on the centre-line. The measured perturbations on any one section line are also widely variable between separate measurement runs (*e.g.* compare the measured flux perturbations for Runs 1 and 2 on the right flank, Figures

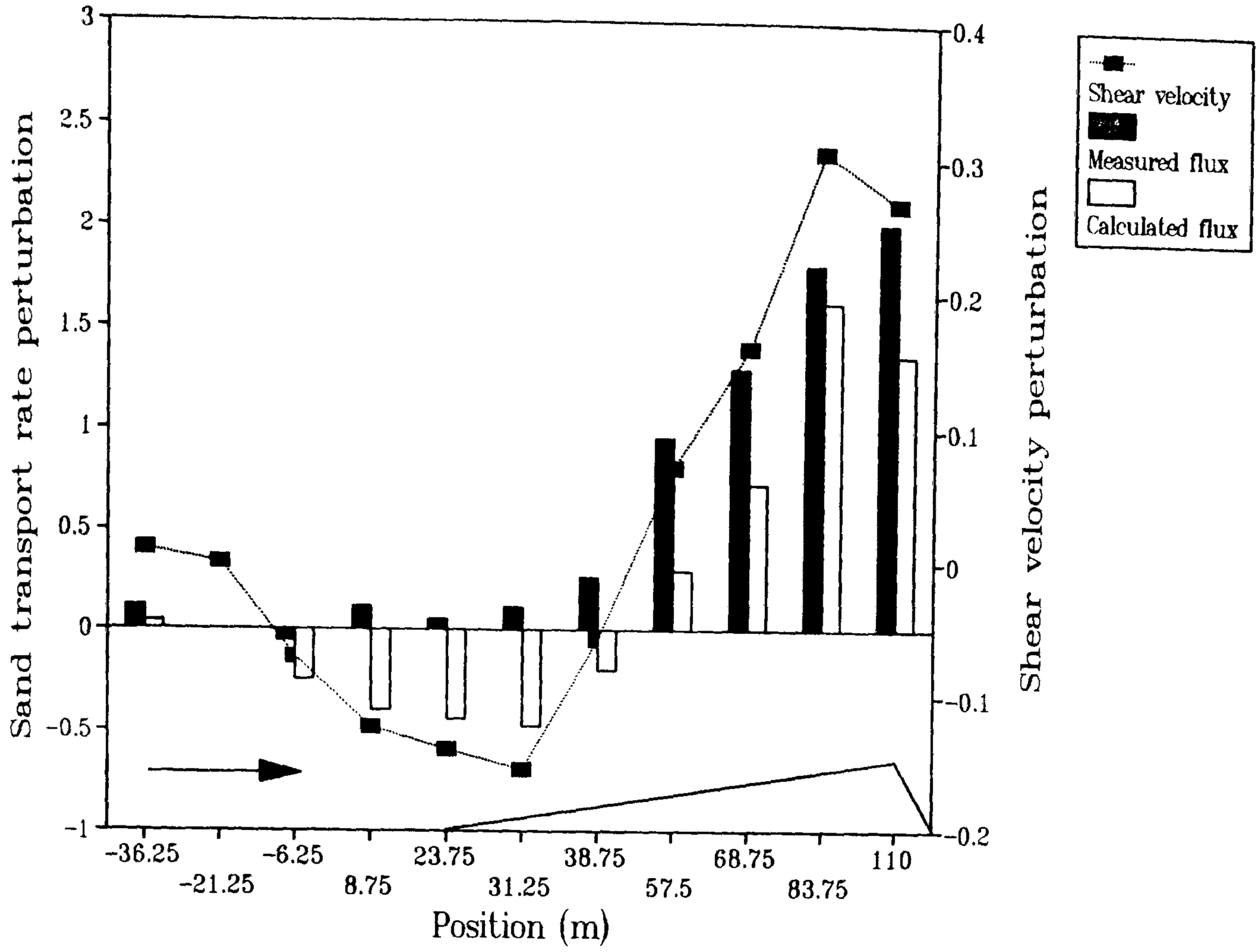

Figure 7.7 Observed and field-predicted sand transport rate perturbations on the centre-line of the dune (run 1).

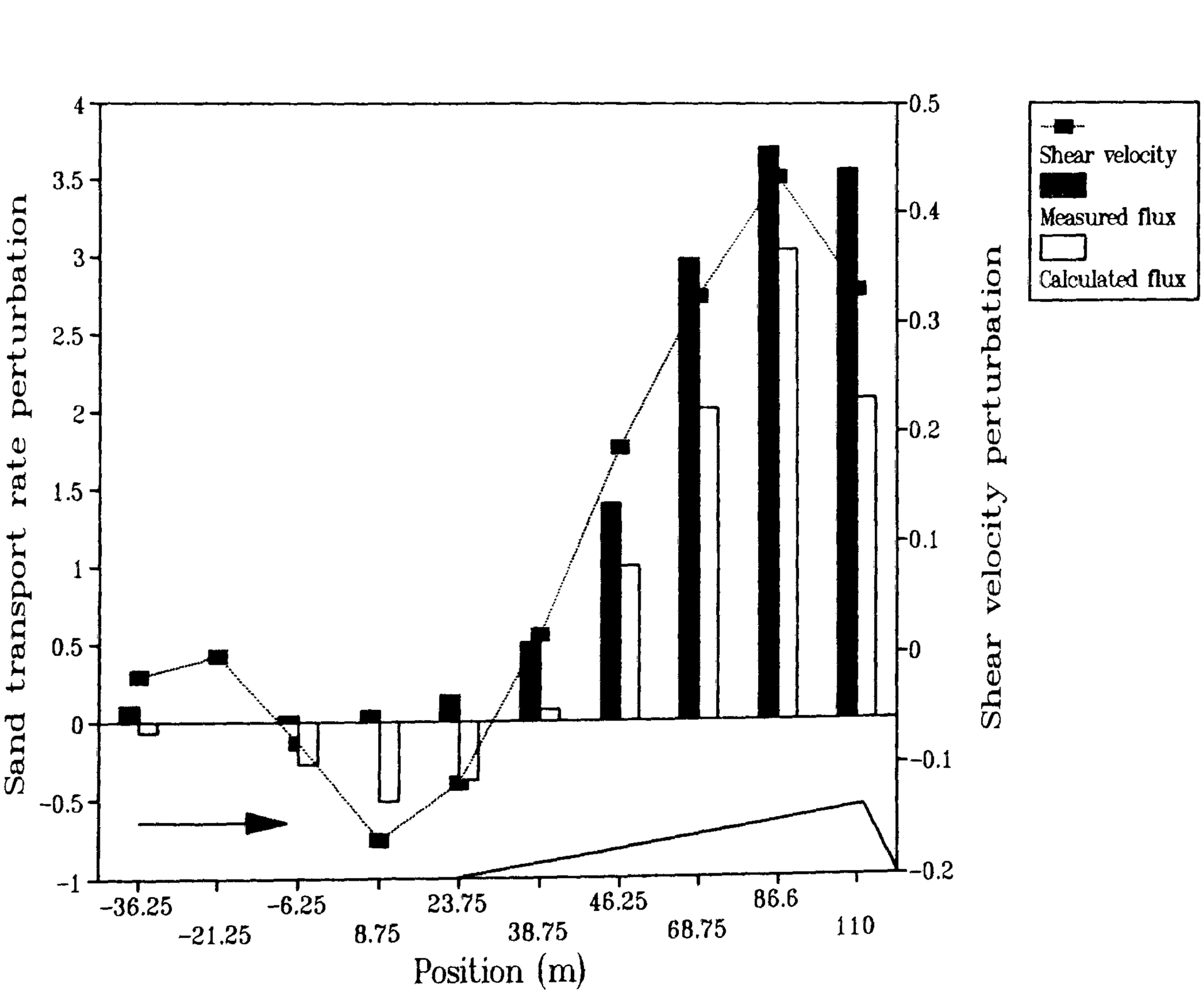

Figure 7.8 Observed and field-predicted sand transport rate perturbations on the centre-line of the dune (run 2).

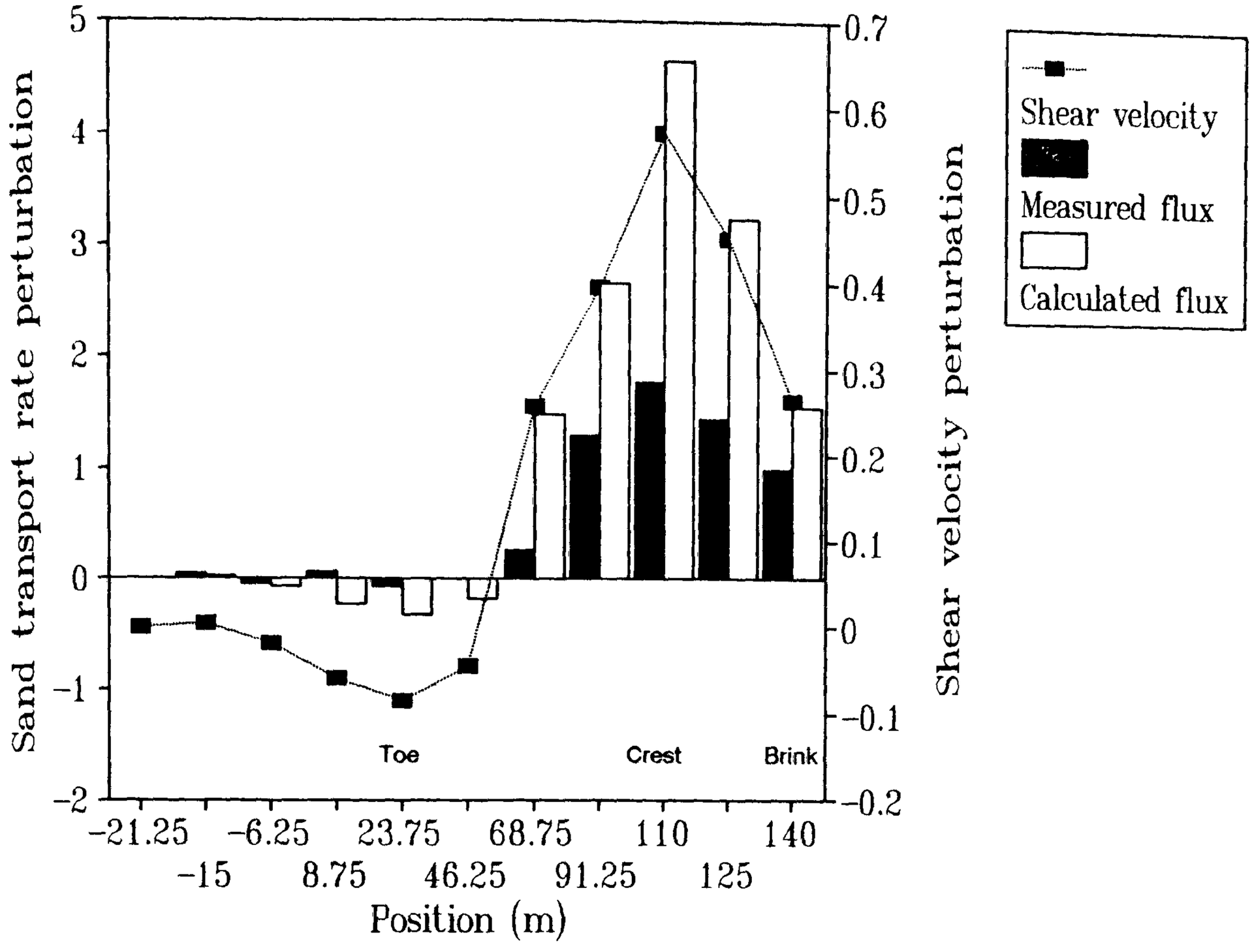

Figure 7.9 Observed and field-predicted sand transport rate perturbations on the left flank of the dune (run 1).

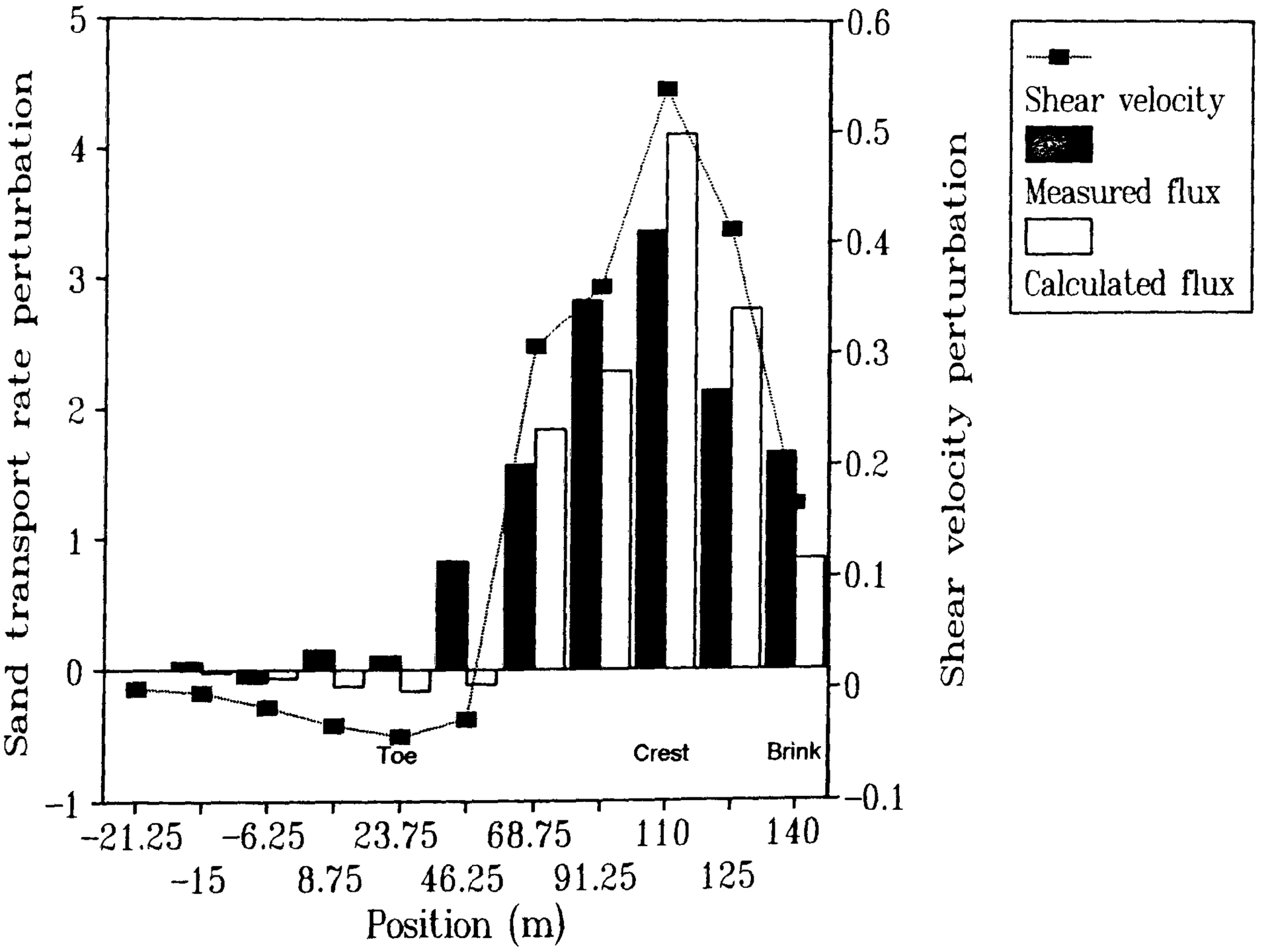

Figure 7.10 Observed and field-predicted sand transport rate perturbations on the left flank of the dune (run 2).

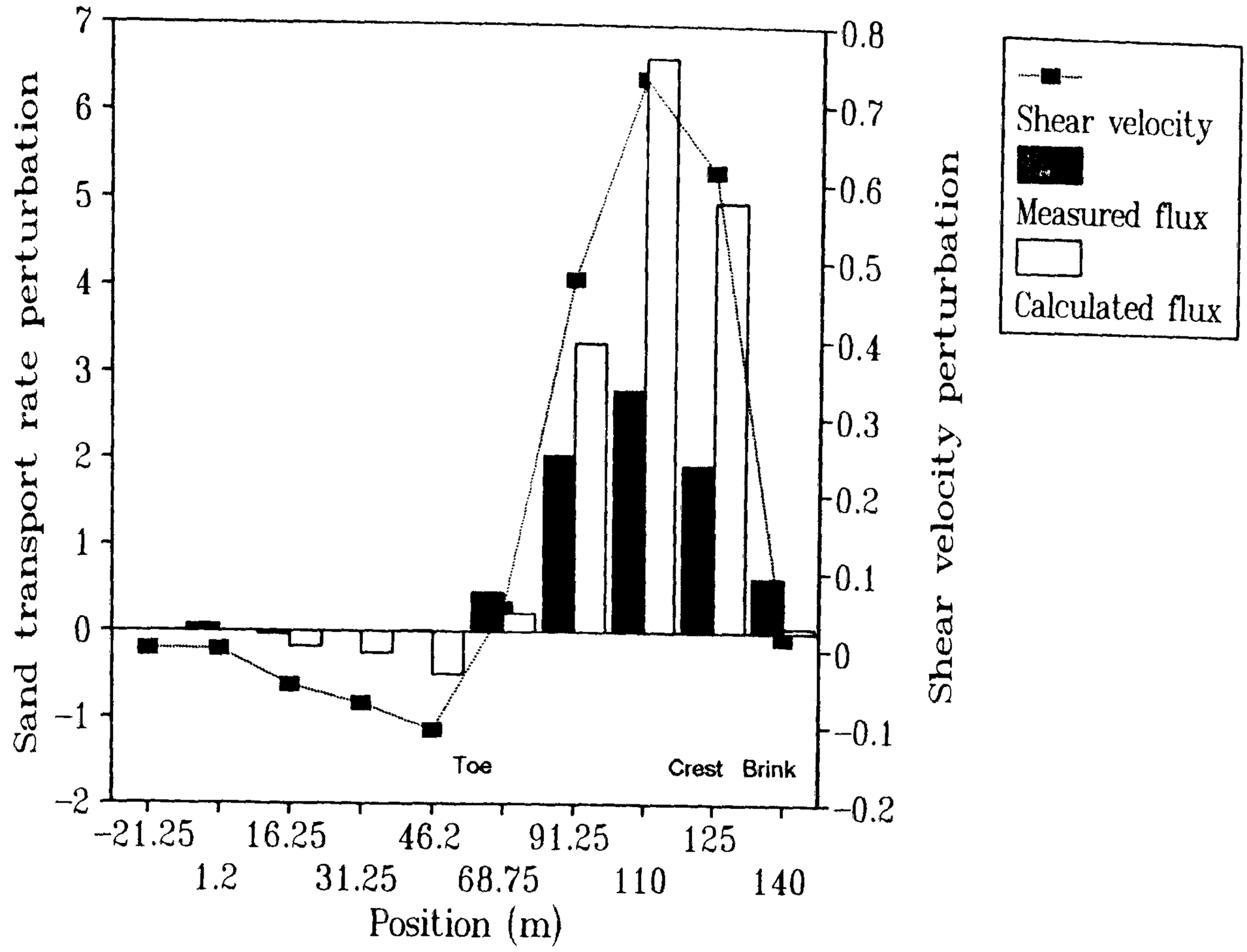

Figure 7.11 Observed and field-predicted sand transport rate perturbations on the right flank of the dune (run 1).

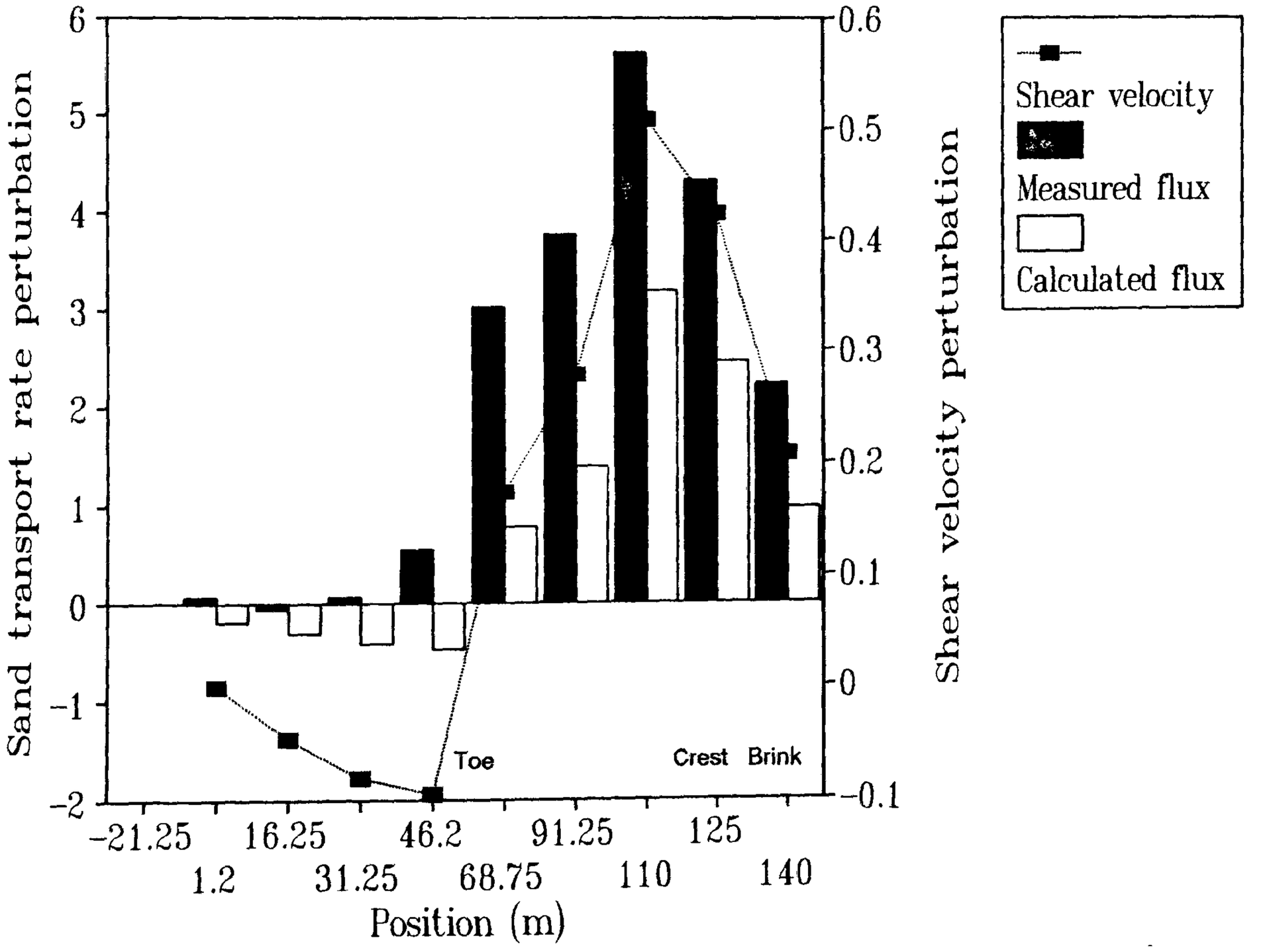

Figure 7.12 Observed and field-predicted sand transport rate perturbations on the right flank of the dune (run 2).

7.11 and 7.12). However, it should be noted that the 'shapes' of the measured and calculated flux perturbations on the windward slope of the dune are very similar. On the centre-line both the measured and calculated perturbations reach maxima in the crestal region. On both flanks the maximum perturbations are always found at the crest, with a reduction in transport rate (both calculated and measured) toward the brink.

Comparisons between predicted sand transport rates and those measured in the field have shown only moderate agreement (Rasmussen & Mikkelsen, 1988; Pye & Tsoar, 1990; McEwen, 1991). Berg (1983) calculated rates an order of magnitude higher than measured rates. The reasons for these discrepancies have been examined by Pye & Tsoar (1990). They noted that one of the major problems is accurately measuring sand transport rate in the field, although McEwen (1991) states that the problem is caused by the fact that the sand transport rate formulae were developed in uniform wind tunnel conditions, with extrapolation of the relationships to the field being unpredictable.

One reason for the less discernible relationship between measured and calculated flux on the windward slope and in the crest region in the present study may be the reduction of sand trap efficiency on the sandy surface of the dune. In Chapter 2 the efficiency of the sand trap used in this study was estimated at about 50%. However, this value is likely to vary across the dune as the conditions into which the traps are placed vary. For example, upwind of the dune on the hard gravel surface the efficiency of air capture is likely to be similar to the value found in the wind tunnel because the surface conditions in the two environments are fairly similar. However, at the crest of the dune where there is a great deal of sand moving and the bed onto which the trap is placed is soft, the efficiency of the trap is likely to be reduced. In this high sand transport and high wind velocity environment there is a probability of increased turbulence around the base of the trap resulting in expanded scouring of the sand surface. This effect might be combined with increased back-pressure caused by rapid filling of the trap due to the high transport conditions. Both of these effects would result in a decreased efficiency. Therefore, care should be taken in the interpretation of sand trap results where comparisons are being made between sand traps placed in differing environments.

The presence of turbulent gusts may also help to explain irregularities such as those described above. The measurements presented in Figures 7.7 to 7.12 are averages of measured and predicted transport rate taken over a period of several minutes. Hence, they do not take account of short-period turbulent bursts which may, for instance, permit sand transport to occur even if the average u_* is below the threshold for entrainment. The importance of turbulence in sand

transport rate modelling has been stressed by McEwen (1991) and Butterfield (1991). Lee (1987) found that the prediction of sand transport rate was not improved by taking variations in wind gustiness into account, although he defined "short-term" as being of the order of 0.5 seconds whereas Butterfield (1991) considered it to be of the order of 0.1 seconds. However, Butterfield (1991) also found no unequivocal relationship between q and u_* with short-period measurements, although logical argument suggests that there should be.

It seems likely that the relationship between measured and predicted sand transport rate in this study could be improved with the employment of traps with a more efficient design and possibly by taking the effects of turbulent gusts into account. Alternatively, the correlation might be enhanced by using a different method of u_* derivation. In Chapter 6 differences in the assessment of u_* over the dune were noted between the three techniques of study (field, wind tunnel and mathematical modelling). In the next section the differences in the ability of the three techniques adequately to predict measured sand transport rates (described above) and dune surface change are discussed.

7.4 Predicted Sand Transport Rates: comparisons between the techniques

By applying Equation 7.3 to the u_* perturbations produced by each technique (described in Chapter 6) sand transport rate perturbations were calculated. Because the same equation was used for each of the three techniques to calculate sand transport rate, the results shown in this section are only a slight extension on those in Chapter 6, where u_* comparisons were discussed. The results presented for the wind tunnel on the centre-line are those derived from the pulse-wire probe. However, on the flanks, where only a few measurements using this technique were carried out, the results presented are derived from the high extrapolation of u_* gained from the cross-wire probe measurements (see Chapter 4.2.2 and 6.5).

The Centre-line

Figure 7.13 shows the sand transport rate (q) perturbations calculated along the centre-line for each of the techniques. The scale of the graph makes comparisons difficult between the techniques upwind and on the windward slope of the dune. It is clear, however, that all of the techniques show a progressive increase in sand transport rate from near the toe region toward a maximum around the crest. The most striking aspect of Figure 7.13 is the large peak in sand transport rate perturbation at the crest predicted by FLOWSTAR. The inability of the

FLOWSTAR program to model highly turbulent reverse flow resulted in a peak in u_* perturbation at the crest of 1.15 (Chapter 6). This, in turn, has caused a peak in sand transport rate perturbation of 15 (1500% more sand in transport than at the upwind reference site). For comparison, the wind tunnel and field sand transport rate perturbations reach maxima in the crestal region of only 3.0 and 5.0 respectively.

Figure 7.14 ignores the extreme FLOWSTAR prediction of sand transport rate at the crest and hence shows the same data as Figure 7.13 but at a larger scale. Also included in Figure 7.14 are the field measurements of actual sand transport (run 1 and run 2) described in Chapter 7.3. A comparison between the predicted and observed transport rate perturbations is not strictly appropriate in this case because the measurement periods were quite different. The wind tunnel and FLOWSTAR predictions were based on 'average' conditions established from several hours of field measurement and the field-predicted sand transport rates were derived from measurements over a one hour period. This is in contrast to the sand trap measurements which were of only several minutes duration. Nevertheless, it is useful to plot the data collectively as it allows general discussion concerning the differences between the two sets of measurements.

From Figure 7.14 it can be seen that upwind of and at the toe of the centre-line (between x = -20 m and +45 m) both the field- and FLOWSTAR-predicted q perturbations become negative (signifying less sand in transport than at the reference site). The field data suggest a progressive reduction in q to a minimum at the toe of less than 50% of the reference site value. Downwind of the toe, the field-predicted q increases toward a maximum at the crest (where the perturbation is +5). The FLOWSTAR-predicted transport rate shows significant negative perturbations only downwind of the toe. The FLOWSTAR minimum occurs at x = +35 m (12 m downwind of the toe) and is of a similar magnitude (at -0.6) to the field-predicted minimum. Downwind of x = +45 m the FLOWSTAR-predicted q increases along the windward slope to an (excessive) maximum at the crest (discussed above). The negative perturbations in sand transport rate upwind of and at the toe of the dune predicted from the field and FLOWSTAR techniques are in contrast to the wind tunnel-predicted perturbations. The wind tunnel q perturbations demonstrate no significant perturbations upwind of the dune centre-line. Downwind of x = +30 m the wind tunnel data show an increasing positive perturbation toward a maximum just upwind of the crest.

The lack of a reduction in sand transport rate upwind of the toe of the dune demonstrated by the wind tunnel data, is consistent with the measured sand transport in the field (as shown in Figure

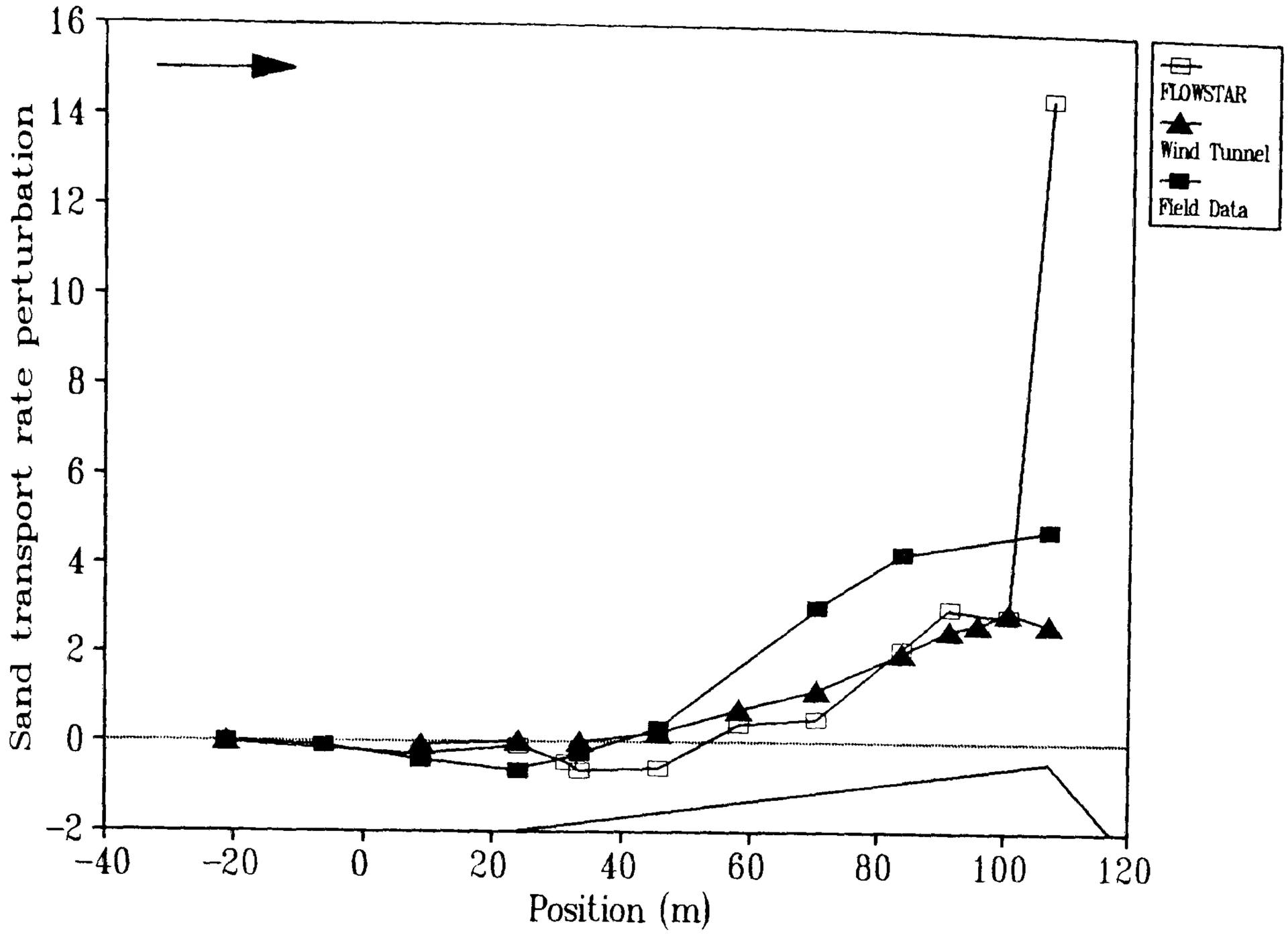

Figure 7.13 Comparison between the sand transport rate predicted by each of the techniques on the centre-line of the dune.

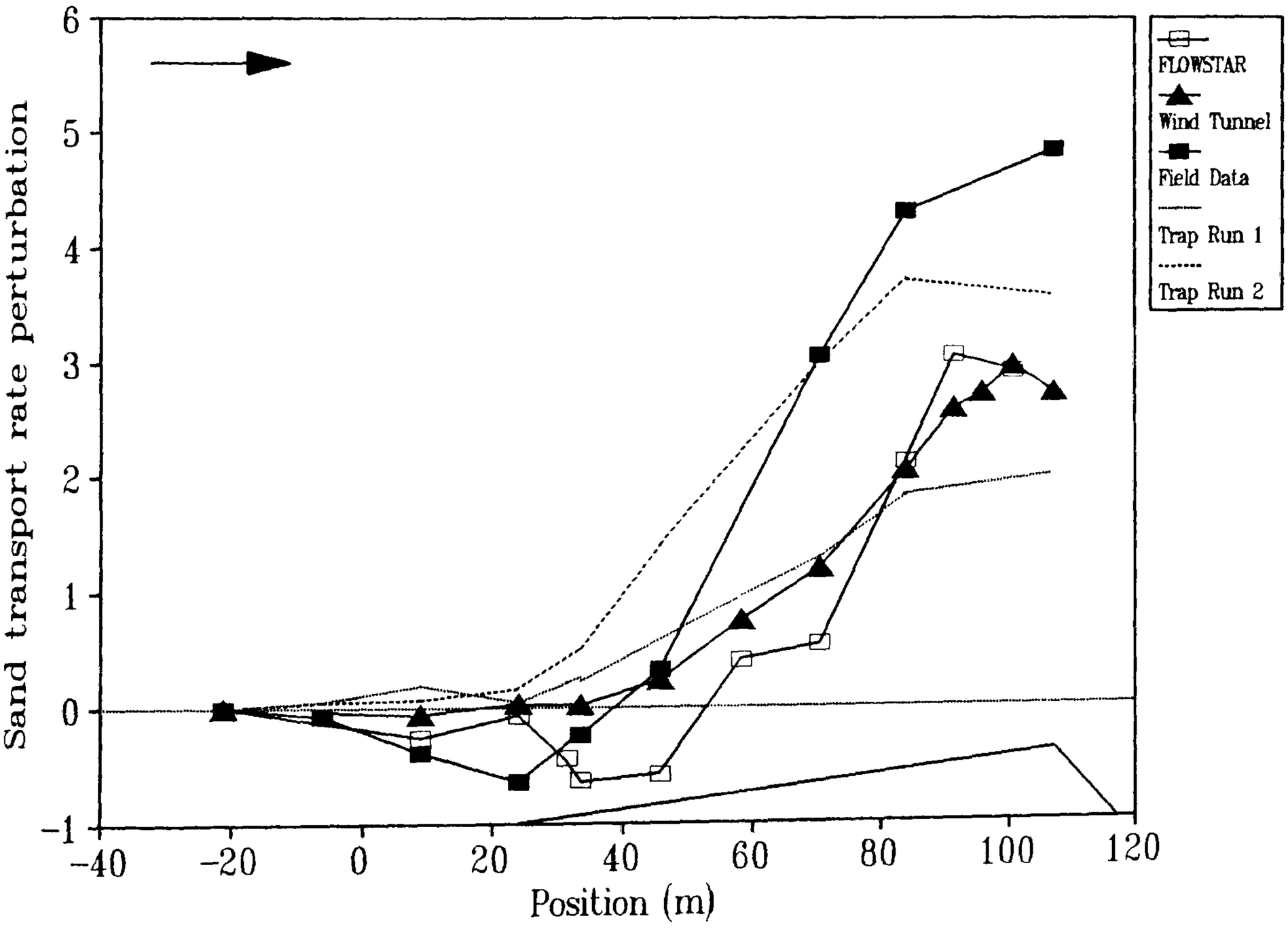

Figure 7.14 Comparison between the sand transport rate predicted by each of the techniques on the centre-line of the dune (excluding FLOWSTAR prediction at the brink).

7.14) which displays no significant perturbation upwind of the dune. On the windward slope and in the crestal region the wind tunnel and FLOWSTAR q perturbations are fairly similar (excepting the FLOWSTAR prediction at the crest itself). In the crestal region both of these techniques display a perturbation of about 3.0. This is in contrast to the field-predicted perturbations which are larger than either the wind tunnel or FLOWSTAR results along the whole of the windward slope (downwind of x = +45 m) and reach a maximum at the crest of 5.0. Notwithstanding the additional errors associated with the observed transport rate perturbations on the windward slope (discussed in Chapter 7.3) it can be seen from Figure 7.14 that all three techniques (wind tunnel, field and mathematical model) display a similar trend to the observed rates, except at the toe.

The Flanks

Similar relationships to those described above for the centre-line are repeated on the flanks. Figures 7.15 and 7.16 show the calculated q perturbations for the three techniques along the left and right flanks respectively. The FLOWSTAR predictions on the left flank (Figure 7.15) display negative q perturbations upwind and in the toe region reaching a minimum of -0.5 more than 20 m downwind of the toe (at x = 42 m). The field predictions in this region do not show such large negative perturbations, although they still reach -0.2 at the toe itself. Both the field- and FLOWSTAR-predicted perturbations show downwind increases to positive values reaching maxima in the crestal region of 2.0 and 1.7 respectively (although the FLOWSTAR maximum is in fact 15 m upwind of the crest itself). Downwind of the crest both the field and FLOWSTAR techniques display decreasing sand transport rate perturbations toward the brink (excepting the FLOWSTAR prediction at the brink itself). The wind tunnel results shown in Figure 7.15 display no significant reduction in q upwind of the toe of the left flank. Just downwind of the toe (at x = +40 m) the wind tunnel perturbations show a positive rise toward a maximum near the crest of +1.0. The perturbations are reduced downwind of the crest toward the brink. As on the centre-line, the calculated wind tunnel q perturbations upwind of the left flank describe the measured q perturbations better than the field- or FLOWSTAR-predictions. Also, downwind of x = 65 m (half-way up the windward slope) the wind tunnel perturbations display less of a perturbation than the other two techniques.

The q perturbations on the right flank (Figure 7.16) reflect those on the left flank (Figure 7.15) almost exactly. Both the field- and FLOWSTAR-predictions show negative perturbations upwind of and at the toe whilst the wind tunnel perturbations maintain their upwind level. The field predicted data show a perturbation at the toe of -0.25 before rising downwind toward a crestal

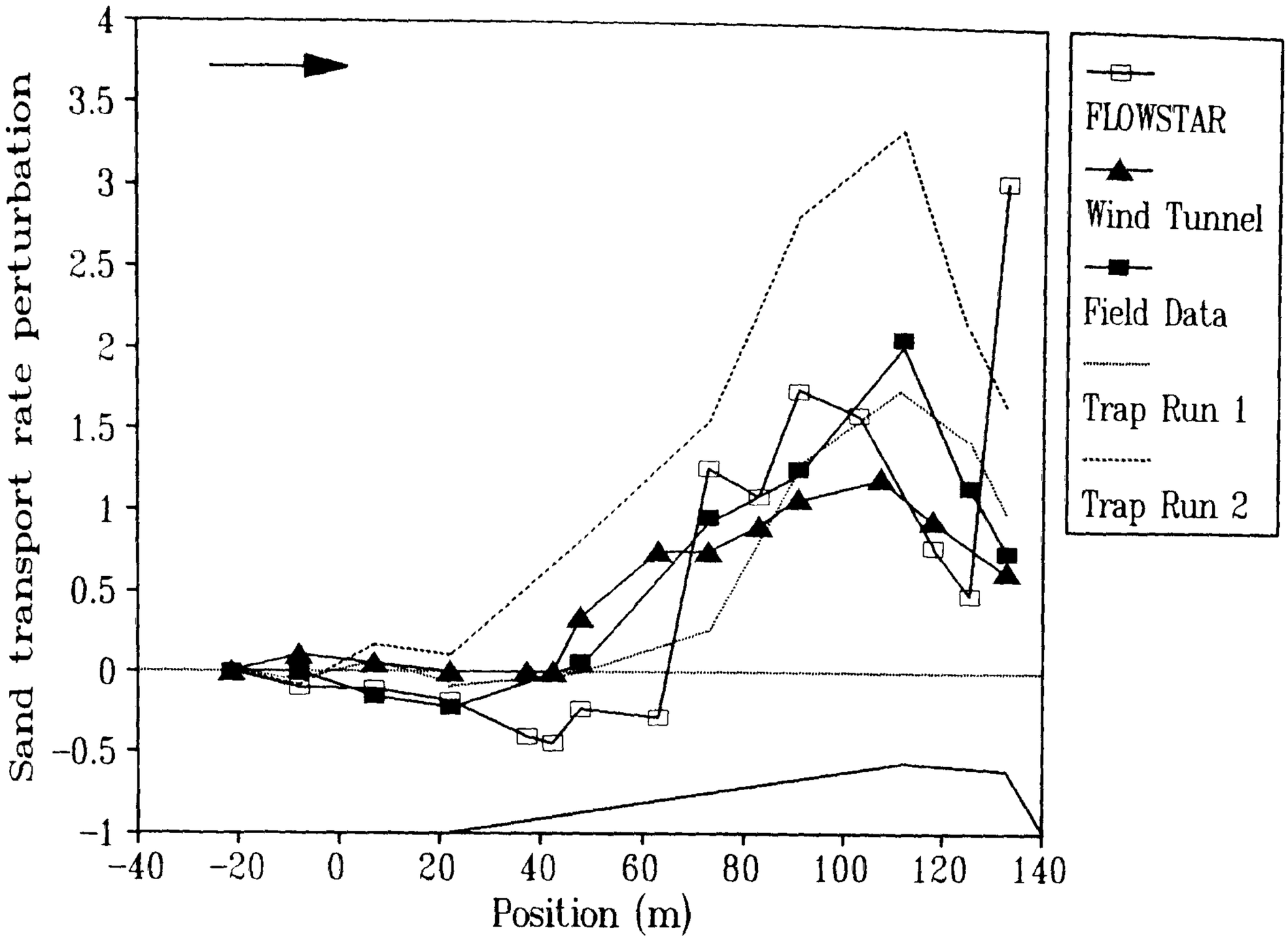

Figure 7.15 Comparison between the sand transport rate predicted by each of the techniques on the left flank of the dune.

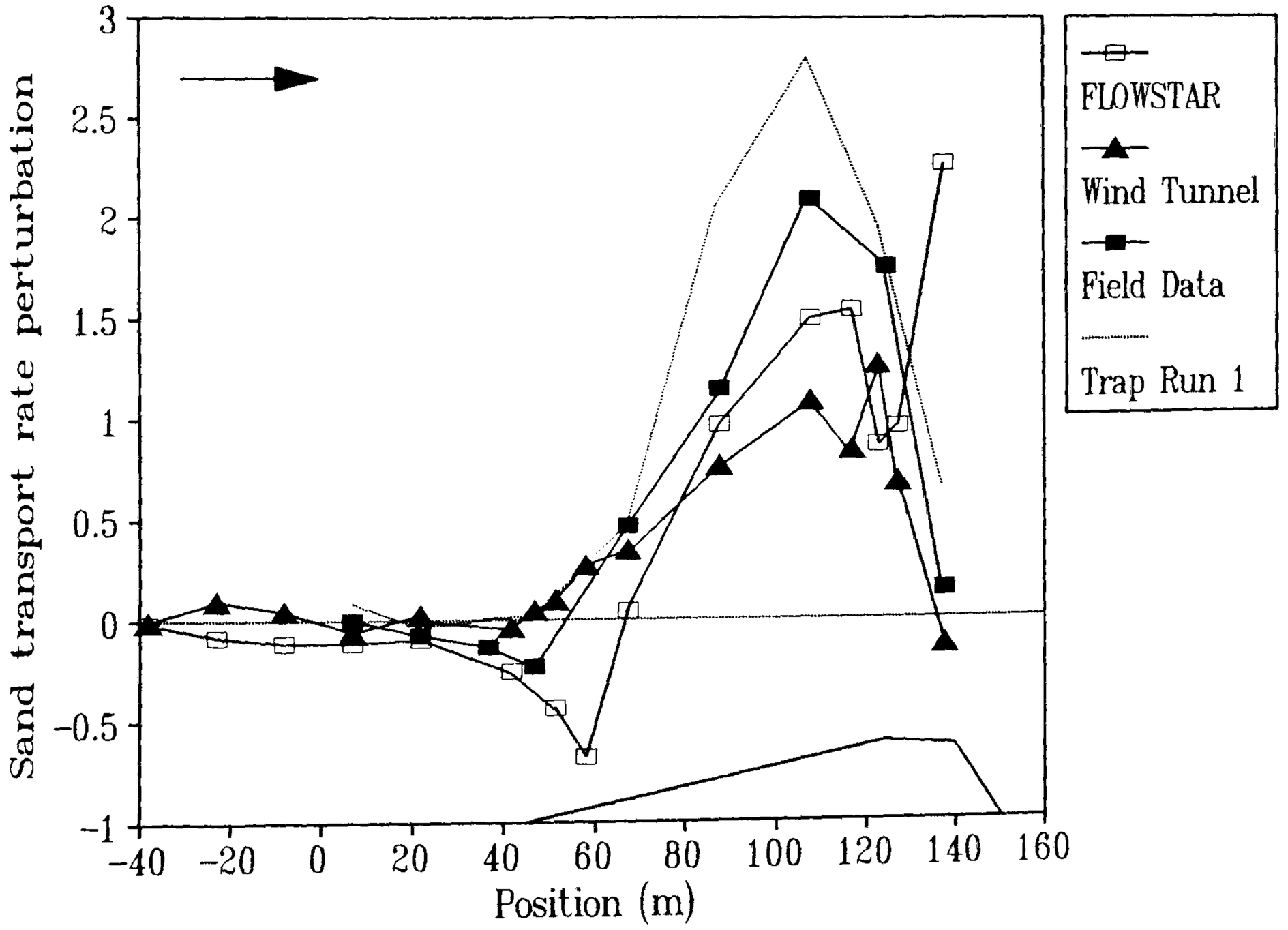

Figure 7.16 Comparison between the sand transport rate predicted by each of the techniques on the right flank of the dune.

maximum of 2.0. The FLOWSTAR predictions attain a perturbation of -0.7 at x = 55 m (15 m downwind of the toe) before they too rise to a maximum at the crest of 1.6. As on the left flank, the wind tunnel perturbations on the right flank are lower than the field and FLOWSTAR perturbations from half-way up the windward slope (downwind of x = 70 m). The maximum wind tunnel perturbation at the crest is also lower at 1.3. Between the crest and brink each of the three techniques displays a reduced sand transport rate (excepting the FLOWSTAR prediction at the brink itself) and the wind tunnel q perturbation actually becomes negative at the brink.

Conclusion

From Figures 7.14 to 7.16 some general trends in the prediction of sand transport rate by each of the three techniques can be identified. On the windward slope and in the crest regions the predicted transport rate perturbations gained from each of the techniques reflect the observed (measured) sand transport rate. The trend is an increase in q on the windward slope of the dune compared with upwind levels leading to a maximum around the crest and, where appropriate, a reduction in transport between the crest and brink. At the brink, however, the over-prediction of u_* by FLOWSTAR results in a substantial over-prediction of q. Unlike the observed transport rates (which were measured over a period of only a few minutes) the 'average' conditions represented by the wind tunnel, FLOWSTAR and extended field measurements reveal larger extremes of q perturbation on the centre-line than on the flanks. It is also noted that the perturbations predicted by the wind tunnel downwind of the mid-windward slope are smaller than those predicted by the other two techniques.

An important difference between the observed and predicted rates of sand transport seems to occur upwind of and at the toe. The field wind data and FLOWSTAR both predict a reduction in sand transport in this region (by more than 50% on the centre-line). This is in contrast to the wind tunnel which predicts a maintenance of upwind sand transport rates, a state more consistent with the measured values. Sand transport equations tend to provide over-estimates of the maximum rate of transport in given wind and topographical conditions (Pye & Tsoar, 1990). However, in this case they appear to be under-estimating the actual amount of sand transport and inaccurately predicting the trend in sand transport rate development at and around the toe of the dune. Considering that the pattern of erosion and deposition on the dune is governed by the relative rates of sand transport on the windward slope this difference may have important implications for the dynamics of the dune.

7.5 Surface Change: comparisons between observed and predicted rates

In order to find how well each of the techniques predicted the observed change in dune form (examined in Chapter 2) it was first necessary to convert the predicted sand transport rate perturbations into a form comparable with the erosion pin measurements. It is quite simple to convert the transport rate perturbations into rates of erosion ($\delta h/\delta t$), but the question remains as to the time period over which the predicted rates should be compared to the actual rates.

The erosion pins were measured every 24 hours over the three-day period that the field wind data were collected. Wind velocity measurements were also recorded over a continuous 24 hour period within this measurement interval so a 'typical' daily wind regime was known. A sensible period over which to compare the observed and predicted erosion would therefore seem to be 24 hours. However, the accuracy of measurement of the erosion pins was, at best, only ±2.5 mm. With a maximum recorded daily erosion amount of 40 mm this involves a considerable margin of error. Of more importance than predicting the actual erosion on the dune is the identification of zones of erosion and deposition. It was considered that this could be achieved more accurately by comparing the predicted erosion with that observed over a 28 day period. The relationships between the daily and monthly (28 day) surface change as measured with the erosion pins on the three section lines are shown in Figures 7.17 to 7.19. From these Figures it can be seen that an 'average' assessment of the location of zones of erosion and deposition is more easily gained from the monthly aggregate of measurements than from the daily sequences. This is a result of a lower margin-of-error in the measurement technique and hence a more accurate interpolation of the actual surface change.

7.5.1 Methods of Calculation

The relationship between the erosion and deposition pattern on the dune and the sand transport rate can be described by:

$$\frac{\delta h}{\delta t} = \frac{1}{\gamma}\left(\frac{q}{l}\frac{\delta l}{\delta x} + \frac{\delta q}{\delta x}\right)$$

where:

$\delta h/\delta t$ = change in height over time

γ = bulk density of sand (2.65)

q = sand transport rate (per unit time per unit width)

l = distance between streamlines

x = distance

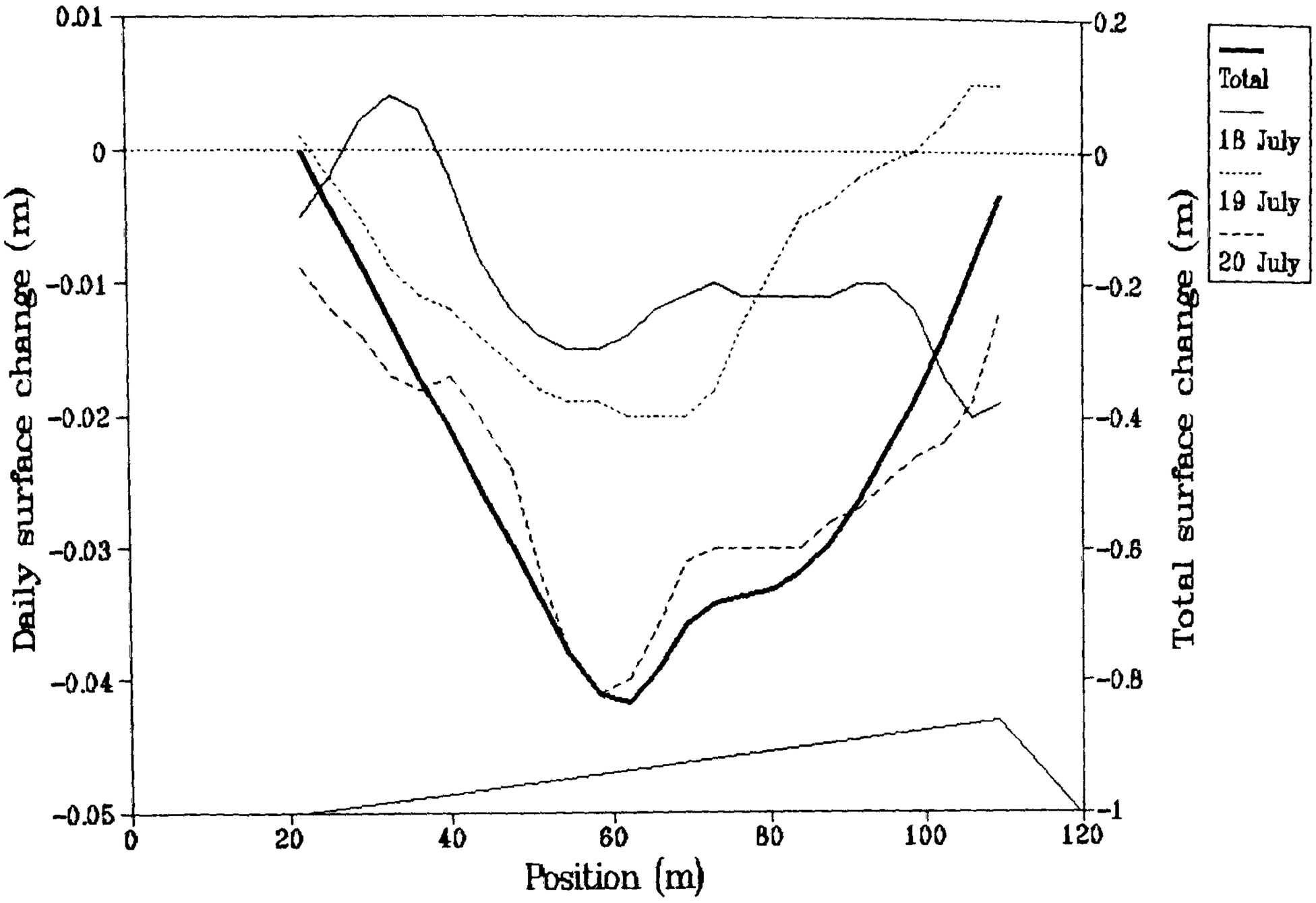

Figure 7.17 Comparison between daily measured surface change and the total (28-day) surface change on the centre-line of the dune.

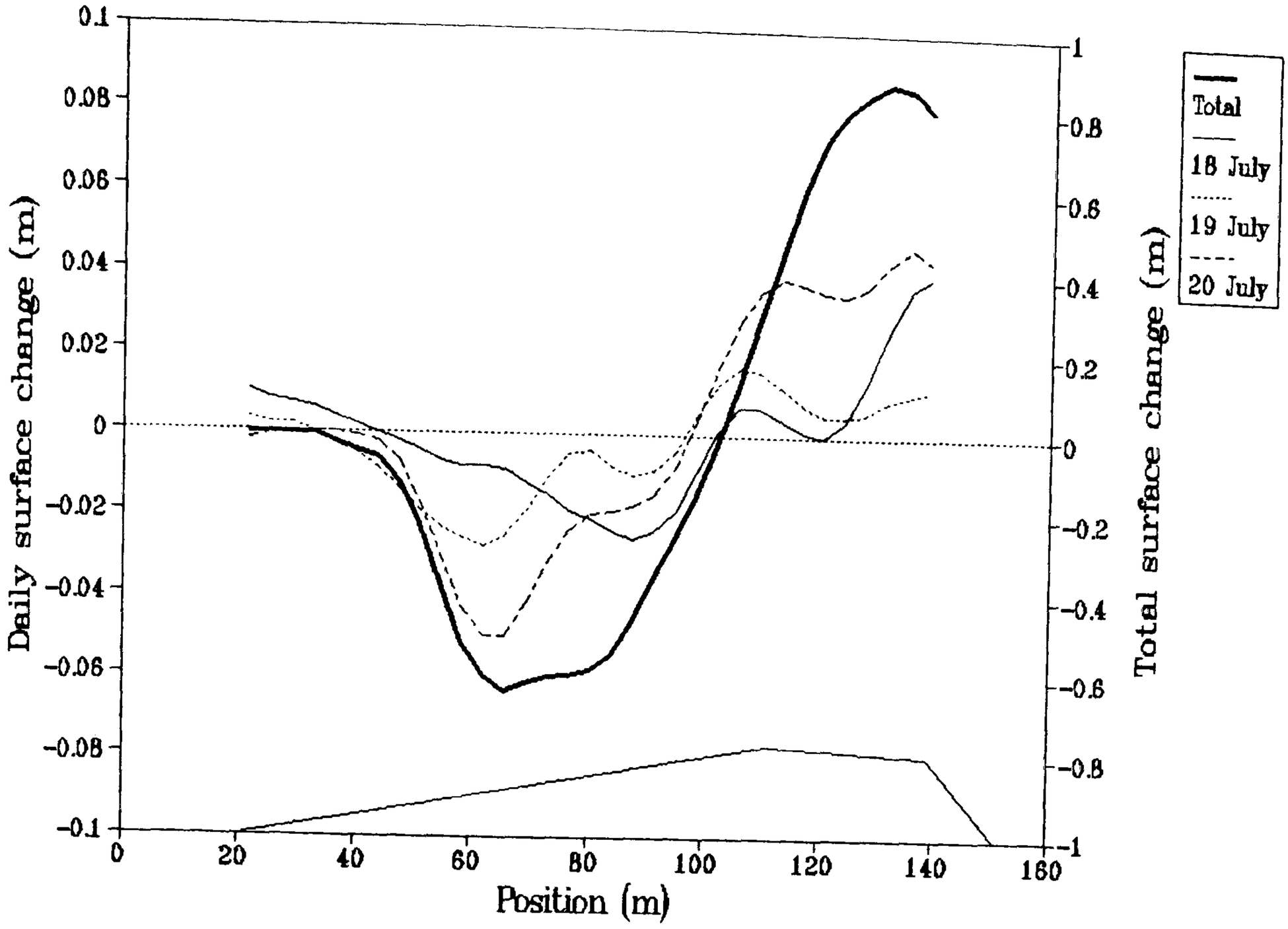

Figure 7.18 Comparison between daily measured surface change and the total (28-day) surface change on the left flank of the dune.

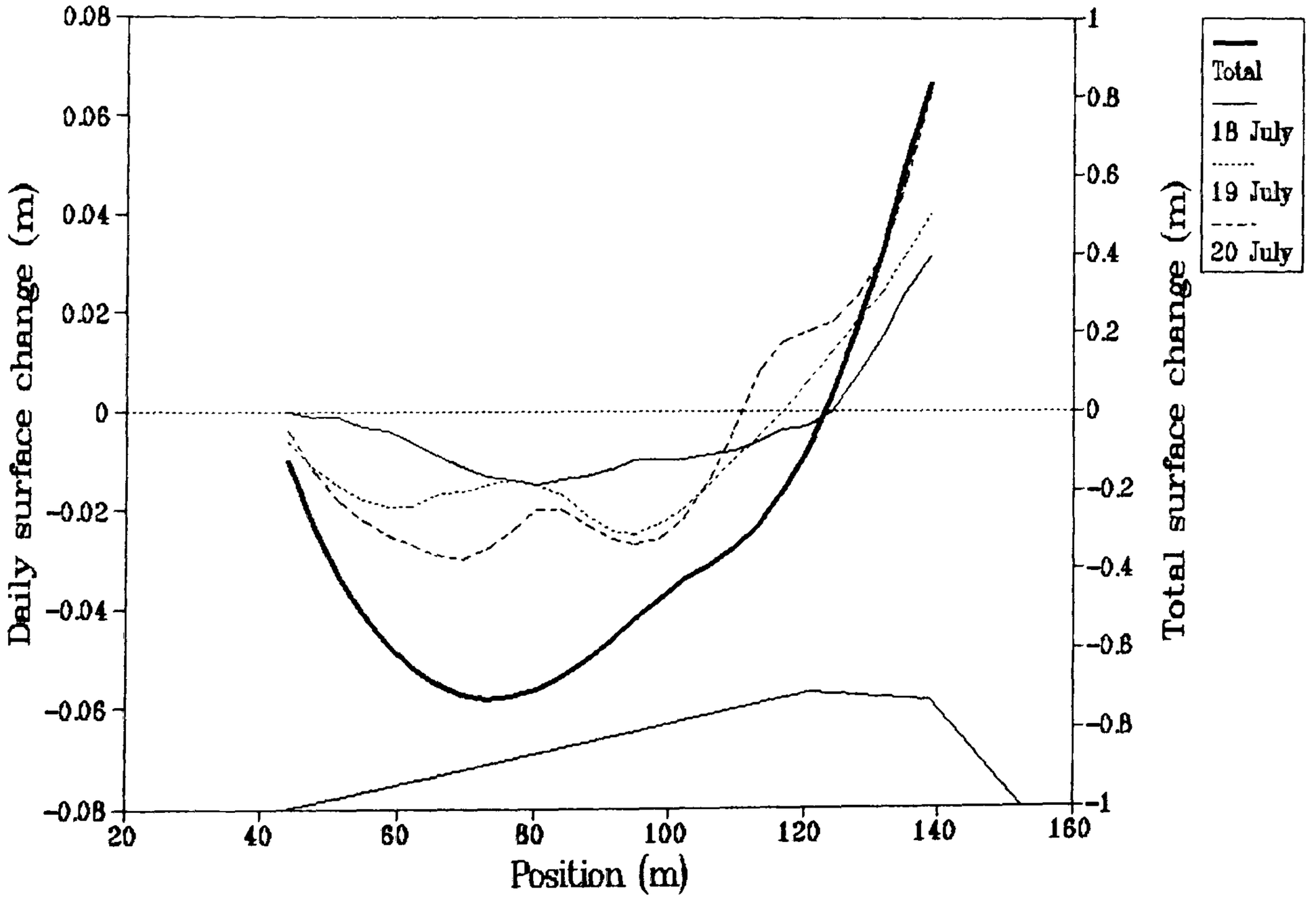

Figure 7.19 Comparison between daily measured surface change and the total (28-day) surface change on the right flank of the dune.

This was the relationship used by Howard *et al.* (1977). It takes into account not only the downwind change in transport rate ($\delta q/\delta x$) but also the divergence of streamlines in its calculation of rate of surface change. However, in the present study no account was made of streamline divergence because no significant alteration in the direction of airflow around the dune was found (Chapters 2.4, 3.4 and 4.3). Also, Howard *et al.* (1977) found that shear velocity was much more important in determining erosion and deposition than was the direction of transport. The change in surface elevation due to the downwind modification of sand transport rates predicted by each of the techniques was therefore determined from Equation 7.7, the sediment continuity equation (Rubin & Hunter, 1982):

$$\delta h/\delta t = -\delta Q/\delta x \qquad (7.7)$$

where:

h = surface elevation
t = time
Q = local volumetric transport rate ($1/\gamma[\delta q/\delta x]$) where γ is the bulk density of sand and q is the local sand transport rate.
x = distance

This equation has also been used by Lancaster (1985, 1987) to predict patterns of surface change on sand dunes.

The sand transport rate perturbations predicted from the field data, wind tunnel and mathematical model (discussed above) were converted into actual transport rates by assuming a mean upwind rate (15 $gm^{-1}s^{-1}$) which was consistent with the mean value of u_* measured in Chapter 2. This gave an average sand transport rate over the dune for each of the techniques in $gm^{-1}s^{-1}$. These values were converted to a volumetric measure by multiplying by $1/\gamma$, where γ is the bulk density of the sand. Howard *et al.* (1977) took γ to be 2.65, the density of quartz. This assumption ignores the compaction of dune sands, and by assuming 100% perfect packing is likely to underestimate erosion and deposition. An investigation of the bulk density of the deposited sands in this study revealed an average value of 1.69 which was the figure used in all subsequent calculations.

The application of Equation 7.7 to the calculated sand transport rates determines the rate of change of height between each measurement point over a period of one second. In order to compare this to the actual erosion and deposition pattern over a 28 day period the $\delta h/\delta t$ for each second was multiplied by the amount of time that sand was moving during a 24 hour period (determined from upwind shear velocity measurements) and then multiplied by 28.

In order to take into account the variation in wind velocity it was assumed (after Bagnold, 1956) that:

$$q \sim (u_* - u_{*_t})^3$$

where:

u_*= upwind shear velocity (evaluated at a height of 0.35 m from Equation 6.3)

u_{*_t}= threshold shear velocity for grain movement (u_{*_t} as defined in Equation 7.3 = 0.18 ms^{-1})

This method of calculating the erosion rate evident from the three techniques over a 28 day period entails making several assumptions and manifest errors. It was assumed that the wind conditions evident over a 24 hour period were repeated for the following 27 days. The fact that sand can be in transport on the upper windward slopes of the dune despite low upwind windspeeds was also ignored. However, it was considered that this calculation procedure provided results which at least identified the major zones of erosion and deposition evident from each technique and hence allowed an assessment of the ability of each of the techniques to predict the observed change in dune form.

In addition to a visual comparison of the measured and observed erosion rates (achieved by graphing the results), the degree of agreement between the two was quantified using the following statistical measures:

1. Difference of Means Test (Norcliffe, 1982)

The standard deviation of the sampling distribution of the means is estimated from;

$$\sigma_{x1-x2} = \sqrt{(\sigma_1^2/N_1)+(\sigma_2^2/N_2)}$$

This is then used to find whether the two means of the distributions are significantly different by comparing it to the *t* distribution;

$$t = X_1 - X_2/\sigma_{x1-x2}$$

Where $t<t_{crit}$ the null hypothesis (H_o = the mean erosion and deposition do not differ between the measured and calculated samples) is accepted.

2. Analysis of Variance (Howard *et al.* 1977)

The degree of variation between the calculated (c_i) and measured rates (m_i), corrected for bias, is given by the variance of the differences (v):

$$v = E(c_i - m_i - b)^2/(N-1)$$

where the bias (*b*) is given by:

$$b = E(c_i - m_i)/N$$

A small variance reflects a good agreement between observed and predicted values.

3. Regression Analysis

Regression analysis between observed and predicted surface change allowed a comparison of x-coefficients, constants and correlation coefficients (Pearson's r) between each of the techniques. A perfect prediction of observed surface change is given where the constant is zero, the x-coefficient is 1.0 and the correlation coefficient is 1.0. As it is the identification of zones of erosion and deposition which is of interest, the value of the constant is of less importance than the correlation and x-coefficients.

7.5.2 Results and Analysis

The Centre-line

Comparisons between the predicted surface change on the centre-line of the dune evident from the different techniques of study and the measured surface change over a 28 day period are shown in Figures 7.20 to 7.25.

On the windward slope of the centre-line the surface change predicted from the field u_* assessments generally reflects the measured surface change (Figure 7.20). The point of maximum erosion (at x = 60 m) is accurately predicted and the rates of surface change both upwind and downwind of this position are satisfactorily estimated. However, the reduction in sand transport rate upwind of the toe of the dune has resulted in the prediction of a zone of deposition. No deposition in the toe region of the dune was measured in the field. If the field-predicted surface change accurately reflected the actual dynamics of the dune, then in the 28 day measurement period the dune would have grown more than 60 m in an upwind direction to a maximum depth of 0.35 m. This was not observed.

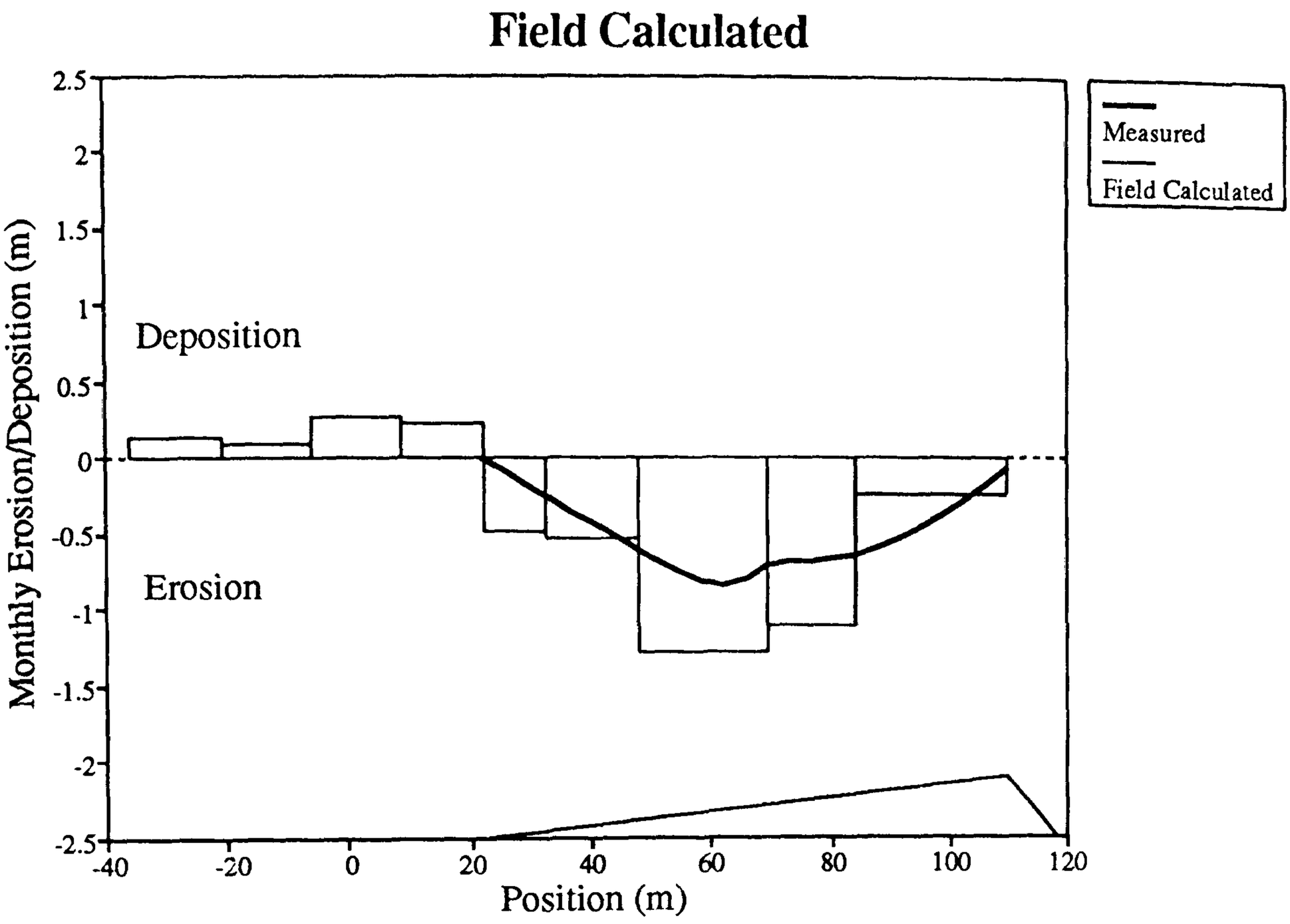

Figure 7.20 Comparison between measured and field-calculated surface change on the centre-line of the dune.

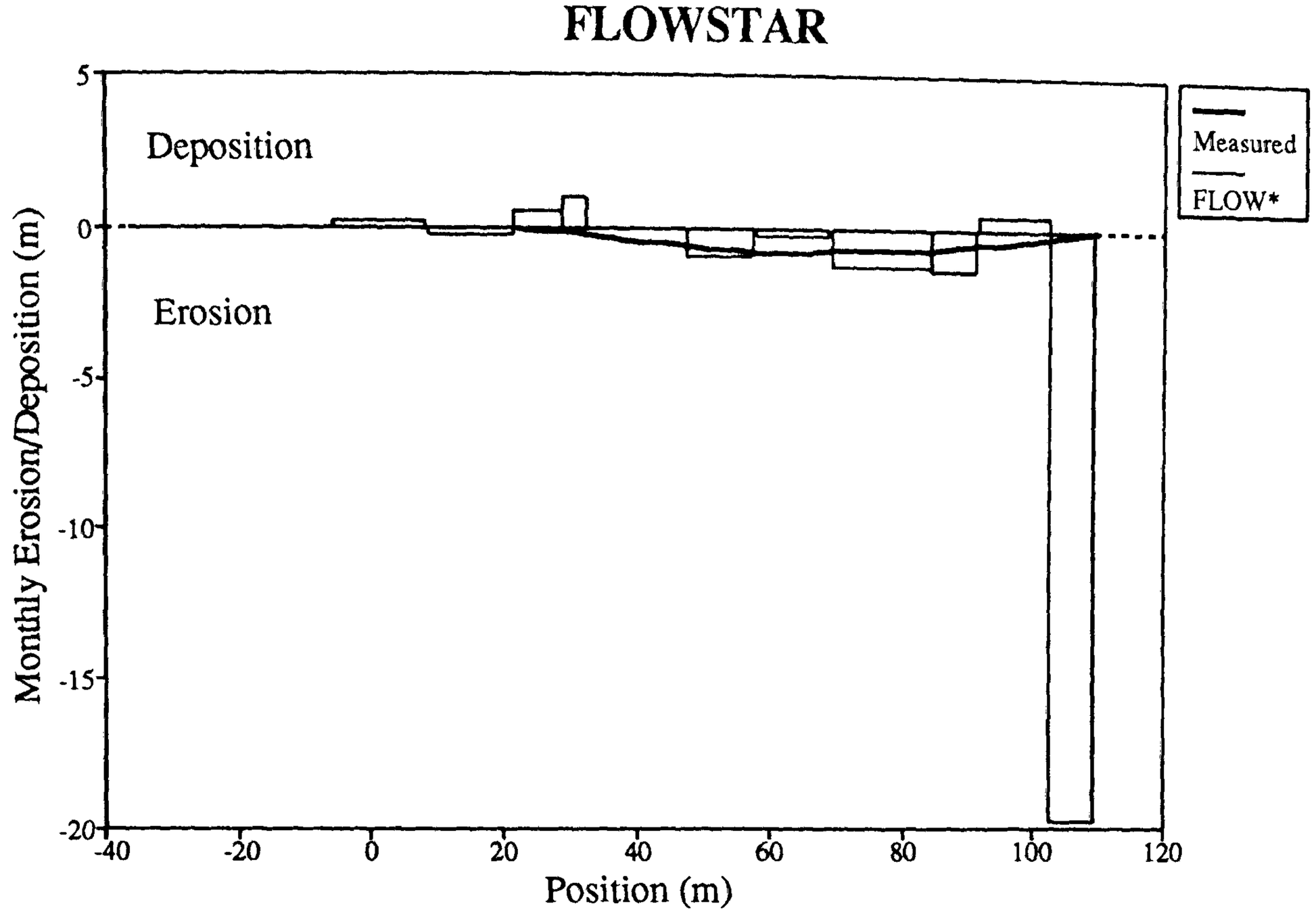

Figure 7.21 Comparison between measured and FLOWSTAR-calculated surface change on the centre-line of the dune.

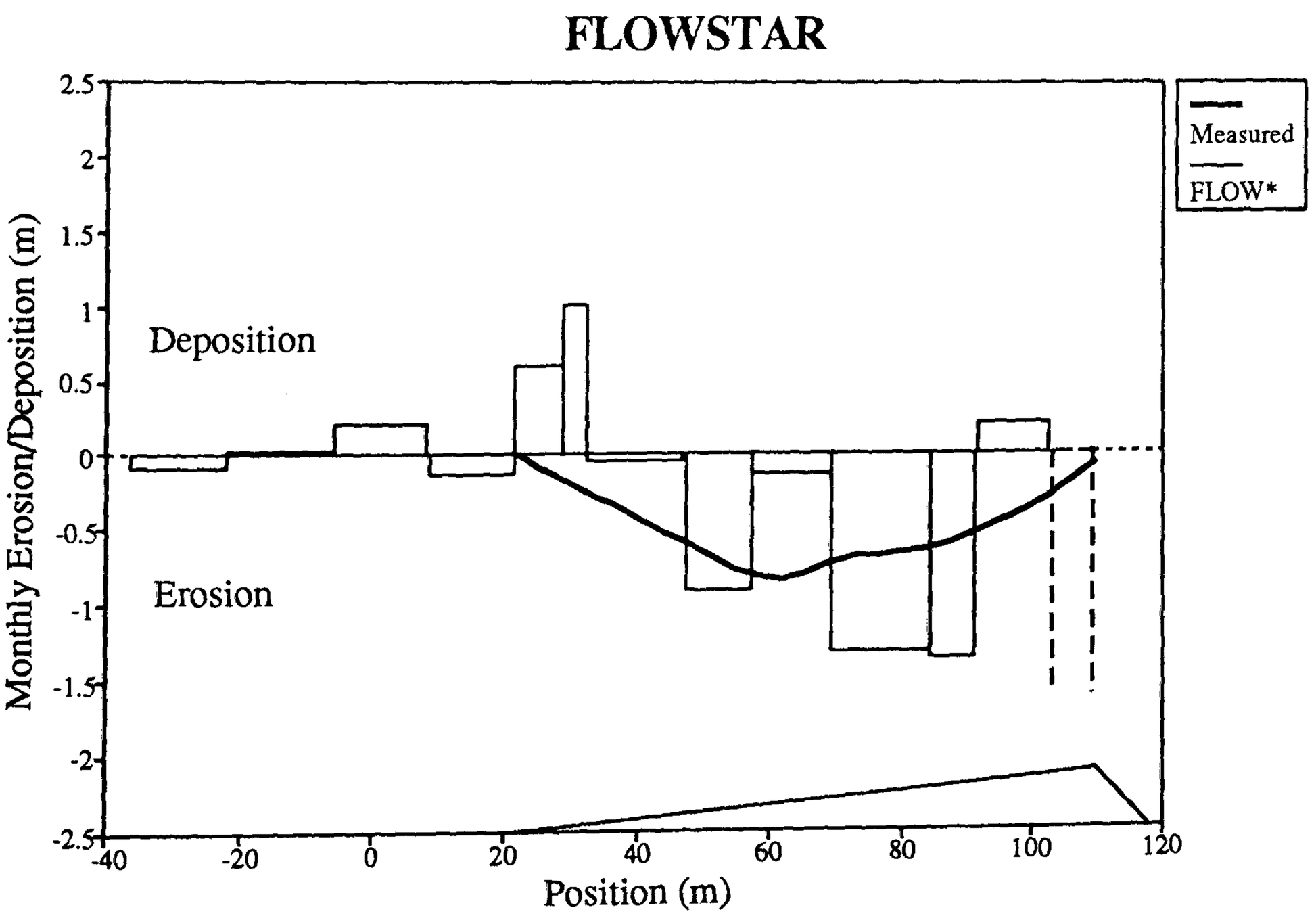

Figure 7.22 Comparison between measured and FLOWSTAR-calculated surface change on the centre-line of the dune (excluding prediction at the brink).

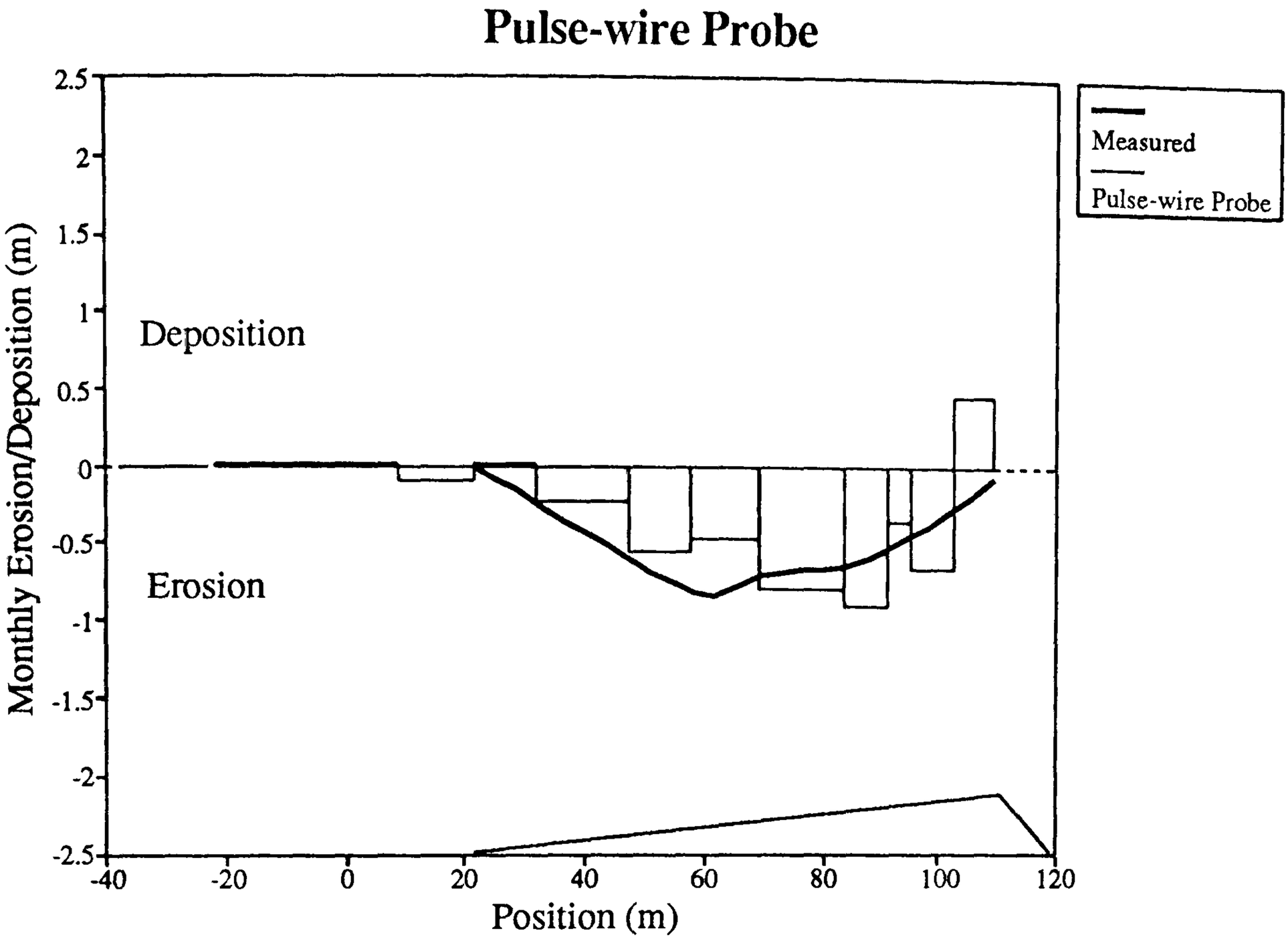

Figure 7.23 Comparison between measured and pulse-wire probe-calculated surface change on the centre-line of the dune.

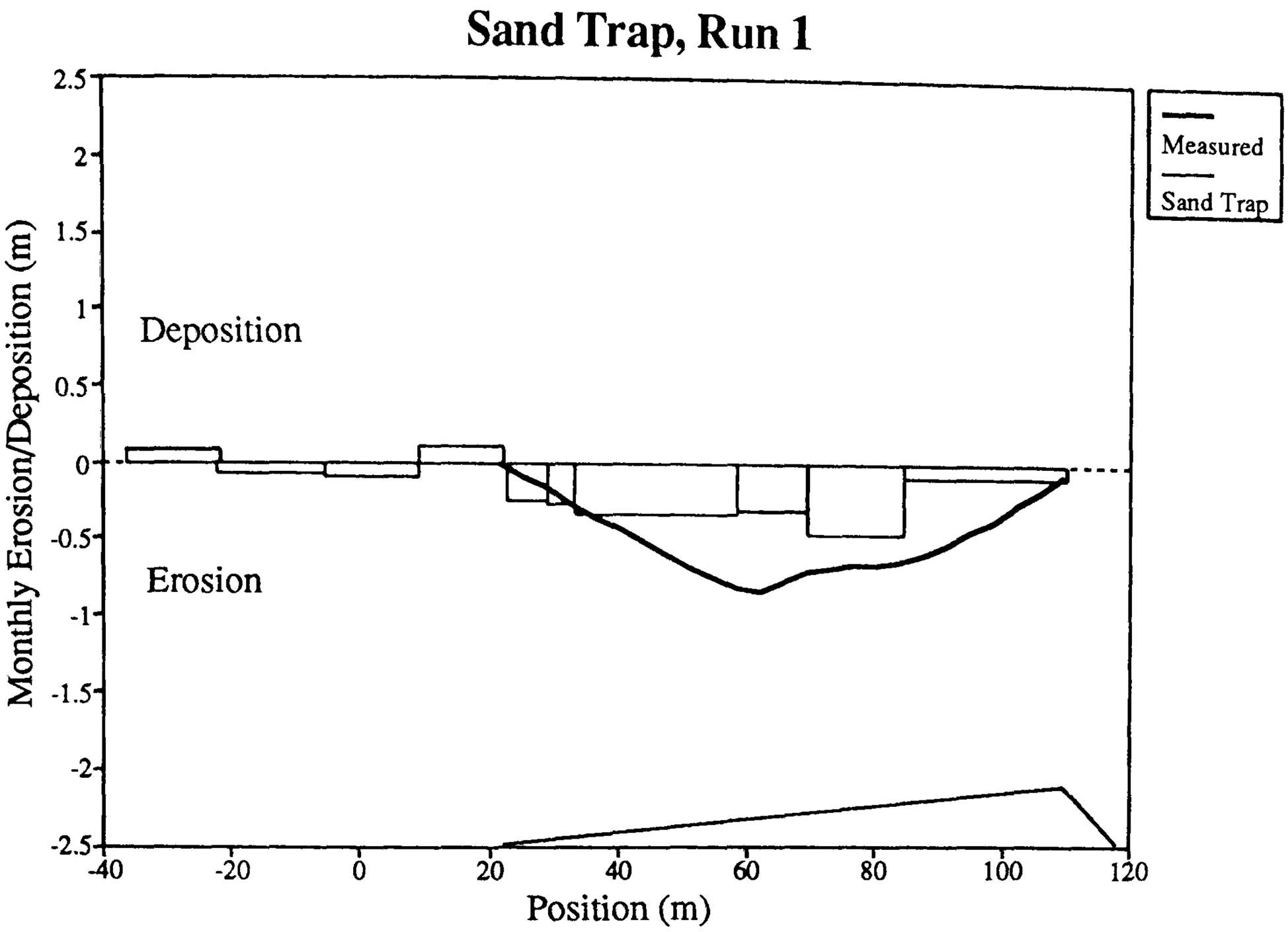

Figure 7.24 Comparison between measured and sand trap-calculated surface change on the centre-line of the dune (run 1).

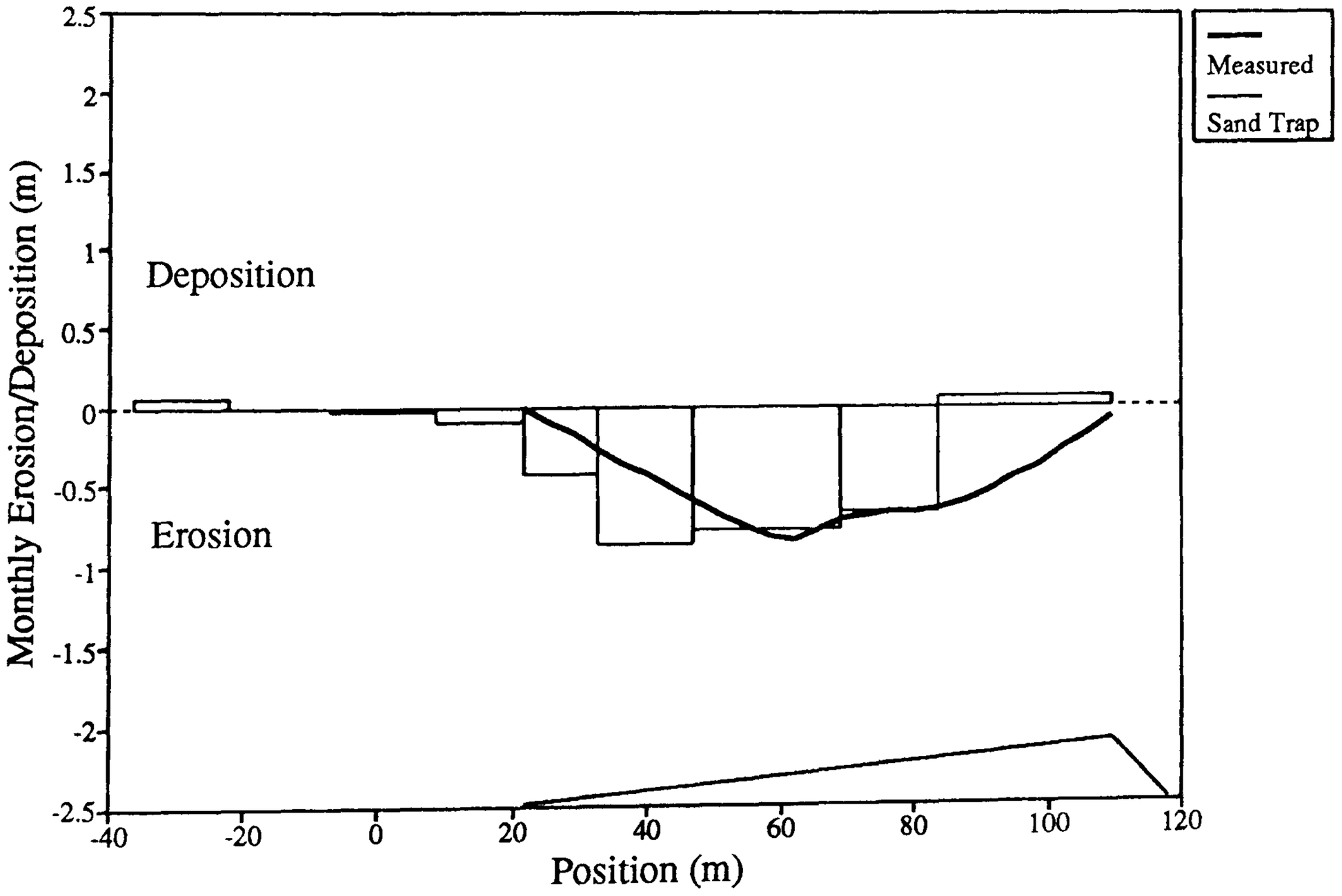

Figure 7.25 Comparison between measured and sand trap-calculated surface change on the centre-line of the dune (run 2).

The FLOWSTAR predictions of surface change on the centre-line are shown in Figures 7.21 and 7.22. Figure 7.21 is at too small a scale for a detailed comparison of the measured and predicted rates to be made, but it does emphasise the large amount of erosion (nearly 20 m) predicted by the model at the brink of the dune due to the over-prediction of u_* at this point. Figure 7.22 shows the same data but at a larger scale, disregarding the brink prediction. From this Figure it can be seen that the FLOWSTAR predictions of surface change are erratic. At the toe of the dune the model predicts over one metre of deposition in 28 days, despite none being observed. At x = 60 m (where the maximum amount of erosion was observed in the field) it displays almost no erosion, in contrast to the immediately adjacent upwind and downwind points which show 1.0 and 1.5 m of erosion respectively. Excepting the erosion predicted by the model at the brink, the point of maximum erosion is estimated to be at x = 90 m, 30 m downwind of the observed point of maximum erosion.

The wind tunnel (pulse-wire probe) assessments of surface change are similar to the observed rates (Figure 7.23). No significant surface change is predicted upwind of the dune or at the toe. However, the wind tunnel measurements estimate the point of maximum erosion to be 25 m downwind (at x = 85 m) of the observed position. In the region of the crest the predictions also appear to be quite irregular, culminating in the calculation of 0.5 m of deposition at the brink. These irregularities at the crest may be explained by the fact that the distance interval between the measurement points near the crest was quite small. This results in any errors or irregularities in the measurements of u_* being magnified out of proportion.

Figures 7.24 and 7.25 show the surface changes predicted from the sand transport rate (sand trap) measurements on the centre-line. The predictions from the first run (Figure 7.24) are not entirely consistent with the observed erosion rates, although it should be noted that the predictions do not show progressive deposition at or near the toe. The fact that the estimates of surface change on the windward slope itself do not reflect the observed rates is not surprising considering the short period of transport rate measurement and the errors associated with the sand traps (see Chapter 2 and above). The second run predictions (Figure 7.25) resemble the observed surface changes much more closely than the first run. Figure 7.25 shows no deposition upwind of the dune and the shape of the 'curve' of erosion on the windward slope is a good estimation. However, the estimated point of maximum erosion (at x = 40 m) is 60 m upwind of the actual location and some sand deposition is predicted at the brink.

The Flanks

Figures 7.26 and 7.27 show the field-calculated surface change on the left and right flanks respectively compared to the observed surface change. The field estimations on both of the flanks broadly reflect the actual surface change by showing erosion on the windward slope and deposition between the crest and brink. However, on neither flank is the point of maximum erosion accurately predicted, being 30 m downwind of the observed location in each case. In a similar manner to the centre-line, the field-predictions for both flanks show some deposition upwind of the toe, although in the case of the right flank this is only a very small amount.

The FLOWSTAR predictions of surface change on the left flank (Figure 7.28) are as erratic as those on the centre-line (Figure 7.22). Ignoring the substantial overestimation of erosion at the brink, Figure 7.28 broadly identifies the windward slope as a zone of erosion (despite several instances of deposition) and the crest-brink zone as a region of deposition. The location of the point of maximum erosion on the windward slope is also well defined. As on the centre-line, the toe of the left flank is identified as a zone of deposition, despite no deposition being observed. On the right flank (Figures 7.29 and 7.30) the FLOWSTAR predictions also identify the toe as a region of deposition, in contrast to the observed surface change. Figure 7.29 clearly shows the magnitude of the over-prediction of erosion and deposition in the crest-brink zone. However, on the windward slope of the right flank the agreement between the observed and predicted rates of erosion is good (Figure 7.30).

The wind tunnel predictions of surface change on the flanks (Figures 7.31 and 7.32) are based on the high extrapolations of u_* from the cross-wire measurements. On the left flank (Figure 7.31) the distinction between erosion and deposition just upwind of the crest is well defined by the cross-wire predictions. However, a large amount of erosion is predicted at the toe and this is not evident from the field observations. In agreement with the measured changes, no significant deposition is predicted at the toe or upwind of the left flank. On the right flank (Figure 7.32) the cross-wire measurements also display little or no deposition at the toe of the dune. They also correctly identify the windward slope as a zone of erosion and the crest-brink region as an area of deposition. However, at the crest (where x = 120 m) the predictions become quite erratic and are not in good agreement with the observed changes. It should be noted that as these predictions of surface change are based only on the high extrapolations of u_* from the cross-wire measurements, they do not necessarily reflect accurate estimates of surface change. This is because the true value of $\delta u_*/\delta x$ (which governs the pattern of erosion) may lie anywhere between the low and high extrapolations.

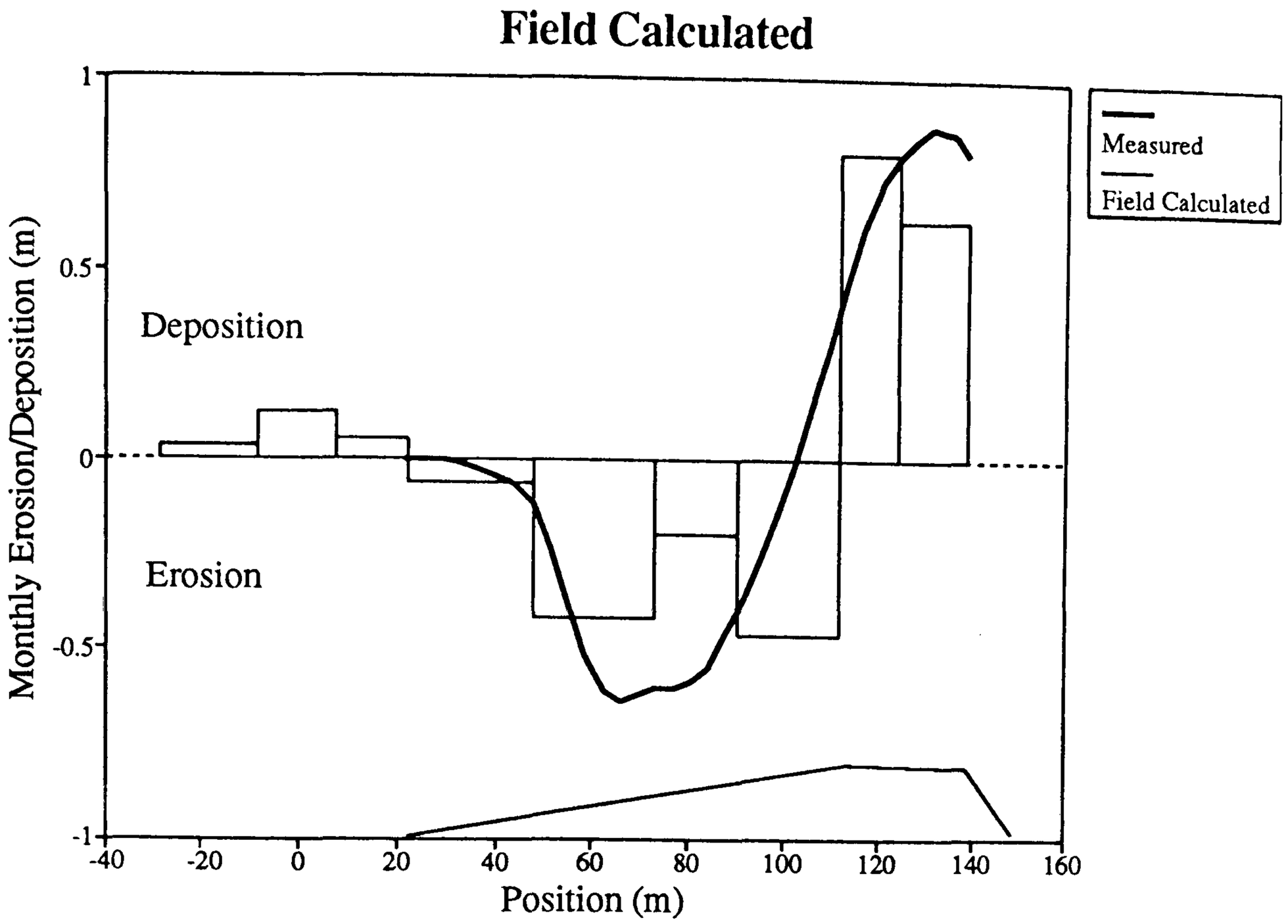

Figure 7.26 Comparison between measured and field-calculated surface change on the left flank of the dune.

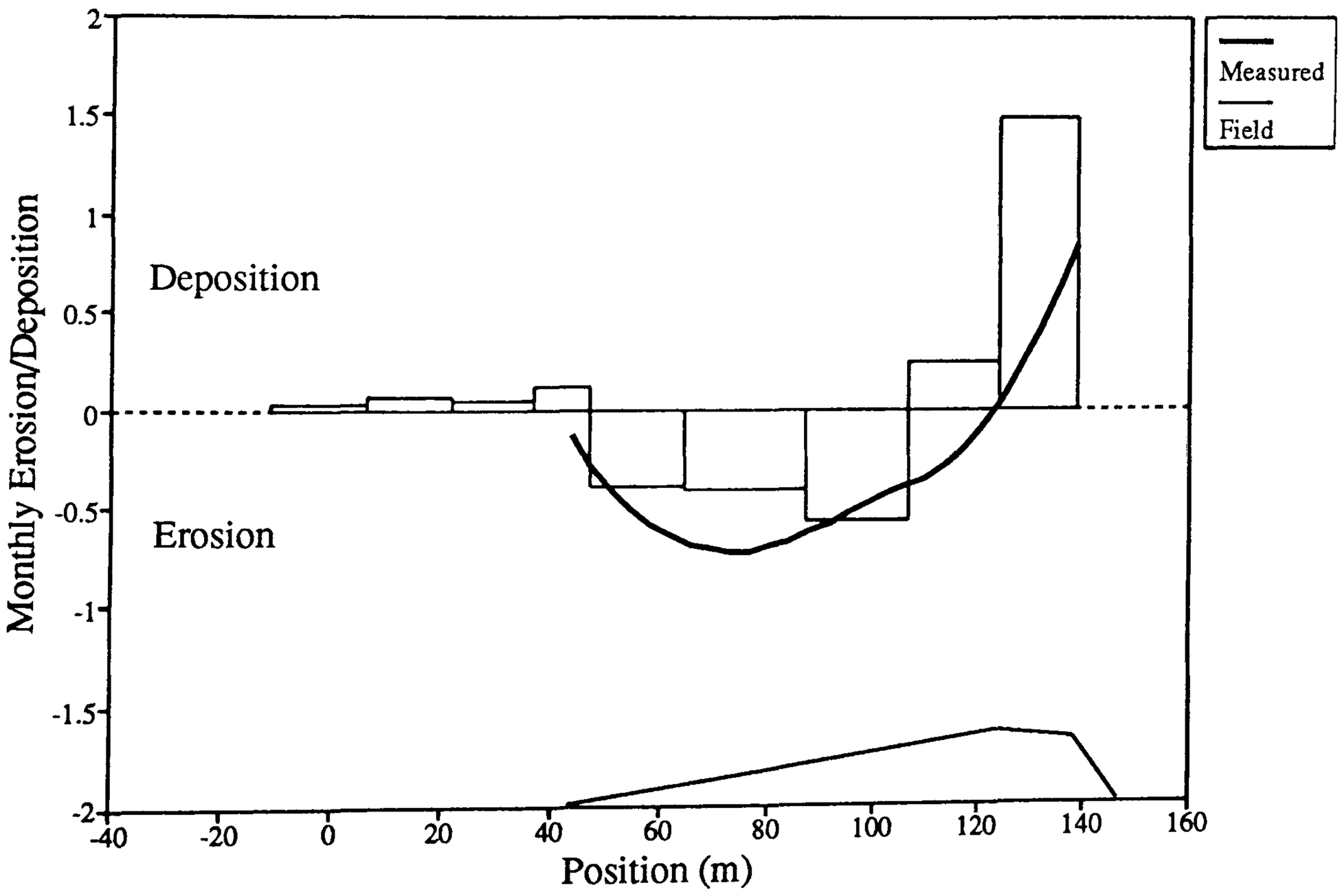

Figure 7.27 Comparison between measured and field-calculated surface change on the right flank of the dune.

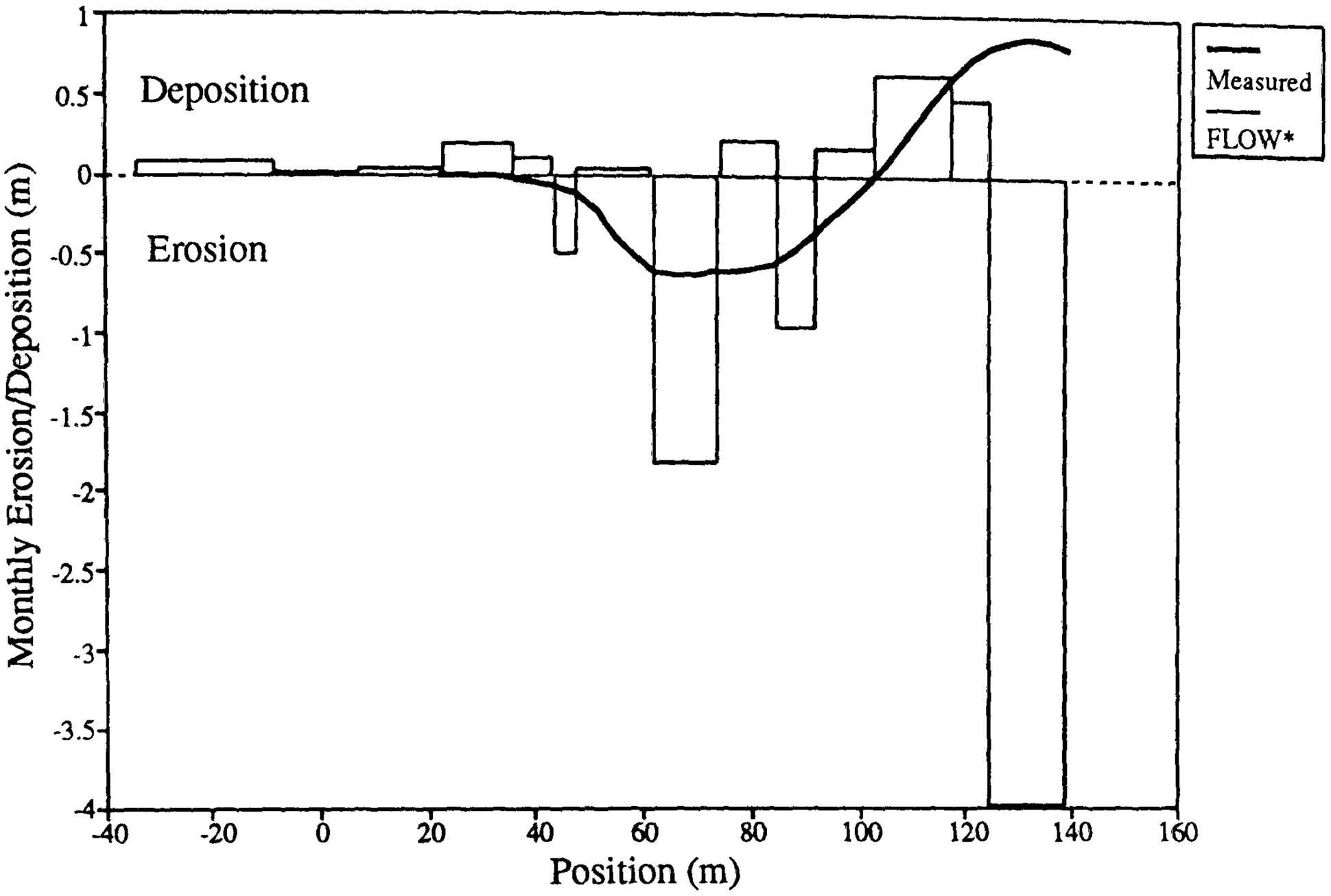

Figure 7.28 Comparison between measured and FLOWSTAR-calculated surface change on the left flank of the dune.

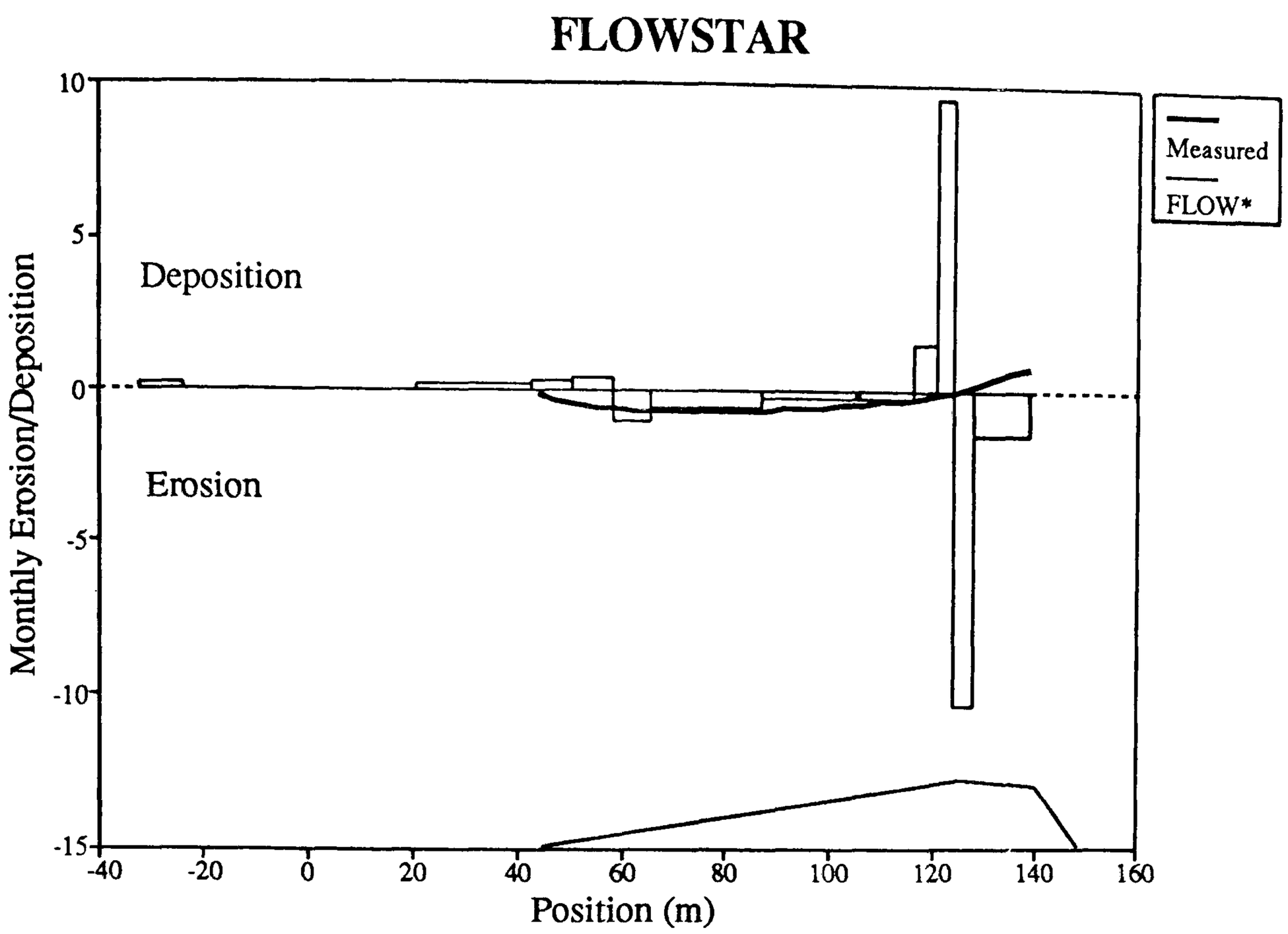

Figure 7.29 Comparison between measured and FLOWSTAR-calculated surface change on the right flank of the dune.

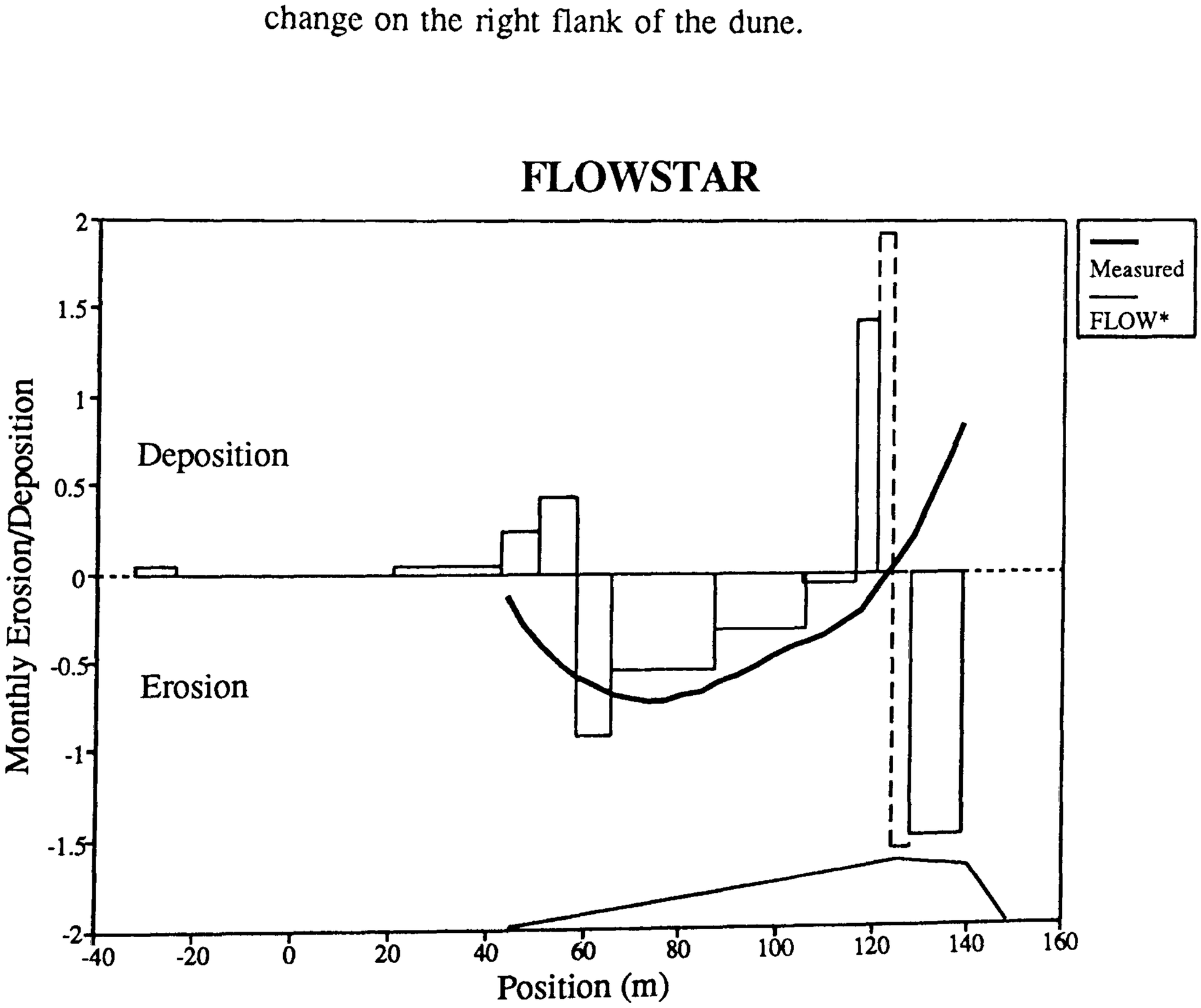

Figure 7.30 Comparison between measured and FLOWSTAR-calculated surface change on the right flank of the dune (excluding prediction at the brink).

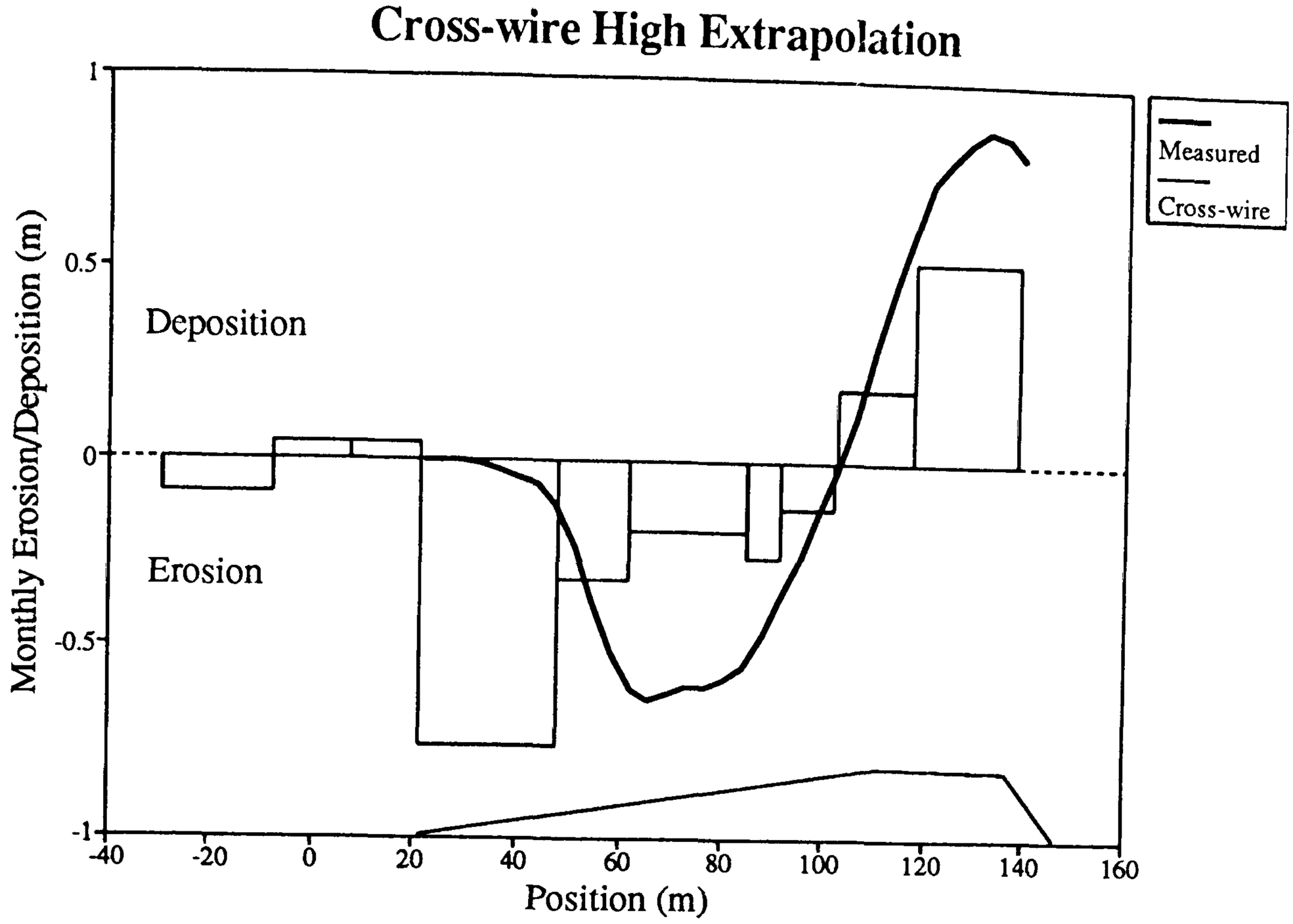

Figure 7.31 Comparison between measured and cross-wire-calculated (high extrapolation) surface change on the left flank of the dune.

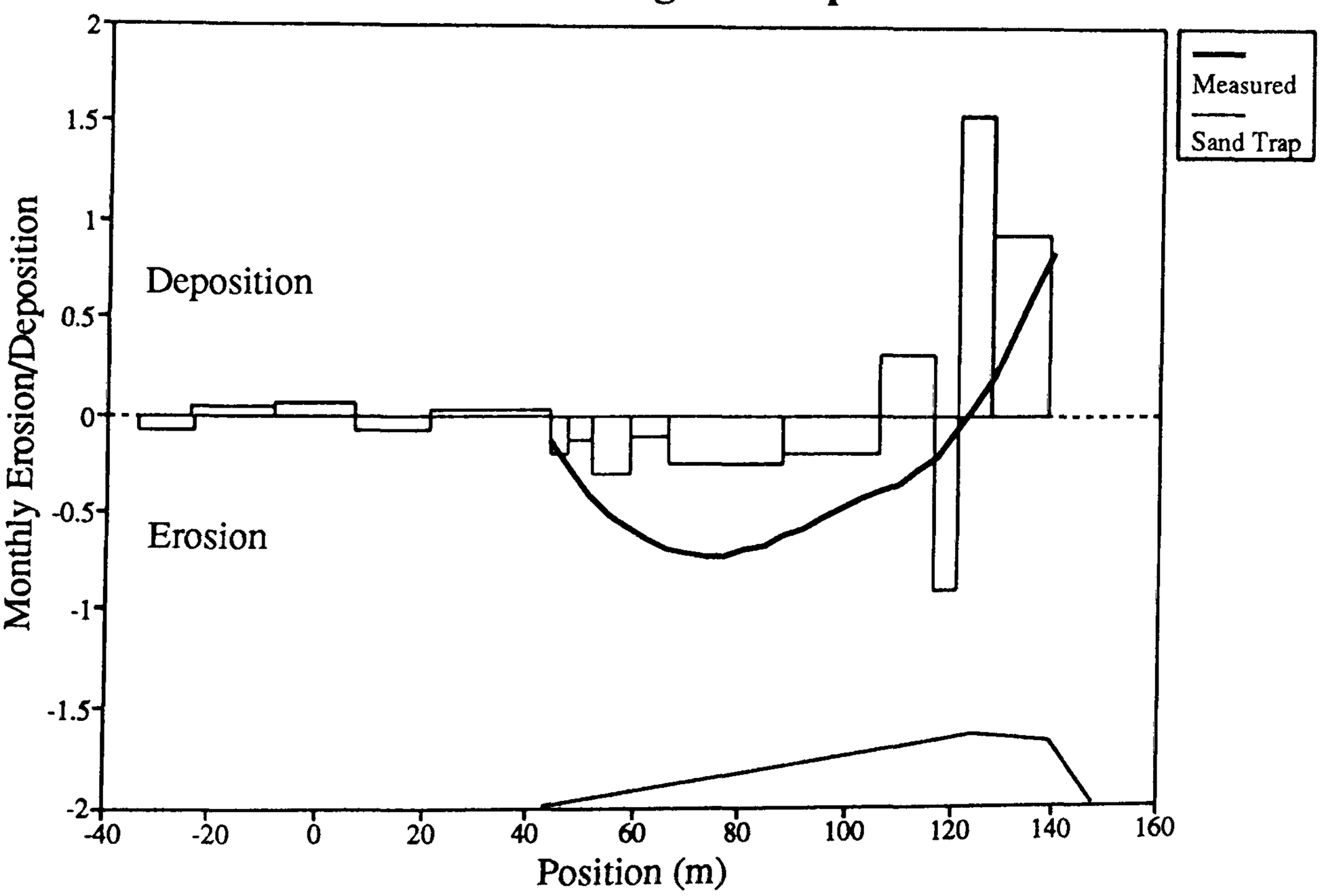

Figure 7.32 Comparison between measured and cross-wire-calculated (high extrapolation) surface change on the right flank of the dune.

Owing to the differences between the low and high extrapolations (noted in Chapter 4) this allows for a large margin of error in the prediction of surface change.

The surface change on the flanks predicted from the sand transport rate measurements are shown in Figures 7.33 to 7.36. On both flanks the predictions accurately define the major zones of erosion and deposition and in all except Figure 7.36 the point of maximum erosion on the windward slope is correctly described. In none of these Figures is there a definite zone of deposition evident at the toe of either flank.

Statistical Analysis

Figures 7.37 to 7.43 show amalgamated comparisons between the measured surface change over a 28 day period on all three section lines and that predicted by each of the techniques. The diagonal lines on each Figure correspond to a 1:1 relationship between measured and predicted surface change. Two graphs are presented for the FLOWSTAR and cross-wire extrapolation results, one for each inclusive of all the data (Figures 7.38 and 7.41) and a further one exclusive of those predicted data-points which show a large variance from the measured values.

Table 7.2 summarises the results of the difference of means tests, analysis of variance (described above) and results of regression analysis (x-coefficient and constant) between the observed and predicted values (x_p signifies the predicted values using technique x whilst x_m denotes the field values measured at the same location). The secondary figures provided for the FLOWSTAR and cross-wire predictions are those calculated after values of high variance (identified from regression analysis) were excluded from the computations. This is of particular importance for the FLOWSTAR predictions as the results show the degree of agreement between predicted and observed values which would be expected if the over-prediction of u_* at the brink was corrected.

Table 7.2 and Figure 7.37 demonstrate good agreement between the field-measured ($Field_m$) and field-predicted ($Field_p$) surface change. The means, standard deviations and sample variances are very similar and the regression equation constant and x-coefficient are near to zero and 1.0 respectively. The strong positive correlation coefficient (of 0.83) shows a close association between the two variables and this is reflected in the low variance (Table 7.2). However, close inspection of Figure 7.37 reveals excess deposition predicted where the measured surface change is zero. This group of points at zero on the x-axis is a result of the field technique predicting deposition of sand upwind of and at the toe of the dune.

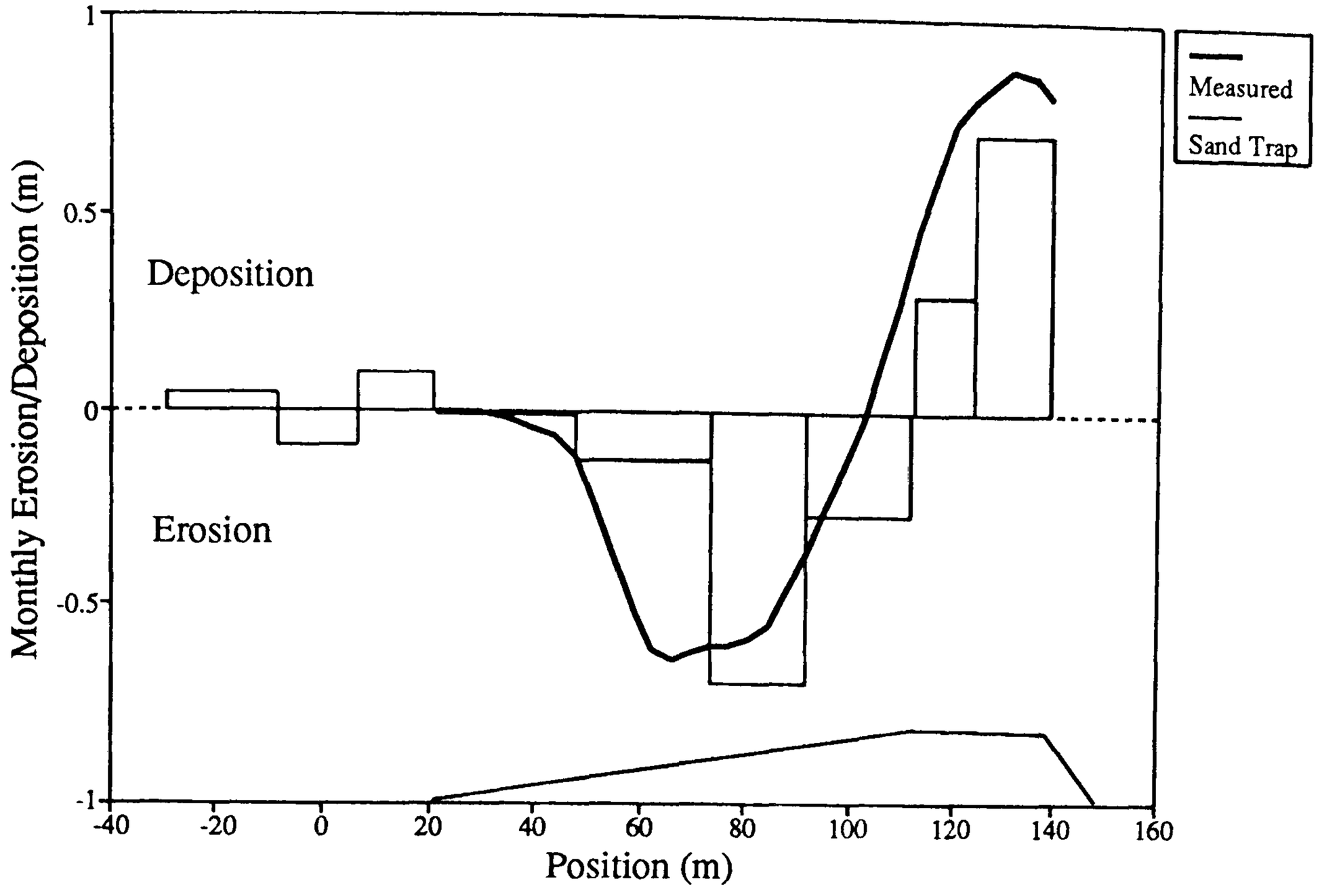

Figure 7.33 Comparison between measured and sand trap-calculated surface change on the left flank of the dune (run 1).

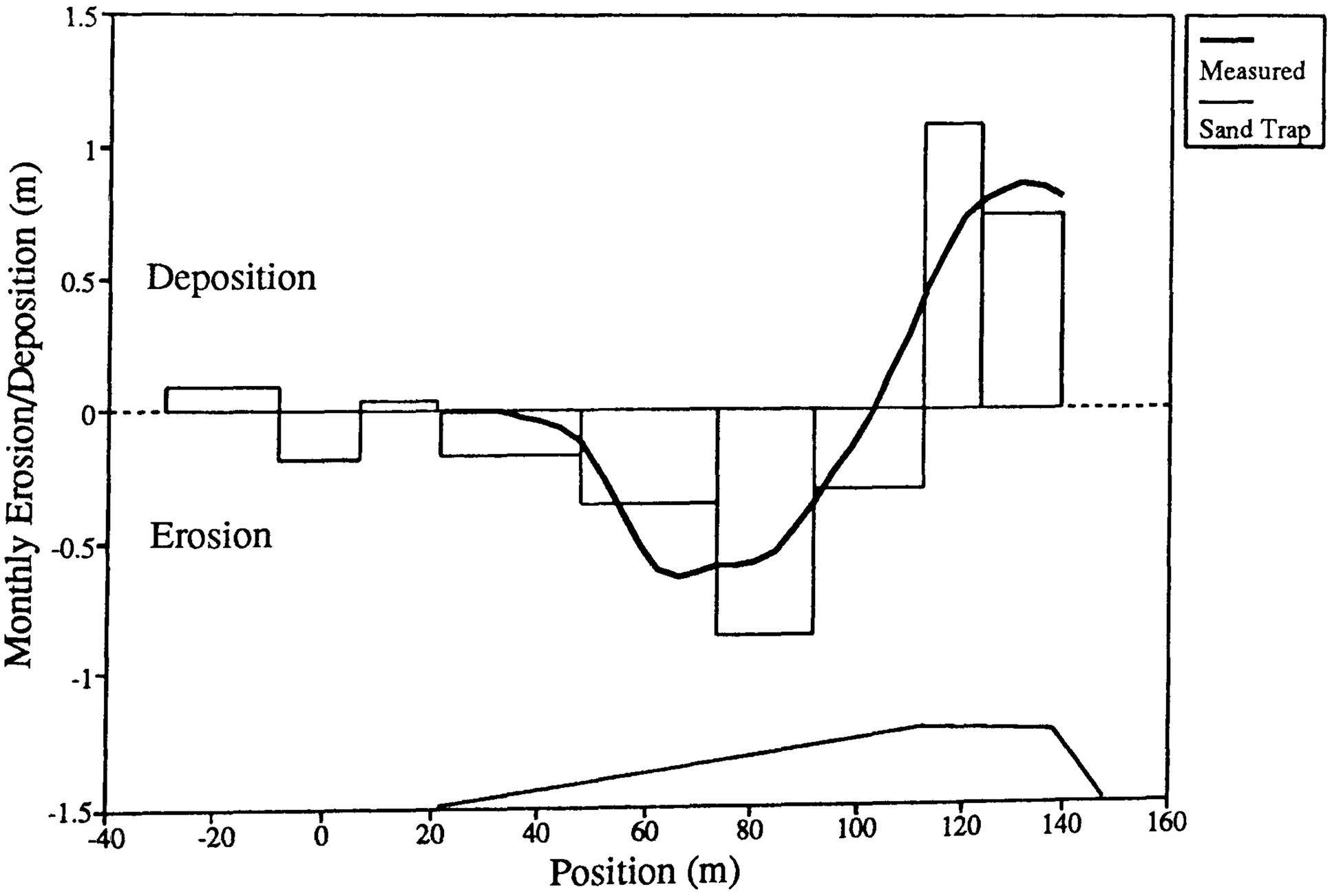

Figure 7.34 Comparison between measured and sand trap-calculated surface change on the left flank of the dune (run 2).

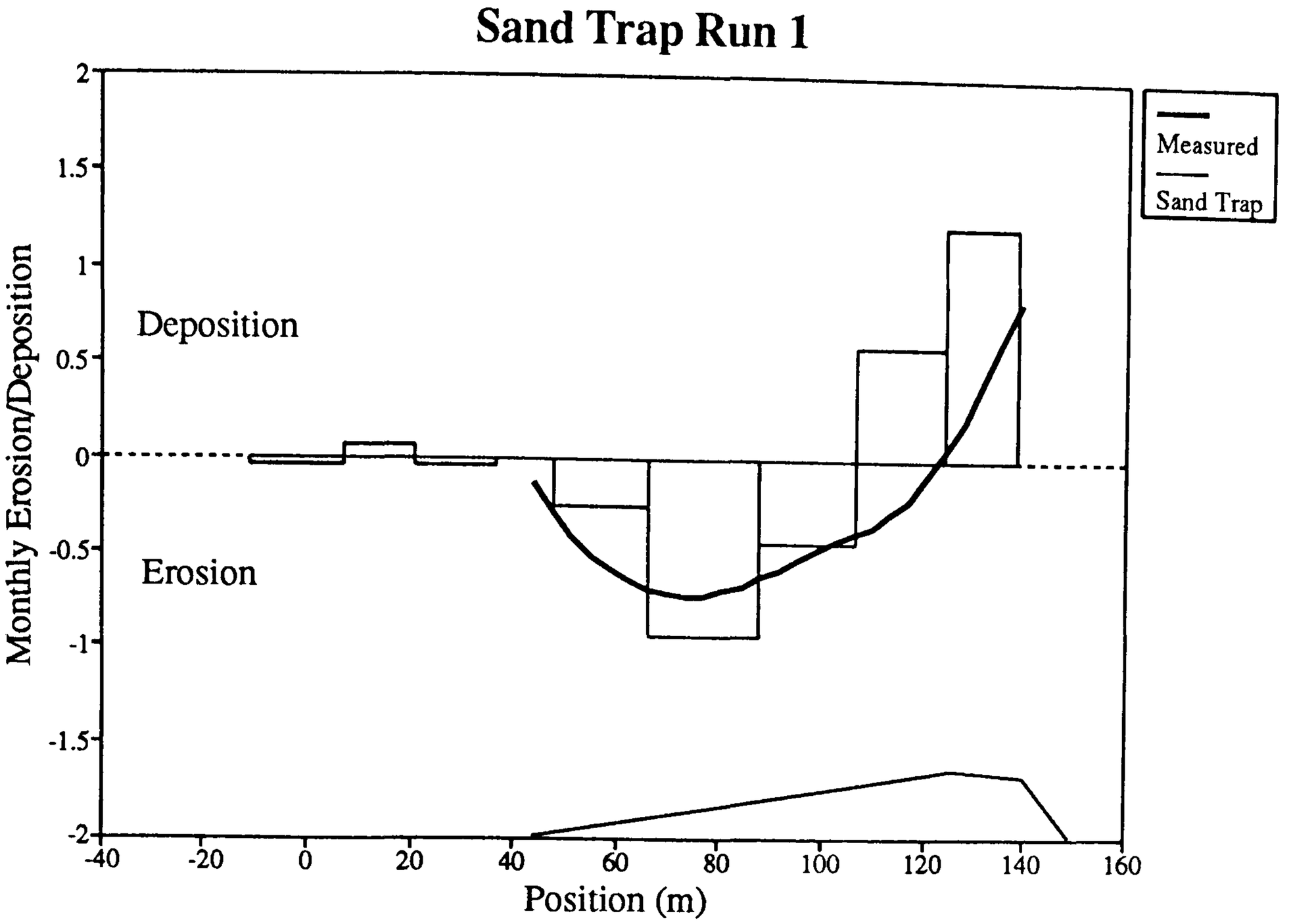

Figure 7.35 Comparison between measured and sand trap-calculated surface change on the right flank of the dune (run 1).

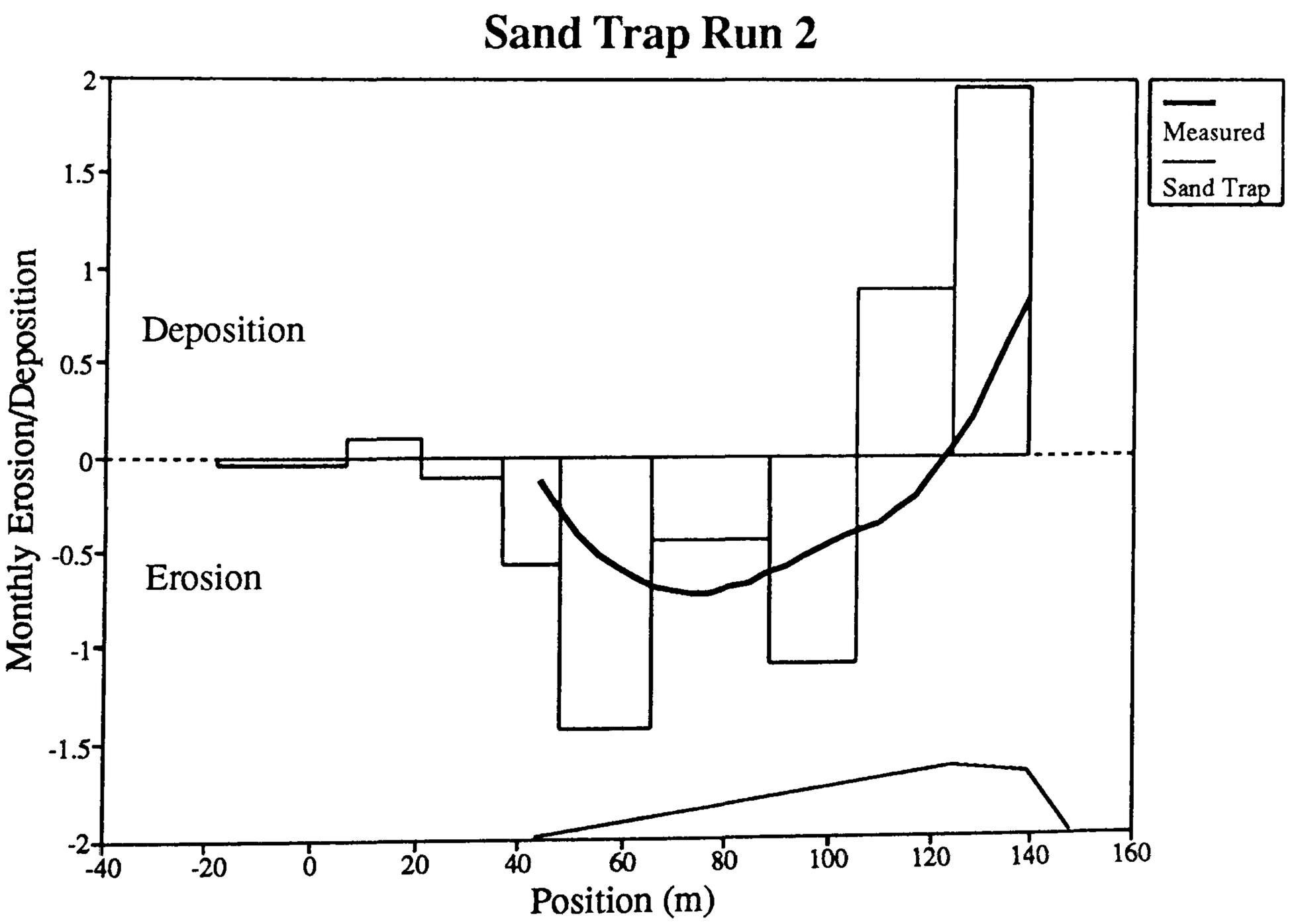

Figure 7.36 Comparison between measured and sand trap-calculated surface change on the right flank of the dune (run 2).

Table 7.2 Summary of the statistical analysis between predicted and observed surface change over a 28-day period on all three section lines

	General Statistics				Difference of Means	Analysis of Variance	Regression Analysis		
	N	Mean	STD	Sample Variance	STD of Means		Const.	x-coeff.	Corr. Coeff.
$Field_m$	29	-0.083	0.421	0.177	0.126	0.091	0.014	1.048	0.83
$Field_p$	29	-0.073	0.534	0.285					
$FLOW^*_m$	44	-0.142	0.395	0.156	0.573	14.625	-0.744	-0.624	-0.07
$FLOW^*_p$	44	-0.660	3.780	14.288					
$FLOW^{*2}_m$	40	-0.181	0.379	0.144	0.119	0.069	-0.025	0.489	0.28
$FLOW^{*2}_p$	40	-0.113	0.652	0.425					
PWA_m	20	-0.170	0.431	0.186	0.147	0.056	0.057	1.021	0.88
PWA_p	20	-0.177	0.499	0.249					
$X\text{-}wire_m$	40	-0.178	0.379	0.144	0.144	0.623	-0.027	0.727	0.33
$X\text{-}wire_p$	40	-0.156	0.830	0.689					
$X\text{-}wire^2_m$	39	-0.176	0.383	0.147	0.098	0.130	0.065	0.652	0.52
$X\text{-}wire^2_p$	39	-0.049	0.482	0.232					
$Trap_m$	59	-0.088	0.420	0.176	0.090	0.118	0.008	1.028	0.78
$Trap_p$	59	-0.083	0.552	0.305					

Figure 7.38 shows the total FLOWSTAR data-set. It demonstrates the excessive predictions of erosion and deposition, mainly at the brink. These outlying data-points have a large effect on the statistical analysis between the observed and predicted values. From Table 7.2 it can be seen that the unadjusted FLOWSTAR predictions ($Flow^*_p$) do not show good agreement with the measured values ($Flow^*_m$). The mean, standard deviation and sample variances are very different and the correlation coefficient and x-coefficient from the regression analysis are negative (demonstrating an inverse relationship between predicted and observed surface change). The agreement is improved when the four values showing the largest variance are removed from the data-set (Figure 7.39). From Table 7.2 ($Flow^{*2}_p$) it can be seen that this considerably improves the agreement between the means, standard deviations and sample variances (although they are not in as close agreement as the field values). The correlation coefficient and x-coefficient also become positive (although very low at 0.28 and 0.489 respectively) and the variance statistic is notably improved.

The pulse-wire probe surface change predictions also show good agreement with the measured values (although a scarcity of data exists in the positive surface change region which is dominated by the crest-brink measurements on the flanks) (Figure 7.40). The means, standard deviations and sample variances presented in Table 7.2 for the PWA predictions (PWA_p) are in close accord to the observed values (PWA_m) (at least as close as the field predictions) and the correlation coefficient and x-coefficient are an improvement on the field predictions. Analysis of variance between the PWA estimates and observed surface change also reveals low values, comparable to the field calculations. A point to note is the absence of deposition predicted where the measured surface change is zero (Figure 7.40), in contrast to the field estimates (Figure 7.37).

The cross-wire predictions of surface change ($X\text{-}wire_p$) are not in as good agreement with the observed changes as the PWA estimates. Figure 7.41 demonstrates a wide scatter around the 1:1 ratio line between the measured and predicted values and this is reflected in Table 7.2 where the standard deviation and sample variance of the predicted values are much larger than the measured values. Furthermore, the correlation coefficient is not high (at only 0.33) and the x-coefficient is only 0.727. The high value for the analysis of variance also indicates poor agreement. The agreement between the observed and predicted changes is considerably improved when the single point with large variance is disregarded in the calculations (Figure 7.42). This single point was the result of measurements at the crest of the centre-line where the near-surface u_* gradient was very strong. This made the extrapolation of a surface u_* from the data very difficult and probable errors in the deduction have been compounded to produce the excessive

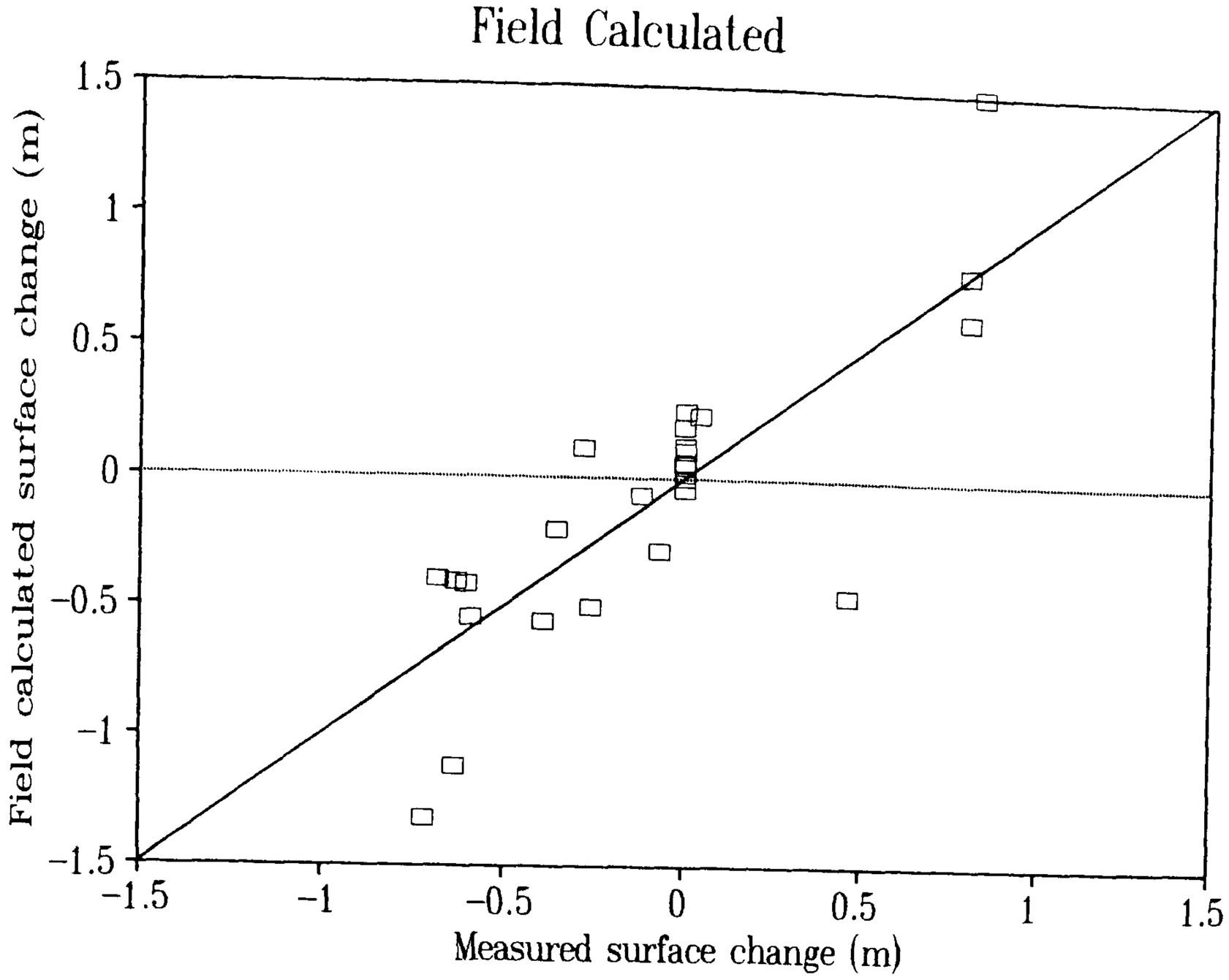

Figure 7.37 Comparison between measured and field-calculated surface change on all three section lines.

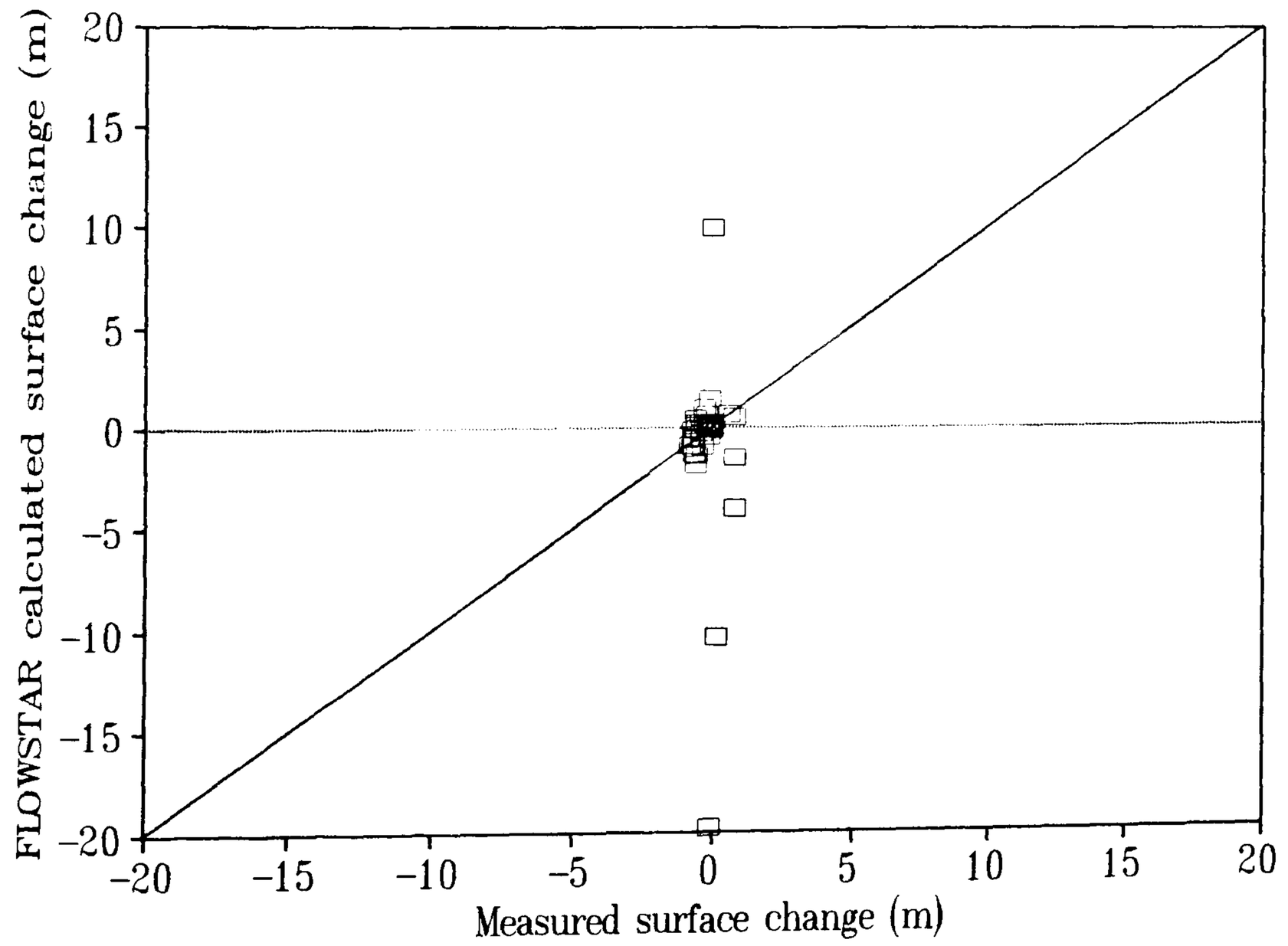

Figure 7.38 Comparison between measured and FLOWSTAR-calculated surface change on all three section lines.

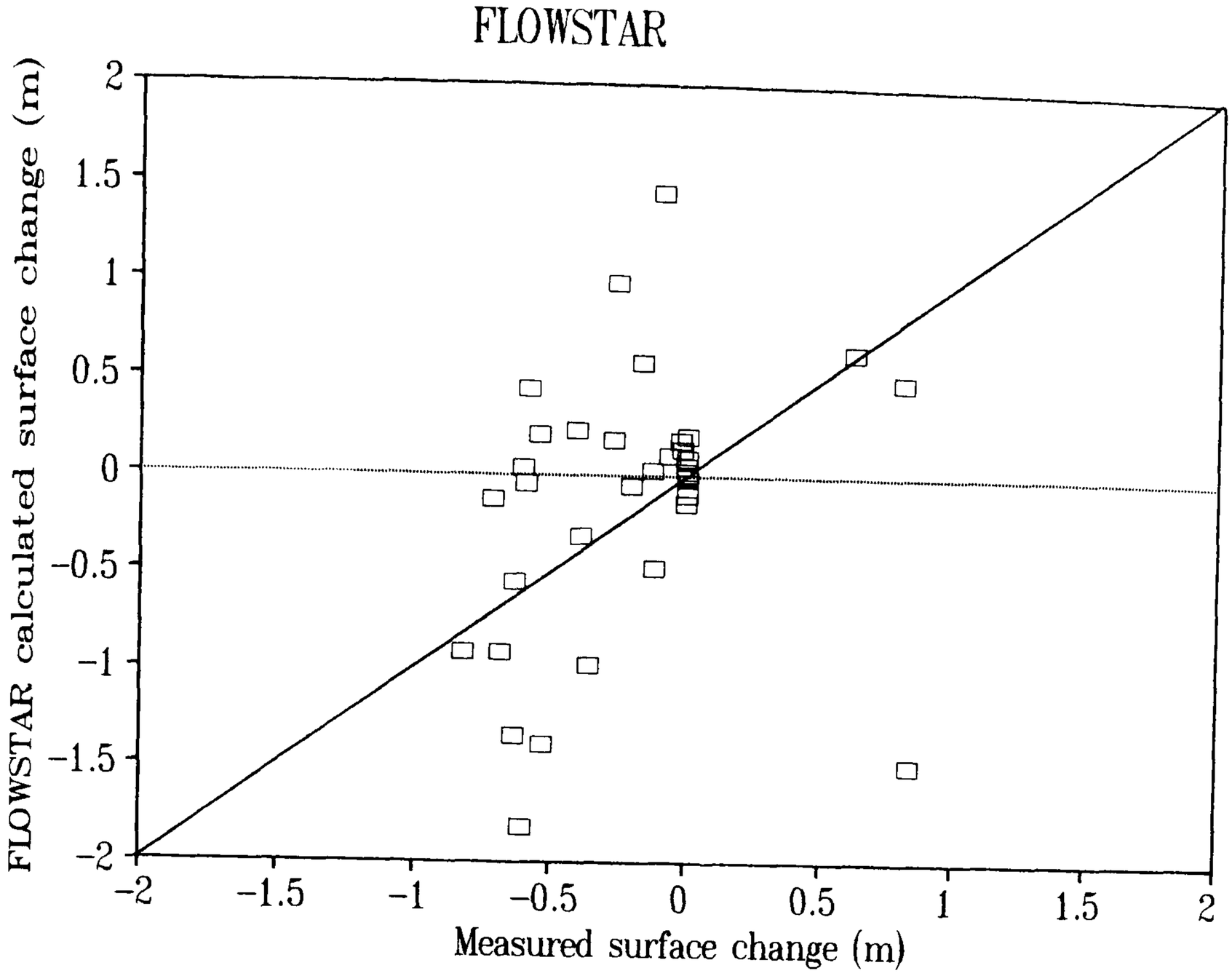

Figure 7.39 Comparison between measured and FLOWSTAR-calculated surface change on all three section lines (excluding prediction at the brink).

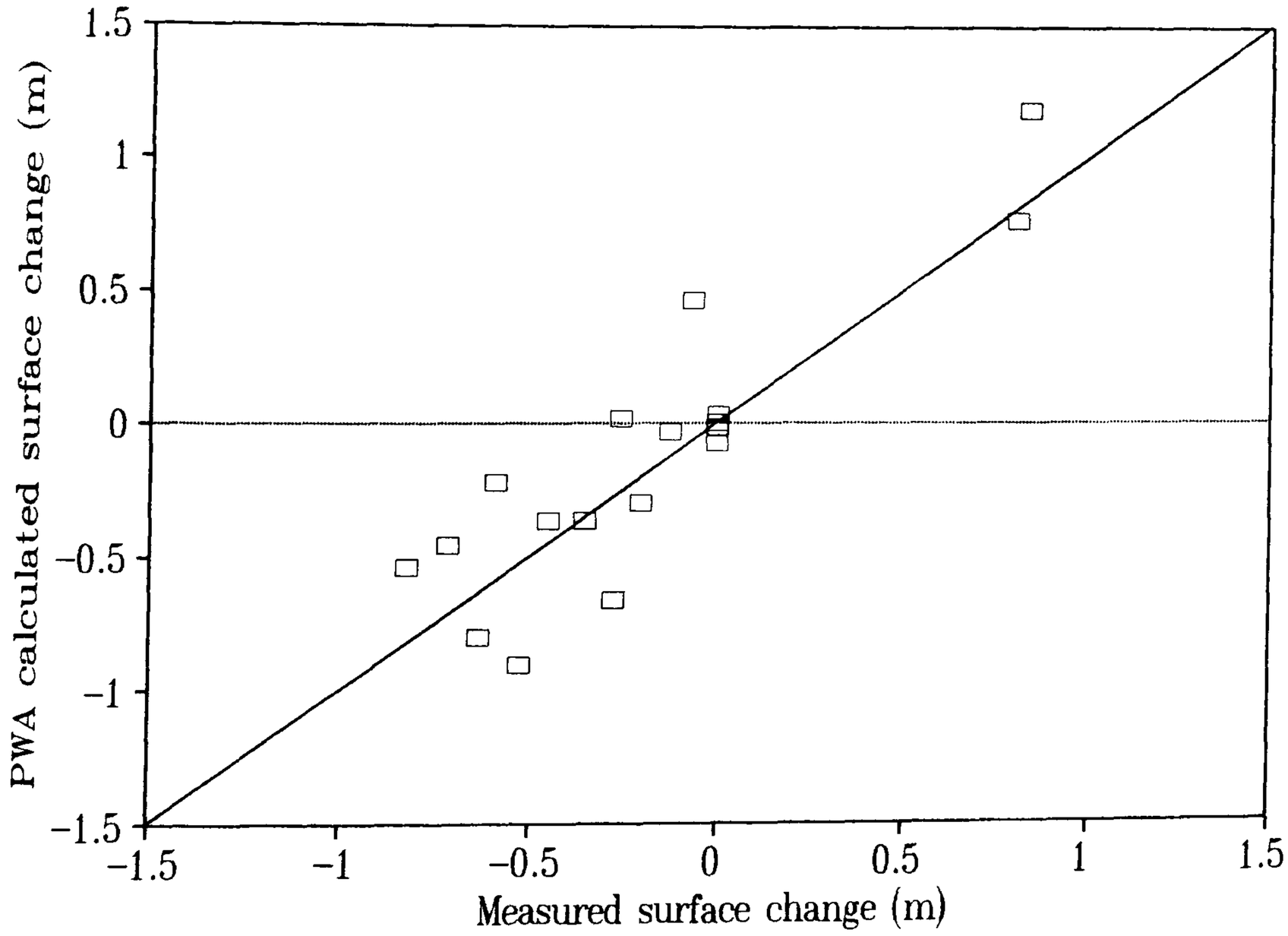

Figure 7.40 Comparison between measured and pulse-wire probe-calculated surface change on all three section lines.

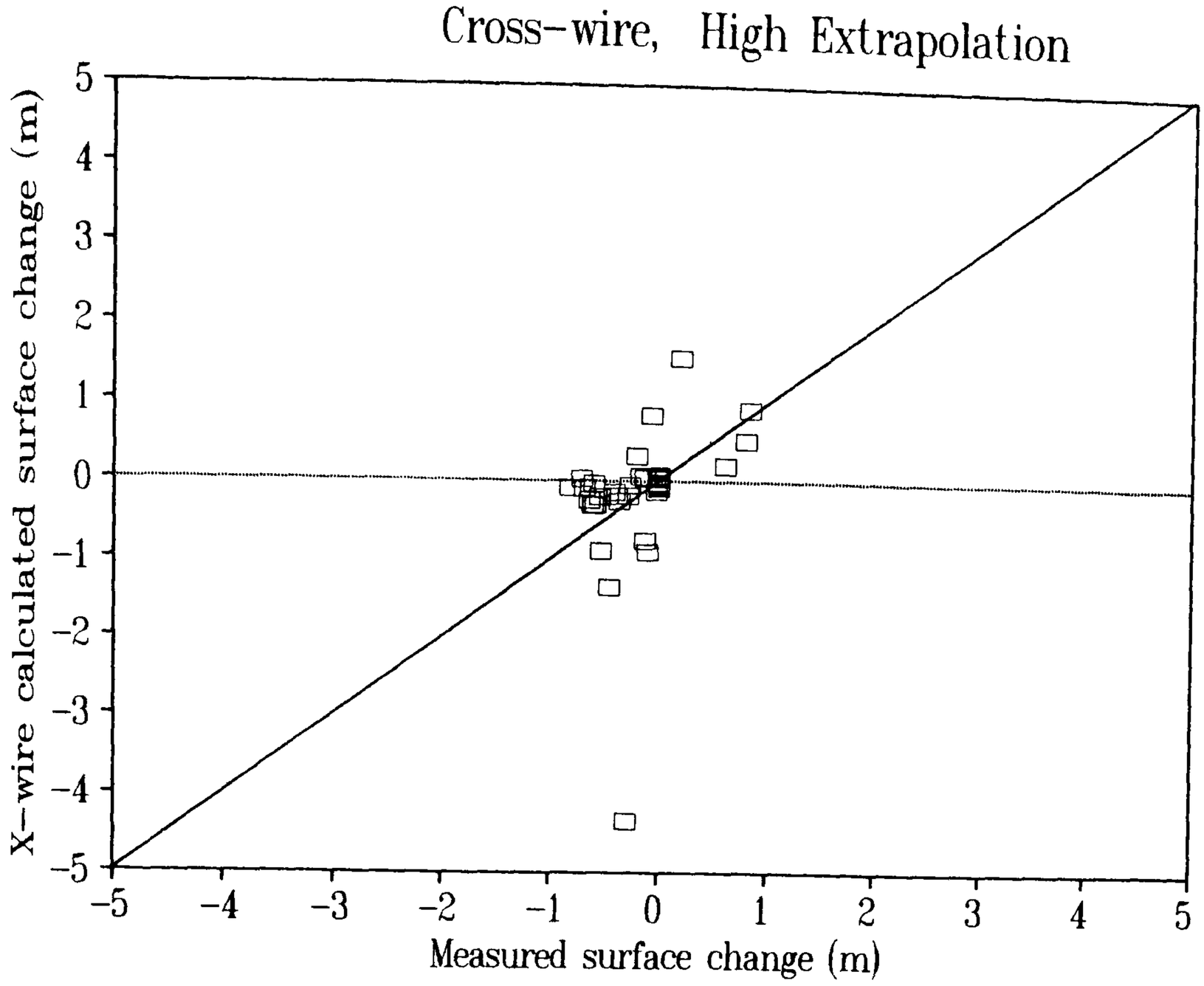

Figure 7.41 Comparison between measured and cross-wire-calculated (high extrapolation) surface change on all three section lines.

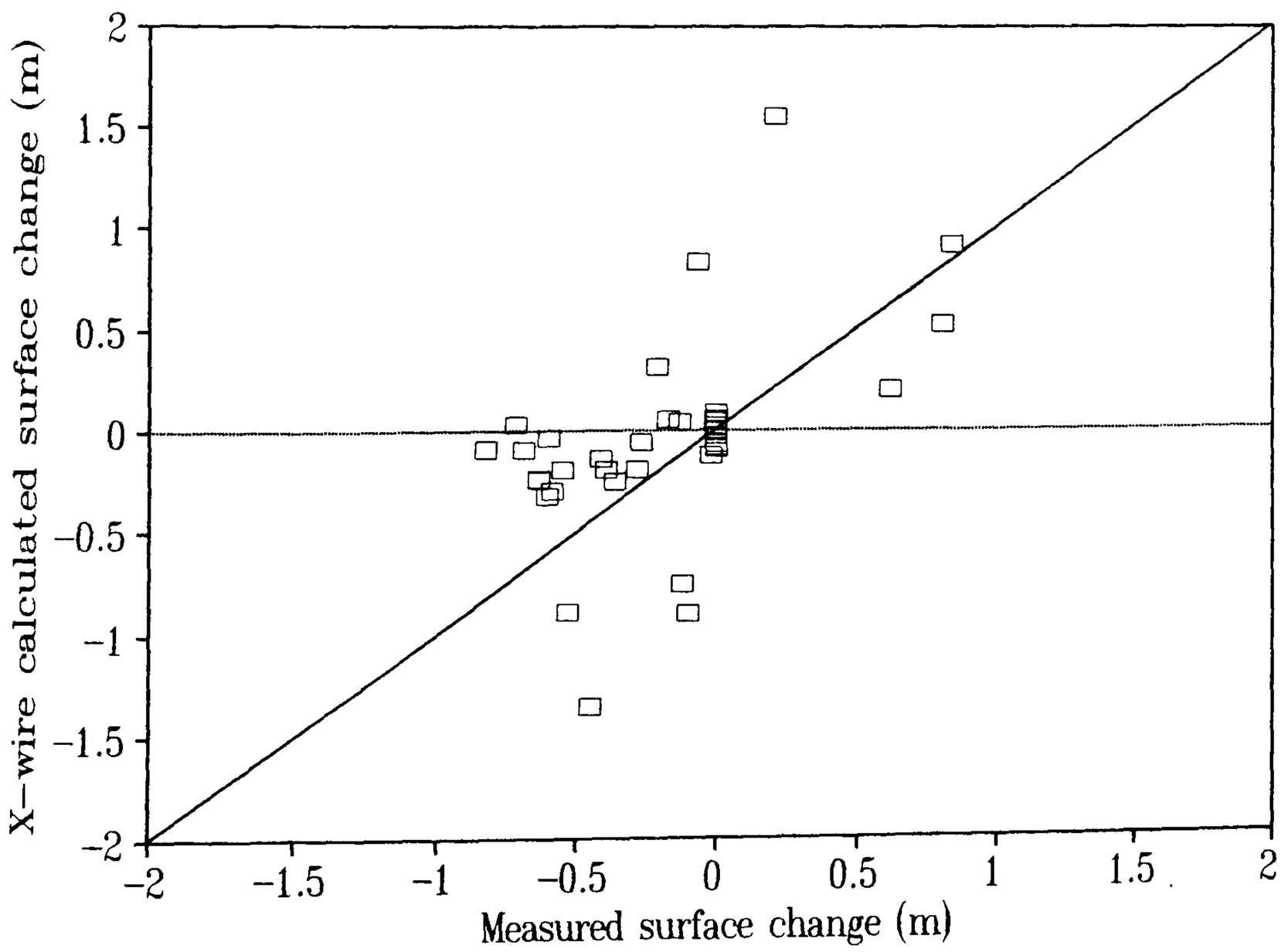

Figure 7.42 Comparison between measured and cross-wire-calculated (high extrapolation) surface change on all three section lines (excluding values of high variance).

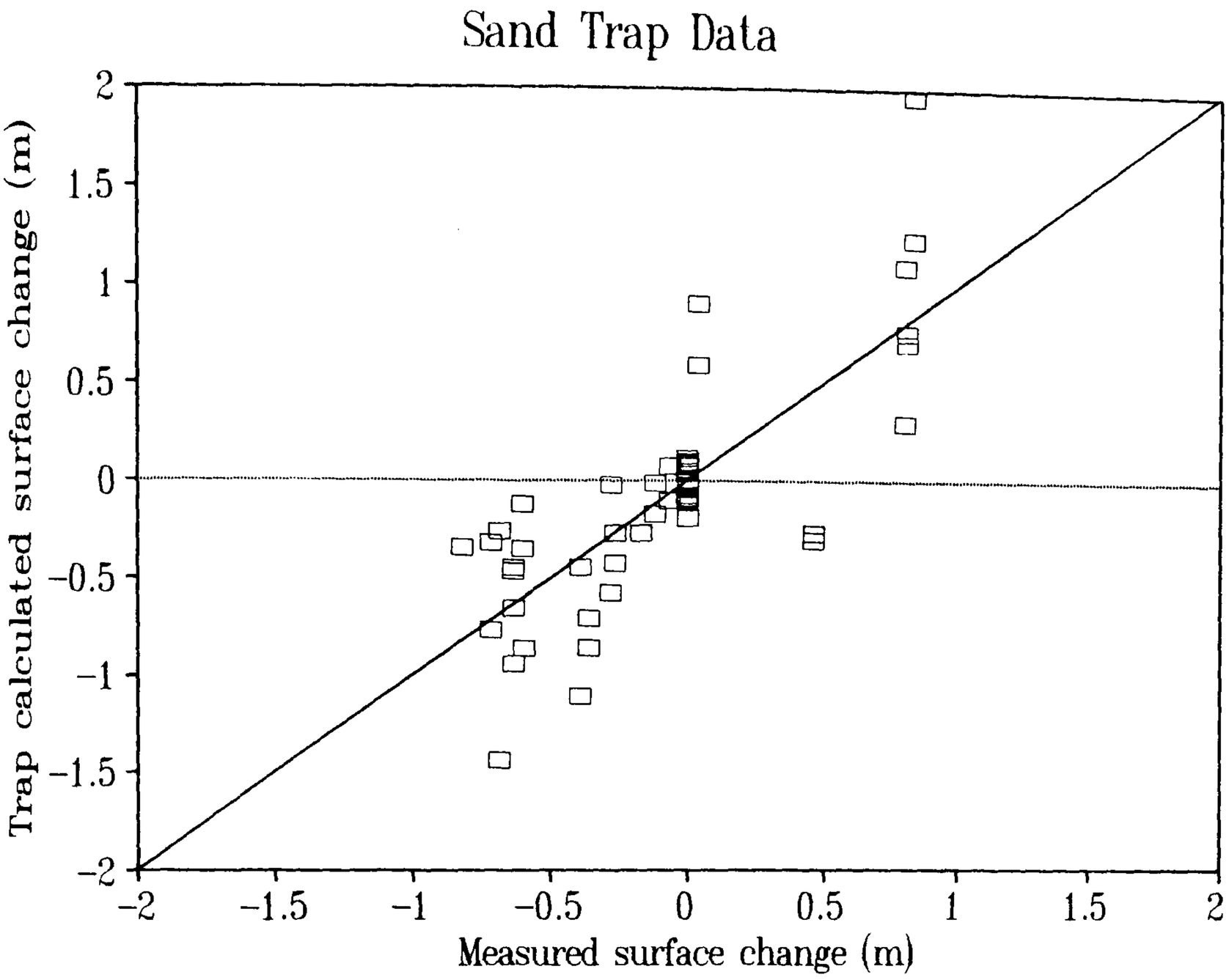

Figure 7.43 Comparison between measured and sand trap-calculated surface change on all three section lines (including all run data).

overestimate of erosion shown in Figure 7.41. The exclusion of this value in the statistical analysis is therefore reasonable. However, the fact that this point has to be ignored because of its considerable influence on the comparative statistics is testimony to the significant problems of accurately assessing shear velocity where a strong near-surface u_* gradient exists. Ignoring the data point improves the agreement between observed and predicted surface change in terms of standard deviation, sample variance and analysis of variance (X-wire^2_p in Table 7.2). The correlation coefficient is also improved. However, the regression line x-coefficient is reduced to 0.652 (further from unity than with the unadjusted data-set) and the agreement between the mean values also deteriorates.

There is good agreement between the measured values of surface change and those predicted from an amalgamation of the sand transport rate measurements (Figure 7.43). Table 7.2 shows similar values between the two variables for mean, standard deviation and sample variance and low values result from the analysis of variance. This is also reflected in the regression analysis with a high correlation coefficient (0.78), an x-coefficient close to unity and a small constant.

The difference of means test applied to the data did not reveal any significant differences between the observed and predicted values for any of the techniques (Table 7.2). It is therefore not considered to be a satisfactory procedure for comparing the ability of the techniques to predict the change in dune form.

However, the statistical significance of the x-coefficients and constants of the regression equations (presented in Table 7.2) were also tested using the technique described below:

i. Testing the significance of the x-coefficient

H_o, $ß = 0$; there is no relationship between predicted and observed surface change.

H_1, $ß \neq 0$; there is a relationship between predicted and observed surface change.

$t_{calc} = ß\text{-}ß^*/S_ß$, where ß is the x-coefficient, $ß^*$ is the expected value of ß (*i.e.* 0) and $S_ß$ is the standard deviation of the estimate of ß.

Where $t_{calc} > t_{crit}$ the null hypothesis can be rejected.

ii. Testing the significance of the intercept (constant)

H_o, $\alpha = 0$; the intercept does not differ significantly from zero.

H_1, $\alpha \neq 0$; the intercept term differs significantly from zero.

$t_{calc} = \alpha\text{-}\alpha^*/S_\alpha$, where α is the intercept of the regression line, α^* is the expected value (*i.e.* 0) and S_α is the standard deviation of the estimate of α.

Where $t_{calc} > t_{crit}$ the null hypothesis can be rejected.

Applying the above technique to the x-coefficient and constant terms presented in Table 7.2 revealed that none of the constants differed significantly from zero at the 95% confidence limit. Hence, each technique adequately predicts the observed surface change at low values. There is no significant offset, either positive or negative, from zero.

The significance tests on the x-coefficients from the regression equations also showed that a significant relationship existed between the observed and predicted values of surface change (at the 95% confidence limit) for all techniques except FLOWSTAR. For the FLOWSTAR predictions (even excluding the highly variant points from the data [FLOW*[2] in Table 7.2]) no significant relationship was found, and so it can be concluded that the FLOWSTAR model does not adequately predict the change in dune form.

7.5.3 Conclusion

All the techniques described in Table 7.2 adequately predict erosion on the windward slope of the dune and deposition between the crest and brink. However, it is quite clear that some techniques are better at predicting the observed changes on certain portions of the dune than others.

Statistical analysis has shown that FLOWSTAR is not capable of predicting surface change to a significant degree. The program is particularly poor at estimating actual surface change at the toe (where it estimates deposition) and the brink (where it estimates substantial erosion). The statistical power of its predictions is not substantially improved even when the over-predictions of erosion at the brink are ignored. This is due partly to the inability of the program to calculate airflow parameters in regions of reverse flow and partly due to the sensitivity of its u_*

predictions to small changes in surface topography (described in Chapter 3). It is likely that numerically smoothing the u_* predictions would increase the predictive power of the model by minimising the erratic nature of the erosion estimates on the windward slope.

The field technique is a good predictor of observed surface change on the windward slope of the dune. Considering the likely inadequacies of the field method of determining u_* (described in Chapter 6.3) this is a surprising result. However, the field technique seems unable accurately to predict observed sand transport rates or surface change upwind of or at the toe of the dune where, like FLOWSTAR, it estimates sand deposition. This is in contrast to the wind tunnel measurements. Neither the PWA nor cross-wire measurements in the wind tunnel predict deposition at the toe. Overall, in comparison with observed sand transport rates and surface change, the PWA measurements were most accurate in their predictions, particularly in the upwind and toe region of the dune. It should also be noted that the sand trap data also reliably predicted the observed surface change. This is particularly surprising as the transport rates were measured over a duration of only a few minutes. It is clear, however, that in the stable conditions of the field site, useful data can be collected in a very short period of time.

In terms of the dynamics of the dune, the results described above may have important consequences. Both the field and wind tunnel estimates were unable to predict the correct location of the point of maximum erosion on the steepest part of the windward slope with any consistency. This may be due, in part, to the inadequacy of the present sand transport equations where the slope of the surface may have a significant effect. Reliable empirical testing of the equations (with a range of grain diameters) is necessary to overcome this difficulty. Other sources of error may include slight differences in geometry and shape between the field dune and wind tunnel and FLOWSTAR models. However, the most notable and consistent feature of the results is the inability of the field and FLOWSTAR techniques accurately to predict the observed surface change upwind of and at the toe of the dune. Both techniques predict a piling up of sand at the toe and upwind. This prediction occurs on all three section lines and appears to be a progressive and distinct trend rather than an irregularity in the data. The consequences of this prediction for the dynamics of the dune are growth of the toe in an upwind direction (more than 60 m in a month as predicted by the field technique) and, as erosion is taking place on the windward slope, a downwind progression of the rest of the dune mass. Using the FLOWSTAR and field techniques a stretching of the dune would therefore be predicted. There is therefore a need to explain how, with a falling u_* (and calculated sand transport rate) upwind of the dune, observed sand transport rates maintained their level and no upwind deposition was observed.

7.6 The Upwind Anomaly Between Observed and Predicted Surface Change

The identification of a region of possible deposition in the basal region of sand dunes is not new. Several other investigations have recorded a zone of decreasing u_* and windspeed immediately upwind of sand dunes and low hills. However, the implications of the existence of this depositional zone for dune dynamics has so far been ignored and explanations for its occurrence have not been forthcoming.

Howard *et al.* (1977), in their comparison of simulated and observed erosion rates on a barchan dune in the Salton Sea, recorded the largest discrepancy between the two on the windward slope near the toe. The contradiction between the observed and simulated patterns of erosion was a large underestimate of erosion at the toe and a zone of strong deposition (not observed) along the base of the wing-tips. In fact, close inspection of the results of Howard *et al.* (1977) reveals that the 'simulated underestimation of erosion at the toe' was in fact quite strong deposition in a zone where none was observed in the field. Further evidence for the existence of this depositional zone is given in Tsoar (1985). Although it remains unmentioned in the text, all of Tsoar's results for the calculated amplification factor (A_z) over convex and triangular shaped hills reveal a considerable reduction below upwind levels near the toe. If it is assumed, as Tsoar does, that $q \propto u_*^3$ and that u_* is dependent upon wind velocity, then a reduction in wind velocity at the toe must be associated with deposition in this zone. In Tsoar's subsequent arguments concerning dune dynamics this fact is disregarded. In their study of airflow over Askervein hill Jensen & Zeman (1985) calculated a reduction in u_*^2 in front of the hill. They recognised the importance of this in terms of dune dynamics but did not discuss it at any length.

There are two ways in which the anomaly may be explained. First, there may be some factor not considered in this study which maintains sand transport upwind of the dune irrespective of the value of u_*. Such components may be due to a roughness change or systematic alteration in wind direction. Secondly, it might be assumed that the evaluations of u_* from the field technique and FLOWSTAR model are inadequate in their estimates of actual u_*. For this explanation to be acceptable a reason for the maintenance of u_* derived form the wind tunnel measurements must be shown.

7.6.1 Maintenance of Upwind Sand Transport Rates

Transport Rate Definition

The sand transport rate (q) equation (Equation 7.3) used in Chapter 7.4 for the calculation of the patterns of surface change only gives results for the *potential* rate of sand transport in given wind conditions. Hence it identifies the maximum amount of sand transport achievable and, as such, all subsequent calculations based on their estimates necessarily assume a sand-saturated wind. If the wind in the field were not sand-saturated then a fall in the *potential* rate of sand transport upwind of the dune (as identified in the field and FLOWSTAR predictions) would not necessarily result in a reduction in *actual* transport rate. Deposition of sand at the toe in these circumstances would only occur if the *potential* q dropped below *actual* q. Hence, a reduction in calculated q upwind of the dune would not necessarily result in deposition.

Figure 7.5, however, shows the *potential* q at the toe of the centre-line dropping below the *actual* q, but with no observed deposition. The magnitude of the *potential* transport rate depends to a large extent upon which equation is used in the calculation. In this study the equation used was the one which showed the highest statistical association with the *actual* transport rates (Equation 7.3), with the assumption that the wind during the study period was sand-saturated. An alternative equation might not have shown the *potential* q fall below the *actual* q because it might have predicted higher values of *potential* q. However, given the free supply of dry sand upwind of the dune and the consistency of the wind (described in Chapter 2) it seems reasonable to assume that the wind was indeed sand-saturated, in which case any fall in *potential* q should be accompanied by deposition.

The fact that the calculated sand transport rates only give estimates of maximum q is therefore not considered to be a valid explanation of the apparent anomaly between observed and predicted surface change upwind of and at the toe of the dune.

Wind Direction Fluctuations

The argument favoured by Howard *et al.* (1977) to explain the under-prediction of erosion at the toe of their study dune was the 30° fluctuation in wind direction measured across the centre-line. They reasoned that when the wind fluctuated from the line of symmetry the 'hump' of the dune on the centre-line windward slope would be more strongly eroded than in the case of a uni-directional wind, because of the additional exposure of the centre-line for skewed winds. Hence, calculations based on a uni-directional wind tended to under-predict total erosion in this region.

In the present study the maximum fluctuation of wind direction in sand driving conditions was only 15° and the Howard *et al.* argument does not explain the absence of sand deposition upwind of the dune, only an under-prediction of erosion on the windward slope. The fluctuation in wind direction around the centre-line of the dune is therefore not considered to be a satisfactory explanation of the anomaly between observed and predicted surface change upwind of and at the toe of the dune.

Roughness Changes

There is likely to be a change in roughness between the upwind gravel surface and the sand surface at the toe of the dune which could affect saltation mechanics and maintain transport rates in the basal region. This possibility was also considered by Howard *et al.* (1977). According to Bagnold (1941) the saltation height (and hence kinetic energy of the grains) is higher on a hard gravel surface than on a soft sand surface because the rebound of the grains is higher. On a sand surface more energy is dissipated on impact and so the rebound of the grains is reduced. Therefore, on the gravel surface upwind of the dune the saltation process is more efficient than on the dune surface. In addition, a surface yielding larger saltation heights introduces an additional drag on the wind velocity profile and therefore increases both z_0 and u_* (Antonia & Luxton, 1971; Rasmussen *et al.*, 1985; Anderson & Haff, 1991; McEwan & Willetts, 1991)).

The hypothesis, therefore, is that the reduction in u_* caused by a drop in wind velocity upwind of the dune is offset by an increase in u_* as a consequence of the roughness change between interdune and dune. Measurements by Antonia & Luxton (1971) showed that, at a smooth-to-rough transition, u_* increased to a peak at the point of change and then reduced to a new equilibrium level downwind. This argument would have relevance to the present study if the roughness change from dune to interdune was from smooth to rough, but a significant problem is correctly assessing the type of roughness change (smooth-to-rough or rough-to-smooth). This is particularly difficult in the dune environment because of the constantly changing slope and surface material. Available models which describe the effect of a roughness change on airflow parameters (Larsen *et al*, 1982) are based on measurements and theoretical analyses (*e.g.* Hunt & Simpson, 1982) far downwind of roughness transitions. The relevance of these models to roughness changes in a dune environment where conditions are constantly changing is therefore questionable. Additionally, the sensitivity of z_0 to surface characteristics (*e.g.* grain diameter, ripple spacing *etc.*) means that the nature of the roughness change is difficult to predict. Tsoar (pers. comm.) has found both types of roughness change between dune and interdune.

The difference in z_0 between the dune and interdune surface in the present study could not be accurately defined. This was because of the large statistical errors associated with defining the roughness from logarithmic velocity profiles (see Chapter 2.4 and Wilkinson 1983/1984). However, if it is assumed that the wind approaching the dune is sand-saturated and that the saltation efficiency on the gravel surface is higher than on the dune surface, then a roughness change from rough-to-smooth (in the wrong direction to explain the anomaly) is the likely scenario. In any case, the effect on downwind u_* due to a roughness change does not help to explain the maintenance of sand transport upwind of the roughness change (at least 60 m upwind according to Figure 7.13).

In addition to the change in u_* associated with a change in z_0 there is also a change in turbulence (Hunt & Simpson, 1982). Irrespective of the nature of the transition (smooth-to-rough or rough-to-smooth) a dominant process is that of production and dissipation of turbulent energy. Small, stationary, turbulent vortices perpendicular to the direction of flow may therefore exist at the rough-to-smooth transition at the toe of the dune, maintaining sediment transport. The size and strength of these potential vortices is not clear, but they are likely to be at the roughness length scale and hence too small to be of importance in maintaining sediment transport.

The data available from this study did not allow a competent examination of the effects of roughness change on sediment transport. However, considering the uncertainties surrounding the likely change in roughness between interdune and dune surfaces and the consequences for airflow parameters, further research into the subject is recommended.

Increased Turbulence

Increased turbulence around the toe region of the dune due to the increasing pressure gradient caused by the obstruction of the airflow by the dune mass was recorded in the wind tunnel measurements (Chapter 4). Both McEwen (1991) and Butterfield (1991) have stressed the importance of turbulence in transport rate modelling (although this has been contested by Lee (1987); Chapter 7.3). It seems plausible that the increased turbulence (and the associated peaks in u_*) upwind of and at the toe of the dune could be responsible for the maintenance of sand transport. The argument satisfies the apparent anomaly of a reduction in mean u_* coupled with the maintenance of sand transport rates upwind of and at the toe of the dune. However, the relationship between turbulence and sand transport rate has yet to be established (Butterfield, 1991) and the measurements taken in the field in the present study were not of sufficient resolution to allow an adequate investigation. It is suggested that further investigation into this aspect of the study would prove fruitful.

7.6.2 Errors Associated with the Assessment of shear velocity

The arguments above, which attempt to explain the anomaly at the toe of the dune by finding a process which maintains sand transport rate whilst also allowing a reduction in average u_*, ignore the fact that the wind tunnel measurements successfully described the observed surface changes in this region by not predicting a reduction in u_* (Chapter 7.5). If the wind tunnel assessments of u_* are relied upon, then no alternative transport mechanisms need be sought. The argument, therefore, is that the assessments of u_* in the field and from FLOWSTAR are inadequate in the toe region.

The field method used to evaluate u_* (Chapters 6.2 and 6.3) relies heavily on the assumption of z_0 constancy and wind velocity as the only determinant. Such a dependence will always result in a reduction in calculated u_* at the toe because of the divergence of streamlines and reduction in wind velocity in this region (Chapter 5.2). However, u_* is not controlled by wind velocity alone. In Chapter 4.4 the sensitivity of u_* to streamline curvature was discussed. It was emphasised that at the toe of a low hill or dune there is concave curvature , with turbulent structures of high velocity being conveyed into regions of lower velocity, thus causing flow instability and an increase in u_*. The additional stresses resulting from such curvature are not apparent in mean velocity profiles and so they are not accounted for in the field method of calculating u_*. Nor are such effects accounted for in the FLOWSTAR calculations. The additional stresses are, however, apparent in the Reynold's-stress profiles and so were evident in the cross-wire and PWA assessments of u_*.

Evidence for the existence of streamline curvature was provided in Chapter 4 by the graphs of the relationships between the Reynold's stress terms (usb and uwb). It was also noted that near-surface streamline curvature was present upwind of the dune (on the interdune flat) in response to the 'flexing' of airflow over the dune mass. Hence, unstable flow and additional curvature-induced shear stresses are likely to be present upwind of the dune, enabling the maintenance of sand transport rates despite a falling mean wind velocity. This was shown in Figures 7.14 to 7.16 which displayed the calculated sand transport rates for each of the techniques across the three section lines of the dune. In the toe region of the dune it was noted that the q predicted by the wind tunnel technique demonstrated no reduction upwind of or at the toe of the dune, in contrast to the field and FLOWSTAR estimates. In the crestal region of the dune and on the upper windward slope (Figures 7.14 to 7.16) it was noted that the wind tunnel q perturbations were smaller than both the field and FLOWSTAR perturbations. This might be explained by the presence of convex streamline curvature (described in Chapter 4), damping the wind tunnel measurements of u_* and hence providing smaller perturbations in q than the other techniques

which take no account of the convex curvature. The differences in sand transport rates predicted by each of the techniques can therefore be adequately explained by the presence or absence of flow curvature terms in the shear velocity calculation technique.

7.6.3 Conclusion

The hypothesis which best explains the anomaly at the toe of the dune involves streamline curvature as the mechanism that maintains shear stress at the surface. This hypothesis explains the lack of sand deposition upwind of the dune despite a reduction in wind velocity. It also explains the deposition predicted by the field and FLOWSTAR techniques in this region, for neither technique accounts for streamline curvature. The effects of streamline curvature may therefore have an important impact on dune dynamics which has so far been overlooked.

This conclusion does not detract from the possible importance of the other factors described above (*i.e.* roughness change, increased turbulence *etc.*). Indeed, they are likely to be closely inter-linked. For example, streamline curvature encourages the downward movement of high velocity turbulent parcels in the vertical profile. Therefore the increased turbulence measured at the toe of the dune in the wind tunnel might also be a response to concave streamline curvature. The streamline curvature hypothesis could be tested with more detailed Reynold's stress measurements in both the field and wind tunnel working in streamline (rather than cartesian) co-ordinates. From such measurements the degree of curvature apparent in the flow could be calculated and the resulting additional surface shear stresses determined. Assuming that streamline curvature is important to the morphological maintenance of the dune then a new model of dune dynamics can be devised which takes its effects into account.

7.7 A New Model of Dune Dynamics

It has been shown that streamline curvature might contribute additional shear stresses to the flow over the study dune (Chapters 4.4 and 7.6). These stresses (additional to those supplied by flow acceleration) appear to have an effect on sand transport rates and are therefore important to the dynamics of the dune. In Chapter 4.4 it was argued that concave streamline curvature and streamwise acceleration both increased shear stress (relative to mean values), whilst convex curvature and deceleration had the opposite effect (Finnigan *et al.*, 1990). A new model of dune dynamics can therefore be developed in which an equilibrium is reached between the form of

the windward slope, the degree of streamline curvature and the degree of streamwise acceleration.

Figure 7.44 shows a two-dimensional representation of a crest-brink separated dune, similar to the flank section lines on the study dune, in an assumed unidirectional and sand-saturated wind. The windward slope is divided into three geomorphologically and aerodynamically distinct zones. The following discussion explores the relationships between form and process within each of these zones.

Zone A

This zone comprises the upwind interdune and concave toe region of the dune. The upwind portion of this region is characterised by flow deceleration and concave flow curvature. The upstream flow is decelerated because the mass of the dune induces an adverse (increasing) pressure gradient and the streamlines upwind of the dune are curved as an initial response to the deflection of flow over the windward slope. In terms of shear stress generation these two processes act in opposition. Flow deceleration decreases shear stress and concave flow curvature increases it. The dynamics in this zone must therefore be reflected in a balance between these two opposing forces.

Deposition would occur at the toe and upwind of the dune if the angle of the windward slope were steep enough for flow separation to occur at the base. Such separation is characterised by a region of intense streamwise deceleration which would significantly reduce the shear stress and sand transport capacity of the wind. The positive (shear stress increasing) effects of concave curvature would be insignificant in this region because the streamline pattern would be disrupted by the separation. The overall shear stress budget (the balance between the processes which increase and decrease shear stress) would therefore become negative (*i.e.* decreasing) due to flow deceleration and hence deposition would occur.

Once deposition had reached the extent where flow separation no longer occurred in Zone A and the angle of the windward slope had been reduced to a value comparable to that of the angle of concave streamline curvature then an equilibrium would be reached. In this case additional deposition would be inhibited by the extra stresses present as a result of concave curvature and excessive erosion would be arrested by the over-steepening of the slope and subsequent flow deceleration.

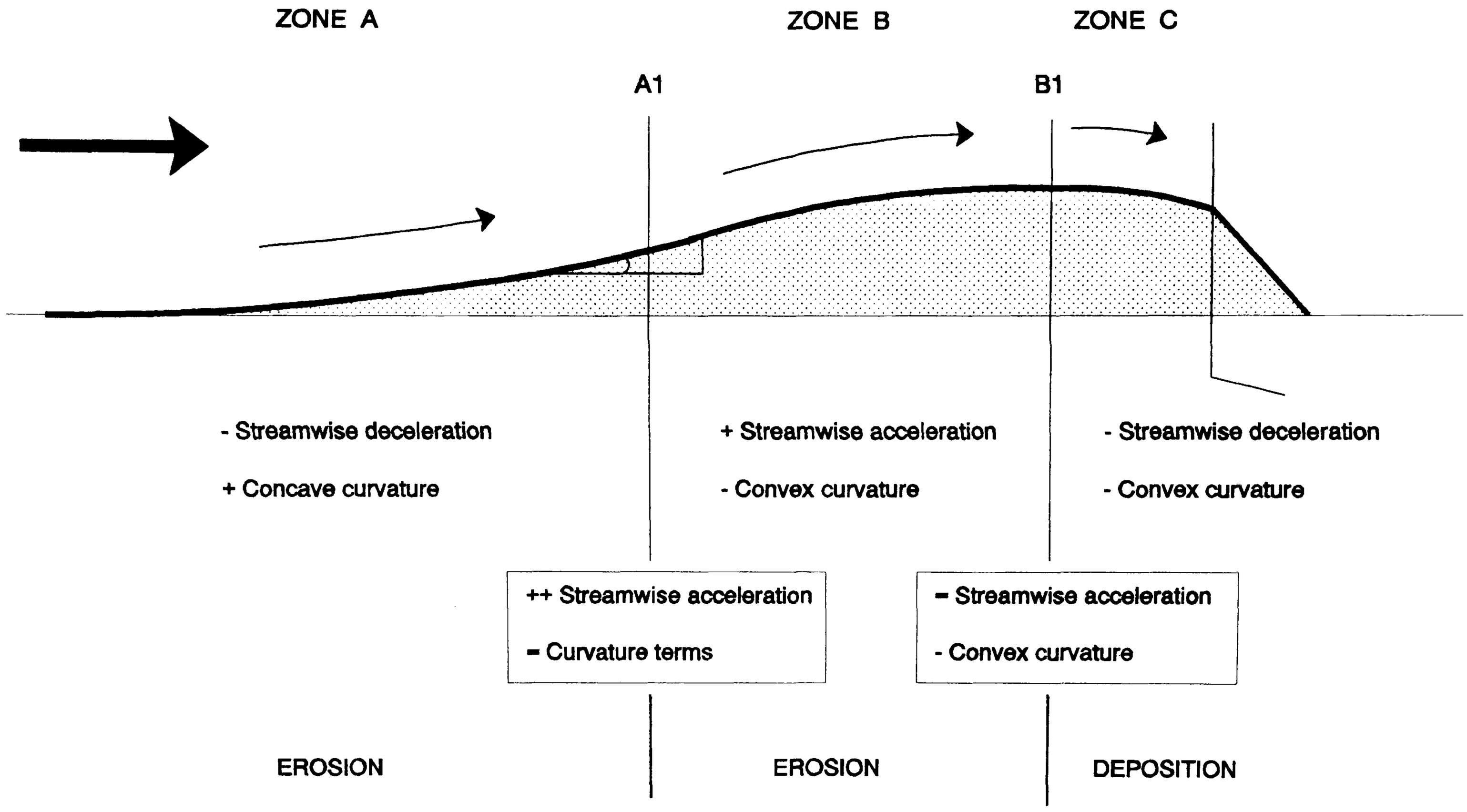

Figure 7.44 A new model of dune dynamics based on an equilibrium between slope morphology and the effects on shear stress production of stream-wise acceleration and streamline curvature.
(-) = decreasing (negative) effect on shear stress;
(+) = increasing (positive) effect on shear stress;
(=) = no effect on shear stress.

Flow deceleration is at its most extreme at the toe itself, so downwind of this point streamwise acceleration and concave curvature effects operate in concert, both increasing shear stress. Overall, this makes the concave toe region of the dune a zone of erosion. Hence, it migrates downwind with the rest of the dune at an angle which represents an equilibrium between the effects of streamwise deceleration, streamwise acceleration and concave streamline curvature.

Zone B

This zone comprises the convex portion of the windward slope between the point of maximum slope (A1) and the crest (B1). It is characterised by streamwise acceleration and convex streamline curvature. As in Zone, A the two processes are operating in opposition, but this time in the opposite way. Streamwise acceleration promotes an increase in shear stress whilst convex curvature encourages flow stabilisation and a decrease in shear stress.

At the point of maximum slope (A1) the curvature term passes from concave to convex. So, at A1 itself, streamline curvature is in a transitional state and has no effect on the shear stress. In contrast, streamwise acceleration reaches a maximum at this point. The overall shear stress budget is therefore strongly positive (increasing) and this is reflected by the fact that maximum erosion is found here.

On the convex slope in Zone B streamline curvature is also convex, inhibiting the production of shear stress. However, this is offset by an increase in shear stress caused by streamwise acceleration, resulting in erosion of the windward slope. As the crest is reached, flow acceleration is reduced and the importance of the convex curvature becomes relatively more important. Therefore, at the rounded crest (B1) on the profile shown in Figure 7.44, the tendency is for deposition to take place. This is because flow acceleration is negligible at the crest so no stresses caused by this process are available. However, the damping effect of convex streamline curvature is still operational as the streamlines flex around into the crest-brink separated region (Zone C). The stabilisation of the flow at B1 reduces the shear stress and deposition occurs at the crest. This hypothesis allows for deposition at the crest until the stabilising effect of streamline curvature is terminated. This would occur once the crest of the dune had built up to a sharp triangular shape with no crest-brink separation. In this case the absence of a flexing of the streamlines into the crest-brink separated zone would reduce the effect of the curvature at the crest and any excess deposition would be offset by erosion caused by streamwise acceleration.

Zone C

Between the crest and brink the effects of streamwise acceleration and streamline curvature act in unison. The flow is decelerated downwind of the crest and the decreases in shear stress consequent on this are bolstered by the negative (shear stress reducing) effects of strong convex curvature. The crest-brink region is therefore characterised by a strong reduction in shear stress and significant deposition. With this model the crest-brink regions of dunes would always be exemplified by sand deposition and vertical height gain. The distance between the crest and brink would therefore always be decreasing and the angle of the crest-brink slope would continually steepen. This growth would continue until a sharp-crested dune was generated in which no crest-brink separation occurred.

Conclusion

The model of dune dynamics presented here is attractive because it not only explains the lack of deposition at the toe of the dune and maximum erosion on the steepest part of the windward slope, which is necessary for an equilibrium dune form to develop, but it also allows for deposition at the crest. This is something that has long been a problem when trying to explain dune dynamics merely in terms of flow acceleration (Lancaster, 1985, 1987; Watson, 1987). For, if flow acceleration continues right to a dune crest, then observed deposition and height growth at the crest cannot be explained. The flow curvature hypothesis allows for such growth on round-topped (crest-brink) separated dunes. It follows that the model predicts an equilibrium dune form as one which has a sharp brink and no crest-brink separation.

The model of a sharp-crested dune being the equilibrium form adopted by transverse dunes is not, however, entirely appropriate for the dune investigated in this study. The discussion concerning the movement of the dune as measured by erosion pins over a 28-day period (Chapter 2.4.2) revealed that the right flank section line progressed downwind without significantly altering in form, despite being crest-brink separated. If the curvature model were applicable then one would have expected the crest and crest-brink slope on this flank to have gained in height. In contrast, the left flank developed as predicted by the model by increasing in height at the crest to a more sharp crested form. The centre-line, which was sharp-crested with no crest-brink separation, also migrated as predicted with no significant change in form. It should be stated, however, that the model described above is the result of a simple analysis. It makes many assumptions. In particular, it is assumed that there is no lag between the effects of streamwise acceleration (or deceleration) on shear stress and the effects of streamline curvature. In Chapter 4.4 it was noted that there was a delay between the onset of streamline curvature and its effect on shear stress. This is in contrast to the immediate effects of flow acceleration or

deceleration. Flow curvature can therefore only partly be responsible for the maintenance of shear stress upwind of and in the toe region of the dune. Other factors which may sustain shear stress, but for which no allowance is made in the current model, include the effect of a changing effective windward slope morphology due to a change in wind direction, the three-dimensional nature of the dune and changes in surface roughness. Despite these difficulties and omissions, the curvature model does provide a starting point from which further investigations can be commenced.

CHAPTER 8 SUMMARY AND CONCLUSIONS

Data concerning airflow structure over a barchan sand dune have successfully been collected using three techniques of study; field experiments, mathematical modelling and wind tunnel modelling.

All three techniques demonstrated similar assessments of velocity, confirming the acceleration of flow up the windward slope and deceleration between the crest and brink on the flanks. The maximum velocity was found to be in the crest region. Significant deceleration of flow was also found upwind of the dune, reaching a maximum in the region of the toe. The mathematical model (FLOWSTAR) failed accurately to simulate velocity at the brink of the dune, where it severely over-predicted the magnitude of velocity. This failure was due to the inability of the model to assess airflow in the region of reverse flow in the lee of the dune.

All three techniques showed that the acceleration of flow up the windward slope caused the velocity profile to deviate from its upwind log-linear character on the windward slope and at the crest and brink. To a lesser degree, deviations from a log-linear profile were also recorded upwind of the dune and in the region of the toe where airflow was decelerated. The maximum flow acceleration and deceleration (and hence the deviations of the velocity profile from a log-linear character) were found to occur within the inner-layer. However, the depth of the inner-layer could not be consistently recognised from the height of the maximum flow acceleration (δs_{max}), as this was found to vary in height across the windward slope. A more substantial investigation of the inner-layer depth could have been achieved if vertical velocity profiles had extended to heights above 1.5 m in the field.

A better characterisation of the depth of the inner-layer was provided by the wind tunnel measurements and FLOWSTAR predictions of Reynold's stress. Despite the fact that the simulated boundary layer in the wind tunnel was not fully rough (hence allowing measurements within the inner-layer), the measurements of velocity and Reynold's stress were comparable to previous studies of flow over hills. The wind tunnel measurements and FLOWSTAR simulations showed a strong shear stress gradient close to the surface. This gradient appeared to reach a minimum at a height above the surface comparable to the depth of the inner-layer, confirming the re-analysis of Hunt *et al.* (1988a). The horizontal development of Reynold's stress across the windward slope of the dune was therefore characterised by an increase in stress toward the crest within the inner-layer, and a decrease toward the crest above the inner-layer, with an opposite progression between the crest and brink. This progressive development was not easily recognised

from the near-surface FLOWSTAR predictions because, like other mathematical models for turbulent flow, they appear to be very sensitive to small-scale terrain irregularities, resulting in a 'noisy' data-set. Shear stress at the brink was also poorly predicted by FLOWSTAR. It is likely that improved near-surface predictions could be achieved were the FLOWSTAR terrain data 'smoothed' prior to testing.

The acceleration of flow up the windward slope of the dune and the identification of a non-log-linear velocity profile (manifested in a strong near-surface shear stress gradient) made the calculation of shear velocity from the field data very difficult. Regression analysis on vertical velocity profiles was found to be unsatisfactory and the Owen (1964) technique suffered from low data resolution and a lack of field validation. The Bagnold / Mulligan approach to shear velocity calculation provided the most reasonable results, despite theoretical misgivings concerning the constancy of z_0 and the apparent absence of a velocity-ray focus.

Comparisons of shear velocity from the three techniques (field, FLOWSTAR and wind tunnel) revealed significant differences, particularly upwind of the dune and in the toe region. Both the field evaluations of u_* (using the Bagnold / Mulligan approach) and the FLOWSTAR predictions exhibited a reduction in u_* upwind of and at the toe of the dune. This was in contrast to the u_* measured in the wind tunnel, using a near-surface pulse-wire probe, which maintained upwind levels before increasing up the windward slope. All three techniques showed a maximum u_* in the crest region and a reduction between crest and brink (although FLOWSTAR vastly over-predicted u_* at the brink). Evidence from the wind tunnel measurements of Reynold's stress suggested that the maintenance of upwind u_* might be a result of additional stresses in the region created by concave (unstable) streamline curvature. Supporting evidence was provided by calculations of upwind streamline angle, the recognition of the fact that neither the field or FLOWSTAR techniques acknowledged stresses imposed by curvature, and the identification of the steepest part of the windward slope (where it changes from concave to convex) as being important to the development of rate-of-change of u_*.

From the evaluations of u_* from each technique it was possible to calculate potential sand transport and erosion and deposition and to compare these predictions with measurements of actual sand transport (using sand traps) and observed surface change (from erosion pin measurements). All three techniques generally correctly predicted erosion on the windward slope of the dune and deposition between the crest and brink. However, the wind tunnel measurements (using the pulse-wire probe) provided the best estimate of observed surface change because both the field and FLOWSTAR techniques incorrectly predicted deposition upwind of and at the toe

of the dune. Due to the over-prediction of u_* at the brink, FLOWSTAR also massively over-predicted erosion in this region. It was shown that FLOWSTAR was unable to predict observed surface change to a statistically significant degree.

The apparent anomaly of declining u_* and sand transport upwind of the dune (as predicted by the field and FLOWSTAR techniques) and yet no observed deposition in the field, was best explained by the existence of concave streamline curvature maintaining shear stress but not being registered by the field technique or FLOWSTAR prediction. From the recognition of streamline curvature as having a possibly important effect on the airflow structure over the dune, a new (2-D) model of dune dynamics was developed, incorporating its influence. The new model, relying on the development of an equilibrium between windward slope morphology, streamline curvature and streamwise acceleration, explains the lack of deposition at the toe, the maximum erosion on the steepest slope and the possibility of deposition at the crest, allowing the dune to grow. However, the equilibrium form predicted by the new model is that of a sharp-crested dune and it does not entirely explain the observed morphology of the study dune.

From these observations several points can be noted:

1. There is no adequate method currently available for evaluating shear stress over a sand dune from wind velocity measurements in a field situation.

2. The inability of FLOWSTAR to account for highly turbulent regions of reverse flow and its sensitivity to small-scale terrain irregularities restrict its use for prediction of sand dune dynamics.

3. Valuable results concerning airflow over dunes can be obtained from wind tunnel measurements where the obligation for a fully-rough boundary layer has been relaxed.

4. A significant portion of the total shear stress at the toe and crest of the dune might be provided by streamline curvature.

5. The windward slope of the dune may be in a delicate equilibrium with shear stresses imposed by streamline curvature and streamwise acceleration.

For further progress to be made it is necessary to be able accurately to assess the short term fluctuating shear stress and sand transport in the field. This would enable confirmation of the

curvature hypothesis and accurate determination of the relationship between shear stress and sand transport. Such shear stress measurements might be accomplished with the development of a suitably armoured cross-wire probe. This would permit the measurement of Reynold's stresses very close to the surface within the saltation layer and perhaps lead to more accurate assessments of roughness change over the dune and between the dune and inter-dune. However, the calibration and use of such a probe could prove problematic in the constantly changing dune environment. Short-term sand transport measurements may also be possible over dunes with the new generation of isokinetic traps and development of infra-red and sonic technology. Such technological advances might allow the true nature of the shear stress distribution over sand dunes to be interpreted.

The FLOWSTAR program could be improved in two ways. First, the effect of the reverse flow region on the upwind predictions at the brink could be falsely constrained. This might improve the predictions of airflow on the windward slope without the necessity of having to predict separated flow. However, statistical analysis in this study suggested that no significant improvement was made by disregarding the brink predictions. Secondly, flow curvature terms could be incorporated into the model to improve the upwind and toe region predictions of velocity and shear stress. This might also act as a test for the flow curvature hypothesis by allowing a comparison with the wind tunnel measurements of surface shear stress.

In the constant flow conditions of the wind tunnel it may also be possible to evaluate the effect of the three-dimensionality of the barchan dune on shear stress generation and modulation. Only cursory measurements of airflow deflection around the dune have been accomplished in the present study and no attempt has been made to explain the 3-D shape of the dune. Near-surface cross-wire and pulse-wire measurements of shear stress across the whole of the windward slope might clarify the effects of the measured flow deflection at the toe and convergence at the brink. Such measurements may elucidate the role of vortex stretching on shear stress generation, whereby spanwise roll vortices induce additional surface stresses as they are stretched around the dune mass.

The merging of the three techniques of study (field, mathematical model and wind tunnel) has proven valuable in this investigation of dune dynamics. The similarities and differences between the results have prompted the development of a new model of dune dynamics which, whilst not comprehensively applicable, provides a basis from which other studies may be instigated. The question remains, however, as how best to study dune dynamics. The field technique suffers from constantly changing wind patterns and dune morphology and inadequate methods of sand

transport and shear stress evaluation. Mathematical modelling is, as yet, unable to account for regions of separated flow and is liable to erratic predictions caused by small-scale terrain irregularities. The wind tunnel technique is hounded by problems of scale and lack of sediment in transport. It is suggested that FLOWSTAR requires more empirical testing before it is relied upon accurately to predict dune dynamics. However, with advances in probe technology and better understanding of the relationships between sand surfaces and near-surface airflow and sand transport, valuable research could be accomplished in the field and wind tunnel environments.

BIBLIOGRAPHY

Allen, J.R.L. (1968) *Current Ripples: their relation to patterns of water and sediment motion.* North Holland, Amsterdam.

Allen, J.R.L. (1970) A quantitative model of climbing ripples and cross laminated deposits. *Sedimentology*, **14**, 5-26.

Allen, J.R.L. (1974) Reaction, relaxation and lag in natural sedimentary systems: general principles, examples and lessons. *Earth Science Reviews*, **10**, 263-342.

Anderson, R.S. & Hallet, B. (1986) Sediment transport by wind: toward a general model. *Geological Society of America Bulletin*, **97**, 523-535.

Anderson, R.S. & Haff, P.K. (1988) Simulation of eolian saltation. *Science*, **241**, 820-823.

Anderson, R.S. & Haff, P.K. (1991) Wind modification and bed response during saltation of sand in air. *Acta Mechanica [Suppl.]*, **1**, 21-51.

Anderson, R.S., Sϕrensen, M. & Willetts, B.B. (1991) A review of recent progress in our understanding of aeolian sediment transport. *Acta Mechanica [Suppl.]*, **1**, 1-19.

Antonia, R.A. & Luxton, R.E. (1971) The response of a turbulent boundary layer to a step change in surface roughness. *Journal of Fluid Mechanics*, **48(4)**, 721-761.

Bagnold, R.A. (1941) *The Physics of Blown Sand and Desert Dunes*. Methuen, London.

Bagnold, R.A. (1956) The flow of cohesionless grains in fluids. **249**, 29-297.

Belly, P.Y. (1964) *Sand Movement by Wind.* U.S. Army Coastal Engineering Research Centre, Technical Memo 1.

Berg, N.H. (1983) Field evaluation of some sand transport models. *Earth Surface Processes & Landforms*, **8**, 101-114.

Besler, H. (1975) Messungen zur Mobilitätvon Dünensanden am Nordrand der Dünen-Namib (SüdwestAfrika). *Mitteilungen der Geographischen Geselschaft, Würzburg*, **43**, 135-147.

Besler, H. (1980) Die Dünen-Namib: Entstehung und Dynamik eines Ergs. *Stuttgarter Geographische Studien*, **96**.

Blackader, A.B. (1962) The vertical distribution of wind and turbulent exchange in a neutral atmosphere. *Journal of Geophysical Research*, **67(8)**, 3095-3102.

Bradbury, L.J.S. & Castro, I.P. (1971) A pulse wire technique for turbulence measurements. *Journal of Fluid Mechanics*, **49**, 657-691.

Bradley, E.F. (1980) An experimental study of the profiles of wind speed, shearing stress and turbulence at the crest of a large hill. *Quarterly Journal Royal Meteorological Society*, **106**, 101-123.

Bradshaw, P. (1971) *An Introduction to Turbulence and its Measurement.* Pergamon, Oxford.

Britter, R.E., Hunt, J.C.R. & Richards, K.J. (1981) Air flow over a two-dimensional hill: studies of velocity speed-up, roughness effects and turbulence. *Quarterly Journal Royal Meteorological Society*, **107**, 91-110.

Burkinshaw, J.R. & Rust, I.C. (1992) Aeolian dynamics on the windward slope of a reversing transverse dune, Alexandria coastal dunefield, South Africa. *Earth Surface Processes and Landforms* (in press).

Businger, J.A., Wyngaard, J.C., Izumi, Y. & Bradley, E.F. (1971) Flux-profile relationships in the atmospheric surface layer. *Journal of Atmospheric Sciences*, **28**, 181-189.

Butterfield, G.R. (1991) Grain transport rates in steady and unsteady turbulent airflows. *Acta Mechanica [Suppl.]*, **1**, 123-134.

Carruthers, D.J., Hunt, J.C.R & Weng, W.S. (1988) A computational model of stratified turbulent airflow over hills - FLOWSTAR I. *In* Zanetti (ed) *Computer Techniques in Environmental Studies*. Springer, Berlin.

Castro, I.P. (1979) Relaxing wakes behind surface-mounted obstacles in rough wall boundary layers. *Journal of Fluid Mechanics*, **93**, 631-659.

Castro, I.P. (1984) Modern developments in turbulence studies. *Physics in Technology*, **15(3)**, 143-163.

Castro, I.P. (1986) The measurement of Reynold's stresses. *Encyclopedia of Fluid Mechanics*. Gulf, Houston.

Castro, I.P. (1991) Pulsed wire anemometry. Paper presented at *Second World Conference on Experimental Methods in Heat Transfer, Fluid Mechanics and Thermodynamics, Dubrovnik, 1991.*

Castro, I.P. & Snyder, W.H. (1982) A wind tunnel study of dispersion from sources downwind of three-dimensional hills. *Atmospheric Environment*, **16(8)**, 1869-1887.

Castro, I.P. & Dianat, M. (1990) Pulsed wire velocity anemometry near walls. *Experiments in Fluids*, **8**, 343-352.

Castro, I.P., Dianat, M. & Bradbury, L.J.S. (1987) The pulsed wire skin-friction measurement technique. *Turbulent Shear Flows*, **5**, 278-290.

Cekirge, H.M., Gunay, N. & Fraga, R.J. (1982) Movements of sand dunes: i. two-dimensional model. *Mathematical Modelling*, **3**, 371-384.

Cekirge, H.M., Fraga, R.J. & Gunay, N. (1983) Movements of sand dunes: ii. The application of airfoil theory. *Mathematical Modelling*, **4**, 301-306.

Cekirge, H.M., Fraga, R.J., Lehr, W.J. & Gunay, N. (1984) Movements of sand dunes: iii. Erosion due to geostrophic wind. *Mathematical Modelling*, **5**, 161-169.

Cermak, J.E. & Arya, S.P.S. (1970) Problems of atmospheric shear flow and their laboratory simulation. *Boundary-Layer Meteorology*, **1**, 40-60.

Chapman, D.M. (1990) Aeolian sand transport - an optimised model. *Earth Surface Processes and Landforms*, **15**, 751-760.

Chappell, A. (1991) *The implications of grain-size variations for sand transport mechanisms over a barchan sand dune in Oman.* Unpublished BSc. dissertation, Coventry Polytechnic, Coventry.

Charnock, H. (1955) Wind stress on a water surface. *Quarterly Journal Royal Meteorological Society*, **81**, 639-640.

Chepil, W.S. (1945) Dynamics of wind erosion: 1. Nature of movement of soil by wind. *Soil Science*, **60**, 305-320.

Chepil, W.S. (1959) Equilibrium of soil grains at the threshold movement by wind. *Proceedings of the Soil Science Society of America*, **23**, 422-428.

Chepil, W.S. & Woodruff, N.P. (1963) The physics of wind erosion and its control. *Advances in Agronomy*, **15**, 211-302.

Chiu, T.Y. (1972) Sand transport by wind. *Department of Coastal and Oceanographic Engineering, University of Florida, Technical Report, TR-040.*

Cockerell, D.J. & Lee, B.E. (1966) Production of shear profiles in a wind tunnel by cylindrical rods placed normal to the stream. *Journal of the Royal Aeronautical Society*, **3**, 724-736.

Cook, N.J. (1977) *Wind Tunnel Simulation of the Adiabatic Atmospheric Boundary Layer by Roughness, Barrier and Mixing-Device Methods.* Building Research Establishment, Paper 6, Department of the Environment.

Counihan, J. (1969) An improved method of simulating an atmospheric boundary layer in a wind tunnel. *Atmospheric Environment*, **3**, 197-214.

Counihan, J. (1970) Further measurements in a simulated atmospheric boundary layer. *Atmospheric Environment*, **4**, 259-275.

Cowdrey, C.F. (1967) *A Simple Method for the Design of Wind-Tunnel Velocity-Profile Grids.* National Physical Laboratory Aerodynamics Division, Aero Note 1055

Crofts, R. (1971) Sand movement in the Emlyberg dunes, Co. Mayo. *Journal of Irish Naturalists*, **17**, 132-136.

Davenport, A.G. & Isyumov, N. (1967) The application of the boundary layer wind tunnel to the prediction of wind loading. *Wind Effects on Buildings and Structures*, University of Toronto Press.

Dyer, A.J. (1974) A review of flux-profile relationships. *Boundary-Layer Meteorology*, **7**, 363-372.

Dyer, K. (1986) *Coastal and Estuarine Sediment Dynamics.* Wiley, Chichester.

Elder, J.W. (1959) Steady flow through non-uniform gauzes. *Journal of Fluid Mechanics*, **5(3)**, 355-371.

Finnigan, J.J., Raupach, M.R., Bradley, E.F. & Aldis, G.K. (1990) A wind tunnel study of turbulent flow over a two-dimensional ridge. *Boundary-Layer Meteorology*, **50**, 277-317.

Fryrear, D.W., Stout, J.E., Hagen, L.J. & Vories, E.D. (1991) Wind erosion: field measurement and analysis. *Transactions of the American Society of Agricultural Engineers*, **34(1)**, 155-160.

Gerety, K.M. (1985) Problems with determination of u_* from wind-velocity profiles measured in experiments with saltation. *Proceedings of International Workshop on Physics of Blown Sand*, Memoirs **8**, Department of Theoretical Statistics, Aarhus University, Denmark.

Gillette, D. & Goodwin, P.A. (1974) Microscale transport of sand-sized soil aggregates eroded by wind. *Journal of Geophysical Research*, **79(27)**, 4080-4084.

Goh, C.B. (1981) *Blockage Removal in Topographic Modelling*. Unpublished PhD. thesis, University of Auckland.

Gong, W. & Ibbetson, A. (1989) A wind tunnel study of turbulent flow over model hills. *Boundary-Layer Meteorology*, **49**, 113-148.

Greeley, R. (1986) Aeolian landforms: laboratory simulations and field studies. *In* Nickling, W.G. (ed) *Aeolian Geomorphology, Proceedings of the 17th Annual Binghampton Symposium, September 1986*, 195-211.

Greeley, R. & Iversen, J.D. (1985) *Wind as a Geological Process*. Cambridge University Press, Cambridge.

Handford, M. & Bradshaw, P. (1989) The pulsed wire anemometer. *Experiments in Fluids*, **7**, 125-132.

Hanna, S.R. (1969) The formation of longitudinal sand dunes by large helical eddies in the atmosphere. *Journal of Applied Meteorology*, **8**, 874-883.

Hardisty, J. & Whitehouse, R.J.S. (1988) Evidence for a new sand transport process from experiments on Saharan dunes. *Nature*, **332**, 532-534.

Havholm, K. & Kocurek, G. (1988) A preliminary study of the dynamics of a modern draa, Algodunes, southeastern California. *Sedimentology*, **35**, 649-669.

Hesp, A.P. (1983) Morphodynamics of incipient foredunes in N.S.W., Australia. *In* Brookfield, M.E. & Ahlbrandt, T.S. (eds) *Developments in Sedimentology*, Elsevier, New York.

Hesp, A.P. (1988) A review of biological and geomorphological processes involved in the initiation and development of incipient foredunes. *In* Gimingham, C.H., Ritchie, W., Willetts, B.B. & Willis, A.J. (eds) *Coastal Sand Dunes, Proceedings of the Royal Society of Edinburgh*, **96(B)**, 181-202.

Hesp, P., Illenberger, W., Rust, I., McLachlan, A. & Hyde, R. (1989) Some aspects of transgressive dunefield and transverse dune geomorphology and dynamics, south coast, South Africa. *Zeitschrift fur Geomorphologie [Suppl. Bd.]*, **73**, 111-123.

Högström, U. (1988) Non-dimensional wind and temperature profiles in the atmospheric surface layer: a re-evaluation. *Boundary-Layer Meteorology*, **42**, 55-78.

Horikawa, K. & Shen, H.W. (1960) Sand movement by wind action - on the characteristics of sand traps. *U.S. Army Corps of Engineers, Beach Erosion Board, Technical Memo*, **19**.

Howard, A.D. & Walmsley, L. (1985) Simulation model of isolated dune sculpture by wind. *Proceedings of International Workshop on Physics of Blown Sand*, Memoirs **8**, Department of Theoretical Statistics, Aarhus University, Denmark.

Howard, A.D., Morton, J.B., Gad-el-Hak, M. & Pierce, D.B. (1977) *Simulation Model of Erosion and Deposition on a Barchan Dune*. NASA Contractor Report, CR-2838, Washington, D.C.

Hsu, S.A. (1971) Wind stress criteria in eolian sand transport. *Journal of Geophysical Research*, **76(36)**, 8684-8686.

Hsu, S.A. (1973) Computing eolian sand transport from shear velocity measurements.*Journal of Geology*, **81**, 739-743.

Hunt, J.C.R. & Simpson, J.E. (1982) Atmospheric boundary layers over non-homogeneous terrain. *In* Plate, E.J. (ed) *Engineering Meteorology*. Elsevier, Amsterdam.

Hunt, J.C.R. & Nalpanis, P. (1985) Saltating and suspended particles over flat and sloping surfaces i. modelling concepts. *Proceedings of International Workshop on Physics of Blown Sand*, Memoirs **8**, Department of Theoretical Statistics, Aarhus University, Denmark.

Hunt, J.C.R., Leibovich, S. & Richards, K.J. (1988a) Turbulent shear flows over low hills. *Quarterly Journal Royal Meteorological Society*, **114**, 1435-1470.

Hunt, J.C.R., Richards, K.J. & Brighton, P.W.M. (1988b) Stably stratified shear flow over low hills. *Quarterly Journal Royal Meteorological Society*, **114**, 859-886.

Jackson, P.S. (1977) A theory for flow over escarpments. *In* Eaton, K.J. (ed) *Wind Effects on Buildings and Structures*. Cambridge University Press, Cambridge.

Jackson, P.S. (1979) *The Influence of Local Terrain Features on the Site Selection for Wind Generating Systems*. Report BLWT-1-1979, University of Western Ontario, Ontario, Canada.

Jackson, P.S. & Hunt, J.C.R. (1975) Turbulent wind flow over a low hill. *Quarterly Journal Royal Meteorological Society*, **101**, 929-955.

Jensen, N.O. & Zeman, O. (1985) Perturbations to mean wind and turbulence in flow over topographic forms. *Proceedings of International Workshop on Physics of Blown Sand*, Memoirs **8**, Department of Theoretical Statistics, Aarhus University, Denmark.

Jensen, J.L., Rasmussen, K.R., Sϕrensen, M. & Willetts, B.B. (1984) The Hanstholm experiment 1982: sand grain saltation on a beach. *Research Report No. 125, Department of Theoretical Statistics, University of Aarhus*.

Jones, J.R. & Willetts, B.B. (1979) Errors in measuring uniform aeolian sand flow by means of an adjustable trap. *Sedimentology*, **26**, 463-468.

Kadib, A.A. (1965) A function of sand movement by wind. *University of California Technical Report, HEL-2-12*.

Kaganov, E.I. & Yaglom, A.M. (1976) Errors in windspeed measurements by rotation anemometers. *Boundary-Layer Meteorology*, **10**, 229-244.

Kawamura, R. (1951) Study of sand movement by wind (in Japanese). *Report of the Institute of Science and Technology, University of Tokyo*. Translated to English in *NASA Technical Transactions, F14*.

Kay, S. (1988) Dune movement: techniques for data collection and analysis. *Journal of Oman Studies Special Report*, **3**, 181-184.

Knott, P. (1979) *Structure and Pattern of Dune-forming Winds*. Unpublished PhD. thesis, University of London.

Knott, P. & Warren, A. (1981) Aeolian processes. *In* Goudie, A. (ed) *Geomorphological Techniques*, Allen & Unwin, London.

Lai, R.J. & Wu, J. (1978) *Wind erosion and deposition and deposition along a coastal sand dune*. Sea Grant Program, University of Delaware, Report DEL-SG-10-78.

Lancaster, N. (1983) Controls of dune morphology in the Namib sand sea. *In* Brookfield, M.E. & Ahlbrandt, T.S. (eds) *Developments in Sedimentology*, Elsevier, New York.

Lancaster, N. (1985) Variations in wind velocity and sand transport on the windward flanks of desert sand dunes. *Sedimentology*, **32**, 581-593.

Lancaster, N. (1987) Reply: variations in wind velocity and sand transport on the windward flanks of desert dunes. *Sedimentology*, **34**, 511-520.

Lancaster, N. (1988) Controls of eolian dune size and spacing. *Geology*, **16**, 972-975.

Lancaster, N. (1989a) Star dunes. *Progress in Physical Geography*, **13(1)**, 67-91.

Lancaster, N. (1989b) The dynamics of star dunes: an example from the Gran Desierto, Mexico. *Sedimentology*, **36**, 273-289.

Lancaster, N., Greeley, R. & Rasmussen, K.R. (1991) Interaction between unvegetated desert surfaces and the atmospheric boundary layer: a preliminary assessment. *Acta Mechanica [Suppl.]*, **2**, 89-102.

Larsen, S.E., Hedegaard, K. & Troen, I. (1982) The change of terrain roughness problem extended to mesoscale fetches. *First International Conference on Meteorology and Air/Sea Interaction of the Coastal Zone, Hague, Netherlands. American Meteorological Society, Boston.*

Leatherman, S.P. (1978) A new aeolian sand trap design. *Sedimentology*, **25**, 303-306.

Lee, J.A. (1987) A field experiment on the role of small scale wind gustiness in aeolian sand transport. *Earth Surface Processes and Landforms*, **12**, 331-335.

Lettau, K. & Lettau, H.H. (1978) Experimental and micrometeorological field studies on dune migration. *In* Lettau, H.H. & Lettau, K. (eds) *Exploring the World's Driest Climate*, University of Wisconsin-Madison, Institute for Environmental Studies, Report 101, 110-147.

Livingstone, I. (1985) *The Dynamics of Sand Transport on a Namib Linear Dune.* Unpublished D.Phil thesis, University of Oxford.

Livingstone, I. (1986) Geomorphological significance of windflow patterns over a Namib linear dune. *In* Nickling, W.G. (ed) *Aeolian Geomorphology, Proceedings of the 17th Annual Binghampton Symposium, September 1986*, 97-112.

Livingstone, I. (1987) Photographic evidence of seasonal change in a secondary form on a 'complex' linear dune. *Madoqua*, **17(3)**, 237-241.

Livingstone, I. (1988) New models for the formation of linear sand dunes. *Geography*, **73**, 105-115

Livingstone, I. (1989) Monitoring surface change on a Namib linear dune. *Earth Surface Processes and Landforms*, **14**, 317-332.

Livingstone, I. (1990) Desert sand dune dynamics: review and prospect. *In* Seely, M.K. (ed) *Namib Ecology: 25 years of Namib research*, Transvaal Museum Monograph, **7**, 47-53.

MacCready, P.B. (1965) Dynamic response characteristics of meteorological sensors. *Bulletin of the American Meteorological Society*, **46(9)**, 533-538.

MacCready, P.B. & Jex, H.R. (1964) Response characteristics and meteorological utilization of propeller and wind vane sensors. *Journal of Applied Meteorology*, **3**, 182-193.

McEwan, I.K. (1992) Sand transport by wind: a review of the current conceptual model. *Geological Society Special Publication*, Blackwell, Oxford (in press).

McEwan, I.K. & Willetts, B.B. (1991) Numerical model of the saltation cloud. *Acta Mechanica [Suppl.]*, **1**, 53-66.

McIntosh, D.W. & Thom, A.S. (1981) *Essentials of Meteorology*. Taylor & Francis, London.

McKee, E.D. (1979) Introduction to the study of global sand seas. *In* McKee, E.D. (ed) *A Study of Global Sand Seas*. United States Geological Survey Professional Paper, **1052**, 3-19.

Marston, R.A. (1986) Maneuver-caused wind erosion impacts, south-central New Mexico. *In* Nickling, W.G. (ed) *Aeolian Geomorphology, Proceedings of the 17th Annual Binghampton Symposium, September 1986*, 273-306.

Mason, P.J. (1986) Flow over the summit of an isolated hill. *Boundary-Layer Meteorology*, **37**, 385-405.

Mason, P.J. & King, J.C. (1985) Measurements and predictions of flow and turbulence over an isolated hill of moderate slope. *Quarterly Journal Royal Meteorological Society*, **111**, 617-640.

Mason, P.J. & Sykes, R.I. (1979) Flow over an isolated hill of moderate slope. *Quarterly Journal Royal Meteorological Society*, **105**, 383-395.

Mickle, R.I., Cook, N.J., Hoff, A.M., Jensen, N.O., Salmon, J.R., Taylor, P.A., Tetzlaff, G. & Teunissen, H.W. (1988) Vertical profiles of wind and turbulence. *Boundary-Layer Meteorology*, **43**, 143-169.

Mulligan, K.R. (1988) Velocity profiles measured on the windward slope of a transverse dune. *Earth Surface Processes & Landforms*, **13**, 573-582.

Nalpanis, P. (1985) Saltating and suspended particles over flat and sloping surfaces ii. experiments and numerical simulations. *Proceedings of International Workshop on Physics of Blown Sand*, Memoirs **8**, Department of Theoretical Statistics, Aarhus University, Denmark.

Nielson, J. & Kocurek, G. (1987) Surfaces processes, deposits, and development of star dunes: Dumont dune field, California. *Geological Society of America Bulletin*, **99**, 177-186.

Norcliffe, A.S. (1982) *Multivariate Analysis*. Pergamon, London.

Nϕrstrud, H. (1982) Wind flow over low arbitrary hills. *Boundary-Layer Meteorology*, **23**, 115-124.

Owen, P.R. (1964) Saltation of uniform grains in air. *Journal of Fluid Mechanics*, **20**, 225-242.

Owen, P.R. & Gillette, D. (1985) Wind tunnel constraint on saltation. *Proceedings of International Workshop on Physics of Blown Sand*, Memoirs **8**, Department of Theoretical Statistics, Aarhus University, Denmark.

Pankhurst, R.C. (1952) *Wind Tunnel Techniques*. Pitman, London.

Panofsky, H.A. & Dutton, J.A. (1984) *Atmospheric Turbulence: Models and Methods for Engineering Applications*. Wiley, New York.

Pearse, J.R., Lindley, D. & Stevenson, D.C. (1981) Wind flow over ridges in simulated atmospheric boundary layers. *Boundary-Layer Meteorology*, **21**, 77-92.

Pye, K. & Tsoar, H. (1990) *Aeolian Sand and Sand Dunes*. Unwin Hyman, London.

Rasmussen, K.R. (1989) Some aspects of flow over coastal dunes. *In* Gimingham, C.H., Ritchie, W., Willetts, B.B. & Willis, A.J. (eds) *Coastal Sand Dunes, Proceedings of the Royal Society of Edinburgh*, **96(B)**, 129-148.

Rasmussen, K.R. & Mikkelsen, H.E. (1988) Aeolian transport in a boundary layer wind tunnel. *Geoskrifter*, **29**, Geologisk Institut Aarhus Universitet, Denmark.

Rasmussen, K.R. & Mikkelsen, H.E. (1991) Wind tunnel observations of aeolian transport rates. *Acta Mechanica [Suppl.]*, **1**, 135-144.

Rasmussen, K.R., Sϕrensen, M. & Willetts, B.B. (1985) Measurement of saltation and wind strength on beaches. *Proceedings of International Workshop on Physics of Blown Sand*, Memoirs **8**, Department of Theoretical Statistics, Aarhus University, Denmark.

Raupach, M.R. (1991) Saltation layers, vegetation canopies and roughness lengths. *Acta Mechanica [Suppl.]*, **1**, 83-96.

Rubin, D. & Hunter, R.E. (1982) Bedform climbing in theory and nature. *Sedimentology*, **29**, 129-138.

Sarre, R.D. (1987) Aeolian sand transport. *Progress in Physical Geography*, **11**, 157-181.

Sarre, R.D. (1988) Evaluation of aeolian sand transport equations using intertidal-zone measurements, Saunton Sands, England. *Sedimentology*, **35**, 671-679.

Schumm, S.A & Lichty, R.W. (1965) Time, space and causality in geomorphology. *American Journal of Science*, **263**, 110-119.

Sherman, D.J. (1990) Discussion: evaluation of aeolian sand transport equations using intertidal-zone measurements, Saunton Sands, England. *Sedimentology*, **37**, 385-392.

Sykes, R.I. (1980) An asymptotic theory of incompressible turbulent boundary-layer flow over a small hump. *Journal of Fluid Mechanics*, **101**, 647-670.

Taylor, P.A. & Teunissen, H.W. (1987) The Askervein hill project: overview and background data. *Boundary-Layer Meteorology*, **39**, 15-39.

Taylor, P.A., Mason, P.J. & Bradley, E.F. (1987) Boundary-layer flow over low hills. *Boundary-Layer Meterology*, **39**, 107-132.

Teunissen, H.W., Shokr, M.E., Bowen, A.J., Wood, C.J. & Green, D.W.R. (1987) The Askervein hill project: wind-tunnel simulations at three length scales. *Boundary-Layer Meteorology*, **40**, 1-29.

Tsoar, H. (1978) *The Dynamics of Longitudinal Dunes*. Final Technical Report, European research Office, U.S. Army, London, DA-ERO 76-G-072.

Tsoar, H. (1983) Dynamic processes acting on a longitudinal (seif) sand dune. *Sedimentology*, **30**, 567-578.

Tsoar, H. (1985) Profiles analysis of sand dunes and their steady state signification. *Geografiska Annaler*, **67A(1-2)**, 47-61.

Tsoar, H., Rasmussen, K.R., Sϕrensen, M. & Willetts, B.B. (1985) Laboratory study of flow over dunes. *Proceedings of International Workshop on Physics of Blown Sand*, Memoirs **8**, Department of Theoretical Statistics, Aarhus University, Denmark.

Tutu, N.K. & Chevray, R. Cross-wire anemometry in high intensity turbulence. *Journal of Fluid Mechanics*, **71**, 785-797.

Ungar, J.E. & Haff, P.K. (1987) Steady state saltation in air. *Sedimentology*, **34**, 289-299.,

Walmsley, J.L. & Howard, A.D. (1985) Application of a boundary-layer model to flow over an eolian dune. *Journal of Geophysical Research*, **90**, 10631-10640.

Walmsley, J.L. & Salmon, J.R. (1984) A boundary-layer model for wind flow over hills: comparisons of model results with Askervein '83 data. *Proceedings of the European Wind Energy Conference*. Hamburg, West Germany.

Walmsley, J.L., Salmon, J.R. & Taylor, P.A. (1982) On the application of a model of boundary-layer flow over low hills to real terrain. *Boundary-Layer Meteorology*, **23**, 17-46.

Ward, J.D. (1984) *Aspects of the Cenozoic Geology in the Kuiseb Valley, Central Namib Desert*. Unpublished PhD. thesis, University of Natal.

Warren, A. (1988a) A note on sand movement and vegetation in the Wahiba Sands. *Journal of Oman Studies Special Report*, **3**, 251-255.

Warren, A. (1988b) The dunes of the Wahiba Sands. *Journal of Oman Studies Special Report*, **3**, 131-160.

Warren, A. & Kay, S. (1986) Dune movement. *In* Dutton, R.W. (ed) *Oman Wahiba Sands Project Rapid Assessment Document*. Royal Geographical Society, London.

Warren, A. & Kay, S. (1987) Dune networks. *In* Frostick, L. & Reid, I. (eds) *Desert Sediments: Ancient and Modern*, Geological Society Special Publication, **35**, 205-212.

Wasson, R.J. & Hyde, R. (1983) Factors determining desert dune type. *Nature*, **304**, 337-339.

Watson, A. (1987) Discussion: variation in wind velocity and sand transport on the windward flanks of desert sand dunes. *Sedimentology*, **34**, 511-520.

Weng, W.S., Hunt, J.C.R., Carruthers, D.J., Warren, A., Wiggs, G.F.S., Livingstone, I. & Castro, I. (1991) Air flow and sand transport over sand dunes. *Acta Mechanica [Suppl.]*, **2**, 1-22.

Werner, B.T. (1990) A steady-state model of wind-blown sand transport. *Journal of Geology*, **98**, 1-17.

White, B.R. (1979) Soil transport by winds on Mars. *Journal of Geophysical Research*, **84(B9)**, 4643-4651.

Whitehouse, R.J.S. & Hardisty, J. (1988) Experimental assessment of two theories for the effect of bedslope on the threshold of bedload transport. *Marine Geology*, **79**, 135-139.

Wilkinson, R.H. (1983/1984) A method for evaluating statistical errors associated with logarithmic velocity profiles. *Geo-Marine Letters*, **3**, 49-52.

Willetts, B.B. & Rice, M.A. (1986a) Collisions in aeolian saltation. *Acta Mechanica*, **63**, 255-265.

Willetts, B.B. & Rice, M.A. (1986b) Collisions in aeolian transport: the saltation/creep link. *In* Nickling, W.G. (ed) *Aeolian Geomorphology, Proceedings of the 17th Annual Binghampton Symposium, September 1986*, 1-18.

Williams, G. (1964) Some aspects of the eolian saltation load. *Sedimentology*, **3**, 257-287.

Wilson, I.G. (1972) Aeolian bedforms - their development and origins. *Sedimentology*, **19**, 173-210.

Wippermann, F.K. & Gross, G. (1986) The wind-induced shaping and migration of an isolated dune: a numerical experiment. *Boundary-Layer Meteorology*, **36**, 319-334.

Wyngaard, J.C. (1990) Scalar fluxes in the planetary boundary layer. *Boundary-Layer Meteorology*, **50**, 49-75.

Zeman, O. & Jensen, N.O. (1987) Modification of turbulence characteristics in flow over hills. *Quarterly Journal Royal Meteorological Society*, **113**, 55-80.

Zeman, O. & Jensen, N.O. (1988) *Progress Report on Modelling Permanent Form Sand Dunes*, Risφ National Laboratory Report, Risφ-M-2738, Denmark.

Zingg, A.W. (1953) Wind tunnel studies of movement of sedimentary material. *Proceedings of 5th Hydraulic Conference Bulletin*, **34**, 111-134.